Advances in Intelligent Systems and Computing 283

Ewa Pietka
Jacek Kawa
Wojciech Wieclawek *Editors*

Information Technologies in Biomedicine, Volume 3

Springer

Advances in Intelligent Systems and Computing

Volume 283

Series editor

Janusz Kacprzyk, Polish Academy of Sciences, Warsaw, Poland
e-mail: kacprzyk@ibspan.waw.pl

For further volumes:
http://www.springer.com/series/11156

About this Series

The series "Advances in Intelligent Systems and Computing" contains publications on theory, applications, and design methods of Intelligent Systems and Intelligent Computing. Virtually all disciplines such as engineering, natural sciences, computer and information science, ICT, economics, business, e-commerce, environment, healthcare, life science are covered. The list of topics spans all the areas of modern intelligent systems and computing.

The publications within "Advances in Intelligent Systems and Computing" are primarily textbooks and proceedings of important conferences, symposia and congresses. They cover significant recent developments in the field, both of a foundational and applicable character. An important characteristic feature of the series is the short publication time and world-wide distribution. This permits a rapid and broad dissemination of research results.

Advisory Board

Ewa Pietka · Jacek Kawa
Wojciech Wieclawek
Editors

Information Technologies in Biomedicine, Volume 3

Springer

Editors
Ewa Pietka
Silesian University of Technology
Faculty of Biomedical Engineering
Gliwice
Poland

Wojciech Wieclawek
Silesian University of Technology
Faculty of Biomedical Engineering
Gliwice
Poland

Jacek Kawa
Silesian University of Technology
Faculty of Biomedical Engineering
Gliwice
Poland

ISSN 2194-5357 ISSN 2194-5365 (electronic)
ISBN 978-3-319-06592-2 ISBN 978-3-319-06593-9 (eBook)
DOI 10.1007/978-3-319-06593-9
Springer Cham Heidelberg New York Dordrecht London

Library of Congress Control Number: 2008926730

Preface

In clinical application we deal with problems that have to be solved in a fast and objective way. However, human observation is influenced by internal (coming form the observer) as well as external (often independent from the observer) impacts. The objectivity of classification is restricted by the receptivity of human senses which are influenced by the experiences or level of training, psychological conditions (tiredness, haste, etc.), as well as external conditions (lighting, destructive noise, etc.) A failure in perception questions the entire recognition process. The recognition process itself, influenced also by the above mentioned conditions, may cause a slowdown and/or lead to a false diagnosis.

New computerized approaches to various problems have become critically important in healthcare. Computer assisted diagnosis has been extended towards a support of the clinical treatment. Mathematical information analysis, computer applications together with medical equipment and instruments have become standard tools underpinning the current rapid progress with developing Computational Intelligence. We are witnessing a radical change as technologies have been integrated into systems that address the core of medicine, including patient care in ambulatory and in-patient setting, disease prevention, health promotion, rehabilitation and home care. A computerized support in the analysis of patient information and implementation of a computer aided diagnosis and treatment systems, increases the objectivity of the analysis and speeds up the response to pathological changes.

This book aims to present a variety of state-of-the-art information technology and its applications to the networked environment to allow robust computerized approaches to be introduced throughout the healthcare enterprise. Image and signal analysis are the traditional parts that deal with the problem of data processing, recognition and classification. Bioinformatics has become a dynamically developed field of computer assisted biological data analysis. Patients' safety and shortening of the rehabilitation time requires a more rapid development of minimally invasive surgery supported by image navigation techniques. Home care, remote rehabilitation assistance, safety of the elderly require new areas to be explored in telemedicine and telegeriatrics.

This book set is a continuation of a book series. This set contains two volumes. *Information Technologies in Biomedicine, Volume 3* discusses Image analysis techniques and their applications in healthcare, as well as some Bioinformatics issues. *Information Technologies in Biomedicine, Volume 4* consists of six parts including Computer Aided Surgery, Telemedicine, Telegeriatrics,

We would like to express our gratitude to the authors who contributed their original research papers as well as the reviewers for their valuable comments.

Ewa Pietka

Contents

Part I: Image Analysis and Applications

Part II: Bioinformatics

Part I

Image Analysis and Applications

Applications of Ray-Casting in Medical Imaging

Maciej Borzęcki[1], Adam Skurski[1], Marek Kamiński[1], Andrzej Napieralski[1], Jarosław Kasprzak[2], and Piotr Lipiec[2]

[1] Department of Microelectronics and Computer Science, Lodz University of Technology, Łódź, Poland
mborzecki@dmcs.pl
[2] Department of Cardiology, Medical University of Lodz, Łódź, Poland

Abstract. The authors present applications of ray casting as segmentation and analysis method for processing of medical imaging data. The first application features ray casting based image segmentation for extraction of a region enclosing heart structures from a series of CT scans. Proposed method yields significant gains in reduction of the data set size, that are of importance in applications such as Transesophageal USG simulations on mobile devices or web platforms.

Another application, utilizes ray casting determining location of characteristic points of *left ventricle* (LV). The points are used as reference during automatic fusion of ECHO Automated Function Imaging output with a 3D model of LV.

Keywords: ray casting, image segmentation, computed tomography.

1 Introduction

Ray casting is a method that has seen wide use in a plethora of applications in different fields. Object picking within a 3D scene or collision detection are examples of traditional uses of ray casting [1, 2]. The method has also been successfully applied in the field of image processing for segmentation and extraction purpose. Example applications as described in [3, 4], indicate a level of success when method is applied for segmentation of medical imaging.

The core idea behind use of ray casting in image segmentation or feature location is largely unchanged from the typical approach. Virtual rays are emitted in a number of directions from a single origin point. For each iteration, a boundary condition is evaluated, indicating whether for the current location of the tip of the ray, the propagation can continue. In case of image segmentation, the boundary condition is typically a function testing if given point is within the desired data set. The concept is briefly visualized in Fig. 1.

Once the points where the ray propagation has ceased are established further steps are taken in order to create a mask or an outline of the identified structure. Typically employed methods are neighbor contour tracing [5] or construction of polygon by connecting the end points.

E. Pietka, J. Kawa, and W. Wieclawek (eds.), *Information Technologies in Biomedicine, Volume 3*, Advances in Intelligent Systems and Computing 283,
DOI: 10.1007/978-3-319-06593-9_1,

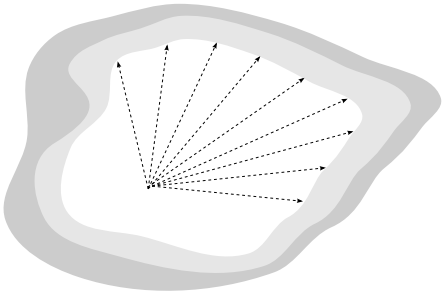

Fig. 1. Ray casting for image segmentation

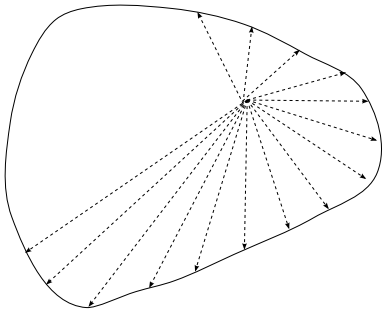

Fig. 2. Ray casting within a convex shape

Ray casting as a method is a subject to a number of problems that need to tackled with. The first problem is the shape of the object under consideration. As shown in Fig. 2, convex shapes usually yield good results.

For concave shapes, such as one shown in Fig. 3, location of ray origin point poses a problem. Misplaced origin will amplify the shadowing, the effect of which needs to be taken into consideration.

If the structure being extracted is relatively large, one needs to consider how many rays need to cast in order to obtain a reasonably good set of points for analysis. The problem is caused by the fact that only a certain number of rays is practical for most applications. In case of image segmentation, too few points may negatively affect the process of establishing object contour.

In the following sections the authors discuss ray casting as a method for processing medical imaging data, where Section 2 describes application in image segmentation, and Section 3 covers automated location of features in a 3D model.

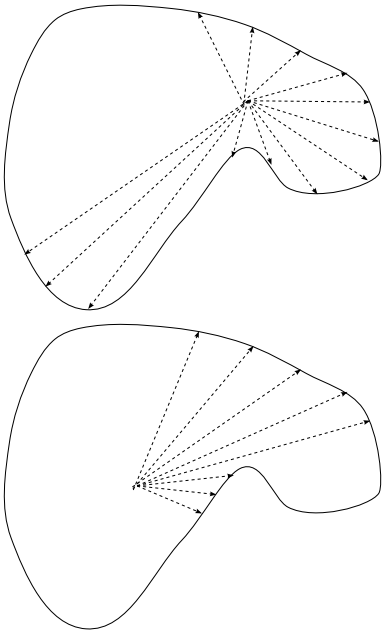

Fig. 3. Ray casting origin location for concave shapes

2 Heart Region Extraction for USG Simulations

The problem of ultrasound simulation has gained wide interest starting from fundamental work based on physical models [6], towards medical applications such as [7, 8]. With advent of cheap, multi-core processing the simulation algorithms have been successfully applied for GPGPU as in [9] and [10]. At the same time new simplified, but effective, processing algorithm such as [11] were proposed. Applications such as [12, 13] conform to the trend of utilizing simulations as a training tool in medicine that right now is considered a necessity [14, 15].

Simulation of Transesophageal Echocardiography commonly makes use of medical imaging collected during patient examination. A TEE simulator applies online algorithms transforming an input data set obtained in CT examination into a simulated USG image. This section discussed a ray casting based input data preprocessing method that provides a significant size reduction of the input data.

Given the physical properties of the USG imaging, the input needs to contain only the heart image and the position of the esophagus. Neighboring organs can be discarded without losing the educational value of the program. A raw data set of size 1-2GB is common for CT scans of a chest. Inclusion of temporal information, so that depiction of heat's cycle is possible, increases it's size significantly. Reduction of the input set size enables latency and processing limited applications to gain wider use.

The authors propose a ray-casting based method for segmentation of CT scan image and *Region of Interest* (ROI) extraction for the purpose of TEE simulation [16]. The method is based on generation of ROI mask for each of the relevant images in the input data set. The next step is superpositioning of all the masks, so that an aggregate mask enclosing all identified ROIs is obtained. The aggregation step allows for generating a 3D volume that is effectively encloses only the data that is relevant for the simulation process. The process is shown in Fig. 4.

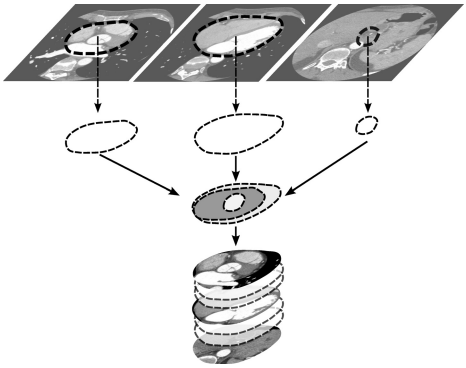

Fig. 4. Processing pipeline - segmentation of CT scan series, preparation of aggregate mask, ROI volume extraction

The concept for heart image segmentation is presented in Fig. 5. The threshold condition for ray propagation is set such that the ray should stop at the pericardium.

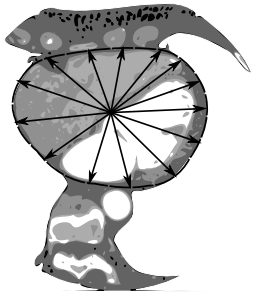

Fig. 5. Heart muscle outline using ray casting

A simple heuristic is used for selection of the origin point based on locating the center of mass of the image. Presence of contrast agent results in areas filled by blood exhibiting higher pixel values in CT images. Heart structures - ventricles,

atria, muscle tissue are thus well visible. Given that, the center of mass will be found inside the area enclosed by heart. The resulting position for 2 samples is shown in Fig. 6.

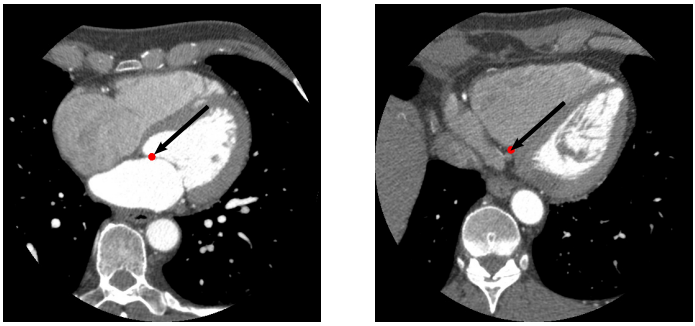

Fig. 6. Ray origin positioning

The threshold value for attenuation was empirically found to be $20HU$ and roughly corresponds to the values expected for area occupied muscle tissue. The value was confirmed by examining a number of data sets, however all images were obtained using the same CT device. The authors strongly suggest to perform additional verification and examine data collected using a particular CT scanner. The Hounsfield value is converted to pixel brightness based on metadata stored in DICOM [17, 18]. Lower values indicate lower measured attenuation, most likely the ray has entered pericardial cavity or lungs.

The result of ray casting is shown in Figure 7(b). One can clearly observe that at the sides, most of the rays stopped at pericardium, mainly due to the large difference in pixel intensity, and thus attenuation, between lungs and heart. However in anterior and posterior regions, the rays propagated farther than desired.

The boundary condition may not be met as the intensity level at the position where the ray propagation should cease is higher than expected. This may be caused by too large ray increase step, amplified by deficiency of the imaging method or existence tissue with similar properties in direct neighborhood. This problem of *mask leakage* can be limited by post processing ray casting points.

The heart can be considered to have a smooth surface, hence any abrupt changes in ray length are improbable and indicate mask leakage. The problem is displayed in Fig. 8. Significant change in ray length is visible both at the center and at the edges of the graph correspond to rays propagating towards ribs at the top and towards aorta at the bottom in Fig. 7(b). Application of a median filter with empirically selected window length alleviates the problem. The resulting ray lengths are shown in Fig. 8 using dashed line. The final shape of the mask obtained in segmentation process is displayed in Fig. 7(c).

Evaluation has been performed by verifying if the resulting masks completely enclose outlines of most significant heart regions (ventricles, atria, pericardium).

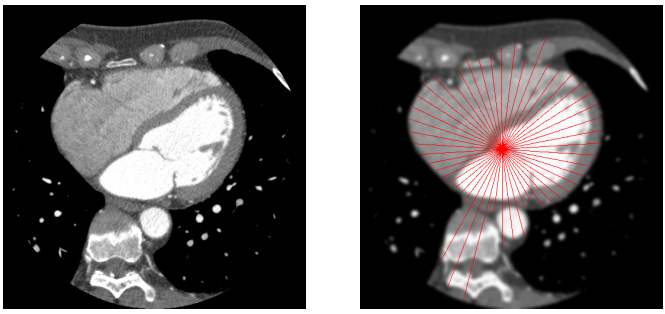

(a) Original image (b) Ray casting

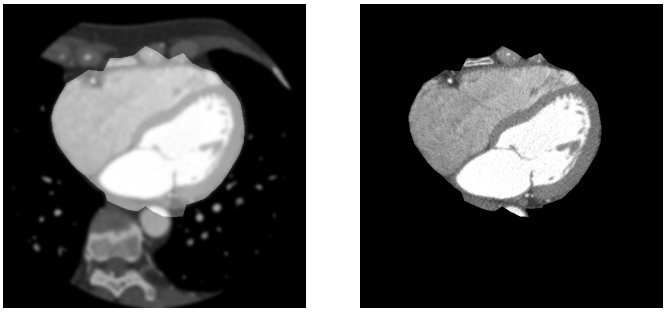

(c) Mask after ray filtering (d) Masked input image

Fig. 7. Segmentation using ray casting

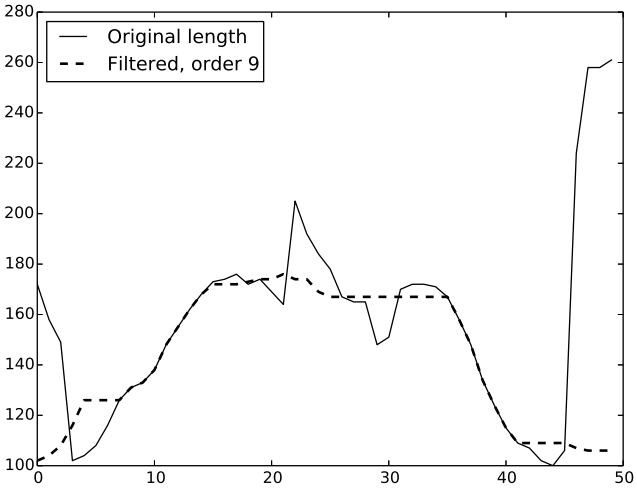

Fig. 8. Consecutive ray lengths from Fig. 7(b) (starting at bottom center, counter-clockwise), before and after filtering

For this purpose a test data with an outline of heart muscle was prepared. The obtained segmentation masks, were then verified to completely contain the reference regions. The graph showing comparison of the obtained mask to the reference area is shown in Fig. 9.

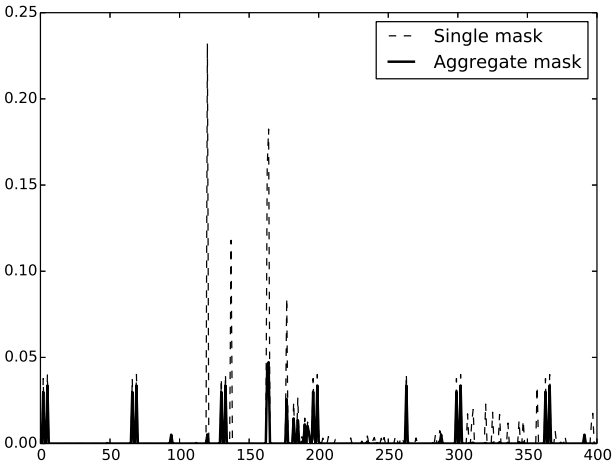

Fig. 9. Measured reference area not included in the mask, relative to mask size

There is a clear difference between the results for individual mask and an aggregate mask. Clearly, single masks have disadvantage in case the ray casting process failed to perform segmentation correctly. However, as assumed previously, the effect is compensated by use of aggregate mask. For all of reference samples, the missing area is below 5% of the mask size. Further analysis revealed that the missing area is at the edge of pericardium and does not impede the final outcome of the segmentation process. It may be expected that inclusion of a dilation step will yield an improvement and cover the missing regions.

After compression the original data set size has been reduced by factor of 18. Further steps that employed ray casting for image segmentation and extraction of the region of interest resulted in another size reduction by a factor of 2.5. Thus a single slice stored in 16-bit PNG format has been downsized to 50kB of data. At the same time the region that needs to be processed during the simulation pass has been marked and reduced significantly, as the relative area occupied by the heart is at most, less than 40% of a single horizontal slice.

3 Automated Identification of Left Ventricle Characteristic Points

Fusion of medical data is a widely regarded practice that aims at improving the diagnostic value individual imaging methods by providing a combined interpretation, thereby revealing indirectly visible aspects of the medical data.

Fusion of morphological data obtained in CT and functional information from SPECT (perfusion at rest and stress) allows for comprehensive evaluation of location and severity of ischemia, thereby increasing the diagnostic and prognostic value of noninvasive imaging techniques [19, 20].

Another application of ray casting plays a significant step in a fusion of ECHO AFI (Automated Function Imaging) [21] output with a 3D model of LV[22]. Combination of a bull's-eye representation of LV [23] stretched on a 3D mesh extracted from a series of CTA (CT Angiography) scans is vital from diagnostic point of view. The method may lower the need for performing classical, invasive angiography or can augment the analysis and interpretation of unclear CTA results. The result of the fusion process is presented in a single view, where the measured LV function is correlated spatially with a 3D model of LV [22].

Successful fusion requires knowledge of characteristic points on the left ventricle that allow for proper positioning of the bull's-eye diagram as a texture. Given the spatial reference of bull's-eye diagram, at least three distinct points need to be found on a 3D mesh. Apex and two additional points at the base of LV, near interventricular septum, were identified as sufficient, see Figure 10.

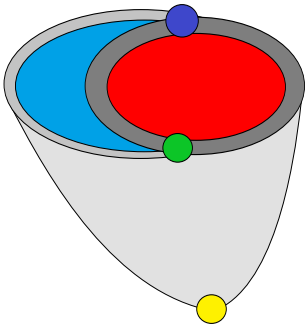

Fig. 10. Characteristic points of left ventricle: apex, two points at the base, near interventricular septum

A 3D mesh, automatically extracted by CT software does not directly contain the required information. The authors propose a ray-casting based method for location of two characteristic points at the base of LV, both points marked in Figure 10 with blue and green markers.

Each of the points if found by evaluating the conditions that refer to the locality of certain features in the 3D mesh.

The blue marker is found by iteratively casting rays, while rotating towards the back of the heart, and measuring distance between pericardium and LV wall. With each iteration, the distance is compared with previous value. Conducted analysis showed that at least 25% increase in distance is a sufficient estimate. Once, the condition has been met, the characteristic point is known to be located at the previous ray position.

The green marker is found using a similar approach. However, the distance is measured between the wall of LV and aortic sinus. The point of interest is located on the ray for which distance measurement was the smallest.

The concept is visualized in Figure 11.

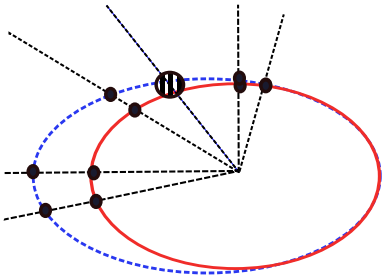

Fig. 11. Locating points of interest (marked with dashed circle) using ray casting

Presented implementations of modified ray-casting method for tracking LV anatomical points of interest provide the opportunity to define a constellation of markers essential for the images fusion performance, presented on Fig. 12.

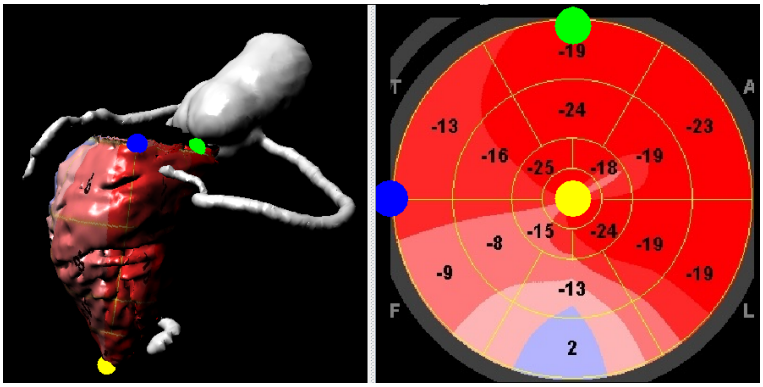

Fig. 12. Fusion of 3D model of LV with ECHO

4 Improvements

While ray casting as algorithm do not provide room for improvement, the respective implementations can be enhanced for greater performance. The algorithm may be easily extended to support a multi-threaded implementation. An inherent data level parallelism allows for work partitioning at the input image level. Lack of dependency between respective rays, allow an approach like in Fig. 13.

The profiling analysis revealed that a large portion of execution time is spent in the process of ray casting, with only little time allocated to ray length filtering, which is a sequential process. Thus, according to Amdahl's law [24, 25], splitting of ray casting task between a number of threads should yield a considerable speedup.

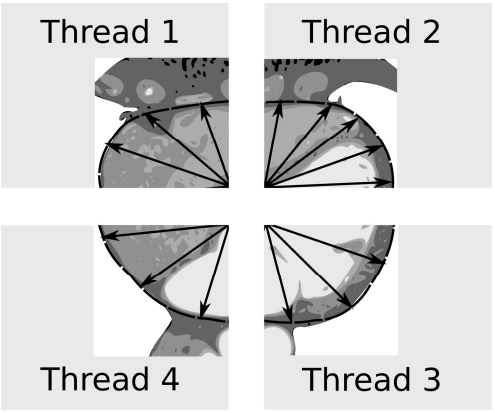

Fig. 13. Parallel ray casting implementation

Another improvement that is possible to apply is to exploit the aliasing effect of the ray propagation near the origin. The input image, as indicated in the introductory section, has a limited resolution. If a large number of rays is used, each ray will, at least for a certain length, starting from the origin, trace the same path as it's neighbors. The authors propose a use of a look-up table, addressed by coordinates of each pixel. The table would hold a binary flag indicating if a pixel was already claimed by a ray. Since all rays are checked against the same boundary condition, the flag allows for pixels that were already tested to be skipped.

5 Conclusions

The authors have presented two successful applications of ray casting for processing of medical imaging data. Although the core method is well known, it's application and enhancements proposed by authors bring a deal of novelty.

Application of ray casting in the segmentation process, although already providing good results, still needs some improvement. It has been observed that for certain samples, not all of the reference area is included within the segmentation mask. Especially at points where transition between pericardium to lungs appears, the segmentation process may partially fail, with ray not propagating far enough. It is expected that the problem can be easily addressed with a dilation step, however this would result in unnecessary increase of the whole mask.

Ray casting implementation for locating characteristic points of LV is a part of software package for supporting CAD (coronary artery disease) diagnosis. Purpose of presented algorithm is to prepare mapping for final texturing step in a fully automated manner. Should the algorithm fail or yield inadequate results, the operator has a possibility to move the markers freely, using the found positions as starting points. Tests in clinical environment using non-pathologic samples are in progress and show promising results. Still the authors have not yet verified the performance of the algorithm in case the input data set contains anomalies such as hypertrophy of the left ventricular wall.

References

1. Bowman, D.A., Hodges, L.F.: An evaluation of techniques for grabbing and manipulating remote objects in immersive virtual environments. In: Proceedings of The 1997 Symposium on Interactive 3D Graphics, I3D 1997, pp. 35–38. ACM, New York (1997)
2. Myszkowski, K., Okunev, O., Kunii, T.: Fast collision detection between complex solids using rasterizing graphics hardware. The Visual Computer 11(9), 497–511 (1995)
3. Moltz, J.H., Bornemann, L., Kuhnigk, J.M., Dicken, V., Peitgen, E., Meier, S., Bolte, H., Fabel, M., Bauknecht, H.C., Hittinger, M., et al.: Advanced segmentation techniques for lung nodules, liver metastases, and enlarged lymph nodes in CT scans. IEEE Journal of Selected Topics in Signal Processing 3(1), 122–134 (2009)
4. Bomans, M., Hohne, K.H., Tiede, U., Riemer, M.: 3-D segmentation of MR images of the head for 3-D display. IEEE Transactions on Medical Imaging 9(2), 177–183 (1990)
5. Dobkin, D.P., Wilks, A.R., Levy, S.V.F., Thurston, W.P.: Contour tracing by piecewise linear approximations. ACM Trans. Graph. 9(4), 389–423 (1990)
6. Jensen, J.A.: Simulation of advanced ultrasound systems using Field II. In: IEEE International Symposium on Biomedical Imaging: Nano to Macro, pp. 636–639. IEEE (2004)
7. Shams, R., Hartley, R.I., Navab, N.: Real-time simulation of medical ultrasound from CT images. In: Metaxas, D., Axel, L., Fichtinger, G., Székely, G. (eds.) MICCAI 2008, Part II. LNCS, vol. 5242, pp. 734–741. Springer, Heidelberg (2008)
8. Sun, B., McKenzie, F.: Real-time sonography simulation for medical training. International Journal of Education and Information Technologies 5(3), 328–335 (2011)
9. Kutter, O., Shams, R., Navab, N.: Visualization and GPU-accelerated simulation of medical ultrasound from CT images. Computer Methods and Programs in Biomedicine 94(3), 250–266 (2009)
10. Burger, B., Bettinghausen, S., Radle, M., Hesser, J.: Real-time GPU-based ultrasound simulation using deformable mesh models. IEEE Transactions on Medical Imaging 32(3), 609–618 (2013)
11. Piórkowski, A., Kempny, A.: The Transesophageal Echocardiography simulator based on Computed Tomography images. IEEE Trans. Biomed. Engineering 60(2), 292–299 (2013)
12. Goksel, O., Salcudean, S.E.: B-mode ultrasound image simulation in deformable 3-D medium. IEEE Transactions on Medical Imaging 28(11), 1657–1669 (2009)

13. Piórkowski, A., Werewka, J.: A concept of eTraining platform for cardiology learning based on SOA paradigm. In: Maciaszek, L.A., Cuzzocrea, A., Cordeiro, J. (eds.) ICEIS (3), vol. 3, pp. 261–264. SciTePress (2012)
14. Kunkler, K.: The role of medical simulation: an overview. The International Journal of Medical Robotics and Computer Assisted Surgery 2(3), 203–210 (2006)
15. Amitai, Z., Small, S.D., Wolpe, P.R.: Patient safety and simulation-based medical education. Medical Teacher 22(5), 489–495 (2000)
16. Borzęcki, M., Skurski, A., Balcerzak, B., Kamiński, M., Napieralski, A., Kasprzak, J., Lipiec, P.: Computed Tomography image processing for diagnostic and training applications in medicine. Journal of Medical Informatics and Technologies 19, 67–73 (2012)
17. Clunie, D.A.: DICOM structured reporting. PixelMed Publishing (2000)
18. Bidgood, W.D., Horii, S.C., Prior, F.W., Van Syckle, D.E.: Understanding and using DICOM, the data interchange standard for biomedical imaging. Journal of the American Medical Informatics Association 4(3), 199–212 (1997)
19. Gaemperli, O., Schepis, T., Valenta, I., Husmann, L., Scheffel, H., Duerst, V., Eberli, F.R., Luscher, T.F., Alkadhi, H., Kaufmann, P.A.: Cardiac image fusion from stand-alone SPECT and CT: clinical experience. Journal of Nuclear Medicine 48(5), 696–703 (2007)
20. Gaemperli, O., Bengel, F.M., Kaufmann, P.A.: Cardiac hybrid imaging. European Heart Journal 32(17), 2100–2108 (2011)
21. Belghiti, H., Brette, S., Lafitte, S., Reant, P., Picard, F., Serri, K., Lafitte, M., Courregelongue, M., Dos Santos, P., Douard, H., et al.: Automated function imaging: a new operator-independent strain method for assessing left ventricular function. Archives of Cardiovascular Diseases 101(3), 163–169 (2008)
22. Skurski, A., Borzęcki, M., Balcerzak, B., Kamiński, M., Napieralski, A., Kasprzak, J., Lipiec, P.: Image processing methods for diagnostic and simulation applications in cardiology. International Journal of Microelectronics and Computer Science 3(4), 146–151 (2012)
23. Murta Jr., L., Pazin-Filho, A., Schmidt, A., Almeida-Filho, O., Marin-Neto, J., Maciel, B.: Segmental quantitative analysis of myocardial contrast echocardiography images using a bullseye representation. In: Computers in Cardiology, pp. 177–180. IEEE (2003)
24. Amdahl, G.M.: Validity of the single processor approach to achieving large scale computing capabilities. In: Proceedings of the Spring Joint Computer Conference, April 18-20, pp. 483–485. ACM (1967)
25. Lee, V.W., Kim, C., Chhugani, J., Deisher, M., Kim, D., Nguyen, A.D., Satish, N., Smelyanskiy, M., Chennupaty, S., Hammarlund, P., et al.: Debunking the 100X GPU vs. CPU myth: an evaluation of throughput computing on CPU and GPU. In: ACM SIGARCH Computer Architecture News, vol. 38, pp. 451–460. ACM (2010)

A New Aortic Aneurysm CT Series Registration Algorithm

Joanna Czajkowska[1,2], Christian Feinen[2], Marcin Grzegorzek[2], Matthias Raspe[3], and Ralph Wickenhöfer[4]

[1] Silesian University of Technology, Faculty of Biomedical Engineering, Department of Informatics and Medical Equipment, Zabrze, Poland
[2] University of Siegen, Institute for Vision and Graphics, Research Group for Pattern Recognition, Siegen, Germany
[3] SOVAmed GmbH, Koblenz, Germany
[4] Herz-Jesu-Krankenhaus, Dernbach, Germany
joanna.czajkowska@polsl.pl

Abstract. Nowadays, vascular diseases are the most challenging health problems in developed countries. Despite the fast development of modern contrast-enhanced Computed Tomography (CT), providing complex 3D datasets, the tremendous amount of problems still remain unsolved. The vascular segmentation as well as registration techniques are the topics of past and on-going research activities. In this work we focus on an abdominal aortic aneurysm registration technique. The developed approach makes it possible to match all voxels belonging to the aorta from pre- and post-operative CT data. The presented technique is based on aorta lumen segmentation and graph matching method. To segment the lumen area a hybrid level-set active contour approach is used. The matching step is performed based on a path similarity skeleton graph matching procedure. The registration results have been tested on the database of 8 patients, for which two different contrast-enhanced CT series were acquired. All registration results achieved with our system and verified by an expert prove the efficiency of the approach and encourage to further develop this method.

Keywords: Hybrid Level-Set Active Contour, Graph Matching, Image Registration, Skeletonization.

1 Introduction

Nowadays, vascular diseases belong to the most challenging health problems in developed countries. An abdominal aortic aneurysm (AAA), addressed in our approach, is a dilated and weakened segment of the abdominal aorta. It is an abnormal ballooning of the abdominal portion of the aorta, that occurs as a consequence of aortic medial degeneration and can break open causing death. An AAA can develop in anyone, however it is mostly seen in males over 60, having one or more risk factors. During last 30 years, the occurrence of AAA has increased threefold. To prevent from rupturing, interventional radiologists offer

E. Pietka, J. Kawa, and W. Wieclawek (eds.), *Information Technologies in Biomedicine, Volume 3*, Advances in Intelligent Systems and Computing 283,
DOI: 10.1007/978-3-319-06593-9_2,

minimally invasive treatment for abdominal aortic aneurysm, which is specially important when it reaches 5 centimeters in diameter. Currently, there are different AAA treatment options. The open surgical repair by a vascular surgeon is the most commonly used for a large, unruptured aneurysm. The less invasive and relatively new technique, eliminating the need for a large abdominal incision, is placing a graft within the aneurysm. It redirects blood flow and stops direct pressure from being exerted on the weak aortic wall [2, 1]. An exemplary 3D volume rendering of CTA series of pre- and post-operative study created using Osirix software is shown in Fig. 1.

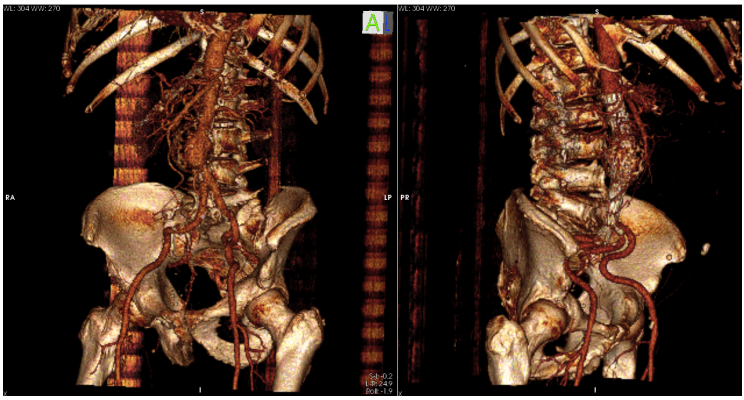

Fig. 1. 3D volume rendering of CTA series of pre- (left) and post-operative (right) study of aortic aneurysm provided by Osirix software

The AAA is mostly diagnosed by a physical examination as a soft mass in the abdomen. For more accurate and efficient diagnosis the development of imaging techniques provides numerous tools used to examine vessels and display their details. A contrast-enhanced CT angiography (CTA), which replaced a conventional angiogram, is an imaging technique commonly used in vascular diagnosis. Despite the fast development of modern contrast-enhanced Computed Tomography (CT), providing complex 3D datasets, the tremendous amount of problems still remain unsolved. The vascular segmentation [3] and registration techniques are the topics of past as well as on-going research activities.

From the medical background of AAA, two region of interests: aorta lumen and thrombus, can be defined. An exemplary manual segmentation results of both of them in a CT scan are shown in Fig. 2. The newest approaches in AAA segmentation [3, 5, 6] address either both of the problems or only a chosen one. An automated method for the segmentation of thrombus in abdominal aortic aneurysms from CTA data is presented in [5]. The Active Shape Model (ASM) fitting is performed in sequential slices. As the starting point for the analysis the results obtained for the adjacent slice are used. The full 3D segmentation technique in CTA is reported in [6]. The system analyses both global features,

incorporating a priori knowledge of the intensity, volume, and shape of the aorta and other structures, and the local information like voxel location, intensity, and texture information. All of them are used for training and driving a support vector machine classifier. As reported in [3] the current state of the art in AAA segmentation is modelling, feature analysis or their combination, and in all these areas different efficient techniques can be found. However, the authors also claim, that there are some problems, which still remain unsolved. There is no standardly accepted databases and validation criteria for most vascular segmentation applications and the direct performance comparisons of the segmentation results have not been performed yet.

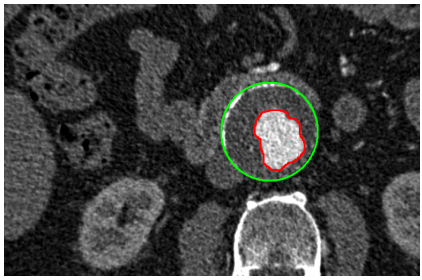

Fig. 2. An example of an contrast-enhanced CT scan of an abdominal aortic aneurysm with segmented thrombus (outer green contour) and lumen (inner red contour)

Despite the fact that the segmentation of vascular structures is valuable for diagnosis assistance, treatment and surgery planning the currently developed computer aided diagnosis (CAD) software target in efficient image registration. It does not only allow measurements of lumen or thrombus volume, but combining different image information is also useful for treatment planning and monitoring. Thanks to it, the comparative analysis of consecutive (pre- and post-operative) CTA studies as well as matching of different image modalities is possible.

Depending on the application, various registration techniques have been reported [7–11]. The registration methods, which address the problem of simultaneous analysis of different image modalities are given in [7–10], whereas the pre- and post-operative CTA sequence matching algorithm is presented in [11]. The authors of [9] propose a registration technique based on the overlaying the preoperative 3D model of the aorta onto the intraoperative 2D X-ray images. The presented technique utilizes two X-ray images showing the abdominal aorta from different angles in an integrated way. They developed a hierarchical registration scheme deployed by a sensible partition of the registration parameter space based on the image acquisition protocol and the patients motion constraint.

The 2D/3D registration technique is also addressed in [7]. The non-rigid method enables information from the CT to be overlaid onto the fluoroscopy images during the implantation procedure. The authors have investigated the

use of manually picked landmarks and the thin plate spline algorithm to deform the CT surface so it more accurately represents the interventional scene. The automatic movement compensation in 2D/3D registration of fluoroscopy and preoperative volumetric data is presented in [10]. The paper proposes a pelvis boundary detection method that enables real time monitoring of patient movement and an automatic 2D/3D re-registration algorithm that compensates for it.

The idea of a graph-based approach in this context is presented in [8]. The introduced 2D/3D registration method is there formulated on a 3D graph and applied for AAA interventions. As an input, the algorithm takes the 3D graph generated from a segmentation of the CT volume and the 2D distance map calculated from the 2D X-ray image. For computing the graph similarity, different measures are then used in a length preservation and a smoothness regularization term.

In this work we focus on 3D abdominal aortic aneurysm registration technique. The developed approach makes it possible to match the aorta segmented in pre- and post-operative CTA data. The presented technique is based on an aorta lumen segmentation and graph matching technique. In the segmentation step a hybrid level-set active contour approach is employed. The applied hybrid medical image segmentation method in the level-set framework [12] uses the object's boundary as well as region information. In this approach a boundary gives the information concerning object location, whereas the region features help to avoid the boundary leakage. The matching step is performed based on a path similarity skeleton graph matching procedure introduced in [21].

In the following section, a short introduction to the hybrid active contour approach [12] applied for AAA lumen segmentation is given. In Section 3, the 3D skeletonization algorithm for graph extraction is described. Section 4 introduces the graph matching technique and Section 5 presents the experiments and the obtained results. Then, the last section (Section 6) concludes the work and outlines plans for the future.

2 Abdominal Aortic Aneurysm Segmentation Method

The active contour model for image segmentation was originally developed by Kass at. all [13] and the energy minimization techniques in image segmentation have attracted researches in the last two decades. The basic idea of the snake method [13] is to iteratively evolve the initial contour towards the regions described by some certain features. The movement of the energy minimizing-spline is guided by the geometry of the evolving curve (internal force) and influenced by image features (external force). The image information pull the contour into the lines, edges or terminations. Local minima of the contour energy correspond to desired image properties. Since the classical implementation of the snake method [13] was introduced, different modifications and improvements dictated by its new applications were incorporated. Active contour model expanded by gradient vector flow is presented in [14]. This efficient algorithm remains limited

to the segmentation of structures with well defined contours. Geodesic active contour model [15] and Chan-Vese approach [16] are two most important techniques improving this segmentation technique standing out for boundary-based and region-based methods.

In all the cases mentioned above, the image segmentation methods are based on minimizing a predefined energy functionals. To solve the curve evolution partial differential equations (PDEs) different numerical methods are applied. In a classical approach the finite set of contour points approximates the parametric contour $\Psi(s) = (x(s), y(s)),\ s \in [0,1]$ and the contour changes in time $\Psi(s,t) = (x(s,t), y(s,t)),\ s \in [0,1], t = \mathbf{R}_+ \cup \{0\}$ - the contour evolves with the points movement. Geodesic [15], Chan-Vese [16] and the hybrid active contour [12] used in this paper belong to the models developed in a level-set framework. In the implementation [15] the solution of the particular energy snakes model is given by a geodesic curve in a Riemannian space, being induced form the image. The Chan-Vese active contour model [16] is based on the mean curvature motion. The curve C is implicitly represented via a Lipschitz function ϕ and by $mathitC = \{(x,y)|\phi(x,y) = 0\}$. The initial contour is defined by the set $\{(x,y)|\phi_0(x,y) = 0\}$ and the evolution of the curve is given by the zero-level curve at time t of the function $\phi(t,x,y)$. To solve the PDE the curve C evolves in normal directions with the speed F [16]

$$\frac{\partial \phi}{\partial t} = |\nabla \phi| F, \phi(0,x,y) = \phi_0(x,y). \tag{1}$$

2.1 Hybrid Level-Set Method

The same as in the active contour given in [16] in the hybrid technique [12], employed in our work, the active contour C is represented by the zero set of embedding function ϕ, such that $C = \{x|\phi(x) = 0\}$. The points inside and outside the contour have positive and negative ϕ values, respectively. The minimized functional in image I domain Ω is defined as

$$E(\phi) = -\alpha \int_\Omega (I - \mu) H(\phi) d\Omega + \beta \int_\Omega g |\nabla H(\phi)| d\Omega, \tag{2}$$

where $g = g(|\nabla I|)$ is a boundary feature map related to the image gradient. The parameters α and β balance the two terms of (2), and μ indicates the lower bound of the gray-level of the target object. Thanks to it, the curve evolves to enclose the regions greater than μ. The PDE of the functional (2) is derived from the Gateaux derivative gradient flow [12]

$$\phi_t = |\nabla \phi| \left[\alpha (I - \mu) + \beta div \left(g \frac{\nabla \phi}{|\nabla \phi|} \right) \right], \tag{3}$$

and the explicit curve evolution PDE is represented by [12]

$$C_t = \alpha (I - \mu) \overrightarrow{N} - \beta \langle \nabla g \cdot \overrightarrow{N} \rangle \overrightarrow{N} + \beta g \kappa \overrightarrow{N}. \tag{4}$$

The direction of the curve normal $\overrightarrow{N}$ is defined to point outward the curve and $\overrightarrow{N} = -\frac{\nabla\phi}{|\nabla\phi|}$. The curvature κ is given by $\kappa = div\left(\frac{\nabla\phi}{|\nabla\phi|}\right)$. The used iterative curve evolution algorithm, based on additive operator splitting (AOS) approach is in detail described in [12]. Some preprocessing steps and parameter set up are described in Sections 2.2 and 5, respectively.

2.2 Preprocessing and Initial Surface Selection

The analysed CTA series are affected by artefacts and noise, which can influence the final segmentation results. Therefore, as a preprocessing step a 3D adaptive filtering procedure was employed. The selected filtering technique based on anisotropic diffusion [18] increases the Signal-to-Noise Ratio (SNR) and preserves the edges.

In the hybrid level-set implementation applied to volumetric CT data, the authors of [12] used a sphere as an initial surface. The results presented by them show that it successfully converges to the target object. However, the performed experiments proved, that the time to converge the hybrid level-set algorithm [12] strongly depends on this surface. In our work, the size of the analysed AAA CTA data ($512 \times 512 \times n$, where $n \in [220, 680]$) determined the clustering-based initial surface selection procedure. For this, we used a weighted fuzzy c-means clustering procedure introduced in [17]. The initial surface was then created by all the voxels belonging to the cluster with the highest mean gray intensity value.

Thanks to this two preprocessing techniques the hybrid level-set algorithm enables fast and robust AAA segmentation. An exemplary final 3D segmentation results of abdominal aorta lumen in CT series are shown in Fig. 3.

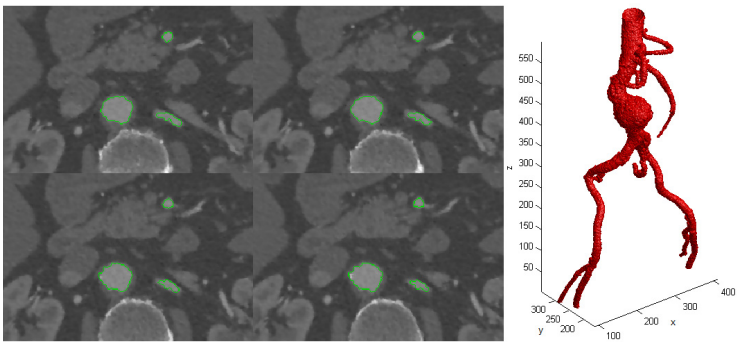

Fig. 3. An example of 3D abdominal aorta lumen segmentation results in an image view (left) and volume rendering (right)

3 Skeletonization

The CTA volume matching procedure being an overall goal of our work is based on graph matching step described in the next section. For this a 3D skeletonization step is incorporated. The 3D skeleton is obtained using the method described in [19]. This automatic algorithm computes subvoxel precise skeleton of volumetric data based on subvoxel precise distance field. The advantage of the subvoxel approach over a voxel precise skeleton is, that it computes an accurate, more precise and centered skeleton also for objects that are less than a single voxel thick. The authors of [19] have proven, that it is a proper solution for the accurate measurements of the object, such as vessel cross section or volume.

The input for the skeletonization method described in [19] is a subvoxel precise distance field. To obtain this field the authors suggest a two steps preprocessing technique. First, a level set time-crossing map calculation followed by a distance field computation is performed. Then, a sampled level set time-crossing map with the embedded zero-crossing isosurface is estimated. In our approach, the isosurface required for this, which yields the object's true boundary is created based on the previously obtained segmentation results. Having a implicit representation of the boundary, we estimate the subvoxel precise Euclidean distance transform for n-dimensional data [20].

The Euclidean distance field is then used to find the point with the largest distance from the boundary and to determine a speed image used as an input for the fast matching propagation step. The speed image being a function of the distance field (d - distance value and D - maximum distance value)

$$v = \left(\frac{d}{D}\right)^2 \tag{5}$$

is used to determine the curve evolution velocity for each pixel. The point at the global maximum distance from the objects boundary is calculated in a single pass through the distance field. The first one encountered in scanline order is used in the situation, if no unique maximum point exists. It is a start point for a fast marching propagation algorithm, in which the obtained speed image is used. The fast marching propagation is augmented to calculate the geodesic distance (Manhattan distance) inside the object starting at the global maximum point of the distance field. Based on the obtained results the branch points are then estimated. The furthest point of the model from the global maximum distance point is used as the start point of the branch. The remaining points of the branch are determined by performing a gradient descent, back-tracking procedure on the fast marching time-crossing map. This process is repeated for each branch of the created skeleton [20]. The exemplary results of application of this method to AAA data are shown in Fig. 4.

4 Graph Matching

The previously obtained aorta skeletons are now matched to properly register the two analysed 3D CTA series for each examination. The registration procedure

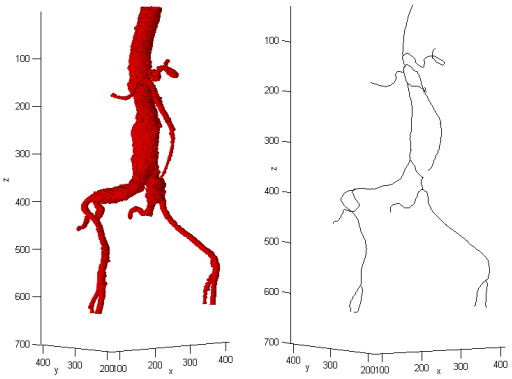

Fig. 4. An exemplary result of applying 3D skeletonization procedure (right) to an abdominal aorta surface (left)

we used is based on the algorithm presented in [21]. In contrast to existing approaches to skeleton similarity, the main idea of this approach is to match the skeleton graphs by comparing the geodesic paths between their endpoints. Therefore, the authors do not explicitly consider the topological structure of the skeleton trees or graphs.

According to the definition given in [21] the so called skeleton path is "a shortest path between a pair of end nodes on a skeleton graph". Based on the previously obtained segmentation and skeletonization results, and using a distance transform $DT(t)$ we are able to approximate the radius $R_{m,n}(t)$ of the maximum disk at each skeleton point with index t in a skeleton path $p(v_m, v_n)$ connecting the end nodes v_m and v_n. Therefore, the path is sampled by K equidistantly distributed points. Due to the fact, that the CTA series also differ in the voxel size, the normalization term proposed in [21] making the method invariant to the scale is also required.

To define the similarity/dissimilarity between two skeleton paths R and R' the authors of [21] suggest a path distance measure as

$$p_d(p(u,v), p(u',v')) = \sum_{i=1}^{M} \frac{(r_i - r'_i)^2}{r_i + r'_i} + \alpha \frac{(l - l')^2}{l + l'}, \tag{6}$$

where l and l' are the lengths of paths $p(u,v)$ and $p(u',v')$ and α is a weighting factor.

Let the two CTA series be described by two ordered graphs G and G' with $K+1$ and $N+1$ nodes ($K \leq N$) respectively. The matching cost $c(v_i, v'_j)$ between end nodes v_i and v'_j is estimated based on the paths to all other vertices in G and G' that emanate from v_i and v'_j. The dissimilarity value between the end nodes is estimated using the optimal subsequence bijection (OSB) method introduced in [24]. The advantage of the OSB algorithm is, that it finds a subsequence a' in sequence a that best matches b' in b skipping possible outlier elements. To prevent

from skipping too many elements of sequence a the authors of [21] suggest a penalty term b_∞, being an additional element of b. The distance function d computes the dissimilarity between a and b, that is, $d(a_i, b_j)$ is given for all $(i, j) \in \{1, \ldots, m\} \times \{1, \ldots, n, \infty\}$, where m and n stand for the length of a and b, respectively. As distance function d the path distance p_d, defined in (6), is used. The distance to the additional element $d(a_i, b_\infty)$ is a constant for all $i \in \{1, \ldots, m\}$ determining the cost of skipping any given element on the sequence a. The so called "jumpcost" j_c is computed as

$$j_c = \mu + \sqrt{\frac{1}{m} \min_{j=1,\ldots,n} (d(a_i, b_j) - \mu)^2}, \quad \mu = \sum_{i=1}^{m} \frac{1}{m} \min_{j=1,\ldots,n} (d(a_i, b_j)). \tag{7}$$

Then, for any given correspondence, the distance between two sequences is defined in [21]

$$d(a, b, f) = \frac{1}{m} \sum_{i=1}^{m} (d(a_i), b_{f(i)})^2. \tag{8}$$

Therefore, an optimal correspondence $\widehat{f}$ of elements in the sequence a to elements in the sequence b over all possible correspondences f is defined as

$$\widehat{f} = arg \min\{d(a, b, f)\}. \tag{9}$$

The optimal correspondence is found with the shortest path algorithm on a directed acyclic graph (DAG), in detail described in [21].

The already described OSB is applied to the matrix of the path distances between the two sequences $v_{i0}, v_{i1}, \ldots, v_{iK}$ in G ($v_i = v_{i0}$) and $v_{j0}, v_{j1}, \ldots, v_{jN}$ in G' ($v_j = v_{j0}$). For the two analysed graphs G and G' all the dissimilarity costs between their end nodes are estimated and stored in a matrix $C(G, G')$. The total dissimilarity $c(G, G')$ between G and G' computed in [21] with the Hungarian algorithm on $C(G, G')$ is here replaced by the algorithm proposed in [23]. The authors presented there Maximum Weight Subgraphs (MWS) which can be expressed as an integer quadratic problem:

$$\max\ g(\mathbf{x}) = \mathbf{x}^T A \mathbf{x} \qquad \text{subject to} \qquad \mathbf{x}^T M \mathbf{x} = 0, \quad \mathbf{x} \in [0, 1]^n, \tag{10}$$

where A is a symmetric $n \times n$ affinity matrix with $\forall i, j = 1 \ldots, n : A_{i,j} \geq 0$ and $M \in \{0, 1\}^{n \times n}$ represents a symmetric mutex matrix. The size of A corresponds to the number of feature points that have been detected and the diagonal of A is created using the output values obtained by the OSB. Since A expects similarity data, the OSB cost values have to be converted. For this, a Gaussian function with $\mu = 0.2$ and $\sigma = 10$ is used. To populate the non-diagonal elements of A, a pairwise distance consistency value is generated between two assignments.

$$A(u, v) = \exp(\frac{(d(i, j) - d(i', j'))^2}{2\sigma^2}), \tag{11}$$

where $u = (i, i')$ and $v = (j, j')$ are the two assignments, the Euclidean distance $d(i, j)$ is calculated.

The exemplary results of matching two CTA series, or more accurately their skeletons is shown in Fig. 5.

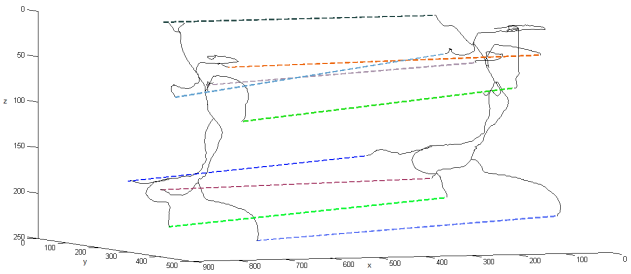

Fig. 5. The exemplary results of matching two AAA skeletons

5 Results

The presented segmentation/registration framework was tested on the database provided by the SOVAmed GmbH[1]. It consists of 8 pairs of of CTA series to be segmented and matched. The examinations contain pre- as well as post-operative data with the resolution of (512×512) and the number of slices in the volume varying form 220 to 680. In the preprocessing step, anisotropic diffusion filtering with a conduction coefficient function $q(x, y, z, t) = \frac{1}{1+\left(\frac{\nabla I}{\nu}^2\right)}$ proposed by Perona and Malik in [18] is used. The ν is the gradient modulus threshold that controls the conduction experimentally set to 70. Based on the normalized CTA data the number of clusters used in initial surface construction was set to 5. In the employed hybrid level-set segmentation technique [12], a boundary feature map related to the image gradient is a decreasing function g such as $g = \frac{1}{1-c|\nabla I|^2}$, with the constant c controlling the slope set to 5. The parameters required for (2) are set to $\alpha = 0.5$ and $\beta = 0.2$, respectively. The proposed set-up makes it possible to efficiently segment the aorta in all 16 analysed series. The obtained segmentation results were then used in a matching/registration step.

For all the analysed pairs of volumetric data the skeletonization procedure and matching algorithm were used. The proper skeletons were obtained for all the 8 pairs. All of them were then matched and the matching results were verified by an expert. As matching results, a labelled skeleton points on both the series were marked, so that the expert was able to verify them. In 4 for 8 analysed examinations the registration was correct. 4 of them required some manual improvements. However, the analysis was performed on a real dataset, not prepared for the analysis in any special way. The the difficulties in matching step were caused by a different resolution of the series as well as their different length. In all the cases, the series did not show exactly the same part of a patient body. However, the need of the manual intervention will be reduced in a future work. For this, we plan to incorporate a DICOM positioning information and modify the matching algorithm so that it will be invariant to the resolution and the length.

[1] `www.sovamed.com/en`

6 Conclusions and Future Work

The paper presents a preliminary study in a 3D registration of abdominal aortic aneurysm in CTA. The developed method consists of 3D segmentation part and graph based registration procedure. The promising results obtained for 8 examinations consisting of 2 CTA series each encourage to further develop this technique. In our work we plan to improve the segmentation as well as registration results incorporating a DICOM positioning information. One of the ideas is to use an algorithm for automatic understanding medical images presented in [22]. For future work an extended database is also considered.

Acknowledgement. This work was funded by the German Research Foundation (DFG) as part of the research training group GRK 1564 "Imaging New Modalities".

The experimental data was provided by SOVAmed GmbH.

References

1. Abdominal Aortic Aneurysm, Society of Interventional Radiology, Enhanced Care Trough Advanced Technology
2. Zarins, C.K., White, R.A., Schwarten, D., Kinney, E., Diethrich, E.B., Hodgson, K.J., et al.: AneuRx Stent Graft Versus Open Surgical Repair of Abdominal Aortic Aneurysms: Multicenter Prospective Clinical Trial. J. Vascular Surg. 29, 292–308 (1999)
3. Lesage, D., Angelini, E.D., Bloch, I., Funka-Lea, G.: A review of 3D vessel lumen segmentation techniques: Models, features and extraction schemes. Medical Image Analysis 13(6), 819–845 (2009)
4. Xiang, B., Latecki, L.J.: Path Similarity Skeleton Graph Matching. IEEE Transactions on Pattern Analysis and Machine Intelligence 30(7), 1282–1292 (2008)
5. de Bruijne, M., van Ginneken, B., Niessen, W.J., Maintz, J.B.A., Viergever, M.A.: Active-shape-model-based segmentation of abdominal aortic aneurysms in CTA images. In: Proc. SPIE 4684, Medical Imaging: Image Processing, p. 463 (May 2002)
6. Zhuge, F., Rubin Geoffrey, D., Shaohua, S., Sandy, N.: An abdominal aortic aneurysm segmentation method: Level set with region and statistical information. Medical Physics 33, 1440–1453 (2006)
7. Raheem, A., Carrell, T., Modarai, B., Penney, G.: Non-rigid 2D-3D image registration for use in endovascular repair of abdominal aortic aneurysms. In: Medical Image Understanding and Analysis, pp. 153–157 (2010)
8. Liao, R., Tan, Y., Sundar, H., Pfister, M., Kamen, A.: An Efficient Graph-Based Deformable 2D/3D Registration Algorithm with Applications for Abdominal Aortic Aneurysm Interventions. In: Liao, H., "Eddie" Edwards, P.J., Pan, X., Fan, Y., Yang, G.-Z. (eds.) MIAR 2010. LNCS, vol. 6326, pp. 561–570. Springer, Heidelberg (2010)
9. Shun, M., Liao, R., Pfister, M.: Toward smart utilization of two X-ray images for 2-D/3-D registration applied to abdominal aortic aneurysm interventions. In: 2011 4th International Conference on Biomedical Engineering and Informatics (BMEI), October 15-17, vol. 1, pp. 550–555 (2011)

10. Liang, D., Bo, D., Shun, M., Pfister, M., Rui, L.: Visual check and automatic compensation for patient movement during image-guided Abdominal Aortic Aneurysm (AAA) stenting. In: 2012 5th International Conference on Biomedical Engineering and Informatics (BMEI), October 16-18, pp. 391–394 (2012)
11. Sun, Z., Helical, C.T.: angiography of fenestrated stent grafting of abdominal aortic aneurysms. Biomed. Imaging Interv. J. 5(2) (April-June 2009)
12. Zhang, Y., Matuszewski, B.J., Shark, L.-K., Moore, C.J.: Medical Image Segmentation Using New Hybrid Level-Set Method. In: IEEE International Conference on Biomedical Visualisation, MEDi08VIS, London, pp. 71–76 (July 2008)
13. Kass, M., Witkin, A., Terzopoulos, D.: Snakes: Active contour models. International Journal of Computer Vision 1(4), 321–331 (1998)
14. Xu, C., Prince, J.L.: Snakes, shapes, and gradient vector flow. IEEE Transaction on Image Processing 7(3), 359–369 (1998)
15. Caselles, V., Kimmel, R., Sapiro, G.: On geodesic active contours. International Journal of Computer Vision 22(1), 61–79 (1997)
16. Chan, T.F., Vese, L.A.: Active contours without edges. IEEE Transactions on Image Processing 10(2), 266–277 (2001)
17. Kawa, J., Pietka, E.: Kernelized Fuzzy C-Means Method in Fast Segmentation of Demyelination Plaques in Multiple Sclerosis. In: Proceedings of the 29th Annual International Conference of the IEEE EMBS (August 2007)
18. Perona, P., Shiota, T., Malik, J.: Anisotropic Diffusion. Geometry-Driven Diffusion in Computer Vision 3, 73–92 (1994)
19. Van Uitert, R., Bitter, I.: Subvoxel precise skeletons of volumetric data based on fast marching methods. Medical Physics 34(3), 627–638 (2007)
20. Uirert, R.V., Bitter, I.: Subvoxel accurate Euclidean distance transforms for n-dimensional data (unpublished)
21. Bai, X., Latecki, L.J.: Path similarity skeleton graph matching. IEEE Transactions on Pattern Analysis and Machine Intelligence 30(4), 1282–1292 (2008)
22. Tadeusiewicz, R.: What Does It Means "Automatic Understanding of the Images?". In: IEEE International Workshop on Imaging Systems and Techniques, IST 2007, pp. 1–3 (May 2007)
23. Ma, T., Latecki, L.J.: Maximum weight cliques with mutex constraints for video object segmentation. In: IEEE CVPR, pp. 670–677. IEEE (2012)
24. Latecki, L.J., Wang, Q., Koknar-Tezel, S., Megalooikonomou, V.: Optimal Subsequence Bijection. In: ICDM, pp. 565–570 (2007)

Angular Resolution Study of Vectors Representing Subtle Spiculated Structures in Mammograms

Magdalena Jasionowska[1] and Artur Przelaskowski[2]

[1] Warsaw University of Technology, The Faculty of Electronics and Information Technology, 00-665 Warsaw, Nowowiejska 15/19, Poland
mjasiono@ire.pw.edu.pl
[2] Warsaw University of Technology, The Faculty of Mathematics and Information Science, 00-662 Warsaw, Koszykowa 75, Poland
arturp@mini.pw.edu.pl

Abstract. In this paper various multiscale transformations, such as contourlets, curvelets, tensor and complex wavelets, were examined in terms of the precise representation of texture directionality in medical images. In particular, subtle radiating and spiculated structures in mammograms were modeled with sparse vectors of the image linear expansions. Important properties of angular resolution, angular selectivity and shift invariance have been evaluated with simple phantoms. According to the experimental results, the complex wavelets have been proved to be the most effective tool in mammogram preprocessing to extract and uniquely represent relevant spicular symptoms for accurate diagnosis.

Keywords: angular resolution and selectivity, shift (rotate) invariant, multiscale transform, spiculed structures enhancement.

1 Introduction

Effective and of good quality imaging is important for further medical decision making. Radiologist interprets medical images, describing the physical components of potential visualized findings, such as shape, growth, and density tissue. Precise characteristic of observed structures or some objects in the background of imaged tissue tends to be significant issue to make an early and correct diagnosis by both radiologists and computer-aided systems. In the case of some pathological findings, for example architectural distortion in mammography, directionality of their structures (commonly called spicules) is one of the main important features to determine these pathology, observed on mammograms.

1.1 Mammographic Spicules

Architectural distortion is a breast lesion in which the normal structure of the breast parenchyma is distorted as if being pulled into a central point, without a

E. Pietka, J. Kawa, and W. Wieclawek (eds.), *Information Technologies in Biomedicine, Volume 3*, Advances in Intelligent Systems and Computing 283,
DOI: 10.1007/978-3-319-06593-9_3,

visible central density [3]. Briefly and clearly saying, it is a group of spicules radiating from a certain area – not the visible mass. In contrast to other pathological lesions in mammography, i.e. microcalcifications, oval or spiculated masses, architectural distortions are not well-defined [5]. Moreover, interpretation process of mammograms is significantly affected by image quality, conditioning of content assessment, individual radiologist knowledge and experience etc. affecting cognitive errors. Therefore, architectural distortions as a subtle ambiguous directional findings are commonly misdiagnosed even by the most experienced radiologists [21]. The only typical feature of this type of pathology in mammography is radiating spicules, but orientation distribution of these subtle mammographic structures is often not clearly defined.

From the viewpoint of image processing, a model of architectural distortion can be assumed piecewise lines propagated in different directions. Such an approach is used in many research studies on automatic recognition of this type of abnormalities on mammograms. In order to extract spicules, the analysis of local oriented edges [14, 15], statistical analysis of a map of pixel orientations [13], skeleton analysis [16] or top-hat partial reconstruction [10–12] were conducted. Moreover, the Dixon and Taylor line enhancement algorithm with a line strength map (as their result) indicated the potential presence of oriented lines [23], estimation of a mean curvature sign and the concentration index [17, 18], Gabor filtering and phase portrait [4, 20] or a curvilinear structure (CLS) ridge detection [6] were used.

Additionally, conducting image structure analysis our attention should be paid to image noise. Therefore, it is worth noting that noise of digital mammogram can be model as spatially correlated Poisson noise [1, 2, 22] and the noise power is closely related to breast tissue (glandular to adipose tissue) [19].

1.2 Spicule Representation in Adjusted Transform Domain

Because of redundancy and limited quality of source image domain, the appropriate spicule representation requires an optimally adjusted image transform domain that allows precise extraction of piecewise structures of different orientations in analyzed image. Therefore, an angular resolution and selectivity, shift (rotation) invariance seem to be decisive to identify the effective image transformation. Moreover, low transform-domain redundancy and low computational complexity play also a significant role in design of useful numerical descriptors of subtle mammographic structures with differentiated directionality. The abovementioned three major properties can be interpreted for our research as follows:

- angular resolution – the number of possible to distinguish directions in image,
- angular selectivity – the ability to distinguish between closely located objects in image (so-called angular separation),
- shift (rotation) invariant – the same image (spectrum) in transform domain independent of small shift (rotation) of objects in input image.

There are many various methods for global image analysis of texture directionality. It is possible to capture dominant orientations in a whole image using these global transformations, but it sometimes affects a noticeable number of false positives in image processing (in case of architectural distortions). Such approach associated with global directional characteristics, for instance based on 2D polar FFT, could be applied at one initial stage of recognition process to select the regions of interests (ROIs) with increased sensitivity of detection procedures [7]. However, it is realized at the expense of permissible false positives reduced at next stages based on more precise analysis of local structure directionality.

Local multiscale analysis of image texture could be adjusted to specific features of selected ROIs providing better results of spicule detection [8]. However, certain conditions should be fulfilled. First, local analysis should be matched to the scale range of real informative structures in order to enhance only image structures of interests and consequently to avoid false positives in detection process. Second, too high computational complexity, which is often accompanied by local image texture analysis (e.g. using Gabor filters [7]) as well as too high domain redundancy of complex data correlation limit achieved performance.

The main goal of research presented in this paper is to investigate the suitability of some local multiscale transformations for extraction of relevant directional structures in mammograms. For this purpose, the selected bases/frames of tensor wavelets, complex wavelets, contourlets and curvelets have been experimentally studied and verified according to criteria of representation clarity of proposed modeled multidirectional spicules.

Our attention has been paid to directional precision in determining of piecewise linear structure orientations due to improve of distributed spicule description and consequently increase of its recognition efficiency. The structures were modeled in domains of four selected multiscale image transformations which have been found to be useful for multiscale analysis of many advantageous applications. In particular, an influence of the size of clearly represented line structures, possible to distinguish the distance of close-lying structures, and the target sensitivity due to the rotation of line structures have been tested. To facilitate correct interpretation information compaction in as sparse as possible object representation in multiscale domain has been investigated.

2 Experimental Test of Angular Resolution

The angular resolution of new image domain should be matched to real needs, i.e. the size of analyzed spicules, and the relation between these spicules (signal) and surrounding background (noise). The size of example spicules in mammograms was experimentally established in previous studies [9]. Thus, two phantoms containing two closely-lying line structures (Fig. 1 - left) were tested. The sample line width of 9 pixels and the line length of 89 or 189 pixels were adopted. To provide adequate (relative to mammographic image) relationship between line structures and background, Gaussian white noise of mean = 0.1 and variance = 3 was added (Fig. 1 – in the middle).

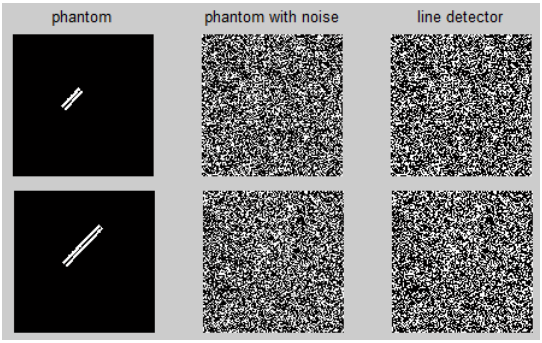

Fig. 1. Two simple phantoms containing: a) two short lines of width 9 pixels and length 89 pixels, b) two longer line structures of width 9 pixels and length 189 pixels. Left to right: phantom of closely-lying lines (rotation angle equals 45 degree), phantom with added noise, and inefficient result of line detector for noisy phantom.

2.1 Angular Resolution versus Structure Rotation

It is commonly known that only some image transformations are shift (rotate) invariant. To verify this aspect, important in line structure recognition process, a simple test was carried out – the line structures on the created phantom were rotated by 20, 50, 90 degrees, respectively. To compare the effectiveness of selected multiscale transformations appropriate MATLAB toolboxes were used. The achieved results presented in Fig. 2 confirm that complex wavelets tend to be the least susceptible to rotation – the image of reconstructed lines are regardless of the rotation angle. In case of complex wavelets there are visible relatively small blur at the ends of the lines on reconstructed images. The accuracy of phantom reconstruction appears to be definitely lower for wavelets, contourlets, and curvelets than complex wavelets. Using wavelets, additional undesirable shadows appear around the reconstructed lines. There is a similar but less visible effect for contourlet transform. However, the curvelets proved to be the least effective tool to enhance the input signal with a small number of coefficients. Curvelets identify and restore lines by isolated "dots", even if a large number coefficients is used. Thus, it is almost impossible to achieve continuous-lines. It is worth noting that the above-mentioned effects will be far more important in interpretation of mammogram contents due to the degree of noise.

2.2 Angular Resolution versus Structure Size

Next, an influence of the number of transformation coefficients on angular resolution was investigated. It has been observed that angular resolution and selectivity is significantly correlated with the number of transformation coefficients. However, it is worth mentioning that the number of coefficients, required to effective line structure reconstruction, depends on several factors. Firstly, it depends on

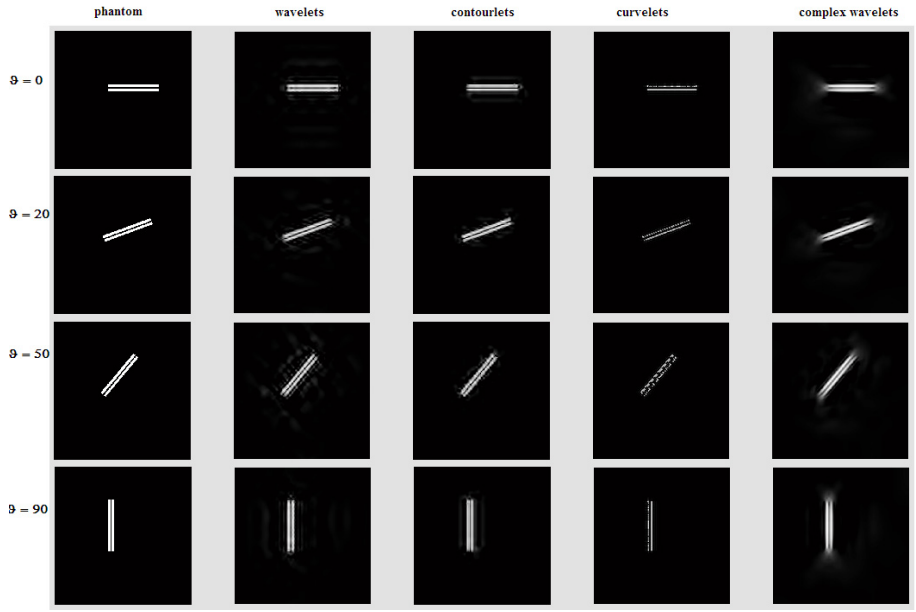

Fig. 2. The phantom of two closely-lying lines of 189 length and four reconstructed images using only 100 significant coefficients of wavelets, contourlets, curvelets, and complex wavelets (left to right). The rotation angle of lines $\theta = 0, 20, 50, 90$ is tested.

the size of analyzed object in image. Secondly, the distance between objects is not meaningless. Therefore, the noisy phantom with lines of $d = 89, 189, 289$ pixels length and the distance between them equal $\Delta = 5$ or 10 pixels, respectively, has been tested. The exemplary results are presented graphically in Fig. 3(a) and Fig. 3(b) – for only $N = 60$ of significant coefficients, and in Fig. 4(a) and Fig. 4(b) – for a much larger number of coefficients, i.e. for $N = 500$.

Comparing the reconstructed image containing lines with different distance (Fig. 3(a) with Fig. 3(b) and Fig. 4(a) with Fig. 4(b)) it appears that line distance is not as significant as length of line. Therefore, further discussion will focus on correlation between the length of different oriented lines and the possibility of their identification.

In order to objectively assess whether two lines are detected in the reconstructed images, the Matlab function *Demirel Edge Detector* was used. Two required parameters were determined experimentally: $T = 0.5$ – a threshold between 0 - 1, and $t = 8$ – the thickness of the line to indicate the edge (the t is 1 pixel smaller than the width of the phantom line due to slightly smaller size of lines in the reconstructed image). The miserable effect of line detector for noisy

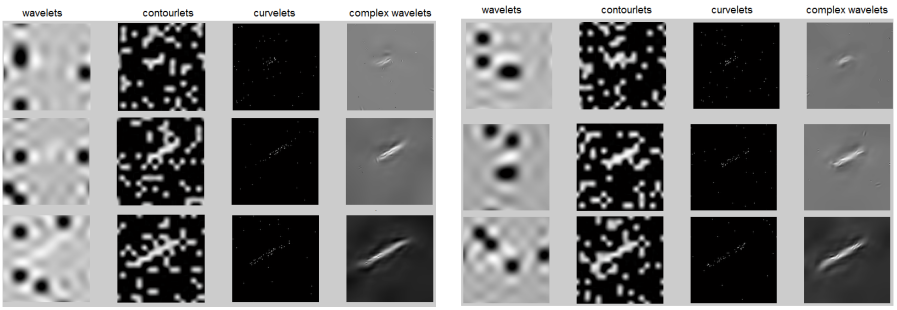

(a) $N = 60, \Delta = 5$ (b) $N = 60, \Delta = 10$

Fig. 3. Visual representation of the impact of line length (from top to bottom: $d = 89, 189, 289$ pixels, respectively) for reconstruction using only $N = 60$ significant coefficients of wavelets, contourlets, curvelets, and complex wavelets (left to right). The rotation angle of line $\theta = 30$, the line distance $\Delta = 5$ or 10 pixels.

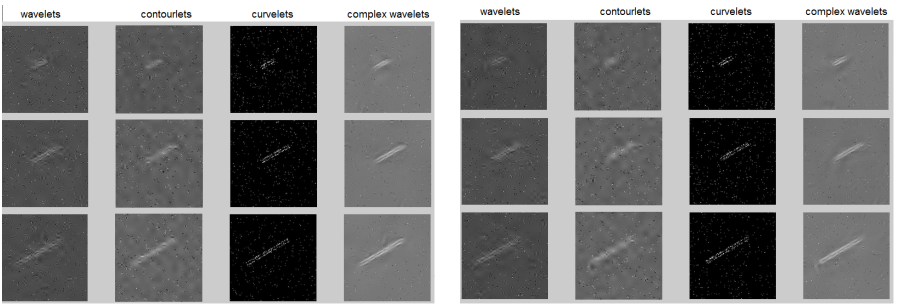

(a) $N = 500, \Delta = 5$ (b) $N = 500, \Delta = 10$

Fig. 4. Visual representation of the impact of line length (from top to bottom: $d = 89, 189, 289$ pixels, respectively) for reconstruction using only $N = 500$ significant coefficients of wavelets, contourlets, curvelets, and complex wavelets (left to right). The rotation angle of line $\theta = 30$, the line distance $\Delta = 5$ or 10 pixels.

phantom of closely-lying lines with distance between them $\Delta = 5$ pixels can be seen in Fig. 1 - right. The noise dominates the signal (line structures). However, the detection of these lines is possible in a situation when the detector is used on the reconstructed images obtained after the removal of a certain number of coefficients. The results for noisy phantom with 189-pixels lines rotated by $\theta = 30$ degree are shown in Fig. 6.

Based on achieved results, it is noteworthy that input signal enhancement, without unnecessary noise, is enabled only using the small number of complex wavelet coefficients (about $N = 60 - 100$). This is also confirmed by the graph in Fig. 5, obtained by use of four multiscale transformations of the noisy phantom

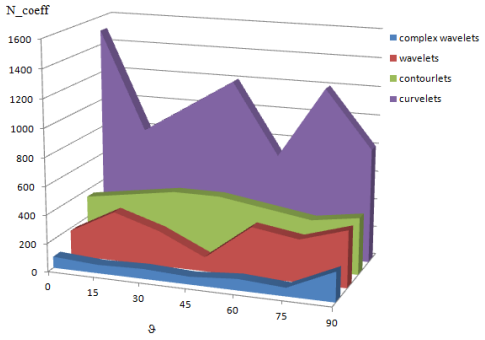

Fig. 5. A sample graph showing a dependence of the number of transformation coefficients N_{coeff} on the rotation angle θ for wavelets, contourlets, curvelets, and complex wavelets, accordingly. This result is achieved for phantom with lines of length $d = 189$ pixels and distance between them $\Delta = 5$.

with 189-pixels lines rotated by angle $\theta = 0 - 90$ degrees. However, it should be mentioned that the number of transformation coefficients required for effective line reconstruction seems to be independent on the length of analyzed structures.

Interpreting the results achieved for wavelets, it is apparent that using the similar to the case of complex wavelets number of coefficients (see in Fig. 6, $N = 400$ and 1000) the reconstruction of two closely-lying lines is also possible, but simultaneously extra noise (constituting useless informations) is extracted. In addition, only for $\theta = 0, 45, 90$ closely-lying lines are quite accurately reconstructed. For other value of θ these line structures connect locally (e.g. for $\theta = 30$ in Fig. 6).

Furthermore, using increasing number of contourlets coefficients to distinguish two closely-lying lines of different rotation angles is impossible. In this situation the energy coefficients focuses not only on the signal but also the noise. Thus, the number of coefficients, useful for the line reconstruction, is limited (see in Fig. 6, $N = 400$ and 1000).

In the case of curvelet transform coefficients failed to keep the continuity of the reconstructed lines (Fig. 3(a), Fig. 4(a), and Fig. 6). Therefore, it is suspected that reconstructed structures tend to be discontinuous even using significantly number of the curvelet transform coefficients.

Summarizing, it is undoubtedly that complex wavelets tend to be very useful tool to investigate image texture directionality due to structure rotate and size invariant. For the same number of the complex wavelet coefficients both the short and long line structures can be enhanced on reconstructed images. Additionally, to reconstruct the input signal without noise the smallest number of the complex wavelet coefficients is sufficient (in comparison to other transformations).

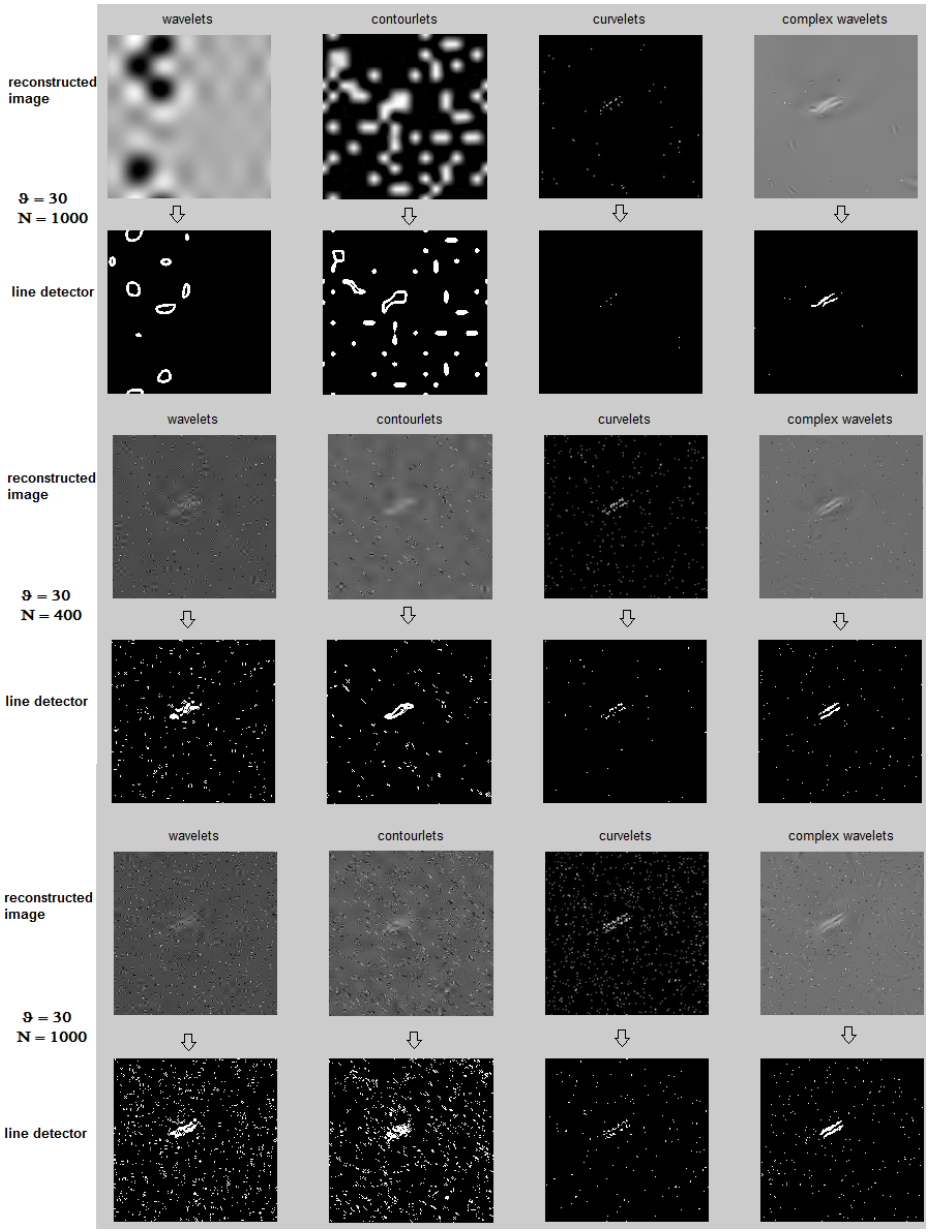

Fig. 6. Noisy phantom of two closely-lying lines ($d = 89$, $\Delta = 5$ pixels) and four reconstructed images using respectively $N = 60, 400, 1000$ significant coefficients of wavelets, contourlets, curvelets, and complex wavelets (from left). Additionally, the effect of line detector was presented. The rotation angle of line $\Theta = 30$ is shown for example.

3 Conclusions

Based on the performed experiment, it can be concluded that complex wavelets tend to have appropriate angular resolution and angular selectivity needed to extract radiating spicules from the noisy image, such as mammogram. Moreover, it appears that it is possible to capture diagnostically significant image content using a small number of transformation coefficients. However, there are two main problems in determining the angular resolution of image transformations. First, an approximation of the directional domain is used – converting Cartesian coordinates to polar coordinates is inaccurate. Therefore, the precise determination of image texture orientation is difficult. Another problem lies in the proposal of some measures to clearly assess both the angular resolution and selectivity of multiscale transformations which are characterized by considerably different transform-domain redundancy.

Acknowledgement. This publication was funded by the National Science Centre (Poland) based on the decision DEC-2011/03/B/ST7/03649.

References

1. Adel, M., Zuwala, D., Rasigni, M., Bourennane, S.: Noise reduction on mammographic phantom images. Electronic Letters on Computer Vision and Image Analysis 5(4), 64–74 (2006)
2. Barnes, G.T., Chakraborty, D.P.: Radiographic mottle and patient exposure in mammography. Radiology 145, 815–821 (1982)
3. American College of Radiology (ACR): Breast Imaging Reporting and Data System BI-RADS, 3rd edn. American College of Radiology (1998)
4. Chakraborty, J., Rangayyan, R.M., Banik, S., Mukhopadhyay, S., Desautels, J.E.L.: Statistical Measures of Orientation of Texture for the Detection of Architectural Distortion in Prior Mammograms of Interval Cancer. Journal of Electronic Imaging 21(3), 033010:1–13 (2012)
5. Dziukowa, R.J.: Mammografia w diagnostyce raka sutka, Warszawa (1998)
6. Ichikawa, T., Matsubara, T., Hara, T., Fujita, H., Endo, T., Iwase, T.: Automated detection method for architectural distorion areas on mammograms based on morphological processing and surface analysis. In: Medical Imaging: Image Processing, vol. 5370, pp. 920–925 (2004)
7. Jasionowska, M., Przelaskowski, A., Rutczynska, A., Wroblewska, A.: A two - step method for detection of architectural distortions in mammograms. In: Piętka, E., Kawa, J. (eds.) Information Technologies in Biomedicine. AISC, vol. 69, pp. 73–84. Springer, Heidelberg (2010)
8. Jasionowska, M., Przelaskowski, A.: Subtle directional mammographic findings in multiscale domain. In: Piętka, E., Kawa, J. (eds.) ITIB 2012. LNCS, vol. 7339, pp. 77–84. Springer, Heidelberg (2012)
9. Jasionowska, M., Przelaskowski, A., Jóźwiak, R.: Charaxteristics of architectural distortions in mammograms - extraction of texture orientation with Gabor filters. In: Bolc, L., Tadeusiewicz, R., Chmielewski, L.J., Wojciechowski, K. (eds.) ICCVG 2010, Part I. LNCS, vol. 6374, pp. 420–430. Springer, Heidelberg (2010)

10. Jiang, H., Tiu, W., Yamamoto, S., Iisaku, S.: Automatic recognition of spicules in mammograms. In: Del Bimbo, A. (ed.) ICIAP 1997. LNCS, vol. 1311, pp. 396–403. Springer, Heidelberg (1997)
11. Jiang, H., Tiu, W., Yamamoto, S., Iisaku, S.: Detection of spicules in mammograms. In: Proc. of IEEE ICIP 1997, vol. III, pp. 520–523 (1997)
12. Jiang, H., Tiu, W., Yamamoto, S., Iisaku, S.: A method for automatic detection of spicules in mammograms. Journal of Computer Aided Diagnosis of Medical Images 2, 23–31 (1998)
13. Karssemeijer, N., Te Brake, G.M.: Detection of stellate distortions in mammograms. IEEE Transactions on Medical Imaging 15(5), 611–619 (1996)
14. Kegelmeyer Jr., W.P.: Evalution of stellate lesion detection in a standard mammogram data set. In: Bowyer, K.W., Astley, S. (eds.) State of the Art in Digital Mammographic Image Analysis, pp. 262–279. World Scientific (1993)
15. Kegelmeyer Jr., W.P.: Computer detection of stellate lesions in mammograms. In: Proc. 1992 SPIE, Conf. on Biomedical Image Processing and 3-D Microscopy, vol. 1660, pp. 446–454 (1992)
16. Kobatake, H., Yoshinaga, Y.: Detection of stellate distortion in mammograms. IEEE Trans. Med. Imaging MI-15(3), 235–245 (1996)
17. Matsubara, T., Fukuoka, D., Yagi, N., Hara, T., Fujita, H., Inenaga, Y., Kasai, S., Kano, A., Endo, T., Iwase, T.: Detection method of architectural distortion based on analysis of structure of mammary gland on mammograms. International Congress Series, vol. 1281, pp. 1036–1040 (2005)
18. Nemoto, M., Honmura, S., Shimizu, A.: A pilot study of architectural distortion detection in mammograms based on characteristics of line shadows. Int. J. CARS 4, 2736 (2009)
19. Pachoud, M., Lepori, D., Valley, J.F., Verdun, F.R.: A new test phantom with different breast tissue compositions for image quality assessment in conventional and digital mammography. Physics in Medicine and Biology 49, 5267–5281 (2004)
20. Rangayyan, R.M., Banik, S., Desautels, J.E.L.: Computer-Aided Detection of Architectural Distortion in Prior Mammograms of Interval Cancer. Journal of Digital Imaging 23(5), 611–631 (2010)
21. Sampat, M.P., Markey, M.K., Bovik, A.C.: Computer-aided detection and diagnosis in mammography. IEEE Publication (2004); Selesnick, I.W., Baraniuk, R.G., Kingsbury, N.G.: The Dual-Tree Complex Wavelet Transform. IEEE Signal Processing Magazine, 124–151 (November 2005)
22. Webb, S.: The Physics of Medical Imaging. IOP Publishing, Adam Hilger, Bristol, Philadelphia (1988)
23. Zwinggelaar, R., Astley, S.M., Boggis, C.R.M., Taylor, C.J.: Linear structures in mammographic images: detection and classification. IEEE Trans. on Medical Imaging 23(9), 1077–1086 (2004)

Line Segment Based Approach to Pattern Detection in Mammographic Images

Jagoda Lazarek and Piotr S. Szczepaniak

Institute of Information Technology
Lodz University of Technology
Wólczańska 215, 90-924 Łódź, Poland
jagoda.lazarek@p.lodz.pl

Abstract. This paper describes a practical application of our novel method for detecting the boundaries between areas of different brightness to microcalcifications detection. We focus on microcalcifications detection step, whereas their classification, next important stage, is out of the scope of this paper. Microcalcifications are tiny specks of calcium, which may be an early sign of cancer. Because of that, their analysis based on mammographic examination is very important. Segments of boundaries are described by the coordinates of the start and the end point. Such representation of the boundary simplify further analysis of their shape. Some results of microcalcifications detection are presented. Parameters influence on results is shown.

Keywords: medical imaging, mammograms, breast cancer, computer-aided diagnosis, image processing, object detection.

1 Introduction

Image analysis, pattern detection and pattern recognition play an important role in our lives, making them easier and safer. Vision systems are widely used in security systems, transport, medicine and much more domains. They provide information, based on image analysis, which may support human decisions. The area on which we focused on in this paper is medical imaging.

Analysis of medical images is a subject of CAD systems (computer-aided detection and computer-aided diagnosis). There are several types of images which may be analysed, e.g. X-ray images, CT (computer tomography), MRI (magnetic resonance imaging), PET (positron emission tomography), USG (ultrasonography). They differ in methods of examination and in consequence in result images. Thus, analysis of them requires the application of various methods.

Mammography is an example of X-ray examination, which is commonly used for examination of breast (MLO, CC views). The aim of this examination is analysis of breast structure and detection of early signs of disease [3, 4]. Early and precise diagnosis increases the chances of recovery [5]. The types of abnormalities may be divided in two groups - masses and calcifications (microcalcifications), each of them may be benign or malignant. Signs of the benign or malignant

E. Pietka, J. Kawa, and W. Wieclawek (eds.), *Information Technologies in Biomedicine, Volume 3*, Advances in Intelligent Systems and Computing 283,
DOI: 10.1007/978-3-319-06593-9_4,

abnormalities are reflected in their appearance in mammograms. Due to different characteristics of masses and calcifications, their analysis is usually applied separately [5].

Microcalcifications (tiny specks of calcium) are regarded to be the very important signs in early breast cancer. The problem of their analysis is divided in two subproblems - detection and classification (as benign or malignant). Classification is out of the scope of this paper. Malignancy of microcalcifications is determined by their shape and distribution. Detailed classification is described by BI-RADS scale.

Difficulty in detection of microcalcifications is caused by their non a priori known shape. On the other hand their are relatively bright in opposite to rest of breast. It is caused by different density of tissue. Analysis of microcalcifications and mammograms in general is addressed by many authors, as a challenging and useful area of research. Bellow some of the existing approaches are outlined.

One of the most common approaches to abnormalities is founded on the pixel-based methods [5], the main idea of which is to analyse the mammogram pixel by pixel. By doing so, one can determine if the pixel is suspicious, i.e. whether it belongs to the abnormality area (e.g. mass, calcification) or not. Another popular approach makes use of the region-based methods. The latter are founded on the extraction of the regions of interest and their classification. The target regions are classified into two classes - suspicious or normal [5].

Detection of microcalcifications requires different methods which are developed by researchers focused on analysis of such abnormalities in mammographic images. Among variety of methods used to solve this problem, there are for example active contours [19, 20], morphological operations (e.g. reconstruction) [17, 18], multiresolutional analysis [21], fuzzy logic techniques [22, 23], machine learning algorithms [14–16], histogram or wavelet analysis [9–13]. These solutions are conceptually different from method presented in this paper.

The paper is organized as follows. Section 2 briefly describes the boundary line segments detection method, which was also described in [8]. Section 3 describes microcalcifications specificity and their role in breast cancer diagnosis. Section 4 presents how the method can be applied to microcalcifications analysis. This is followed by the discussion of the possibilities of the approach. We conclude in Section 5.

2 Boundary Line Segments Detection Method

In this section, the idea of our method is described. The method is used to detect the edge between two areas of different brightness, where the boundary between these areas is not clearly visible. The lack of boundary is caused by the tonal transition from one area to another. Our method solves this problem by separating areas of different brightness and gives coordinates of boundary segments in one step — in a contrast to edges which are extracted by filters like Sobel filter or Canny filter. Furthermore, obtained boundaries are very thin, what is important in the next steps of analysis, which will be introduced in the next stage of research.

Let us analyse the images shown in Figs. 1 and 2. In Fig. 1, the boundaries between two areas are clearly visible, as opposed to the boundaries depicted in Fig. 2. It is easy to notice that there are no straight boundaries which separate those two areas. The edges are ragged and the areas are not homogeneous, but when we look at these images from distance, such details are no more visible. We can see only two areas, a darker one and a brighter one, and a boundary between them. This observation has given rise to the idea of a method which can give the possibility to define this boundary.

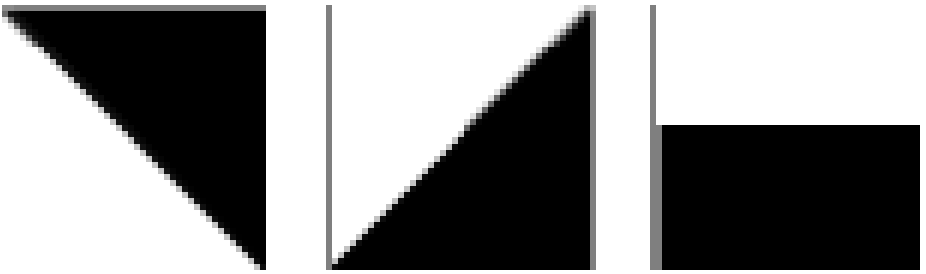

Fig. 1. Clearly visible boundaries between two areas, where (a) the boundary from the left upper corner to the right bottom corner, (b) the boundary from the left bottom corner to the right upper corner, (c) the horizontal boundary, in the middle of the image

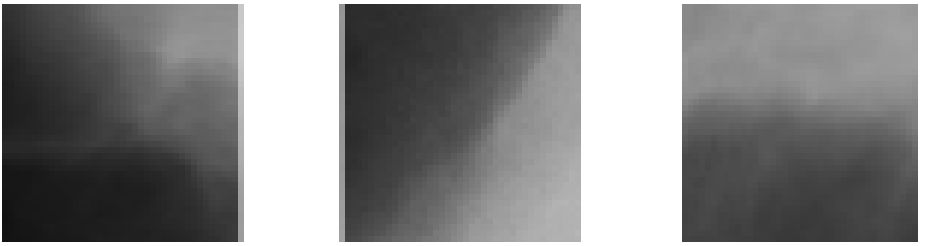

Fig. 2. Unclearly visible boundaries between two areas, where (a) the boundary from the left upper corner to the right bottom corner, (b) the boundary from the left bottom corner to the right upper corner, (c) the horizontal boundary, in the middle of the image

The above observations have led us to formulate an inverse task – not to find boundaries on the image but to create artificial boundaries and check if they are correct. Let us imagine that the images shown in Figs. 1 and 2 have four artificial, predefined boundaries. These boundaries define the areas. On the basis of calculations and analysis, we decide which boundary is correct.

Let e_1, e_2, e_3 and e_4 be the boundaries, which are defined as follows (where the given coordinates represent the coordinates of the start and the end point of the boundary, respectively) and presented on the image in Fig. 3:

- $e_1 \rightarrow ((x_0, y_0), (x_2, y_2))$,
- $e_2 \rightarrow ((x_0, y_2), (x_2, y_0))$,
- $e_3 \rightarrow ((x_1, y_0), (x_1, y_2))$,
- $e_4 \rightarrow ((x_0, y_1), (x_2, y_1))$.

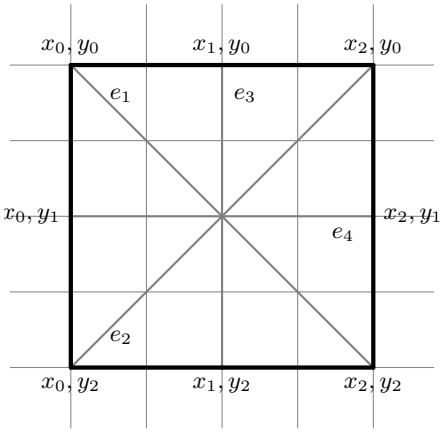

Fig. 3. Mask with artificial boundaries

Boundaries belong to one of the two types - horizontal and vertical boundaries (type 1.) or diagonal boundaries (type 2.). Boundaries of each of the types have to be analysed in pairs – e_1 with e_2 and e_3 with e_4. Such boundaries are opposites to each other, they are mutually exclusive. If one of them exists, second does not. For each pair, the calculation of average brightness for the area above and below the boundaries is done:

- a_{n_1} – average brightness above boundary n_1,
- b_{n_1} – average brightness below boundary n_1,
- a_{n_2} – average brightness above boundary n_2,
- b_{n_2} – average brightness below boundary n_2

where n_1 and n_2 are the analysed pair of boundaries, so there are two cases:

- $n_1 = e_1$, $n_2 = e_2$
- $n_1 = e_3$, $n_2 = e_4$

Values a_{n_1}, b_{n_1}, a_{n_2}, b_{n_2} are used to calculate d_{n_1} and d_{n_2}. These coefficients are needed to decide if and which boundary exists.

$$d_{n_1} = |a_{n_1} - b_{n_1}| \tag{1}$$

$$d_{n_2} = |a_{n_2} - b_{n_2}| \tag{2}$$

$$\frac{d_{n_1}}{d_{n_2}} \geq \alpha, \quad where \quad d_{n_2} > 0 \tag{3}$$

$$\frac{d_{n_2}}{d_{n_1}} \geq \alpha, \quad where \quad d_{n_1} > 0 \tag{4}$$

$$|d_{n_1} - d_{n_2}| > \beta \tag{5}$$

Where:

- d_{n_1} is the absolute value of the difference between average brightness above boundary n_1 and average brightness below boundary n_1,
- d_{n_2} is the absolute value of the difference between average brightness above boundary n_2 and average brightness below boundary n_2.

If conditions Eq. 3 and Eq. 5 are fulfilled, boundary n_1 exists; else if conditions Eq. 4 and Eq. 5 are fulfilled, boundary n_2 exists; else neither boundary n_1 nor boundary n_2 exists. Parameters α and β are defined experimentally – $\alpha = 3$ and $\beta = 15$. Choice was based on correctness of boundaries detection from prepared training set.

3 Microcalcifications Specificity and Their Role in Breast Cancer Diagnosis

As it was mentioned in the Introduction, microcalcifications may be in various shapes and have different spatial distributions. These features indicate the level of malignancy from 0 to 6, according to BI-RADS classification.

Benign microcalcifications are relatively large, homogeneous in shape and size, rounded, small in number, diffusely distributed. Malignant microcalcifications are small, irregular, heterogeneous in shape and size, clustered. More detailed characteristics of both of the types of microcalicifications are presented in tables below — Tab. 1 and 2.

Usual steps of microcalcifications detections are as follows:

- detection of ROIs (regions of interests),
- segmentation,
- classification.

We focused on detection of microcalcification boundaries, because of the crucial meaning of their shape in microcalcification classification. Classification is out of the scope of this paper, but this step will be introduced in the future research. Our initial solution is presented in the next Section.

Table 1. Calcifications morphology [24]

Benign	Intermediate concern	Malignant
skin	amorphous	fine linear
vascular	coarse heterogeneous	branching
popcorn		pleomorphic
plasmacell mastitis		
fat necrosis		
milk of calcium		
dystrophic		
eggshell		
suture		

Table 2. Calcifications distribution [24]

Benign	Intermediate concern	Malignant
diffuse	clustered	linear
regional		segmented

4 Method Application to Microcalcifications Detection

Since the meaning of microcalcification shape is crucial, we tried to adopt our method described in [8] and Section 2 to this task. This method connects three advantages - it deals with tonal transitions between microcalcifications and rest of tissue, is local and provides boundary segments (with coordinates of the start and the end point) which are useful for shape analysis.

Similarly to the our approach described in [8] the process of detection is performed using a mask with defined dimensions $a \times a$. The mask is moved over the image with step δ. For each area below the mask, calculations based on equations from Eq. 3 to Eq. 5 are done and boundaries are created. The parameters a and δ can be freely changed. The value of parameter a reflects in length of detected boundary segment.

Bellow some of results are presented, different values of parameters a and δ have been used. The analysed mammograms belong to the MIAS dataset [1], which contains set of digitised mammograms with information of localization and type of abnormality for each image.

As can be seen on Figs. 6, 7, 8, 10, 4 each or almost each microcalcification has been found. The boundaries of them are represented by groups of line segments in four possible directions. Such representation simplify shape analysis which will be provided in next steps of the solution.

Precise evaluation is impossible at the current stage of the research. Reference datasets contain information of localization of the whole group of microcalcifications but there are not information of expected and proper segmentation of single microcalcifications. Because of that, expert knowledge (radiologist) is needed to assess results.

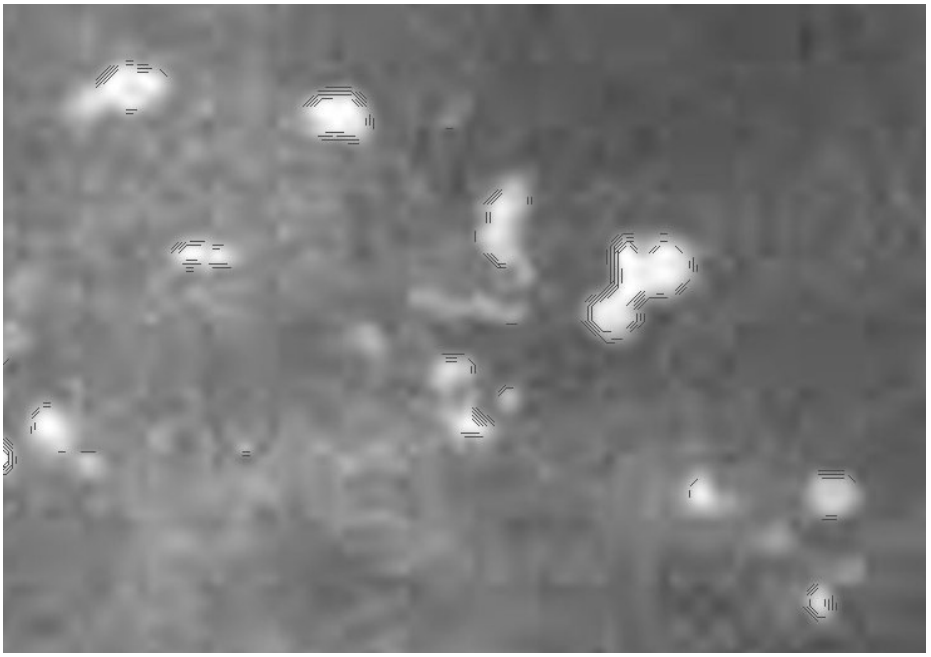

Fig. 4. Detected microcalcifications, parameters — $a = 5$, $\delta = 3$

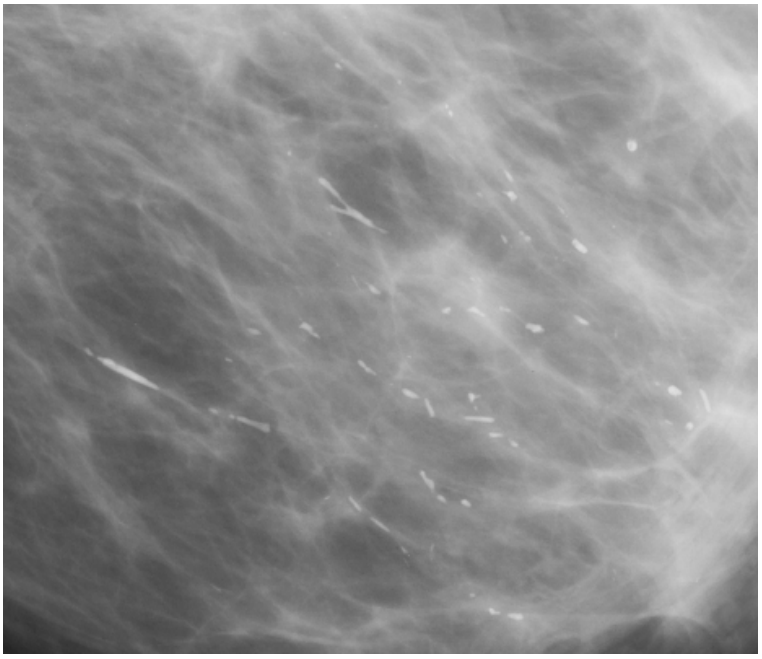

Fig. 5. Example of microcalcifications (mdb148 from MIAS dataset)

Fig. 6. Detected microcalcifications (Fig. 5), parameters — $a = 5$, $\delta = 3$

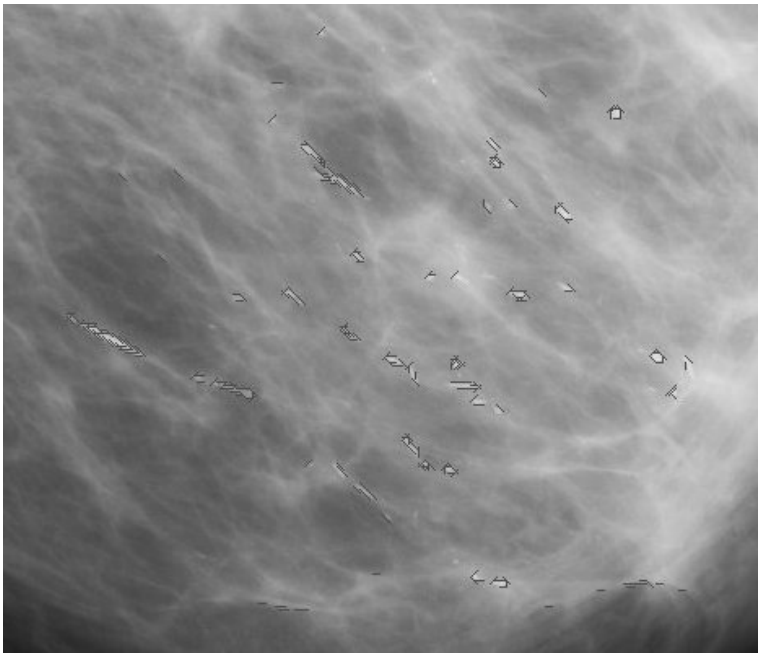

Fig. 7. Detected microcalcifications (Fig. 5), parameters — $a = 4$, $\delta = 2$

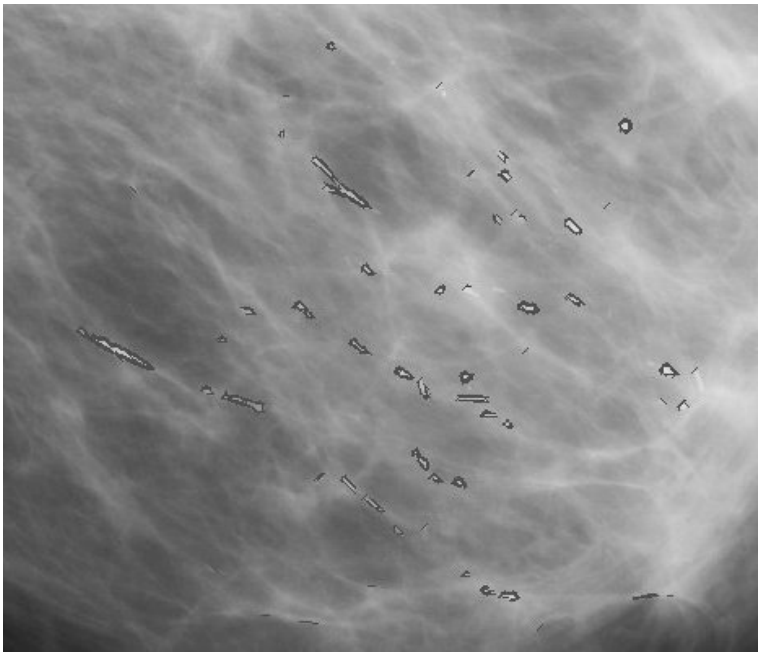

Fig. 8. Detected microcalcifications (Fig. 5), parameters — $a = 3$, $\delta = 1$

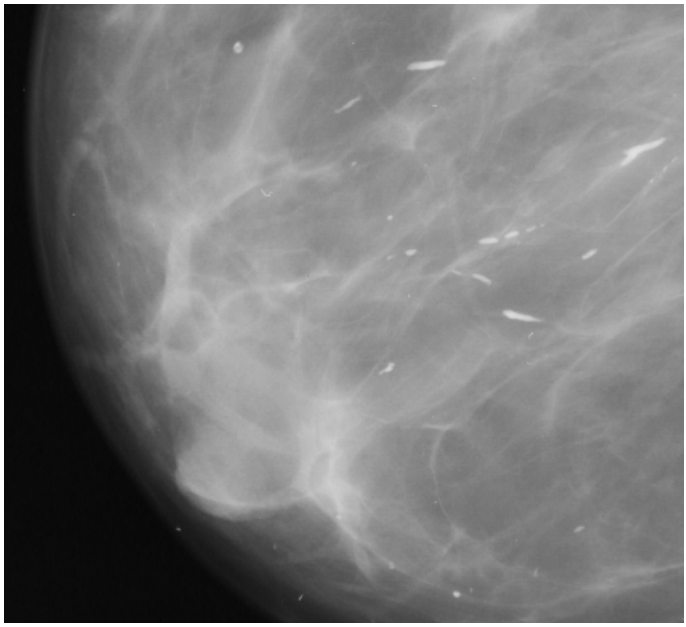

Fig. 9. Example of microcalcifications (mdb147 from MIAS dataset)

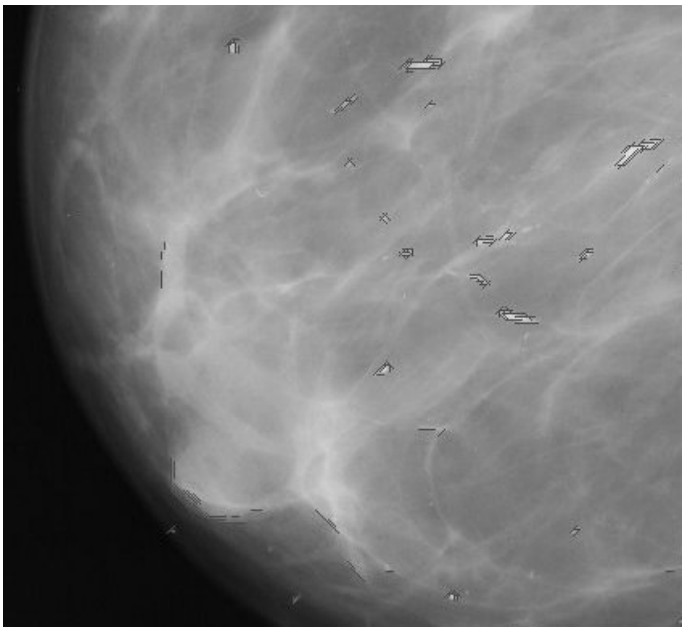

Fig. 10. Detected microcalcifications (Fig. 9), parameters — $a = 4$, $\delta = 3$

5 Conclusions and Future Research

In this paper, we have outlined the problem of microcalcifications detection. Afterwards our solution of the problem was presented. Concept of method is based on our previous research – the method for detecting the boundaries between areas of different brightness. Method has been modified for detection of very small and varied in shape objects. Than it was tested on several images, on which different types of microcalcifications were visible. Achieved results lead us to conclusion that this method may be useful for detection of microcalcifications and analysis of their shape, due to classification.

As we mentioned in the Introduction, classification of microcalcifications is out of the scope of this paper, since that is an important stage we plan to introduce it in aim to provide complete solution. To sum up, the further research will focus on microcalcifications shape analysis, classification and results evaluation by radiologists.

References

1. Mias dataset. MIAS dataset, `http://peipa.essex.ac.uk/info/mias.html`
2. Guliato, D., Rangayyan, R., Carnielli, W., Zuffo, J., Desautels, J.: Segmentation of breast tumors in mammograms by fuzzy region growing in. In: Proceedings of the 20th Annual International Conference of the IEEE Engineering in Medicine and Biology Society, vol. 2, pp. 1002–1005 (1998)

3. Huo, Z., Giger, M., Vyborny, C., Metz, C.: Breast cancer: Effectiveness of computer-aided diagnosis – observer study with independent database of mammograms. Radiology 224(2), 560–568 (2002)
4. Rangayyan, R.M., Ayres, F.J., Desautels, J.L.: A review of computer-aided diagnosis of breast cancer: Toward the detection of subtle signs. Journal of the Franklin Institute, Special Issue: Medical Applications of Signal Processing, Part I 344(34), 312–348 (2007)
5. Sampat, M., Markey, M., Bovik, A.: others: Computer-aided detection and diagnosis in mammography. In: Handbook of Image and Video Processing, vol. 2, pp. 1195–1217 (2005)
6. Pryczek, M., Tomczyk, A., Szczepaniak, P.S.: Active Partition Based Medical Image Understanding with Self Organized, Competitive Spatch Eduction. Journal of Applied Computer Science 18(2), 67–78 (2010)
7. Tomczyk, A., Szczepaniak, P.S., Pryczek, M.: Cognitive hierarchical active partitions in distributed analysis of medical images. Journal of Ambient Intelligence and Humanized Computing, 1–11 (2012)
8. Łazarek, J., Szczepaniak, P.S., Tomczyk, A.: Method of Pattern Detection in Mammographic Images. In: Korbicz, J., Kowal, M. (eds.) Intelligent Systems in Technical and Medical Diagnostics. AISC, vol. 230, pp. 235–245. Springer, Heidelberg (2013)
9. Yoshida, H., Doi, K., Nishikawa, R.: Automated detection of clustered microcalcifications in digital mammograms using wavelet transform techniques. In: Loew, M.H. (ed.) Proceedings of the International Society for Optical Engineering, vol. 2167, pp. 868–886 (1994)
10. Yoshida, H., Doi, K., Nishikawa, R., Giger, M., Schmidt, R.: An improved computer-assisted diagnostic scheme using wavelet transform for detecting clustered microcalcifications in digital mammograms. Acad. Radiol. 3, 621–627 (1996)
11. Zhang, W., Yoshida, H., Nishikawa, R., Doi, K.: Optimally weighted wavelet transform based on supervised training for detection of microcalcifications in digital mammograms. Med. Phys. 25, 949–956 (1998)
12. Wang, N., Karayiannis, T.C.: Detection of microcalcifications in digital mammograms using wavelets. IEEE Trans. Med. Imaging 17(4), 498–509 (1998)
13. Chen, C., Lee, G.: On digital mammogram segmentation and microcalcification detection using multiresolution wavelet analysis. Graphical Models and Image Processing 59(5), 349–364 (1997), http://dx.doi.org/10.1006/gmip.1997.0443
14. Cordella, L., Tortorella, F., Vento, M.: Combining experts with different features for classifying clustered microcalcifications in mammograms. In: Proceedings of the International Conference on Pattern Recognition, vol. 4, pp. 324–327 (2000)
15. Edwards, D., Kupinski, M., Nagel, R., Nishikawa, R., Papaioannou, J.: Using a Bayesian neural network to optimally eliminate false-positive microcalcification detections in a CAD scheme. In: Yaffe, M. (ed.) Digital Mammography, pp. 168–173. Medical Physics Publishing, Madison (2000)
16. El-Naqa, I., Yang, Y., Wernick, M., Galatsanos, N., Nishikawa, R.: A support vector machine approach for detection of microcalcifications. IEEE Trans. Med. Imaging 21(12), 1552–1563 (2002)
17. Halkiots, S., Botsis, T., Rangoussi, M.: Automatic detection of clustered microcalcifications in digital mammograms using mathematical morphology and neural networks. Signal Processing 87(1), 1559–1568 (2007), http://dx.doi.org/10.1016/j.sigpro.2007.01.004

18. Stojic, T., Reljin, I., Reljin, B.: Local contrast enhancement in digital mammography by using mathematical morphology. In: ISSCS 2005: Proceedings of the International Symposium on Signals, Circuits and Systems 2005, Iasi, vol. 2(1), pp. 609–612 (2005), http://dx.doi.org/10.1109/ISSCS.2005.1511314
19. Arikidis, N., Karahaliou, A., Skiadopoulos, S., Korfiatis, P., Likaki, E., Panayiotakis, G., Costaridou, L.: Size-adapted microcalcification segmentation in mammography utilizing scale-space signatures. Computerized Medical Imaging and Graphics 34(6), 487–493 (2010), http://dx.doi.org/10.1016/j.compmedimag.2009.12.009
20. Paquerault, S., Yarusso, L., Papaioannou, J., Jiang, Y.: Radial gradient-based segmentation of mammographic microcalcifications: observer evaluation and effect on CAD performance. Medical Physics 31(9), 2648–2657 (2004), http://dx.doi.org/10.1118/1.1767692
21. Netsch, T., Peitgen, H.-O.: Scale-space signatures for the detection of clustered microcalcifications in digital mammograms. IEEE Trans. Med. Imaging 18(9), 774–786 (1999)
22. Pandey, N., Salcic, Z., Sivaswamy, J.: Fuzzy logic based microcalcification detection. In: Widrow, B., et al. (eds.) Proceedings of the IEEE Neural Networks for Signal Processing Workshop X, pp. 662–671. IEEE Press (2000)
23. Gravielides, M., Lo, J., Floyd Jr., C.E.F.: Parameter optimization of a computer-aided diagnosis scheme for the segmentation of microcalcification clusters in mammograms. Medical Physics 29(4), 475–483 (2000), http://dx.doi.org/10.1118/1.1460874
24. Smithuis, R., Pijnappel, R.: Breast - Calcifications Differential Diagnosis, Radiology department, Rijnland Hospital, Leiderdorp and Martini Ziekenhuis, Groningen, the Netherlands, http://www.radiologyassistant.nl/en/p4793bfde0ed53 (publication date May 11, 2008)

Breast Phantom Imaging Results from an Ultrasound Computer Tomography Research System

Krzysztof J. Opieliński[1], Piotr Pruchnicki[1], Tadeusz Gudra[1], Przemysław Podgórski[2], Tomasz Kraśnicki[2], Jacek Kurcz[2], and Marek Sąsiadek[2]

[1] Faculty of Electronics, Wrocław University of Technology, Wyb. Wyspiańskiego 27, 50-370 Wrocław, Poland
{krzysztof.opielinski,piotr.pruchnicki,tadeusz.gudra}@pwr.wroc.pl
http://www.weka.pwr.wroc.pl

[2] Department of Radiology, Wrocław Medical University, Borowska 213, 50-556 Wrocław, Poland
{przemyslaw.podgorski,tomasz.krasnicki, jacek.kurcz,marek.sasiadek}@umed.wroc.pl
http://www.umed.wroc.pl/radiologia

Abstract. Today, in the age of computerization, experts not only strive to perfect methods of ultrasonographic (US) imaging of tissue structure, but also intensively develop transmission methods, focusing especially on ultrasound transmission tomography (UTT) (analogous to X-ray computed tomography - CT) and ultrasound reflection tomography (URT) based on synthetic aperture method used in radar imaging. The following paper presents and analyses the results of ultrasound transmission tomography of the internal structure of a biopsy CIRS Model 052A breast phantom. The imaging was performed with an internally designed ultrasound computer tomography research system. The obtained results were compared to the imaging results from dual energy CT, MR mammography and traditional US.

Keywords: ultrasound computer tomography (UCT), ultrasonography (US), ultrasound transmission tomography (UTT), computed tomography (CT), magnetic resonance (MR) mammography, breast biopsy phantom.

1 Introduction

The most common diagnostic tests used for early detection of malignant breast lesions include palpation (manual), X-ray mammography, traditional ultrasonography (US) and magnetic resonance (MR) mammography [1]. If a suspicion of breast malignancy is raised then cytological or histopathological tests of biopsy-obtained specimens are performed. There are also other diagnostic methods that can be used for preventive breast examinations, such as [2]: elastography (USE),

E. Pietka, J. Kawa, and W. Wieclawek (eds.), *Information Technologies in Biomedicine, Volume 3*, Advances in Intelligent Systems and Computing 283,
DOI: 10.1007/978-3-319-06593-9_5,

thermography, electrical impedance tomography (EIT), single photon emission computed tomography (SPECT) and positron emission tomography (PET). It became clear that ultrasound transmission (UTT) and reflection tomography (URT) can also be used for imaging and early detection of malignant lesions in women's breasts [2–7]. Several research centres around the world (including the Faculty of Electronics at Wroclaw University of Technology) are currently working to construct a prototype of an ultrasound computer tomograph dedicated for women's breast examination [2–7].

The paper we present discusses and analyses the results of ultrasound transmission tomography imaging of the internal structure of a biopsy CIRS Model 052A breast phantom used for ultrasonography assisted biopsy training. The scans were performed using an ultrasound computer tomography research system that was designed with the assistance of a private investor. The obtained results were compared with scans obtained using dual energy CT, MR mammography and traditional US.

2 Materials and Methods

2.1 Measurement Setup

Block diagram of the designed ultrasound computer tomography research system is presented in Fig. 1. Ultrasound computer tomography research system's main element is a circular array of piezoelectric transducers [8] with the internal diameter of 260 mm. 1024 piezoceramic sending-receiving transducers with dimensions of 0.5 x 18 mm, located evenly 0.2 mm apart on the internal side of the

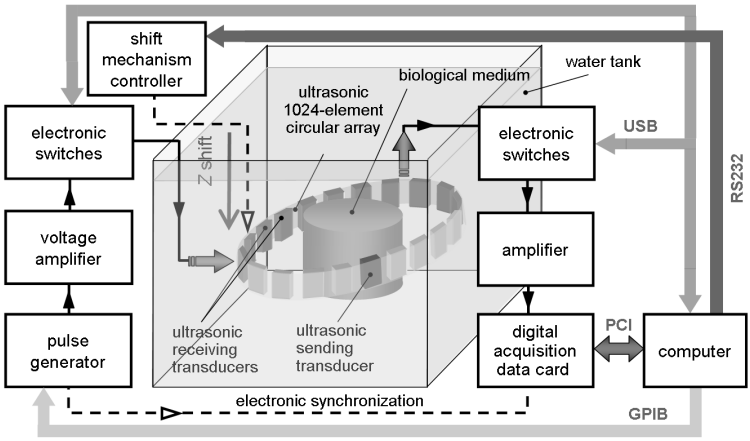

Fig. 1. Block diagram of the designed ultrasound computer tomography research system

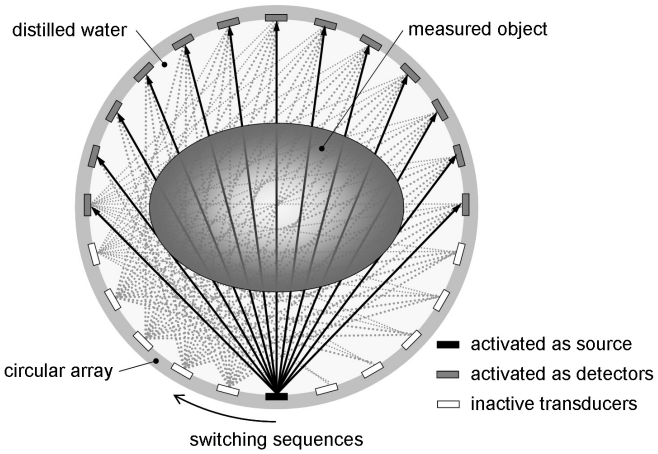

Fig. 2. A method of tomographic scanning of a section structure of the measured object in divergent projection geometry

mounting ring of the array, are driven during transmission by short rectangular pulse signals with the length of 5 cycles, frequency of 2 MHz and amplitude of 60 V_{pp}, using a voltage amplifier system and a demultiplexer system. Pulse generator is controlled via a GPIB connection from a computer. The signals passing through the studied biological medium (submerged in distilled water and located inside the array's ring) are received by means of a multiplexer and a low noise amplifier. The received signals are recorded by a computer using a digital card for acquisition of signals. Tomographic, transmission images of the sections of the internal structure of the studied biological medium are reconstructed using a suitable software with implemented algorithms for measurement of acoustic parameters of ultrasonic pulse [2, 7] (esp. its runtime [9]). One transmitting transducer and several hundred (usually half of the available amount) receiving transducers operate during one of the 1024 measurement cycles (Fig. 2). A computer controls the switching of transmitting and receiving transducers via an USB port. The measurements are performed in distilled water that fills the inside of a circular ultrasonic array, using a base, which allows precise vertical movement of the studied object. A complete measurement of one section of the object's structure (for a selected vertical base position) performed using the ultrasound computer tomography research system takes about 10 minutes. In the currently developed device prototype, the total measurement time for one cross-section will be reduced to below one second. This will be achieved due to parallel acquisition and processing of received signals and the use of fast FPGA circuits. Time of reconstruction of transmission images of a single cross-section of the studied object should not exceed a few milliseconds.

2.2 Breast Biopsy Phantom

The biopsy CIRS Model 052A breast phantom, selected for ultrasound tomographic study, imitates average values of acoustic parameters of tissues occurring in woman's breast for the purpose of training in thin-needle biopsy, assisted by real-time ultrasonography. The size (150:120:70 mm, volume: 600 cm^3 and shape of the phantom mimics female breast in supine body position. The phantom is made of Zerdine^{TM} gel, which imitates tissue and contains liquid and solid inclusions that mimic pathological lesions in the form of cysts and solid lesions (compact masses), respectively. According to the manufacturer's specifications, ultrasonic wave propagation velocity in Zerdine^{TM} gel is about $1500 \div 1540$ m/s depending on temperature. The CIRS Model 052A phantom has 6 amorphous (not spherical in shape) $8 \div 15$ mm green inclusions that imitate cysts and 6 amorphous $6 \div 12$ mm black inclusions that imitate solid lumps. The position of the inclusions in the phantom is random. One of the advantages of the phantom, in relation to its use for tomographic studies in water, is its smooth surface, which minimizes attenuation of oblique incident ultrasonic wave.

2.3 Ultrasound Tomography Imaging Conditions

Average velocity of ultrasound in distilled water during the phantom tests was $c \approx 1491.63$ m/s ($t \approx 23.13$ °C, temperature fluctuation $\Delta t \approx \pm 0.38$ °C).

28 cross-sections of the phantom were measured in coronal planes (the base of the phantom was perpendicular to the surface of the array's transducers), with a 2 mm vertical step, in the range of 54 mm from the base of the object (Fig. 3). 511 circular array receiving transducers positioned symmetrically opposite a transmitting one were used for each of the 1024 sequences of the successively activated transmitting transducers (Fig. 2). The diameter of the reconstructed area is 182.4 mm. UTT images were reconstructed using an algorithm of filtered backprojection with Hamming filter, and rectilinear propagation of ultrasonic waves from the source to the detector was assumed [10, 11]. The resolution of the obtained UTT images is 457 x 457 pixels with the size of 0.4 mm.

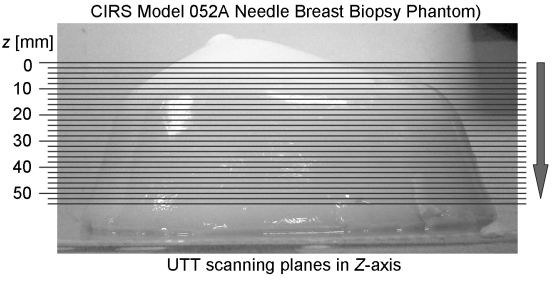

Fig. 3. The measured coronal cross-sections of the CIRS Model 052A phantom

3 Alternative Imaging Methods

For the purpose of comparison, the internal structure of the studied phantom was visualized using standard techniques utilised in breast diagnostics: MR mammography and US. Dual energy CT was used as a high resolution reference imaging.

CT and MRI examinations of the phantom were performed in the Department of General Radiology, Interventional Radiology and Neuroradiology of the Wroclaw Medical University Hospital, using Discovery CT 750HD (GE Healthcare) and MR Signa HDxt 1.5T (GE Healthcare) scanners, respectively.

The CT phantom examination was performed using a dual-energy protocol (80 keV and 140 keV in single acquisition). Then, dedicated software (GSI Viewer, GE Healthcare) was used to obtain secondary reconstruction of images for 75 keV energy. The phantom was positioned so that its base was parallel to the surface of the gantry hole and perpendicular to the axis of the bed surface (Fig. 4(a)). CT acquisition parameters were as follows: slice thickness 0.625 mm, field of view (FOV) 266 mm, acquisition matrix was 512 x 512 pixels with the size of 0.52 x 0.52 x 0.625 mm.

For the MRI examination the T_2 FSE sequence was used with the following parameters: repetition time $T_r = 5000$ ms and echo time $T_e = 86.968$ ms. The phantom was examined using an 8ch HD Breast Array (8-channel coil dedicated for breast imaging). The phantom was positioned in a special breast grip, with the side parallel to the gantry hole (Fig. 4(b)). MRI acquisition parameters were as follows: slice thickness 5 mm, FOV 195 mm, acquisition matrix 512 x 512 resulting in pixel dimension of 0.38 x 0.38 x 5 mm.

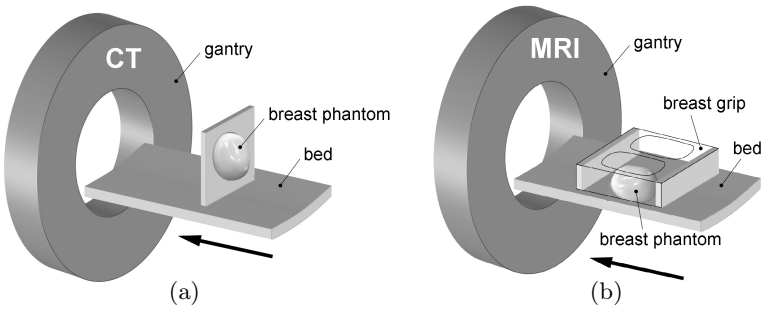

Fig. 4. The method of imaging the structure of breast phantom using: (a) CT, (b) MRI

In the traditional US method, the sections of the phantom were imaged using a 3.5 MHz ultrasonic linear probe (operating with a Picker LS2400 apparatus), that was submerged in distilled water and moved along the phantom on a special base (Fig. 5) with 5 mm step.

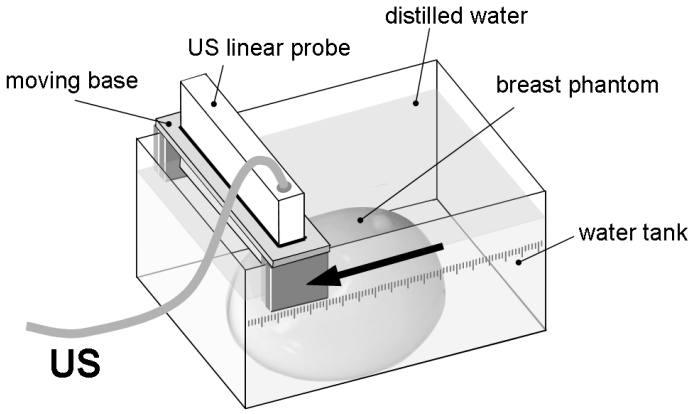

Fig. 5. The method of imaging the structure of breast phantom using US

4 Results

Images reflecting the distributions of local ultrasound velocity values were reconstructed (in greyscale, form black to white) from the digitally determined values of runtime of ultrasonic pulses, recorded using the designed ultrasound computer tomography research system (Fig. 1) in individual coronal cross-sections of the CIRS Model 052A breast phantom (Fig. 3), in divergent geometry setup (Fig. 2). Selected results of UTT examinations for two coronal cross-sections of the studied phantom (in the form of cross-section images and distributions of pixel values along dashed lines marked on the images) are presented in Fig. 6.

Two images for the cross-sections measured using the UTT method were selected from the set of CT images of the CIRS Model 052A breast phantom cross-sections reconstructed in coronal planes, based on measurements performed on a Discovery CT 750HD device (Fig. 4(a)). They are shown in Fig. 7.

MRI images of the sections of the CIRS Model 052A breast phantom in sagittal planes were reconstructed based on measurements performed on a MR Signa HDxt 1.5T device (Fig. 4(b)). Layered images in coronal planes that were obtained using multiplanar reconstruction (MPR) were used to acquire images in sagittal planes. Two of those images representing cross-sections measured using UTT and CT are presented in Fig. 8.

Examples of US images of sections of the CIRS Model 052A breast phantom (range of distance between the linear probe axis from the edge of the tank: 4.5 $\div$ 9 cm) obtained using a Picker LS2400 device, are presented in Fig. 9.

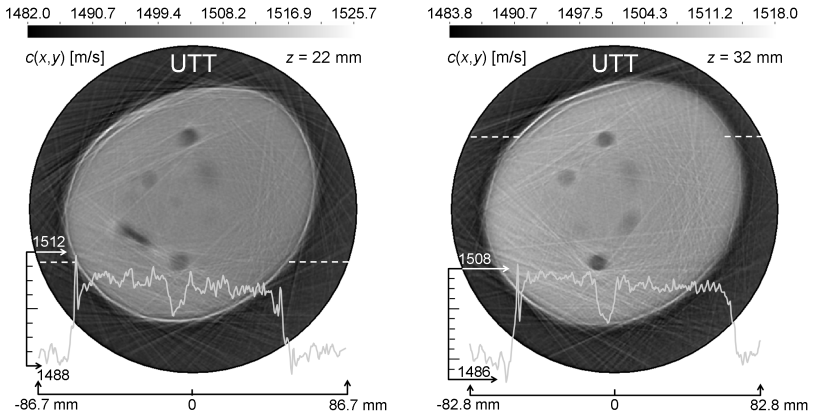

Fig. 6. Tomographic images of distribution of local values of ultrasound velocity for two coronal cross-sections of the CIRS Model 052A breast phantom, reconstructed based on runtime measurements

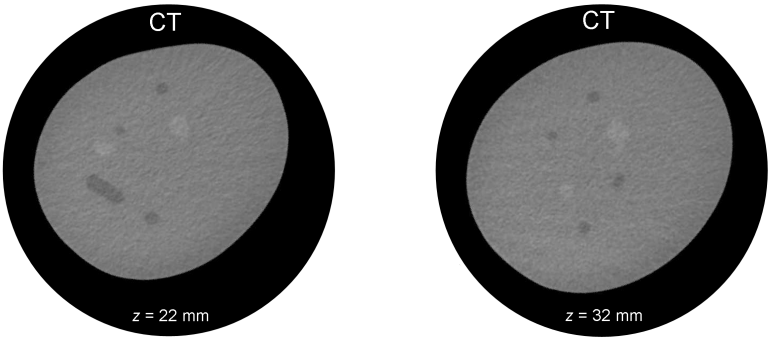

Fig. 7. CT images of two coronal cross-sections of the CIRS Model 052A breast phantom for the cross-sections measured using UTT method

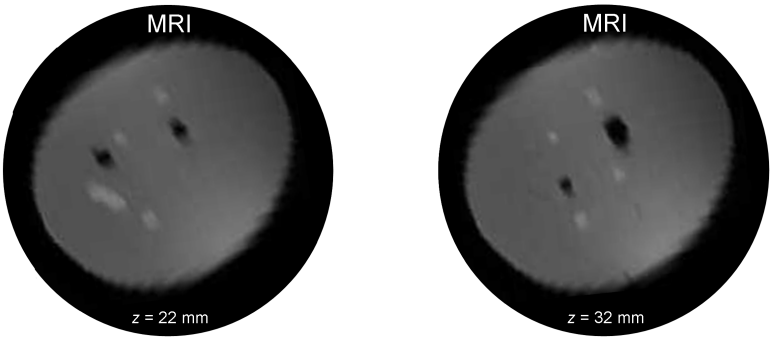

Fig. 8. MRI images of two coronal cross-sections of the CIRS Model 052A breast phantom for the cross-sections measured using UTT and CT

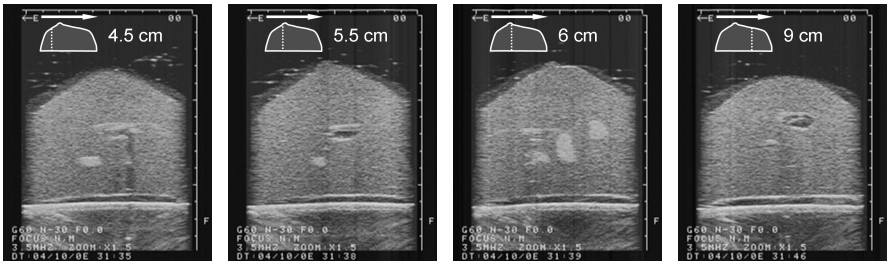

Fig. 9. Examples of US images of sections of the CIRS Model 052A breast phantom for various distances of the linear probe axis from the edge of the tank (based on the position of inclusions)

5 Comparative Analysis

The following section includes comparative analysis of images of the examined breast phantom acquired using various methods and a discussion concerning spatial and contrast resolutions. The authors did not use objective descriptors to compare image pixel values, because they are not diagnostically useful in this case. The visualised values, e.g. around a heterogeneity are distorted and every quantitative parameter for the analysis of correspondence with a reference sample of average pixel values of the compared images in the selected areas shows significant discrepancies. This, however, does not mean that the structures and their sizes are not detected correctly. Additionally, the examined phantom (made of soft gel) was measured in various positions (similarly as in the case of *in vivo* breast examinations), in various conditions (air, water). Therefore, it is impossible to assure ideal positioning of the examined structures – there are slight variations in the position resulting from deformation of the soft gel structure.

In this paper, the CT method was selected in order to obtain high resolution reference images of the structure of the studied phantom. The CT method is characterised by soft tissue contrast resolution of about 0.2 %. Possible spatial resolutions achievable in CT systems are about $0.2 \div 0.3$ mm [12]. Radiological density (the level of X-ray opacity) and Hounsfield scale (based on radiodensity), which is a linear transformation of the original linear attenuation coefficient measurement for X-rays are the differentiating parameters. Radiodensity of distilled water in standard temperature and pressure is defined as zero on Hounsfield scale (HU – Hounsfield units), while air density in typical conditions is -1000 HU [12]. In dual-energy CT imaging the value of beam's linear attenuation coefficient for two different energies is simultaneously tested. Then, based on the coefficient value, HU values of the tested material are calculated for specific energy. It needs to be highlighted, that CT technique is not used for women's breast examination, because of radiation beam rigidity (typically 120 kV). As a result the differences in radiation attenuation in tissues are too low. The imaged

inclusions (Fig. 7) have sharply delineated margins but are hardly distinguishable form the background (phantom gel).

The reconstructed UTT images of distribution of local values of ultrasound velocity in the cross-sections of the studied phantom (Fig. 6) are quantitative images, which make it possible to identify heterogeneities from the background (the difference in ultrasound velocity is a single [m/s]). Average ultrasound velocity in gel varied in the range $1503 \div 1507$ m/s. The range of ultrasound velocity variability $\Delta c \approx 4$ m/s in gel, results predominantly from changing measurement conditions (e.g. temperature differences). It is also possible to visualise both continuous and stepped changes (Figure 6 shows water penetrating the edges of the phantom gel as lower velocity values). One disadvantage of this imaging modality is fuzzy edges, associated with errors in evaluation of the size of small inclusions and distorted ultrasound velocity values in small heterogeneous areas caused by multipath effect during ultrasonic wave propagation in a heterogeneous structure [13]. The most significant distortions occur near the heterogeneity borders due to loss and dropout of the transmitted signal and refraction of ultrasonic wave beam (Fig. 6). The structure of the phantom on the cross-sections visualised in the UTT images is very similar to the structure shown on reference CT images – the same inclusions are visible (compare Fig. 6 and Fig. 7). Lateral resolution of the UTT method (horizontal plane scanning density) primarily depends on the resolution of the ultrasonic array (the number, width and spacing of the elementary transducers). In case of the 1024-element probe, used in this research, the lateral resolution can be estimated to be about 0.4 mm. If the longitudinal resolution of an UTT image (axial, along the path of the wave beam) is assumed to be half of the wavelength, the obtained value will also be around 0.4 mm. Horizontal resolution (height) primarily depends on horizontal scanning density (layer thickness), with a limitation resulting from the transducer's height, and in this case is about 5 mm. This can, however, be improved by horizontal focusing (mechanical or electronic) of ultrasonic wave beam. As a result of such a low vertical resolution, structures located above and below the examination plane appear on UTT images (compare Fig. 6 and Fig. 7–9). UTT contrast resolution is considerably dependent on the examined structure. Calculations show that if the total precision of determining projection values of ultrasound velocity is 0.01 m/s (disregarding the measurement uncertainty, which can be much greater), it will be possible to distinguish, in an UTT image, heterogeneous areas that differ from the surrounding tissue in the value of ultrasound velocity: 1 m/s with the size of > 2.3 mm, 2 m/s with the size of > 1.2 mm, 5 m/s with the size of > 460 μm, 10 m/s with the size of > 240 μm, 15 m/s with the size of > 160 μm, 20 m/s with the size of 120 $mathrm\mu$m [9]. Figure 10 shows the relation of the relative resolution of UTT imaging of the distribution of local values of ultrasound velocity inside a structure to its dimensions, against the average velocity of 1540 m/s in soft tissue.

MR mammography is a method that makes it possible to detect even small focal breast lesions that with high probability can be identified as early-stage malignancy. However, it usually requires contrast medium to be injected into

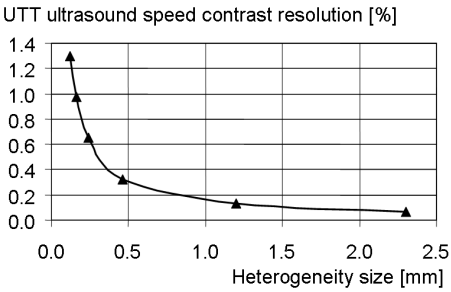

Fig. 10. The relation of the relative resolution of UTT imaging of the distribution of local values of ultrasound velocity inside a structure to its dimensions, against the average velocity of 1540 m/s in soft tissue

patient's body, which cannot be safely performed in case of patients with renal failure or allergy to contrast agents [12]. Additionally, MRI examination exposes patients to strong magnetic field and is contraindicated in patients with metal instruments or implants. Magnetic resonance tomography reflects concentration of nuclei of hydrogen atoms (protons) [12], which results in observable changes of signals of resonance emission, caused by hydrogen atoms present in water molecules in tissues. As a result MRI is the optimal technique for detecting conditions associated with increased amount of fluid in areas of pathological lesions (i.a. some tumours, infections and inflammations). Resolution of MR images depends on the number of water protons, both free and as part of macromolecules, in a medium. The resolution of magnetic resonance imaging can be as high as about $0.4 \div 1$ mm. The contrast resolution of MRI images is significantly affected by the specifications of the measurement equipment (level of magnet's induction, gradient force, receiving system, the coil used, etc.) and parameters of the scanning sequence [12] selected by the operator. Seemingly unimportant changes in the basic imaging parameters can result in obtaining slightly different data, which enable various diagnostic interpretations. Despite significantly lower resolution, in comparison to CT images, MRI visualisations of the examined breast phantom clearly demonstrate the same inclusions in its structure. Inclusion borders are slightly fuzzy. Another problem was related to the examination method (similar to one faced in *in vivo* breast examination). The phantom was positioned in a special breast grip, at an angle, with the side parallel to the gantry hole (Fig. 4(b)). As a result it was difficult to match and compare sections with other imaging types. Additionally, the resolution of scanning of sections of the phantom was just 5 mm.

Ultrasonography (US) is a method of diagnostic imaging of breasts that is routinely used as the primary or complementary test in relation to X-ray mammography [1]. This method allows, for example, to distinguish cysts from solid lesions (lumps) and is useful for precise localisation of a lesion, especially before a planned thin-needle biopsy and in young and middle-aged female patients, whose

breast tissue is usually to dense for diagnostically reliable X-ray mammography. The additional use of Doppler-US allows for lesion vascularity to be assessed. This method, however, does not make it possible to unequivocally distinguish malignant lesions from benign ones. Reflections of ultrasonic wave pulses from microcalcifications (the sizes of which start from a few μm) mean that signals received by the US-scanner can be obtained. This, however, does not mean that such signals will always be distinguished in an US image from many other signals received from the border of the adipose, fibrous, glandular tissue and their heterogeneities (tissue noise) [14]. US imaging produces limited viewing area, is subjective (depends on the examining person's assessment) and generates results that are an effect of a compromise between ultrasonic wave penetration depth and image resolution. The probability of early breast cancer detection using US is estimated to be about 50 % [15]. Looking at the US images of the studied breast phantom cross-sections, it is possible to identify heterogeneity of the object's structure and distinguish cysts from lumps. Acoustic impedance is the differentiating parameter in this case. US is a qualitative type of imaging and visualises heterogeneity borders but does not provide data on their quantitative characteristics.

6 Conclusions

The obtained UTT, CT, MRI and US images of the CIRS Model 052A breast phantom structure show comparable (in the context of size and location) heterogeneities inside the object. They are hardly distinguishable from the background on CT images and slightly more visible on MRI images, but have more fuzzy edges. The UTT images of distribution of ultrasound velocity clearly demonstrate continuous and stepped changes of density. The edges of small inclusions are slightly fuzzy. UTT image is a quantitative type, because of high precision of digital determination of runtime. As a result it is potentially possible to identify the character of a breast lesion (benign vs. malignant) based on pixel values in the lesion area in relation to the background. These are valuable diagnostic data.

The obtained results show that, after the scanning process is accelerated making it possible to perform *in vivo* examinations, the developed UTT method can successfully be used to detect and diagnose focal lesions in women's breasts. Lesions that cannot be visualised using the traditional ultrasonography can be imaged thanks to the UTT method. It combines the advantages of US (no X-rays and contrast media used, no contraindications in case of ferromagnetic implants) with transmission technology used in CT, making it an innovative, sensitive and potentially powerful diagnostic method.

Acknowledgments. The authors would like to thank DRAMIŃSKI Medical Instruments Company for financing the research as part of a process of introducing an ultrasonic transmission tomograph for examining women's breasts to the market.

References

1. Basset, L.W., Jackson, V.P., Fu, K.L., Fu, Y.S.: Diagnosis of Diseases of the Breast. Elsevier Saunders, Philadelphia (2005)
2. Opielinski, K.J.: Application of transmission waves for characterization and imaging of biological media structures. Printing House of Wroclaw University of Technology, Wroclaw (2011) (in Polish)
3. Opielinski, K.J.: Ultrasonic Tomographic Imaging of Soft Tissue. In: Leniowska, L., Branski, A. (eds.) Progress of Acoustics, pp. 23–52. Polish Acoustical Society, Rzeszow Department, Rzeszow (2013) (in Polish)
4. Duric, N., Littrup, P., Poulo, L., Babkin, A., Pevzner, R., Holsapple, E., Rama, O., Glide, C.: Detection of breast cancer with ultrasound tomography: First results with the Computed Ultrasound Risk Evaluation (CURE) prototype. Med. Phys. 34(2), 773–785 (2007)
5. Ruiter, N.V., Schwarzenberg, G.F., Zapf, M., Gemmeke, H.: Conclusions from an Experimental 3D Ultrasound Computer Tomograph. In: IEEE Nuclear Science Symposium Conference Record, pp. 4502–4509. IEEE Press, New York (2008)
6. Wiskin, J., Borup, D., Johnson, S., Andre, M., Greenleaf, J., Parisky, Y., Klock, J.: Three-dimensional nonlinear inverse scattering: Quantitative transmission algorithms, refraction corrected reflection, scanner design and clinical results. POMA 19, 075001 (2013)
7. Opielinski, K.J., Pruchnicki, P., Gudra, T., Podgorski, P., Krasnicki, T., Kurcz, J., Sasiadek, M.: Ultrasound Transmission Tomography Imaging of Structure of Breast Elastography Phantom Compared to US, CT and MRI. Arch. Acoust. 38(3), 321–334 (2013)
8. Gudra, T., Opielinski, K.J.: The ultrasonic probe for the investigating of internal object structure by ultrasound transmission tomography. Ultrasonics 44, e679–e683 (2006)
9. Opielinski, K.J., Gudra, T.: Multi-parameter ultrasound transmission tomography of biological media. Ultrasonics 44(1-4), e295–e302 (2006)
10. Opielinski, K.J., Gudra, T.: Ultrasonic Transmission Tomography. In: Sikora, J., Wojtowicz, S. (eds.) Industrial and Biological Tomography, pp. 263–338. Book Publishing of Institute of Electrotechnics, Warsaw (2010)
11. Kak, A.C., Slaney, M.: Principles of Computerized Tomographic Imaging. IEEE Press, New York (1988)
12. Pruszynski, B.: Radiology, RTG, CT, USG, MRI Image Diagnostics and Radioisotopes. PZWL, Warsaw (2000) (in Polish)
13. Crawford, C.R., Kak, A.C.: Multipath artifact corrections in ultrasonic transmission tomography. Ultrasonic Imaging 4, 234–266 (1982)
14. Filipczynski, L.: Detect ability of calcifications in breast tissues by means of ultrasonic echo method. Arch. Acoust. 18(3), 223–240 (1983) (in Polish)
15. Wronkowski, Z., Zwierno, M.: Brest cancer – practical information – interview, diagnostics, classification of changes. Health Service 24-26, 2917–2919 (2000) (in Polish)

Adaptive Preprocessing of X-ray Hand Images

Marzena Bielecka and Adam Piórkowski

Department of Geoinfomatics and Applied Computer Science, AGH University of Science and Technology, A. Mickiewicza 30 Av., 30059 Cracow, Poland
pioro@agh.edu.pl
http://www.geoinf.agh.edu.pl

Abstract. In this paper an algorithm based on gradient methods and binarization threshold selection is proposed. The finger bones contourisation, the finger joints localization, the fingers segmentation and the noise elimination are the considered tasks. The introduced method gives promising results.

Keywords: image preprocessing, radiograms, X-ray hand images.

1 Introduction

X-ray imaging is one of the most important diagnostic tools in contemporary medicine [8, 9, 13, 21–23]. In comparison with other methods of medical imaging, such as computer tomography or magnetic resonance, X-ray pictures remain popular due to low cost and simplicity. The application of computers to automatic image analysis makes X-ray imaging even more attractive. In a such approach, however, good preprocessing of the radiograms is required [5, 19].The existing algorithms of medical X-ray images preprocessing do not give satisfactory results. In the field of rheumatology there are several diseases detectable by using X-ray pictures, especially in palm region [23]. Several methods of preprocessing have been proposed on various levels [5, 7, 12]. The preprocessed image is analyzed on account of interesting features, like contour or joints detection [3, 7, 11, 14]. Detection of pathological changes in joint spaces and bone contours are done as well [1, 2, 4, 6, 18, 19, 21]. Further research employs pattern recognition and image understanding [17, 24] in order to create computer-aided medical diagnostic system [15]. Processing of X-ray pictures is more difficult than pictures taken in visible spectrum for various reasons: high noise level, low contrast between soft tissue and background and high variability in the level of gray. Differences in tissue thickness between the finger area and the wrist area are the main issues associated with X-ray pictures. The hand extraction from the raw picture is the main goal of the preprocessing of the hand radiograms. Low contrast between soft tissue and background and high variability in luminance cause problems with binarization. Moreover, high noise level causes failing of direct application of visible spectrum pictures preprocessing algorithm to X-ray images. Due to the aforementioned problems, the satisfied algorithm of the medical X-ray images preprocessing has not been worked out so far. The adaptive preprocessing of the

E. Pietka, J. Kawa, and W. Wieclawek (eds.), *Information Technologies in Biomedicine, Volume 3*, Advances in Intelligent Systems and Computing 283,
DOI: 10.1007/978-3-319-06593-9_6,

palm radiograms is the topic of this paper. The finger bones contourisation, the finger joints localization, the finger segmentation and the noise elimination are the considered tasks. This paper is a continuation of studies described in [5, 16].

2 Input Data

Sixty pairs of left and right hand radiograms, made since 2006 until 2010, are processed images. Both the images quality and their sizes are different. Therefore, it is crucial to work out adaptive algorithm effective for all data set. The radiograms are digital data in DICOM format. As it has been mentioned, the size of images are different and varies from [1301×2320] to [2311×3480] pixels. Therefore, algorithms which use relative metrics should be used. A range of pictures brightness, corresponding to $X - ray$ absorption varies from [0-1018] to [0-4095]. Differences occur even between pictures of left and right hand in images made for the same patient at the same day - see Fig. 1.

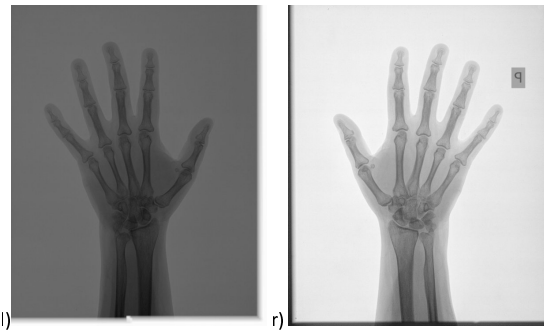

Fig. 1. An example of different ranges of brightness of hand images of the same patient (left and right)

Although in fields bit stored and bit allocated the 16 bit brightness resolution was declared it seems that the used AC converter had 12 bit brightness resolution. Therefore the brightness range [0-4095] was assumed. According to differences in brightness the applied algorithms should check difference between brightness levels instead of ascribing the meaning of the brightness levels. Hands are presented in vertical positions. The higher brightness of the picture, the lower X-rays absorption in the examined tissue. A 3D surface plot for a hand image is presented in Fig. 2. It should be stressed that it is not a 3D reconstruction. The following conclusion can be reached on the basis of Fig. 2 :

– The X-rays absorption varies depending on the picture region - brightness of bones at the tip of fingers is the same as the brightness of muscles at the wrist region. Therefore analysis based only on the brightness levels cannot be effective.

– Finger joints are hinged ones (ginglymus). In such joints one bone is rotund whereas the second one is a bowl which absorbs X-rays in a specific way. At radiograms it causes a characteristic descending slopes of brightness.

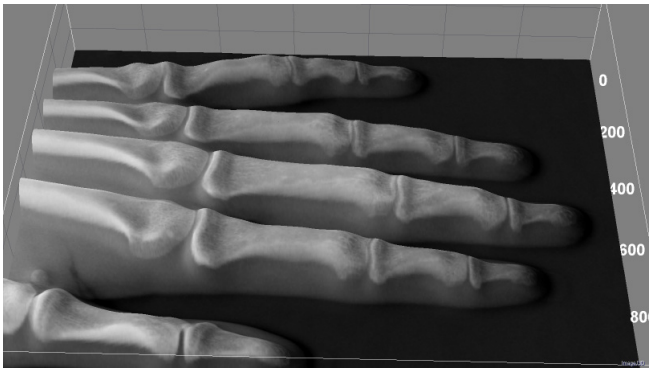

Fig. 2. A 3D surface plot for a hand image; this is not a 3D reconstruction

2.1 The Structure Identification on the Basis of Brightness Levels

The brightness range of images is a starting point of the analysis. In the case of the hand radiograms the brightness range which correspond to bones or muscles is often disparate among different images. Thus, the analysis of horizontal profile is proposed - see Fig. 3. In a such case, it should be possible to distinguish bones, muscles and skin by using the given profile. The following conclusion can be reached on the basis on Fig. 3:

– It is needed to distinguish bones, muscles and skin for each finger.
– The brightness range for both sides of the given finger is not the same what make hard to determine thresholds separating bones and muscles.
– The brightness profile of bones does not determine univocally the place of bones.

Therefore, this method is not accurate enough.

3 The Algorithm of Outlining the Joint Spaces in the X-Ray Pictures

Taking into consideration the results from the previous section the following steps of finding of joint spaces is proposed:

– Application of a directional differential mask A in order to finding a steep descending slope of phalange.

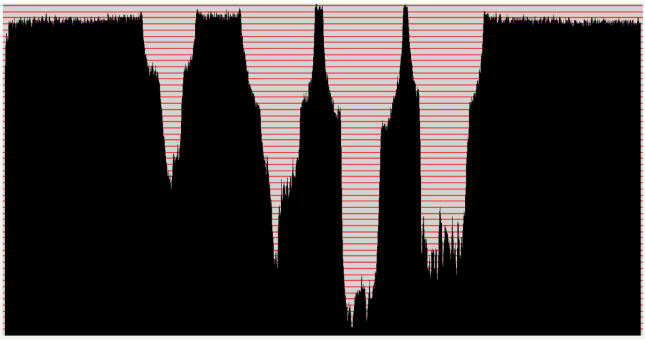

Fig. 3. The horizontal profile of hand image

– Application of a directional mask B detecting of valleys in order to finding places corresponding to joint spaces.

In the process of finding of joint spaces two images are received as a result of application of the mask A and B – see Fig. 4. Next, for a given binarization threshold, determined separately for each mask, the binary images are created. The descending slopes and outlines of valleys are distinguished in the images. In the preprocessing image joint spaces constitute clear valleys surrounded by descending slopes in vertical direction. Therefore, they can be detected by using the mask B. Some effects of filtration by using the mask A covers with the result of filtration by using the mask B. Finally, the joint space is outlined as a result of filtration by using the mask B where the result of filtration by using the mask A is adjoined to it from up side - see Fig. 8. The depicted joint space can be used both to analysis of degenerated joints and to segmentation of hand phalange. The scheme of the proposed algorithm is presented in Fig. 5.

-1	-1	-1	-1	-1	-1	-1	-1	-1	-1
-1	-1	-1	-1	-1	-1	-1	-1	-1	-1
-1	-1	-1	-1	-1	-1	-1	-1	-1	-1
-1	-1	-1	-1	-1	-1	-1	-1	-1	-1
0	0	0	0	0	0	0	0	0	0
1	1	1	1	1	1	1	1	1	1
1	1	1	1	1	1	1	1	1	1
1	1	1	1	1	1	1	1	1	1
1	1	1	1	1	1	1	1	1	1

(a)

-4	-4	-4	-4	-4	-4	-4	-4	-4	-4
-2	-2	-2	-2	-2	-2	-2	-2	-2	-2
-1	-1	-1	-1	-1	-1	-1	-1	-1	-1
2	2	2	2	2	2	2	2	2	2
10	10	10	10	10	10	10	10	10	10
2	2	2	2	2	2	2	2	2	2
-1	-1	-1	-1	-1	-1	-1	-1	-1	-1
-2	-2	-2	-2	-2	-2	-2	-2	-2	-2
-4	-4	-4	-4	-4	-4	-4	-4	-4	-4

(b)

Fig. 4. Mask A and B for detecting of joint outlines

3.1 Noise Filtering

The proposed algorithm does not require noise removing. However, the number of objects disturbing the correct outline of joint spaces decrease by application of a median mask 3×3 and averaging filtration by using mask 7×7 with elements equal to 1 according to the pattern of a rhomb.

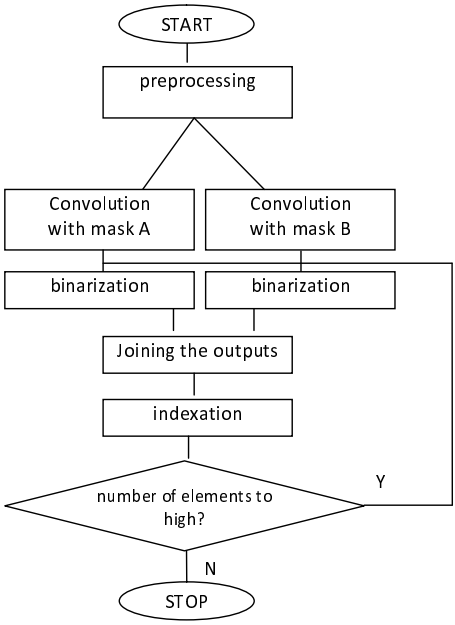

Fig. 5. The scheme of the proposed algorithm

3.2 Threshold Binarization

The algorithm of finding the proper threshold binarization consists in constant increasing of the value of the threshold binarization. If the number of elements outside of join spaces is below 20, then the threshold value is proper. The disturbing elements constitute small dense groups of pixels in shape of square or rectangle. They do not have elongated shape, i.e. such shape that the width is at least five times greater than the height, what makes easy to distinguish them from the joint spaces. The setting of proper binarization threshold value is important. Too low threshold value makes the number of places being possibly outlines of joints increases. Too high threshold value leads to lose information about a joint like for an example shortening of its outline or loss of information about pathological deformation. In Fig. 6 there are shown results for two images of left (L) and right (R) hand for the same patient (TE) differ in quality. Each input image (with (p) and without preprocessing (n)) has different the optimal threshold binarization.

The same was done for the more patients and depicted in Fig. 7.

On the basis of the two above figures the following conclusions are obtained:

– Preliminary filtration by using the proposed filters precipitated determination of the proper binarization threshold. The mentioned filtration allowed us to group radiograms whereas lack of regularity of brightness variability was observed when filtration had not been used.

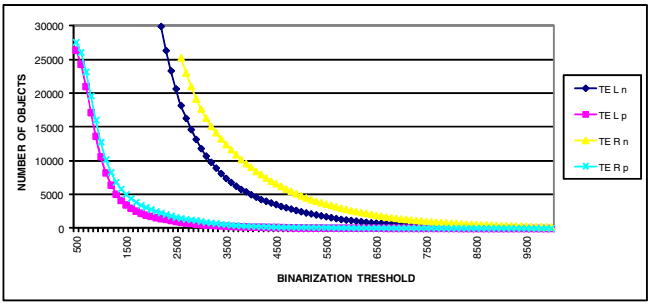

Fig. 6. The results for images without preprocessing (n) and with preprocessing (p) for two different pictures of left hand (L) and right hand (R) for the same patient (TE)

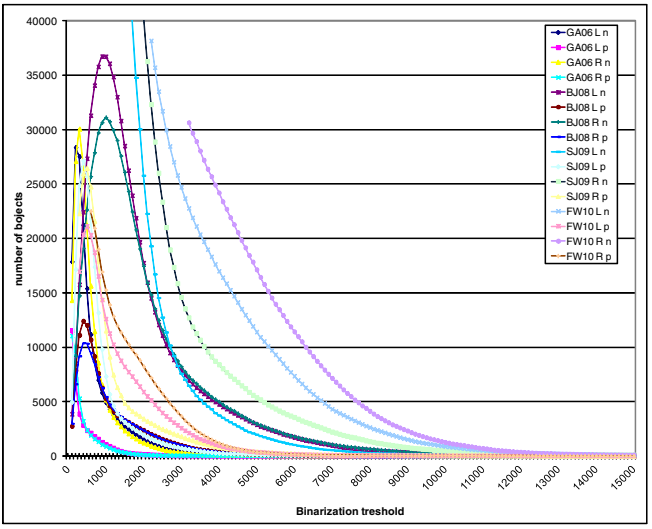

Fig. 7. The results for images without preprocessing (n) and with preprocessing (p) for two different pictures of left hand (L) and right hand (R) for more patients

– If preliminary filtration was used, then the adjusting threshold value was approximately the same for the left and right hand for the same patients.

The number of objects detected on the radiograms as a function of the threshold value has a clear maximum. Below this maximum detected objects joints into one big structure whereas for threshold values greater than this maximum diminished small objects, which is, in general, positive. Therefore, the optimal threshold value should be searched above the mentioned maximum. On the basis of the algorithm application for the whole data set it was found that the threshold for which 200-500 objects were detected in the hand radiograms allowed us find the joints effectively and additional detected objects that are meaningless, are

significantly smaller than the detected joints and separated clearly, so they can be removed easily.

3.3 The Algorithm Application

An example of the algorithm application is presented in Fig. 8. Structures detected by using the mask A are marked in blue colour whereas in yellow are marked valleys detected by using the mask B. The common region, i.e. the region detected by both the mask A and B, is marked in green. The region detected by the mask B - yellow and blue regions in Fig. 8 - is the finish result.

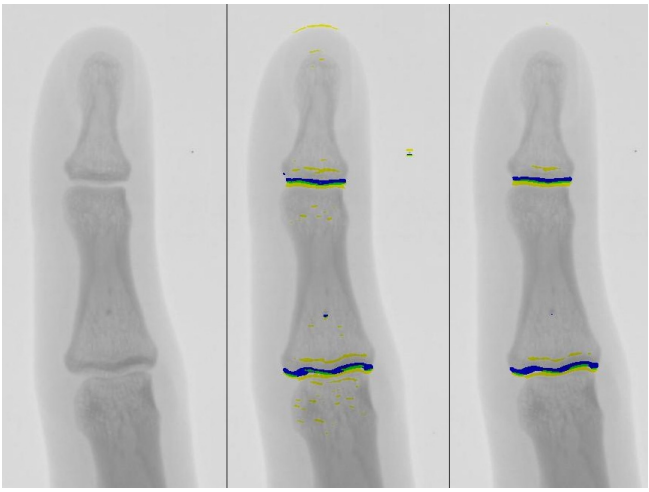

Fig. 8. An example of joint contours detecting, dark blue - mask A, yellow - mask B, green - intersection: original (left), without preprocessing (middle), with preprocessing (right)

4 Fingers Segmentation

Fingers segmentation was done by using analysis of differences in brightness. The maximum of results obtained from four directional filters was selected. The similar approach is presented in [20]. The masks depicted in Fig. 10 were applied in order to obtain bones edges. Threshold binarization is the next step of the algorithm. The threshold value should be selected in such a way that large structures, such as bones, palm contour, preserve their spatial continuity and small isolated object that are a noise, are removed. After binarization, the detected joins are removed from the picture in order to separate clearly finger bones. Then, the indexation is done in order to select finger structures and filter small, meaningless objects. Edges thinning, in order to obtain clear contours, is the finish step of the algorithm. The effects of the sequence of the algorithm steps is presented in Fig. 9 where the joint region between distal and intermediate phalanges is put as an example.

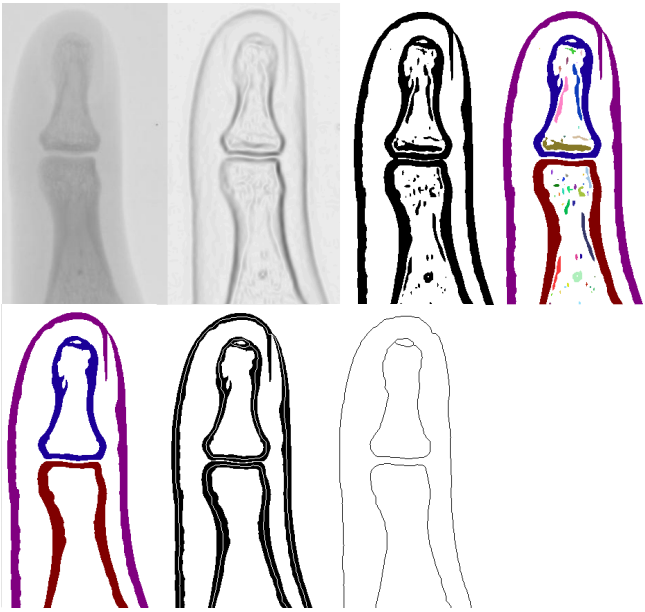

Fig. 9. An example of finger bones extraction and countourization. From left to right and top-bottom: original, after edge detection, after binarization, after finger bones separating and indexation, after small object filtration, after thinning.

(a)

-3	-3	-3	-3	-3	-3	-3
-2	-2	-2	-2	-2	-2	-2
-1	-1	-1	-1	-1	-1	-1
0	0	0	0	0	0	0
1	1	1	1	1	1	1
2	2	2	2	2	2	2
3	3	3	3	3	3	3

(b)

3	3	3	3	3	3	3
2	2	2	2	2	2	2
1	1	1	1	1	1	1
0	0	0	0	0	0	0
-1	-1	-1	-1	-1	-1	-1
-2	-2	-2	-2	-2	-2	-2
-3	-3	-3	-3	-3	-3	-3

(c)

3	2	1	0	-1	-2	-3
3	2	1	0	-1	-2	-3
3	2	1	0	-1	-2	-3
3	2	1	0	-1	-2	-3
3	2	1	0	-1	-2	-3
3	2	1	0	-1	-2	-3
3	2	1	0	-1	-2	-3

(d)

-3	-2	-1	0	1	2	3
-3	-2	-1	0	1	2	3
-3	-2	-1	0	1	2	3
-3	-2	-1	0	1	2	3
-3	-2	-1	0	1	2	3
-3	-2	-1	0	1	2	3
-3	-2	-1	0	1	2	3

Fig. 10. Directional filters for edges of a hand detecting

5 Concluding Remarks

As it has been aforementioned, radiograms preprocessing algorithms are far from satisfactory ones. Therefore, not only already applied methods are tried to be improved but also new approaches are looked for. According to the results described in this paper, it seems that the proposed method gives promising results. It should be emphasized, however, that preprocessing done by humans,

i.e. localization of joints and bones contours is far more effective than the existing algorithms. The human preprocessing is based on the predefined knowledge - an expert knows where bones contours, joint spaces and other characteristic anatomic structures should exist and he estimates the radiograms in the frame of this knowledge. Therefore, it seems that preprocessing algorithm based on the anatomic knowledge, encoded as a type of artificial intelligence system as it was proposed in [1, 2, 17, 24], is a promising approach to medical radiograms preprocessing.

Acknowledgement. This work was financed by the AGH - University of Science and Technology, Faculty of Geology, Geophysics and Environmental Protection, Department of Geoinformatics and Applied Computer Science as a part of statutory project.

References

1. Bielecka, M., Bielecki, A., Korkosz, M., Skomorowski, M., Wojciechowski, W., Zieliński, B.: Application of shape description methodology to hand radiographs interpretation. In: Bolc, L., Tadeusiewicz, R., Chmielewski, L.J., Wojciechowski, K. (eds.) ICCVG 2010, Part I. LNCS, vol. 6374, pp. 11–18. Springer, Heidelberg (2010)
2. Bielecka, M., Skomorowski, M., Zieliński, B.: A fuzzy shape descriptor and interference by fuzzy relaxation with application to description of bones contours at hand radiographs. In: Kolehmainen, M., Toivanen, P., Beliczynski, B. (eds.) ICANNGA 2009. LNCS, vol. 5495, pp. 469–478. Springer, Heidelberg (2009)
3. Bielecki, A., Korkosz, M., Wojciechowski, W., Zieliński, B.: Identifying the borders of the upper and lower metacarpophalangeal joint surfaces on hand radiographs. In: Rutkowski, L., Scherer, R., Tadeusiewicz, R., Zadeh, L.A., Zurada, J.M. (eds.) ICAISC 2010, Part I. LNCS (LNAI), vol. 6113, pp. 589–596. Springer, Heidelberg (2010)
4. Bielecka, M., Bielecki, A., Korkosz, M., Skomorowski, M., Wojciechowski, W., Zieliński, B.: Modified Jakubowski shape transducer for detecting osteophytes and erosions in finger joints. In: Dobnikar, A., Lotrič, U., Šter, B. (eds.) ICANNGA 2011, Part II. LNCS, vol. 6594, pp. 147–155. Springer, Heidelberg (2011)
5. Bielecki, A., Korkosz, M., Zielinski, B.: Hand radiographs preprocessing, image representation In the finger regions and joint space width measurments for image interpretation. Pattern Recognition 41, 3786–3798 (2008)
6. Bottcher, J., Pfeil, A., Rosholm, A., Petrovitch, A., et al.: Digital X-ray radiogrammetry combined with semiautomated analysis of joint space widths as a new diagnostic approach in rheumatoid arthritis: a cross-sectional and longitudal study. Arthritis and Rheumatism 52, 3850–3859 (2005)
7. Choi, S., Lee, G.J., Hong, S.J., Park, K.H., Urtnasan, T., Park, H.K.: Development of a joint space width measurement method based on radiographic hand images. Computers in Biology and Medicine 41, 987–998 (2011)
8. Choi, S., Lee, Y., Hong, S., Lee, G., Kang, S., et al.: Evaluation of inflammatory change and bone erosion using a murine type II collagen-induced arthritis model. Rheumatology International 31, 595–603 (2011)

9. Choi, S., Su-Jin Chae, S., Kang, S., Cheong, Y., Hong, S., Park, H.: Non-invasive screening of progressive joint defects in the type II collagen - induced arthritis animal model using radiographic paw images. Inflammation Research 60, 447–456 (2011)
10. Chun, H., Jun, L., Junwei, H.: Image edge detection method based on the direction feature of fuzzy entropy. In: Proc. 6th International Conference on Natural Computation, pp. 3581–3584 (2010)
11. Davis, L., Theobald, B.J., Toms, A., Bagnall, A.: On the extraction and classification of hand outlines. In: Yin, H., Wang, W., Rayward-Smith, V. (eds.) IDEAL 2011. LNCS, vol. 6936, pp. 92–99. Springer, Heidelberg (2011)
12. He, X.Q., Ran, L.K., Tan, P.C., Jin, J.: Hand radiographs preprocessing and improved k-cosine algorithm in location method for phalangeal key points. Journal of Clinical Rehabilitative Tissue Engineering Research 15, 4817–4820 (2011)
13. Jantan, S., Hussain, A., Mustafa, M.M.: Distal radius bone age estimation based on fuzzy model. In: Proceedings of Conference on Biomedical Engineering and Sciences, IECBES, pp. 427–432 (2010)
14. Kaufmann, J., Slump, C.H., Bernelot Moens, H.J.: Segmentation of hand radiographs by using multi-level connected active appearance models. In: Proceedings of the SPIE, vol. 5747, pp. 1571–1581 (2005)
15. Klooster, R., Hendrics, E.A., Watt, I., et al.: Automatic quantification of osteoarthritis in hand radiographs: validation of a new method to measure joint space width. Osteoarthritis and Cartilage 16, 18–25 (2008)
16. Korkosz, M., Bielecka, M., Bielecki, A., Skomorowski, M., Wojciechowski, W., Wójtowicz, T.: Improved fuzzy entropy algorithm for X-ray pictures preprocessing. In: Rutkowski, L., Korytkowski, M., Scherer, R., Tadeusiewicz, R., Zadeh, L.A., Zurada, J.M. (eds.) ICAISC 2012, Part II. LNCS, vol. 7268, pp. 268–275. Springer, Heidelberg (2012)
17. Ogiela, M.R., Tadeusiewicz, R., Ogiela, L.: Image languages in intelligent radiological palm diagnostics. Pattern Recognition 39, 2157–2165 (2006)
18. Pfeil, A., Botcher, J., Seidl, B.E., Heyne, J.P., et al.: Computer-aided joint space analysis of the metacarpal-phalangeal and proximal-interphalangeal finger joint: normative age-relate and gender-specific data. Skeletal Radiology 36, 853–864 (2007)
19. Pfeil, A., Botcher, J., Schafer, M.L., Seidl, B., et al.: Normative reference values of joint space width estimated by computer-aided joint space analysis CAJSA: The Distal Interphalangeal Joint. Journal of Digital Imaging 21(suppl. 1), 104–112 (2008)
20. Piorkowski, A., Gronkowska-Serafin, J.: Analysis of corneal endothelial image using classic image processing methods. In: The Computer-Aided Scientific Research, XVIII, vol. 217, pp. 283–290. The Works of Wroclaw Scientific Society (2011)
21. Sharp, J., Gardner, J., Bennett, E.: Computer-based methods for measuring joint space and estimating erosion volume in the finger and wrist joints of patients with rheumatoi arthritis. Arthritis and Rheumatism 43, 1378–1386 (2000)
22. Szostek, K., Gronkowska-Serafin, J., Piorkowski, A.: Problems of corneal endothelial image binarization. Schedae Informaticae 20, 211–218 (2011)
23. Staniszewska-Varga, J., Szymanska-Jagiello, W., Luft, S., Korkosz, M.: Rheumatic diseases atlas. Medycyna Praktyczna, Kraków (2003) (in Polish)
24. Tadeusiewicz, R., Ogiela, M.R.: Picture languages in automatic radiological palm interpretation. International Journal of Applied Mathematics and Computer Science 15, 305–312 (2005)

Cruciate Ligaments of the Knee Joint in the Computer Analysis

Piotr Zarychta

Faculty of Biomedical Engineering, Silesian University of Technology, Zabrze, Poland
piotr.zarychta@polsl.pl

Abstract. The main aim of this research is the feature vector of the cruciate ligaments finding. This feature vector has to clearly define the ligaments structure and make easier diagnose their. The feature vector finding is based on the successive steps in extraction process of both anterior and posterior cruciate ligaments. In the first stage a region of interest including cruciate ligaments (CL) is outlined. The automatic method of location of the CL on the T1-weighted (T1W) MRI knee images is based on fuzzy C-means (FCM) algorithm with median modification. The next step of that process is an extraction of the cruciate ligament structure using the fuzzy connectedness approach. In the last stage the feature vector is built.

Keywords: feature vector of the cruciate ligaments, cruciate ligaments, fuzzy c-means, fuzzy connectedness.

1 Introduction

Cruciate ligaments (Anterior Cruciate Ligament - ACL and Posterior Cruciate Ligament - PCL) are a very important anatomical structure of the knee joint. They are main stabilizers of the knee joint in the sagittal plane. Together with the shape of articular surface and muscles ensure proper arthrokinematics. They play a very important role during the passive and active motion. During passive motion of the knee joint cruciates help to change rolling into sliding movements. and during active motion resist translations and reduce shear forces. It is worth remembering that cruciate ligaments with collateral ligaments ensure rotational stability of the extended knee joint [1].

Although, the first surgical reconstruction of the cruciate ligament has been executed about one hundred years ago (Mayo Robson, General Infirmary in Leeds, 1895), the dispute over the appropriate treatment method of the instability of the knee joint ended in a general disagreement [2]. The success of cruciate ligaments reconstructive procedure depends on many factors, mainly an accurate diagnosis based on the location, segmentation and 3-dimensional visualization of the anatomical structures. Construction of a vector containing an appropriate set of features can improve the diagnosis yet.

E. Pietka, J. Kawa, and W. Wieclawek (eds.), *Information Technologies in Biomedicine, Volume 3*, Advances in Intelligent Systems and Computing 283,
DOI: 10.1007/978-3-319-06593-9_7,

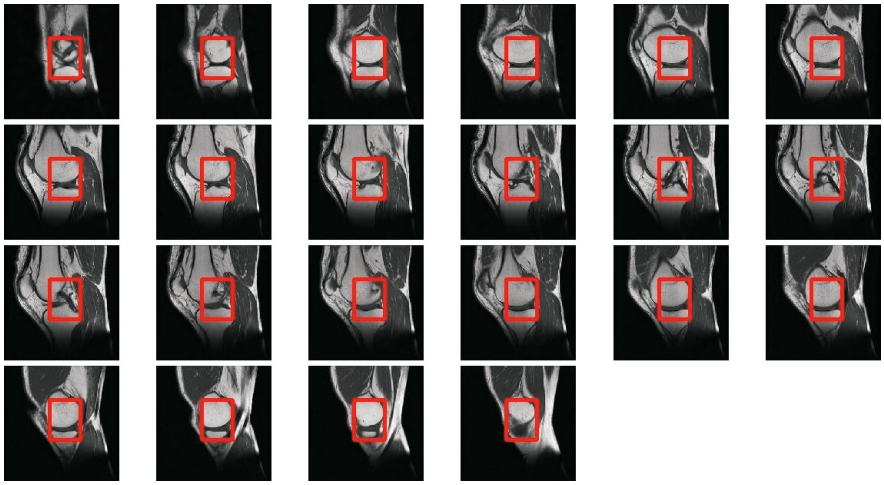

Fig. 1. T1W MRI series - signal from data base clinical hospital with 2-dimensional region of interest including the ACL and PCL

Magnetic resonance imaging (MRI) is today the primary method for the diagnostics of the knee joint cruciate ligaments lesions. However conventional radiography is an irreplaceable method in evaluation of the bone injuries. In case of soft tissue injuries, especially intra knee joint structures, MRI is the method of choice. Therefore in this paper, computer analysis of the cruciate ligaments is shown on the example of MRI of the knee joint (Fig. 1).

In this paper the methodology finding 2-dimensional region of interest including cruciate ligaments (ACL and PCL), the extraction process of the cruciate ligaments structure from T1W MRI series are not widely described. The exhaustive description can be found in [3, 4]. This article discusses the selection of the feature vector and their impact on the diagnostics of the cruciate ligaments lesions.

2 Methodology

In order to lower of the computational complexity and to increase of the efficiency an automatical procedure of the extracting 2-dimensional region of interest (ROI) that include the anterior and posterior cruciate ligaments structures has been implemented (Fig. 1). This procedure has been based on the analysis of the T1-weighted MRI slices in a sagittal series (the resolution of the T1-weighted MRI slices of the knee joint is usually 256×256 pixels) and the processed area has been reduced meanly three times (the average length of the ACL and PCL 2D ROI is about 100×100 pixels). The 3-dimensional ROI including the anterior and posterior cruciate ligaments of the knee joint is obtained by mapping the 2D ROI on all of the T1-weighted MRI slices of the knee joint. The 3D ROI is presented in Fig. 2.

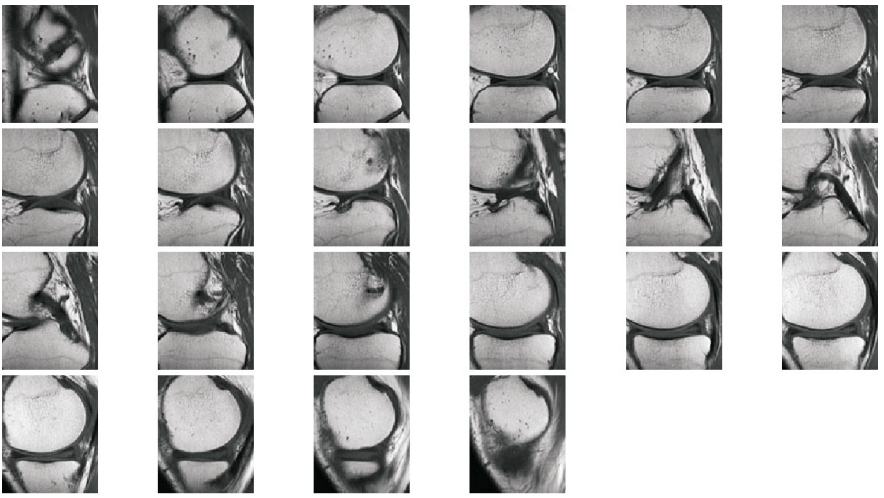

Fig. 2. The 3-dimensional ROI including the ACL and PCL

In this study the location procedure of the ACL and PCL on the T1-weighted MRI slices of the knee joint based on the entropy and energy measures of fuzziness and Fuzzy C-Means (FCM) algorithm with median modification is implemented. This procedure has been widely described in [3, 4].

The segmentation process of the ACL and PCL structures based on a fuzzy connectedness concept is described in Section 3 and results are presented in Section 4.

The block diagram of the presented methodology providing the major outline of the overall algorithm is given in Fig. 3.

3 ACL and PCL Structures Segmentation

In this paper the segmentation process of the anterior and posterior cruciate ligaments structures used a fuzzy connectedness concept. In the literature can find the generalized definition of fuzzy connectedness [5]. This definition is based on the fuzzy affinity relation and introduces an iterative method, permitting the fuzzy connectedness to be determined with respect to the chosen image pixel - seed point. This paper is based on the simplified graph-based view for Z^2 [6], using a digital topology approach. Let $z_i = (z_{i1}; z_{i2})$ denote an image pixel, and $f(z_i)$ its signal intensity. Let all the image pixels z_i constitute the nodes of a graph. In the practical approach, within the graph, each pixel is connected with all its spatially adjacent pixels. The adjacency may be defined in terms of a 2D fuzzy relation, but usually an intuitive [6] crisp relation of 9- or 25-connectedness is used. Every direct link $z_i - z_j$ in the graph has the strength (assigned to it) equal to the value of the reflexive and symmetric fuzzy affinity relations for two connected nodes $mf_{\kappa\upsilon}(z_i; z_j)$. The fuzzy affinity relation models

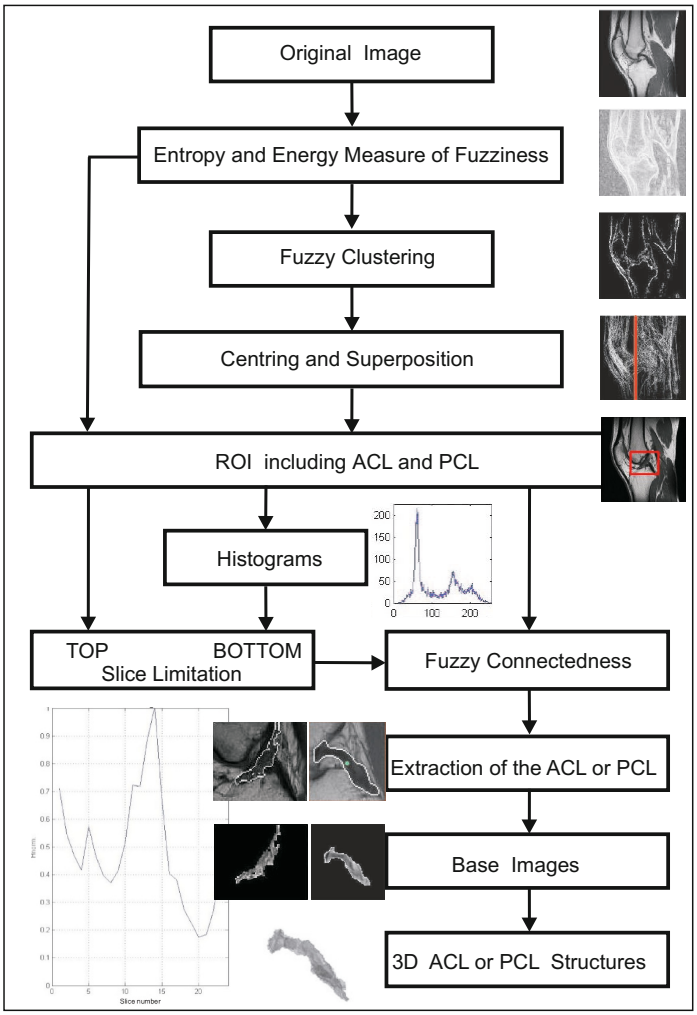

Fig. 3. Block diagram

the similarity of adjacent pixels. Within the graph, for each two pixels z_k and z_l, a path consisting of zero or more links can be found. The set of all existing paths from z_k to z_l is denoted as $P_{z_k z_l}$. The strength $mf_N(p)$ is assigned to each path p from $P_{z_k z_l}$, as the strength of its weakest link, i.e. the lowest value of affinity for two constituting nodes ($[0, 1]$). The fuzzy connectedness can then be defined as a fuzzy relation

$$\forall z_k, z_l : mf_\kappa(z_k, z_l) = \max_{p \in P_{z_k z_l}} [mf_N(p)]. \tag{1}$$

The object segmentation is possible by thresholding the fuzzy connectedness relation (FC-based labelling and object extraction) or by comparing the fuzzy connectedness determined with respect to the given segmentation seed points belonging to the object and background (relative FC approach) [7]. In both direct, and relative FC-based segmentation tasks, the fuzzy affinity $mf_{\kappa\upsilon}$ is used to model the notion of similarity of adjacent pixels within the extracted object. Usually [5] a membership function is employed, depending on the signal level of compared pixels, the local signal gradient and the properties of the extracted object (defined in terms of mean and standard deviation parameters)

$$mf_{\kappa}(z_k, z_l) = \begin{cases} 1 & \text{if } z_k = z_l \\ \omega \cdot G_1(z_k, z_l) + (1-\omega) \cdot G_2(z_k, z_l) & \\ \quad \text{if } z_k \neq z_l \text{ and adjacent} & \\ 0 & \text{otherwise} \end{cases}, \tag{2}$$

where $\omega \in [0;1]$ and G_1, G_2 are selected from

$$g_1(z_k, z_l) = \exp\left((-1) \cdot \frac{1}{2s_1^2}\left(\frac{f(z_k) + f(z_l)}{2} - m_1\right)^2\right), \tag{3}$$

$$g_2(z_k, z_l) = \exp\left((-1) \cdot \frac{1}{2s_2^2}(|f(z_k) - f(z_l)| - m_2)^2\right), \tag{4}$$

$$g_3(z_k, z_l) = 1 - g_1(z_k, z_l), \tag{5}$$

$$g_4(z_k, z_l) = 1 - g_2(z_k, z_l). \tag{6}$$

Functions $f(z_k)$ and $f(z_l)$ denote the signal levels of z_k and z_l [7] and the affinity parameters m_1, s_1, m_2 and s_2 correspond to the intensity average and standard deviation, respectively.

4 Numerical Results

The researches have been tested on 68 clinical T1-weighted MRI studies. This group consists of 56 healthy (e.g. Fig. 2) and 12 pathological (e.g. Fig. 6) cases of the anterior and posterior cruciate ligaments. On the basis of the testing studies it can be prove the following elements. On the basis of comparing the original T1-weighted MRI slices of the knee joint with the segmented ACL structures the radiologists stated that in 63 (92%) cases the proposed anterior cruciate ligament segmentation and extraction method yielded correct results (e.g. Fig. 4c). The evaluation has been performed by two radiologists and in 63 studies (92%) the ACL segmentation has pasted the test. Quite similar results were obtained for the PCL structures. The radiologists stated that in 62 (91%) cases the proposed posterior cruciate ligament segmentation and extraction method yielded correct results (e.g. Fig. 5c).

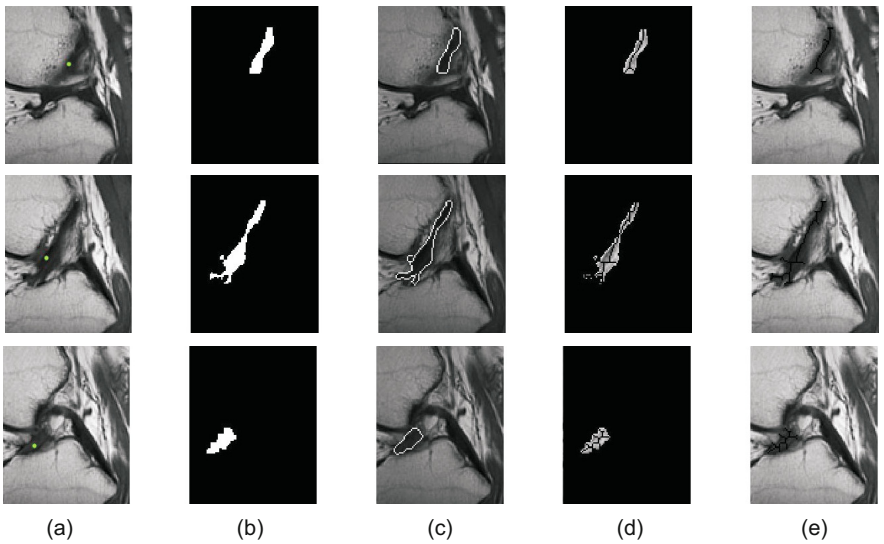

Fig. 4. Stages in the segmentation and extraction process of the ACL: (a) original image with seed point, (b) result after fuzzy connectedness operation with respect to the seed point and morphological operations (c) result superimposed onto the original image (d) skeleton of the ACL structure (e) skeleton superimposed onto the original image

The incorrect location and lack of capacity to perform the correct segmentation of the cruciate ligaments has been caused by the following factors: ligament displaced caused by the broken thighbone (2 cases), a lack alignment of the thighbone and tibia along the same axis (3 cases) and a location of the knee joint in the extreme part of the slice (1 case).

The breaking of thighbone structures in the vicinity of the knee joint excludes the possibility of using the proposed algorithm for finding the 2-dimensional ROI, which includes the cruciate ligament. This kind of pathology is not a common case. Its diagnosis is not a difficult problem for radiologists and does not require from them a time-consuming analysis of the T1-weighted MRI slices of the knee joint.

The presented methodology does not yield correct results in case of a lack of thighbone and tibia location along the same axis. The envelop of the family of selected profiles widely described in [3], allows for a deviation of twenty degrees between both bones. The deviation of more than twenty degrees was found in patients with degeneration in the knee joint and causes an incorrect location of the 2-dimensional ROI.

Ligamentous injuries of the knee are growing both social and medical problems. Injuries of the cruciate ligaments are diagnosed on the base of MRI study. However, each medical study can be misinterpreted. The most important criterium

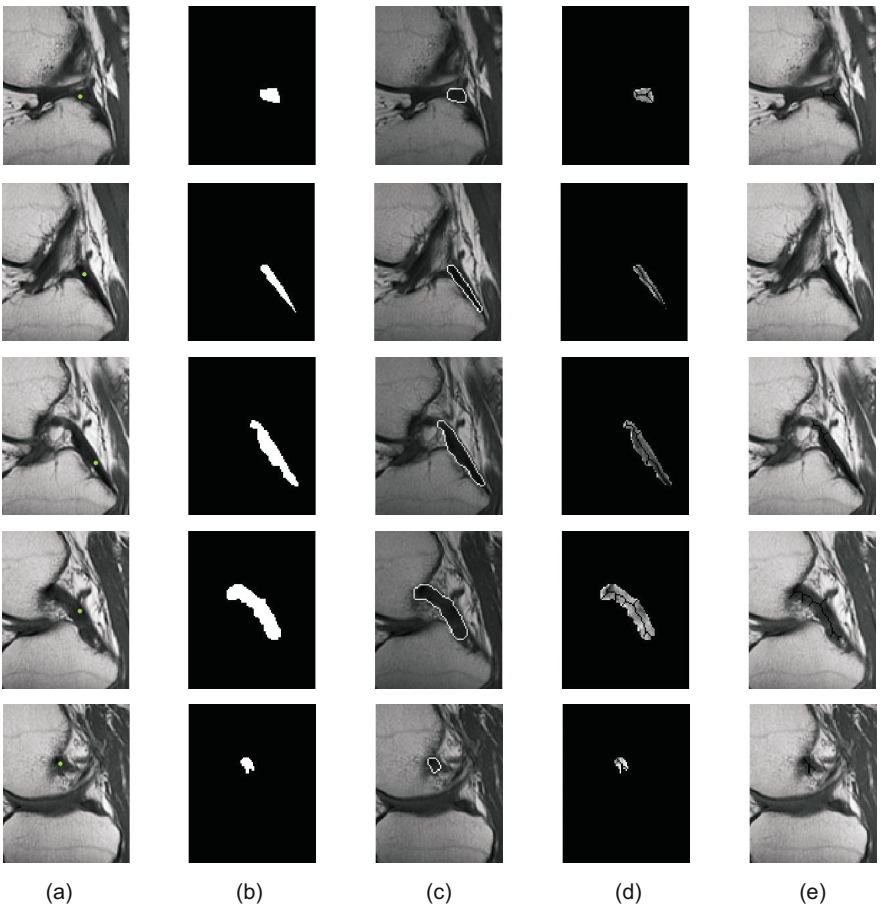

Fig. 5. Stages in the segmentation and extraction process of the PCL: (a) original image with seed point, (b) result after fuzzy connectedness operation with respect to the seed point and morphological operations (c) result superimposed onto the original image (d) skeleton of the PCL structure (e) skeleton superimposed onto the original image

in the cruciate ligaments diagnosis are the surface area and shape cruciate structures. Therefore the feature vector has to include the surface area and skeleton of the segmented and extracted structures of the cruciate ligaments (Fig. 4d,e and Fig. 5d,e).

Comparison of surface area normal and pathological structures of the cruciate ligaments (for the corresponding slices) gives the following results.

The surface area value for the case of the pathological structures can be much lower or much higher than the corresponding values for the healthy case. Considerably lower values are obtained for a complete disruption of the CL structures.

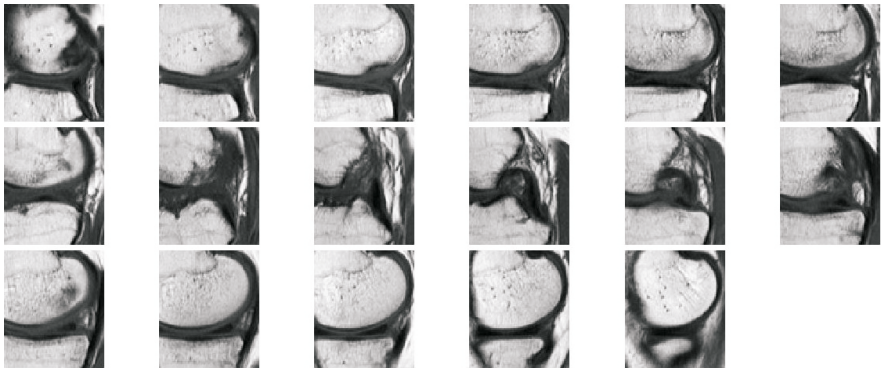

Fig. 6. The 3-dimensional ROI including the pathological ACL and PCL

Then the segmented is just one part completely disrupted the structure of CL. Much higher values of the surface area are obtained for a incomplete disruption of the CL structures. This is associated with the case of the partial damage.

The injuries of the anterior cruciate ligaments of the knee joint are much more often than the injuries of the posterior cruciate ligaments. Its injuries diagnosis is based upon several criteria dependent on the type of injury and the time

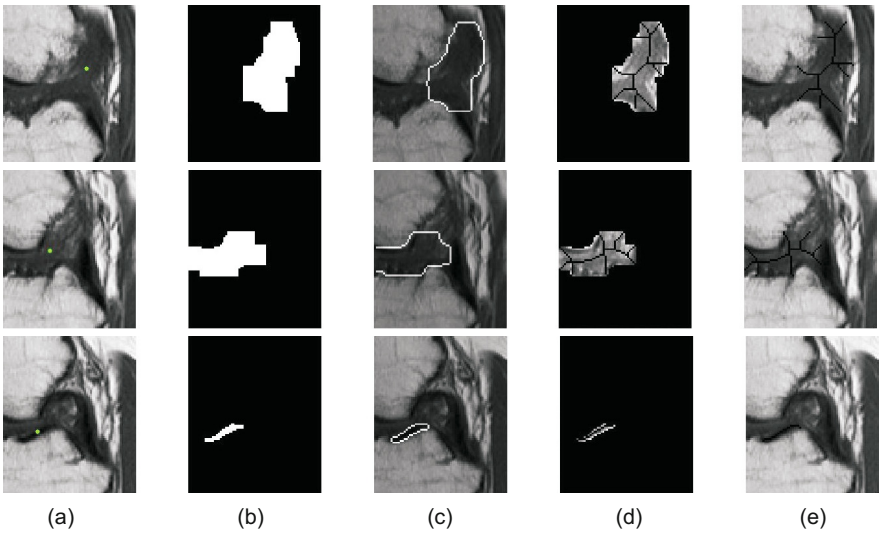

Fig. 7. Stages in the segmentation and extraction process of the pathological ACL: (a) original image with seed point, (b) result after fuzzy connectedness operation with respect to the seed point and morphological operations (c) result superimposed onto the original image (d) skeleton of the ACL structure (e) skeleton superimposed onto the original image

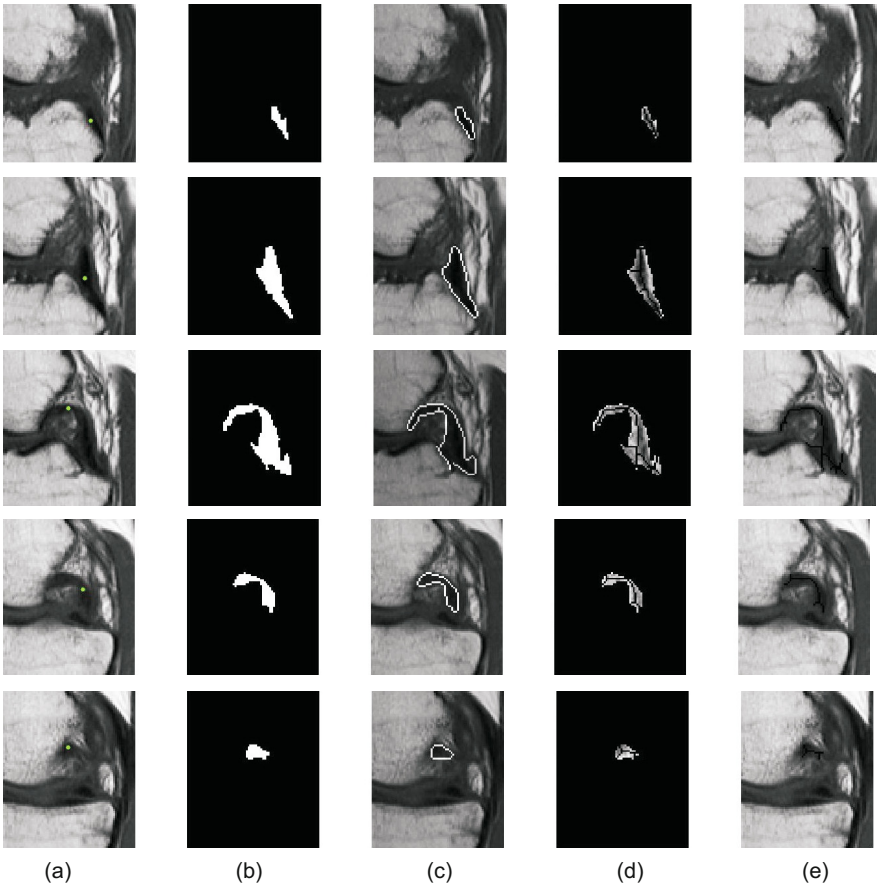

Fig. 8. Stages in the segmentation and extraction process of the pathological PCL: (a) original image with seed point, (b) result after fuzzy connectedness operation with respect to the seed point and morphological operations (c) result superimposed onto the original image (d) skeleton of the PCL structure (e) skeleton superimposed onto the original image

elapsed from the ruptured ligament injury. The basic criteria used in the injuries diagnosis of the ACL and PCL are following: increase the ligament signal in the entire volume in all of sagittal slices and swelling ligament. Often, an additional criterion of the PCL injury is S-shape of the ligament. Therefore, the skeleton of the segmented structure of PCL is another important feature.

Ligament rupture on the type of "shaving brush" in opinion two experts: radiologist and orthopaedist is the most common injuries of the anterior cruciate ligament, and also the posterior. It is characterized in the MRI study by massive swelling and fraying ligament fibers over their entire length.

Additionally, the partial damage in case of the PCL is characterized by irregular signal of the ligaments in MRI study, swelling and disruption following structures of the CL [8].

5 Conclusion

The automatic method of location of the CL on the T1W MR knee images, and segmentation and extraction procedure based on the of the fuzzy connectedness approach in my opinion seem to be a very effective and promising method in the 3-dimensional visualization process of that structure. The MRI study is a gold standard in diagnostics of the cruciate ligaments injuries. However, keep in mind the consequences of performing this study in the wrong class equipment, or in the wrong way. Thus, each additional element supporting a diagnosis is important. Such is the role of the proposed feature vector. This vector is the next stage in computer aided diagnosis of the knee joint, including the three-dimensional models of the following structures: bones as well as posterior and anterior cruciate ligaments.

References

1. Pasierbiński, A., Jarząbek, A.: Biomechanika więzadeł krzyżowych. Acta Clinica 4(1), 284–293 (2001)
2. Dziak, A.: Uszkodzenia więzadeł krzyżowych kolana. Acta Clinica 4(1), 271–274 (2001)
3. Zarychta, P.: Location and 3D visualization of the cruciate ligament in the MR knee images on the basis of fuzzy logic. PhD Thesis, Silesian University of Technology, Gliwice (2006)
4. Zarychta, P., Zarychta-Bargieła, A.: Anterior and posterior cruciate ligament-extraction and 3D visualization. In: Piętka, E., Kawa, J. (eds.) Information Technologies in Biomedicine. AISC, vol. 69, pp. 115–122. Springer, Heidelberg (2010)
5. Udupa, J., Samarasekera, S.: Fuzzy Connectedness and Object Definition: Theory, Algorithms, and Applications in Image Segmentation. Graph. Models Image Processing 58, 246–261 (1996)
6. Eckhardt, U., Latecki, L.: Topologies for the Digital Spaces Z^2 and Z^3. Computer Vision and Image Understanding 90, 295–312 (2003)
7. Kawa, J., Pietka, E.: Automated Fuzzy-Connectedness-Based Segmentation in Extraction of Multiple Sclerosis Lesions. In: Pietka, E., Kawa, J. (eds.) Information Technologies in Biomedicine. ASC, vol. 47, pp. 149–156. Springer, Heidelberg (2008)
8. Czyrny, Z.: Diagnostyka uszkodzeń więzadeł krzyżowych w badaniu rezonansu magnetycznego. Acta Clinica 4(1), 331–339 (2001)

Trabecular Bone Microstructure Investigation

Paulina Popik[1], Marcin Binkowski[1], Łukasz Cyganik[1], Filip Bolechała[2], Roman Nowak[3], Antoni John[4], and Zygmunt Wróbel[1]

[1] X-ray Microtomography Lab, Department of Biomedical Computer Systems, Institute of Computer Science, Faculty of Computer and Materials Science, University of Silesia, 75 Pułku Piechoty 1, budynek H, segment C, pok. P7, 41-500 Chorzów, Poland
{ppopik,marcin.binkowski,cyganik,zygmunt.wrobel}@us.edu.pl
[2] Medical College, Jagiellonian University, Grzegórzecka 16, 31-531 Kraków, Poland
[3] Medical University of Silesia, Medyków 1, Sosnowiec, Poland
[4] Institute of Computational Mechanics and Engineering, Silesian University of Technology, Konarskiego 18A, 44-100 Gliwice, Poland

Abstract. Assessment of bone histomorphometry allows to determine the condition of the bones and thus to predict the occurrence, course, treatment planning and recovery for certain conditions within the skeletal system. Noninvasive acquisition of information about the structure of the bone on the basis of image data makes it possible in a relatively fast and easy way to determine a number of key parameters describing the bone. As part of the study, the number of histomorphometric parameters for samples from different patients and various areas of cancellous bone were determined and compared based on images from X-ray microcomputed tomography. Samples of cancellous bone, in the form of cubes, derived from healthy subjects and patients diagnosed with a osteoarthritis and also from the core of the femoral head and from peripheral areas. The results demonstrate the significant differences in the structure of trabecular bone tissue derived from different people.

Keywords: trabecular bone, histomorphometry, X-ray microcomputed tomography.

1 Introduction

The acquisition of all the information, also about human anatomy and physiology is becoming faster and easier. This is caused by the development of technology which translates into ever wider and more accurate knowledge of the world. In the field of orthopaedics the evaluation of structural properties of bone tissue is carried out for many years in a non-destructive manner by means of medical imaging [1–4]. In clinical practice in line with WHO recommendations, the most important indicator of the structure of the bone is a bone mineral density (BMD), calculated on the basis of image data. Determination of additional bone histomorphometric parameters including: bone volume/total volume (BV/TV), trabecular thickness ($Tb.Th$), trabecular separation ($Tb.Sp$), porosity allows for

E. Pietka, J. Kawa, and W. Wieclawek (eds.), *Information Technologies in Biomedicine, Volume 3*, Advances in Intelligent Systems and Computing 283,
DOI: 10.1007/978-3-319-06593-9_8,

comprehensive assessment of bone microarchitecture and thereby to determine whether it is in the physiological state, whether there is defined within it a pathology [5–11]. These parameters describe the dimensions of the elements of the bone structure quantitatively (*Tb.Th*, *Tb.N*, *BV*, *TV*, *connectivity*), their distance apart (*Tb.Sp*), characterize pores occurring (*porosity*), determine the degree of anisotropy of the structure *(DA*) whereas structure model index indicates the relative prevalence of rods and plates in a 3D structure such as trabecular bone. Nevertheless, in order to obtain additional information for instance about the mechanical properties of bone a number of histomorphometric parameters should be the set of input data for the three-dimensional model of cancellous bone structure followed by mechanical testing analysis using FEA. From the standpoint of clinical practice, identifying a set of histomorphometric parameters considerably facilitates the description and characterization of well-known, as well as the new disorders of the skeletal system. In addition improves the diagnosis, treatment, rehabilitation, and prevention in the field of orthopaedics also the planning and conducting of many surgical procedures.

Research carried out in the techniques such as Computed tomography (CT) and X-ray microcomputed tomography (XMT) are the main tool for assessing the condition as well as characterizing the mechanisms and course of various diseases of bone tissue [2, 4, 12–14]. Using XMT the images of individual cross-sections of the tested object are obtained with high spatial resolution which allows to create three-dimensional models based on surface or volume rendering. On the basis of 2D and 3D images the parameters of the structure are calculated with high accuracy corresponding to a given resolution [8, 9, 12, 15–17].

The aim of this study was to investigate the structural properties of human trabecular bone for samples of different origins determining microstructure observed based on XMT imaging. Evaluation of the structure was based on the analysis of the histomorphometric parameters describing the spatial structure and relationships between the components of trabecular bone in details. Range of histomorphometric parameters of cancellous bone for extreme clinical cases was calculated in order to determine the dispersion of possible results for different samples.

2 Material and Methods

2.1 Sample Preparation

From 57 trabecular bone samples extracted from 14 femoral heads a three with extremely different origin, both in terms of location as well as the health of the donor [see Table 1] were selected. Due to the fact that the individual femoral heads differed from each other in internal structure and the condition of surface, the number of samples prepared in a further step was different for the various bones. Eleven femoral heads were taken from patients undergoing total hip replacement surgery (Provincial Specialist Hospital No. 5 in Sosnowiec, Poland) and other three from cadavers (Department of Forensic Medicine, Jagiellonian University Medical College in Cracow, Poland). The donors were aged 38-77. The

hip specimens from the hospital were collected by permission of the Bioethics Committee from the Medical Silesian University in Katowice, Poland.

In the first step of preparation the main trabecular direction (MTD) was identified and marked on the femoral head using the XMT scout views (Figure 1 a). All the cubic specimens were cut out from the femoral heads, using a precision saw machine with a diamond-coated cut-off wheel (STRUERS Secotom – 15, Willich, Germany, 2200 rpm, $f = 0.1$ mm/s). The trabecular bone layers, with the target thickness of the layers of 10 mm, were cut out of the femoral heads according to MTD. After the MTD was marked on the each layer afresh the cubic samples were cut out of individual layers (Figure 1 b). Subsequently, the spatial orientation of the specimens in the femoral heads was also marked on the surface: a single dot – planes parallel to the anterior-posterior axis, two dots – planes perpendicular to MTD (Figure 1 c,d).

All the cut out specimens were fixed in 70% ethanol and stored in 4^oC.

Table 1. Data concerning selected samples of cancellous bone

Sample number	The patient's age	Sex of the patient	Condition of the patient	Location in the femur head
1	70	female	advanced osteoarthritis, hip endoprosthesis	core
2	74	female	osteoarthritis	side
3	77	male	healthy	border region between core and side

2.2 X-ray Microcomputed Tomography Scanning

All the specimens were scanned using laboratory ex-vivo (also called an industrial) small size X-ray microtomography scanner (v|tome|x s, GE Sensing & Inspection Technologies, Phoenix|x-ray, Wunstorf, Germany). The device is a scanner equipped with both tungsten cathode (filament) and anode (target) consisting of two open X-ray tubes: transmission nanotube (180kV) and direct tube (240kV) which was applied in this study. The polychromatic X-ray cone-beam is used there. The specimens are located on the rotary table in the scanner chamber. The results of X-ray beam attenuation propagated through the sample is recorded by the 16" Flat Panel Detector (2.024x2.024 pixels, pixel size $= 200\mu m^2$). The Datos 2.0 software provided by the manufacturer was applied to obtain projection and image reconstruction. The greyscale was stored using 256 gray levels (8 bits per voxel) which resulted in a single set of data volume of 5.491GB. The image of all samples was reconstructed in cubic grid with dimensions 1700x1900x1700 voxels. Identical for all samples the size of the grid provided repetitive measurement conditions.

In order to obtain the view of the total specimen to identify the main trabecular direction (MTD) the whole femoral heads were preliminary imaged (scout

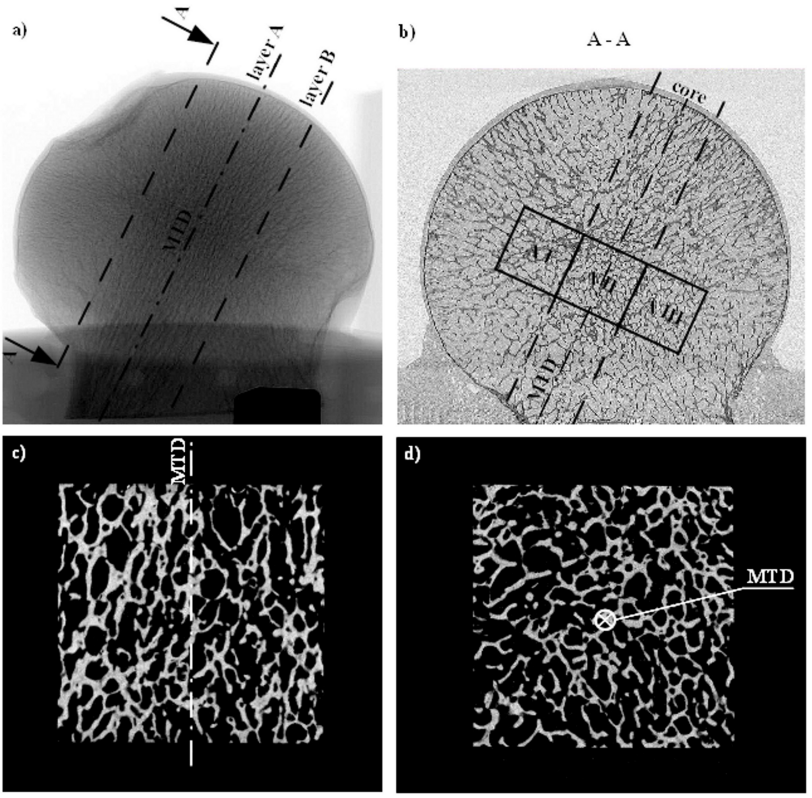

Fig. 1. Sample preparation: (a) Scout view of femoral head showing the main trabecular direction (MTD), the position of layers and the position of A-A cross-section, (b) A-A cross-section showing the surface of layer A with marked position of specimens: the area between the dashed lines is classified into the "core" category, (c) XMT image of a plane of a cubic specimen, perpendicular to the MTD, (d) XMT image of a plane of a cubic specimen in the MTD

view). Having the proper orientation of MTD, the cubic samples dissected from the specimen were tested using higher scanning resolution. The scanning parameters were presented in Table 2.

2.3 Histomorphometric Parameters Calculating

Calculation of the histomorphometric parameters describing cancellous bone tissue was performed using the software CT Analyser 1.13.2.1 + (SkyScan, Belgium). In order to obtain the best results of morphometric measurements a number of tests for eight different sizes ROI's, that are multiples of three-dimensional image voxel size (10.247 microns) were performed on a random sample. On the basis of the results a ROI size of 9499x9499 μm^2 was selected to perform the

Table 2. Scan parameters for femoral heads and the cubic samples

		Scanned object	
		Femur head	Cubic sample
Scan parameters	Magnification	5.985	19.518
	Voxel size [μm]	33.416	10.246
	Scan time [min]	34	26
	Number of images	1000	
	Image size	2024x2024	
	Timing [ms]	500	
	Average	3	2
	Skip	1	
	Voltage [kV]	140	70
	Current [μA]	200	140
	Filter	Cu 0.5	Cu 0.1

calculations for all samples of cancellous bone (Figure 2). The whole ROI is included in the sample area with the elimination of peripheral areas, which can cause undesirable edge effects associated with the machining process at a cutting samples (inequalities, detached pieces). In addition, through the use ROI size smaller than the dimensions of the sample the surface areas of the samples contaminated with correction fluid for determining the directions of the forces acting on the bone was eliminated. As a result elements of the corrector differing in structure, chemical composition and properties will not be taken into account during the subsequent research, and thus will not adversely floated on the final results.

Histomorphometric parameters are calculated by CT-analyser in 3D based on a volume model. For VOI dimensions of 9499x9499x9499 μm^3 (927x927x927 pixels) with the same range of thresholding for all samples (130–190 on a scale of 0 to 255) the following histomorphometric parameters were computed: bone volume (BV) [mm^3], total volume (TV) [mm^3], BV/TV [%], trabecular thickness ($Tb.Th$) [μm], trabecular number ($Tb.N$) [μm^{-1}], trabecular separation ($Tb.Sp$) [μm], Structure Model Index (SMI), total porosity [%], Degree of anisotropy (DA), Connectivity. The 3D volume measurement of BV and TV is based on the hexahedral marching cubes volume model of: the binarised objects within the VOI for BV and the whole VOI for TV. BV/TV parameter is the proportion of the VOI occupied by binarised solid objects. $Tb.Th$ is determined as an average of the local thickness at each voxel representing bone, $Tb.N$ implies the number of traversals across a trabecular structure made per unit length on a linear path through a trabecular bone region, and $Tb.Sp$ is the thickness of the spaces as defined by binarization within the VOI. SMI indicates the relative prevalence of rods and plates in a 3D bone structure and also involves a measurement of surface convexity. Porosity is the area of fully enclosed spaces as a percent of the total area of binarised objects and isotropy is a measure of 3D symmetry or the presence or absence of preferential alignment of structures along a particular directional axis and it's expressed by DA parameter.

This set of parameters was selected to answer the following questions: What is the amount of the bone tissue in the different locations of femoral head? How the shape and number of trabeculae is changing with the location? How much the anisotropy of trabecular bone is changing from the core to the peripheral areas? Getting the answers to the questions above is significant for instance in accurate prediction of mechanical strength of the trabecular bone and to identify the pathological conditions.

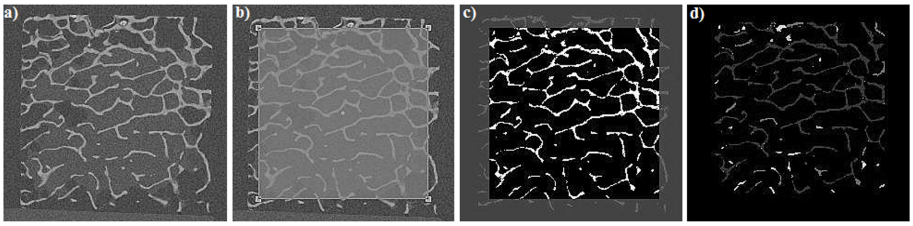

Fig. 2. The individual steps of preparing a 3D model to determine the histomorphometric parameters in the CT Analyser: (a) the loading of the reconstructed image of the sample, (b) selecting ROI, (c) binarization within the area, (d) calculations

3 Results

Summary of results of histomorphometric parameters of the selected samples are presented in Table 3.

The analysis of the results obtained for samples from different patients and from different places in the femoral heads resulted in the following observations. The biggest differences in the values of individual histomorphometric parameters occur between samples 1 and 2, while the results for sample No. 3 are in the range where lower and upper limits are the results of samples 1 and 2 (the total volume is the same for all samples due to the identical ROIs).

For the ratio of BV/TV the maximum difference $diff_{BV/TV} = 35.562\%$, maximum difference percentage $percdiff_{BV/TV} = 292.757\%$, and the mean value $mean_{BV/TV} = 28.191\%$. In the case of BV parameter $diff_{BV} = 304.804mm^3$, $percdiff_{BV} = 292.757\%$, $mean_{BV} = 241.626mm^3$. Results for the $Tb.Th$ are: $diff_{Tb.Th} = 36.227\mu m$, $percdiff_{Tb.Th} = 33.806\%$, $mean_{Tb.Th} = 125.314\mu m$, for $Tb.N$ are: $diff_{Tb.N} = 0.0022\mu m^{-1}$,$percdiff_{Tb.N} = 194.690\%$, $mean_{Tb.N} = 0.0021\mu m^{-1}$, and for $Tb.Sp$: $diff_{Tb.Sp} = 568.101\mu m$,$percdiff_{Tb.Sp} = 221.381\%$, $mean_{Tb.Sp} = 581.185\ \mu m$.

The remaining results: $diff_{SMI} = 12.686$, $percdiff_{SMI} = 1237.619\%$, $mean_{SMI} = -6.010$, $diff_{porosity} = 35.562\%$, $percdiff_{porosity} = 68.009\%$, $mean_{porosity} = 71.808\%$, $diff_{DA} = 0.815$, $percdiff_{DA} = 59.063\%$, $mean_{DA} = 1.717$, and $diff_{connectivity} = 395975$, $percdiff_{connectivity} = 361.146\%$, $mean_{connectivity} = 289029$.

Table 3. Histomorphometric parameters for individual samples of cancellous bone

Parameter, unit	Sample number			Maximum differences value	Maximum differences percentage	The mean value
	1	2	3			
BV/TV, %	47.709	12.147	24.716	35.562	292.757	28.191
BV, mm^3	408.919	104.115	211.846	304.804	292.757	241.626
TV, mm^3	857.094	857.094	857.094	-	-	857.094
Tb.Th, μm	143.391	107.163	125.387	36.227	33.806	125.314
Tb.N, μm^{-1}	0.00333	0.00113	0.00197	0.0022	194.690	0.0021
Tb.Sp, μm	256.616	824.717	662.222	568.101	221.381	581.185
SMI	-13.711	-1.02503	-3.29605	12.686	1237.619	-6.010
Total porosity, %	52.290	87.852	75.283	35.562	68.009	71.808
DA	1.380	2.196	1.576	0.815	59.063	1.717
Connectivity	505619	109644	251824	395975	361.146	289029

4 Discussion

The conducted research indicates a strong relationship between trabecular bone microstructure and area of sampling as well as the physical condition of the patient.

The most compact microstructure within the meaning of the spatial was distinguished sample No. 1. It is characterized by relatively high: BV/TV ratio, bone volume, trabecular thickness, trabecular number per unit area and connectivity. The values of: trabecular separation, structure model index, total porosity and degree of anisotropy are lower than the results of samples No. 2 and 3. The results obtained for this case are affected by the fact that the sample came from the centre of the femoral head where the greatest loads are transferred. The patient from whom the sample was taken suffered from advanced osteoarthritis which also resulted in an increase in trabecular thickness, BV/TV ratio etc. which is confirmed by the literature [14, 18, 19].

For the sample cut from a peripheral area of the femoral head (No. 2) the results of BV/TV ratio differed by 292.757% from specimen No. 1. Similarly, in the case of other parameters the values of which indicate a significantly higher porosity of the microstructure at the level of 87.852%. Furthermore, trabecular number per unit area, trabecular thickness and connectivity are lower than for sample No. 1 and trabecular separation, degree of anisotropy and structure model index are higher.

Individual parameter values for the sample No. 3 obtained in the studies are in the range of values obtained for the other two samples. This confirms the rule that structure parameters are dependent on the location of the sample in the whole bone. The trabeculae in the middle of the femoral head are more numerous, thicker and more densely spaced. At the edge of the femoral head occurs a opposite phenomenon and also a greater anisotropy. Indirectly, this fact can be observed at the stage of the XMT scanning (see Figure 1 a,b). Significant impact on the differences between the results for the sample No.

3 and the samples 1 and 2 is the fact that it comes from a man qualified as a healthy person. For this specimen there is no an excessive increase in bone volume or its local weakness characteristic or various stages of osteoarthritis as demonstrated by samples 1 and 2.

The study is a demonstration of the level of differences in the properties of trabecular bone depending on the origin and the position of the specimen in the femoral head. The weakness of the work is small number of the specimens and for this reason the statistical analysis have not been performed. However, for demonstration purposes three specimens are sufficient.

The different results for different regions of the femoral head point to strong connection between microarchitecture of cancellous bone and its location in femoral head. Significant differences in values are also observed for cases of degenerated bone in the course of osteoarthritis characterized by changes in bone structure. The intensity of increasing bone decreases from the core towards the peripheral areas of bone with the development of osteoarthritis [20, 21]. The conducted as part of the present study research shows that the scope of histomorphometric parameters emanating from different patients or from various parts of the body is wide. Therefore, in the research the medical data of patients and the location of sampling must always be taken into account. The obtained results suggest that the differences in the properties of trabecular bone may be high and the quantitative research with more specimens and statistical analysis should be performed.

The paper presents the results indicating that the range of variation of the human histomorphometric parameters of cancellous bone is very wide, which should pay particular attention to conducting research in this area, which is often neglected by authors of similar works. By accessing to a large number of patients and thereby the possibility of obtaining a large number of samples those with extreme values were chosen. Thanks to this a real range of parameter values for bone conditions from physiological to a pathological was determined. Paying attention to the significant differences in the histomorphometric parameters in a direct manner points to the future that the critical point of any study of bone histomorphometry must be an appropriate choice of research material for a specific application. The choice of random samples without information about patients from whom samples were taken can generate significant errors in the obtained results.

Acknowledgement. The authors: Paulina Popik and Łukasz Cyganik are beneficiaries of the "Silesian Cooperation: Innovations For Efficient Development (SWIDER)" project realized within Human Capital Operational Programme, Priority VIII: Regional human resources for the economy, 8.2 Transfer of knowledge, Sub-measure 8.2.1 Support for cooperation of scientific environment and enterprises. Project partially funded from European Union Project based on European Social Funds. Marcin Binkowski was partially supported by postdoctoral fellowship (KOLUMB) and supportive grant from the Foundation for Polish Science, Warsaw, Poland. The project was partially supported by grant no. N N518 425036 from the Ministry of Science and Higher Education, Warsaw, Poland.

References

1. Browne, J.G., Mesallati, T., Picard, C., Reeve-Arnold, K., Reilly, P.O., Daly, J.S., Casey, M.C., Walsh, J.B., Taylor, D.: Investigating bone quality in patients with hip fractures using newer bioengineering techniques. Bone 47(1), 80–81 (2010)
2. Genant, H.K., Gordon, C., Jiang, Y., Lang, T.F., Link, T.M., Majumdar, S.: Advanced imaging of bone macro and micro structure. Bone 25(1), 149–152 (1999)
3. Issever, A.S., Vieth, V., Lotter, A., Meier, N., Laib, A., Newitt, D., Majumdar, S., Link, T.M.: Local differences in the trabecular bone structure of the proximal femur depicted with high-spatial-resolution MR imaging and multisection CT. Academic Radiology 9(12), 1395–1406 (2002)
4. Donnelly, E.: Methods for assessing bone quality: a review. Clinical Orthopaedics and Related Research 469(8), 2128–2138 (2011)
5. Parfitt, A.M., et al.: Bone Histomorphometry: Standarization of Nomenclature, Symbols, and Units. Journal of Bone and Mineral Research 2(6), 595–610 (1987)
6. Topoliński, T., Mazurkiewicz, A., Jung, S., Cichański, A., Nowicki, K.: Microarchitecture parameters describe bone structure and its strength better than BMD. The Scientific World Journal, Article ID: 502781 (2012)
7. Perilli, E., Baleani, M., Ohman, C., Fognani, R., Baruffaldi, F., Viceconti, M.: Dependence of mechanical compressive strength on local variations in microarchitecture in cancellous bone of proximal human femur. Journal of Biomechanics 41(2), 438–446 (2008)
8. Kazakia, G.J., Burghardt, A.J., Cheung, S., Majumdar, S.: Assessment of bone tissue mineralization by conventional x-ray microcomputed tomography: Comparison with synchrotron radiation microcomputed tomography and ash measurements. Medical Physics 35(7), 3170–3179 (2008)
9. Laib, A., Rüegsegger, P.: Calibration of trabecular bone structure measurements of in vivo three-dimensional peripheral quantitative computed tomography with 28-microm-resolution microcomputed tomography. Bone 24(1), 35–39 (1999)
10. Barger-Lux, M.J., Recker, R.R.: Toward Understanding Bone Quality. Transilial Bone Biopsy and Bone Histomorphometry. Clinical Reviews in Bone and Mineral Metabolism 4(3), 167–176 (2006)
11. Tanck, E., Homminga, J., van Lenthe, G.H., Huiskes, R.: Increase in bone volume fraction precedes architectural adaptation in growing bone. Bone 28(6), 650–654 (2001)
12. Tamminen, I.S., Isaksson, H., Aula, A.S., Honkanen, E., Jurvelin, J.S., Kröger, H.: Reproducibility and agreement of micro-CT and histomorphometry in human trabecular bone with different metabolic status. Journal of Bone and Mineral Metabolism 29(4), 442–448 (2011)
13. Griffith, J.F., Genant, H.K.: Bone mass and architecture determination: state of the art. Best practice & research. Clinical Endocrinology & Metabolism 22(5), 737–764 (2008)
14. Perilli, E., Baleani, M., Öhman, C., Baruffaldi, F., Viceconti, M.: Structural parameters and mechanical strength of cancellous bone in the femoral head in osteoarthritis do not depend on age. Bone 41, 760–768 (2007)
15. Boutroy, S., Vilayphiou, N., Roux, J.-P., Delmas, P.D., Blain, H., Chapurlat, R.D., Chavassieux, P.: Comparison of 2D and 3D bone microarchitecture evaluation at the femoral neck, among postmenopausal women with hip fracture or hip osteoarthritis. Bone 49(5), 1055–1061 (2011)

16. Nazarian, A., Snyder, B.D., Zurakowski, D., Müller, R.: Quantitative micro-computed tomography: a non-invasive method to assess equivalent bone mineral density. Bone 43(2), 302–311 (2008)
17. Goulet, R.W., Goldstein, S.A., Ciarelli, M.J., Kuhn, L.J., Brown, M.B., Feldkamp, L.A.: The relationship between the structural and orthogonal compressive properties of trabecular bone. Journal of Biomechanics 27(4), 375–389 (1994)
18. Srikanth, V.K., Fryer, J.L., Zhai, G., Winzenberg, T.M., Hosmer, D., Jones, G.: A meta-analysis of sex differences prevalence, incidence and severity of osteoarthritis. Osteoarthritis and Cartilage 13(9), 769–781 (2005)
19. Hochberg, M., Lethbridge-Cejku, M., Tobin, J.: Bone mineral density and osteoarthritis: Data from the Baltimore Longitudinal Study of Aging. Osteoarthritis and Cartilage 12, 45–48 (2004)
20. Burr, D.B., Gallant, M.A.: Bone remodelling in osteoarthritis. Nature Reviews Rheumatology 8(11), 665–673 (2012)
21. Lajeunesse, D., Pelletier, J.P., Martel-Pelletier, J.: Osteoporosis and osteoarthritis: bone is the common battleground. Medicographia 32(4), 391–398 (2010)

The Three Dimensional Visualization Growth of Bone Tissue in Microstructure of Surface Analysis Using Drishti Open-Source Software

Mateusz Stolarz[1,2,3], Krzysztof Ficek[3], Marcin Binkowski[1], Anna Wójcicka[1,4], and Zygmunt Wróbel[1]

[1] X-ray Microtomography Laboratory, Department of Biomedical Computer Systems, University of Silesia, Institute of Computer Science Bedzinska 39, 41-200 Sosnowiec, Poland
matstolarz@gmail.com,
{marcin.binkowski,zygmunt.wrobel}@us.edu.pl
[2] Department of Orthopedics and Traumatology, City Hospital in Zabrze, Zamkowa 4, 41-803 Zabrze, Poland
[3] Galen-Orthopaedics, Jerzego 6, 43-150 Bierun, Poland
galen@galen.pl
[4] Department of Technology and Engineering of Material Pedagogical University, Institute of Technology Podchorążych 2, 30-084 Cracow, Poland
aniawojcicka@gmail.com

Abstract. Nowadays, computed tomography and three dimensional visualization provide anatomic images structures with an impressive richness of anatomical details. They are ubiquitous used in various fields of medical knowledge. In addition, X-ray microtomography (XMT) next to standard quantitative computed tomography (QCT) provide data with much higher spatial resolution. Use them for three dimensional visualization of the surface of animal tissue for macroscopic and microscopic analysis of the structure of tissue is a tool of immense possibilities that successfully is widely use in structural studies of hard tissues. The research article presents the disadvantages and advantages of the creation and use of three dimensional visualization of images using Drishti open-source software on the example of growth of sheep bone tissue.

Keywords: Three dimensional visualization, bone tissue, animal studies, X-ray microtomography.

1 Introduction

Three-dimensional visualization of Computed Tomography (CT) images plays an important role in medicine and related sciences. In addition, thanks to the development of X-ray Microcomputed Tomography (XMT) following the standard CT it is the ability to obtain three-dimensional images in much higher resolution, allowing to visualize the smallest details. The basis of 3D visualization is a multiplanar reconstruction (MPR). MPR is a unique technique for computing

E. Pietka, J. Kawa, and W. Wieclawek (eds.), *Information Technologies in Biomedicine, Volume 3*, Advances in Intelligent Systems and Computing 283,
DOI: 10.1007/978-3-319-06593-9_9,

arbitrarily oriented planar slices from volume imaging data for instance CT data. By examining arbitrarily oriented slices it is possible to elucidate information about 3D relationships which is not evident when examining slices oriented in the acquisition plane [15].

Then, computer programs by volume rendering and MPR model image is created, which depending on the analysis, more or less corresponds to the actual image. The practice of medicine and study of biology visualizations help to understand the relationship between anatomical structures and their biological functions as well as in the detection and treatment of diseases and injuries which disturb or threaten normal life processes. Locked within 3D biomedical images is significant information about the objects and their properties from which the images are derived [6, 17].

The value of biomedical visualized images depends largely upon the context from which they are obtained and the medical interest and goals that motivate their production and use. The continuing evolution of visualization imaging promises even greater capabilities for accurate noninvasive clinical diagnoses and treatment, as well as for quantitative biological investigations and scientific exploration, targeted at ever increasing our understanding of the human condition and how to improve it [17]. Visualization is a special value-added in orthopedics where it is used to the 3D imaging musculoskeletal injuries, especially bone fractures and displacement of the fractured bone fragments. Three dimensional projections of anatomical structure damages effectively support operational planning, selecting proper instrumentation, virtual repositioning of broken bones, choosing the right technique, which incredibly helps the surgeon during the operation, as well as after surgery in control of the process of fixation and bone healing [9, 18].

The aim of article was to present the advantages and disadvantages of the creation and use of three dimensional visualization of images using Drishti with bone tissue surface analysis. As an example of images XMT data of sheep bone tissue was used for research.

2 X-ray Microtomography

Imaging with high-resolution and accurate study of various structures e.g. bone tissue is possible by Computed Microtomography (XMT). In recent years, XMT has been developed rapidly, what is more introduction of commercial scanners disseminated researches in many centers in the world. In this chapter, the authors will briefly analyze and describe use of XMT.

The X-ray microtomography was pioneered by Elliot and Dover in 1982 [4]. It is just as computed tomography (CT) non-invasive diagnostic method, which in contrast to the CT allows to obtain images of structures having much higher resolution. Until now, the high quality of the data has been used in many fields of knowledge, for instance in biology [7, 12, 21] paleontology [3], anthropology [14], physics [20], and above all in the various fields of medicine and biomedical science [1, 2, 8].

XMT is an reliable approach to image and quantify bone tissue in three dimensions. The field was pioneered by Feldkamp et al. [5]. Authors used a microfocus X-ray tube as a source, an image intensifier as a 2D detector, and cone-wave reconstruction to made a three dimensional object [5]. XMT allows fast and very precise measurement of trabecular and compact bone in unprocessed biopsies. What is more XMT imaging might help to investigate the relative importance of bone architecture, damage accumulation, density, bone strength and mineralization in the characterization of bone quality [1, 2, 11, 13].

Bone studies were performed in laboratory equipped with the GE phoenix v|tome-|x XMT scanner (GE Measurement & Control, Wunstorf, Germany) with versatile CT system suitable for a wide range of CT applications. With its 240 kV/320W directional X-ray tube and precision manipulator allows scanning objects with voxel sizes less than 2 micrometers. Applying three dimensional visualization of the bone samples scanned can gain insight into microscopic structure of the material which enables an efficient analysis. It is very important in the use of 3D visualization to the analyze of structural materials is possible to obtain images in high resolution. This allows to look at the macroscopic structure of bone samples (Fig. 1a), to distinguish between areas of the revised structure as well as using magnification to look at the microstructure or the individual trabecular bone (Fig. 2b).

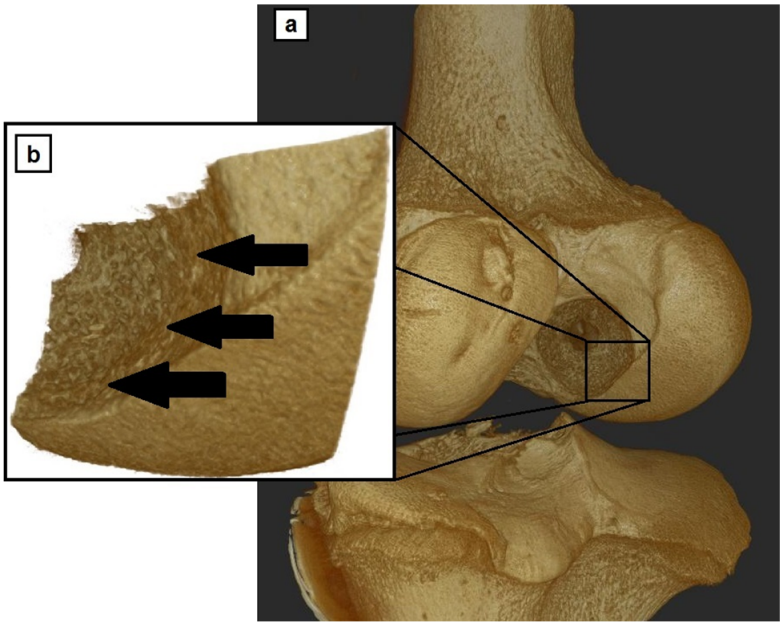

Fig. 1. Macroscopic structure of sheep bone samples (a), and microstructure of trabecular bone (b)

3 The Materials and Methods

Studies included eight male sheeps, twelve months old, weighing 35 - 40 kg (Ethics Committee approval 820/2010). The animals were divided into two groups, each consisting of four animals (four subjects for six weeks, and four subjects for twelve weeks).

The first stage of research was to perform reconstruction surgery within the knee joint. The surgery was performed in The National Research Institute of Animal Production in Krakow-Balice. Prior to ligament reconstruction, the native anterior cruciate ligament (ACL) was cut and removed from the joint. The natural ACL insertions served as the footprints to drill the tibial and femoral bone tunnels. The tunnels were arranged in proximal tibia methaphysis medially and in distal femur methaphysis laterally. Diameters of bone tunnels were 1 mm wider than their grafts. The autograft tendon, harvested from the Achilles was then pulled through the tunnels. The graft's ends were fixed extracortically to the femoral and tibial parts with an Endobutton system. All 8 animals were euthanized 6 or 12 weeks after the surgery. Then sheep knee joints were surgically excised, with the bones within the knee joint. Excision were performed carefully to keep all parts of bone tunnels.

Knees were tested using an XMT scanner. Acquisition of the X-ray images was performed using 140kV Voltage, 350 mA current, filter 0.5 Cu and 2000 projections with 2048x2048 pixels stored in 16 bit non-compressed TIFF files. After reconstruction of the 8 bit cross-sectional images, the spatial resolution reflected a voxel size equal to 50x50x50 μm. The reconstructed data files were imported into Drishti software, in which the data were processing and finally three-dimensional visualization were performed.

4 Drishti Open-Source Volume Exploration and Presentation Tool

Creating a three dimensional visualization has become very simply and more popular thanks to dedicated programs, both paid and free to facilitate their implementation. Commercial, advanced solutions such as: MIMICS [25], Avizo Fire [24], VG Studio [28], Amira [23], requires extensive knowledge, skills and costs. These programs are primarily dedicated to medical graphic designers, and biomedical engineers having advanced structure and number of modules. For medical visualization are enough free programs - often have comparable or even superior modules to work then commercial programs [10]. One of the free programs created by Ajay Limaye from The Australian National University is Drishti shortly described as open-source Volume Exploration and Presentation Tool with a powerful visualization tools for a wide variety of applications [10]. Program is written using OpenGL [26] with Qt [27] for the user interface. The main feature of Drishti is to support a unique mesh generation and coloring options that are currently not available in any of the commercial or free software [10]. The Drishti user interface is shown in Fig. 2. On the left window,

there is a preview of the three dimensional visualization. Drishti allows very quick creation of three dimensional preview of hundreds of images for instance from XMT, which is the essence of improvement in relation to other applications of this type. On the right side of interface are the sections responsible for the picture layout, where you can adjust lot of transfer functions (shadows, lightning, light position etc.).

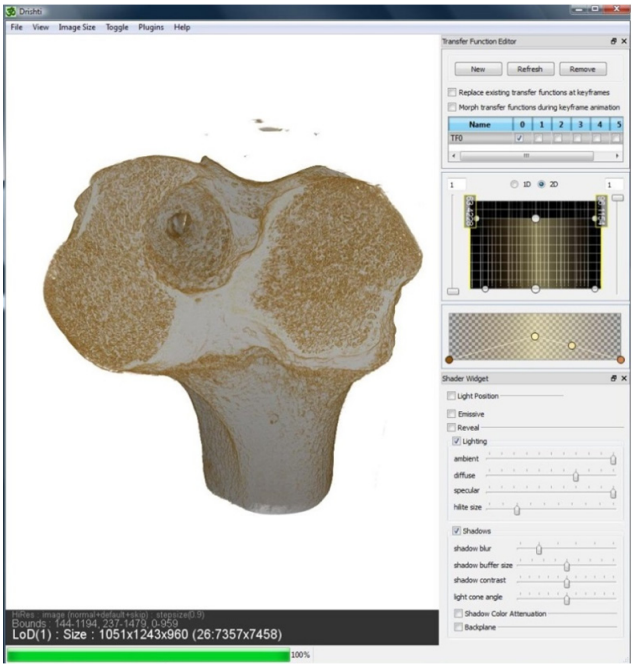

Fig. 2. Drishti interface; on the left side is display window for volume rendered images; on the right side is the graphical user interface; display window can be switched to show entire volume or selected sub volume

5 The Creation of Three Dimensional Visualization

Creating a three dimensional visualization has become very easy and more popular thanks to special programs. One of the open-source software is Drishti–direct volume rendering tool. Describes the Drishti workspace, and feature sections which can be used to modify the resulting three dimensional visualization. This chapter describes the step by step how to perform a 3D visualization of the surface of a bone tissue on the example of the sheep bone tissue taken during ACL reconstruction. At the beginning, the data obtained as a result of the XMT study were imported into Drishti. Then and automatic segmentation process is carried out. Three-dimensional model obtained by the segmentation is shown in

Fig. 2. Presented in the picture interface is intuitive and relatively easy to learn to use. It does not require complicated instructions, and only requires practical exercises. After creating the model, it should be fitted to spatial view for further analysis. View required to further sample analysis can be adjusted with the mouse. The right mouse button is used to shift the object in model space, while double-clicking the left button allows its rotation, so that it is possible to observe the object from all sides. To zoom in or out of the property is made via a scroll mouse.

Then, using the sculping tools, there is removed unwanted items object in order to visualize the internal structure, which is then analyzed. Drishti provides sculpting facility via clipping planes, cropping, blending, dissection, reveal, path tools and bricks [10]. Fig. 3 shows a 3D model of partially visualized internal structure obtained by "clip" tools. If the image has too many artifacts in the form of noise, you can remove unwanted parts by using the "mop".

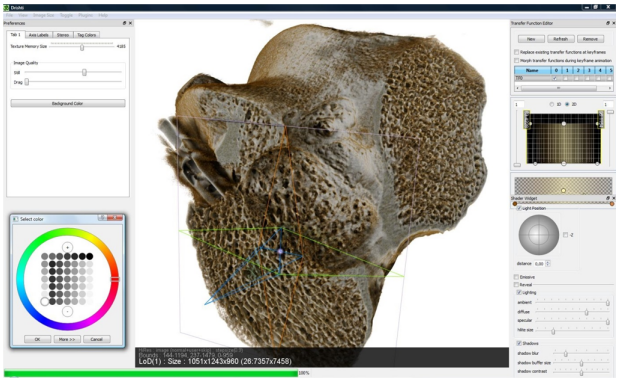

Fig. 3. Three dimensional image editing

An important element of visualization is to match the appropriate background color. A well-chosen background color can effectively expose visualized object. Drishti has a wide range of colors that can be individually adapted to the model. An example of the use of light background is shown in Fig. 3, the darker is shown in Fig. 1. As can be seen in some cases, choosing a darker background gives more favorable results. An important function is to choose the appropriate lights position. The angle of incidence of the light may be perpendicular to the image as well as to fall from one of the sides. This option allows you to fill by light small holes or curvatures, where visibility is necessary for the final result.

Next step is to choose the appropriate resolution of the image ("Image Quality") and enable shadowing that allow you to obtain from the object (Fig. 4a), the model much better visualizing bone structure (Fig. 4b).

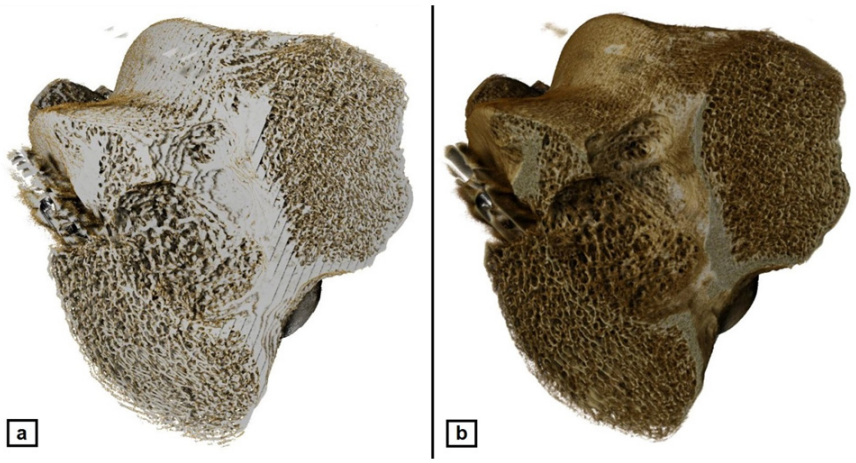

Fig. 4. Source image imported to Drishti (a) and after implementation of high resolution and shadowing (b)

The final step in creating a three-dimensional model is giving a real appearance of bone tissue by setting the parameters of Lightening and Shadows. Lightening is adjusted by options: ambient, diffuse, specular, hilite size, as well as shadowing, which is adjusted by options: blurr shadow, shadow buffer size and shadow contrast. These modifications obtain desired texture of the bone tissue. It should be noted that the process of selection of these parameters is personally subjective and also depends on the availability of different functions, and computing power. The final effect of this process of creating a three-dimensional model of the bone structure of a sheep is shown in Fig. 5 and Fig. 6. Thanks to the use and the appropriate choice of many parameters, the final image visualization very well corresponds to the natural bones. Chosen colors correlate with the original, anatomical colors of bone tissue. It is important for precise visualize, because mismatched colors can lead to errors in interpretation. Three dimensional visualization of the strategic projections may be saved in different formats dependent on user needs. They could be presented as images, showed in this article, but also as powerful animations. Animations in Drishti are generated by function "keyframe based animation". Users choreograph camera moves and various parameters and saves important frames in an animation sequence. These saved frames are named "keyframes". A keyframe saves all important information to generate the required image. The animations can be rendered as a set of images or can be saved in one of movie format [10]. The possibility of movie imaging of samples and smooth viewing slide by slide subsequent layers of the sample can well reveal changes of the microstructure occurring in different parts of the sample.

These data indicate that the three dimensional visualization is incredibly useful tool for the analysis of the structure so that an insight into the micro and

macrostructure is done without having to invasive (e.g. biopsy) observation of what is becoming increasingly popular among researchers from different fields of science [10, 16, 19]. Unfortunately, program is the lack of opportunities for precise measurement and calculation of parameters such as bone density, porosity, trabecular thickness etc.

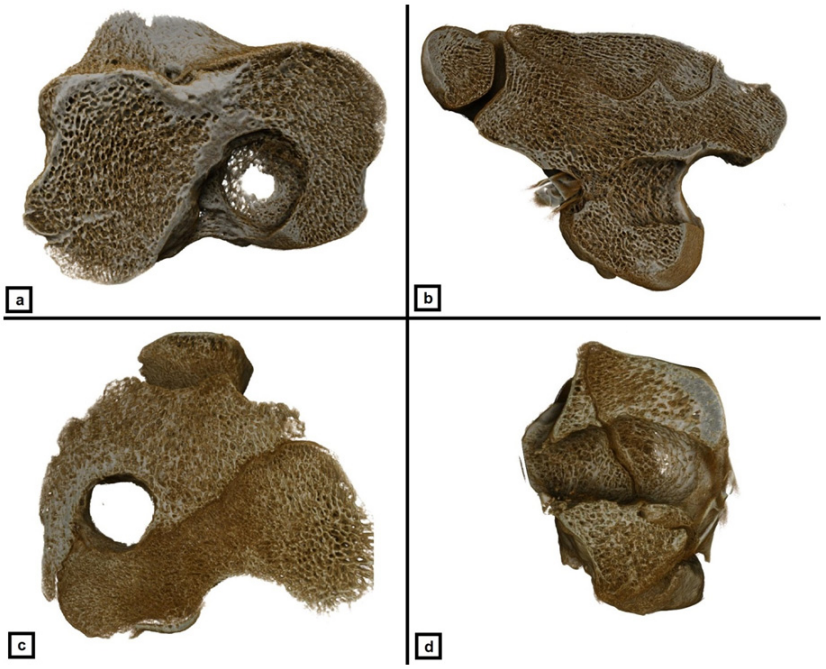

Fig. 5. Three dimensional visualization of bone structure, sheep group after 6 weeks; femur: the cross-section (a) and longitudinal-section (b), the tibia cross-section (c) and longitudinal section (d)

6 Results

The final result of implementation of the three dimensional visualization of the surface of the sheep bone tissue samples are presented in pictures (Fig. 5–7). Visualization with high resolution allowing to perform an precise visual analysis of microstructure of trabecular bone. Great advantage of the 3D visualization is to obtain 3D images which can be viewed from all sides in few seconds. In one moment it is possible find the microstructure of the desired area, which saves valuable time.

Analysis of visualized XMT images using Drishti showed microstructure of bone remodeling at the site of observations on the border between bone tissue and transplanted ligament. In many cross-sections (Fig. 5–7) there are shown

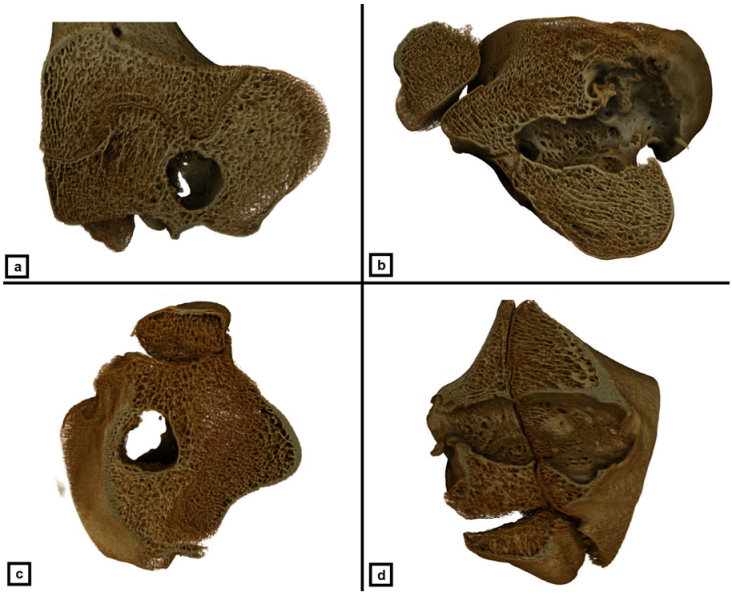

Fig. 6. Three dimensional visualization of bone structure, sheep group after 12 weeks; femur the cross-section (a) and longitudinal-section (b), the tibia cross-section (c) and longitudinal section (d)

different microstructure of the bone depending on the placement. In relation to bone tunnel, there is shown layers of bone tissue, with varied density. The layer directly adjacent to the tunnel presents the highest concentration of trabecular. It corresponds to the forming callus, as well as the bone remodeling processes. In addition, visualizations show the entry and exit of the bone tunnel, where bone tissue has a much greater density, which corresponds with the compact bone (it occurs in the outer portion of the long bones). Three dimensional images of bone structure showed in different planes in three-dimensional visualization of the sheep show in the group after 6 weeks (Fig. 5) process of remodeling in early phase. Trabecular bone near the bone tunnel start to be treated by osteoclasts and osteoblasts. In each case in a group after 12 weeks (Fig. 6, Fig. 7) in relation to the group after 6 weeks (Fig. 5, Fig. 7) the remodeling processes are more advanced. Comparing the images from the surrounding tunnel bone structure (Fig. 7) show the increase in bone density, and bone volume as well. It corresponds to forming callus and implantation of fibrous tissue from transplanted graft. These changes correspond to healing between bone and graft which has been histologically well described [22]. Implemented features of Drishti as well as setting the relevant parameters such as ambient, diffuse, specular, hilite size, shadowing, blurr shadow, shadow buffer size and shadow contrast etc. allowed accurately show different bone microstructure, and changes over time.

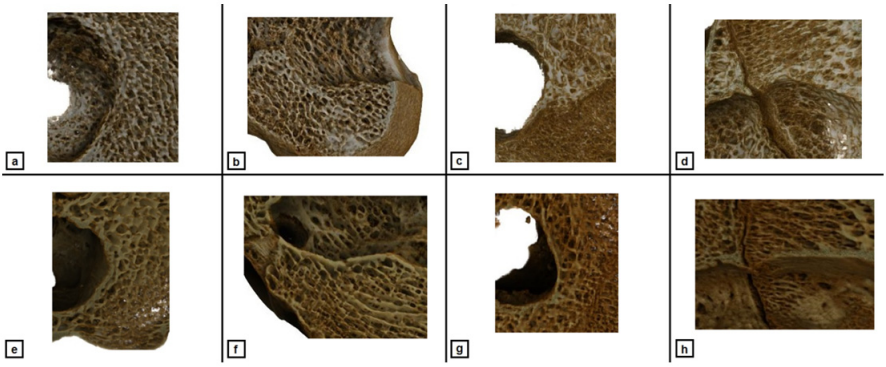

Fig. 7. Three dimensional visualization of bone ingrowth around bone tunnel; sheep group after 6 weeks: part of femur (a,b), and tibia (c,d); a comparative group of sheeps after 12 weeks: part of femur (e,f) and tibia (g,h)

7 Conclusions

- The three dimensional visualization is incredibly powerful and useful tool for analyzing the structure of materials is gaining more and more popular among researchers in various field,
- The three dimensional visualization high-resolution allows to precise quantitative analyze microstructure sample surface, especially bone tissue structure,
- Drishti open-source software can perform three dimensional visualization with impressive colorful and high quality of generated images,
- Drishti software is an advance presentation tool which can be used for three dimensional visualization of hard tissues especially bone, and ingrowth of this tissue,
- Drishti program interface is simple and intuitive, which helps in rapid execution of the intended visualizations,
- The disadvantage of the program is the lack of opportunities for precise measurement and calculation of parameters such as density.

Acknowledgments. Mateusz Stolarz and Anna Wójcicka are beneficiary of Silesian Silesian Cooperation: Innovations For Efficient Development (SWIDER). Project realized within Human Capital Operational Programme, Priority VIII: Regional human resources for economy, 8.2 Transfer of knowledge, Sub-measure 8.2.1 Support for cooperation of scientific environment and enterprises. Project partially funded from European Union Project based on European Social Funds.

Authors want to thank Martyna Czaja for her great technical support, and thank to dr Stodolak-Zych for her help in preperation and to dr Jaroslaw Wieczorek for animal care.

Finally authors would like to acknowledge to Ajay Limaye from The Australian National University, Australia for his training and continues support.

References

1. Binkowski, M., et al.: Differences in trabecular bone mechanical strength measured by the x-ray microcomputed tomography and compressive test. Journal of Medical Informatics & Technologies 15, 163–168 (2010)
2. Binkowski, M., et al.: Quantitative Measurement of the Bone Density by X-Ray Micro Computed Tomography. In: IFMBE Proceedings, vol. 31, pp. 856–859 (2010)
3. Błażejowski, B., et al.: X-ray Microtomography (XMT) of Fossil Brachiopod Shell Interiors for Taxonomy. Acta Palaeontologica Polonica 56(2), 439–440 (2011)
4. Elliott, J.C., Dover, S.D.: X-ray microtomography. Journal of Microscopy 126(2), 211–213 (1982)
5. Feldkamp, L.A., et al.: The direct examination of three-dimensional bone architecture in vitro by computed tomography. Journal of Bone and Mineral Research 4(1), 3–11 (1989)
6. Hofer, M., et al.: CT Teaching Manual: A Systematic Approach to CT Reading. Journal of Nuclear Medicine 48(3), 494 (2007)
7. Van de Kamp, T., et al.: A biological screw in a beetle's leg. Science 333(6038), 52 (2011)
8. Kohler, T., et al.: Compartmental bone morphometry in the mouse femur: reproducibility and resolution dependence of microtomographic measurements. Calcified Tissue International 77(5), 281–290 (2005)
9. Langford, J.R., et al.: Pelvic Fractures: Part 2. Contemporary Indications and Techniques for Definitive Surgical Management. Journal of the American Academy of Orthopaedic Surgeons 21(8), 458–468 (2013)
10. Limaye, A.: Drishti: a volume exploration and presentation tool. In: SPIE Developments in X-Ray Tomography VIII, vol. 8506, p. 85060X (2012)
11. Marinozzi, F., et al.: Technique for bone volume measurement from human femur head samples by classification of micro-CT image histograms. Ann. Ist. Super Sanitr. 49(3), 300–305 (2013)
12. Mizutani, R., Suzuki, Y.: X-ray microtomography in biology. Micron 43(2-3), 104–115 (2012)
13. Müller, R., Rüegsegger, P.: Micro-tomographic imaging for the nondestructive evaluation of trabecular bone architecture. Studies in Health Technology and Informatics 40, 61–79 (1997)
14. Nowaczewska, W., et al.: The tooth of a Neanderthal child from Stajnia Cave, Poland. Journal of Human Evolution 64(3), 225–231 (2013)
15. Owen, S.: Visualization in Medicine, `http://www.siggraph.org/education/HyperVis-/applicat/medical/intro.htm`
16. Ribi, W., et al.: Imaging honey bee brain anatomy with micro-X-ray-computed tomography. Journal of Neuroscience Methods 171(1), 93–97 (2008)
17. Robb, R.: 3-Dimensional Visualization in Medicine and Biology. In: Handbook of Medical Imaging: Processing and Analysis, pp. 685–712. Academic Press, San Diego (2000)
18. Sheth, N.P., et al.: Femoral Bone Loss in Revision Total Hip Arthroplasty: Evaluation and Management. Journal of the American Academy of Orthopaedic Surgeons 21(10), 601–612 (2013)
19. Short, K.M., et al.: Tomographic quantification of branching morphogenesis and renal development. Kidney International 77(12), 1132–1139 (2010)
20. Sinha, P.K., et al.: Quantification of Liquid Water Saturation in a PEM Fuel Cell Diffusion Medium Using X-ray Microtomography. Electrochemical and Solid-State Letters 9(7), A344 (2006)

21. Sulikowska-Drozd, A., et al.: The evolution of shell apertural barriers in viviparous land snails (Gastropoda, Pulmonata, Clausiliidae). Canadian Journal of Zoology (2014)
22. Weiler, A., et al.: Tendon Healing in a Bone Tunnel. Part II: Histologic Analysis After Biodegradable Interference Fit Fixation in a Model of Anterior Cruciate Ligament Reconstruction in Sheep. Arthroscopy: The Journal of Arthroscopic and Related Surgery 18(2), 124–135 (2002)
23. Amira, http://www.vsg3d.com/amira/overview
24. Avizo® Fire, http://www.vsg3d.com/avizo/fire
25. Mimics, http://biomedical.materialise.com/mimics
26. OpenGL, http://www.opengl.org
27. Qt, http://qt.nokia.com
28. VG Studio, http://www.volumegraphics.com/en/products/vgstudio-max.html

Fractal Texture Analysis in the Irregular Region of Interest of the Healing Process Using Guided Bone Regeneration

Marta Borowska[1], Edward Oczeretko[1], and Janusz Szarmach[2]

[1] Bialystok University of Technology, Faculty of Mechanical Engineering, Department of Materials and Biomedical Engineering, Wiejska 45C, 15-351 Białystok, Poland
m.borowska@pb.edu.pl
[2] Medical University of Bialystok, Department of Oral Surgery, M. Curie-Skłodowskiej 24A, 15-276 Białystok, Poland

Abstract. A fractal texture analysis technique was introduced for assessment of the healing process using Guided Bone Regeneration (GBR) after bone loss in resected and cystic areas. Fractal dimension may be used for the characterization of surface topography of medical images. In this paper we attempted to analyse fractal surface in the irregular regions of interest (irregular ROI-s) using two methods: Chen's method and variogram. In our study a significant change for the values of fractal dimension was found.

Keywords: fractal texture analysis, irregular region of interests, guided bone regeneration, xenografts.

1 Introduction

Apicoectomy is the treatment method standing for resection of the root apex along with inflammatory changes. The periapical surgery with cyst enucleation is strictly related to enormous bone loss that heals for a long period of time and moreover does not close up completely. System called Guided Bone Regeneration is the one recommended in filling bone deficits appearing after root end resection with total cyst enucleation. Xenografts (of animal origin) are commonly used materials when introduced into the habitat bone, goes under osseointegration, shows long-term stability in a living organism and demonstrates osteoinductive abilities of a new bone creation [1–5]. Radiological investigation is used for assessment of the healing process after bone loss in resected and cystic areas. In standard radiology, spongy bone properties are identified using indirect symptoms such as reduced shadow density in a radiogram. The interpretation of the image depends on who does it, which causes a large margin of uncertainty. Subjective evaluation of changes observed during the healing process after bone loss, encourages a search for measurable algorithms.

In the last decades, many researchers have used various texture analysis approaches. Many of this methods represent the local behavior of the texture [6–8], structural [9–12] or spectral [13–16] properties of the image. However, these

E. Pietka, J. Kawa, and W. Wieclawek (eds.), *Information Technologies in Biomedicine, Volume 3*, Advances in Intelligent Systems and Computing 283,
DOI: 10.1007/978-3-319-06593-9_10,

methods do not distinguish between the many natural textures, which show non-periodic structure. Natural textures exhibit random, durable patterns. These include, for example, images of clouds, smoke, surfaces of the leaves, etc. Fractals a relatively new tool within mathematics, offer an alternative to these methods. Benoit Mandelbrot [17] developed this discipline in the $1960s$ and $70s$ grasp the model of complex, chaotic systems occuring naturally. Now, the concept of fractals has successfully been applied in many areas of science and technology. The fractal objects are characterized by [18]: a large degree of heterogeneity, fine structure, irregularity, self-similarity, fractional dimension. The term "irregularity" means that fractals defy the explanatory tools of traditional geometry. And the notion "self-similarity" means that small-scale structures of fractal set resemble large-scale structures.

Many surfaces can be characterized by the fractal dimension (the Hausdorff-Besicovitch dimension) D [19, 20] that is defined as the exponent:

$$M \propto R^D \tag{1}$$

where M is a measure, R is a scale, D is related to fractal dimension. Equation 1 applies to Euclidian objects, for which the exponent D equals 1, 2, or 3, respectively. For different surfaces the values of the fractal dimension are ranging from 2 to 3. When the surface roughness is extremely high the fractal dimension is about 3. For the smooth surfaces fractal dimension is about 2.

Existing algorithms for computing the fractal dimension are either based on geometrical or stochastic approach. Geometrical algorithms: planar triangles method [21, 22], covering blanket method [23], flat structuring element method [24], box dimension and lacunarity [25, 26], regard the graph of an image as a three-dimensional object. Stochastical algorithms based on fractal Brownian function: variogram [27], power spectrum [28, 29], a particular class of fractals with well defined statistical properties. These algorithms were used in the analysis of medical images [30–35] in regular region of interest. In this paper we apply the fractional Brownian motion methods in the irregular region of interest in radiovisiographic images, because near boundary between different structures the values of fractal dimensions changed significantly [36, 37].

2 Fractal Dimension Computing Methods

Many methods exist to compute fractal dimension: each method has its own mathematic basis. This fact requires using different methods for computing fractal dimension for the same feature. Although, the practical algorithms differ, they can be realized in the three steps:

- measure the quantities of the object using various step sizes,
- plot of measured quantities versus step sizes on the log-log scale and fit least-square regression line to the data points,
- estimate fractal dimension D as the slope of the regression line.

In this paragraph we present the fractional Brownian motion methods in the irregular region of interests.

2.1 The Fractional Brownian Motion

Developed by Mandelbrot [38] fractional Brownian motion (`fBm`) is the most common mathematical model for random fractal textures found in nature. Many properties of `fBm` have been tested [39], [38], [40]. The grey level intensity medical image regards naturally occurring rough surface as the end results of random walks [38]. Therefore, the `fBm` model can be used for the analysis of radiological images.

The texture of the intensity image $I(x, y)$ can be modeled by a fractional Brownian function [18]:

$$Pr(\frac{I(x_2, y_2) - I(x_1, y_1)}{(\sqrt{(x_2 - x_1)^2 + (y_2 - y1)^2})^H} < y) = F(y) \tag{2}$$

where $I(\cdot)$ is the intensity of pixel x, y, $F(y)$ - the cumulative distribution function and H is called the Hurst coefficient in the range $0 < H < 1$. Small values of H give too many details in fractal surface with a high degree of fragmentation, whereas high values of H - a smooth undulating surface. There exists a correlation between fractal dimension D and the Hurst exponent H expressed as

$$D = 3 - H \tag{3}$$

Defining

$$\triangle I_{\triangle r} = |I(x_2, y_1) - I(x_1, y_1)| \tag{4}$$

and

$$\triangle r = \sqrt{(x_2 - x_1)^2 + (y_2 - y_1)^2} \tag{5}$$

from (2) we can calculate [41]:

$$E\{(\triangle I_{\triangle r})^2\} = \sigma^2 |\triangle r|^{2H} \tag{6}$$

where $E\{\cdot\}$ denotes the expected value of the quantity of brackets, σ^2 is the variance of the $F(y)$, $|\cdot|$ denotes the Euclidan distance.

If we take the logarithm of (6), we obtain:

$$\log E\{(\triangle I_{\triangle r})^2\} = 2 \log \sigma^2 + 2H \log |\triangle r| = \log C + 2H \log |\triangle r| \tag{7}$$

Because C is a constant, the parameter H can be concluded from the linear regression to estimate the slope of $E\{(\triangle I_{\triangle r})^2\}$ as a function of $|\triangle r|$ by choosing $\triangle r_{max}$ and $\triangle r_{min}$ (Fig. 1).

2.2 Intensity Difference Scaling Methods

Chen et al. introduced intensity difference scaling method [42]. Given on $M \times M$ image the grey level intensity vector is defined as follows:

$$MIDV = [id(1), id(2), ..., id(n)] \tag{8}$$

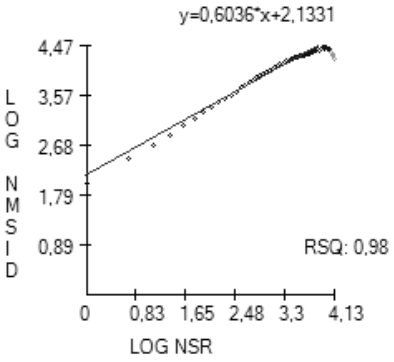

Fig. 1. The parameter H is estimated from the linear regression as the slope of $E\{(\triangle I_{\triangle r})^2\}$ as a function of $|\triangle r|$ by choosing $\triangle r_{max}$ and $\triangle r_{min}$

where n is the maximum possible scale, $id(i)$ is the average of the absolute intensity difference of all pixel pairs with scale i. The realization of estimation fractal dimension can be defined as:

$$id(i) = \frac{1}{N_i} \sum_{x_1=0}^{M-1} \sum_{y_1=0}^{M-1} \sum_{x_2=0}^{M-1} \sum_{y_2=0}^{M-1} |I(x_2, y_2) - I(x_1, y_1)| \tag{9}$$

where N_i is the number of pairs for scale i with distance $((x_2-x_1)^2+(y_2-y_1)^2)^{\frac{1}{2}}$.

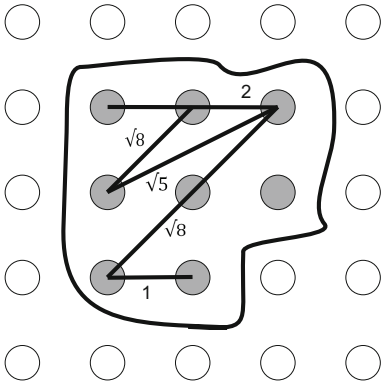

Fig. 2. 5×5 image. There are 14 possible scales. The total number of pixel pairs is 300. Manually drawn irregular region of interest with 8 pixels and 5 possible scales.

Fig. 2 shows 5×5 image with manually drawn irregular region of interests with 8 pixels and 5 possible scales. In calculation only pixels which belong to the region were used. For 5×5 image the number of possible scales is 14 (1,

$\sqrt{2}$, 2, $\sqrt{5}$, $\sqrt{8}$, 3, $\sqrt{10}$, $\sqrt{13}$, 4 $\sqrt{17}$, $\sqrt{18}$, $\sqrt{20}$, 5, $\sqrt{32}$), and the total number of pixel pairs analyzed of these scales is 36, for 63×63 image the number of possible scales is 1529, and the total number of pixel pairs analyzed of these scales is 31505922. For big region of interest the total number of all scales is too large. Chen et al. [42] proposed normalized $NMIDV$ vector to reduce the number of elements of $MIDV$ vector. This vector includes only integer scales occurring. Non-integer scales were set in integer scale, for example, information from scales: $\sqrt{5}$, $\sqrt{8}$ (2.2361, 2.8284) were set in scale 2. For fractal surfaces the relationship between $MIDV$ and scale i is ruled by a power-law:

$$MIDV = Ci^H \tag{10}$$

2.3 Variogram Methods

The variogram method is estimated on the statistical Gaussian modeling of images. The variogram is defined as

$$\gamma(r) = E[(I(x_2, y_2) - I(x_1, y_1))^2] \tag{11}$$

where $\gamma(r)$ is variogram at distance r, $I(\cdot)$ - the intensity of pixel (x, y) and $E\cdot$ is the expectation.

Fractal distribution is characterized by a variogram model of following form:

$$\gamma r = \gamma_0 r^{2H} \tag{12}$$

where H - Hurst exponent.

The fractal dimension is obtained from the `log-log` plot of expected differences in radiance versus distance in terms of number of bands between the point pairs.

3 Results

Implementation of two methods was done on an `Intel I5 Machine` workstation. The code was written in `C++` (Borland International) and Visual Basic (Microsoft .NET Framework 3.5).

3.1 Evaluation of the Algorithms on Synthetic Textured Images

In order to test our implementation of fractal dimension estimation methods, we applied these methods to a set of synthetic textured images (63×63 pixels in size) with known fractal dimension ranging from 2.05 to 2.95 (2.05, 2.10, 2.20, 2.30, 2.40, 2.50, 2.60, 2.70, 2.80, 2.90, 2.95). The synthetic textured images were generated by means of Matlab function **synth2**, that is a part of *FracLab* (Fractal Analysis Software [43]). In this software incremental Fourier synthesis method was implemented. Fig. 3 shows generated surfaces with fractal dimension ranging from 2.20 to 2.80 and 3-D representation of this texture.

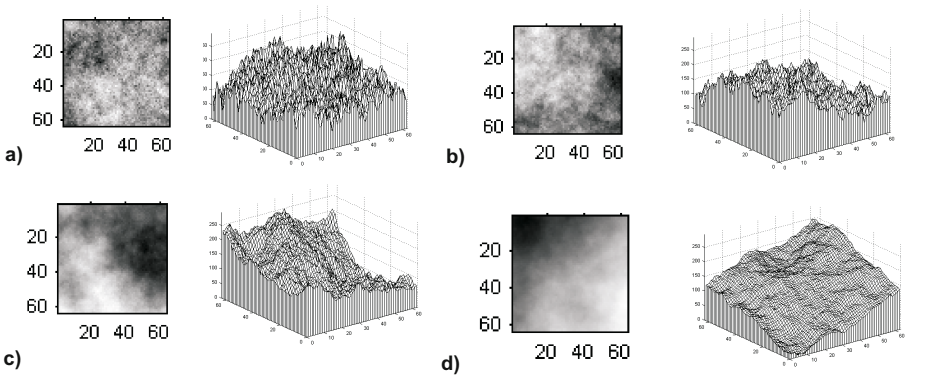

Fig. 3. a) Synthetic fractal texture with fractal dimension $D = 2.80$ with 3-D representation of this texture, b) Synthetic fractal texture with fractal dimension $D = 2.60$ with 3-D representation of this texture, c) Synthetic fractal texture with fractal dimension $D = 2.40$ with 3-D representation of this texture, d) Synthetic fractal texture with fractal dimension $D = 2.20$ with 3-D representation of this texture

Results of fractal dimension for synthetic surfaces calculated in irregular regions of interest using intensity difference scaling method and variogram method are presented in Fig. 4. Fig. 4a) shows that implemented algorithm of Chen's method in the irregular region of interest is able to calculate D close to the theoretical values. The calculated values increased monotonically as the true values increased. For the variogram method, calculated values differed from the theoretical values, but they increased monotonically. Another problem was to select the regression points in the range from $\triangle r_{min}$ to $\triangle r_{max}$. To calculate the linear regression the coefficient of determination RSQ was calculated. The assumed RSQ value was above 0.97.

3.2 Application of Fractal Dimension to Radiogram Texture Characterization

Case Study was conducted in the Oral Surgery Department in Bialystok, where 26 patients (18 females, 8 males) aged $18 - 53$ yr. (average 35.6) were examined according to the clinical symptoms and radiographic images of the root cysts. Clinical evaluation was performed 2 weeks before the apical surgery (15 images) and repeated 12 months after that, hence (26 images). Intraoral images were taken directly after surgical procedure (14 images) and then 12 months later (26 images) with the KODAK set RVG 6100 with resolution above $14pl/mm$ using collimator narrowing the radiation bundle in a straight angle technique with a constant exposure time of $0.08s$. Images were recorded as MPG graphic files, then archived and analyzed. All bone loss areas mentioned were filled with xenogenic `BioOss` material (spongious bone granulation with gradation of $0.25 - 1mm$) and then covered with resorbable membrane `BioGide`. `BioOss` material

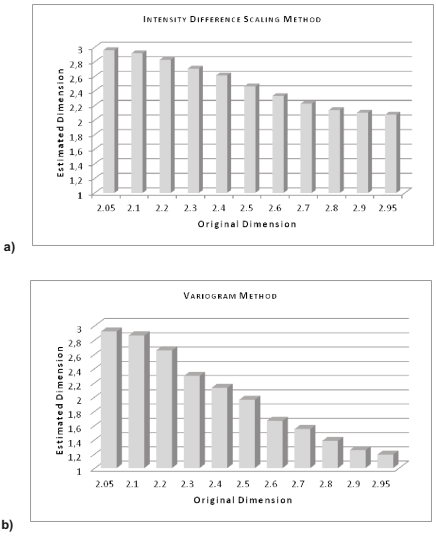

Fig. 4. Fractal dimension for synthetic surfaces calculated in irregular regions of interest using a) intensity difference scaling method, b) variogram method

[4] introduced to deficit zones is a totally decalcified specimen of natural origin. Fig. 5 shows radiovisiographic images with marked 4 irregular regions of interest a) before the apical surgery, b) directly after surgical procedure, c) then 12 months later. For the analysis four regions of interest were taken, because one large region would result in a long calculation time. In this paper images after surgical procedure (I group) and 12 months later (II group) were compared. Images before the apical surgery differ from the post surgical state in a visible way. Radiological investigation is used for the assessment of the healing process after bone loss in resected and cystic areas.

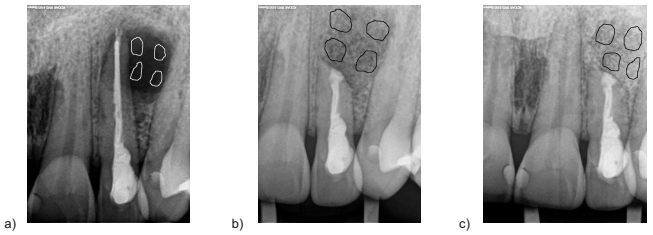

Fig. 5. Radiovisiographic images with marked 4 irregular region of interest a) before the apical surgery, b) directly after surgical procedure, c) then 12 months later

Fig. 6 shows results of fractal dimension in irregular `ROI-s` using Chen's method. The mean value of fractal dimension for $Igroup$ was $D = 2.5741 \pm 0.0585$, and for $IIgroup$ was $D = 2.4919 \pm 0.0656$. Statistical analysis was performed by means of non-parametric `Mann-Whitney test` (statistically significant differences $p < 0.05$, $p = 0.0007$).

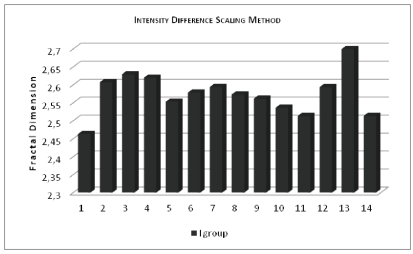

a)

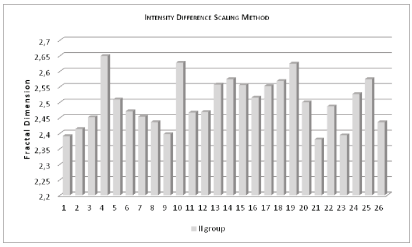

b)

Fig. 6. Results of fractal analysis in irregular region of interest using Chen's method a) I group, b) II group

Fig. 7 shows results of fractal dimension in irregular `ROI-s` using variogram method. The mean value of fractal dimension for $Igroup$ was $D = 2.1747 \pm 0.0976$, and for $IIgroup$ was $D = 2.0469 \pm 0.1056$. Statistical analysis was performed by means of non-parametric `Mann-Whitney test` (statistically significant differences $p < 0.05$, $p = 0.0010$).

Fig. 8 shows results of fractal dimension in irregular `ROI-s` between images in the same patients taken after surgical procedure and then 12 months later using variogram method. The mean value of fractal dimension of Chen's method (Fig. 8a)) was $D = 2.5741 \pm 0.0585$ for images after surgical procedure, and $D = 2.4677 \pm 0.0500$ for images studied 12 months later. Statistical analysis was performed by means of paired-sample `T-test` (statistically significant differences $p < 0.05$, $p = 0.00000012$). The mean value of fractal dimension of variogram method (Fig. 8b)) was $D = 2.1747 \pm 0.0976$ for images after surgical procedure, and $D = 2.0436 \pm 0.0980$ for images studied 12 months later. Statistical analysis was performed by means of paired-sample `T-test` (statistically significant differences $p < 0.05$, $p = 0.0000012$).

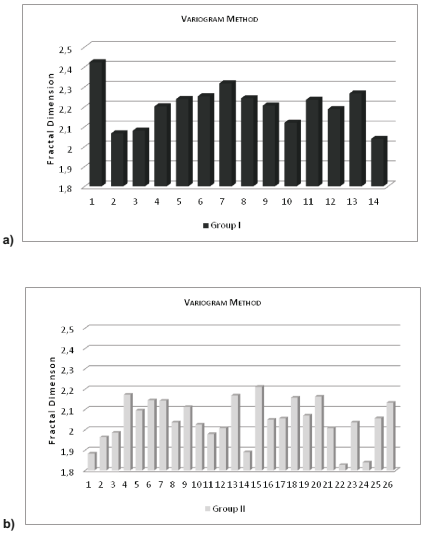

Fig. 7. Results of fractal analysis in irregular region of interest using variogram method a) I group, b) II group

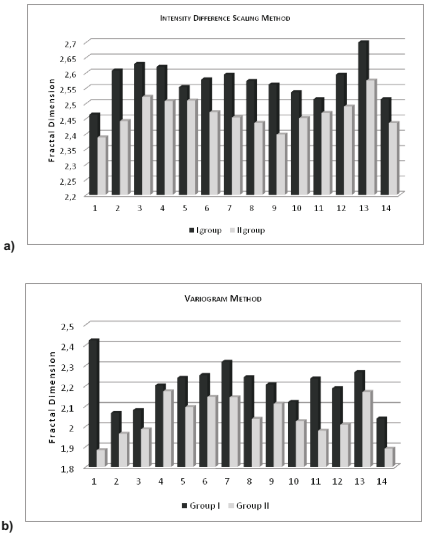

Fig. 8. Results of fractal analysis in irregular region of interest between images taken after surgical procedure and then images taken 12 months later using a) Chen's method, b) variogram method

4 Conclusion

We presented two methods of calculation fractal dimension in the irregular region of interest. It is difficult to fit the whole regular region of interest and to avoid the influence of boundaries and the other body structures. Our methods of calculating fractal dimension in the irregular region of interests solve these problems. Implementation of these methods needs extensive adjustments of heuristic parameters. This was achieved using theoretical surface models generated by fractional Brownian motion. Results of estimation of fractal dimension using the intensity difference scaling method were similar to theoretical fractal dimension. In the case of dental radiographic images the difference between images after surgical procedure and images taken 12 months later was showed with the latter surfaces being less complicated. The diagnostic information lies in the texture.

References

1. Kim, Y.K., Yun, P.Y., Kim, S.G., Lim, S.C.: Analysis of the healing process in sinus bone grafting using various grafting materials. Oral Surg. Oral Med. Oral Pathol. Oral Radiol. Endod. 107(2), 204–211 (2009)
2. Ribeiro, F.V., Suaid, F.F., Ruiz, K.G.S., Rodrigues, T.L., Carvalho, M.D., Nociti, F.H., Sallum, E.A., Casati, M.Z.: Effect of autologous bone marrow-derived cells associated with guided bone regeneration or not in the treatment of peri-implant defects. Int. J. Oral Maxillofac. Surg. 41(1), 121–127 (2012)
3. Baldini, N., De Sanctis, M., Ferrari, M.: Deproteinized bovine bone in periodontal and implant surgery. Dent. Mater. 27(1), 61–70 (2011)
4. Kim, S.G., Kim, H.K., Lim, S.C.: Combined implantation of particulate dentine, plaster of Paris, and a bone xenograft (Bio-Oss) for bone regeneration in rats. J. Craniomaxillofac. Surg. 29(5), 282–288 (2001)
5. Mokbel, N., Naaman, N., Nohra, J., Badawi, N.: Healing patterns of critical size bony defects in rats after grafting with bone substitutes soaked in recombinant human bone morphogenetic protein-2: histological and histometric evaluation. Br. J. Oral Maxillofac. Surg. 51(6), 545–549 (2013)
6. Chen, Y.Q., Nixon, M.S., Thomas, D.W.: Statistical geometrical features for texture classification. Pattern Recogn 28(4), 537–552 (1995)
7. Xu, C.L., Chen, Y.Q.: Classifying image texture with statistical landscape features. Pattern Anal. Appl. 8(4), 321–331 (2006)
8. Chandraratne, M.R., Kulasiri, D., Samarasinghe, S.: Classification of lamb carcass using machine vision: Comparison of statistical and neural network analyses. J. Food Eng. 82(1), 26–34 (2007)
9. Vilnrotter, F.M., Nevatia, R., Price, K.E.: Structural Analysis of Natural Textures. IEEE T. Pattern Anal. 8(1), 76–89 (1986)
10. Keller, J.M., Chen, S., Crownover, R.M.: Texture description and segmentation through fractal geometry. Comput. Vision Graph 45(2), 150–166 (1989)
11. Zhang, J., Tan, T.: Brief review of invariant texture analysis methods. Pattern Recogn. 35(3), 735–747 (2002)
12. Ghali, A., Daemi, M.F., Mansour, M.: Image structural information assessment. Pattern Recogn. Lett. 19(5-6), 447–453 (1998)

13. Azencott, R., Wang, J.P., Younes, L.: Texture classification using windowed Fourier filters. IEEE T. Pattern. Anal. 19(2), 148–153 (1997)
14. Jain, A.K., Farrokhnia, F.: Unsupervised texture segmentation using Gabor filters. Pattern Recogn. 24(12), 1167–1186 (1991)
15. Randen, T., Husoy, J.H.: Filtering for texture classification: A comparative study. IEEE T. Pattern Anal. 21(4), 291–310 (2002)
16. Bresch, M.: Optimizing filter banks for supervised texture recognition. Pattern Recogn. 35(4), 783–790 (2002)
17. Mandelbrot, B.B.: The fractal geometryof nature. Freeman, New York
18. Nelson, T.R.: Fractals: physiologic complexity, scaling, and opportunities for imaging. Invest. Radiol. 25, 1140–1148 (1990)
19. Besicovitch, A.: On the fundamental properties of linearity measurable plane setsof points. Math. Ann. 98, 422–464 (1928)
20. Hausdorff, F.: Dimension und äußeres Maß. Math. Ann. 79, 157–179 (1918)
21. Caldwell, C.B., Moran, E.L., Bogoch, E.R.: Fractal dimension as a measure of altered trabecular bone in experimental inflamatory arthritis. J. Bone Miner. Res. 13(6), 978–985 (1998)
22. Clarke, K.C.: Computation of the fractal dimension of topographic surfaces using triangular prism surface area method. Comp. Geosci. 12, 713–722 (1986)
23. Peleg, S., Naor, J., Hartley, R., Avnir, D.: Multiple resolution texture analysis and classification. IEEE Trans. Pattern Anal. Mach. Intell. 6(4), 518–523 (1984)
24. Maragos, P., Sun, F.K.: Measuring the fractal dimension of signals: morphological covers and iterative optimization. IEEE Trans. Signal Process. 41(1), 108–121 (1993)
25. Voss, R.: Random Fractals: Characterization and measurement. In: Pynn, R., Skjeltorp, A. (eds.) Scaling Phenomena in Disordered Systems, pp. 1–11. Plenum, New York (1986)
26. Chen, S.S., Keller, J.M., Crownover, R.M.: On the calculations of fractal features from images. IEEE Trans. Pattern Anal. Mach. Intell. 15(10), 1087–1090 (1993)
27. Bianchi, F., Bonetto, R.: FERImage: an interactive program for fractal dimension, d(per) and d(min) calculations. Scanning 23(3), 193–197 (2001)
28. Dennis, T.J., Dessipris, N.G.: Fractal modelling in image texture analysis. IEEE Proc. F Radar and Signal Process. 136, 227–235 (1989)
29. Super, B.J., Bovik, A.C.: Localized measurement of image fractal dimension using gabor filters. J. Visual Commun. Image Represent. 2, 114–128 (1991)
30. Losa, G.A., Merlini, D., Nonnemacher, T., Weibel, E.R. (eds.): Fractals in Biology and Medicine, vol. II. Birkhäuser Verlag, Basel (1998)
31. Losa, G.A., Merlini, D., Nonnemacher, T., Weibel, E.R. (eds.): Fractals in Biology and Medicine, vol. III. Birkhäuser Verlag, Basel (2002)
32. Losa, G.A., Merlini, D., Nonnemacher, T., Weibel, E.R. (eds.): Fractals in Biology and Medicine, vol. IV. Birkhäuser Verlag, Basel (2005)
33. Chappard, D., Guggenbuhl, P., Legrand, E., Basle, M.F., Audran, M.: Texture analysis of X-ray radiographs is correlated with bone histomorphometry. J. Bone Miner. Metab. 23, 24–29 (2005)
34. Iftekharuddin, K.M., Jia, W., Marsh, R.: Fractal analysis of tumor in brain MR images. Mach. Vision and Appl. 13, 352–362
35. Mustonen, T., Koivisto, T., Vanninen, E., Vanninen, R., Kuikka, J.: Cerebral perfusion heterogeneity and complexity in patients with acute subarachnoid haemorrhage. Nucl. Med. Commun. 27(2), 157–164 (2006)

36. Oczeretko, E., Rogowski, F., Jurgilewicz, D.: Fractal analysis of nuclear medicine scans. In: Losa, G.A., Merlini, D., Nonnemacher, T.F., Weibel, E.R. (eds.) Fractals in Biology and Medicine, vol. II. Birkhäuser Verlag, Basel (1998)
37. Oczeretko, E., Borowska, M., Kitlas, A., Borusiewicz, A., Sobolewska-Siemieniuk, M.: Fractal analysis of medical images in the irregular regions of interest. In: 8th IEEE International Conference on Bioinformatics and BioEngineering, Athens (2008)
38. Mandelbrot, B.B., Van Ness, J.W.: Fractional Brownian motions, fractional noises, and applications. SIAM Rev. 10, 422–437 (1968)
39. Flandrin, P.: On the spectrum of fractional Brownian motions. IEEE Trans. Inform. Theory 35, 197–199 (1989)
40. Peitgen, H.O., Saupe, D. (eds.): The Science of Fractal Images. Springer, New York (1988)
41. Gärdig, J.: Properties of fractal intensity surfaces. Pattern Recog. Lett. 8, 319–324 (1988)
42. Chen, C.C., Daponte, J.S., Fox, M.D.: Fractal feature analysis and classification in medical imaging. IEEE Trans. Med. Imaging 8, 133–142 (1989)
43. Fractal Analysis Software, `http://www.scilab.org`

A New Method of Automatic Craniometric Landmarks Definition and Soft Tissue Thickness Measurement Based on MRI Data

Iryna Gorbenko[1], Krzysztof Mikołajczyk[1], Iaroslav Iarovyi[2], Tomasz Kubik[1], and Krzysztof Kałużyński[1]

[1] Warsaw University of Technology, Faculty of Mechatronics, Institute of Metrology and Biomedical Engineering, Department of Biomedical Engineering, Św. Andrzeja Boboli 8, 02-525 Warsaw, Poland
i.gorbenko@mchtr.pw.edu.pl

[2] Warsaw University of Technology, Faculty of Electronics and Information Technology, Institute of Electronic Systems, Department of Microsystems and Measurement Systems, Nowowiejska 15/19, 00-665 Warsaw, Poland

Abstract. An automatic method for definition of the craniometric landmarks and soft tissues thickness measurement in these landmarks is proposed. The method uses MRI data and is based on the non-rigid registration of the target image to the template. Three MRI templates for three Body Mass Index ranges were created. Each template has 20 pairs of landmarks on the skull and on the face surface. To validate the proposed method the soft tissue thickness was measured using data from the IXI database. These were 18 MRI images obtained in Caucasian adult females, having the BMI in the range 20-25 [kg/m^2]. For each landmark the mean value, the standard deviation, the minimum and the maximum values of thickness were estimated. The obtained values are close to those obtained using the ultrasonic method. The method doesn't introduce errors resulting from contact with the subject nor from operator skills.

Keywords: facial soft tissue thickness measurement, craniometric landmarks, forensic facial reconstruction, non-rigid registration.

1 Introduction

Forensic facial reconstruction is based on the values of the soft tissue thickness at the craniometric points, called craniometric landmarks, which are located on the surface of a skull. The reconstruction uses a database of soft tissue thickness in craniometric points. The completeness and accuracy of such a database affect strongly the final result of the reconstruction. There is a constant need to enlarge the soft tissue thickness databases and to improve the accuracy of soft tissue thickness measurements. Many of the existing data Tables [1–4] contain results of the soft tissue thickness measurements using "needle thickness probing method", radiography and ultrasonography [1, 5]. Needle thickness probing method was

E. Pietka, J. Kawa, and W. Wieclawek (eds.), *Information Technologies in Biomedicine, Volume 3*, Advances in Intelligent Systems and Computing 283,
DOI: 10.1007/978-3-319-06593-9_11,

used on cadavers and suffers from errors resulting from the process of soft tissue decomposition and from the measurement technique. Pressing the skin with a needle compresses the soft tissue and results in a decreased thickness values [2, 5]. Radiography enables a precise measurement of the soft tissue thickness on the Median Sagittal plane of the skull. However, at all other landmarks the same precision can not be achieved because in the corresponding positions of the head the resulting image is distorted. The ionizing radiation presents a hazard for the patient [1, 6]. Ultrasound method is noninvasive and easy to use [1, 7]. It is a contact method and the results suffer from errors [1].

The Computed Tomography (CT) and Magnetic Resonance Imaging (MRI) are the most frequently used methods to provide data for the soft tissue thickness measurement nowadays [5]. These are non-contact methods and ensure higher precision of the measurement [1]. The main disadvantage of the CT is the ionizing radiation. This limitation does not allow creation of a big database. The MRI method does not have this drawback and provides better images of the soft tissue. Major problems of the soft tissue thickness measurement using MRI data are the possible distortion and difficulties in accurate localization of the craniometric landmarks on the skull in the most popular sequences.

The craniometric landmarks in MRI and CT images were usually identified manually. This approach is time-consuming. The next significant disadvantage of this solution is its dependence on manual skills and experience of the operator. In order to make the process of craniometric landmarks localization on the skull surface quicker, to minimize operator influence and to increase the accuracy of the soft tissue thickness measurement, methods for automatic definition of craniometric landmarks and face reconstruction were developed.

Within the great number of computerized forensic facial reconstruction methods the most promising are methods based on non-rigid registration of the target skull to template [8, 9]. The mesh deformation is carried out using methods such as the energy minimization, the mass-spring model, the local affine transformations, the trilinear transformation, the graph and manifold matching, the octree-splines and the thin-plate spline (TPS) [9]. Methods based on matching can be also used for automatic definition of the craniometric landmarks and for the measurement of the soft tissue thickness. In this case the set of the craniometric landmarks on the skull surface and measured soft tissue thickness at these landmarks will be obtained instead of face surface reconstruction. Below a new method for soft tissue thickness measurement is presented, which speeds up and facilitates this measurement. There are numerous methods of automatic landmarks definition. Examples of them are: non-rigid matching of reference model to a target model using facial planes [9], significant lines detection and pattern matching algorithm [10], fitting 3D parametric intensity models [11] and using expectation window and template-matching algorithm [12]. The novelty of the method proposed is that it performs the inverse transform on the set of craniometric points instead of performing it on the surface of a template face (as it is used in [6] for face reconstruction).

2 Materials and Methods

A MRI head template, with known parameters and with defined set of the craniometric landmarks on it, is needed as a basis for application of a non-rigid registration method. A plane which is common for both the template and target images must be defined. The Anterior Commissure - Posterior Commissure (AC-PC) plane inside of the brain was used as this reference. This plane is easy to define in the MRI data and enables orientation of all the MRI images in the same way.

Data from the public MRI database Information eXtraction from Images (IXI) were used in this study. This database contains nearly 600 MRI images from healthy human subjects [13]. Only T1-weighted MR images were used in this study. Each record of the database is characterized by such parameters as the race, the sex, the age, the height and the weight. The BMI was calculated in each case based on last two parameters. To determine which of these parameters have the greatest influence on the results of the elastic matching, experiments for different templates were made. The conclusion of these experiments is that the most important parameter for elastic matching quality is the BMI which is correlated with weigth and height. In [14] it is stated that the BMI has the greatest influence on the soft tissue thickness measurement.

The data was divided into classes depending on the BMI value [15]. An analysis of matching quality of 14 selected subjects to the templates for each class was carried out. The criterion of matching quality was the sum of the differences between craniometric landmark, marked manually by the operator in the analysed MRI image, and landmark obtained as result of elastic matching of the MRI image to template.

2.1 The Algorithm for MRI Templates Creation Based on BMI Ranges

The template is created as a product of averaging of a number of MRI images coming from the same class, according to the BMI value.

1. *Selection of initial image.*
   First (initial) image is an MRI image from IXI database with the smallest noise according to visual assessment. This data is transformed so that AC-PC line in MRI image becomes horizontal.
2. *Selection of other MRI images from database.*
   A number of low noise images (visual assessment – images without dental restoration signals) from the database is selected. These data should have a uniform signal intensity. These data contain whole head with all dependent parts (including soft tissues).
3. *Denoising of selected data (optional).*
   The optional denoising may be applied to the all the images selected, using the Non-Local Means filter [16].

4. *Elastic matching of two images.*
   Two images are matched. At the first step these are the images from the database, at further steps – the running template and the next image from selected ones. As a method for elastic matching the SPM (Statistical Parametric Mapping) was used as implemented in PMOD [17], a kind of the spatial normalization which uses mutual information as a cost function. Usually this method is used for matching brain images of different patients. In this study this method was used for the whole head.
5. *Averaging of the matched MRI images; saving averaged result to a temporary image variable.*
   The images matched in the previous step are averaged. The result will be used as a reference (running template) for the next MRI image from the list.
6. *Repeat operations mentioned in points 4 and 5 for remaining MRI images.*
   The next MRI image is matched to the running template and the product of their averaging will become the new running template. The number of averages is set by the operator and amounts from 3 to 5, based on the assessment of a preliminary matching of the running template and another image from the database.
7. *Smoothing of the template (optional).*
   Depending on chosen options a template smoothing with Gaussian filter may be executed (full width at half maximum (FWHM) 3 [mm] in each direction).
8. *Mask creation.*
   Head segmentation based on thresholding and morphological operations was applied.

When the template creation process was finished, the operator defined craniometric landmarks set, consisting of 20 basic landmarks (see Table 1). There is a landmark on the face surface corresponding to each craniometric landmark on the skull surface. As the result a set of 20 pairs of landmarks for each template was obtained.

2.2 The Algorithm for Automatic Craniometric Landmarks Definition Along with Soft Tissue Thickness Measurement in Landmarks

1. *Enter parameters.*
   Parameters for analysed MRI images (race, sex, age, height, weight, BMI) are entered into the program.
2. *Chose template which corresponds to the set of entered parameters.*
   A template from the previously created templates is chosen on the basis of data entered in the previous step.
3. *Elastic matching of the analyzed MRI image to the template.*
   The same approach is used for the elastic matching as during the template creation. Calculation of straight and inverse transformation matrix.
4. *Application of the inverse transformation to the template landmark set (transferring landmarks to the space of analyzed MRI image).*

Table 1. Basic craniometric landmarks used for testing of the algorithm of automatic craniometric landmarks definition, ∗ – symmetrical (paired) landmarks

Nr	Craniometric landmark name	Short name	Description [19]
1	Glabella	g	The most anterior midline point on the frontal bone, usually above the frontonasal suture.
2	Nasion	n	The midline point where the two nasal bones and the frontal intersect.
3	Rhinion	rhi	The midline point at the inferior free end of the internasal suture.
4	Nasospinale	ns	the point where a line tangent to the inferiormost points of the two inferior curves of the anterior nasal aperture margin crosses the midline.
5	Pogonion	pg	The most anterior midline point on the chin of the mandible.
6	Gnathion	gn	The most inferior midline point on the mandible.
7	Prosthion	pr	The midline point at the most anterior point on the alveolar process of the maxillae.
8	Infradentale superius	ids	The midline point at the inferior tip of the bony septum between the upper central incisors.
9	Incision	inc	The point at the occlusal surface where the upper central incisors meet.
10	Infradentale	id	The midline point at the superior tip of the septum between the mandibular central incisors.
11	Opisthocranion	op	An instrumentally determined point at the rear of the cranium. It is defined as the midline ectocranial point at the farthest chord length from glabella.
12	Inion	i	An ectocranial midline point at the base of the external occipital protuberance.
13	Alare	al*	Instrumentally determined as the most lateral point on the margin of the anterior nasal aperture.
14	Orbitale	or*	The lowest point on the orbital margin.
15	Supraorbital	sor*	Centered on eyepupil, just above eyebrow.
16	Zygion	zy*	The instrumentally determined point of maximum lateral extent of the lateral surface of the zygomatic arch.

For transferring the craniometric landmarks set from space of the template to space of the target data the inverse transformation matrix is applied.

5. *Soft tissue thickness measurement at craniometric landmarks.*
   Soft tissue thickness measurement in craniometric landmark is made using the Euclidean distance calculation between craniometric landmark on the skull surface and the corresponding landmark on the face surface.

The basics of the above algorithm described as original in [8] is normally used for facial reconstruction. In this research it is proposed to perform soft tissue thickness measurement using the author's modification of the original algorithm.

To validate the implemented algorithm the soft tissue thickness was measured in basic craniometric landmarks (Table 1). From IXI database 18 MRI images were chosen. These were Caucasian adult females, aged from 18 to 29 years and having the BMI in the range 20-25 [kg/m^2]. For each landmark the following statistical parameters were estimated:

– Mean – mean value of soft tissue thickness in a landmark, [mm];
– S.D. – standard deviation of soft tissue thickness in a landmark, [mm];
– Min – minimum value of soft tissue thickness in a landmark, [mm];
– Max – maximum value of soft tissue thickness in a landmark, [mm].

The software PMOD version 3.5 was used as a image processing tool to implement and to test the methodology [17]. Program package R was used for statistical calculations [18].

3 Results

The results of matching quality evaluation are gathered in Table 2 and Table 3. The age is presented in [years], BMI – in [kg/m^2].

Table 2. Evaluation of matching quality of analysed MRI images with low BMI to templates with boundary values from BMI range SDIF – the sum of the differences in [mm] between craniometric landmark, marked manually by the operator in the analysed image, and the landmark received as the result of automatic matching MRI image to template; MX – Asian or Asian British; EX – White; F – Female; M – Male

Parameters in test group					SDIF	SDIF
Nr	Race	Sex	Age	BMI	BMI < 25	$30 \leq$ BMI < 60
1	MX	F	52.53	22.8	93	103
2	EX	F	42.15	21.1	101	152
3	EX	F	42.22	19.8	76	72
4	MX	M	50.4	19.9	94	97
5	EX	M	24.88	21.1	98	109
6	EX	M	54.69	20.1	97	100
7	EX	F	66.86	21.0	108	86

SDIF values from Table 2–3 show that MRI images obtained for low BMI cases are matched better to the template for low BMI, whereas MRI images obtained for high BMI cases are better matched to the template with high BMI. The matching quality depends thus on the template used in the matching process. Since the differences in the matching quality criterion are not so big, there is no need to increase the number of BMI ranges and the number of templates.

Table 3. Evaluation of matching quality of analysed MRI images with high BMI to templates with boundary values from BMI range SDIF – the sum of the differences in [mm] between craniometric landmark, marked manually by the operator and the landmark obtained from of automatic matching; AN – Black or Black British; EX – White; F – Female; M – Male

Parameters in test group					SDIF	SDIF
Nr	Race	Sex	Age	BMI	BMI < 25	$30 \leq$ BMI < 60
1	AN	F	49.92	30.5	149	81
2	EX	F	74.64	31.3	99	111
3	EX	F	62.96	35.5	109	83
4	EX	F	42.97	39.5	94	56
5	EX	F	51.66	43.6	124	91
6	EX	M	52.89	36.3	107	85
7	EX	M	37.95	35.1	132	103

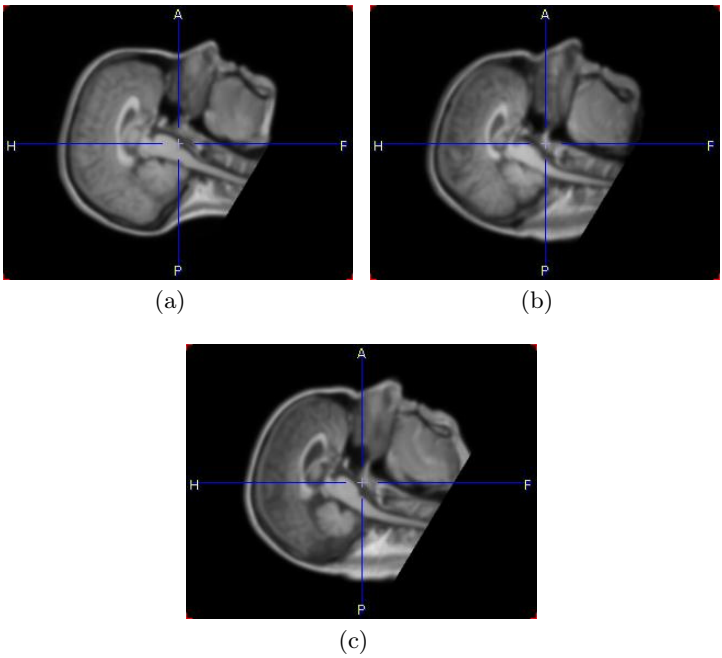

(a) (b)

(c)

Fig. 1. Templates with different BMI: (a) BMI$<$ 25, (b) $25 \leq$ BMI < 30, (c) $30 \leq$ BMI < 60

Based on preliminary experiments 3 templates according to BMI ranges were created (Fig. 1):

– BMI<25 – normal body constitution;
– $25 \leq$ BMI < 30 – overweight;
– $30 \leq$ BMI < 60 – obesity class I-III.

Examples of automatically localized craniometric landmarks obtained using the proposed algorithm is presented in Fig. 2. The red squares present the craniometric landmarks on the skull surface. The green squares present the landmarks on the face surface corresponding to each craniometric landmark on the skull surface. Soft tissue thickness is measured as a distance between each pair of landmarks.

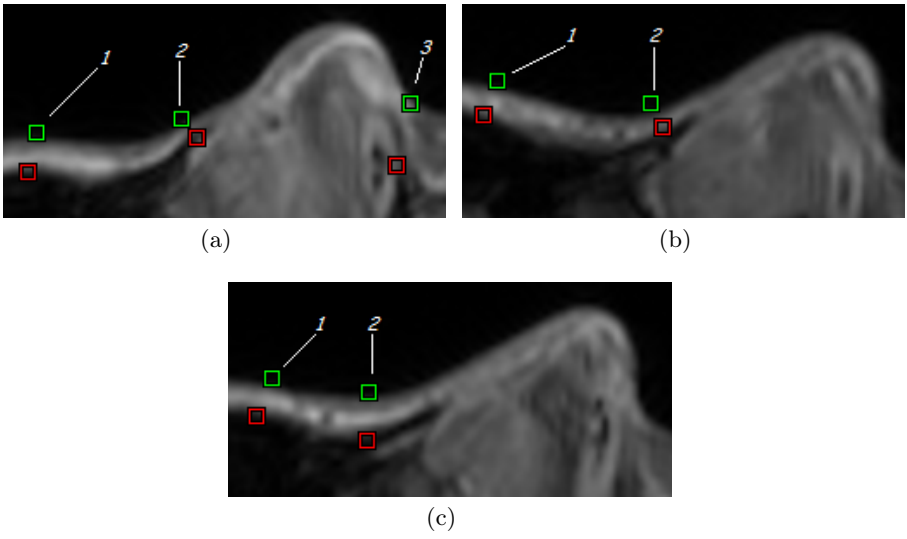

(a) (b)

(c)

Fig. 2. Presentation of automatically localized craniometric landmarks without location correction (a) Glabella, (b) Nasion, (c) Rhinion

The statistical parameters obtained for the selected set of 18 MRI images are presented in the Table 4 and Fig. 3. The measurements are presented in millimetres and rounded to one fractional digit.

The obtained values of soft tissue thickness in the craniometric landmarks were compared with data presented in [3], collected for group of subjects selected using the same criterion.

Table 4. Soft tissue thicknesses measured for Caucasian females 18 – 29 years and BMI 20 – 25 [kg/m^2], x_r – landmark located on the right side of the head, x_l – landmark located on the left side of the head

Nr	Craniometric landmark	Mean	S.D.	Min	Max
1	g	5.77	0.48	4.98	6.58
2	n	7.06	0.36	6.5	7.77
3	rhi	4.06	0.17	3.77	4.33
4	ns	10.57	0.43	9.81	11.25
5	pg	11.76	0.61	10.41	12.87
6	gn	7.97	0.52	7.19	9.06
7	pr	13.0	0.53	11.89	13.85
8	ids	12.51	0.56	11.34	13.52
9	inc	4.35	0.21	3.92	4.69
10	id	10.59	0.47	9.61	11.3
11	op	6.18	0.61	5.13	7.35
12	i	7.66	0.8	6.21	8.88
13	al_r	10.1	0.48	9.24	11.00
14	al_l	10.51	0.44	9.62	11.21
15	or_r	6.25	0.39	5.64	6.89
16	or_l	6.79	0.37	6.15	7.43
17	sor_r	6.91	0.47	6.21	7.76
18	sor_l	6.99	0.49	6.32	7.9
19	zy_r	7.28	0.73	6.36	8.62
20	zy_l	6.45	0.63	5.65	7.65

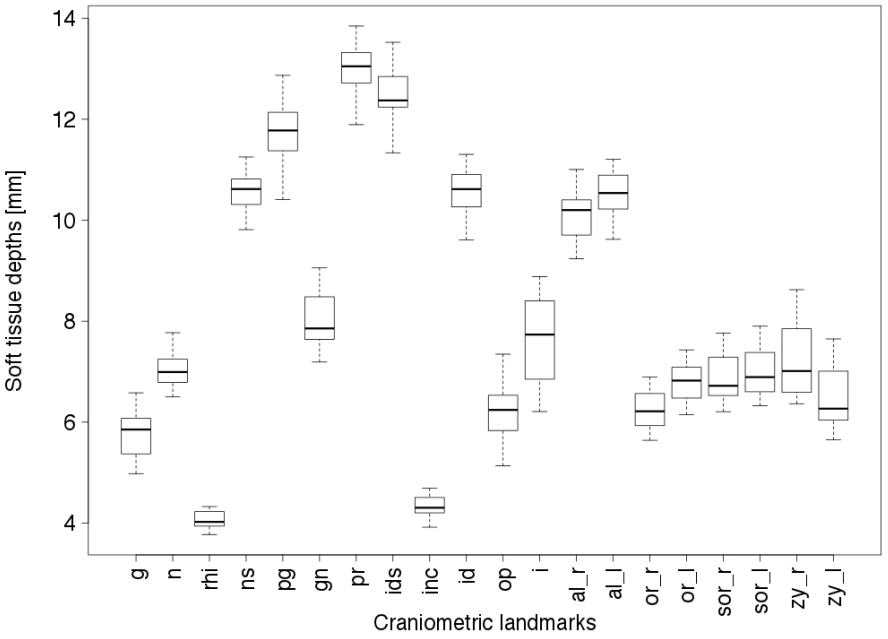

Fig. 3. Box plot shows soft tissue thickness [mm] measured automatically in craniometric landmarks

Table 5. Comparison of measurement results with published data; DM (18) – measured soft tissue thicknesses data for 18 patients; DL (149) – soft tissue thicknesses literature data for 149 patients [3]

Nr	Craniometric landmark	DM (18)			DL (149)		
		Mean	S.D.	Range	Mean	S.D.	Range
1	g	5.8	0.5	5 – 6.6	5.1	0.8	3.4 – 7.5
2	n	7.1	0.4	6.5 – 7.8	6.3	1.2	4.0 – 9.4
3	rhi	4.1	0.2	3.8 – 4.3	2.6	0.8	1.6 – 9.2
4	pg	11.8	0.6	10.4 – 12.9	9.6	1.7	6.7 – 14.3
5	gn	8.0	0.5	7.2 – 9.1	5.6	1.3	3.3 – 10.2
6	pr	13.0	0.5	11.9 – 13.9	9.8	1.6	2.6 – 13.6
7	ids	12.5	0.6	11.3 – 13.5	10.0	1.7	5.6 – 13.8
8	id	10.6	0.5	9.6 – 11.3	11.0	2.0	6.9 – 15.5
9	al_r	10.1	0.5	9.2 – 11.0	9.5	1.3	5.8 – 12.6
10	al_l	10.5	0.4	9.6 – 11.2	9.7	1.3	5.8 – 12.6
11	or_r	6.3	0.4	5.6 – 6.9	9.4	2.1	3.3 – 14.2
12	or_l	6.8	0.4	6.2 – 7.4	9.5	2.1	3.3 – 14.2
13	sor_r	6.9	0.5	6.2 – 7.8	5.4	1.0	3.8 – 10.9
14	sor_l	7.0	0.5	6.3 – 7.9	5.6	1.0	3.8 – 10.9
15	zy_r	7.3	0.7	6.4 – 8.6	6.7	1.5	3.6 – 11.3
16	zy_l	6.5	0.6	5.7 – 7.7	6.5	1.5	3.6 – 11.3

4 Discussion

The comparison and analysis of own measurement results and literature data [3] indicates that method proposed here gives close results to those obtained using the ultrasonic method. However, 75% of measurement results based on ultrasonography are smaller than the values obtained in the same landmarks using the method proposed here. The systematic error in such situation most probably results from the fact, that the ultrasonic measurement requires probe contact with the skin and this provokes some soft tissue deformation. Because of this the results based on the ultrasonic method are strongly operator-dependent. Our method operates on data obtained without any contact with the soft tissue.

43.75% values of our data are within the range mean+/-SD of the literature data. The remaining 56.25% are within the range mean+/-2SD of literature data.

Important differences in SD values appeared because of quite big soft tissue thickness spread in particular craniometric landmarks in the literature data. These data were collected from much bigger quantity of patients [3]. It explains why they have such a wide range of soft tissue thickness values.

5 Conclusion

An automatic, non-contact method for the definition of the craniometric landmarks and soft tissue thickness measurement in these landmarks is proposed. The

method uses the MRI for data collection, is non-invasive and has no counter-indications in widespread use. The novelty of the method proposed is that it performs the inverse transform on the set of craniometric points instead of performing it on the surface of a template face.

The full automatization of measurement greatly speeds up the process of soft tissue measurements and also gives a possibility to acquire results for large population within shorter time. A comparison of own results with literature data allows to state, that the proposed method on the current stage of development gives similar results to literature data. Another advantage of the method is the limited role of the operator during the process of soft tissue thickness measurement as compared to e.g. needle probing or ultrasonic methods. In the proposed method the operator defines craniometric landmarks only on the template which will be used in future matching. It is also a weakness of the method, as an erroneous definition of the craniometric landmark in the template can make the error propagate to further MRI images. In order to eliminate this disadvantage the following step in the development of the algorithm will be the automatic correction of craniometric landmarks in MRI data. Another task is to propose and validate an objective measure for the selection of number of averagings when creating the template.

References

1. Stephan, C.N., Simpson, E.K.: Facial Soft Tissue Depths in Craniofacial Identification (Part I): An Analytical Review of the Published Adult Data. Journal of Forensic Sciences 53(6), 1257–1272 (2008)
2. Gerasimov, M.M.: Vosstanovlenie lica po cerepu. Akademii Nauk SSSR, Moskva (1955)
3. De Greef, S., Claes, P., Vandermeulen, D., Mollemans, W., Suetens, P., Willems, G.: Large-scale in-vivo Caucasian facial soft tissue thickness database for craniofacial reconstruction. Forensic Science International 159S, 126–146 (2006)
4. Facial-Soft-Tissue-Depth Data Store, `http://www.craniofacialidentification.com/CFSTDDS.html`
5. Kurkcuoglu, A., Pelin, C., Canan, S., Zagyapan, R., Sahinoglu, Z., Ozsoy, O.P.: A comparison of facial soft tissue thickness in Anatolian pre-pubertal and post pubertal subjects in relation to different facial patterns. Anatomy 5, 7–17 (2011)
6. Dementieva, S.: Ivan Groznyi, volevoi i brezglivyi, `http://wsyachina.narod.ru/technology/physio_restor.html`
7. El-Mehallawi, I.H., Soliman, E.M.: Ultrasonic assessment of facial soft tissue thicknesses in adult Egyptians. Forensic Science International 117, 99–107 (2001)
8. Clement, J.G., Marks, M.K.: Computer-graphic facial reconstruction. Elsevier, Academic Press, Burlington (2005)
9. Zhang, K., Cheng, Y., Leow, W.K.: Dense Correspondence of Skull Models by Automatic Detection of Anatomical Landmarks. In: Wilson, R., Hancock, E., Bors, A., Smith, W. (eds.) CAIP 2013, Part I. LNCS, vol. 8047, pp. 229–236. Springer, Heidelberg (2013)
10. Grau, V., Alcaniz, M., Juan, M.C., Monserrat, C., Knoll, C.: Automatic Localization of Cephalometric Landmarks. Journal of Biomedical Informatics 34, 146–156 (2001)

11. Worz, S., Rohr, K.: Localization of anatomical point landmarks in 3D medical images by fitting 3D parametric intensity models. Lecture Notes in Computer Science, 76–88. Springer (2003)
12. El-Feghi, I., Sid-Ahmed, M.A., Ahmadi, M.: Automatic localization of craniofacial landmarks for assisted cephalometry. Pattern Recognition 37, 609–621 (2004)
13. IXI dataset, http://www.brain-development.org/
14. De Greef, S., Vandermeulen, D., Claes, P., Suetens, P., Willems, G.: The influence of sex, age and body mass index on facial soft tissue depths. Forensic Science, Medicine, and Pathology 5, 60–65 (2009)
15. National Institutes of Health, National Heart, Lung, and Blood Institute, North American Association FOR The Study of Obesity: The Practical Guide Identification, Evaluation, and Treatment of Overweight and Obesity in Adults. NIH Publication Number 00-4084 (2000)
16. Buades, A., Coll, B., Morel, J.M.: A non-local algorithm for image denoising. In: IEEE Computer Society Conference on Computer Vision and Pattern Recognition (CVPR 2005), vol. 2, pp. 60–65 (2005)
17. PMOD software documentation, http://www.pmod.com/technologies/products/products.html
18. R software documentation, http://www.r-project.org/
19. White, T.D., Black, M.T., Folkens, P.A.: Human osteology, 3rd edn. (2012)

The Assessment of Brain Volume in the Postoperative Craniosynostosis

Anna Fabijańska[1], Jarosław Gocławski[1], and Wanda Mikołajczyk-Wieczorek[2]

[1] Lodz University of Technology, Institute of Applied Computer Science,
18/22 Stefanowskiego Str., 90-924 Lodz, Poland
{anna.fabijanska,jaroslaw.goclawski}@p.lodz.pl
[2] Polish Mother's Memorial Hospital, Research Institute,
281/289 Rzgowska St., Lodz, Poland
drwanda@tlen.pl

Abstract. This paper considers the problem of brain volume assessment in children with craniosynostosis using the algorithms of image processing and analysis. In particular the postoperative craniosynostosis is considered. In this case the quantitative assessment of brain volume is very challenging due to missing fragments of the skull. These are removed during the corrective surgery and make image segmentation algorithms fail when applied to the brain extraction. The approach introduced in this paper overcomes this problem by combining morphological processing with the 3D random walk segmentation. The details of the introduced approach are explained in the paper contents. The results of the brain segmentation and brain volume assessment for the postoperative subjects are presented, analysed and discussed.

Keywords: image segmentation, brain volume assessment, craniosynostosis, random walker.

1 Introduction

The craniosynostosis is a serious abnormality of infancy and childhood, which occurs in 1 in 2500 births. It is defined as premature fusion of cranial sutures resulting in compensatory growth in other areas of the skull [2]. Craniosynostosis is classified as involving a single suture versus multiple sutures and as either syndromic or nonsyndromic. Unlike the syndromic type, nonsyndromic synostosis is not associated with other dysmorphisms of the face, trunk or extremities. Furthermore, nonsyndromic craniosynostoses typically involve a single suture, the most common types being sagittal, unicoronal, bicoronal, metopic and lambdoidal [1]. Aims of the surgical correction of these conditions are to counteract the cosmetic and functional anomalies of the craniofacial skeleton, to restore the normal spatial relationship between the skull and the contained neural and vascular structures, to correct the possibly associated abnormalities of the cerebral blood flow and cerebrospinal fluid circulation as well as to re-orientate the deviated growth vectors of the skull base and vault. The types of techniques

E. Pietka, J. Kawa, and W. Wieclawek (eds.), *Information Technologies in Biomedicine, Volume 3*, Advances in Intelligent Systems and Computing 283,
DOI: 10.1007/978-3-319-06593-9_12,

include: strip craniectomy and fronto-orbital advancement with calvarial vault remodeling [7]. In general, they all are performed by the removal of the deformed fragments of skull.

The traditional postoperative assessment of the craniosynostosis is most commonly performed based on linear measurements of the brain characteristic dimensions obtained from CT scans. These measurements are performed manually by the specialist and as a result are often inaccurate, unrepeatable and subjective. Additionally, they include only the information contained in the most representative slices what limits the accuracy of the case assessment.

One of the indicators which could be applied to the postoperative assessment of craniosynostosis is brain volume. However, determination of this parameter requires the segmentation of intra-cranial region from CT or MRI scans. Manual segmentation of this region usually involves laborious and time consuming brain image editing and cannot be applied in everyday clinical routine. Therefore an automatic brain segmentation algorithm seems to be the best choice to quickly obtain the brain volume information.

The task of the brain segmentation has been widely discussed over the years and numerous approaches to this problem have already been proposed. However, most of the existing approaches require the presence of a continuous skull which limits the brain region. As a result they cannot be applied for brain segmentation in the postoperative craniosynostosis, where significant parts of the skull are missing and its borders remain discontinuous. Therefore there is a need of developing dedicated brain segmentation algorithms and another algorithms for further quantitative analysis of this region.

The problem of application of image processing and analysis algorithms for a quantitative assessment of craniosynostosis is generally new. To the best of our knowledge only a few research projects in this topic have already been reported. These regard mostly preoperative cases and consider automatic classification of the disease type based on skull properties [9, 10, 13]. Research dedicated to the postoperative cases is mostly concerned with modelling of skull shape after surgical treatments [3, 4, 12]. There is also work on assessment of brain volume in the postoperative craniosynostosis [11]. However, the authors consider only MRI images and do not reveal any details about the image segmentation algorithm used in the research.

Having in mind the above-mentioned, this paper considers the problem of brain segmentation and brain volume estimation in the postoperative craniosynostosis.

The following part of this paper is organized as follows. Firstly, in Section 2 the regarded problem is briefly outlined. This is followed in Section 3 by the description of medical data used in this research. The more detailed description of the introduced approach is given in Section 4. The results are presented and discussed in Section 5. Finally, Section 6 concludes the paper.

2 Problem Definition

The estimation of brain volume requires separation of the brain region from CT scans of the whole head using appropriate segmentation algorithm. In the case of the head with a complete skull this task is rather simple, as borders of the brain are clearly delineated by the skull. However, in the case of the postoperative craniosynostosis pieces of the skull are missing as they are removed during the corrective surgery. This problem is illustrated in Figure 1 which shows exemplary CT slices and 3D views of a skull in the postoperative craniosynostosis.

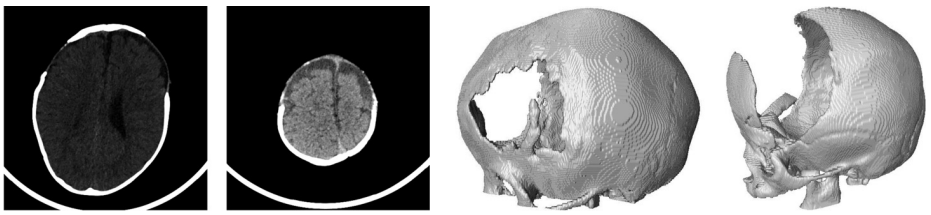

Fig. 1. Exemplary CT slices and 3D view of skull in the postoperative craniosynostosis

Due to the discontinuities of the skull the brain segmentation is a challenging task in the postoperative craniosynostosis. The missing pieces of the skull make image segmentation algorithms fail, when applied to the extraction of brain region. In particular, many segmentations with the traditional algorithms [5] are affected by the phenomenon of brain over-segmentation out of its real space, known as "leakage". Then the revealed brain region can include the pieces of skin. This effect is presented in Figure 2, where the "leakages" are indicated by arrows.

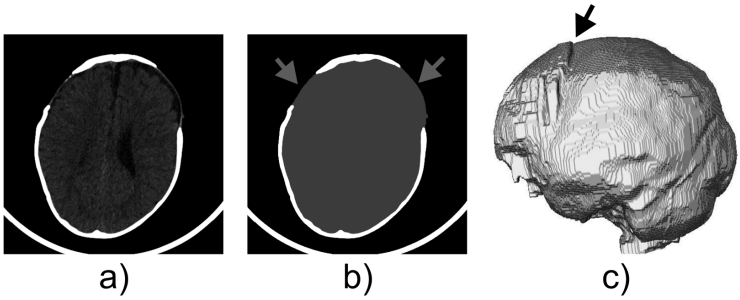

Fig. 2. The segmentation leakages in the postoperative craniosynostosis (indicated by arrows); a) exemplary slice; b) segmentation result compared to the input slice; c) 3D view of the extracted brain space

The over-segmentation falsely increases brain size and thus its volume. It also deteriorates the real brain shape. All these factors influence further diagnosis of the disease. Therefore, in the considered problem, the brain segmentation algorithm must to be robust to skull discontinuity.

Having in mind this requirement, a new approach introduced in this paper is based on the random walker (RW) approach [6]. One of the most important properties of the RW method is that it obeys weak and discontinuous borders.

The RW algorithm is dedicated to image segmentation into number of regions based on seeds provided for each region. Image division is obtained by assigning each unlabeled node a label which represents one of the output regions. Labels are assigned with respect to the probability that a random walker released from each unlabeled pixel will firstly reach one of the seeds. The random walk occurs on a weighted and undirected pixel adjacency graph. The final segmentation is obtained by including a pixel into a region for which the greatest probability exists.

The detailed description of the introduced approach is given in the following sections.

3 Input Data Windowing

Three dimensional CT brain scans of the postoperative craniosynostosis were examined. The slices were provided with 16-bit resolution and stored as signed 16-bit monochromatic images of the resolution 512 x 512 pixels and stored in the DICOM file format. Individual slices of each image were stacked into a 3D space representing volumetric data set. The number of slices in the dataset varied between 100 and 200.

Before the main processing, input data $i(\mathbf{x})$ was normalized to the range of intensities $[0, 1]$. The normalization, performed in accordance with Equation 1, highlighted intensities from 0 HU to 150 HU corresponding to the brain tissues and attenuated intensities below 0 and above 150 HU, corresponding to the surrounding air and the dense tissues respectively.

$$j(\mathbf{x}) = \begin{cases} 1 & \text{if } i(\mathbf{x}) \geq \mathbf{150} \\ 0 & \text{if } i(\mathbf{x}) \leq \mathbf{0} \\ i(\mathbf{x})/\mathbf{150} & \text{otherwise} \end{cases} \tag{1}$$

After normalization, the skull is represented by the intensity value equal to 1, while the intensity equal to 0 is assigned to air outside head.

4 The Proposed Approach

The main steps of the introduced approach to the evaluation of brain volume in the postoperative craniosynostosis are depicted in Figure 3. The method starts from the preprocessing stage, which aims at the determination of background and object seeds for the random walk segmentation performed in the following

step. During the post processing stage the brain surface is smoothed and the errors of segmentation are corrected using approximation techniques. Finally, the brain volume is determined based on the segmentation result.

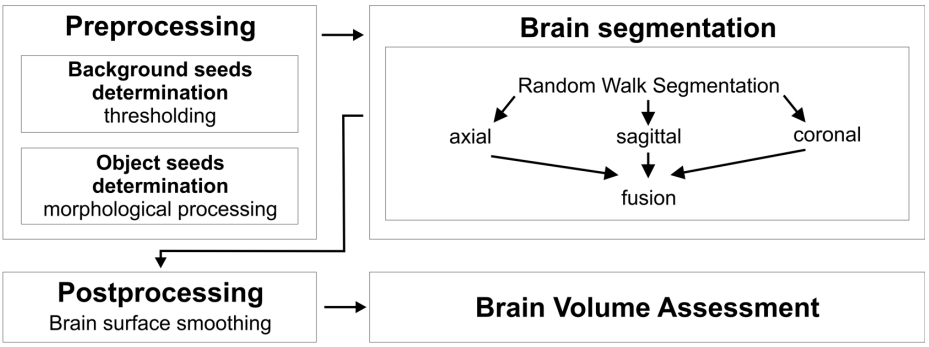

Fig. 3. The consecutive steps of the introduced approach

The consecutive steps are described in details in the following subsections.

4.1 Preprocessing

The introduced brain segmentation algorithm is based on the random walk approach [6], which requires initialization by object and background seeds. These seeds are created in the preprocessing step.

The background seeds are identified as pixels belonging to the skull and are easily determined by a simple thresholding of the image, performed in accordance with Equation 2.

$$s(\mathbf{x}) = \begin{cases} 1 & \text{if } j(\mathbf{x}) = \mathbf{1} \\ 0 & \text{if } j(\mathbf{x}) < \mathbf{1} \end{cases}, \tag{2}$$

where $\mathbf{x} = \{x_1, x_2, x_3\}$ denotes pixel coordinates, s is the binary image of the skull and i represents the input CT image after windowing (see Sect. 3).

Object seeds are determined using morphological processing. Firstly, the binary image is produced as shown in Equation 3.

$$b_1(\mathbf{x}) = \begin{cases} 1 & \text{if } j(\mathbf{x}) = 0 \text{ or } j(\mathbf{x}) = 1 \\ 0 & \text{otherwise} \end{cases}. \tag{3}$$

The image b_1 shows the pixels of intensities different from 0 and 1, i.e. the pixels which do not belong to the skull or the region surrounding the head. However, in the image b_1 there are pixels corresponding both to the brain space and other regions adjacent to the brain (e.g. eyes, nose, ears, head skin etc.; see Fig. 4b,c). Therefore, in the next step image erosion [5] with big structuring element followed by median filtration [5] are performed in accordance with

Equation 4 in order to disconnect these regions from the brain region and to smooth its surface respectively.

$$b_2 = median(b_1 \ominus s_e, [n, n, n]), \tag{4}$$

where s_e is a large structuring element and $n = 5$ is a dimension of median filter. In particular s_e is a cube of dimensions equal to $0.2Z$ where Z is a number of slices in the dataset.

Finally, the largest 3D connected component b_3 is selected from the binary image b_2 (see Fig. 4d,e). This component contains the pixels belonging to the brain region and is used as object seeds for the random walk segmentation performed in the next step.

The exemplary visual results of the consecutive steps of seeds determination are shown in Figure 4. In particular, an exemplary CT brain slice is shown in Figure 4a. This is followed in Figures 4b and c by the presentation of pixels with intensities different from 0 and 1 in the 3D and planar views respectively. The 3D and 2D views of object seeds only are shown in Figures 4d and e. Figure 4f contains the 3D view of object and background seeds.

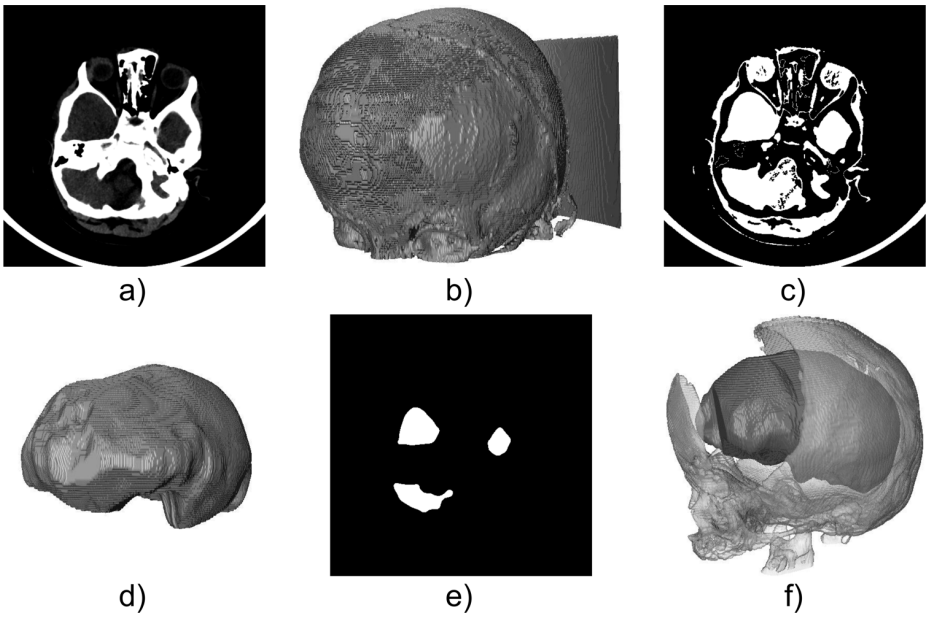

Fig. 4. The consecutive steps of seeds determination; a) exemplary CT slice; b) pixels of intensities different from 0 and 1 - 3D view; c) pixels of intensities different from 0 and 1 - exemplary CT slice; d) object seeds - 3D view; e) object seeds - exemplary CT slice; f) 3D view of object and background seeds

4.2 Brain Segmentation

The determination of object and background seeds is followed by the random walk segmentation. In particular, the procedure is performed slice-by-slice separately in three orthogonal view-planes i.e. the axial plane, the sagittal plane and the coronal plane. The results of the segmentation for single slices obtained in each plane are stacked together into a volumetric space. The volumes formed independently for every plane are next combined together, in order to perform the first approximation (coarse segmentation) of the brain region. This idea is explained in Figure 5. In particular, the consecutive columns of the figure present the results of the brain image segmentation performed in the axial, sagittal and coronal directions respectively. In the last column the fusion effect of these partial results is shown. The fusion of binary components means their logical sum in a three dimensional space according to Equation 5.

$$b_4(\mathbf{x}) = b_a(\mathbf{x}) \cup b_s(\mathbf{x}) \cup b_c(\mathbf{x}), \tag{5}$$

where $\mathbf{x}$ denotes an image voxel, $b_4(\mathbf{x})$ is the fusion result, $b_a(\mathbf{x})$, $b_s(\mathbf{x})$, $b_c(\mathbf{x})$ represent respectively the axial, sagittal and coronal component images.

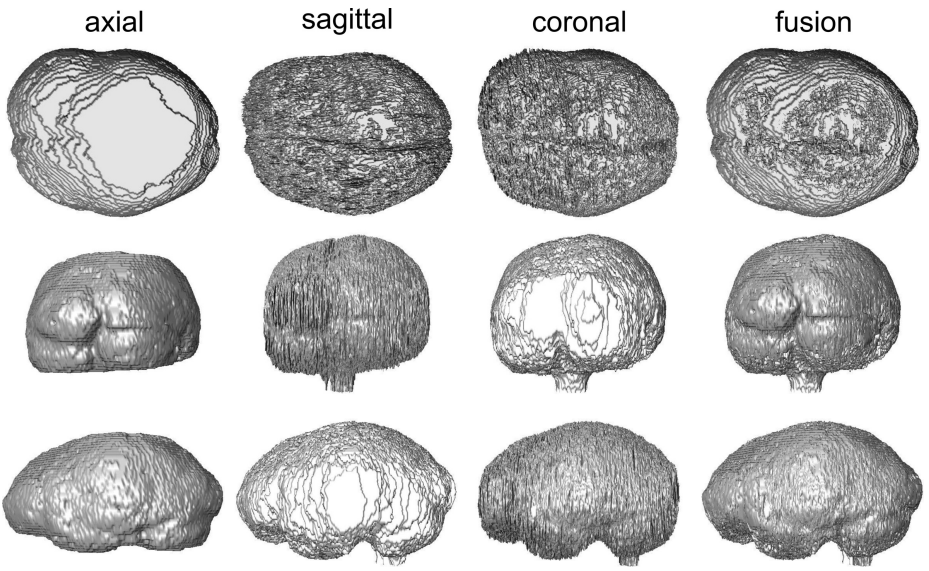

Fig. 5. The results of the random walk segmentation performed in the axial, the sagittal and the coronal directions. The last column shows the fusion of partial results.

Exemplary CT slices with the results of the random walk segmentation applied to each of the regarded directions are shown in Figure 6. These are shown in light grey. Additionally, the seeds for the segmentation are visualised in dark gray.

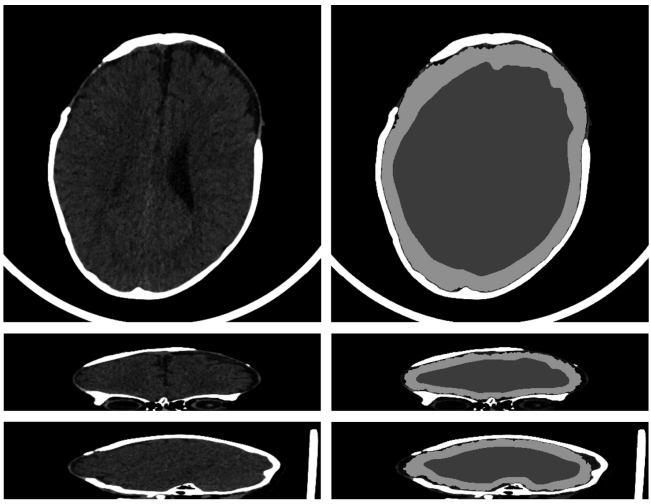

Fig. 6. Exemplary CT slices presenting results of the random walk segmentation performed in the axial, sagittal and coronal directions; left column - original images, right column - segmentation results

4.3 Post Processing

During the post processing the brain surface is smoothed in order to remove artefacts caused by the image segmentation performed slice-by-slice in the three orthogonal directions. The removal is obtained by applying median filtration. In order to utilize the information contained in all views 3D filtration is applied using the mask of 5 x 5 x 5 pixels. The size of this mask was adjusted experimentally.

4.4 Brain Volume Evaluation

After the brain region has been segmented, its volume can be easily determined by counting all of its pixels. In particular, each pixel is regarded as a cuboid of dimensions equal to $d_x \times d_y \times d_z$, where d_z is the slice thickness, d_x and d_y represent the pixel spacing in X and Y directions respectively. All these parameters are stored in the header of each DICOM file including a slice of the CT image. The volume V_p of a single pixel can be determined from Equation 6, while the volume V_b of the brain is described by Equation 7.

$$V_p = d_x d_y d_z. \tag{6}$$

$$V_b = V_p \sum_{z=1}^{Z} \sum_{y=1}^{Y} \sum_{x=1}^{X} b_4(\mathbf{x}), \tag{7}$$

where X and Y are the dimensions of a single slice, Z is the number of slices and b_4 denotes the binary mask image of a brain.

5 Results and Discussion

Visual results of applying the introduced segmentation approach to 4 exemplary subjects with the postoperative craniosynostosis are presented in Figure 7. For every case three randomly selected slices in the axial, the sagittal and the coronal views are presented. Additionally, 3D views of a brain and a skull are provided. The case ID is indicated at the beginning of each row. The corresponding brain volumes determined from the segmentation results are listed in Table 1. Additionally, they are compared with the volumes obtained by the radiological specialist using a manual method for labelling pixels in the regions of interest. The volume data are accompanied by the values of the Dice coefficient [8] located in the third column. It represents one of the known similarity measures between data sets. In the considered case it can be expressed as in Equation 8.

$$Dice(R_{AUTO}, R_{REF}) = \frac{2\,|R_{AUTO} \bigcap R_{REF}|}{|R_{AUTO}| + |R_{REF}|}, \tag{8}$$

where $|\ \cdot\ |$ is the symbol of set cardinality and R_{AUTO} and R_{REF} denote the pixel sets of brain regions identified with the automatic or reference method respectively.

The visual results of brain segmentation presented in Figure 7 clearly show that the introduced approach was successful in extracting the intracranial region. Although in the regarded cases significant parts of skulls were missing, the brain was successfully extracted and the leakages outside the intracranial space were effectively avoided.

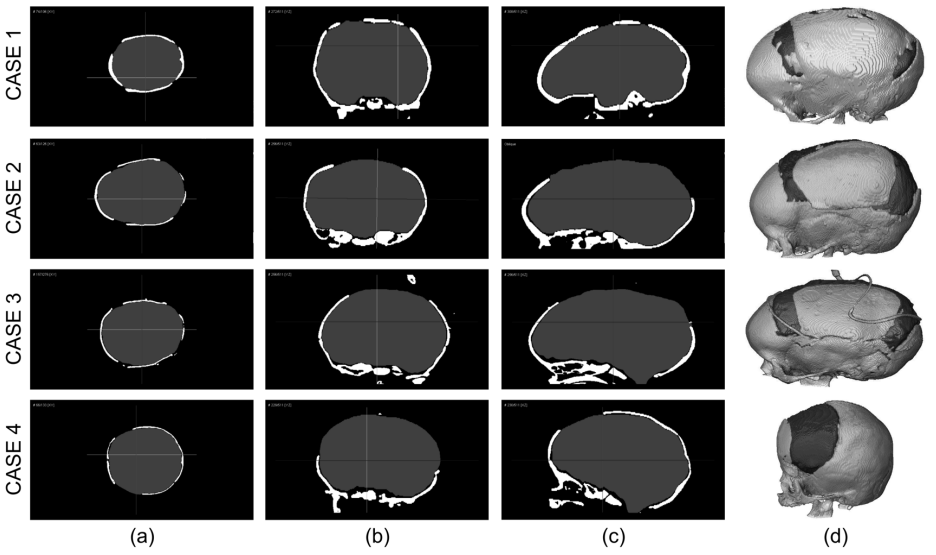

Fig. 7. The results of brain segmentation using the introduced approach; (a) axial view; (b) sagittal view; (c) coronal view; (d) 3D view of a brain and a skull

Table 1. The comparison of the brain region volumes determined automatically V_{AUTO} with the referential ones V_{REF} at the level of region similarity verified by the Dice coefficients

Case ID	V_{AUTO} $[dm^3]$	V_{REF} $[dm^3]$	Dice [%]
1	0.9797	0.9931	97.3927
2	1.1386	1.2521	93.6140
3	0.9079	0.9965	95.8531
4	1.0777	1.1536	96.5613

The results of volume measurement included in Table 1 show that the volumes obtained with the automatic method in all considered cases differ less than 10% from the results of the manual method. In particular, the brain object volumes obtained by the automated method are slightly and systematically underestimated. The relative error of volume estimation fits in the range $[-1.3, -9.1\%]$ with the average value of -6.5%. Such results obtained by the proposed segmentation can be regarded as good enough keeping in mind that the measurements refer to the volume of a complex biological structure with partially ambiguous or disappearing boundaries. The manual method often exploits very complex expert knowledge to classify the pixels of a brain image, not only grey-levels or simple texture features. This extra knowledge used in the segmentation process is difficult to verbalise or translate for programming language. Moreover, the differences up to 10% in the location of the organ by experts are also acceptable.

Simultaneously both of the methods (i.e. the automatic one and the manual one) show high similarities of the detected brain regions. This is shown by the Dice coefficient in Table 1 which is very high. It varies from about 94% to about 97% (i.e. only in the range of 3.8%). This proves that not only the volume but also the brain shape is properly mapped compared with the manual method. The sources of mapping error reside both in the human factor of the manual method and in the approximation of brain boundary mapping by the computer method. In future research, the authors will try to correct the little of the brain volume, based on interviews with experts performing the reference manual measurements.

At the end it should be underlined, that the goal of this paper is only to present the ability to detect the brain region from CT scans using the new method. For now the algorithm has been temporarily developed in the MATLAB 2012 environment with the support of functions from *Image Processing Toolbox*. The method is still under development, therefore the computational complexity of the algorithm has not been estimated yet. This will be done in the nearest future, when the algorithm is rebuild in the C++ environment under Windows.

6 Conclusions

The change of brain volume can be regarded as an important indicator applied to the post surgical assessment of craniosynostosis. In practice this parameter

is usually unused and often replaced by the linear measurements of brain characteristic dimensions as mentioned in Section 1. This happens because manual determination of the volume is extremely laborious and time consuming. Therefore the authors propose an automatic brain CT image segmentation method to extract the brain space as a serious alternative to the linear measurements or manual volume labelling by experts. The example results of the volume measurement presented in Section 5 show high compatibility with the results determined based on the manual segmentation. The proposed method was not developed yet in the form of a commercial application but its execution for the example images takes only several minutes, which is still much faster than the manual method requiring up to half an hour of expert work. After the implementation of the method in C++ code the authors plan to apply fully three-dimensional morphological preprocessing of the image and three dimensional random walker approach, which will probably take more time but may allow better volume measurement accuracy than the currently achieved.

Acknowledgement. The research was funded by the Ministry of Science and Higher Education of Poland from founds for science in years 2013-2015 in a framework of project no. IP 2012 011272.

References

1. Cohen, M.M., MacLean, R.E.: Craniosynostosis: Diagnosis, Evaluation, and Management. Oxford University Press, Oxford (2000)
2. David, D.J., Poswillo, D., Simpson, D.: The Craniosynostoses: Causes, Natural History, and Management. Springer (2013)
3. Elias de Oliveira, M., Hallila, H., Ritvanen, A., Buchler, P., Paulasto, M., Hukki, J.: Postoperative Evaluation of Surgery for Craniosynostosis Based on Image Registration Techniques. In: Proc. Ann. Int. Conf. Engineering in Medicine and Biology Society, pp. 5620–5623 (2010)
4. Elias de Oliveira, M., Hallila, H., Ritvanen, A., Buchler, P., Paulasto, M., Hukki, J.: Feature-Invariant Image Registration Method for Quantification of Surgical Outcomes in Patients with Craniosynostosis: a Preliminary Study. J. Pediatr. Surg. 46(10), E1–E8 (2011)
5. Gonzalez, R.C., Woods, R.E.: Digital Image Processing. Prentice-Hall Inc. (2006)
6. Grady, L.: Random Walks for Image Segmentation. IEEE Trans. Pattern Anal. Mach. Intell. 28(11), 1768–1783 (2006)
7. Hayward, R., Jones, B., Dunaway, D.: Clinical Management of Craniosynostosis. Mac Keith Press (2004)
8. Labatut, V., Cherifi, H.: Accuracy measures for the comparison of classifiers. CoRR, arXiv:1207.3790 (2012), http://arxiv.org/abs/1207.3790
9. Lin, H.J., Ruiz-Correa, S., Sze, R.W., Cunningham, M.L., Speltz, M.L., Hing, A.V., Shapiro, L.G.: Efficient Symbolic Signatures for Classifying Craniosynostosis Skull Deformities. In: Liu, Y., Jiang, T.-Z., Zhang, C. (eds.) CVBIA 2005. LNCS, vol. 3765, pp. 302–313. Springer, Heidelberg (2005)

10. Mendoza, C.S., Safdar, N., Myers, E., Kittisarapong, T., Rogers, G.F., Linguraru, M.G.: Computer-Based Quantitative Assessment of Skull Morphology for Craniosynostosis. In: Drechsler, K., Erdt, M., Linguraru, M.G., Oyarzun Laura, C., Sharma, K., Shekhar, R., Wesarg, S. (eds.) CLIP 2012. LNCS, vol. 7761, pp. 98–105. Springer, Heidelberg (2013)
11. Paniagua, B., Emodi, O., Hill, J., Fishbaugh, J., Pimenta, L.A., Aylward, S.R., Andinet, E., Gerig, G., Gilmore, J., van Aalst, J.A., Styner, M.: 3D of Brain Shape and Volume After Cranial Vault Remodeling Surgery for Craniosynostosis Correction in Infants. In: Proc. SPIE, vol. 8672 (2013), doi:10.1117/12.2006524
12. Wolański, W., Larysz, D., Gzik, M., Kawlewska, E.: Modeling and Biomechanical Analysis of Craniosynostosis Correction with the Use of Finite Element Method. Int. J. Numer. Method. Biomed. Eng. 29(8), 916–925 (2013)
13. Yang, S., Shapiro, L.G., Cunningham, M.L., Speltz, M., Le, S.: Classification and Feature Selection for Craniosynostosis. In: Proc. 2nd ACM Conf. Bioinformatics, Computational Biology and Biomedicine, pp. 340–344 (2011)

Multi-Image Texture Analysis in Classification of Prostatic Tissues from MRI. Preliminary Results

Dorota Duda[1], Marek Kretowski[1], Romain Mathieu[2], Renaud de Crevoisier[3], and Johanne Bezy-Wendling[3]

[1] Faculty of Computer Science, Bialystok University of Technology, Poland
{d.duda,m.kretowski}@pb.edu.pl
[2] Department of Urology, Pontchaillou University Hospital, Rennes, France
[3] LTSI, INSERM U1099, University of Rennes 1, France

Abstract. In the work, a (semi)automatic multi-image texture analysis is applied to the characterization of prostatic tissues from Magnetic Resonance Images (MRI). The method consists in a simultaneous analysis of several images, each acquired under different conditions, but representing the same part of the organ. First, the texture of each image is characterized independently of the others, using the same techniques. Afterwards, the feature values corresponding to the different acquisition conditions are combined in one vector, characterizing a multi-image texture. Thus, in the tissue classification process different tissue properties are considered simultaneously. We analyzed three MRI sequences: contrast-enhanced T1-, T2-, and diffusion-weighted one. Two classes of tissue were recognized: cancerous and healthy. Experiments with several sets of textural features and four classification methods showed that the application of multi-image texture analysis could improve the classification accuracy in comparison to single-image texture analysis.

Keywords: computer-aided diagnosis, tissue characterization, feature extraction, multi-image texture, classification.

1 Introduction

According to *Global Cancer Statistics* [1], prostate cancer is the second most frequently diagnosed cancer worldwide, and the sixth most frequent cause of cancer death in males. In 2008 it represented 14% of the total new cancer incidences (903,500 reported cases) and 6% of the total cancer deaths (258,400 cases) in males. In this context, the search for the methods allowing to detect a prostate pathology as early as possible and to determine its type (benign or malign) is crucial for reducing prostate cancer-caused mortality rates.

Admittedly, there exist some diagnostic tools for prostate cancers: the PSA (prostate-specific antigen) serum screening, the needle biopsies, or an ensemble of the MRI techniques enabling to visualize different prostatic tissue properties. However, the first two tools have many deficiencies and their use still remains

E. Pietka, J. Kawa, and W. Wieclawek (eds.), *Information Technologies in Biomedicine, Volume 3*, Advances in Intelligent Systems and Computing 283,
DOI: 10.1007/978-3-319-06593-9_13,

under discussion. For example, a 10-year experiment on 76,693 men conducted by Andriole *et al.* [2] revealed that there were no significant benefits of screening for prostate cancer with PSA serum testing. According to another report, in some cases prostate cancer screening could lead to over-treatment [3]. Furthermore, the use of needle biopsy, which is the current standard when discovering high PSA values, carries a risk of serious complications. Also, a needle may miss an important tumor case, when it does not hit the right place.

Considering the above facts, a large hope can be placed in a correct interpretation of MR prostate images, especially that their acquisition is not too invasive or harmful to health. However, the correct recognition of image content may go beyond the capacity of a non-equipped physician. It is important, therefore, to develop appropriate tools for computer-aided diagnosis (CAD).

The aim of present study is to validate methods for the texture-based analysis of MR prostate images and to examine their usefulness in prostatic tissue classification. In this process, we analyze simultaneously textures corresponding to different MR image sequences (contrast-enhanced T1-, T2-, and diffusion-weighted) and referring to the same prostate slice. According to our knowledge, no one has yet proposed a CAD system designed for prostate tumor recognition based on multi-image texture analysis from MR images. However, there exist few works on multi-image texture analysis concerning other organs and other imaging modalities. They have already shown that such an approach is promising in the process of tissue characterization and recognition.

The next section includes a short overview of existing CAD systems, incorporating methods for a simultaneous analysis of several images acquired under different conditions and representing the same part of an organ. In Sect. 3 our system for the classification of multi-image textures is presented. Experimental validation of the proposed methods is described in Sect. 4. Conclusions and future works follow in the last section.

2 Related Work

The earliest studies on the usefulness of multi-image texture analysis were presented in [4] and [5]. In both works, triples of CT liver images were analyzed simultaneously, in order to recognize the normal liver and its two primary malignant tumors: hepatocellular carcinoma (HCC) and cholangiocarcinoma. The images in a triple corresponded to the same liver slice. Each of them was acquired with different concentration of the contrast product injected to the patient. The first image was taken without the contrast, the next two ones – after its injection in the arterial and portal phase of its propagation in hepatic vessels. The multi-image texture was characterized by sets of features corresponding to each acquisition moment and placed all together in one vector. Experiments conducted separately for each of the three acquisition moments, and for the multi-image case proved the considerable potential of multi-image texture analysis.

The latter work, concerning the classification of liver pathologies from CT images, also showed the high usefulness of the multi-image approach for tissue characterization. In [6] four moments of contrast product propagation were considered: a pre-injection phase, and three after-injection phases: arterial, portal, and late. The CT images were analyzed in quadruples. Five types of liver lesions (cysts, adenomas, hemangiomas, HCC and metastasis) were recognized. Also here, a set of four textures was characterized by one vector composed of features calculated separately for each of the four acquisition moments.

Nagarajan *et al.* [7] used a multi-image texture analysis for breast lesion classification from dynamic contrast-enhanced (DCE) MR images. In order to differentiate two types of small lesions (benign and malign) five post-contrast images were analyzed simultaneously. A multi-image texture was characterized by five values of the same textural feature, each corresponding to a different moment of contrast product propagation. The study showed that the characterization of the lesion enhancement pattern could improve the classification accuracy of the considered, diagnostically challenging, breast lesions.

Quite different approach to multi-image texture analysis was presented in [8]. This study introduces the notion of "textural kinetics" that characterizes texture evolution under contrast product propagation in DCE-MRI. At first, textural features are calculated at each moment of contrast product propagation, and the "textural kinetics curve" is created basing on the set of feature values. Afterwards, a third order polynomial is fitted to such curve in order to characterize its shape. Four polynomial coefficients constitute the feature vector. Such a method was applied to the recognition of benign and malignant breast lesions and proved to be superior to lesion intensity profile dynamics.

Finally, Bhooshan *et al.* [9] combined textural features from both DCE T1- and T2-weighted MR images in order to recognize benign and malignant breast lesions. For the T1-weighted sequences, only the first post-contrast image was used for texture analysis. In this case, contrast product propagation was characterized by typical kinetic parameters obtained from signal-to-time curves. The experiments showed, that the combination of texture characteristics, obtained from both T1-, and T2-weighted images may outperform the conventional analysis of T1-weighted contrast-enhanced sequences.

To the best of our knowledge, there is no such a CAD system that combines texture characteristics corresponding to different MRI sequences (like T1-, T2-, or diffusion-weighted) in order to characterize prostatic tissue in classification process. There exist a few systems that use information about the propagation of contrast product based on T1-weighted DCE-MR sequences (e.g. [10]). Nevertheless, they use only pharmacokinetic models, employing the signal-to-time curves in order to find perfusion parameters. The aim of our work is, therefore, to assess the utility of multi-image texture analysis in the characterization of prostatic tissue from MRI. The images belonging to different MRI sequences will be analyzed simultaneously.

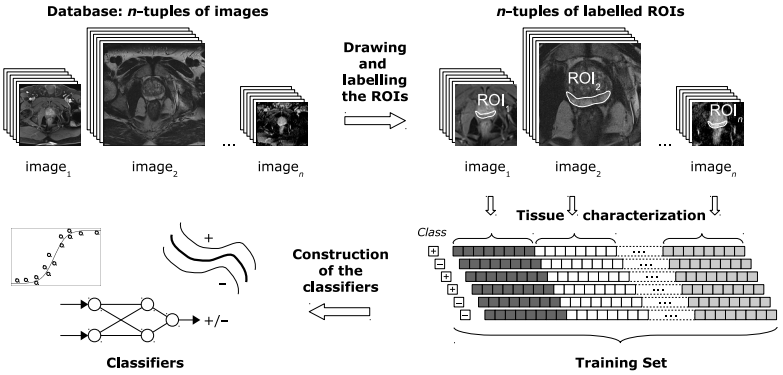

Fig. 1. A system for tissue classification based on multi-image texture analysis; the first stage of work: the construction of classifiers from a database of image n-tuples

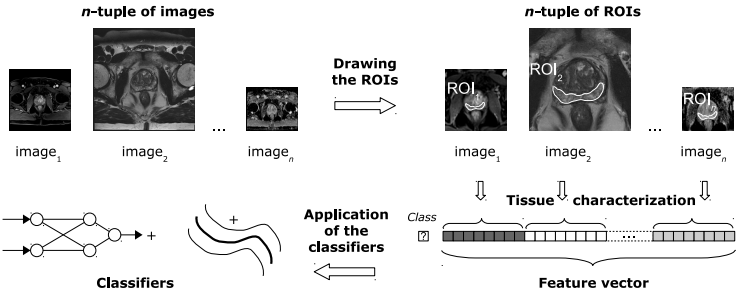

Fig. 2. A system for tissue classification based on multi-image texture analysis; the second stage of work: the application of classifiers to aid diagnosis

3 Methods

Two stages of work of a typical, image-based CAD system can be distinguished [11]. The first one, called *training* (or *learning*), consists in the preparation of the system for the recognition of several predefined tissue classes. In practice, this means constructing classifiers from a database of images which represent only diagnosed cases. The second stage is the application of the system in order to aid diagnosis.

The system which we are working on also follows the above-described, two-stage scheme. What distinguishes our system among others, is that the n images representing the same tissue slice but acquired under different acquisition conditions (e.g. different scanner settings) are combined in the n-tuples and analyzed simultaneously. The first stage of work of our system is presented in Fig. 1.

After the creation of a database, the n-tuples of images are formed. Depending on the number of considered image sequences, an n-tuple can comprise two, or more images. The order of images in each n-tuple is fixed. For example, a triple of

MRI prostate images might contain the T1-, the T2-, and the diffusion-weighted image on the first, the second, and the third position respectively.

An optional step here can be image pre-processing. It is used to improve the contrast, to eliminate the noise or the artifacts, or to equalize ranges of pixel values corresponding to different studies (which is the case in our database).

The next step is to outline the Regions of Interest (ROIs). A ROI covering the same part of the organ is outlined on each of the images forming an n-tuple. An n-tuple of thus obtained ROIs is analyzed simultaneously in order to characterize the tissue. First, the same set of textural features is calculated for each ROI in an n-tuple. Next, the features corresponding to different images in the n-tuple are combined in one "complex" vector characterizing a multi-image texture. In the simplest case, such a vector is formed by concatenating the sets of features corresponding to each considered sequence. Its parameters can also be a function of several feature values obtained with the same method and corresponding to different sequences. At this point, the doctor-specialist specifies the tissue class (label) which is attributed to each complex vector of features. The label reflects a pathology affecting the organ under consideration and is determined on the basis of a verified diagnosis. Labeled feature vectors form the so-called *training* (or *learning*) set. On the basis of such a set one or more classifiers are constructed.

Another optional step can be feature selection that takes place either before or during the construction of classifiers. It allows finding the most relevant features and rejecting redundant or inefficient ones. It also results in the reduction of memory and computation time required for the following processing steps.

Once the classifiers are constructed, the second stage of system work can take place: the system can be applied to identify new, yet undiagnosed cases. The key details of this process are depicted in Fig. 2.

At this stage, an n-tuple of images representing the same part of the organ is necessary. The order of the sequences from which subsequent images derive is the same as it was in the first stage of system work. Also the image pre-processing and the texture feature extraction techniques remain the same. After outlining the ROI on each of the images composing an n-tuple, the extraction of textural features for each ROI takes place. Next, a complex vector characterizing a n-tuple of textures is created. If feature selection was applied in the first stage, only the selected features are used here. Finally, the classifiers available in the system are applied and the most probable tissue class is indicated.

4 Experiments

The aim of the experiments was to assess the usefulness of the proposed method in the characterization of prostatic tissues from MR images. Three image sequences (contrast-enhanced T1-, T2-, and diffusion-weighted) were considered simultaneously in the classification of two tissue types: cancerous and healthy. Complex feature vectors were created by concatenating the parameters corresponding to the three sequences. For comparison, also pairs of image sequences were tested, as well as the one-sequence cases.

4.1 Database Description

The images were gathered in Pontchaillou University Hospital in Rennes, France, between August 2009 and April 2010. They were derived from 19 patients. One study per patient was available. The acquisitions were performed on a 3T Siemens *Verio* magnetic resonance scanner. The images were recorded in DICOM format. The T1-weighted sequences were taken after injection of a gadolinium-based contrast agent, *Dotarem*®, in an amount of 13 to 20 ml. 30 different moments of contrast agent propagation were visualized. The time interval between consecutive moments was 7 seconds. The fat suppression (FS) method was applied for the T1 sequences. Slice thickness was the same for all the images of the same sequence: 3 mm for the T1-, and T2-wighted sequences, 6 mm for the diffusion-weighted ones. Image size in pixels was: 192×192 for the T1-weighted images, 320×320 (for 16 patients) or 448×448 (for 3 patients) for the T2-weighted ones, and 160 $times136$ for diffusion-weighted. An example of the three corresponding images of considered sequences is given in the Figure 3.

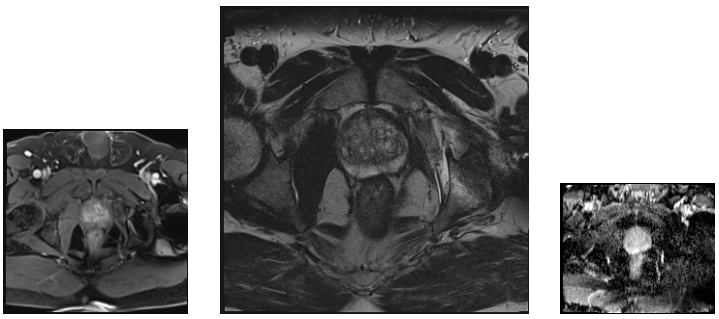

(a) T1-weighted (b) T2-weighted (c) diffusion-weighted

Fig. 3. Three MR images of prostate acquired at the same slice position; the proportions between images of each sequence were kept

In total, 180 ROIs were outlined for prostatic tissue, 60 for each of the three considered image sequences. Due to the fact that image sizes differed between sequences, the average sizes of ROIs corresponding to different sequences were also different. They amounted to 91, 456, and 85 pixels respectively.

For most studies, ROIs were outlined only within one of the two available classes (healthy or tumorous), which resulted in a certain inconvenience. It was not possible to determine the moment of contrast agent propagation in which the differences between texture characteristics corresponding to healthy and tumorous tissue were the most significant. For this reason, for our analyses, we always chose the middle image (15^{th} of the available 30) from the T1-weighted sequences.

4.2 Image Conversion

An important drawback of our database was that the full range of pixel values possible to occur in the images (image resolution in pixel values) could not be determined from the DICOM headers. It is known that pixel values describing each organ fall into a certain part of the full range. Basing on pixel value histograms, obtained for the ROIs within the prostate, for the entire hips (not affected by tumor), and for the entire images, we hypothesized that image resolutions in pixel values might be different for each of the considered studies.

Therefore, in order to equalize the ranges of pixel values corresponding to different studies (separately for each sequence), the preliminary step of image processing was image conversion. Due to the fact that the ROIs outlined for the prostate were very small, and, for most studies, corresponded to only one tissue class, it would have been difficult to convert images basing only on the pixel values describing the prostate. Such a conversion was thus conducted in order to obtain the same range of pixel values (the smallest possible) corresponding to ROIs covering the hips.

In total, 1601 ROIs covering the hips were considered among which 678, 522, and 401 ROIs corresponded to T1-, T2-, and diffusion-weighted sequences respectively. Average ROI areas were about 547, 2404, and 412 pixels respectively. For each study and for each sequence, the range of pixel values was found separately. Each time, 5% of the brightest and the darkest pixels were not taken into account.

For the diffusion-weighted images the ranges of pixel values did not differed considerably. The widest of them were not even twice wider than the narrowest ones. The largest differences in ranges of pixel values were observed for T2 sequences. The widest range was more than nine times wider than the narrowest one. For T1 sequences it was above four times wider. The range centers obtained for different studies and the same series were located in different places.

Finally, the pixel values of the images of the T1-, and T2-weighted sequences were subjected to a linear transformation with integer coefficients. After the conversion, the range of gray levels sufficient to characterize all the pixels belonging to the prostate ROIs did not exceed 256, for each of the considered sequences. This allowed the images to be processed as if they were in a 8-bit BMP format.

4.3 Feature Extraction

The 30 texture features were calculated separately for each image in a triple. Six different approaches to texture analysis were used. They based on: autocorrelation (AC) [12], first order statistics (FO), gradients (GB), fractals (FB) [13], co-occurrence matrices (COM) [14], and run length matrices (RLM) [15, 16]. The names of features are given in Table 1.

For the COM and RLM methods, the number of gray levels was reduced to 64 and 32 respectively. The co-occurrence matrices were constructed separately for 4 standard directions (0°, 45°, 90°, and 135°), and for 2 different distances between the pixel pairs, 1 and 2. The run length matrices considered the 4 aforementioned

Table 1. Calculated textural features; the name of a feature set is created by adding the number of features (as a subscript index) to the name of the extraction method

Set	Feature Names
AC_2	(d)*Autocorr*, where $d = 1, 2$ is a pixel distance
FO_4	*Avg*, *Var*, *Skew*, *Kurt*
GB_4	*GradAvg*, *GradVar*, *GradSkew*, *GradKurt*
FB_1	*FractalDim*
COM_{11}	*AngSecMom*, *InvDiffMom*, *Entropy*, *Correlation*, *SumAvg*, *DiffAvg*, *SumVar*, *DiffVar*, *SumEntropy*, *DiffEntropy*, *Contrast*
RLM_8	*ShortEmp*, *LongEmp*, *GLNonUni*, *RLNonUni*, *Fraction*, *LowGLREmp*, *HighGLREmp*, *RLEntropy*

directions of pixel runs. Features obtained for different pixel distances and/or for different directions were averaged.

The normalized autocorrelation coefficients (AC method) were also calculated separately for 4 standard directions, and for 2 different pixel distances: 1, and 2. Only features corresponding to different directions were averaged.

The FB method was based on the fractional Brownian motion model [17] and also considered only 2 pixel distances, 1 and 2.

In total, 11 different feature sets were tested. Six of them contained features derived from one extraction method only. Another three sets combined features derived from several methods: All_{23} (COM, RLM, and FO), All_{25} (COM, RLM, FO, and AC), and All_{30} (all available features). Moreover, two sets of selected features were considered: Sel_F, and Sel_B. They contained features selected from the 30·3 possible ones (30 features corresponding to the 3 image sequences), using two searching directions, respectively *Forward*, and *Backward*. The selection of features was performed with the *Weka* software [18]. The following selection settings were applied: the wrapper method (called *WrapperSubsetEval* in *Weka*) – as an evaluator of each tested subset of features, the *C4.5* tree [19] (*J48*) – as a classifier, and the *BestFirst* searching strategy.

4.4 Classification Results

Several classifiers were used in order to assess the potential of the multi-image texture analysis, and to compare it to that of one-sequence texture analysis. Among them were: logistic regression – LR (algorithm called *Logistic* in *Weka*), neural network – NN (*MultilayerPerceptron*), and support vector machines – SVM (algorithm *SMO*). The NN used a backpropagation algorithm and a sigmoid activation function. It had one hidden layer, wherein the number of neurons was equal to the average value of the number of features and the number of classes. The SVM used two kernels: the Gaussian kernel (*RBFKernel*), GK,

and the polynomial (*PolyKernel*) one, PK. The classification accuracies were estimated by 10-fold cross-validation, repeated 10 times.

The Table 2 presents selected results obtained for the classification of simple textures (when each sequence was considered separately) and multi-image textures (when three or two sequences were analyzed simultaneously). Each line of the table contains results obtained by the same classifier, for the same set of features, but for different image sequences (T1, T2 or diffusion) or image sequence combinations (T1 and T2, T1 and diffusion, T2 and diffusion, T1 and T2 and diffusion). We will always compare the results located in the same row of the Table 2 – obtained with the same classifier, and for the same set of features.

As for the cases of simple texture analysis, we can conclude that the most useful piece of information for the process of prostatic tissue classification was extracted from the T2- and the diffusion-weighted images. The advantage of the T2-weighted images was certainly that they were the biggest in size. Their drawback was the necessity of pre-conversion, as, initially, they showed the largest differences in the ranges of pixel values. Finally, taking into account the results obtained with T2-weighted images, we could estimate that the applied image conversion probably did not affect the classification results (too) negatively. Therefore, pre-conversion could be a good solution when no information about the full range of image pixel values is available in DICOM headers. In turn, inferior results obtained for a T1-weighted sequence may indicate the need to develop a method for choosing the most appropriate moment (in terms of tissue characterization) of contrast agent propagation.

The best classification results for the simple texture problem were: 94.83%, 95.67%, 93.00%, and 96.17% of correctly classified cases for the LR (with the Sel_F feature set), the NN (with COM_{11}), the SVM-GK (with Sel_F), and the SVM-PK (with All_{25}) classifiers respectively. Such results were obtained when the diffusion-weighted sequences (the case of the first three classifiers) or the T1-weighted sequences (the case of the last two classifiers) were considered.

Comparing classification results obtained for simple and multi-image textures, we can notice that there always exists at least one combination of two sequences that leads to better tissue recognition in comparison with the best possible one achieved for a single-sequence case. This is observed for each classifier, and for each feature set. The simultaneous analysis of images in triples almost always guaranties better results than the analysis of pairs of images. Finally, it is with the analysis of the three-image textures that the best overall classification result was achieved: 99.19%, for the combination of the SVM-PK classifier and the All_{23} feature set. With other classifiers the results slightly differed from the best possible one: 98.00%, 97.83%, and 98.00% obtained for the LR (with COM_{11}), NN (with RLM_8), and SVM-GK (with RLM_8 feature set) classifiers respectively.

The highest differences between the best results for the multi-image and the single-image case were observed with RLM_8 feature set: 7.00%, 6.33%, 6.50%, and 4.84% for the LR, the NN, the SVM-GK, and the SVM-PK classifiers respectively.

Table 2. Classification accuracy [%] (and standard deviation) obtained for simple and multi-image textures; three image sequences, T1-, T2-, and diffusion-weighted one ("Diff"), and four combinations of sequences were considered; the results were obtained using the four classifiers: logistic regression (LR), neural network (NN), support vector machines with a Gaussian kernel (SVM-GK) and with a polynomial kernel (SVM-PK)

	Set of Features	Simple (One-Sequence) Textures			Multi-Image Textures			
		T1	T2	Diff	T1 and T2	T1 and Diff	T2 and Diff	T1 and T2 and Diff
LR	COM_{11}	68.67 (9.79)	87.33 (6.06)	93.50 (4.42)	96.17 (3.72)	91.17 (5.49)	92.83 (4.92)	98.00 (2.97)
	RLM_8	75.17 (8.98)	90.00 (6.27)	85.00 (7.63)	91.17 (5.49)	87.33 (6.17)	89.33 (5.62)	97.00 (3.63)
	Sel_F	82.83 (7.54)	93.00 (5.32)	94.83 (4.39)	91.67 (5.23)	96.33 (4.03)	94.83 (4.39)	96.33 (4.03)
	All_{23}	67.50 (9.87)	89.33 (5.87)	88.17 (6.41)	91.17 (5.62)	93.17 (5.31)	91.67 (5.49)	93.67 (5.14)
	All_{25}	70.83 (9.28)	89.17 (6.09)	86.33 (7.05)	91.17 (5.98)	94.00 (4.82)	92.17 (5.36)	94.83 (4.84)
	All_{30}	70.17 (8.73)	86.00 (6.13)	89.00 (6.29)	90.17 (5.82)	94.67 (4.57)	94.00 (5.37)	95.00 (4.67)
NN	COM_{11}	78.17 (8.27)	90.67 (5.96)	95.67 (4.21)	96.83 (3.29)	95.33 (3.95)	95.83 (4.65)	96.50 (3.98)
	RLM_8	77.50 (8.33)	91.50 (5.74)	90.17 (5.82)	97.83 (2.82)	87.83 (6.14)	92.00 (5.62)	97.33 (3.50)
	Sel_F	79.50 (7.19)	93.33 (5.43)	92.83 (4.92)	92.83 (5.33)	96.33 (4.03)	92.83 (4.92)	96.33 (4.03)
	All_{23}	75.50 (7.99)	92.50 (5.35)	94.67 (4.87)	95.50 (3.72)	94.50 (4.28)	92.67 (4.93)	97.50 (3.43)
	All_{25}	78.67 (8.79)	91.33 (5.36)	93.50 (5.29)	96.17 (3.90)	95.83 (4.00)	94.50 (4.89)	96.33 (3.86)
	All_{30}	78.33 (8.91)	92.67 (4.93)	94.00 (4.02)	94.67 (4.42)	96.33 (3.67)	94.33 (4.77)	96.00 (4.29)
SVM-GK	COM_{11}	67.67 (8.77)	92.17 (5.23)	88.67 (5.67)	88.83 (6.09)	93.00 (4.91)	93.67 (4.40)	94.83 (4.39)
	RLM_8	73.00 (9.24)	91.50 (5.49)	89.67 (5.53)	94.33 (4.62)	91.17 (5.09)	96.67 (3.56)	98.00 (2.97)
	Sel_F	84.17 (6.85)	93.00 (4.91)	93.00 (4.62)	94.33 (4.77)	96.67 (3.75)	93.00 (4.62)	96.67 (3.75)
	All_{23}	75.83 (8.90)	92.67 (4.79)	89.50 (5.51)	93.17 (4.75)	94.50 (4.89)	96.33 (3.47)	97.67 (2.91)
	All_{25}	79.33 (7.87)	92.50 (4.80)	89.50 (5.39)	93.67 (5.40)	94.33 (4.77)	95.50 (3.90)	97.00 (3.43)
	All_{30}	79.17 (7.98)	92.33 (5.22)	89.17 (5.61)	91.67 (5.74)	92.17 (5.23)	94.83 (4.69)	97.00 (3.43)
SVM-PK	COM_{11}	77.00 (8.02)	96.00 (4.13)	93.33 (5.43)	96.83 (3.50)	96.17 (3.90)	96.50 (3.80)	98.00 (3.20)
	RLM_8	79.50 (8.02)	93.33 (5.17)	91.00 (5.56)	97.00 (3.43)	93.00 (5.05)	95.50 (4.08)	98.17 (2.62)
	Sel_F	83.00 (7.11)	94.00 (4.52)	94.00 (4.52)	93.33 (4.89)	96.67 (3.75)	94.00 (4.52)	96.67 (3.75)
	All_{23}	81.67 (7.06)	94.33 (4.62)	91.17 (5.62)	95.67 (3.86)	97.50 (3.43)	95.67 (4.37)	99.17 (2.48)
	All_{25}	87.17 (6.79)	96.17 (4.08)	91.33 (5.36)	96.33 (3.86)	98.00 (2.97)	96.00 (4.29)	98.67 (2.56)
	All_{30}	81.67 (7.72)	93.67 (5.14)	95.17 (4.63)	96.33 (3.86)	97.00 (3.63)	96.17 (3.90)	98.33 (2.78)

5 Conclusions and Future Work

In the work, a multi-image texture analysis was applied, for the first time, to the characterization of prostatic tissues from MR images. Images representing the same prostate slice but corresponding to different acquisition conditions (giving the T1-, T2-, and diffusion-weighted sequences) were analyzed simultaneously. Two classes of prostatic tissue were recognized: cancerous and healthy.

Experiments have shown that a simultaneous analysis of two, or three images can improve the recognition of prostatic tissues, in comparison with single-image analysis. The best results obtained for multi-image (two-, or three-image) cases were better than the best corresponding ones achieved for simple-image cases. The best improvement of classification quality reached 7.00%. The analysis of three-image textures proved to ensure the best classification result.

We admit that the preliminary experimental results, although promising, could also be subject to error. This could have been avoided if a key piece of information had been available in the database to process, namely the full ranges of image pixel values, apparently different for different studies. In this case, image conversion based on the analysis of the intervals of pixel values corresponding to another organ (in our case the hips) seemed to be the only solution. Nevertheless, the texture of the hips can also be altered by the presence of various pathological processes, different for each patient. To avoid this problem in the future, either image acquisition protocols should be standardized or images should contain information about the full ranges of pixel values. Furthermore, when acquiring images, a good idea would be to place a "reference object" in view. The texture analysis of such an object could be crucial for the purposes of image conversion aimed at the equalization of pixel value ranges corresponding to different studies.

Finally, it would be desirable to have two types of ROIs (corresponding to cancerous and healthy tissue) delineated for each study or patient. Such an information would allow to analyze changes in texture characteristics under contrast product propagation (in T1-weighted sequences) corresponding to the both types of tissue. Basing on such an analysis one could determine which moment of contrast product propagation is related to the most significant differences in texture characteristics obtained for cancerous and healthy tissue.

In the future, we will try to resolve all of the aforementioned problems. It would be worthwhile to repeat the experiments using a much larger database and to recognize more than two tissue classes. Other MRI sequences, such as FLAIR (fluid-attenuated inversion recovery) or proton density-weighted, can also be considered for multi-image texture analysis. It also seems to be interesting to find a method for characterizing texture evolution under contrast product propagation based on the simultaneous analysis of many contrast-enhanced T1-weighted images related to different concentrations of the contrast product in prostatic vessels.

Acknowledgement. This work was supported by the grant S/WI/2/2013 from Bialystok University of Technology.

References

1. Jemal, A., Bray, F., Center, M.M., et al.: Global cancer statistics. CA: A Cancer J. Clin. 61(2), 69–90 (2011)
2. Andriole, G.L., Crawford, E.D., Grubb, I.R.L., et al.: Mortality Results from a Randomized Prostate-Cancer Screening Trial. N. Engl. J. Med. 360, 1310–1319 (2009)
3. Greene, K.L., Albertsen, P.C., Babaian, R.J., et al.: Prostate Specific Antigen Best Practice Statement: 2009 Update. J. Urol. 182(5), 2232–2241 (2009)
4. Duda, D., Krętowski, M., Bézy-Wendling, J.: Texture-based classification of hepatic primary tumors in multiphase CT. In: Barillot, C., Haynor, D.R., Hellier, P. (eds.) MICCAI 2004. LNCS, vol. 3217, pp. 1050–1051. Springer, Heidelberg (2004)
5. Duda, D., Kretowski, M., Bezy-Wendling, J.: Texture characterization for Hepatic Tumor Recognition in Multiphase CT. Biocybern. Biomed. Eng. 26(4), 15–24 (2006)
6. Quatrehomme, A., Millet, I., Hoa, D., Subsol, G., Puech, W.: Assessing the classification of liver focal lesions by using multi-phase Computer Tomography scans. In: Greenspan, H., Müller, H., Syeda-Mahmood, T. (eds.) MCBR-CDS 2012. LNCS, vol. 7723, pp. 80–91. Springer, Heidelberg (2013)
7. Nagarajan, M.B., Huber, M.B., Schlossbauer, T., Leinsinger, G., Krol, A., Wismüller, A.: Classifying small lesions on breast MRI through dynamic enhancement pattern characterization. In: Suzuki, K., Wang, F., Shen, D., Yan, P. (eds.) MLMI 2011. LNCS, vol. 7009, pp. 352–359. Springer, Heidelberg (2011)
8. Agner, S.C., Soman, S., Libfeld, E., et al.: Novel kinetic texture features for breast lesion classification on dynamic contrast enhanced (DCE) MRI. In: Proc. of SPIE, vol. 6915(69152C) (2008)
9. Bhooshan, N., Giger, M., Lan, L., et al.: Combined use of T2-weighted MRI and T1-weighted dynamic contrast-enhanced MRI in the automated analysis of breast lesions. Magn. Reson. Med. 66(2), 555–564 (2011)
10. Sung, Y.S., Kwon, H.J., Park, B.W., et al.: Prostate cancer detection on dynamic contrast-enhanced MRI: computer-aided diagnosis versus single perfusion parameter maps. Am. J. Roentgenol. 197(5), 1122–1129 (2011)
11. Duda, D.: Medical image classification based on texture analysis. PhD Thesis, University of Rennes 1, Rennes, France (2009)
12. Gonzalez, R.C., Woods, R.E.: Digital Image Processing, 2nd edn. Addison-Wesley, Reading (2002)
13. Chen, C., Daponte, J.S., Fox, M.D.: Fractal feature analysis and classification in medical imaging. IEEE Trans. Med. Imag. 8(2), 133–142 (1989)
14. Haralick, R.M., Shanmugam, K., Dinstein, I.: Textural features for image classification. IEEE Trans. Syst. Man Cybern. 3(6), 610–621 (1973)
15. Galloway, M.M.: Texture analysis using gray level run lengths. Comp. Graph. and Im. Proc. 4(2), 172–179 (1975)
16. Chu, A., Sehgal, C.M., Greenleaf, J.F.: Use of gray value distribution of run lengths for texture analysis. Pattern Recog. Lett. 11(6), 415–419 (1990)
17. Chen, E.L., Chung, P.C., Chen, C.L., et al.: An automatic diagnostic system for CT liver image classification. IEEE Trans. Biomed. Eng. 45(6), 783–794 (1998)
18. Hall, M., Frank, E., Holmes, G., et al.: The WEKA data mining software: an update. SIGKDD Explorations 11(1), 10–18 (2009)
19. Quinlan, J.: C4.5: Programs for Machine Learning. Morgan Kaufmann, San Francisco (1993)

Adaptive Sparse Recovery of Medical Images with Variational Approach – Preliminary Study for CT Stroke

Artur Przelaskowski

Faculty of Mathematics and Information Science, Warsaw University of Technology, Koszykowa 75, 00-662 Warszawa, Poland
arturp@mini.pw.edu.pl

Abstract. Presented research was directed to effective signal recovery problem for computer-aided medical diagnosis. Extracted and visualized information covered in sensed data of imaging systems supports interpretation according to "second look" procedure. The integrated framework of compressive sensing was used to optimize CT acute stroke diagnosis. Previously studied nonlinear approximation of the sparse signals in adjusted dictionaries was extended with variational approach to extract more precisely the content components. Proposed methodology adjusts optimized fidelity norms and regularizing priors to semantic question of image-based diagnosis. Preliminary experimental study was performed to provide selected proof-of-concept results for designed CT hypodensity extractors.

Keywords: computer-aided diagnosis, image recovery, compressed sensing, variational image processing.

1 Introduction

Images are naturally compressible in a sense that the sorted magnitudes of the transformed image coefficients decay quickly to zero according to the power law. In other words, images are approximately sparse in transform atoms (i.e. elementary signal-representing templates). Consequently, image and signal processing predominantly is based on sparse signal model founded on last decade achievements of harmonic analysis, approximation theory and wavelets. Sparse-Land has emerged as one of the leading concepts in a wide range of applications: denoising, restoration, feature extraction, detection, source separation, compression etc. [1].

Moreover, another competing or extending framework, i.e. variational image processing succeeded in developing an explosively fast speed [2], exploits signal sparsity as regularization prior. Rather than viewing images as being sparse in some basis, they are viewed as minimizers to certain energy functionals including adequate regularizers. The classic example is restoring a noisy image using total-variation regularization [3]. Variational image processing treats an image as a reality function whose sampling or sensing corresponds to the matrix form

E. Pietka, J. Kawa, and W. Wieclawek (eds.), *Information Technologies in Biomedicine, Volume 3*, Advances in Intelligent Systems and Computing 283,
DOI: 10.1007/978-3-319-06593-9_14,

of a given discrete image. It enables use of useful concepts of functions, i.e. geometry, shapes, edges, smoothness etc., to achieve sub-pixel level accuracy in high-resolution image processing.

Compressive sensing (CS) integrates sparse signal models with variational image processing to reliably recover images acquired from just a few linear measurements. In general, CS (sometimes called sparse recovery) exploits the sparsity and smoothness/regularity of an unknown signals to be sensed by relatively small number of incoherent linear measurements selected a priori. Exhaustively developed theory assures, under respective conditions of high incoherence of measurement matrix, the signal recovery with relatively high resolution and enough accuracy. Generally, image recovery is optimization procedure (where output is a minimizer of certain functional constituting convex problem) with relaxation of important sparsity prior in terms of more computationally tractable norms, greedy alternatives and adaptively formulated semantic criteria of the accuracy.

Medical image recovery means diagnostic information recovered from data acquired in medical imaging systems to be clearly percepted by experts making correct interpretation. Sparse information recovery (generally based on image acquisition, preprocessing to improve the quality, extraction of imaged content possibly followed by automatic object/pattern recognition and even image interpretation) assumes images being sparse in some basis/frames to separate and reconstruct all necessary information to redundant image domain.

1.1 Acute Stroke Diagnosis

To verify presented concept of image content recovery for more effective diagnosis, two important applications of computer-aided diagnostic imaging were considered. Recognition of ischemic stroke symptoms in CT images and detection of directional breast cancer lesions in mammograms.

Stroke as one of the most frequent and most devastating event among human diseases is the first cause of permanent disability (over 40 years old) worldwide and the third most frequent cause of death. The diagnosis of acute stroke itself is clinical with assistance from the imaging techniques which determine the subtypes. The main method of instrumental stroke diagnosis is computed tomography (CT) widely applicable because of fast, accessible and inexpensive examinations. CT differentiates very well hemorrhagic and ischemic forms of stroke because fresh blood extravasated into brain parenchyma or pericerebral spaces is visible at once as seen at Figure 1. Moreover, CT remains an invaluable method for the detection of hemorrhagic complications, the intermediate signs of necrosis and the emerging threat of uncontrolled intracranial pressure increase followed by herniation and death.

However, there are serious problems with very early discovery of ischemic stroke in CT. In the first hours of ischemic stroke image interpretation is often ambiguous, indirect and not obvious. CT scans (without contrast enhancements; specificity= 96%) during the first 24 hours after the onset in the most cases with ischemic stroke is almost normal. Only direct finding enabling ischemia recognition is the extent of hypodense tissue on baseline CT significantly facilitating

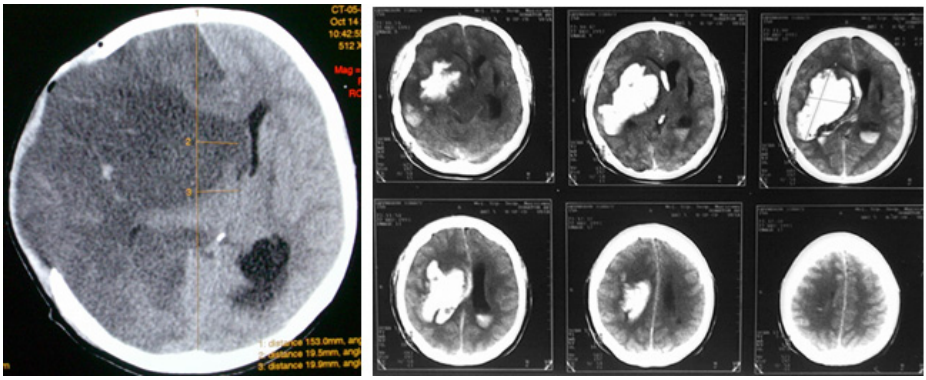

Fig. 1. Ischemic stroke (left) and haemorrhagic stroke (right) manifestation on CT scans

stroke diagnosis. However, such noticeable lowering of brain attenuation coefficients is often perceptually hidden because of unstable technological conditions of image acquisition, distorted linearity, degraded contrast resolution, artifacts, noise etc. Therefore, acute stroke diagnosis needs computerized support to extract reliable signs of stroke, first of all hypodensity.

This introductory paper with preliminary results presents carried out research background as review of CS-based fundamental adjusted to CT stroke recovery problem. Possible optimization of the image recovery with high enough accuracy of diagnostic components was considered, according to reliable requirements of concrete diagnostic imaging. We proposed use of variational approach (VA) to recover separated components of information improving diagnosis of CT acute stroke. Following such concept, we designed and verified fundamental principles of computerized CT stroke diagnosis in order to separate the hypodensity as most important, direct sign of ischemia. Proposed concepts extends image model of sparsity in wavelets to variational recovering of hypodensity distribution.

Adaptation of the optimization criteria was directed to local minima of denoised image function (functional image model) to approximate a variation of tissue density in CT brain images. The framework of compressive sensing was used to verify several concepts of hypodensity extractors.

2 Framework of the Proposed Method

Let's start from compressive sensing problem to explain fundamentals of proposed method. The essential advantages of CS concept applied for medical image recovery are as follows:

- reduced sensing cost (mostly radiation dose for CT because of reduced number of measurements),
- sensing based on sparsifying dictionaries (possible content-dependent adaptivity to selected information components),

- image recovery based on variational approach (possibly content-oriented),
- image processing with the VA to approximate adaptively diagnostic components.

2.1 Sensing with Sparse Image Models

Sparsity of unknown images is exploited to recover the image information from relatively small number of linear measurements, significantly fewer than required by Nyquist-Shannon theorem. Sparsity means that information contained in a signal/image is much smaller than its effective bandwith. However, in most cases of natural signals we have transform's economical signal representation in some dictionary (base, frame) $\mathbf{\Phi}$. Additional necessary condition is incoherence between sensing matrix (i.e. real imaging modality model) and sparsifying $\mathbf{\Phi}$. For example noiselets $\mathbf{\Xi}$ [4] are useful to measure sparse signals because they have pseudorandom dense representation and the signals compact in the wavelet domain are spread out in the noiselet domain.

Long term study has proved sparsity of CT brain images in wavelet or wavelet-like bases [5]. Selected sparsyfing transforms were applied to optimize sparsity with satisfactorily fidelity criterion. Further research was directed to other multiscale and local base/frame with nonseparable kernels in 2D/3D space were verified to optimize approximately sparse representation as content sparse representation. The lineal and nonlinear approximation procedures were used to extract target function of informative components like nonzeros of highly sparse representation. Unrepresented noise, artifacts and other uninformative signal components were excluded from reconstructed image information. Selected results were presented in Section 4.

2.2 Problem to Be Solved

Ill-posed inverse problem of image recovery refers to noisy (η) sensing with full-rank measurement matrix $\mathbf{A} \in \mathbb{R}^{M \times N}$ of

$$\mathbf{y} = \mathbf{A}\mathbf{x}^{(r)} + \eta \tag{1}$$

where compressed (e.g. low resolution or feature-oriented) or degraded measurement vector $\mathbf{y}$ of M observations is used to recover $\tilde{\mathbf{x}}$ with high enough resolution $N \gg M$ as reliable approximation of unknown real $\mathbf{x}^{(r)}$ (possibly with infinitive resolution physically but pragmatically limited to content clarity criteria). The measurement matrix $\mathbf{A}$ is linear operator of underdetermined system having infinitely many solutions. In case of noiselet-based sensing of the signals sparse in wavelet basis, we have $\mathbf{A} = \mathbf{\Xi\Phi}$. In order to estimated unique and well-defined solution additional criteria are necessary. Moreover, such criteria could be fitted to content model and specific characteristics of the images.

2.3 Criteria of the Solution

Inversion of the problem (1) is a variational minimization in the following adaptive form

$$\tilde{\mathbf{x}} = \arg\min_{\mathbf{x}} \kappa(\mathbf{x})F(\mathbf{x}) + \lambda(\mathbf{x})P(\mathbf{x}) \tag{2}$$

with κ-weighted criterion of the fidelity $F(\mathbf{x})$ to the observations (usually l_2 norm-based) and λ-weighted prior $P(\mathbf{x}) \in \mathbb{R}$ that determines regularity of the solution. The prior is low for the image features one is interested in.

Important optimization metrics to assess the efficacy of recovering procedures include: recovery accuracy, computational complexity (possible linear or convex programing) and convergence speed. Fidelity criteria need to take into account the highly structured features of natural/medical images and evident properties of the human visual system (HVS).

Strictly convex minimized function guarantees a unique and computationally tractable solution, what means that squared Euclidean norm l_2^2 (i.e. measure of energy) and l_1 are preferable. However, highly desired in signal processing is sparsity of the signals, especially for image recovery. It forces minimization of pseudo-norm $\|\mathbf{x}\|_0 = \#\{i; x_i \neq 0\}$ what is classical problem of combinatorial search but generally NP-hard. Imposing certain matrix $\mathbf{A}$ conditioning, i.e. incoherence and restricted isometry property (RIP), convex optimization with l_1 or simple greedy algorithms give the sparsest solution of l_0-based optimization. Other way of problem relaxation is solving l_p-minimizing problem where $\|\mathbf{x}\|_p = \sum_i \left(|x_i|^p\right)^{1/p}$ but every choice $0 < p < 1$ gives a concave functional [6]

Fidelity criteria are mostly designed with l_2 norm primarily but other norm are possible as follows

- typically least squares (LS), i.e. squared l_2 as $\|\mathbf{y} - \mathbf{A}\mathbf{x}\|_2^2$; integrated with TV (total variation) prior is preferable for images corrupted by Gaussian noise with satisfactory edges preserving;
- recursive last squares (RLS) that minimizes weighted linear least squares cost function assuming deterministic signal model, able e.g. to estimate consistently the sparse signal's support and its nonzero entries [7];
- mean square error (MSE) or l_2 in the constrained form $\|\mathbf{y} - \mathbf{A}\mathbf{x}\|_p \leq \tau$ [8, 9];
- l_1-norm, used with TV prior is useful for removing impulsive noise [10, 11];
- general l_p fidelity constraint, i.e. $\|\mathbf{y} - \mathbf{A}\mathbf{x}\|_p \leq \tau$ where $p \geq 1$ and τ is chosen depending on the noise pth moment $\mathbb{E}(\|\eta\|_p)$; for uniform quantization noise, $p = \infty$ is good choice [12];
- Dantzig selector [13] that uses indication function of $\|\mathbf{A}^*(\mathbf{y} - \mathbf{A}\mathbf{x})\|_\infty \leq \tau$, where $\mathbf{A}^*$ is adjoint of $\mathbf{A}$; the Dantzig selector is robust against measurement errors and more adaptive in a sense of fidelity criteria - with l_1 prior can be recast as a linear program.

Fundamental priors considered to recover medical image are as follows:

- based on derivatives of the image to impose some smoothness on the recovered image:

  - the Sobolev prior which is l_2 norm of the gradient approximated with a finite difference scheme $P(\mathbf{x}) = \sum_i \| \bigtriangledown x_i \|_2$; it favors uniformly smooth images;
  - the total variation (TV) prior as $P(\mathbf{x}) = \sum_i \| \bigtriangledown x_i \|_1$; it assumes that $\mathbf{x} \in l_1(\Omega)$ (Ω is image domain) and favors piecewise constant images with edge discontinuities of small perimeters [3]; the TV functional is non-differentiable but still convex and causes sparsity of the solution [14];
  - the weighted TV model (WTV) with certain discretization of TV with anisotropic weights defined for 5×5 support of $4/8/16$ pixel neighborhood [15];
- sparsity prior while $\#(\sup \mathbf{x}) \leq K \ll M$ with unknown support distribution; NP_hard solution requires relaxation
  - to convex l_1 minimization (i.e. Laplacian prior) with computationally tractable implementations;
  - to $l_p: \ 0 < p < 1$ minimization;
  - in a form of greedy algorithms.
- sparsifying decompositions that produce sparse representation of natural signals; it is based on a reliable theory of sparse signal models what means that the signals can be well-approximated as a linear combination of only a few elements (vectors) from adaptively adjusted basis or dictionary; we have
  - orthogonal/biorthogonal bases of tensor wavelets, redundant curvelets with nonseparable kernels, contourlets, complex wavelets etc.;
  - SVD, KLT and others signular/independent vector extractors [16].

2.4 Recovery Algorithms

The l_1 minimization is fundamental approach to recover a sparse signal from limited number of measurements. It provides a useful framework to perform accurate recovery by means of convex optimization problems. Stable signal recovery in noise is possible under a variety of common noise models, e.g. uniformly bounded noise or Gaussian noise. Both the RIP and coherence are useful to establish performance guarantees in noise. l_1 -based relaxation of l_0 pseudonorm is realized in standard decoder of basis pursuit (BP) with LS fidelity criterion for noiseless and noisy data (well known realizations of lasso or extended with fidelity criteria of the Dantzig selector).

Moreover, there is a variety of greedy methods to recover sparse signals. Greedy algorithms abandons exhaustive search for a series of locally optimal single-term updates. They rely on iterative approximation of the signal nonzeros (i.e. signal support with refined coefficients), either iterative identifying the support until a convergence criterion is fulfilled or subsequent signal estimation to provide matching to the measured data. Both essential approaches are applied, greedy pursuits (e.g. Orthogonal Matching Pursuit - OMP with iteratively adding new components that are estimated to be nonzeros) and greedy thresholding algorithms with element pruning steps (nonzero elements are removed iteratively from further analysis, e.g. the Iterative Hard Thresholding - IHT).

In greedy pursuit, starting from $\mathbf{x}^{(0)} = 0$ a k-term aproximant $\mathbf{x}^{(k)}$ is iteratively constructed by providing a set of active columns of $\mathbf{A}$ successively expanded at each next stage. The column selected at successive stage maximally reduces the residual l_2 error in approximating $\mathbf{y}$ from the currently active columns. An important example of such greedy strategy is the OMP, where the approximation for $\mathbf{x}$ is updated by projecting $\mathbf{y}$ orthogonally onto the columns of $\mathbf{A}$ representing current support estimate.

The Compressive Sampling Matching Matching Pursuit (CoSaMP) [17] keeps the nonzero support and either adds and remove alements in each iteration; new $\mathbf{x}$ estimate is restricted to new smaller support. Alternative approach for recovery of sparse signals is combinatorial algorithms [18].

2.5 Medical Information Recovery

Image edges, ridges and textures of specific ROI (Region of Interests) or denoised approximation signal (stroke case) tendency play decisive role in content-oriented medical image recovery. Accurate visual perception of extracted diagnostic information (lesion symptoms, signatures or any specific features experienced as direct or indirect sign of pathology) is key condition of correct image interpretation. Thus separation and noticeable extraction of diagnostic components significantly improves medical image recovery.

Instead of local image filtering or transform coefficient thresholding, one can use variational processing embedded in optimization procedure of semantic image recovery. Limited number of measurements in CS scheme adequately models acquisition limitations of real imaging systems with respect to potentially continues, noiseless image model as reliable function of interests. Random matrices simulating acquisition process enable modeling of acquisition limitations due to radiation dose, time and resolution-limits, movement and physical artifacts, technological noise, unstable detector sensitivity and contrast etc. Weighted priors of the iterative recovery are important tool to control semantic recovery of diagnostically improved medical images.

Adaptiveness of the recovery was mainly concentrated on models of sparse, locally limited signal segments of interests able to cope with the space-varying context; instead of an access to the whole sensed data to compute the solution, only local data are used to estimate adaptively and locally sparse solution [19].

3 Proposed Method

Consequently, the design of adaptive image recovery was formulated according to the following adaptive optimization procedure

$$\tilde{\mathbf{x}} = \arg\min_{\mathbf{x},\mathbf{c}(\cdot)} \kappa(\mathbf{x})\|\mathbf{y} - \mathbf{A}\mathbf{x}\|_p + \mu(\mathbf{x})\|\mathbf{\Phi}\mathbf{x}\|_1 + \lambda(\mathbf{x})TV(\mathbf{x}) \tag{3}$$

with matrix $\mathbf{\Phi}$ sparsifying signal $\mathbf{x}$ and three signal-dependent criteria of adapted fidelity with priors of sparsity and smoothness represented by functional vector $\mathbf{c}(\cdot) = [\kappa(\cdot), \mu(\cdot), \lambda(\cdot)]$.

The fidelity metric $\|\mathbf{y}-\mathbf{A}\mathbf{x}\|_p$ should highly correlate to image accuracy for diagnostic and clinical procedures. First of all the specificity includes emphasized regions of interests or selected image components, e.g. high frequency representatives (e.g. signatures of breast cancer in mammograms) or local intensity maxima/minima (stroke case). Image fidelity criterion truncated to extracted a priori or a posteriori information was considered to be adaptive according to specific medical imaging problem (formal semantic model).

Furthermore, instead of fixed prior, the regularization could be enhanced by using a family of weighted prior model $P(x)^{(\mu,\lambda)}$ adapted to l_1 and TV specificity because of image edge, intensity and texture distribution related to content and diagnostic significance. Weighting parameters should be adapted to the noise level and reliability of estimated image model. The possible integration of sparsity estimate (l_1-like or greedy iteration) with TV smoothness prior (e.g. matched to 2D, 3D context models and edge specificity) and adjusted fidelity of reconstruction to optimize image recovery was studied. Initial results of such optimization realized in preliminary study were presented.

Adaptive recovery of diagnostic image content is based on two fundamental assumptions:

a) as accurate as possible basic iterative image reconstruction according to respectively selected fidelity criterion and priors (a priori adaptation),
b) semantic model of extracted information (a posteriori adaptation).

The following subsections shortly characterized possible realizations of the above general concept, adjusted to specificity of CT stroke diagnosis.

3.1 General Scheme of Extractors

General scheme of CT stroke extractors proposed in [5] includes: -image preprocessing to improve the quality, -initial analysis to select regions of interests susceptible to stroke hypodensity, -approximation of hypodensity image component, -optimization of visualized form of pathology extraction. Presented study concentrates only on approximation of hypodensity component. The following extractors were realized and compared in exemplar experiments.

Nonlinear Approximation in Sparsifying Dictionaries. Such concept was realized in our previous study with adjusted bases of orthogonal/biorthogonal wavelets, Fourier transform (FT) and discrete cosine transform (DCT, and block version BDCT), and frames of curvelets, contourlets, surflets, shearlets and complex wavelets (CWT). Nonlinear approximation of decaying magnitudes of transform coefficients orders hypodensity among small set of the highest magnitudes. But the effects significantly depends on the matched dictionary.

VA-Based Image Approximation. Variational approximation was realized according to global minimization of anisotropically discretized TV with weighted fidelity term as follows

$$\tilde{\mathbf{x}} = \arg\min_{\mathbf{x}} \kappa(\mathbf{x}) \|\mathbf{x}^{(r)} - \mathbf{A}\mathbf{x}\|_1 + TV(\mathbf{x}) \tag{4}$$

where $\kappa(\mathbf{x})$ was optimized with combinatorial approach using simple criterion of maximized change of density variation estimate of ischemic region relate to normal region.

Basic on algorithms presented in [20], different schemes of fidelity weighting to strengthen hypodensity extraction was verified. The weights were estimated as normalized factors of image intensity distribution or thresholded indicator of significant or insignificant areas.

CS-Based Image Recovery. This hypodensity extractor extends the optimization procedure according to (4) with two elements:

- sparsity prior of minimized $\|\mathbf{\Phi}\mathbf{x}\|_1$ with adjusted wavelet orthogonal base of coiflets with near symmetric wavelet functions and 12-tap filter banks; second-order cone program (SOCP) with a generic log-barrier algorithm (with Newton solver) was used as implementation[1];
- possible reduction of sensed data to verify possible measurement procedure limited to content-oriented sparsity of the images; however the required solution was possible adaptive concentration of the measurements to region (or component) of interests, only pseudo-random noiselets were verified with 1 to 10 reduction of the number of sensed data.

Therefore, realized concept of the image recovery with approximated hypodensity was as follows:

a) data sensing with reduced number of measurements $M \ll N$; precisely, we used $M = N/10$ in the experiments;
b) initial approximation of sensed data vector with Conjugate Gradients solver [21] (alternatively, additional fast reconstruction with Dantzig selector or CoSaMP were verified);
c) image recovery with enhanced hypodensity according to the following procedure: main iterative loop of l_1 sparsity prior with Dantzig selector (i.e. $\|\cdot\|_\infty$ fidelity term) and recast as linear program (or alternatively log-barrier with LS fidelity term)
   - solving the Newton systems via the Conjugate Gradients;
   - embedded VA-based emphasize of hypodensity (4) where $\kappa(\mathbf{x})$ are normalized intensities of successively recovered image;
d) final VA-based approximation of hypodensity component where $\kappa(\mathbf{x})$ is a thresholded vector of recovered intensity distribution; adaptive histogram-based extraction of hypodense intensity range is required.

[1] `http://users.ece.gatech.edu/~justin/l1magic/`

Because of weighted fidelity in the variational procedure, sparsity prior was weighted having regard to energy concentrated on selected image component. Sparsity adjusted to smoothing pattern controls the weights of fidelity in VA (we have greedy, integrated feedback in iterated recovery procedure). Final recovery was the integration of required component approximation with iterated reconstruction according to controlled sparsity and fidelity constraints.

4 Preliminary Results

Exemplar, representative CT image with perceptible ischemia in the right hemisphere of the brain was used to characterize essential processing effects for three proposed hypodensity extractors. The preliminary results are presented on the following Figures: 2, 3 and 4, respectively.

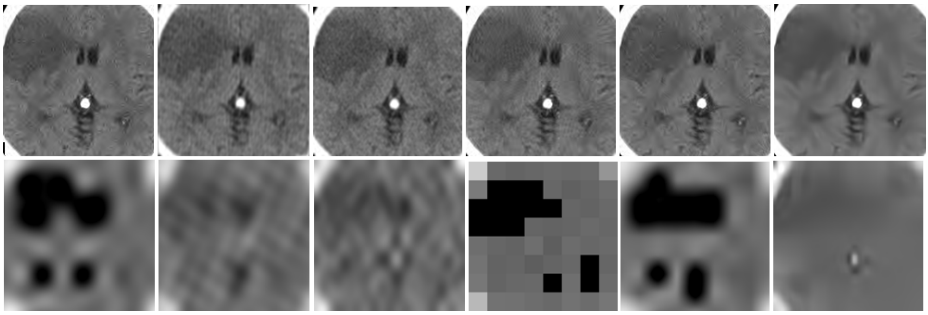

Fig. 2. Nonlinear approximation applied to exemplar, representative CT image of ischemic stroke (original is left image in Fig. 3); first row contains the results of reconstruction with 10% coefficients of wavelets, FT, DCT, BDCT, contourlets and CWT; the second row contains the reconstructions with 0.07% coefficients of the same transforms, respectively

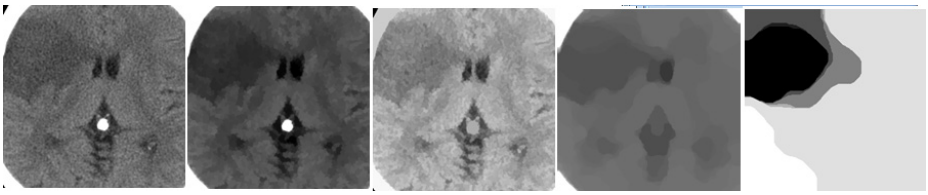

Fig. 3. VA-based image approximation applied to exemplar, representative CT image of ischemic stroke; from left to right the effects of hypodenstity extraction with different weights of fidelity term

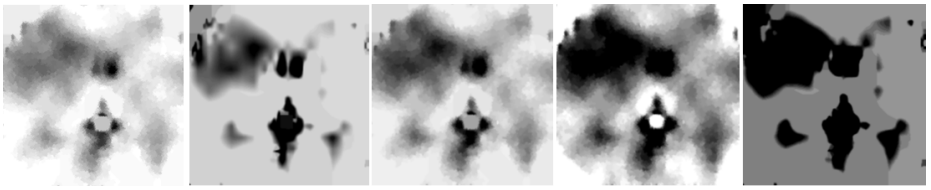

Fig. 4. CS-based image recovery with iterated VA approximation applied to exemplar, representative CT image of ischemic stroke (original is left image in Fig. 3); from left to right the effects of hypodenstity extraction with different combinations of integrated fidelity, sparsity and smoothness constraints

Presented sample of the effects is representative of the preliminary experiments conducted on a larger group of images. At lower level of the coefficient reduction (first raw in Figure 2), nonlinear approximation method allows image denoising (especially for CWT), but the perception enhancement of hypodense area is relatively insignificant. With very sparse image representation of the biggest coefficients, the overall characteristics of reconstructed images is erased, the details are lost. Moreover, distinctly highlighted the area of ischemia (especially for wavelets, BDCT and contourlets) is strongly distorted, the resulting image is blurred, artificial, distant from the original.

In the case of the VA-based approximation, the reconstructed images preserve the details, wherein the enhancement of hypodense area is more significant, with clearly better perception. But at very strong approximation, only the outlines of the structures are reconstructed, the details are lost and image is percepted as artificial. However, smooth shape of ischemic area is reconstructed with a higher accuracy, more precisely, suggestively.

The concept of CS-based image recovery results in clearly exposed areas of tissue with reduced density, maintaining their shape with high precision of the details. Other unimportant components of content disappeared, and the images seem much better emphasize the hypodense nature of the area located in the right hemisphere of the brain. The essential features of this area appear to be significantly enhanced, their perception is definitely the best.

The advantages of the CS-based method was verified in selected several cases of early stroke. CT scans of early examinations with the lack of stroke symptoms and follow-up CT studies with convincing symptoms of hypodensity were processed and ad hoc visualized - see the examples in Figure 5. The pronounced extraction of the reduced density tissue was observed in each of the cases. Such confirmation of stroke occurrence at acute stage of symptom onset is really useful aid of stroke diagnosis. However, the method requires optimized visualization of extraction effects. Additionally, initial segmentation that limits effectively the areas of stroke susceptibility can give more explicit results to provide high enough specificity of such aided diagnosis.

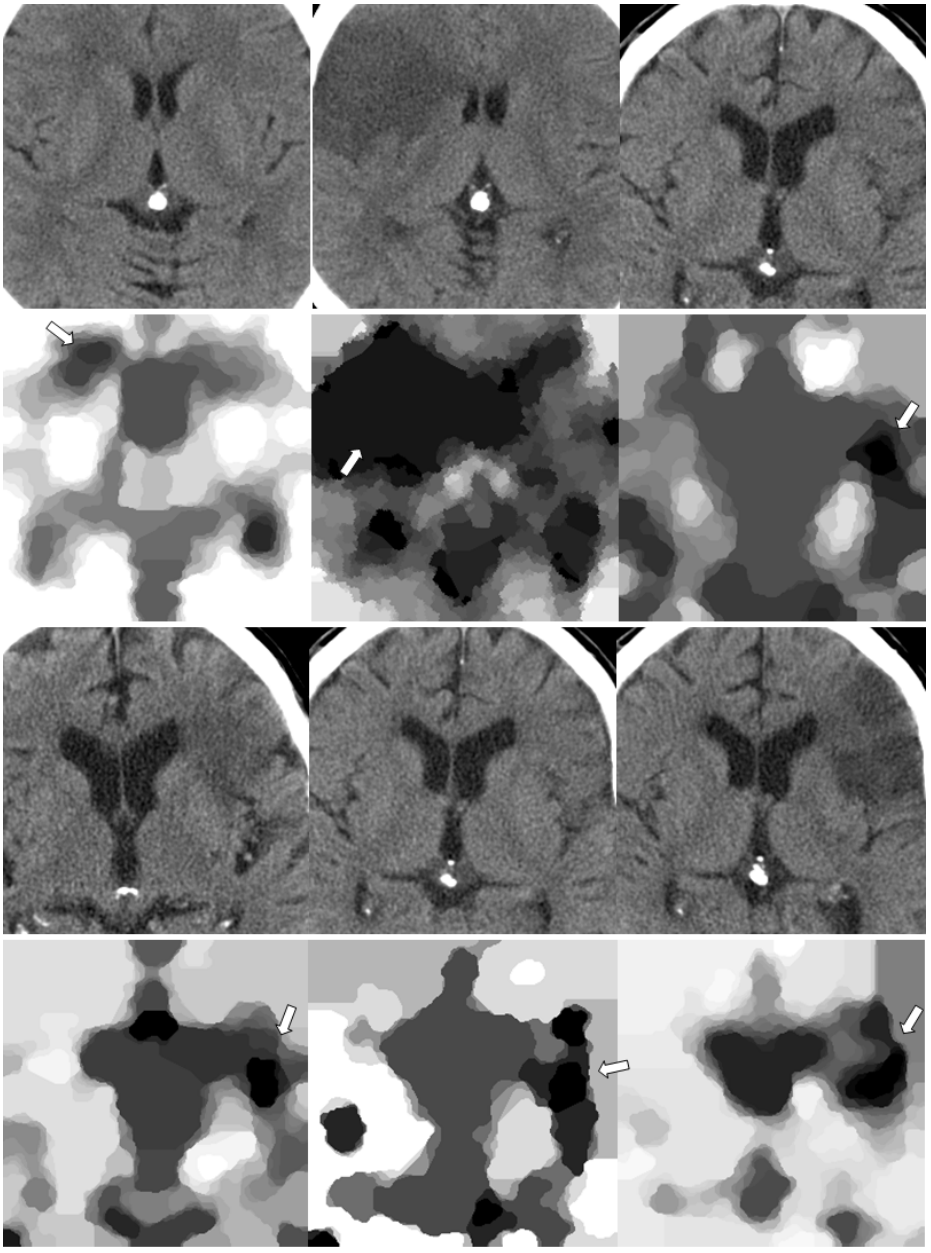

Fig. 5. The results of verification tests for CS-based image recovery; the odd rows contain examples of chosen CT slices – three stroke couples of acute diagnosis and follow-up with confirmed symptom onset; the even raws show their respective recovery with clearly extracted hypodensity, asymmetrically distributed around the axis of the brain, both for imperceptible early symptoms and late confirmations

5 Conclusions

The advantage of image processing and recovery based on integrated CS framework is possibility of more complex, deeper or "genetic" signal analysis to precisely select and reconstruct hidden components of high diagnostic importance. More degrees of freedom and possible forming of image components step-by-step, with adjusted adaptive regularization give opportunity to extract the hypodensity even in very difficult cases. However, design and optimization of such flexible model of whole image recovery is neither convex not numerically tractable problem. Instead of that we have heuristic integration problem of numerically tractable partial subproblems.

Future research will primarily focus on the specific, fast and convergent implementation of the outlined concepts. Especially, medical image applications tend toward perfected adaptation of optimization terms according to semantic models of diagnostic images.

Acknowledgement. This publication was funded by the National Science Centre (Poland) based on the decision DEC-2011/03/B/ST7/03649.

References

1. Starck, J.-L., Murtagh, F., Fadili, J.M.: Sparse image and signal processing. Wavelets, curvelets, morphological diversity. Cambridge University Press (2010)
2. Chan, T.F., Shen, J.H.: Image processing and analysis - variational, PDE, Wavelet, and Stochastic Methods. SIAM Publications, Philadelphia (2005)
3. Rudin, L.I., Osher, S., Fatemi, E.: Nonlinear total variation based noise removal algorithms. Phys D 60, 259–268 (1992)
4. Coifman, R., Geshwind, F., Meyer, Y.: Noiselets. App. Comp. Harm. Anal. 10, 27–44 (2001)
5. Przelaskowski, A., Walecki, J., Sklinda, K., Ostrek, G.: Improving diagnostic value of CT examinations in hyperacute ischemic stroke. Acta Neurochirurgica Supplementum 106, 165–170 (2009)
6. Bruckstein, A.M., Donoho, D.L., Elad, M.: From sparse solutions of systems of equations to sparse modeling of signals and images. SIAM Review 51(1), 34–81 (2009)
7. Angelosante, D., Giannakis, G.B.: RLS-weighted Lasso for adaptive estimation of sparse signals. In: Proc. IEEE ICASSP, pp. 3245–3248 (2009)
8. Candés, E., Romberg, J., Tao, T.: Stable signal recovery from incomplete and inaccurate measurements. Commun. Pur. Appl. Math. 59(8), 1207–1223 (2006)
9. Guleryuz, O.G.: Nonlinear approximation based image recovery using adaptive sparse reconstructions and iterated denoising-Part I: Theory. IEEE Trans. Image Process. 15(3), 539–554 (2006)
10. Nikolova, M.: Weakly constrained minimization: application to the estimation of images and signals involving constant regions. J. Math. Imag. Vis. 21(2), 155–175 (2004)
11. Chan, T.F., Esedoglu, S.: Aspects of total variation regularized L1 function approximation. SIAM J. App. Math. 65(5), 1817–1837 (2005)

12. Candes, E., Tao, T.: Near-optimal signal recovery from random projections: universal encoding strategies? IEEE Tran. Inf. Theory 52(12), 5406–5425 (2006)
13. Candes, E., Tao, T.: The Dantzig selector: Statistical estimation when p is much larger than n. Ann. Statist. 35(6), 2313–2817 (2007)
14. Olshausen, B.A., Field, D.J.: Emergence of simple-cell receptive field properties by learning a sparse code for natural images. Nature 381(6583), 607–609 (1996)
15. Guo, W., Yin, W.: Edge guided reconstruction for compressive imaging. SIAM J. Imaging Sci. 5, 809–834 (2012)
16. Aharon, M., Elad, M., Bruckstein, A.: K-SVD: An algorithm for designing overcomplete dictionaries for sparse representation. IEEE Tran. Sig. Proc. 54(11), 4311–4322 (2006)
17. Needell, D., Tropp, J.A.: CoSaMP: Iterative signal recovery from incomplete and inaccurate samples. Comm. ACM 53(12), 93–100 (2010)
18. Du, D., Hwang, F.: Combinatorial group testing and its applications. World Scientific, Singapore (2000)
19. Dumitrescu, B., Onose, A., Helin, P., Tabus, I.: Greedy Sparse RLS. IEEE Trans. Sign. Proc. 60(5), 2194–2207 (2012)
20. Goldfarb, D., Yin, W.: Parametric maximum flow algorithms for fast Total Variation minimization. SIAM J. Sc. Comp. 31(5), 3712–3743 (2007)
21. Shewchuk, J.R.: An introduction to the conjugate gradient method without the agonizing pain. Manuscript (August 1994) (l_1-MAGIC implementation)

Application of the Digital Curvelet Transform for the Purpose of Image Denoising in MRI

Joanna Świebocka-Więk and Henryk Figiel

AGH University of Science and Technology, Cracow 30-059, PL
Faculty of Physics and Applied Computer Science
jswiebockawiek@gmail.com

Abstract. This paper presents a curvelet-based approach on the image denoising in magnetic resonance imaging (MRI). The method is worth of examination, because it has not been tested so far in case of MRI. The results show how the Digital Curvelet Transform method can be used for the noise reduction. The analysis of the Signal to Noise Ratio (SNR), Normal to Mean value (NM) and edge detection quality is applied. The Digital Curvelet Transform application provides additional possibilities like image compression and image fusion, which could be also useful in the MRI application.

Keywords: curvelet transform, magnetic resonance imaging, noise reduction, edge detection.

1 Introduction

Noise is the unwanted, but integral part of the MRI images, impossible to completely remove. In case of MRI technique, there are 3 basic types of noise, depending on the acquisitions, the physical properties of the sample and methodology for image processing. The image might be noised during its registration and postprocessing as well.

Exact selection of image acquisition terms is also extremely important because of the procedure duration (acquisition time). The magnetic field induction value is one of the most important factors determining the obtained image quality — the lower this value is, the higher noise is observed. In case of the low-field scanners (magnetic field induction lower than 0.35 T), obtaining images comparable with images from high-field scanners requires for example larger number of averages, thicker slices, the smaller size of the matrix, or coil frequency bandwidth. It results in significantly prolonged acquisition time (even up to an hour for 8 averages) and decreasing image diagnostic value in some cases. Therefore, for low-field scanners it is so important to select the best noise reducing method, allowing to obtain images with high quality and short acquisition time as well.

The most reliable and common in use parameter dedicated to noise measurement is Signal to Noise Ratio (SNR). It is relation between average signal measured in the sample homogeneous region and the standard deviation of the

E. Pietka, J. Kawa, and W. Wieclawek (eds.), *Information Technologies in Biomedicine, Volume 3*, Advances in Intelligent Systems and Computing 283,
DOI: 10.1007/978-3-319-06593-9_15,

background signal [1]. This parameter is also used to evaluate and compare MRI tomography scanners.

Finding the best way to increase Signal to Noise Ratio in the MRI is a fundamental part of the image quality improvement. Its value can be increased not only by choosing appropriate image acquisition parameters, but also by using programming methods: from simple averaging algorithms to the modern spatial-frequency transforms [2]. Among the broad spectrum of postprocessing methods, the numerical methods seem to be the most useful.

The Digital Curvelet Transform (DCT) is multiresolution method, allowing sparse representation of signal and images. It was proposed by E. Candes and D. Donoho [3] and it has never been tested in MRI denoising. However it has a wide range of applications among others fields of science, like signal and image processing, seismic surveys, modeling of fluid mechanics or even modeling the dynamics and the state of the combustion of pulverized coal [4]. Image denoising was applied for the first time in 2002, by two research teams: J.L. Starck et al. [4] and E. Candes et al. [7]. Earlier publications about DCT applications reported encouraging results, therefore its verification in MRI is worth of interest [5].

For the purpose of this paper the method was implemented in the MATLAB environment, using Curvelab package [11]. The main goal of this publication is to show and rate the results of the DCT methodology in MRI, taking into consideration the chosen image quality criteria like: visual evaluation, Signal to Noise Ratio (SNR), degree of keeping the edges and typical structures, degree of smoothing the image. Research was performed using fantom and diagnostic images.

2 Digital Curvelet Transform

There are two algorithms based on idea of the curvelet transformation: Curvelet-99 (proposed in 1999) and Curvelet-2nd generation (proposed in 2005 and used in this publication). The method is a development of the discrete wavelet transform (new additional orientation parameter is introduced), enriched using so called heterogeneous scaling law which allows better edge representation (contrast and time-frequency resolution increase) than in case of wavelet transform application. Because of its very promising results, curvelet transform methodology is still in development [6].

2.1 Algorithm Description

The idea of the transform is the decomposition (segmentation) of image using a wavelet transform, then the band analysis using Ridgelet Transform [2]. The image can be analyzed by parts using frequency windows with different sizes.

DCT method has four basic steps:

1. Subband decomposition

Image is decomposed by application of high-pass and low-pass frequency filtration. Each received band (subimage) contains details image representing

specific frequencies. All frequencies are stored in form of the transform coefficients.

2. Partitioning and smoothing
Information contained in each pixel is divided between all bands (subimages). The number of coefficients increases.

3. Renormalisation
All subimages are divided into diadic, unit squares.

4. Ridgelet Transform
The algorithm of the edge detection is applied in each square.

Application of Inverse Digital Curvelet Transform (IDCT) based on reversing these steps yields input image with reduced noise. Figure 1 illustrates consecutive steps of the DCT algorithm.

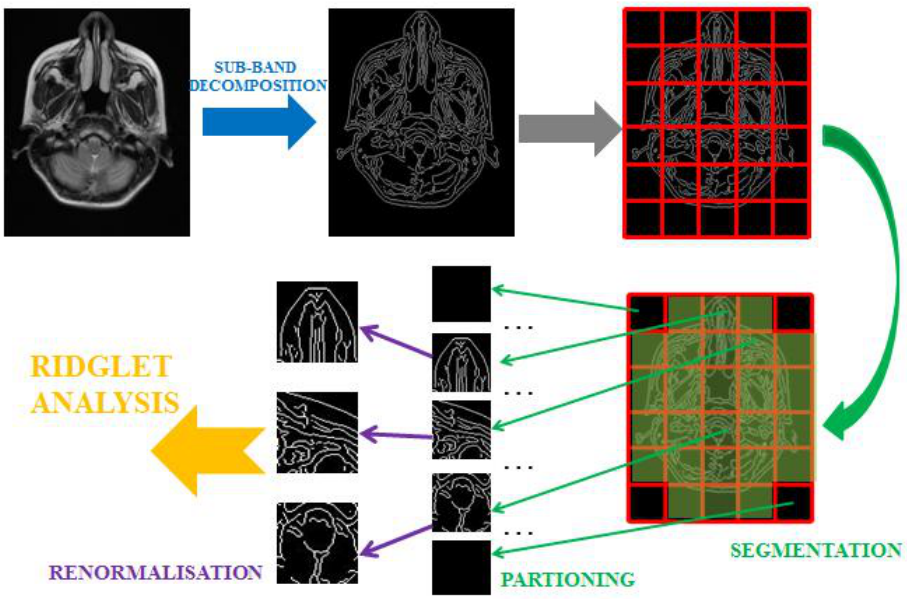

Fig. 1. Consecutive steps of the Digital Curvelet Transform algorithm

2.2 Implementation

Curvelab package can be downloaded (for the academic purpose) from the site `http://www.curvelet.org` [11]. It is a set of programs and procedures, implemented in CPP for MATLAB environment, allowing signal denoising in 1D, 2D or even 3D.

There are 2 versions of the noise removal algorithm that differ in the type of sampling grid :

– wrapping-based method (applied in this publication),
– unequally-spaced Fast Fourier Transform-based (USFFT) method.

In wrapping-based method (standard approach), image is treated as a set of 146 matrices containing transform coefficients. It is possible to consider only the chosen matrix, representing coefficients of interest.

Each matrix corresponds to different level of resolution (scale parameter) and orientation (matrix 1 means the lowest level of resolution, 146 - the highest one). Matrices 2-145 represent the coefficients with different orientation parameter (horizontal details are described in matrices which are placed near to 0° line, vertical details - near to 90° line). Between the lines of 0° and 90° there are matrices describing the oblique details (mixed components). All coefficients are geometrical symmetric relating to the image center (matrix number 1). Figure 2 shows how to encode information using wrapping-based algorithm.

Denoising effect is achieved by the hard thresholding of the curvelet transform coefficients. The threshold point is set as $3\delta_{ij}$ (except of the highest scale where threshold point is $4\delta_{ij}$), where $4\delta_{ij}$ means the standard deviation of the noise level for the scale orientation i, j, calculated as the norm of each curvelet coefficient.

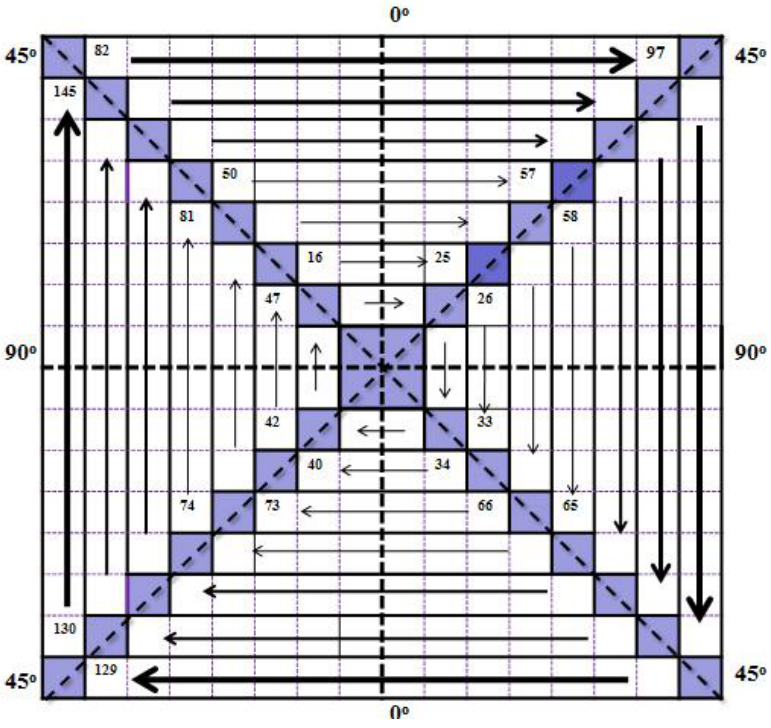

Fig. 2. Image matrices numbering and arrangement in wrapping-based method

3 Results

All images were obtained on low-field MR tomography system (Cirrus Open 0.2T) created and installed in AGH-University of Science and Technology. From the series of 30 images registered with different acquisition parameters, 2 groups of images were selected [10]:

1. characterized by low SNR value,
2. characterized by strong darkening (low visual quality).

Table 1 contains the results of the noise removing filtration applied to images with the low SNR value. The greatest improvement was noted for most dark images, mainly due to a strong decrease of the background standard deviation (SD).

Table 1. Image denoising effect after DCT implementation for the low SNR images

Image No	SNR before DCT filtration	SNR after DCT filtration
1	4.344 (± 0.24)	95.449 (± 4.775)
10	15.752 (± 0.798)	79.848 (± 3.902)
12	8.29 (± 0.422)	50.045 (± 2.502)
18	9.589 (± 0.608)	18.604 (± 0.985)
19	25.354 (± 1.27)	41.441 (± 2.072)

The same kind of analysis was applied for the separate group of darkened images (showed in Table 2), which are difficult to visual evaluation. In all cases, images were slightly brightened and their background standard deviation was decreased at the same time (image homogenous was increased, therefore SNR value increased rapidly as well). All images were also smoothed, which is typical for most of denoising algorithms.

Table 2. Image denoising effect after DCT applied for the darkened images

Image No	SNR before DCT filtration	SNR after DCT filtration
9	4.895 (± 0.328)	61.295 (± 3.064)
24	21.047 (± 1.058)	46.999 (± 2.351)
25	27.238 (± 1.365)	63.741 (± 3.187)

3.1 Normal Mean Value

The Normal Mean value (NM) is a very useful parameter for noise reduction evaluation. It is determined for homogenous image area without any edges. It defines a relation between the variance value of image background after and before filtration:

$$NM = \frac{\mu_{filtr}}{\mu_{original}} \tag{1}$$

where:

μ_{filtr} - a variance of the background image after the filtration,
$\mu_{original}$ - a variance of the background original image (before the filtration)

In Table 3 the NM values for chosen images were shown.

Table 3. NM values for chosen filtered images

Image No	NM value
1	1.65
2	1.05
3	1.11
7	1.19
8	1.15
9	1.14
10	1.21
11	1.09
12	1.12
19	1.11
24	1.14
25	1.13

In case of NM value greater than 1, it indicates the degree of brightening the image after filtration. Higher value means the greater image changes. The highest value was obtained for the NM image with initially the biggest darkening and the lowest SNR value (image number 1).

3.2 Edge and Line Detection

Detection of edges is extremely important part of image quality improvement In this procedure some characteristics important for the image diagnostic utility should be taken into consideration. The most important is the lack of the false edges, detected because of the presence of noise, which must be reduced. The image analysis of the keeping the edges after denoising filtration was performed, using 6 types of filters (Canny, Zero-crossing, Laplacian of Gaussian (LoG), Prewitt, Roberts, Sobel) [9]. Image analysis after filtration allowed to divide the filters into 2 groups:

- Methods detecting false edges (due to noise presence), decreasing the readability and usefulness of diagnostic images (Canny, Zero-crossing and Laplacian of Gaussian (LoG) filters),
- Methods do not detection noise-generated, false edges (Prewitt, Roberts and Sobel filters)

Comparison of the results of selected edge detection filters before and after DCT filtration is given in Figure 3, 4 and 5. Evaluation of the DCT effectiveness

was based on preservation of the existing edges and false-ones discrimination. It is shown that in each case number of false edges was reduced after image denoising (DCT filtration). Best results were obtained for the zero-crossing and LoG filters. Although in all cases the results reflect the course of the edges accurately.

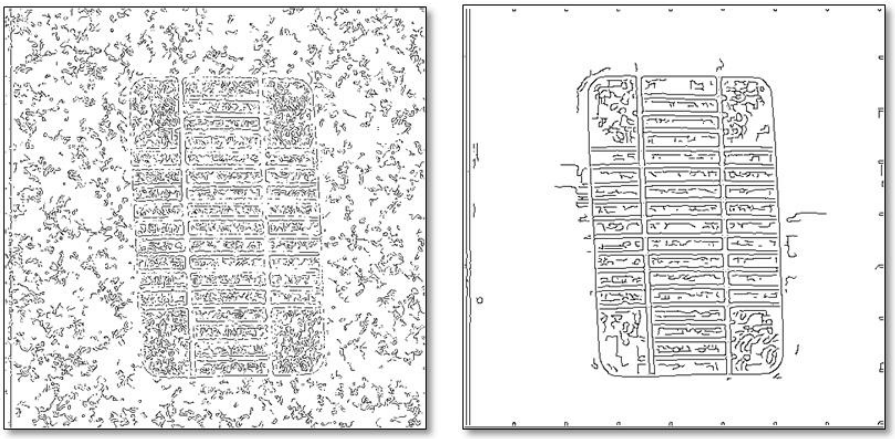

(a) (b)

Fig. 3. Edge detection in fantom image before (a) and after (b) DCT denoising filtration; Canny edge detection algorithm

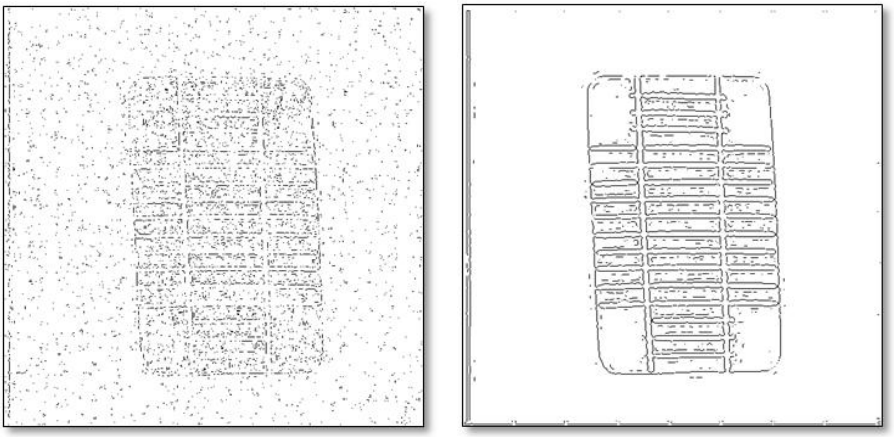

(a) (b)

Fig. 4. Edge detection in fantom image before (a) and after (b) DCT denoising filtration; zero-crossing edge detection algorithm

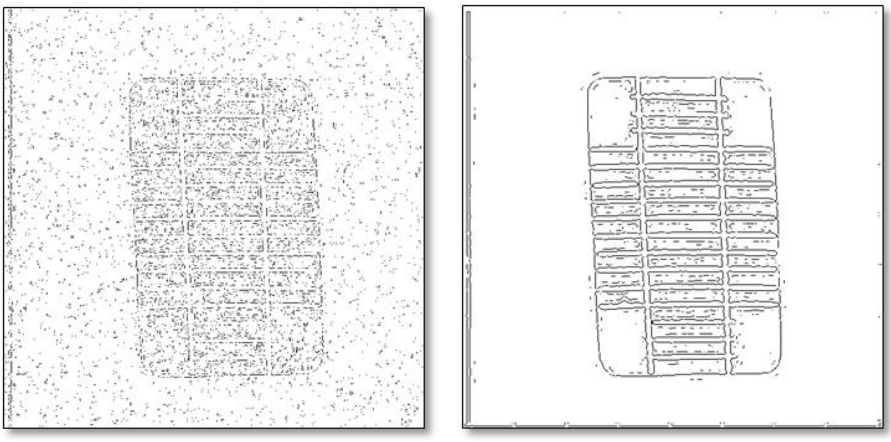

(a) (b)

Fig. 5. Edge detection in fantom image before (a) and after (b) DCT denoising filtration; Laplacian of Gaussian (LoG) edge detection algorithm

3.3 Study of Rabbit Bone Implant

The effectiveness of the method was also tested on noised images presenting implant assimilation in rabbit femur. From a series of images, 4 was chosen based on their low visual quality. All images were recorded with the following acquisition parameters:

- magnetic field induction: 0.2 T,
- 4 averaging,
- slice thickness: 3mm,
- matrix dimension: 192x192,
- FOV: 70x70 (saggital plane), 70x50 (transverse plane).

The results are shown in Table 4. In all cases SNR increased several times. Visual quality was improved as well, by a strong reduction of the background signal standard deviation.

Table 4. SNR value comparison before and after image denoising filtering - rabbit bone implant

Image No	SNR before DCT filtration	SNR after DCT filtration
1	28.52 (± 1.83)	62.97 (± 3.78)
2	32.09 (± 1.97)	83.96 (± 4.51)
3	44.49 (± 2.27)	89.75 (± 4.72)
4	36.27 (± 2.03)	87.11 (± 4.6)

4 Summary and Conclusions

Analysis of the Digital Curvelet Transform as the method of image denoising in MRI based on increasing the SNR and keeping real edges gave very good results. A major advantage of this method is the low computational complexity and high contrast of processed images.

Shown methodology has a great application potential in the analysis of images from low-field MRI systems. The obtained results allow to conclude that the use of this technique in noise reduction applications is an attractive alternative to repeating the measurement sequence, and that is why it permits to reduce the acquisition time while maintaining high-quality images.

The presented results also prove that the application of the DCT method to improve MRI images is very useful although it needs further studies.

Acknowledgement. The Authors express their gratitude to MSc.B. Proniewski and MSc. K. Klodowski for the fantom images.

References

1. Landini, L., Positano, V.: Advanced Image Processing in Magnetic Resonance Imaging. CRC Press (2005)
2. Starck, J.L., Fionn, M.: Sparse Image and Signal Processing. Wavelets, Curvelets, Morphological Diversity. Cambridge University Press (2010)
3. Candes, E., Donoho, D.: Curvelets–a surprisingly effective nonadaptive representation for objects with edges, pp. 105–120. Vanderbilt University Press, Nashville (2000)
4. Starck, J.L., Candes, E., Donoho, D.: The Curvelet Transform for Image Denoising. IEEE Transactions on Image Processing 11(6) (2002)
5. Jagadeeswar, G., Jayachandraprasad, T.: Curvelets with New Quantizer for Image Compression Global. Journal of Computer Science and Technology 12(8) (April 2012)
6. Parlewar, P.K., Bhurchandi, K.M.: A 4-quadrant curvelet transform for denoising digital images. International Journal of Automation and Computing 10(3), 217–226 (2013)
7. Candes, D., Guo, F.: New Multiscale Transforms, Minimum Total Variation Synthesis: Applications to Edge-Preserving Image Reconstruction. Signal Processing 82(11), 1519–1543 (2001)
8. Donoho, D., Duncan, M.: Digital Curvelet Transform: Strategy, Implementation and Experiments. Technical Report, Stanford University (1999)
9. Gonzalez, R.C., Woods, R.E.: Digital Image Processing using Matlab. Pearson Education Inc., NJ (2004)
10. Świebocka-Więk, J.: Effectiveness analysis of selected noise reduction algorithms in magnetic resonance imaging. PhD thesis, AGH University of Science and Technology, Cracov (2013)
11. `http://www.curvelet.org`

Universal Segmentation Framework for Medical Imaging Using Rough Sets Theory and Fuzzy Logic Clustering

Marcin Majak

Department of Systems and Computer Networks, Faculty of Electronics, Wrocław University of Technology, Wybrzeże Wyspiańskiego 27, 50-370 Wrocław, Poland
marcin.majak@pwr.wroc.pl
http://www.kssk.pwr.wroc.pl/

Abstract. The main goal of this paper is to describe universal software framework and its improvements to represent region of interest (ROI) which can be used for precise medical image segmentation. Software reads different image modalities and later applies registration method to align two or more datasets. This article also presents extension for basic segmentation enriching it with Rough sets theory and c-means fuzzy logic application to manage uncertain and vague data. Rough sets method introduces two region of interest for current segmentation: positive one where voxels are certainly included in the ROI and boundary region in which voxels possibly belong to ROI. Such concept description is very valuable in early medical diagnosis especially in oncological treatment. Along with Rough sets algorithm c-means fuzzy logic algorithm has been implemented for clustering data in MRI images.

Keywords: image registration methods, medical image segmentation, Rough sets theory, fuzzy logic clustering.

1 Medical Imaging

Medical image analysis and segmentation algorithms have evolved in the past few years. With the advancement of image processing methods and higher device's precision medical diagnosis can be significantly supported. In the literature one can find many examples of medical image applications: from tumor and soft tissue segmentation in various types to diagnostic tools using pattern recognition and artificial intelligence. Other domain which has been recently developed is image-guided surgery systems used for both: virtual planning and surgery control.

Algorithms described in this article operates on different medical images such as CT, MRI, PET and many others which have been worked out in the last 50 years. Each of the aforementioned modalities provides different information and are valuable for specific treatment. Due to these fact it is required to provide universal framework which can be used in many medical image applications. Basic binary threshold segmentation method has been enriched with Rough sets

E. Pietka, J. Kawa, and W. Wieclawek (eds.), *Information Technologies in Biomedicine, Volume 3*, Advances in Intelligent Systems and Computing 283,
DOI: 10.1007/978-3-319-06593-9_16,

processing module and c-means fuzzy logic clustering algorithm, which gives good results comparing to other algorithms.

The organization of this paper is as follows: Section 2 describes main medical image processing issues which we have to deal with, Section 3 indicates how Rough sets theory and c-means clustering (two the most promising and very interesting algorithm for medical images) can be used in the image segmentation. In Section 4 one can find software description developed for testing and evaluation and in 5 example results are shown with discussion. Whole paper is finished in Section 6 with proposal for future improvements and final conclusions.

2 Medical Imaging Processing Issues

Image registration process is very important in medical imaging. It allows to compare and align images acquired at different time or very often in different modalities. One can wonder if this is really required while we can asses images by looking at them independently. This is crucial part because each image modality unveils different information. Let's consider CT and MRI taken from the same patient. The first one illustrates bone tissues while on the second soft tissue are better visible. Aligning these datasets especially in oncological imaging provides valuable information in the comparison mode. Surgeon can asses not only how cancer affects bone tissue, but additionally how soft tissues are degenerated in the tumor vicinity. Repeated acquisitions of image data from the same patient is a common approach and is used to compare pre- and post-treatment changes, clinical follow-up, evaluation of the treatment, and serial studies [1].

It should be emphasized that image registration procedure is not a trivial task especially between different modalities. Very often images are acquired at different time so it is almost impossible that these two datasets will be spatially aligned due to body movements or different device settings. What it more, images can differ with image dimension, pixel resolution and intensities. There are many different registration methods and it is hard to describe all of them. For more detailed and comprehensive description of registration methods review [2–4]. Each registration algorithm strongly depends on its medical application and requirements. The most commonly used registration methods are: manual registration, external point landmarks registration (skin markers, dental impressions), surface Landmark registration, voxel intensity-based registration and finally hybrid approach [5, 6].

Apart from the registration aspect, another very important issue to reconsider is connected with image interpolation. Due to calculated transformation (rotation and translation) we have to determine pixel intensity at point c from a set of pixels surrounding it. It should be noted that depending on the application a compromise between time complexity and interpolation accuracy is crucial. In the volumetric images each pixel coordinate is defined by integer values: (X, Y, Z), but after transformation pixel's coordinates can be expressed as non-integer values (x, y, z) so interpolation is needed to set pixel intensity in the exact integer position. In the literature one can find many interpolation

algorithms, but in medical images one of the most commonly used are: nearest neighbor, bicubic and trilinear interpolation and sinc interpolation [7].

3 Rough Sets and C-Means Fuzzy Logic Algorithms in Image Segmentation

3.1 Rough Sets Application in Medical Images

Rough sets theory (RST) described by Pawlak in the early 1980's can be easily applied to image processing algorithms. This theory is based on the object's discernibility and can handle uncertainty which is often phenomenon in medical images due to noise and poor acquisition quality [8, 9]. Additionally, RST can reduce feature space by introducing granular knowledge. For example, CT bone is described by group of pixel intensities so the whole bone class in RST can be reduced to one, representative pixel intensity. Another important advantage of RST for image processing comes with approximations which can be used straightforward because whole methodology is directly computed from the input data without strong a priori reasoning. Using pixel intensity or shapes measure it is quite easily to define lower and upper approximations of a given concept. Especially, this approach is very valuable in a direct representation of the region of interest (ROI), when it is very hard to assign to one concept a whole range of noisy pixels in an interchangeable manner. Approximations, which can significantly reduce pixel intensity variance, are desired in medical image segmentation because single threshold value will not determine the exact ROI boundary. The recent applications of RST involves segmentation of the heart on cardiovascular magnetic resonance [10], distinguishing different picture types of the central nervous system and color image segmentation [11, 12] to name only the few.

To introduce RST let U be an universe of discourse and X be a given concept as a subset of U. Over this we can define an equivalence relation R which divides whole set U into subsets of categories $U/R = \{X_1, X_2, \ldots, X_n\}$. Each X_n represents an equivalence class of R. In RST we introduce R_*-lower and R^*-upper approximations of X and define it as:

$$R_*X = \cup\{Y \in U/R | Y \subseteq X\} \tag{1}$$

$$R^*X = \cup\{Y \in U/R | Y \cap X \neq \emptyset\} \tag{2}$$

RST uses three basic regions: positive, negative and the boundary region [13]. Positive one contains approximations which surely describe given concept X, while negative region has values that do not belong to the category X. Finally, a boundary region has values that can possibly describe concept X. Using (1) and (2) we can define RST region as follows:

$$P_R(X) = R_*X \tag{3}$$

$$N_R(X) = R^*X \tag{4}$$

$$B_R(X) = R_*X - R^*(X) \tag{5}$$

Equations (3), (4) and (5) define basic notions in RST and are used in the algorithm construction prepared in this article to describe segmentation ROI. But, here arises the question how to decide if a given approximation should be included in ROI when its value is close to the threshold. For example it could be assigned in two ways: if an averaged intensity value from this granule is greater than defined threshold or the number of pixel which intensity is greater than threshold to other pixels from approximation is greater than one [10]. Another important advantage of RST is than it can be defined on different features such as pixel intensity, distance measure, shape or what is more interesting even various approximations can be combined [14].

3.2 C-Means Fuzzy Logic Application in Medical Images

As described in Section 3.1, RST algorithm requires defining proper threshold values. For basic tissue structures it is quite simple, but sometimes an additional expert knowledge is required to find proper thresholds. Clustering algorithm is something which can deal with this problem. In the past few years c-means fuzzy logic clustering has been significantly developed. It can be used in many domains from filtering and noise removal to finding non-overlapping clusters.

Fuzzy logic c-means (FCM) clustering algorithm was firstly implemented by Dunn in 1973 and later improved by Bezdek in 1981. Since then, many improvements and changes have been proposed [15–17]. In a general approach, FCM works by minimizing cost function described as:

$$J_m = \sum_{i=1}^{N}\sum_{j=1}^{C} u_{ij}^m ||x_i - c_j||^2, 1 \leq m \leq \infty \tag{6}$$

where: m defines the number of clusters, u_{ij} determines how pixel i belongs to the claster j, and c_j is a center point for the claster j. Algorithm works in iterations when in each step coefficients u_{ij}, c_j are updated according to equations (7), (8):

$$u_{ij} = \frac{1}{\sum_{k=1}^{c} (\frac{||x_i - c_j||}{||x_i - c_k||})^{\frac{2}{m-1}}} \tag{7}$$

$$c_j = \frac{\sum_{i=1}^{N} u_{ij}^m \cdot x_i}{\sum_{i=1}^{N} u_{ij}^m} \tag{8}$$

In each iteration every pixel from image is assigned to a given cluster using membership function from range $< 0, 1 >$ [18]. It should be noted that the same pixel can belong to few clusters with different values of the membership coefficient. Additionally, each cluster center from one iteration to the next is translated through whole image to find pixels with the highest similarity.

4 Software Description

As a result of project realization an universal framework software was implemented to assist diagnosis using medical images. Program allows to read various image modalities provided in DICOM format which is a global standard for medical image storing. Software uses two segmentation algorithms: Rough sets and c-means fuzzy logic (according to author, two the most promising and very effective methods). Rough sets theory is used to describe region of interest and c-means fuzzy logic clustering can be used for finding non-overlapping pixel clusters in the image or determining segmentation thresholds. Fig. 1 shows a general flow of information in this system. Firstly, as a preprocessing step, Gauss filtering is applied to remove noise and later CLAHE histogram equalization is performed on each slice. CLAHE algorithm divides the image into regions and performs histogram equalization independently to each part instead of the whole image histogram equalization. This approach ensures that hidden features of the image become more visible. Of course user can alter image display parameters by changing window level and window width coefficients.

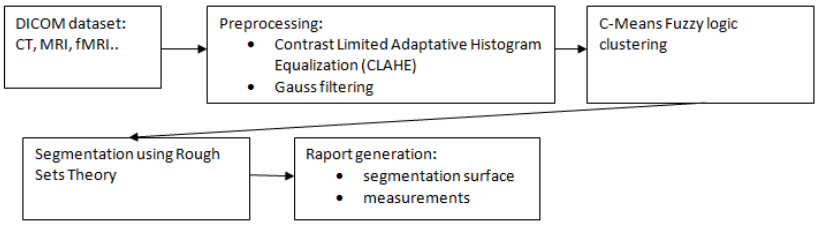

Fig. 1. General scheme of software information flow

4.1 Registration Method

Described application provides different modalities loading so a registration method was required to compare images and segmentation results. This software is strictly dedicated to experienced people having knowledge about medical imaging and after consultations it was decided that fast algorithm with manual modification is required. For examinations performed at different time body movements occur making it almost impossible to match images. In such a situation only a part of image should be registered (for example head without shoulders from CT image). Due to these restrictions, manual registration was implemented and whole process is divided into three stages:

1. landmark point definition and correction using 3D model and 2D slice projections (Axial, Sagittal, Frontal) for two images (example landmark point selection was shown in Fig. 2),
2. 3D objects modifications by surface rotation and translation,
3. transformation matrix calculation and image generation.

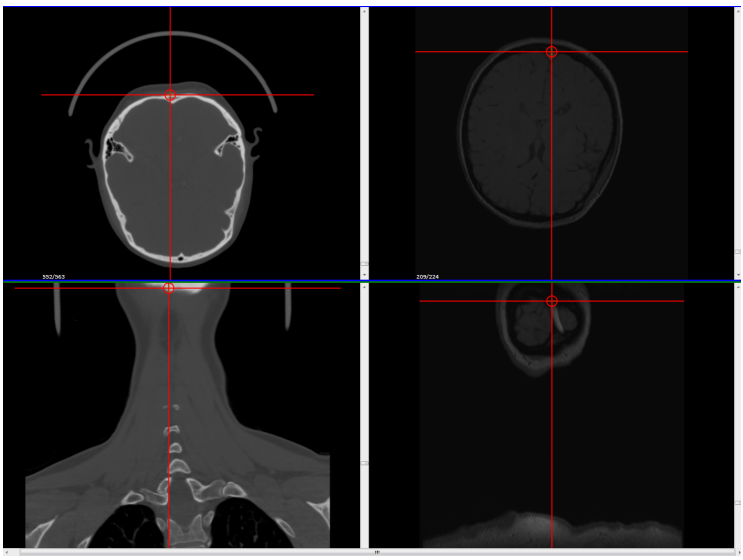

Fig. 2. Landmark point definition on corresponding image's slices for CT (left side) and MRI (right side); after determining landmark position on 3D models, 2D projections are used for precise correction

In this method the basic assumption is that at least three corresponding points are collected. Using these points an initial transformation is calculated and 3D surfaces or 3D volumes are aligned. In the next step, 3D models are used for final corrections. When 3D transformation is performed then FRE (Fiducial registration error) between corresponding landmark is calculated to indicate transformation quality. From many performed tests it was noticeable that 5 to 7 characteristics points are sufficient to obtain satisfactory results.

4.2 Interpolation Method for Image Generation

New image can be generated using transformation matrix, but as described in Section 2 an interpolation method is needed to prepare image without any artifacts. Higher order interpolation requires more memory and computational time so in this paper bicubic interpolation was chosen because it gives consensus between time and image quality. Actually, it is an implementation of Hermite interpolation method while it allows to modify parameters and decide how neighboring pixels affect final pixel intensity calculations.

4.3 Segmentation Algorithms Parameter Settings

When designing segmentation algorithms it is crucial to obey time requirements and ensure that algorithm is easy to understand. Described software provides

two segmentation methods which according to surgeons are very useful in medical diagnosis. The first one is c-means fuzzy logic which is commonly used for global segmentation and finding pixel clusters (for example brain matter in MRI images). The second proposed approach is a Rough sets precise segmentation showing exact ROI with additional boundary region possibly belonging to it. Example segmentation result for these two method was presented in Fig. 3.

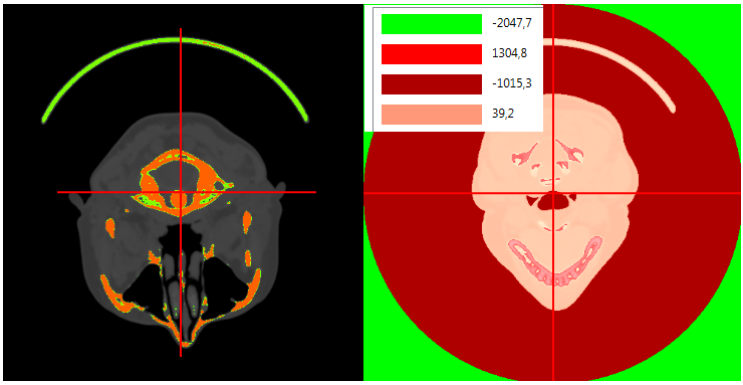

Fig. 3. Example of CT segmentation using proposed algorithms; image on the left is processed by RST (red- positive region, green- boundary region); image on the right: cluster colors and their Hounsfield values

In c-means fuzzy logic clustering method there is always a question how many initial clusters must be chosen. Some literature sources propose that it should be a fixed number with clusters locations selected randomly. In this software two ways are possible: random clusters can be created or a genetic algorithm is applied to find the optimal number of clusters. The main drawback of the first solution involves clusters overlaps, so the second solution if preferred because small clusters are removed by connecting them with greater and similar ones.

Genetic algorithm construction is quite simple and assumes that each allele in the chromosome encodes an intensity value for a single cluster. Additionally, new variable 'invalid' was introduced to indicate that a certain cluster should be excluded from calculations. At the beginning each chromosome is randomly initialized with image pixel intensities. Single chromosome proposes clusterization which is assessed by (6) with extra scaling factor. This coefficient is used to prefer solutions with the smallest number of clusters. As a selection for the next population Roulette Wheel method was chosen, and a single-point cross-over with determined probability was used. Genetic algorithm parameters are shown in Table 1.

In the precise Rough sets segmentation two measures were taken for calculating the final ROI representation: pixel intensity and distance. For the first one whole intensity pixel range was split into 15 sets. In the second measure

Table 1. Genetic algorithm parameter settings used in simulations

Population size	20
Representation	Bit representation
Mutation	0.2
Mutation type	Bit changing
Crossover ratio	0.8

2D image was divided horizontally and vertically into 20 segments creating 400 small grids for 512x512 CT scan image. After performing segmentation using first measure the second stage is applied by visiting each small grid. From single location 3 nearest grids falling into positive or boundary region are searched. If the average distance between current grid and three others is less or equal to the threshold value then this grid is also added to the ROI description. The second phase allows to enlarge boundary region and can significantly deal with noisy places in the image.

5 Results

To test proposed registration and segmentation algorithm 5 CT and 5 MRI real datasets examinations were used. In this paper only example results are shown to prove algorithm usefulness.

Each CT dataset was registered with 3, 5, 8 and 10 anatomical points on the skull. To check registration accuracy FRE measure in mm was calculated from selected landmarks. Additionally, other three points in the corresponding datasets were chosen to calculate TRE (Target Registration Error) errors. Tests were performed by medical expert who is able to determine anatomical landmarks and is experienced in medical imaging area. Example results for two datasets are collected in Table 2 where an average FRE plus TRE error is presented. Each landmark point was firstly selected on 3D model and later its location was adjusted using 2D slices. Apart from the registration accuracy, also time was measured to check procedure efficiency (time devoted only for selecting exact landmark position). Performed tests revealed that even exact landmark point location cannot ensure proper matching matrix. To overcome this problem, user can change calculated transformation by translating and rotating target 3D objects in the reference to source 3D model. In every step FRE and TRE errors are updated to indicate if transformation is proper and gives better results. After consultations, it was decided that 5-7 points are sufficient to obtain satisfactory visual results. This is a compromise between time and proper image quality.

C-means fuzzy logic algorithm with genetic modification (G-FCM) was applied to 5 examinations and its performance was compared with k-Means and basic FCM algorithm using predefined number of clusters. As a fitness measure a validity index was used, introduced by Turi in [19]. Initial chromosome length

Table 2. Registration accuracy and procedure time depending on different number of landmark points for two examination sets

#Landmarks		3	5	8	10
#1	Accuracy [mm]	5.16	4.02	2.21	1.97
	Time [s]	40	70	120	170
#2	Accuracy [mm]	6.19	5.02	2.59	2.46
	Time [s]	55	83	154	200

for G-FCM was set to 10. Comparison results are shown in Table 3 where value in the bracket in the last column indicates final number of clusters reduced from starting 10 clusters. Table 3 shows 8 randomly chosen scans from 5 examinations.

Table 3. Segmentation results performance using Turi's validity index for k-means, basic FCM and genetic FCM algorithm for 8 randomly chosen scans from 5 MRI examinations

Scan	k-means	FCM	G-FCM
1	0.42	0.14	0.12 (4)
2	0.44	0.02	0.02 (5)
3	0.92	0.08	0.07 (3)
4	0.24	0.04	0.02 (6)
5	0.52	0.17	0.18 (2)
6	0.39	0.12	0.12 (8)
7	0.87	0.23	0.20 (7)
8	0.24	0.09	0.09 (4)

Each G-FCM segmentation result has been consulted with expert who assessed visually each image. Algorithm has obtained satisfactory results and what is more important it managed to reduce final number of clusters with no overlaps.

The last test checked Rough sets segmentation validity with a simple binary threshold method. Segmentation surface in cm^2 was used as a quality measure. It should be noted that for Rough sets segmentation a positive and a boundary region was treated as a ROI representation and used in measurements. Procedure investigated bone tissue segmentation on CT scan by two algorithms: RST and binary thresholding and it was done in two stages. The first one measured general Rough sets performance on the same image versus binary thresholding. For the second one each scan was filled with 3% Gaussian noise to check how RST deals with uncertain data. Segmentation results for five CT examinations for 10 randomly chosen scans are presented in Table 4.

Proposed RST algorithm deals quite well with noisy images due to granular knowledge introduction. Additionally, usage of the second distance measure

Table 4. Segmentation results obtained by binary threshold method versus Rough sets segmentation for original images and noisy ones

	Original image		Noisy image	
Scan	Binary	RST	Binary	RST
1	1.44	1.48	1.02	1.39
2	6.09	7.02	5.99	6.81
3	34.92	35.91	31.83	33.21
4	21.11	24.82	20.40	21.01
5	138.92	141.02	137.01	138.02
6	59.60	60.48	57.12	57.92
7	12.49	13.02	10.29	12.11
8	7.02	7.03	6.80	7.00
9	80.23	80.89	78.47	78.51
10	17.42	18.00	17.11	17.74

turned out to be a correct research direction because surrounding grids were taken into account allowing to fill holes in the segmentation area. Even if pixel intensity criteria is not fulfilled, it is a chance that distance measure will assign this grid to ROI basing on other grids knowledge.

6 Conclusions

In this paper segmentation framework was described which can be used in medical treatment and diagnosis. The main goal was to implement universal application allowing to read different medical images in DICOM format and provide advanced tool for segmentation. Taking into account the nature of medical images due to noise and resolution constraints sometimes it is very hard to perform proper segmentation. To overcome this problem Rough sets theory and c-means fuzzy logic were implemented to describe region of interest. Software was tested on images (mainly CT and MRI) provided from M. Skłodowska-Curie Memorial Cancer Center where proper segmentation region and ability to compare this region with CT and MRI plays very crucial part in early diagnosis and oncological treatment. ROI description using Rough sets theory has proved to be a proper direction and gives satisfactory results, but of course more tests should be performed.

In the future it is assumed to develop registration method to support application with non-rigid transformation. What is more, RST algorithm can be enriched with more sophisticated measures, for example shape factor. In the next step software will be tested with greater examination database not only basing on CT and MRI.

Acknowledgement. The work was supported by the statutory funds of the Department of Systems and Computer Networks, Wroclaw University of Technology, Poland and described software was prepared for VIII edition of "Młoda Kadra" project.

References

1. Wang, X.S., Hu, C., Qiu, J., Xu, Z.: A comparative study of three ct and mri registration algorithms in nasopharyngeal carcinoma. Journal of Applied Clinical Medical Physics 10(2), 3–10 (2009)
2. Sannazzari, G., Ragona, R., Ruo Redda, G., Giglioli, F., Isolato, G., Guarneri, A.: Ct-mri image fusion for delineation of volumes in three-dimensional conformal radiation therapy in the treatment of localized prostate cancer. The British Journal of Radiology 75, 603–607 (2002)
3. Gottesfeld, L.: A survey of image registration techniques. ACM Computing Surveys 24(4), 325–376 (1992)
4. Maintz, J., Max, A.: A survey of medical image registration. Medical Image Analysis 2(1), 1–36 (1998)
5. Gai, A., Chen, M., Hu, Q.: Non-rigid registration between brain ct images and mri brain atlas by combining grayscale information, point correspondence on the midsaggital plane and brain surface matching. In: Proceedings of the 2nd International Conference on Computer Science and Electronics Engineering, ICCSEE 2013, pp. 222–225 (2013)
6. Widz, S., Revett, K.R., Ślęzak, D.: An automated mutli-spectral mri segmentation algorithm using approximate reducts. In: Tsumoto, S., Słowiński, R., Komorowski, J., Grzymała-Busse, J.W. (eds.) RSCTC 2004. LNCS (LNAI), vol. 3066, pp. 815–824. Springer, Heidelberg (2004)
7. Lehmann, T., Spitzer, K.: Survey interpolation methods in medical image processing. IEEE Transactions on Medical Imaging 18(11), 1049–1075 (1999)
8. Pattaraintakorn, P., Cercone, N.: Integrating rough set theory and medical applications. Applied Mathematics Letters 21, 400–403 (2008)
9. Komorowski, J., Pawlak, Z., Polkowski, L., Skowron, A.: Rough sets a tutorial. In: Pal, S.K., Skowron, A. (eds.) Rough Fuzzy Hybridization- A New Trend in Decision Making, pp. 3–98. Springer, Heidelberg (1999)
10. Hirano, S., Tsumoto, S.: Rough representation of a region of interest in medical images. International Journal of Approximate Reasoning 40, 23–34 (2005)
11. Xue, J., Pizurica, A., Philips, W., Kerre, E., Van de Walle, R., Lemahieu, I.: An integrated method of adaptive enhancement for unsupervised segmentation of mri brain images. Pattern Recognition Letters 24(15), 2549–2560 (2003)
12. Mushrif, M.M., Ray, A.K.: Color image segmentation rough-set theoretic approach. Pattern Recognition Letters 29, 483–493 (2008)
13. Sankar, K.P., Mitra, P.: Multispectral image segmentation using the rough-set-initialized em algorithm. IEEE Transaction on Geoscience and Remote Sensing 40(11), 2495–2501 (2002)
14. Kovacevic, N., Lobaugh, N., Bronskill, M., Levine, B., Feinstein, A., Black, S.: A robust extraction and automatic segmentation of brain images. NeuroImage 17, 1087–1100 (2002)
15. Hassanien, A.: Fuzzy rough sets hybrid scheme for breast cancer detection. Image and Vision Computing 25(40), 172–183 (2007)
16. Hassanien, A., Bader, A.: A comparative study on digital mamography enhancement algorithms based on fuzzy theory. International Journal of Studies in Informatics and Control 12, 21–34 (2003)

17. Hassanien, A.E., Ali, J.M., Nobuhara, H.: Detection of spiculated masses in mammograms based on fuzzy image processing. In: Rutkowski, L., Siekmann, J.H., Tadeusiewicz, R., Zadeh, L.A. (eds.) ICAISC 2004. LNCS (LNAI), vol. 3070, pp. 1002–1007. Springer, Heidelberg (2004)
18. Sharma, M., Mukharjee, S.: Brain tumor segmentation using hybrid genetic algorithm and artificial neural network fuzzy inference system (anfis). International Journal of Fuzzy Logic Systems 2(4), 31–42 (2012)
19. Turi, H.: Clustering-based color image segmentation. PhD Thesis, Monash University, Australia (2001)

Ultrafast Iterative Model-Based Statistical 3D Reconstruction Algorithm for X-ray Computed Tomography

Robert Cierniak and Michal Knas

Institute of Computational Intelligence,
Czestochowa University of Technology,
Armii Krajowej 36, 42-200 Czestochowa, Poland
cierniak@kik.pcz.czest.pl

Abstract. We present in this paper the orginally formulated 3D reconstruction algorithm for spiral cone-beam x-ray tomography. Proposed here appraoch is based on the fully analytical formulation of the reconstruction problem. Moreover, we take into account the form of noise present in x-ray measurement system at the formulation of this problem. Therefore, this method belongs to the class of the statistical reconstruction methods. Thanks to this fact, this conception significantly improves quality of the obtained after reconstruction images, what allows in consequence for decreasing the x-ray dose reduction absorbed by a patient during examination. The analytical roots of the proposed here algorithm permits to decrease the complexity of the reconstruction problem in comparison with approaches based on the algebraic problem formulation. The carried out computer simulations shown that presented here reconstruction algorithm outperforms conventional analytical methods regarding the obtained image quality. The GPU realization of our algorithm shows that this algorithm can be fully applicable for commercial use in the sense of the obtained image quality and the time of reconstruction process.

Keywords: Image reconstruction from projections, x-ray computed tomography, statistical reconstruction algorithm.

1 Introduction

This paper is concerned with a medical imaging technique called computed tomography CT (more precisely, x-ray computed tomography), in particular with the most important, for development of this technique, problem of the formulation of image reconstruction from projections algorithms. Considering the methods used in medical computed tomography, it should be taken into account the destructive influence of radiation used in this imaging technique. In the case of x-ray CT (transmission tomography), it is x-ray radiation. It is indisputable that this kind of radiation is harmful to health of the examinated patients, and this a main reason why the research is undertaken to decrease the dose of radiation received by these patients. Because the limitation of the intensity of x-ray radiation during examination, and in consequence limitation of x-ray dose absorption)

E. Pietka, J. Kawa, and W. Wieclawek (eds.), *Information Technologies in Biomedicine, Volume 3*, Advances in Intelligent Systems and Computing 283,
DOI: 10.1007/978-3-319-06593-9_17,

implies the deterioration of the obtained images, i.e. the decreasing of the low contrast resolution parameter (one of the most important parameter describing the quality of the scanner), this way is wrong. It is caused by a fact, that in this matter rules the following relationship [1]:

$$SNR \propto \sqrt{D}, \tag{1}$$

where: D is a dose of x-ray radiation absorbed by a patient.

It is relatively strong relationship beetween dose absorption by patient and qality of the reconstructed image. It is clear that x-ray dose absorbed by a patient is proportional to the intensity of the x-ray used during an examination. It is a barrier for the approach of the direct intensity limitation. And so was a new idea to decrease this dose limiting used x-ray intensity without degradation of reconstructed image using only an appropriately formulated reconstruction algorithm. This kind of approach would allow to improve image quality with high resolution and/or to decrease the absorbed dose of x-ray radiation by a patient. Such conception found its exemplification in an idea of the statistical image reconstruction algorithms, which take into account the probabilistic conditions present in measurement systems in CT scanners, so as limit influence of this noise on the obtained using carried out measurements images. So far, there are some developed commercial solutions of such kind algorithms, for example Adaptive Statistical Iterative Reconstruction (ASIR), Iterative Reconstruction in Image Space (ARIS), Adaptive Iterative Dose Reduction (AIDR) or iDose algorithms, which iteratively perform reconstruction processing decreasing noise from obtained images. Details of those algorithms are not open, but their practical usefulness was confirmed by many published papers in radiological journals, for example [2]. Completely different approach, called by authors MBIR (Model-Based Iterative Reconstruction), is presented in such papers as [3, 4], where in an analytical way is derived a statistical model of the measurement signals, and based on its it is formulated an iterative reconstruction algorithm. Generally, one can say that all most significant existing reconstruction algorithms belong to two basic approaches, taking into account the methodology of the used in them signal processing concepts: these are called the analytical methods, and those are assigned to strategy called the algebraic reconstruction technique (ART). We can guess that the implementation of the ART in the historical first CT Haunsfield's apparatus was caused for lack of alternative at that time. In text generations of CT systems were used only reconstruction algorithms based on analytical methodology. It is clear when we take into account the huge sizes of matrices appeared in the algebraic reconstruction problem, and caused by this fact the calculation complexity of reconstruction method based on this methodology. The analytical methodology simplifies drastically the number of neccessary calculation and in this way is more appealing. Afterwards, the algebraic approach was taken into consideration (see e.g. [3, 5]) for design of the statistical reconstruction algorithms because it allows for accurate modelling of the statistics of projection data and it helps to avoid most of distortion caused by them. This conception was a background to establish a commercial solution called the

Veo in 2013. Presented in those reconstruction idea is based on the maximum *a posteriori* probability (MAP) estimation approach. That application of the algebraic reconstruction technique has some significant technical difficulties at practical realization, namely: in the case of algorithms for 3D spiral cone-beam scanners, it is complicated to establish the coefficients of forward model for ART at this geometry of scanner [5–7], and that methodology forces simultaneously calculations for all voxels in range of reconstructed 3D image what makes the reconstruction problem extremely complex.

We could avoid the mentioned above difficulties connected with using of ART methodology using an analytical strategy of the reconstructed image processing. We previously showed how to formulate the analytical reconstruction problem consistent with the ML method for parallel geometry of scanner [8–10], for fan-beams [11], and finally we proposed the scheme of reconstruction method for the spiral cone-beam scanner [12]. In comparison with methods based on algebraic methodology, this analytical statistical 3D reconstruction algorithm has some serious adventages. First of all, reconstruction process is perfored only in one plane in 2D space, what significantly simplify the problem, and this way every reconstruction process can be performed for every cross-section image separately. After this, it is possible to reconstruct whole 3D volume image from set of the reconstructed before 2D images. Additionally, we use during reconstruction process the FFT what drastically decreases the time of a iteration during reconstruction process. In this paper, we present an approach to the analytical statistical reconstruction using methodlology resembling the very popular and regarded FDK (Feldkamp) algorithm.

2 3D Reconstruction Algorithm for Spiral Cone-Beam Scanner

Our algorithm is based on the originally formulated 2D analytical approximate reconstruction problem for parallel geometry of scanner (see e.g. [9, 10]). This conception can be incorporated into the Feldkamp-type reconstruction methodology for design of 3D reconstruction algorithm for the spiral cone-beam geometry of the scanners. In the following subsections, it will be shown how to adapt our orginal idea to the 3D reconstruction problem. The general scheme of the proposed in this paper reconstruction procedure is depicted in Fig. 1.

This iterative statistical reconstruction algorithm operates on projections obtained in a spiral cone-beam scanner. Firstly, a position z_p on the z-axis of the reconstructed cross-section of a body is selected, before the reconstruction of image at this position is performed.

Practically, the reconstruction algorithm can only make use of projections obtained at certain angles and measured only at particular points on the partial cylindrical-shaped screen. In the case of spiral cone-beam scanner, a beam of x-rays reaches the individual detector row $k = 1, 2, \ldots, \mathrm{K}$, where K is a number of rows placed on the screen. In every row, selected rays strike the detectors, each of which is indexed by the variable $\eta = -(\mathrm{H}-1)/2, \ldots, 0, \ldots, (\mathrm{H}-1)/2$,

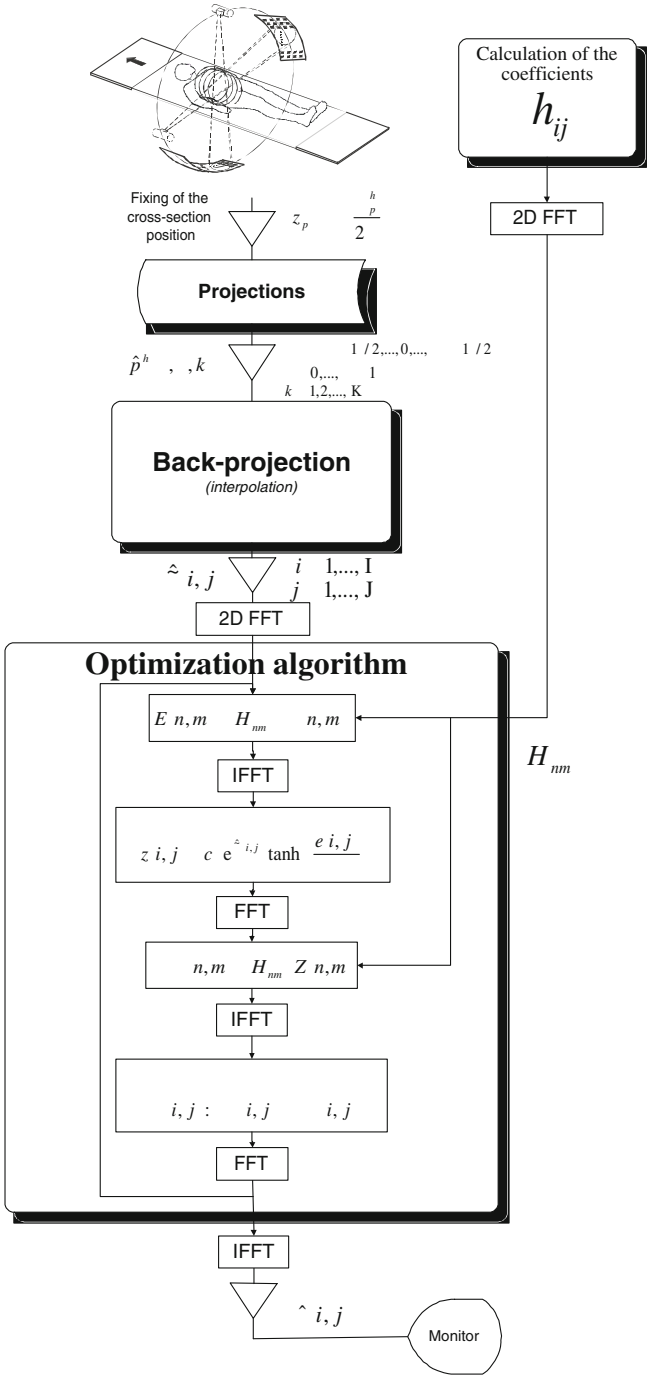

Fig. 1. An image reconstruction algorithm for the cone-beam geometry scanner

where H is an odd number of detectors in each channel of the array. Detectors are placed on the screen separated by a distance Δ_k in each row, and by an angular distance Δ_η in each channel. Furthermore, only a limited number of projections are performed, each of which is indexed by the variable $\theta = 0, \ldots, \Theta - 1$, where $\Theta - 1$ is the total number of projections made during the examination. Every projection is carried out after rotation by Δ_θ. Summarizing, our reconstruction algorithm has available the projection values $p^h\left(\beta_\eta, \alpha_\theta^h, \dot{z}_k\right)$, in the ranges: $\eta = -\left(\mathrm{H}-1\right)/2, \ldots, 0, \ldots, \left(\mathrm{H}-1\right)/2$; $\theta = 0, \ldots, \Theta - 1$; $k = 1, 2, \ldots, \mathrm{K}$.

After acquisition process, all performed in our reconstruction algorithm operations are the same as in the case of the reconstruction algorithm designed for parallel-beam scanner. The only defference between 2D and 3D approaches lies in performance of the back-projejection operation.

2.1 Back-Projection Operation

The first operation of the proposed here reconstruction algorithm is a three-dimensional back-projection. Every point in the coordinate space is given a value equal to the sum of all the projection values from all the rays passing through this point. For the projections $\dot{p}^h\left(\beta_{ij}, \theta, \dot{z}_{ij}\right)$ made at angle θ; $\theta = 0, \ldots, \Theta - 1$, the operation can be written, as follows:

$$\tilde{\mu}\left(i, j, z_p\right) \cong \Delta_\alpha^h \cdot \sum_\theta \dot{p}^h\left(\beta_{ij}, \theta, \dot{z}_{ij}\right), \tag{2}$$

Mostly, x-rays do not pass exactly through the particular voxels (i, j, z_p) and so there is no projection value available to the reconstruction algorithm, and it is necessary to use interpolation to obtain the missing projection value based on measurements $p^h\left(\eta, \theta, k\right)$, using for example the technique of bilinear interpolation:

$$\dot{p}^h\left(\beta_{ij}, \theta, \dot{z}_{ij}\right) = \sum_{n=1}^{4} c_{n,\theta,ij} p_{n,\theta,ij}^h \tag{3}$$

where the coefficients of interpolation $c_{n,\theta,ij}$ can be established in the following way:

$$c_{n,\theta,ij} = \left(1 - \frac{|\Delta\beta|}{\Delta_\eta}\right) \cdot \left(1 - \frac{|\Delta\dot{z}|}{\Delta_{\dot{z}_k}}\right), \tag{4}$$

where the quantities β_{ij} and $\dot{z}_{ij}$ represent the coordinates of the discrete point (i, j, z_p) expressed as parameters of the projection carried out at the angle θ. Parameters $\dot{z}_{ij}$ are calculated in the following way:

$$\dot{z}_{ij}\left(\theta\right) = \frac{\mathrm{R}_f \cdot \left(z_p - z_0\left(\theta\right)\right)}{\mathrm{R}_f - u_{ij}} \tag{5}$$

where R_f is the radius of the circle described by the focus of the tube, and

$$z_0\left(\theta\right) = \lambda \cdot \frac{\theta \Delta_\alpha^h}{2\pi} \tag{6}$$

and

$$u_{ij} = i\Delta_{xy} \cdot \sin\left(\theta\Delta_{\alpha}^{h}\right) - j\Delta_{xy} \cdot \cos\left(\theta\Delta_{\alpha}^{h}\right), \tag{7}$$

where: Δ_{xy} is the interval between individual points on the reconstructed image.

The value of β_{ij} is easily determined using the following formula:

$$\beta_{ij}(\theta) = \arcsin\left(\frac{s_{ij}}{\sqrt{\mathrm{R}_f^2 + \dot{z}_{ij}} - u_{ij}}\right), \tag{8}$$

where

$$s_{ij} = i\Delta_{xy} \cdot \cos\left(\theta\Delta_{\alpha}^{h}\right) + j\Delta_{xy} \cdot \sin\left(\theta\Delta_{\alpha}^{h}\right), \tag{9}$$

and u_{ij} has already been determined in equation (7).

Now, it is clear how are chosen these four projections $p_{n,\theta,ij}^{h}$ used in bilinear interpolation (3). Namely, they are determined as the nearest neighbours of the projection $\dot{p}^{h}(\beta_{ij}, \theta, \dot{z}_{ij})$, taking into account the parameters $\beta_{ij}(\theta)$ and $\dot{z}_{ij}(\theta)$ (equations (8) and (5), respectively).

2.2 Iterative Reconstruction Procedure

After back-projection operation, it is possible to carry out the iterative reconstruction procedure. Thanks to the reformulation of the reconstruction peoblem into the optimization problem we can perform it according to the maximum likelihood (ML) methodology of estimation of expected value of image for certain pixels, holding the analytical scheme of image processing in given reconstruction algorithm. After deep statistical analysis, we propose the following form of objective to be optimized during this iterative reconstruction procedure:

$$\mu_{\min}^{*} = \arg\min_{\mu^{*}}\left(\frac{1}{2}\sum_{i=1}^{\mathrm{I}}\sum_{j=1}^{\mathrm{J}}\frac{1}{\sigma_{\Sigma}^{2}(i,j)}f\left(e(i,j)\right)\right), \tag{10}$$

where:

$$e(i,j) = \sum_{\bar{i}}\sum_{\bar{j}}\mu^{*}(\bar{i},\bar{j}) \cdot h_{\Delta i,\Delta j} - \tilde{\mu}(i,j), \tag{11}$$

and (what can be shown)

$$h_{\Delta i,\Delta j} = h_{i,j} = \Delta_{\alpha} \cdot \sum_{\psi=0}^{\Psi-1} i\bar{n}t\left(i\cos\psi\Delta_{\alpha} + j\sin\psi\Delta_{\alpha}\right), \tag{12}$$

where $i\bar{n}t$ is an interpolation function used in the back-projection operation; $\Delta i = |i - \bar{i}|$, $\Delta j = |j - \bar{j}|$, $\Delta_{\alpha} = \frac{2\Pi}{\Psi}$, and

$$\sigma_{\Sigma}^{2}(i,j) \cong \frac{1}{n_0}\sum_{\psi=0}^{\Psi-1}\sum_{n} c_{n,\theta,ij}^{2}\mathrm{e}^{p_{n,\theta,ij}^{h}}, \tag{13}$$

where n_0 is the initial count of x-ray photons. Thus, it will be possible to find the optimal image μ^* in the sense of estimation of the expected values of the reconstructed image μ. Note, that in Eq. (11) $\tilde{\mu}$ means an image obtained after back-projection operation, $h_{\Delta i,\Delta j}$ are constant coefficients of the convolution, $f(\bullet)$ is a penalty function. We propose the following form of the function $f(\bullet)$:

$$f(e(i,j)) = \lambda \cdot \ln\cosh\left(\frac{e(i,j)}{\lambda}\right) \tag{14}$$

where: λ is a slope coefficient. It is worth to note that the introduction of this function instead of the quadratic form for each pixel is not inconsistent with the main idea of the statistical reconstruction approach – that of matching an appropriate divergence function with the probabilistic distribution present in the measured signals. The form of function (14) overlaps with the quadratic form in the wider neighbourhood of their minimums.

According to the relation (10) it is possible to formulate many solutions to the image reconstruction from projections problem, consistent with ML methodology. Although, there are several methods of searching for the optimal solution, we propose the simplest gradient descent method. Therefore, the pixels in reconstructed image will be adjusted, as follows:

$$\mu^{*(t+1)}(i,j) = \mu^{*(t)}(i,j) - c \cdot \sum_{\bar{i}=1}^{\mathrm{I}} \sum_{\bar{j}=1}^{\mathrm{J}} \frac{1}{\sigma^2_{\Sigma}(\bar{i},\bar{j})} f'\left(e^{(t)}(\bar{i},\bar{j})\right) h_{\Delta i,\Delta j}, \tag{15}$$

where f' is a deriviation of the function (14).

3 Experimental Results

In our experiments, we have adapted the well-known FORBILD phantom of the head (see [13]) for 3D spiral cone-beam projections. Paremeters: λ was set to be 2.5, and R_f to be 1200. During the simulations, we fixed $\mathrm{H} = 1025$ measurement points (detectors) on the screen at virtual parallel projections, and $\mathrm{K} = 121$. The number of projections was chosen as $\Theta = 3220$ rotation angles, and the size of the processed image was fixed at $\mathrm{I} \times \mathrm{J} = 1024 \times 1024$ pixels. The coefficients $h_{\Delta i,\Delta j}$ were precomputed before we started the reconstruction process and these coefficients were fixed for the subsequent processing. We started the actual reconstruction procedure and perform the back-projection operation to get a blurred image of the x-ray attenuation distribution in a given cross-section of the investigated object. The image obtained in this way was then subjected to a process of reconstruction (optimization) using an iterative statistically- tailored procedure. It is worth noting that we can choose the starting point of this procedure to be a result of using any standard reconstruction method, for example a reconstruction Feldcamp-type FBP algorithm. Because the set of possible

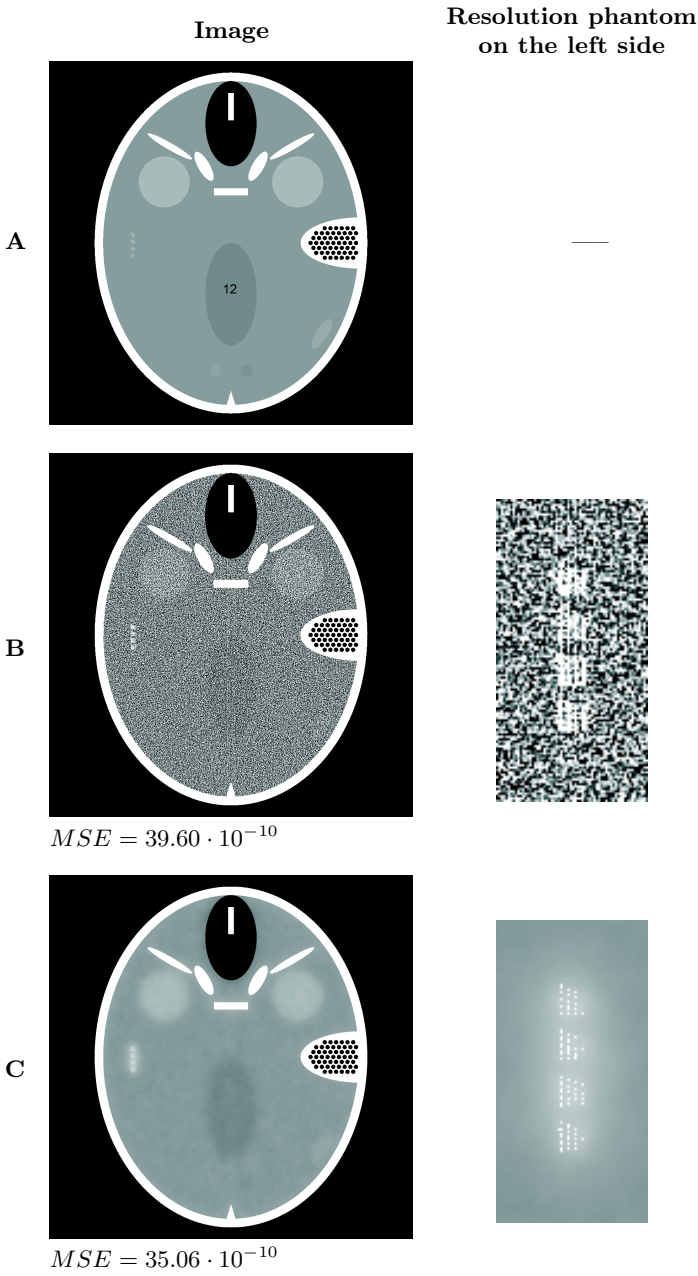

Fig. 2. View of the images (window centre $C = 1.05 \cdot 10^{-3}$, window width $W = 0.1 \cdot 10^{-3}$) when the signals registered by the detectors are stochastic: original image (A); reconstructed image using the standard FBP method with Shepp-Logan kernel (B); reconstructed image using the method described in this paper at $t = 1000$ (C)

states of matrix μ^* is convex and the function from relation (10) is convex, the optimization process starting from any point of the convex set μ^* yields a unique solution. The convolutions in iterative procedure were calculated in frequency domain to accelerate reconstruction procedure. The whole iterative process was implemented for GPUs with the NVIDIA CUDA framework and executed on the GeForce GTX 680 graphics card. In this case, the iterative reconstruction process (3000 iterations) has taken 53s.

Evaluating a reconstruction procedure based only on a view of the reconstructed image is very subjective. That is why the quality of the reconstructed image has been evaluated by an error measure defined as follows

$$MSE = \frac{1}{I^2} \sum_{i=1}^{\mathrm{I}} \sum_{j=1}^{\mathrm{J}} \left(\hat{\mu}^{*(t)}(i,j) - \mu(i,j) \right)^2, \tag{16}$$

where: $\hat{\mu}^{*(t)}(i,j)$ is the reconstructed image after t iterations, $\mu(i,j)$ is the original image of the FORBILD phantom.

Views of the reconstructed images of the mathematical phantom in the cross-section after 3000 iterations are presented (Fig. 2C) for stochastic signals. For comparison, the original phantom image (Fig. 2A) and the image reconstructed by a standard Feldkamp-type FBP reconstruction method (Fig. 2B) are also presented.

4 Conclusion

In this paper, it is presented a fully feasible 3D statistical reconstruction algorithm for spiral tomography with cone shaped beams. Incorporation of analytical scheme of signal processing allows to avoid very serious disadvantages involved with the algebraic reconstruction techniques, which are particularly evident if they are applied to reconstruction algorithms for spiral tomographic scanners. Generally, presented here reconstruction algorithm is very easy and compact. It is wort to underline that in shown here algorithm, there is not used any additional geometrical correction of the projection lines in this approach. Coefficients $h_{\Delta i,\Delta j}$ are precalculated according to the Eq. (11), before we start the actual reconstruction procedure and they are the same for all pixels in the reconstructed image. Some simulations have been carried out, which prove that our reconstruction method is extremely fast (the whole iterative reconstruction process with 3000 iterations takes 53s). It is worth noting that we have introduced of a new form of penalty function which prevents the occurrence of possible instabilities in the reconstruction process. The image of the cross-section of the mathematical phantom was reconstructed with high accuracy compared with the standard method (in our experiments the standard Feldkamp-type algorithm), as measured both in the subjective way and using the objective MSE quality measure.

References

1. Bezug, T.M.: Computed Tomography - from Photon Statistics to Modern Cone-Beam CT. Springer, Heidelberg (2008)
2. Silva, A.C., Lawder, H.J., Hara, A., Kujak, J., Pavlicek, W.: Innovations in CT dose reduction strategy: application of the adaptive statistical iterative reconstruction algorithm. Am. J. Roentgenology 194, 191–199 (2010)
3. Sauer, K., Bouman, C.: A local update strategy for iterative reconstruction from projections. IEEE Tran. Signal Processing 41, 534–548 (1993)
4. Bouman, C., Sauer, K.: A unified approach to statistical tomography using coordinate descent optimization. IEEE Tran. Image Processing 5, 480–492 (1996)
5. Thibault, J.-B., Sauer, K.D., Bouman, C.A., Hsieh, J.: A three-dimensional statistical approach to improved image quality for multislice helical CT. Med. Phys. 34, 4526–4544 (2007)
6. DeMan, B., Basu, S.: Distance-driven projection and backprojection in three dimensions. Phys. Med. Biol. 49, 2463–2475 (2004)
7. Zhou, Y., Thibault, J.-B., Bouman, C.A., Hsieh, J., Sauer, K.D.: Fast model-based x-ray CT reconstruction using spatially non-homogeneous ICD optimization. IEEE Tran. Im. Proc. 20, 161–175 (2011)
8. Cierniak, R.: A novel approach to image reconstruction from projections using Hopfield-type neural network. In: Rutkowski, L., Tadeusiewicz, R., Zadeh, L.A., Żurada, J.M. (eds.) ICAISC 2006. LNCS (LNAI), vol. 4029, pp. 890–898. Springer, Heidelberg (2006)
9. Cierniak, R.: A new approach to tomographic image reconstruction using a Hopfield-type neural network. Int. J. Artificial Intelligence in Med. 43, 113–125 (2008)
10. Cierniak, R.: A new approach to image reconstruction from projections problem using a recurrent neural network. Int. J. Applied Math. Comp. Sc. 183, 147–157 (2008)
11. Cierniak, R.: New neural network algorithm for image reconstruction from fan-beam projections. Neurocomputing 72, 3238–3244 (2009)
12. Cierniak, R.: A three-dimensional neural network based approach to the image reconstruction from projections problem. In: Rutkowski, L., Scherer, R., Tadeusiewicz, R., Zadeh, L.A., Zurada, J.M. (eds.) ICAISC 2010, Part I. LNCS (LNAI), vol. 6113, pp. 505–514. Springer, Heidelberg (2010)
13. Institute of Medical Physics, Friedrich-Alexander-University Erlangen-Nürnberg, `http://www.imp.uni-erlangen.de/forbild/deutsch/results/head/head.html`

Comparison Study of Two Programs Dedicated to X-ray Microtomography Data Analysis

Joanna Śróbka[1], Marcin Binkowski[1], Martyna Czaja[1], Iwona Szarejko[2], and Zygmunt Wróbel[1]

[1] University of Silesia, Faculty of Computer and Materials Sciences, Department of Biomedical Computer Systems, X-ray Microtomography Lab, 75 Pulku Piechoty Str, building H, seg. C, room P8, 41-500 Chorzów, Poland
{jsrobka,marcin.binkowski,martyna.czaja, iwona.szarejko,zygmunt.wrobel}@us.edu.pl

[2] University of Silesia, Faculty of Biology and Environmental Protection, Department of Genetic, Jagiellońska Str. 28, 40-035 Katowice, Poland

Abstract. X-ray Microtomography (XMT) is frequently used to visualize plant's internal 3D structure among many different imaging methods. The obtained data are large volume and difficult to process. Many software packages were developed for XMT data analysis. Dedicated programs are also frequently developed. XMT data may vary in many aspects and consequence could be different level of analysis difficulties. It is important to select properly the program for obtained data. One of aspects is expected analysis effect. Proper software will provides measurable results. This study focus on the comparison of two dedicated to XMT data analysis software. The comparison is based on 3D reconstruction of barley root system growing in sand medium and scanned using XMT.

Keywords: XMT, roots, image analysis.

1 Introduction

Image data analysis plays very important role in almost all science disciplines. With the development of imaging techniques, this kind research possibilities are growing [1]. In addition to techniques such as microscopy, which provide mainly 2D image acquisition, there are many techniques dedicated to three-dimensional (3D) reconstruction of analysed object's structure. Microscopy gives an opportunity to carry out an investigations concerning the surface of microscopic slide (e.g. Light Microscopy) or object (e.g. Scanning Microscopy) [1, 2]. Different approach should be taken into account, if it is necessary to look inside analysed object. Among those approaches there is a modification of the traditional light microscopy, Optical Projection Tomography (OPT), using visible photons [3]. Other methods, such as Positron Emission Tomography (PET) and Magnetic Resonance Imaging (MRI) are also used to obtain structural data in 3D [4]. XMT (X-ray Microtomography), a non-invasive technique, does not cause a destruction of the sample. Initially, this technique was used for medical imaging

E. Pietka, J. Kawa, and W. Wieclawek (eds.), *Information Technologies in Biomedicine, Volume 3*, Advances in Intelligent Systems and Computing 283,
DOI: 10.1007/978-3-319-06593-9_18,

purposes (first use 1971) [5]. Since then, it is still being applied to a broader range of science disciplines like biology, material and earth science [6, 7]. XMT in biological science is used for plant [5, 8, 9], animal [10, 11] and cell studies [12].

In addition to imaging method and sample preparing approach, it is necessary to dispose an appropriate computer software in order to obtain satisfactory results. It is particularly important for high volume data which requires complex computing operations. Through the years many different applications, dedicated XMT data analysis purpose, has been developed. Applications like Drishti [13] or ImageJ [14] are freeware and, by fulfilling hardware requirements, are available for each user. Advanced applications, with various, targeted modules are also available. Among many of them Mimics [15], VG StudioMAX [16] or Avizo [17] are primarily used to XMT data analysis. Dedicated programs are also available for particular purposes. One of them, RooTrack program, is designed to root tracing on XMT images [18]. The main aim of the described research was to check the sandy growth medium influence on the ability to identify root using XMT images. The studies were conducted on barley 7-days-old seedling growing in the sand.

The main issue was to compare two software packages dedicated to XMT data processing and its performance during segmentation of root system from the growth medium. Some technical aspects of the segmentation process were also addressed. In each program the best possible procedures of data segmentation and analysis have been performed.

2 Material and Methods

2.1 Grains

Seed material were barley (*Hordeum vulgare*) grains, "Sebastian" variety. The grains came from field cultivation (Experimental field of Department of Biology and Environmental Protection in Boguchwałowice, University of Silesia in Katowice, Poland).

2.2 Growth Conditions and Growth Medium

Plant growth was conducted in a culture room, under controlled conditions. The temperature during cultivation was $18 - 20^oC$. Photoperiod was 16/8 and light intensity at level 20,000 lux. Relative humidity was maintained at 70-80%. During the growth, plants were watered by water and nutrient $\frac{1}{2}$ MS. Nutrient solution was prepared according to the proportions developed by Murashige and Skoog [19]. Barley was cultured in standard plastic (polypropylene), round pot. Growth medium was sand.

2.3 Scanning

In the 7. day of growth plant was scanned using XMT scanner v|tome|x s (GE Sensing & Inspection Technologies, phoenix|x-ray, Wunstorf, Germany).

The scanner is equipped with two X-ray sources: microfocus 240V/320W and nanofocus 180V/15W. Temperature-stabilized detector DXF 16" provides superior contrast. A rotary table is installed between the X-ray source and the detector, which enables positioning the tested object along the X-ray beam and adjusts magnification which reflects the image resolution. Scans were carried out using microfocus tube and X-ray power lower than voxel size of the data matrix. Scanning parameters and growth environment are presented below (Tab. 1).

Table 1. Scanning and growth environment parameters

Growth container	Pot
Growth medium	Sand
Voltage (kV)	200
Current (μA)	130
Power (W)	26
Filter	Cu 0.1
Number of projections	2000
Resolution (μm)	47,661
Timming (ms)	200
Average	2
Skip	1
Scan time (min)	23

2.4 Image Analysis Using Mimics Program

In order to get root XMT image analysis, the data set was loaded to the Mimics 15.0 (Materialise, Belgium) using a standard template. Size of the dataset, resolution and image orientation were defined by the user. *Thresholding*, *Region Growing* and*Dynamic Region Growing* tools were used first. Manual *Multiple Slice Edit* or, rather, *Slice Edit* tool were used if automatic methods turned out to be unsuccessful in root segmenting from the medium. Moreover, horizontal axis was chosen for manual tracing. Roots tracing started from shoot selection on the first layer and processed down, at intervals of 2 or 3 layers. Each root was traced individually until the end. When the entire root system was successfully segmented, 3D model have been calculated. This model was then a subjected to smoothing operation.

2.5 Image Analysis Using Drishti Program

Drishti software [20] is developed to visualize tomography and electron-microscopy image data i.e. It is online available, on freeware license [13]. Standard loading procedure was followed to visualize object in Drishti 2.3.3. Visualization was processed using various tools, e.g. clip plane (image pruning in different planes), histogram and color gradient manipulation and morphological operations (erosion, dilation, skeletonization). Image visualization process depends on

many factors, such as density in particular image areas, thickness of the layers, scan resolution and quality. In this case histogram manipulations have been chosen to make the root system visible. Then, the remaining noises were removed manually using various tools. Firstly MOP (morphological operation) update off and then MOP carve were used. MOP update off is an operation providing turning of updates to mask buffer. It allows changes making by MOP carve to be saved after histogram manipulation. MOP carve tool is an eraser. A user selects diameter and the depth of the removal area (the number of layer on which tool erases noises). Those operations allowed to remove most of noises from the image and to make segmented area more visible.

3 Results

Work in both programs was conducted separately. Obtained results concerned the same plant. Performed models are independent from each other. It means that each of them can be obtained in a different way. Results also depends on skills of the user.

3.1 Outcome from Mimics Program

The first outcome in Mimics program was complete mask of root system architecture. The entire root system was marked by manual tracing. Mask was additionally checked by tracing each root and supplementation eventual gaps in their continuity (Fig. 1, Fig. 2). Next, 3D model was created to visualize a whole mask (Fig. 3). This model was smoothed twice, usually with smooth factor 1,0. Compensate shrinkage option was also selected. This option prevents from substantial loss of 3D model area during smoothing operation. Final result gives a general overview on the architecture of analysed plant's root system.

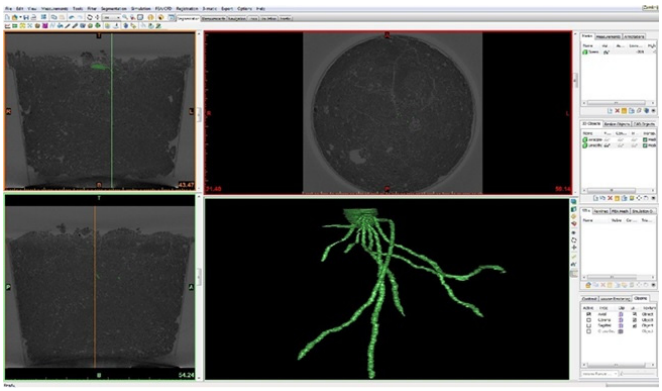

Fig. 1. Dialog window of Mimics program with analysed plant

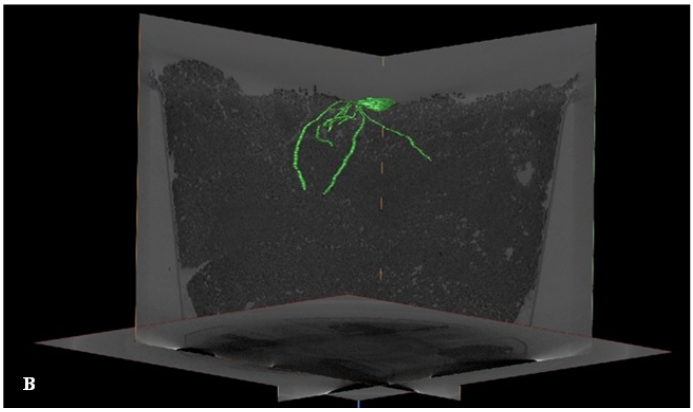

Fig. 2. 3D model of segmented barley root system; it is situated in arrangement created by the selected points on the displayed planes

Fig. 3. Segmented and smoothed barley's 7-days-old root system generated from areas marked on consecutive layers

3.2 Outcome from Drishti Program

Results obtained only by histogram manipulation indicates that it is possible to visualize root growing in sand medium using this method (Fig. 4). Roots, surrounded by partially transparent medium, are visible on this visualization.

Also part of grain and shoot are recognisable. The effect presented on Figure 5 was possible to achieve with the use of Morphological Operations. During segmenting process (histogram manipulations) a top part of root system has been lost and it is not visible on final visualisation.

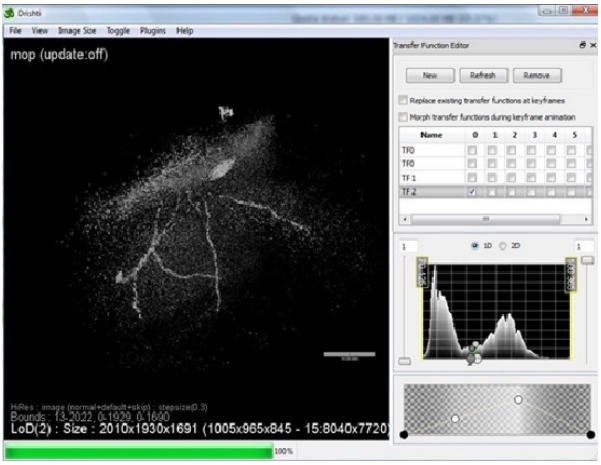

Fig. 4. Drishti program dialog window with analysed plant visualization.Visualization obtained after image segmentation with histogram manipulation use, before manual erasing

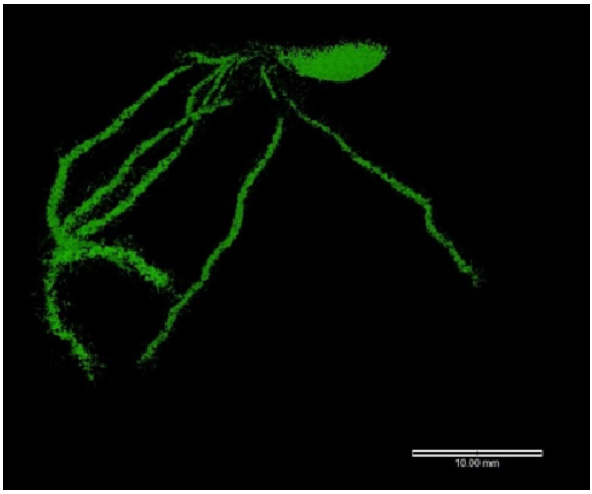

Fig. 5. Segmented visualisation of 7-days-old barley's seedling; most of noises have been removed

4 Discussion

Most common tasks in the field of plant image analysis are image segmentation, motion analysis and tracing. It is also reflected in the literature [21]. Various programs are used for those purposes. The study has focused on the research related to two different software applications. These applications were compared in terms of segmentation ability of barley's root system growing in the sand medium. Both are dedicated to image data analysis. First difference between them is a licence. While Drishti is freeware and open-source, Mimics is software developed by Materialise [15], especially for medical image processing. Mimics relies on differences in grey level value between voxels. A histogram of values corresponding to the differences in density of analysed object is generated. The program could be also used to segment data derived from CT, MRI, XMT, CBCT, Ultrasound and Confocal Microscopy. Depending on the available modules, the program creates a variety of possibilities to work with the data. The most basic possibilities are segmenting data and creating 3D models from segmented masks. Also measuring angles, distances or volumes are possible. More advanced modules, like cardiovascular module, allow i.e. to measure vessels or heart parameters.

Obtaining a visualisation in the Mimics program was time-consuming and labour-intensive. Due to the fact that none of available automatic segmenting tools was suitable, all segmenting processes have been made manually. First, grain position on image has been found. It was a starting point for root tracing on next slices. All roots have their beginning from one point on a grain. This fact was one of the most helpful principals during root tracing. The recognised root was traced along, until the last visible position. The position, shape and dimension of root was chosen by the user. There is an indication that this choice may be slightly different comparing to real root parameters. For this reason, the obtained dimensions cannot be used as fully reliable results for counting root parameters, such as volume or area. There is still a lot of work to be done in preparing well-functioning methods for those kind of analysis. A user needed 2 whole workdays (about 16 hours) to segment and prepare complete 3D model of a whole root system architecture.

Drishti, alike as Mimics, is based on differences in grey level value. This program vary from Mimics in using those differences in segmentation process. Drishti is developed by Ajay Limaye [13]. After downloading it from the website software is instantly ready to use. It is a graphic hardware-based direct volume rendering application. A possibility to real-time exploration and presentation of volumetric data is applicable i.e. in biology, medicine, geoscience and palaeontology. Unlike the Mimics program, Drishti allows user to create expanded animations and also render, cut, colour and export processed data. This software enables viewing large data sets by allowing visualisation of smaller sub-volumes [22].

Visualization using Drishti program took less time than in the Mimics. It depends mainly on the user's skills in using the program. To reduce the influence of noises and make work easier, clip plane tool was used. This tool allows to cut down the visible analysis area in any plane. In this case it appeared to be helpful

because root system occupied a small part of the whole analysed sample. MOP carve was used to remove the remaining noises around the root ball. The upper parts of roots were invisible in established parameters. The probable reason of this situation was a substantial amount of noises in this region. A user needs about half normal work day (4h) to achieve the effect presented on Figure 4.

There are several differences between programs operations. One of the most essential is different histogram functionality (Fig. 6). In Mimics no manipulations of values presented on histogram are possible. Mask of targeted image part is generated. This mask is originally based on values resulting from the reconstructed data. It is a fraction of the analysed object, selected from its grey level value histogram (Fig. 6(a)). In Drishti Import module histogram is adjusted to desirable part of images. There is a possibility to enhance values representing targeted parts of image. Simultaneously, noises and background can be silenced. This enables easier analysis because unnecessary parts are removed (Fig.6(b)).

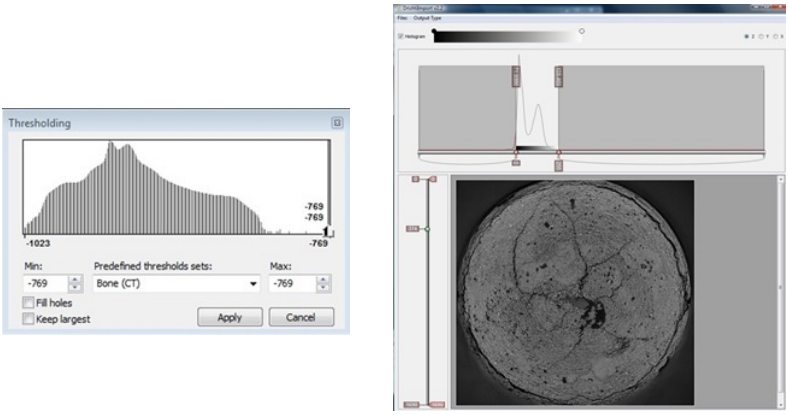

(a) (b)

Fig. 6. Difference in histogram based operations : (a) in Mimics (new mask generating), (b) in Drishti Import (import procedure before loading do Drishti Renderer)

Drishti software is widely used for XMT data analysis. For plant study purpose Mayo et al. [8] used this software to visualize wood of several trees species and Arabidopsis thaliana stem in micron scale. A satisfactory quality visualisation has been obtained using this software. Another example is using Drishti to visualize ultrasonic irrigation (PUI) of calcium hydroxide ($Ca[OH]_2$) removal and to measure the volume and the percentage of $Ca(OH)_2$ remaining in the root canal system. The material in this study were root canals of 46 extracted human mandibular molar teeth [23]. Drishti software has been used with success also in neurobiology. Research was concerned with the internal structure of bee's brains staining by osmium and visualizing using XMT [1]. Drishti was used by Jones et al. [24] in visualization results of the study about bone ingrowth

into two different scaffolds with cellular and strut-like architectures. Presented publication indicates that Drishti is plastic and universal software.

Mimics is mainly used for medical data analysis purpose. However, different uses of this software are known. In soil research Mimics 6.3 was used by Mooney et al. in 2002 [25]. The study focused on visualization and quantification of soil macroporosity and water flow patterns in various soil mediums. CT data were collected using Picker PQ6000 whole-body, medical x-ray CT-scanner. For medical study purpose, Mimics was used to visualise detailed Computational Fluid Dynamics (CFD) simulations during expiration [26]. The aim of the study was investigations the fluid flow in the airway regions. Material for this study has been obtained from anatomically accurate human upper airway model. The model was constructed from multiple MRI imaging axial scans. Also Chen et al. [27] used Mimics software in his work about bone regeneration on nano-fibrous computer-designed scaffolds. Program was employed to visualise ear reconstruction from histological sections and human mandible reconstruction from CT scans. Received results also indicate the usefulness of a presented software.

XMT is one of a few methods which allows the analysis of the object's internal structure. Among other alternative methods OPT should be mentioned. OPT uses visible photon beam instead of an X-ray. It can be used to visualize small objects, 1-10 mm only, with special resolution 5 μm [3]. The example of OPT used is a visualisation of morphology, internal structure and gene expression in Arabidopsis thaliana [28]. Other non-invasive techniques, such as MRI or PET are also widely used in plant science [5]. Measuring medium, used in MRI imaging, provides tomographic reconstructions of cross-sectional images, but at significantly lower resolution [29]. PET scanning uses short life radioactive tracers (like carbon isotopes). Its distribution is detecting and visualizing [30]. Both presented techniques are more useful in studies about physiological processes such as water transport or content (MRI) and C assimilation in plant tissue (PET) [5].

Analysis methodology presents differently in both programs. In Mimics user's interactions relies on choosing a root area on each slice. User manipulations in analysed image quality was limited to contrast manipulations. Difference between minimum and maximum value is still the same, only the position of whole image range of gray level values changes along the histogram. In Mimics, the whole segmentation process is based on original images. In Drishti, source images stock is basis for manipulations. In Drishti Renderer module histogram manipulating is possible. 1D (one dimension) histogram allows thresholding to make visible particular elements of an image. In 2D (two dimensions) histogram more advanced operations are possible. Volume visualization with 2D transfer functions, allows the appearance to be adjusted according to voxel scalar value or gradient [31]. The segmented data processing is the most essential difference in both programs operating. While in Mimics user works on source image, without changing it, whole analysis in Drishti is focused on manipulating in image features. Therefore, results vary between themselves in origin. 3D model generated using Mimics program, is based on areas which are marked by user on a

source image. The model is based originally on mask, which is more accuratly segmented than in Drishti. Drihsti prepares 3D model which is derived from extract parts of source image.

A comparison analysis of barley root system in those two software indicates that both are useful in such kind of image processing. The main advantage of Drishti is saving the time with the possibility to visualize most part of the root system at the same time. It is still valuable for demonstrative visualization of root ball growth direction and architecture. The most disturbing disadvantage is a significant amount of noises which still are present after histogram manipulation. Moreover, also failure to obtain the continuity at the roots basis is an issue. Furthermore, the lack of possibility to look back on original data is also a problem. It stems from nature of the program and is a disadvantage only in certain cases, such as described example. Root surface, obtained even after erasing operation, is not as smooth as the one obtained the Mimics program.

Figure 7 presents summary of two 3D models obtained in the presented study. Main differences between them are the quality of generated model and time necessary to obtain this effect. Mimics software is better to use in order to obtain more comprehensive results. Although more time is required to prepare 3D model of root system architecture in Mimics, the obtained quality is better. Still it can not be used to calculate properly all root parameters, however, there is a possibility to measure some of them (e.g. root diameter) during manual segmentation. In case of a limited amount of time, to achieve measurable effect, Drishti software can be used. The presented effect is of a lower quality, but on the other hand, still gives an overall view of the plant root system architecture. Described research was focused on qualitative analysis of the performance of two software packages. The effects of the presented activities, like segmenting three dimensional shape, can be a subject for further quantitative analysis.

Fig. 7. Comperison of visualisation obtained by (a) Drishti software, (b) Mimics software

Acknowledgement. Joanna Śróbka is beneficiary of Silesian Cooperation: Innovations For Efficient Development (SWIDER) project realized within Human Capital Operational Program, Priority VIII: Regional human resources for the economy, 8.2 Transfer of knowledge, Sub-measure 8.2.1 Support for cooperation of scientific environment and enterprises. Project partially funded from European Union Project based on European Social Funds.

Special thanks to Iwona Szarejko for providing the laboratory for plant breeding.

References

1. Ribi, W., Senden, T.J., Sakellariou, A., Limay, A., Zhang, S.: Imaging honey bee brain anatomy with micro-X-ray-computed tomography. J.Neurosci. Met. 171, 93–97 (2008)
2. Optical Microscopy Primer, `http://micro.magnet.fsu.edu/primer/index.html`
3. Sharpe, J.: Opitical projection tomography. An. Rev. Biomed. Eng. 6, 2009–2228 (2004)
4. Pajor, R., Fleming, A., Osborne, P.C., Rolfe, S.A., Sturrock, C.J., Mooney, S.J.: Seeing space: visualization and quantification of plant leaf structure using X-ray micro-computed tomography. J. Exp. Bot. 64, 385–390 (2013)
5. Dhont, S., Vanhaeren, H., Van Loo, D., Cnudde, V., Inze, D.: Plant structure visualization by high- resolution X-ray computed tomography. Tren Pl. Sci. 15, 419–422 (2010)
6. Cnudde, V., Masschaele, B., Dierick, M., Vlassenbroeck, J., Van Hoorebeke, L., Jacobs, P.: Recent progress in X-ray CT as a geosciences tool. App. Geochem. 21, 826–832 (2006)
7. Dal Ferro, N., Delmas, P., Duwig, C., Simonetti, G., Morari, F.: Coupling X-ray microtomography and mercury intrusion porosimetry to quantify aggregate structures of a cambisol under different fertilisation treatments. Soil Till. Res. 119, 13–21 (2012)
8. Mayo, S.C., Chen, F., Evans, R.: Micron-scale 3D imaging of wood and plant microstructure using high- resolution X-ray phase-contrast microtomography. J. Str. Bio. 171, 182–188 (2012)
9. Tracy, S.R., Black, C.R., Roberts, J.A., Sturrock, C., Mairhofer, S., Craigon, J., Mooney, S.J.: Quantifying the impact of soil compaction on root system architecture in tomato (Solanum lycopersicum) by X-ray micro-computed tomography. Ann. Bot. 110, 511–519 (2012)
10. Tanaka, G., Hou, X., Ma, X., Edgecombe, G.D., Strausfeld, N.J.: Chelicerate neural ground pattern in a Cambrian great appendage arthropod. Nat. 502, 364–367 (2013)
11. Dobrivojević, M., Bohaček, I., Erjavec, I., Gorup, D., Gajović, S.: Computed microtomography visualization and quantification of mouse ischemic brain lesion by nonionic radio contrast agents. Croat. Med. J. 54, 3–11 (2013)
12. Moosmann, J., Ershov, A., Weinhardt, V., Baumbach, T., Prasad, M.S., Labonne, C., Xiao, X., Kashef, J., Hofmann, R.: Time-lapse X-ray phase-contrast microtomography for in vivo imaging and analysis of morphogenesis. Nat. Protoc. 9, 294–304 (2014)
13. Limaye, A.: Drishti: a volume exploration and presentation tool. In: Proc. SPIE Developments in X-ray Tomography VIII, p. 85060X (2006)

14. ImageJ, http://rsbweb.nih.gov/ij/
15. Materialise, http://biomedical.materialise.com/mimics
16. Volume Graphics, http://www.volumegraphics.com/en/products/vgstudio-max.html
17. FEI Visualization Sciences Group, http://www.vsg3d.com/avizo/overview
18. Mairhofer, S., Zappala, S., Tracy, S.R., Sturrock, C., Bennett, M., Mooney, S.J., Pridmore, T.: RooTrak: automated recovery of three-dimensional plant root architecture in soil from x-ray microcomputed tomography images using visual tracking. Plant Physiol. 158, 561–569 (2012)
19. Murashige, T., Skoog, F.: A revised medium for rapid growth and bio-assays with tobacco tissue cultures. Physiol. Plant 15, 473–497 (1962)
20. Drihsti, http://sf.anu.edu.au/Vizlab/drishti/
21. Pridmore, T.P., French, A.P., Michael, P.P.: What lies beneath: underlying assumptions in bioimage analysis. Tr. Plant Sci. 17, 688–692 (2012)
22. iVEC, http://www.ivec.org/ai1ec_event/3866-2/?instance_id=
23. Wiseman, A., Cox, T.C., Paranjpe, A., Flake, M.N., Cohenca, N., Johnson, J.D.: Efficacy of Sonic and Ultrasonic Activation for Removal of Calcium Hydroxide from Mesial Canals of Mandibular Molars: A Microtomographic Study. J. Endo. 37, 235–238 (2011)
24. Jones, A.C., Arns, C.H., Sheppard, A.P., Hutmacher, D.W., Milthorpe, B.K., Knackstedt, M.A.: Assessment of bone ingrowth into porous biomaterials using MICRO-CT. Biomat. 28, 2491–2504 (2007)
25. Mooney, S.J.: Three-dimensional visualization and quantification of soil macroporosity and water flow patterns using computed tomography. Soil Use Manag. 18, 142–151 (2002)
26. Mylavarapu, G., Murugappan, S., Mihaescu, M., Kalra, M., Khosla, S., Gutmark, E.: Validation of computational fluid dynamics methodology used for human upper airway flow simulations. J. Biomech. 42, 1553–1559 (2009)
27. Chen, V.J., Smith, L.A., Ma, P.X.: Bone regeneration on computer-designed nanofibrous scaffolds. Biomat. 27, 3973–3979 (2006)
28. Lee, K., Avando, J., Morrison, H., Blot, L., Stark, M., Sharpe, J., Bangham, A., Coen, E.: Visualizing plant development and gene expression in three dimensions using optical projection tomopraphy. Plant Cell 18, 2145–2156 (2006)
29. Windt, C.W., Gerkema, E., Van As, H.: Most water in the tomato truss is imported through the xylem, not the phloem: a nuclear magnetic resonance flow imaging study. Plant Physiol. 151, 830–842 (2009)
30. Jahnke, S., Menzel, M.I., van Dusschoten, D., Roeb, G.W., Bühler, J., Minwuyelet, S., Blumler, P., Temperton, V.M., Hombach, T., Streun, M., Beer, S., Khodaverdi, M., Ziemons, K., Coenen, H.H., Schurr, U.: Plant J. 59, 634–644 (2009)
31. Manchester X-ray Imaging Facility, http://www.mxif.manchester.ac.uk/index.php-/software/drishti

Object Detail Correspondence Problem in Stereovision

Pawel Popielski, Zygmunt Wróbel, and Robert Koprowski

Institute of Computer Science, University of Silesia,
41-200 Sosnowiec, ul. Bedzinska 39
pawel.popielski@us.edu.pl

Abstract. The authors in their research deal with a broad spectrum of 3D reconstruction problems. In this paper, the authors explore the correspondence problem between some object details imaged with stereo vision head. Since the authors are working on a new matching algorithm based on graph theory, it was decided to test how problematic regions of images match each other. Problematic regions like edges, corners and other shapes with a shaded or motley background seem to create different images for left and right pictures and, in the case of further process, they may cause serious matching difficulties. Images of such problematic object details have been explored with several well-known edge detection methods, which have never been applied to stereovision before.

Keywords: stereo correspondence, stereovision, edge detection.

1 Introduction

Owing to full automation, 3D reconstruction from non-metric images in the visible band can be used in medicine, namely in the diagnosis of faulty posture, metabolic diseases, bone or plastic surgery [2, 10, 11]. Prerequisites for admission of this modern diagnostic method for use in medical practice are, among other things, immediacy of results, non-invasiveness, high accuracy of reconstructed geometry, low cost and compactness of the diagnostic installation [13, 1]. The authors are working on their own 3D reconstruction system that will automatically extract geometrical characteristics which will enable to determine, among others, the stage of scoliosis or the degree of overweight.

3D reconstruction methods previously used in medicine, based on laser scanning or projection of various geometrical elements [11], did not enable to obtain sufficient measurement accuracy, reconstruction completeness and automation.

Throughout the previous century, photogrammetry [8] dealt with 3D reconstruction but finally computer vision allowed to complete the process of full automation of 3D reconstruction from images [16, 3]. Among other things, owing to the development of 3D reconstruction algorithms, it was also possible to work with non-metric cameras (i.e. not having specific, pre-established parameters of interior orientation [5] and fully eliminated aberrations [4]).

E. Pietka, J. Kawa, and W. Wieclawek (eds.), *Information Technologies in Biomedicine, Volume 3*, Advances in Intelligent Systems and Computing 283,
DOI: 10.1007/978-3-319-06593-9_19,

At a certain level of abstraction, it can be assumed that the 3D reconstruction process consists of four main stages [8, 15]. First, the intrinsics and aberrations must be determined. Then the extrinsics must be calculated. In the next step, the matching process has to be completed followed by the calculation of the point's coordinates X,Y,Z.

The third stage is currently in the centre of attention of the paper's authors. Detection of points [14] itself brings many challenges as the object must be covered with a sufficiently dense network of points to provide high accuracy of shape reconstruction [9]. Till now, the authors have matched images mainly with the use of variational methods [7]. During the concept creation of the new matching method based on graph theory, the authors have found that some image regions may cause more problems during matching than others. These problematic regions like edges, corners and other shapes with a shaded or motley background seem to create different images for left and right pictures and, in the case of further process, they may cause serious matching difficulties. The authors were unable to find other studies on this topic so it was decided to describe this problem.

Images of such problematic object details have been explored with well-known edge detection methods, never before applied to stereovision, as an equivalent of further processes which may occur during matching stereo images.

Section 2 shortly presents well-known edge detectors, Section 3 describes the procedure, Section 4 focuses on the obtained results and Section 5 includes a summary.

2 Edge Detectors

The Sobel operator [12] applied by the authors uses two 3×3 kernels which are convolved with the original image to calculate approximations of the derivatives - one for the horizontal changes, and one for the vertical ones. When A is the source image and G_x and G_y are two images which at each point contain the horizontal and vertical derivative approximations, the computations are as follows:

$$G_x = \begin{bmatrix} +1 & 0 & -1 \\ +2 & 0 & -2 \\ +1 & 0 & -1 \end{bmatrix} \otimes A \qquad \text{and} \qquad G_x = \begin{bmatrix} +1 & +2 & -1 \\ 0 & 0 & 0 \\ +1 & -2 & -1 \end{bmatrix} \otimes A$$

where $\otimes$ here denotes a 2-dimensional convolution operation. A different kernel was developed by Judith M. S. Prewitt [12] where

$$G_x = \begin{bmatrix} -1 & 0 & +1 \\ -1 & 0 & +1 \\ -1 & 0 & +1 \end{bmatrix} \qquad \text{and} \qquad G_x = \begin{bmatrix} +1 & +1 & +1 \\ 0 & 0 & 0 \\ -1 & -1 & -1 \end{bmatrix}$$

The oldest Roberts operator [12] uses a 2×2 kernel

$$G_x = \begin{bmatrix} +1 & 0 \\ 0 & -1 \end{bmatrix} \qquad \text{and} \qquad G_x = \begin{bmatrix} 0 & +1 \\ -1 & 0 \end{bmatrix}$$

which also gives interesting results.

The Laplacian of Gaussian (log) method [12] finds edges by looking for zero crossings after filtering an image with a Laplacian of Gaussian filter or with any specified filter (zc).

The Canny operator [12] uses the calculus of variations to find the function which optimizes a given functional. For the purposes of this study, approximation by the first derivative of a Gaussian was applied.

$$B = \frac{1}{159}\begin{bmatrix} 2 & 4 & 5 & 4 & 2 \\ 4 & 9 & 12 & 9 & 4 \\ 5 & 12 & 15 & 12 & 5 \\ 4 & 9 & 12 & 9 & 4 \\ 2 & 4 & 5 & 4 & 2 \end{bmatrix} \otimes A$$

3 Test Procedure

In order to investigate the stereo correspondence problem, the authors used three images from Middlebury Stereo Vision Page i.e. aloe, wood1 and bowling2. Since these images are widely used for matching purposes in stereovision, the authors decided to test these samples as well. Although these samples seem to be quite perfect, the authors also tested their own three images used before in their research i.e. fern, person and arrangement.

All the images were filtered with edge operators and then problematic areas were identified. A unified dimension crop window sized 71×57 pixels was applied to all images. The window size was chosen experimentally so that distinct differences between stereo pairs could be clearly observed at the minimum possible resolution. The threshold was chosen arbitrarily mainly to keep the edges visible, but also to keep the edges distinguishable and distanced from a motley pattern.

Then, using Matlab Image Processing Toolbox, the centroids and length in pixels were calculated for the stereo pairs for the selected elements, which are in the centre of attention of the paper's authors. The edges for which the centroids and length were determined were marked with a white line in the original images. Next, the distances between the nearest centroids and the difference in length of the edges between stereo pairs were calculated. The first analysed sample "aloe" (Table 1) definitely indicates a difference between images created in the left and right pictures. The upper edge of the leaf is visible or even distinguishable in the left image. In the right image, the leaf edge is barely distinguishable or completely invisible probably due to the motley background.

The next analysed image "wood1" (Table 1) is characteristic due to uniformity of the foreground and background. The edge is distinguishable quite well in the original image. The corner in the right image is visible whereas in the left image it is really difficult to notice.

An edge adjoining another edge can be observed in the "bowling2" sample (Table 2), where one edge has much better visibility than the other one due to the colour composition. And again a visible or even distinguishable junction

Table 1. Result of the edge extraction for the sample "aloe" and "wood1"

	aloe		wood1	
	left image	right image	left image	right image
original image	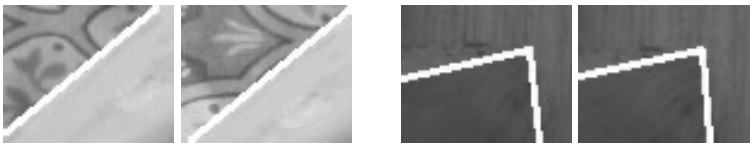			
sobel	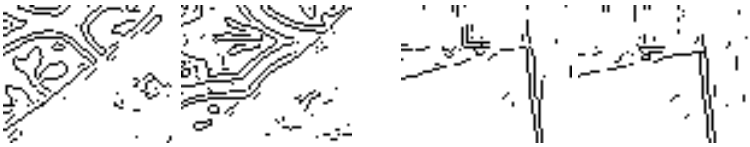			
prewitt	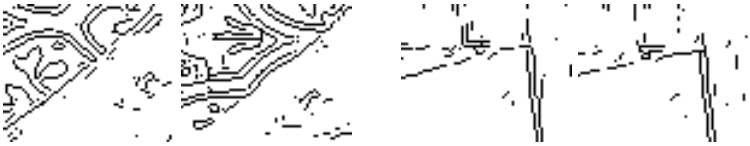			
roberts	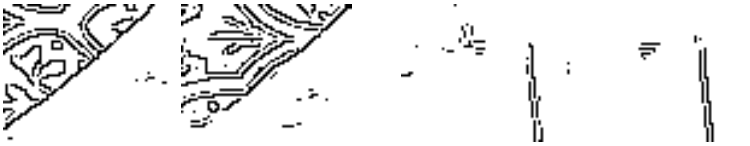			
log				
zerocross				
canny	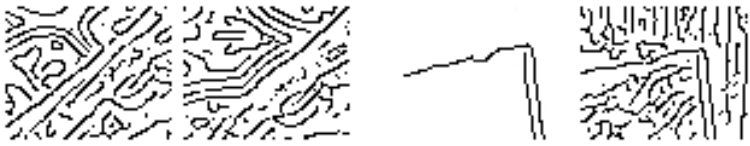			

Table 2. Result of the edge extraction for the sample "bowling2" and "fern"

	bowling2		fern	
	left image	right image	left image	right image
original image	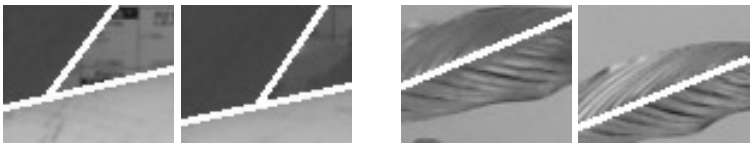			
sobel				
prewitt				
roberts	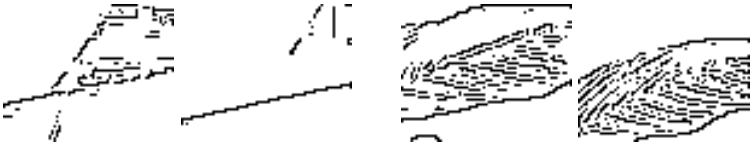			
log	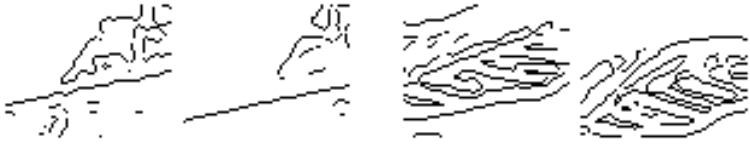			
zerocross	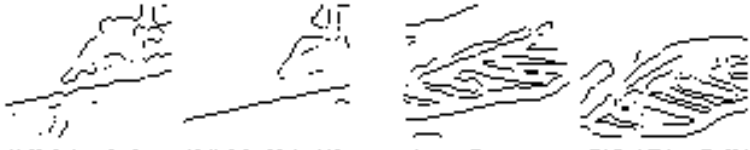			
canny				

Table 3. Result of the edge extraction for the sample "arrangement" and "person"

	arrangement		person	
	left image	right image	left image	right image
original image	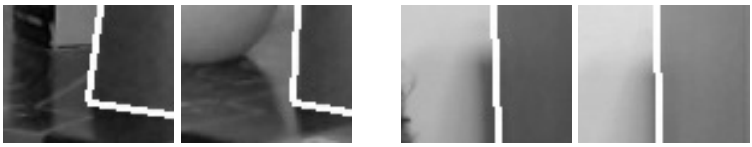			
sobel	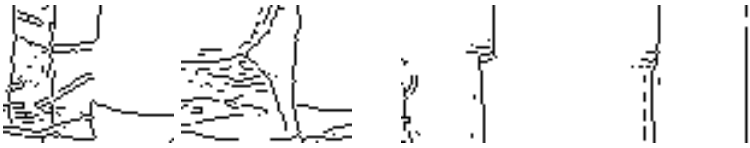			
prewitt	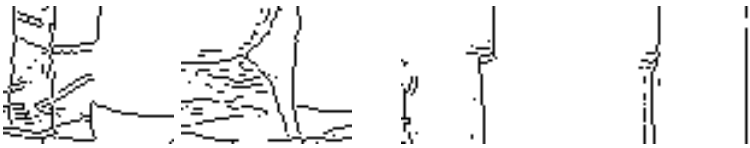			
roberts	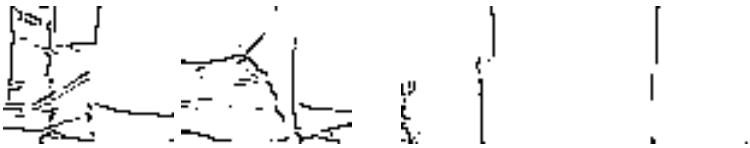			
log	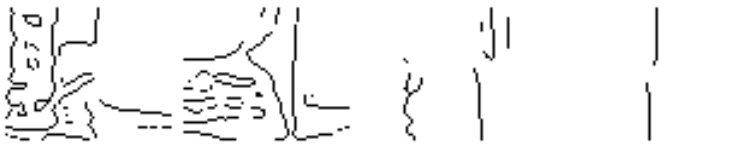			
zerocross				
canny				

of both edges is present in the left image. In the other image, there is no edge junction. In the case of the "fern" sample (Table 2), there is a longitudinal stripe in the middle of the leaf. The stripe can be easily noticed in the left image. However, it is not possible to observe any longitudinal stripe in the right image, probably due to the light reflex.

As for the "arrangement" sample (Table 3), there is a very interesting composition. The table is covered with a motley pattern, which should cause difficulties in the pot edge detection. That is why, it is impossible to observe the pot edge in the left image. In the right image, there is a strong light reflex on the table which makes the motely pattern invisible and, as a result, the pot edge cannot be observed.

In the "person" sample (Table 3)), there is a shade behind the cupboard. The shade edge is not sharp even in the original image. In the left image, the shade is much more visible or distinguishable than in the right image. It definitely results from the fact that there is much more shade in the original left image.

4 Results

Tables from 4 to 9 present in pixels the coordinates of the centroids and the edge lengths of the elements. Table 10 shows the distances between the nearest centroids and the differences in the edge length between stereo pairs of images.

The values in the table for the line "left image - centroids" and "canny" column show the coordinates of three centroids. Horizontal and vertical coordinates in pixels are lowered to a full pixel. The original values calculated as the centre of gravity are real numbers. The edge length in pixels is the total value for all sub-edges overlapping the test edge. The data in all tables are organised in the same way.

Table 4. Centroid coordinates and pixel lengths for Aloe sample

	canny	log	prewitt	roberts	sobel	zc	pix
	22 35	34 30	14 43	23 34	9 46	2 54	
	45 16		32 29	55 8	23 36	19 42	
	55 7		38 23		32 29	37 27	
left image			42 20		38 24	41 25	centroid
			46 16		42 20	54 13	
			56 8		46 16		
					56 7		
	95	**69**	**65**	**111**	**62**	**63**	**length**
	4 55	42 30	10 51	8 50	11 50	23 44	
	9 51		21 43	21 42	21 43	51 23	
	14 48		22 45	48 20	34 31		
right image	20 43		42 26		46 24		centroid
	49 20		61 10		53 17		
			66 6		61 10		
			69 3		68 4		
	87	**56**	**62**	**97**	**58**	**54**	**length**

Table 5. Centroid coordinates and pixel lengths for Wood1 sample

	canny	log	prewitt	roberts	sobel	zc	pix
	39 29	10 27	10 28	3 29	10 28	16 26	
	53 38	25 24	26 24	33 21	26 24	33 23	
		32 22	33 21	53 23	33 21	41 20	
left image		36 21	38 21	53 27	38 21	49 17	centroid
		39 21	44 19	55 27	44 19	51 30	
		43 19	56 35	54 40	55 37	58 35	
		51 30	54 38	56 53		54 48	
		54 48		57 43			
		58 36		58 49			
				58 49			
	136	**107**	**121**	**81**	**121**	**123**	**length**
	14 26	11 27	5 28	28 21	5 28	13 27	
	30 25	28 24	16 26	51 30	16 26	27 26	
	50 31	34 23	22 25	54 38	22 25	50 31	
right image	51 39	44 20	28 23	53 50	28 23	38 27	centroid
		50 39	51 35		51 34	50 38	
		56 37					
	128	**109**	**118**	**85**	**119**	**133**	**length**

Table 6. Centroid coordinates and pixel lengths for Bowling2 sample

	canny	log	prewitt	roberts	sobel	zc	pix
	13 39	36 36	16 39	13 39	16 39	30 37	
	33 19	31 24	24 33	24 31	24 33	26 30	
	37 34	41 9	28 29	30 36	28 29	35 18	
left image	45 2		30 25	30 23	30 25	42 9	centroid
	58 30		35 18	34 17	34 19	65 30	
			44 33	38 33	53 31		
			39 12	38 12	38 13		
			41 10	41 8	39 10		
			43 6	41 5	41 10		
			63 30	43 6	45 5		
				45 4	47 1		
				46 1			
				48 33			
				52 32			
				55 31			
				65 28			
	118	**96**	**94**	**124**	**101**	**93**	**length**
	35 40	36 42	36 41	35 40	36 41	36 42	
	35 36	45 22	35 39	48 18	35 39	41 29	
	45 22	56 5	38 37	54 8	45 23	46 21	
right image	56 5		45 22	57 3	53 13	57 5	centroid
			56 5		56 5		
	108	**94**	**103**	**107**	**106**	**91**	**length**

Table 7. Centroid coordinates and pixel lengths for Fern sample

	canny	log	prewitt	roberts	sobel	zc	pix
	21 25	32 22	1 34	6 32	2 36	3 35	
	47 15		3 32	12 28	1 38	19 26	
	58 10		6 30	19 26	5 33	43 17	
left image	67 6		10 28	31 21	7 31	60 10	centroid
			15 28	45 16	9 31		
			36 17	53 13	20 26		
			60 10	59 9	38 19		
				70 8	57 11		
	77	**63**	**59**	**58**	**60**	**54**	**length**
	3 47	2 55	2 54	2 52	1 54	3 52	
	12 46	5 54	11 46	5 51	10 47	10 48	
	16 45	9 49	18 41	8 50	16 42	19 44	
	24 41	12 47	28 38	12 48	19 42	24 42	
	34 37	20 44	30 38	14 47	25 39	32 38	
	37 36	24 42	37 35	15 44	30 38	39 36	
	43 32	31 38	39 34	23 37	32 37	41 32	
right image	57 28	41 33	42 33	28 36	37 35	42 35	centroid
	68 26	47 31	49 31	41 30	39 34	45 31	
		57 27	53 29	46 29	41 33	56 28	
		67 26	58 28	52 28	45 31	58 25	
			66 26	55 28	52 29	62 25	
			71 25	65 26	57 27	68 23	
				71 26	58 25		
					62 24		
					65 24		
					70 23		
	44	**45**	**46**	**22**	**34**	**39**	**length**

Table 8. Centroid coordinates and pixel lengths for Arrangement sample

	canny	log	prewitt	roberts	sobel	zc	pix
	38 9	37 29	37 19	36 28	37 29	37 29	
	37 22	37 32	37 29	36 31	37 31	39 9	
	37 25	39 9	37 31	39 8	54 44	56 44	
left image	37 28	55 44	40 8	55 44	40 7		centroid
	37 30		54 44				
	53 43						
	60	**48**	**53**	**58**	**50**	**45**	**length**
	47 21	47 25	48 21	47 29	48 21	47 26	
right image	59 42	49 4	60 43	48 15	60 43	49 4	centroid
		61 42		56 42		60 42	
				68 44			
	62	**57**	**65**	**49**	**65**	**58**	**length**

The number of centroids is substantially different between the left and right images, which indicates low stereo correspondence of the edges between stereo pairs.

Coordinates of corresponding centroids for a stereo pair of images should differ by the value proportional to the value of the shooting base.

Differences in edge lengths between left and right images also prove low correspondence of stereo pair images.

The results of various well-known edge detectors confirm the thesis about low correspondence of image elements that are in situations crucial for image analysis.

Table 9. Centroid coordinates and pixel lengths for Person sample

	canny	log	prewitt	roberts	sobel	zc	pix
	35 28	33 41	36 27	32 24	36 27	33 41	
	40 41	38 13		33 43		38 13	
left image				37 23			centroid
				38 10			
	93	**56**	**68**	**62**	**68**	**56**	**length**
	31 28	29 44	26 26	31 34	32 28	29 43	
	34 42	32 13	32 27	31 56	28 31	32 14	
			28 31	33 12	28 38		
			28 38	70 57	28 46		
right image			28 41		28 53		centroid
			28 45		29 26		
			28 53				
			29 26				
	86	**48**	**92**	**42**	**86**	**53**	**length**

The authors have performed the above analyses also for stereo pairs rotated by 5 and 15 degrees. The results agree with the ones obtained above.

The distances between centroids and the differences in length shown in (Table 10) prove that there exists a problem with correspondence between the elements, in the present case the edges, located in the left and right images in particularly difficult areas of the scene. The distances between adjacent centroids strongly fluctuate, reaching a maximum value of 57 pixels for the Person scene and Roberts filter.

Table 10. Distances between centroids and differences between edge lengths

	canny	log	prewitt	roberts	sobel	zc	pix
	8	8	9	8	4	4	
	9		18	14	7	10	
Aloe			27		3		Distance
			6		8		between
			16		11		centroids
			10		16		
					12		
	8	13	3	14	4	9	Difference between lengths
	10	1	5	5	5	3	
	2	3	2	4	10	7	
Wood1		3	4	2	12	1	Distance
		1		5	10	8	between
		9			4	8	centroids
		2					
	8	2	3	4	2	10	Difference between lengths
	21	6	23	13	14	8	
	3	14	11	14	15	13	
Bowling2	15	16	25	9	14	13	Distance
	11		13	10	11	26	between
			13		10		centroids
	10	2	9	17	5	2	Difference between lengths
	16	16	20	19	18	17	
	17		16	20	13	18	
Fern	18		16	11	14	14	Distance
	20		20	15	16	15	between
			19	13	18		centroids
			18	15	16		
			18	19	16		
				17	16		
	33	18	13	36	26	15	Difference between lengths
	10	11	11	11	14	10	Distance
Arrangement	6	11	6	20	6	11	between
		6		2		4	centroids
	2	9	12	9	15	13	Difference between lengths
	4	5	4	10	4	4	
Person	6	6		13		6	Distance
				12			between
				57			centroids
	7	8	24	20	18	3	Difference between lengths

The obvious reason for this difference is the nature of the shadow cast by the wardrobe. The natural shade level varies with the shooting place, which is shown in Fig. 1.

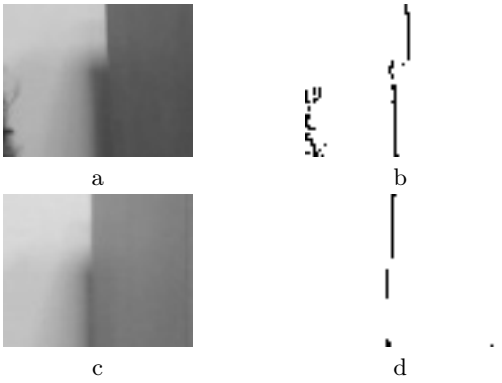

Fig. 1. Probably the most problematic scene with a shade; a, c - stereo images; b, d - the edge detected with the Roberts filter

5 Conclusions

In stereovision, left and right images are taken from different geometric places, which results in different images in both pictures. Sometimes even a small imaging base makes images in both pictures different. It leads to later problems with recognising the same elements present in those pictures.

The background is very important. The more motley the background is, the more problems there occur with edge extraction of the foreground elements. A more contrasting background guarantees much easier edge detection of the foreground elements. But even a motley background can always be neutralised with proper light focusing.

Also a uniform colour of the background and detected objects may cause problems with distinguishing the edge lines. How easy it is to detect such edges depends on the light direction, reflexes and degree of the shade. Also the angle at which the lens axis points at particular object details is very important. The situation is quite different with the shade. It is much easier to extract the edge of a bigger shade in the bright background. It may be assumed that it will be very difficult to detect corners in shaded areas where in one picture the same element is located in the shade but in the other one it is outside the shade. Such a situation can definitely happen when both pictures are taken one after another.

Taking into account all the above issues, the new stereo correspondence algorithm based on graph theory must be reduced to the problem of inexact graph

matching in accordingly defined graphs. When a decision is made to apply segmentation to stereo images, the regions should be properly defined to keep small details still recognisable. The segmentation algorithm must be definitely properly designed.

The discussed analysis is only one of possible approaches to presenting this problem. Other methods which are implemented when presenting similar problems, e.g. [2], may also be applied here.

Acknowledgement. Co-Author Pawel Popielski is a scholarship holder within The Project DoktoRIS - Scholarship Program for Innovative Silesia co-financed by the European Union under the European Social Fund.

References

1. D'apuzzo, N.: Automated Photogrammetric Measurement of Human Faces. In: Archives of Photogrammetry and Remote Sensing, Hakodate, Japan, vol. XXXII(Pt. B5), pp. 402–407 (1998)
2. D'apuzzo, N.: Measurement and modelling of human faces from multi images. International Archives of Photogrammetry and Remote Sensing 34(5), 241–246 (2002)
3. Cyganek, B., Siebert, J.: An Introduction to 3D Computer Vision Techniques and Algorithms. Willey (2009)
4. Fryer, J.G., Brown, D.C.: Lens distortion for close-range photogrammetry. Photogrammetric Engineering and Remote Sensing 52, 51–58 (1986)
5. Heikkila, J., Silven, O.: A four-step camera calibration procedure with implicit image correction. In: Proceedings of the 1997 Conference on Computer Vision and Pattern Recognition, p. 1106 (1997)
6. Korzynska, A., Iwanowski, M.: Multistage morphological segmentation of bright-field and fluorescent microscopy images. Opt-Electron 20(2), 87–99 (2012)
7. Kosov, S., Thormählen, T., Seidel, H.-P.: Accurate Real-Time Disparity Estimation with Variational Methods. In: Bebis, G., Boyle, R., Parvin, B., Koracin, D., Kuno, Y., Wang, J., Wang, J.-X., Wang, J., Pajarola, R., Lindstrom, P., Hinkenjann, A., Encarnação, M.L., Silva, C.T., Coming, D. (eds.) ISVC 2009, Part I. LNCS, vol. 5875, pp. 796–807. Springer, Heidelberg (2009)
8. Kraus, K.: Photogrammetry. Walter de Gruyter, Berlin (2007)
9. Malian, A., Azizi, A., Van Den Heuvel, F.A.: Medphos: A new photogrammetric system for medical measurement. International Archives of the Photogrammetry, Remote Sensing and Spatial Information Sciences 35(B5), 311–316 (2004)
10. Mitchell, H.L.: Applications of digital photogrammetry to medical investigations. ISPRS Journal of Photogrammetry and Remote Sensing 50(3), 27–36 (1995)
11. Mitchell, H.L., Newton, I.: Medical photogrammetric measurement: overview and prospects. ISPRS Journal of Photogrammetry and Remote Sensing 56(5-6), 286–294 (2002)
12. Oskoei, M.A., Hu, H.: A Survey on Edge Detection Methods. University of Essex, UK (2010)
13. Patias, P.: Medical imaging challenges photogrammetry. ISPRS Journal of Photogrammetry and Remote Sensing 56(5-6), 295–310 (2002)

14. Popielski, P., Wróbel, Z.: The Feature Detection on the Homogeneous Surfaces with Projected Pattern. In: Piętka, E., Kawa, J. (eds.) ITIB 2012. LNCS, vol. 7339, pp. 118–128. Springer, Heidelberg (2012)
15. Schenk, T.: Digital Photogrammetry, TerraScience, Laurelville, Ohio, p. 428, 34 (2002); Stockman, G.C.: Computer Vision. Prentice-Hall (1999)
16. Shapiro, L., Stockman, G.C.: Computer Vision. Prentice-Hall (2002)
17. Zhang, Z.: A flexible new technique for camera calibration. IEEE Transactions on Pattern Analysis and Machine Intelligence 22, 1330–1334 (2000)

An Algorithm for the Pore Size Determination Using Digital Image Analysis

Małgorzata Charytanowicz[1,2]

[1] Polish Academy of Sciences,
Newelska 6, PL 01-447 Warsaw, Poland
mchmat@kul.lublin.pl
[2] The John Paul II Catholic University of Lublin,
Konstantynów 1 H, PL 20-708 Lublin, Poland

Abstract. The study is concerned with putting forth a novel method of determination the pore size and its distribution for pores of different shapes. The identification of irregular and branched pores is associated with difficulties in their separation, as well as in the quantification of their size and shape characteristics. Recent developments in digital image processing provides a relatively new technology that allows visualization of the internal structure of objects. Our research was conducted using computer-aided tomography, and in turn, statistical techniques. This seems to be very useful in characterizing the pore volume distribution and in quantifying the differences in pore structures of the investigated materials. In this paper, the methodology is illustrated with a number of soil aggregates which differ in terms of soil fertilization. The approach is universal, and can be successfully applied for many tasks in data mining where pore characteristics are needed.

Keywords: image processing, cumulative distribution function, pore size distribution, pore space, total porosity, statistical methods, soil aggregation.

1 Introduction

The characterization of porous material has been an important topic in the research area. This includes the total porosity, pore size distribution, pore size and shape or interconnectivity [1, 2]. Pore shape is mainly unknown, but it could be approximated by one of the basic pore models: "cylindrical" – with circular cross-section, "ink-bottle" – having a narrow neck and wide body, and "slit-shaped" – with parallel plates. Unfortunately, pore structures do not have any regular or well defined shape, and therefore the use of methods assuming their shape becomes inapplicable. For this reason, some authors have proposed different computational methods to determine the pore size distribution. These techniques can be classified based on the pore size, pore type, amount of pores or nature of measurements. Despite the usefulness of these methods for determining pore size distribution, a combination of different techniques is needed to

E. Pietka, J. Kawa, and W. Wieclawek (eds.), *Information Technologies in Biomedicine, Volume 3*, Advances in Intelligent Systems and Computing 283,
DOI: 10.1007/978-3-319-06593-9_20,

cover the wide range of characteristics describing the pore structure. However, conventional techniques, such as mercury porosimetry, or low-temperature gas adsorption have often been unsatisfactory due to inadequate pore characteristics. Moreover, they are limited in applicably as far as pore size and shape or preferential flow is concerned.

Computed tomography and digital image processing provide new possibilities of identifying pores and quantifying their characteristics. The non-destructive nature of computed tomography scanning allows the same object to be scanned multiple times and provides an opportunity to investigate its particle at any location within a sample. In the last few years, studies indicate that X-ray computer-aided tomography also provides an alternate approach for the non-destructive observing, measuring, and quantifying of the internal microstructure of materials [3, 4]. In our research, the use of image analysis has enabled us to determine pore size distribution.

Classical parametric techniques of density estimation assume that the data can be drawn from one of a known parametric family of distributions, and determined by a few parameters, for example, mean and variance. The density underlying the data could then be estimated by finding the parameters using the data and substituting these estimates into the formula for the chosen density. Such technique requires performing significant tests, such as Chi-square goodness-of-fit, Kolmogorov-Smirnov or Shapiro-Wilk test [5, 6]. The null hypothesis states that our data must follow a specific distribution. A not significant result denoting that the tested hypothesis is not rejected allows us to use the estimated model. Moreover, for skewed distributions, a mathematical transformation, for example, logarithmic, tending the data to normal distribution, is recommended. On the other hand, nonparametric estimation [7–9] assumes that there is no pre-specified functional form for a density function. Some of these methods also have the advantages of being very intuitive and relatively simple to analyze mathematically. Moreover, it is worth noticing that all parameters appearing in the obtained model can be effectively calculated using convenient numerical procedures based on optimizing criteria [10, 11].

In this paper, research was conducted to determine porosity and soil pore size distribution. Pore size distribution is one of the many physical measurements characterizing soil structure as far as plant growth is concerned. Additionally, total porosity, defined by the ratio of the volume of void-space, and the total volume of soil material (including the solid and void components), provides a more useful physical description of a particular soil, such as compaction or the maximum space available for water. A number of scientists have reported studies of employing pore space as a general method for defining soil properties [12]. In this respect, a complete analysis of the soil pore size distribution is used for predicting the gas diffusivity, water conductivity and water availability to plants. The investigated material, suitable for collecting information about the soil porosity, was preprocessed by aggregate preparation, image analysis and statistical methods. Background and information regarding these operations are

described in Section 2 and 3. The two packages that were used to conduct and report research are the Aphelion image analysis package and Statistica software.

2 Materials and Methods

The experiments were conducted on three soil samples differ in terms of fertilization (pig manure, mineral fertilization, control group), and were explored at the Polish Academy of Sciences in Lublin. The investigated material was sampled from the cultivated soil layer, classified as silty loam (Word References Base for Soil Resources – Mollic Gleysols). The proportion of each particle size group in the soil was as follows: sand – 46%, silt – 28%, clay – 26%, pH was: H_2O – 5.9, KCl – 5.4. A long-term fertilization trial was executed on the experimental fields. The manure treatment was 80 ton per ha of composed pig manure. The mineral fertilization was according to plant needs. The control was applied neither mineral nor manure treatment, there were plant residues only. The adopted crop rotation was as follows: a cycle of potato – barley – rye from 1955 to 1989, and sugar – beet – barley – rape – wheat from 1990. Aggregate soil organic matter was measured by the Multi N/C 3100 Autoanalyser (Analitic Jena, Germany). The total organic carbon and total nitrogen contents for three fertilizations (pig manure, mineral fertilization, control) were respectively: 21.50, 14.89, 13.54 g/kg, and 2.10, 1.51, 1.35 g/kg. The total organic carbon shows the same tendency as total nitrogen, i.e. they increase in the same order: the lowest – control, middle – mineral fertilization, the highest – pig manure.

2.1 Soil Sample Preparation

The soil samples used for porosity analysis were air dried in room conditions, divided into smaller quantities, and gently sieved through 2 and 10 mm sieves. The remaining at 2 mm sieve soil aggregates of sizes ranging from 2 to 10 mm, were then detected by means of X-ray computational tomography, using a GE Nanotom S device with a molybdenum X-ray source, 230 μA cathode current, 60 kV voltage and voxel-resolution of 2.5 microns per volume pixel. Three 2D sections of 3D objects, uniformly located within them, were performed to characterize the aggregate structure. After this, tomography sections were processed using the Aphelion 4.0.1 package. Pore size measurements of the aggregate sample were collected by means of image processing techniques [13, 15, 16].

2.2 Image Processing and Data Analysis

The entire procedure was composed of the following steps. Firstly, grayscale tomography sections were preprocessed by removing ring artifacts using the ROI (region of interest) method. Next, the automatic Otsu binarization method was employed. After these preprocessing methods were undertaken, a binary morphological closing with increasing size of structuring element SE (starting with 2×2 square SE), was processed subsequently. Operation closing, consisting of

a dilation followed by erosion, was used to fill in holes and small gaps without changing the aggregate size and original boundary shape. In each step, the source image was subtracted from the target image, and the result volumes were listed, giving soil aggregate pore distribution. The operation was repeated until all pores were filled. A direct subtraction of two images: the transformed image and the original image, gives the total pore volume in the soil sample. A cumulative aggregate porosity $P(i)$ related to a given and smaller structuring element size can be calculated as:

$$P(i) = \frac{S(i) - S(0)}{S(N)} \text{ for } i = 2, 3, \ldots, N, \tag{1}$$

where:

$S(i)$ – surface area of solids and filled by pores less than or equals to SE size i, $i \geq 2$,

$S(0)$ – surface area of solid phase,

$S(N)$ – total area, equals to surface area of solids and pores,

N – size related to the biggest pore,

$P(N)$ – total porosity.

Next, the soil pore size distribution can be calculated as:

$$\frac{1}{P(N)} \frac{dP}{dr} = \frac{P(i+1) - P(i)}{P(N)} \text{ for } i = 2, 3, \ldots, N-1, \tag{2}$$

where $P(N)$ denotes the total porosity.

Figure 1 shows subsequently obtained aggregate section images related to the described method.

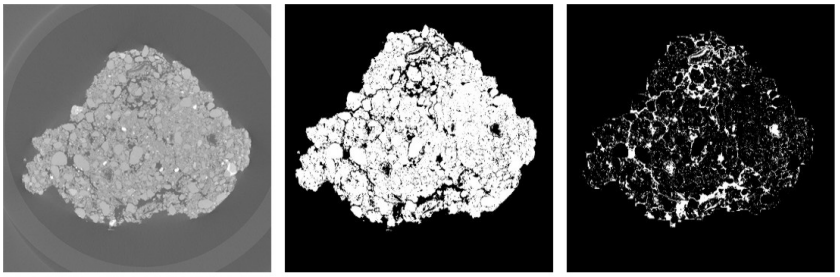

Fig. 1. Cross section of a typical soil with pore space in black (a), a binary soil aggregate section image done by ROI and Otsu methods (b), a binary image of all pores detected by closing operation (c)

The data derived automatically from images was statistically examined using classical methods. For each fertilization (pig manure, mineral fertilization, control), a discrete data set consists of cumulative porosities $P(i)$, $i = 2, 3, \ldots, N$

was explored. Our aim was to present the frequency distribution as a continuous mathematical equation instead of a discrete set of data. We have fitted to the observed data, a known theoretical model of probability distribution function.

Finally, the elaborated procedure for determining the porosity and soil pore size distribution may be explained in the following steps:

The Procedure for Determining the Porosity and Soil Pore Size Distribution

1. Soil sample preparation.
2. X-ray microtomography of soil aggregates.
3. Digital image processing.
   (a) ROI method.
   (b) Otsu thresholding method.
   (c) Binary morphological closing.
4. Frequency analysis.

3 Results

A cumulative porosity of investigated soil aggregates was determined using the image processing methods described in paragraph 2. Figure 2 shows exemplary soil aggregate section images done by ROI and Otsu methods for each type of aggregate.

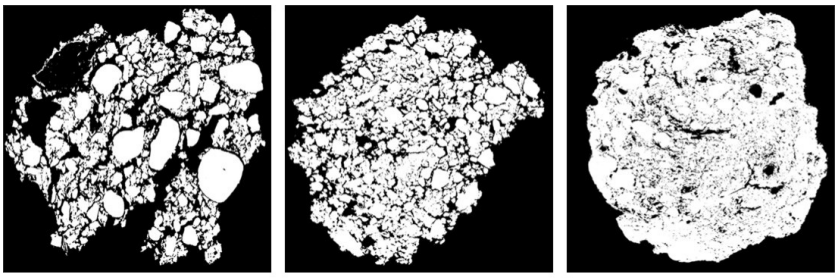

Fig. 2. Exemplary binary images of investigated aggregates: pig manure (a), mineral fertilization (b), control (c)

The total porosity of the investigated aggregates for three fertilizations (pig manure, mineral fertilization, control) calculated as the average of three sections, were equal to 33.28%, 22.95%, 14.2% respectively. The total porosity shows the same tendency as total organic carbon and total nitrogen, i.e. they increase in the same order: the lowest – control, middle – mineral fertilization, the highest – pig manure.

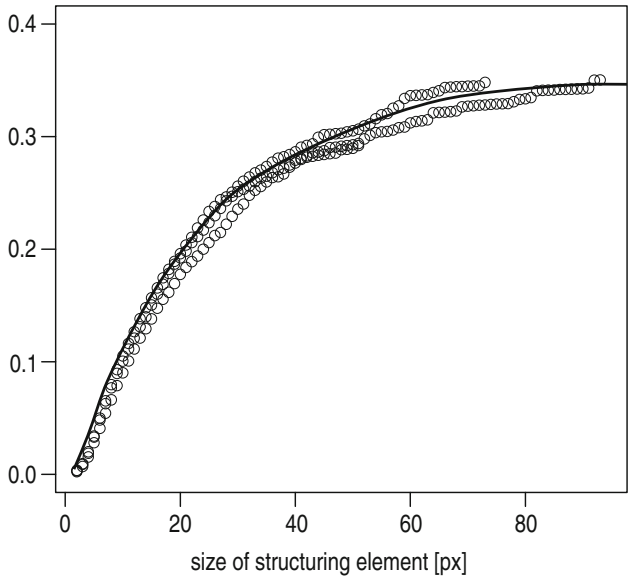

Fig. 3. Cumulative porosity of aggregates treated with pig manure (circle – observed data, line – estimated curve)

Experimental points (x_i, y_i), $i = 2, 3, \ldots, N$ where x_i denotes the size of structuring element (1px = 2.5 microns), and y_i was calculated using formula (1) and denotes cumulative porosity, are shown in Figure 3 – Figure 5.

The function given by the formula:

$$Y = k \cdot ILognorm(x, m, s) \tag{3}$$

where Y denotes the cumulative porosity, x means size of structuring element, k, m, and s constitute the parameters of the models, and $ILognorm(x, m, s)$ denotes the lognormal cumulative distribution function, was fitted to the observed data using nonlinear estimation [14]. The function was selected by means of the minimum square error criterion.

Table 1 shows the parameter values of the model given by the rule (3) and the corresponding coefficients of determination R^2 for the investigated aggregates. The usefulness of such a model is very high, R^2 is shown to be greater than 90% for all the types of fertilization sampled.

The parameter k corresponds to the total porosity of the aggregate, while the larger parameter m corresponds to the higher total porosity of the aggregate.

Pores have traditionally been divided into micropores, mesopores, and macropores, with the division between them being arbitrary. The use of the estimated models allowed us to calculate the cumulative porosity for the arbitrarily given

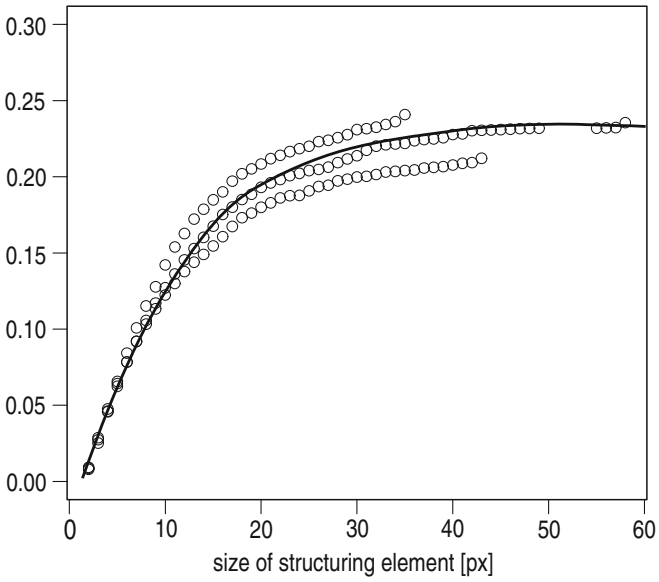

Fig. 4. Cumulative porosity of aggregates treated with mineral fertilization (circle – observed data, line – estimated curve)

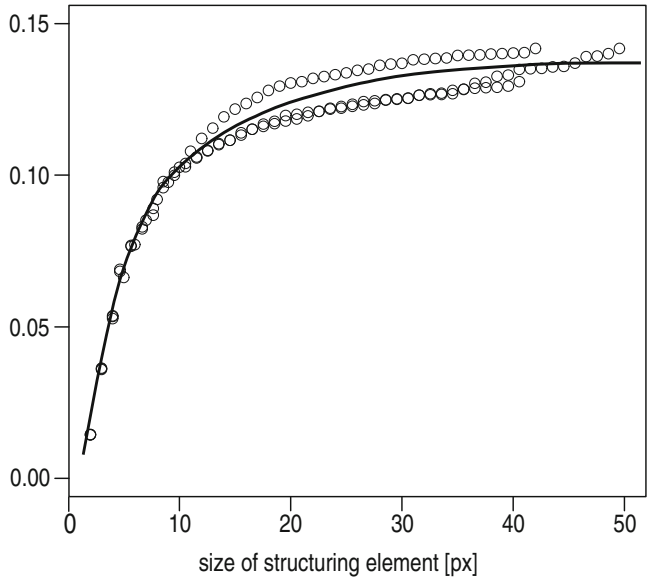

Fig. 5. Cumulative porosity of the control group (circle – observed data, line – estimated curve)

Table 1. The model parameters and the coefficient of determination obtained for the model $Y = k \cdot ILognorm(x, m, s)$

Fertilization	k	m	s	R^2
Pig manure	0.37	2.79	0.89	0.99
Mineral fertilization	0.23	2.16	0.89	0.98
Control	0.14	1.67	1.03	0.95

limits between micropores, mesopores and macropores, equal to 30 microns and 75 microns respectively. This enables to calculate the fractions of micro-, meso-, and macropores for each type of fertilization. The results are given in Table 2.

Table 2. Fractions of micro-, meso- and macropores

Fertilization	Fraction		
	of micropores	of mesopores	of macropores
Pig manure	0.12	0.13	0.09
Mineral fertilization	0.14	0.08	0.02
Control	0.12	0.02	0.001

As can be seen, the largest fraction of mesopores occurs in the soil fertilized with manure, this fraction represents 13% of the total aggregate area. In addition, this sample shows 12% of the total aggregate area to be micropores and 9% to be macropores. This creates the most favorable conditions for plant growth.

Within the aggregate, the second largest fraction of mesopores, equaling 8%, was observed in the soil with mineral fertilization. This soil has a small amount of macropores, equaling 2%, and a quite large amount of micropores, equaling 14%. This creates less favorable conditions for plant growth.

The soil without fertilization (control group) reveals that 12% of the total aggregate area are micropores, 2% are mesopores and 0.1% are macropores. The largest fraction of micropores in comparison with the fractions of meso- and masropores creates the least favorable conditions for plant growth

Next the methodology described above was used to determine the soil pore size distribution. Experimental points (x_i, y_i), $i = 2, 3, \ldots, N$ were done, where x_i denotes the size of structuring element, and y_i was calculated using formula (2). The model fitted takes the form:

$$Y = Lognorm(x, m, s) \tag{4}$$

where

$$Lognorm(x, m, s) = \frac{1}{x\sqrt{2\pi}s} \exp\left(-\frac{(\log(x) - m)^2}{2s^2}\right) \tag{5}$$

is the probability density function of the lognormal distribution with parameters m and s, Y denotes the pore size fraction to be modeled, and positive variable x means the size of structuring element (1px = 2.5 microns).

The results are shown graphically in Figure 6 – Figure 8.

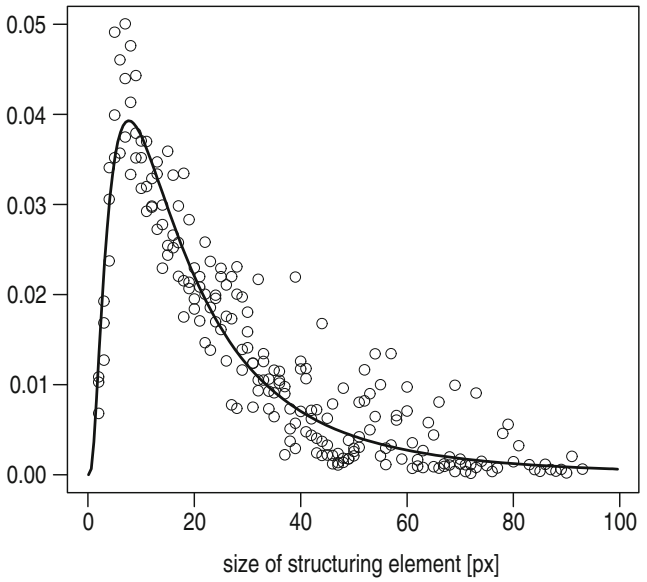

Fig. 6. Frequency distribution of aggregates treated with pig manure (circle – observed data, line – estimated curve)

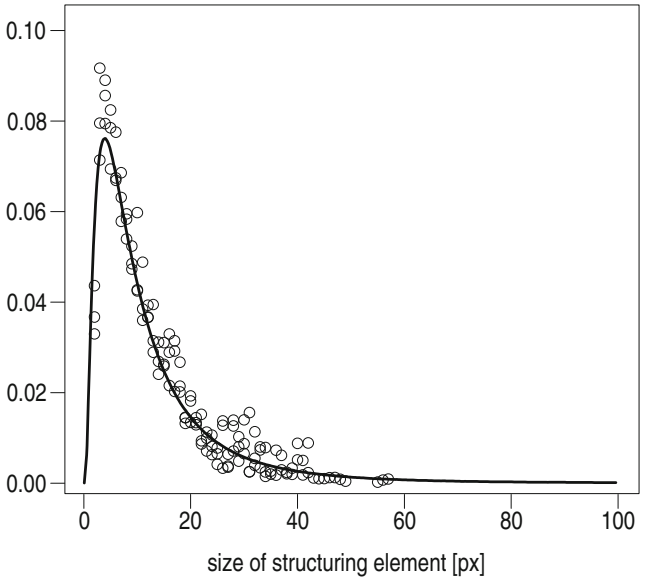

Fig. 7. Frequency distribution of aggregates treated with mineral fertilization (circle – observed data, line – estimated curve)

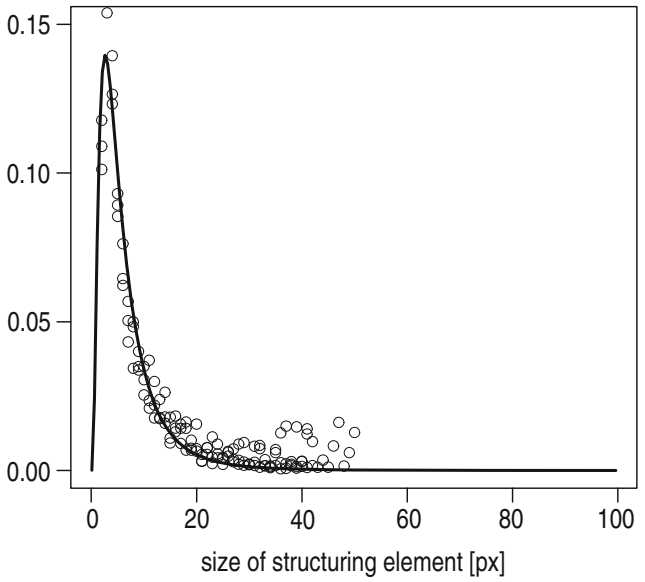

Fig. 8. Frequency distribution of the control group (circle – observed data, line – estimated curve)

Table 3 shows the parameter values of the model (4) and the corresponding coefficients of determination R^2 for the investigated aggregates.

Table 3. The model parameters and the coefficient of determination obtained for the model $Y = Lognorm(x, m, s)$

Fertilization	m	s	R^2
Pig manure	2.83	0.89	0.90
Mineral fertilization	2.17	0.83	0.95
Control	1.59	0.79	0.94

The usefulness of the model is demonstrated to be very high, R^2 is greater than 90% for all the types of sampled fertilization. This indicates that the model has a very good fit to the data. The larger parameter m corresponds to the higher total porosity of the aggregate. The values of parameter m range from 1.59 to 2.83, whilst the values of parameter s are smaller than 1.0 and range from 0.79 to 0.89. As having the same role, the values of these parameters are mostly the same as the corresponding values obtained for the model characterizing the porosity. However, some differences may arise due to the smaller dispersion of the data resulting better fitting the model to cumulative porosity.

The obtained function, characterizing the pore size distribution, reveals their positively skewed and unimodal character. The pore size distribution for pig

manure fertilization evidences a high amount of large pores, whilst the pore size distribution for the control group indicates the presence of a high amount of small pores.

4 Summary

Recently, a notable increase in research in the area of image processing methods, has shown that, together with computed tomography, these techniques provide non-destructive tools for studying the internal structures of objects. This seems very useful in exploring soil aggregates and quantifying their characteristics.

In this paper, a systematic procedure was outlined for using X-ray tomography and frequency analysis to quantify measurements of void ratio, porosity, and pore size distribution. The lognormal probability density function was crucial for description of pore size distributions. The presented algorithm is expected to be more objective than classical methods, where arbitrary assumptions concerning the shape of pores are required.

This approach is also motivated by the current rapid growth in computational power. Hence, improved real-time data processing and algorithm efficiency have importance due to the concurrent increase in the quantity and complexity of the data that are being collected.

References

1. Czachor, H., Lipiec, J.: The effects of manure application on soil aggregation. International Agrophysics 18, 217–223 (2004)
2. Dexter, A.R.: Advances in characterization of soil structure. Soil and Tillage Research 11, 198–238 (1988)
3. Papadopoulos, A., Bird, N.R., Whitmore, A.P., Mooney, S.J.: Investigating the effects of organic and conventional management on soil aggregate stability using X-ray computed tomography. European Journal of Soil Science 60, 360–388 (2009)
4. Peth, S., Nellesen, J., Fischer, G., Horn, R.: Non-invasive 3D analysis of local soil deformation under mechanical and hydraulic stresses by uCT and digital image correlation. Soil and Tillage Research 111, 3–18 (2010)
5. Nowak, P., Romaniuk, M.: Pricing and simulations of catastrophe bonds. Insurance: Mathematics and Economics 52, 18–28 (2013)
6. Swanepoel, C.J., Doku, W.O.: New goodness-of-fit tests for the error distribution of autoregressive time-series models. Computational Statistics and Data Analysis 43, 333–340 (2003)
7. Charytanowicz, M., Kulczycki, P.: Nonparametric Regression for Analyzing Correlation between Medical Parameters. In: Pietka, E., Kawa, J. (eds.) Information Technologies in Biomedicine. ASC, vol. 47, pp. 437–444. Springer, Heidelberg (2008)
8. Kulczycki, P., Charytanowicz, M.: Conditional Parameter Identification with Different Losses of Under- and Overestimation. Applied Mathematical Modelling 37, 2166–2177 (2013)
9. Silverman, B.W.: Density Estimation for Statistics and Data Analysis. Chapman and Hall, London (1986)

10. Lange, K.: Numerical Analysis for Statisticians. Statistics and Computing. Springer, New York (2000)
11. Kincaid, D., Cheney, W.: Numerical Analysis. Brooks/Cole, Pacific Grove (2002)
12. Zdravkov, B., Cermak, J., Sefara, M., Janku, J.: Pore classification in the characterization of porous materials: A perspective. Central European Journal of Chemistry 5, 385–395 (2007)
13. Król, A., Niewczas, J., Charytanowicz, M., Gonet, S., Lichner, L., Czachor, H., Lamorski, K.: Water-stable and non-stable soil aggregates and their pore size distributions. In: 20th International Poster Day and Institute of Hydrology Open Day: Transport of Water, Chemicals and Energy in the Soil – Plant – Atmosphere System, Bratislava, pp. 870–871 (2012)
14. Draper, N.R., Smith, H.: Applied regression analysis. John Wiley and Sons, New York (1981)
15. Pratt, W.K.: Digital Image Processing. John Wiley and Sons, New York (2001)
16. Aphelion 4.0.10 user guide: ADCIS S.A. (1997)

Automatic Car Make Recognition in Low-Quality Images

Paweł Badura and Maria Skotnicka

Silesian University of Technology, Faculty of Biomedical Engineering, Zabrze, Poland
pawel.badura@polsl.pl

Abstract. This paper presents a robust system for automatic car make recognition in real-traffic images of car front, featuring low contrast and compression-based distortions. The system is designed to distinguish and classify a variety of car makes by means of Scale Invariant Feature Transform pattern recognition and matching over a reference database of car brand images. The system framework consists of image preprocessing techniques yielding a car brand region, feature extraction and description, pattern matching procedure and multicriteria decision-making process. The knowledge database is opened and easy to extend in order to cover an increasing number of car makes. Described approach stands for a part of an expert system for car type, make and color recognition, to be designed and build for real traffic supervision.

Keywords: car make recognition, feature extraction, Scale Invariant Feature Transform.

1 Introduction

Automatic systems for detection, recognition and classification of various car features becomes a more explored research topic nowadays. That concerns not only licence plate recognition systems (ALPR), which have been widely designed and applied for years [1]. Number of effective and real-time approaches for visual analysis of a car appearance in various types of image data significantly increases. Car type, make, model, color should be mentioned [2]. They are often collected and closed in a complex expert system designed to provide comprehensive information on the car being inspected [3].

Most of make recognition systems is based on feature extraction and classification methods (e.g. Support Vector Machines – SVM [4, 5], Bayesian methods [6, 7], neural networks [8]). Commonly used feature extraction algorithms are: Canny edge detector [9], square mapped gradients [10], methods based on contour information [11], Curvelet Transform [5], Speeded-Up Robust Features (SURF) [3, 12] and Scale Invariant Feature Transform (SIFT) [3, 13].

Main limitation of all systems is the image quality. High efficiency (96%) of make and model recognition has been reached by applying k-nearest-neighbour and Naive Bayes classifiers [7]. The dataset, however, consisted of pictures of parked cars, taken from small distance (1.5-3 m), whilst most systems have to

E. Pietka, J. Kawa, and W. Wieclawek (eds.), *Information Technologies in Biomedicine, Volume 3*, Advances in Intelligent Systems and Computing 283,
DOI: 10.1007/978-3-319-06593-9_21,

manage with poor quality images of moving cars. Another problem is a number of classes in a database. There is a large number of car models in real traffic and each system should recognize the majority. In [3] the SURF detector and SVM have been used for model recognition with the accuracy of 91.7%, yet with a database of 17 different models. Segmentation precision of 62.53% have been obtained in [14] using local and global object information, with a database of only 10 car makes and models. Another car make recognition problem is the number of car make samples in the database. In [15] the SURF based recognition has been used yielding 45% efficiency due to the small amount of samples used for evaluation. The authors suppose, that a larger dataset could improve the above statistics.

The aim of this study, in reference to the above review, is the design of a system for an automatic recognition of a car make in case of low-contrast, JPEG compressed images of car front. Our system is a component of an expert system for car type, make and color recognition, to be designed and build for a real traffic supervision. Foundations of the car make recognition system might be formulated as follows: (a) since the inspected images feature (by default) low contrast and compression-based distortions, the system is supposed to be robust also for multiple types of real-traffic imaging drawbacks: e.g. lighting, dirt, or weather conditions influence; (b) a wide spectrum of car makes should be recognizable, involving those more or less present on supervised roads; (c) the system should be easily adaptable and enable appending successive makes to the knowledge base without decrease of distinctiveness; (d) since no model recognition is required, the appropriate car make classification should be secured among various models of the same car producer; (e) the system should be fast enough to be a real-time application.

In order to meet the above requirements a system has been designed, composed of image preprocessing procedures, feature extraction and description, pattern matching, and classification based on multicriteria decision-making process. The image preparation contains licence plate recognition, image rotation, car mask and brand region of interest (ROI) extraction. The car brand ROI is subjected to a feature extraction process involving the SIFT paradigms. Then, the SIFT descriptors are matched to the previously collected reference database of car make patterns to produce the matching vector. Finally, a decision is made after a cautious look at the input car brand compared to the reference database samples.

This paper is organized as follows. Section 2 presents the idea of a system: image data specification, image preparation techniques, feature extraction and description, pattern matching, and classification idea. Quantitative verification of the system is shown and discussed in Section 3. Section 4 concludes the paper.

2 Methodology

The system components include (Fig. 1): image preprocessing, feature extraction, pattern matching, and classification. They are discussed in the following sections.

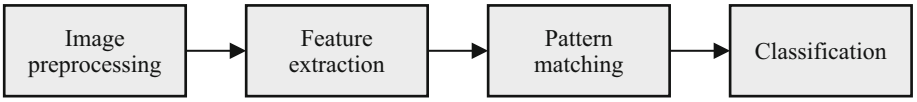

Fig. 1. Automatic car make recognition scheme

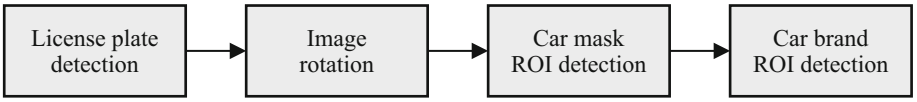

Fig. 2. Image preprocessing scheme

2.1 Image Preprocessing

The image preprocessing procedures are presented in Fig. 2. Before specifying them in details, first the database of images has to be introduced.

Database. Images used in this study have been acquired by a SmartLPR® Speed infrared camera operating in real traffic and used for ALPR. Sample images are shown in Fig. 3. The image size is 752×480 pixels with 8-bit JPEG compression at ca. $0.15 - 0.50$ bits per pixel (bpp). In many cases the images have unsatisfactory contrast due to histogram shift towards low intensities (two bottom rows in Fig. 3). Our system is designed to overcome such problems in a reasonable range. Nonetheless, we found the interpretability limitation for image quality at ca. 0.25 bpp compression. That excludes poor images (bottom row in Fig. 3) from the recognition process, as they do not offer any valuable features.

The license plate and lights are sufficiently apparent in database images, therefore they might be used to position the car mask and establish further detection workflow.

License Plate Detection. The license plate detection consists of (Fig. 4):

1. Bernsen dynamic thresholding of the original image I [16] with parameters $r = 5$ (window size), $l = 48$ (minimum window contrast) and a half of intensity range (128) used for thresholding within low-contrast windows.
2. Morphological corrections employed to eliminate small false positive regions, cut off all links between license plate and possible parts of the car body, filling holes in the license plate region and adjust its edges [17].
3. If multiple candidate regions survive previous operations, a simple voting system is employed to select the proper region. Several object features are taken into consideration, namely: texture parameters based on intensity changes across image rows intersecting the candidate object, region orientation, size proportions, and spatial relation to the image vertical axis.

Fig. 3. Sample car images arranged with decreasing contrast/quality

Image Rotation. Cars, in general, are not positioned parallel to the image horizontal axis, thus the rotation is performed to secure proper position. Rotation angle α_{lp} results from the license plate orientation relative to the image x-axis (Fig. 5).

Car Mask ROI Detection. Based on a wide analysis of possible car brand locations in a car mask, a narrow car mask region of interest has been defined according to the following rules:

1. The license plate is assumed to be placed in a lower part of a car front, symmetrical in the horizontal direction. Thus, its middle column determines the vertical axis of symmetry in the rotated car region.

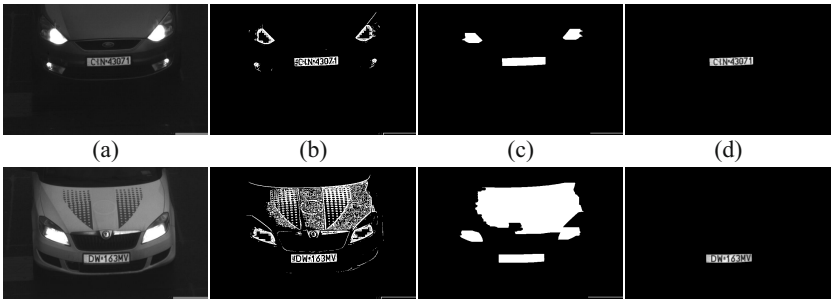

Fig. 4. License plate detection (2 cases); (a) original image I and results of: (b) Bernsen thresholding, (c) morphological corrections, (d) region selection using a voting system

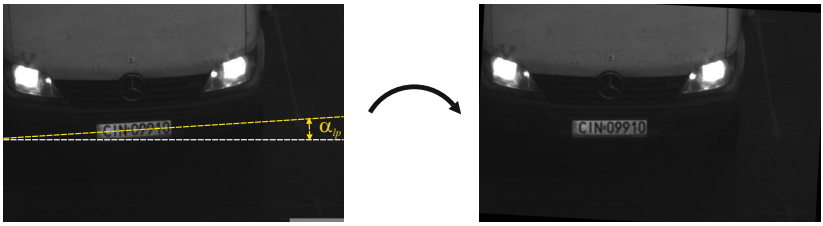

Fig. 5. Image rotation

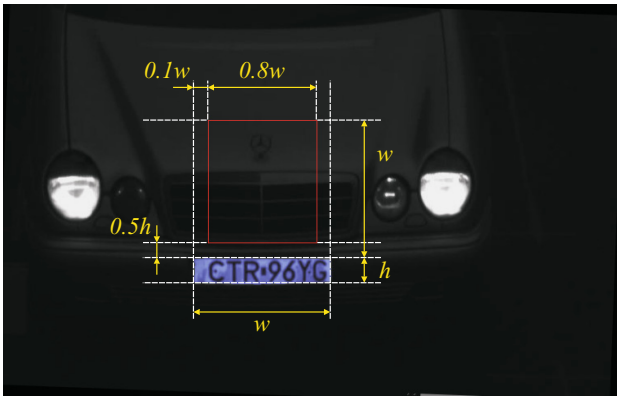

Fig. 6. Definition of a car mask ROI

2. For most of the car makes, the brand and other useful patterns are located in a rectangular region above a license plate. It has been defined based on plate sizes (Fig. 6).

The car mask ROI I_{cm} is cropped from the original image and subjected to a car brand search.

Car Brand ROI Detection. Determination of the car vertical axis of symmetry is crucial, because it crosses the brand in practically all car makes. Our recognition technique relies on textural features distinctive for multiple car makes, yet similar for various models of the same car producer. The car brand seems to be the best choice, also due to particular problems to be solved in a robust manner: diverse contrast, reflections and various appearance, possible lack of the entire car front in an image, etc.

The car brand detection is performed on I_{cm} in the following steps (Fig. 7):

1. Lowpass filtering of I_{cm} using 5×5 Gaussian kernel.
2. Adaptive contrast enhancement. Primary intensity scale is transformed into a narrower scale, based on the ROI histogram.
3. Calculation of the horizontal gradient summed across image rows. This is done iteratively on sub-images enlarged around vertical axis, as the brand

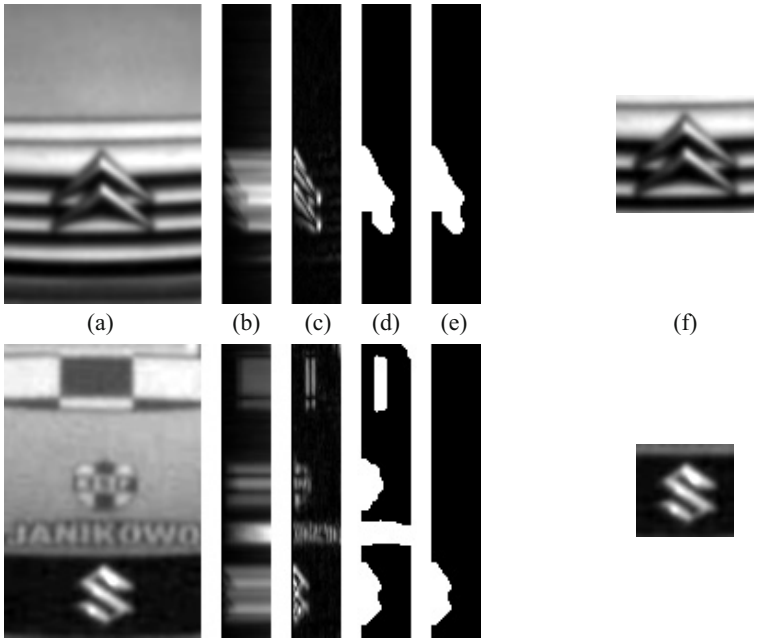

Fig. 7. Car brand ROI detection (2 cases); (a) car mask ROI with enhanced contrast, (b) auxiliary image J_{gs}, (c) vertical edges from (b), (d) initial and (e) final brand mask, (f) detected car brand ROI

pattern usually disrupts the symmetry more than other image regions. As a result, an auxiliary image J_{gs} is created, that might be compared to an image bent along the y-axis with vertical borders folded together (Fig. 7b).

4. Detection of vertical edges in J_{gs} in order to obtain rough boundaries of the car brand (Fig. 7c), grayscale dilation, Otsu thresholding [18], and morphological closing (Fig. 7d).
5. Since the resulting mask may contain false positive objects (bottom case in Fig. 7), additional operations are performed, if necessary. Namely: selection of objects adjacent to the left border (vertical axis in I_{cm}) and simple voting system based on object features.

The finally chosen object (Fig. 7e) determines the bounding box for a car brand in the mask ROI. It is adjusted not to exceed minimum/maximum assumed sizes and cropped to produce the final car brand ROI I_{cb} (Fig. 7f). Fig. 8 shows several images extracted using this methodology. A number of already mentioned concerns arise here: low contrast of the original image related to the JPEG compression leads to more or less significant distortions. All of them have to stay in mind while discussing the design and evaluation of the feature extraction and classification processes.

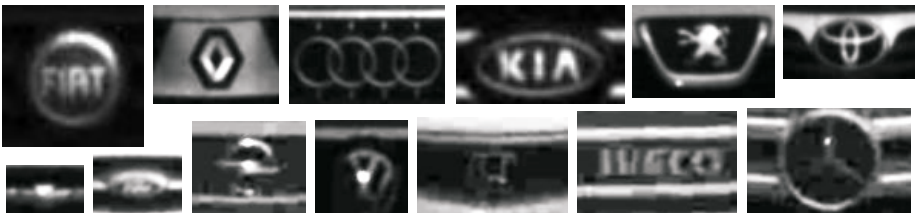

Fig. 8. Sample car brand ROI images arranged with decreasing quality

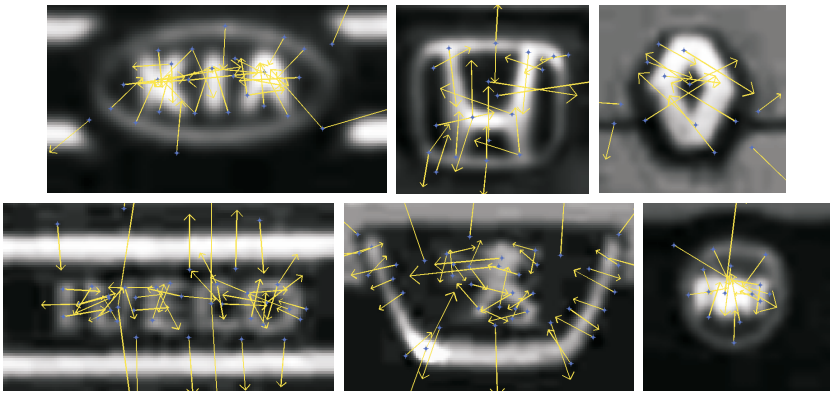

Fig. 9. Sample car brand ROI images with SIFT keypoints; each vector represents a single vector-like oriented keypoint, with initial point at keypoint location and vector length corresponding to scale size

2.2 Feature Extraction

The Scale Invariant Feature Transform (SIFT) is an automatic tool provided by Lowe [19, 20] for extraction of image features and classification by feature-based matching. It relies on detection and description of keypoints – selected extrema in the image scale space [21, 22]. Each keypoint is uniquely represented by its topological location, scale and orientation. Moreover, for each keypoint a feature vector of descriptors is generated to prepare the background for comparison and matching. Fig. 9 shows sample car brand images with SIFT keypoints indicated by vectors.

In this study, we have tested several potential ROI possibilities as a fundament of a SIFT-based object recognition, in terms of keypoints representativeness and repeatability, as well as system efficiency: the full image I, various modes and sizes of a car mask ROI and a car brand ROI, as described in previous section. As a result, a car brand ROI has been chosen after Gaussian filtering and a contrast enhancement (note Fig. 7f). Moreover, the ROI resampling is applied by bicubic interpolation, to preserve the length of the longer image side at 128 pixels. Such a solution enables a generation of ca. 10-60 keypoints per image, with an average amount at ca. 20.

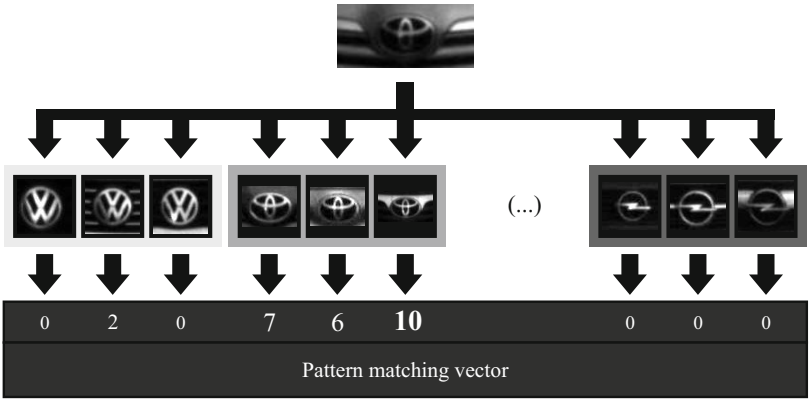

Fig. 10. Pattern matching scheme

2.3 Pattern Matching

The fundamentals of SIFT enable flexible, scale- and rotation-invariant analysis of correspondence between patterns in images. Two images might be compared by a distance measure between pairs of keypoints taken from both sources. Euclidean distance between normalized descriptor vectors is used: with keypoint k_i generated by the first image, a single keypoint l_j is chosen as a candidate match from a set of L keypoints describing the second image being the closest neighbour of k_i. To provide a full automation of matching process, a comparative system has been proposed to verify such candidate k_i-l_j match [20]: it is approved only if the ratio of distance measures of the closest and the second-closest keypoints does not exceed a predefined value of r_d. Authors report $r_d = 0.8$ to be the generally best suited value for object recognition by SIFT analysis. We have tested our system to adjust the r_d value and found 0.65-0.75 to be more profitable.

A set of car brand SIFT patterns have been prepared to stand for a reference database. It consist of $N_g = 25$-40 groups of $N_{ppb} = 3$-5 patterns – representatives of particular car makes. Engaging multiple patterns per brand makes the system more robust, but also slows it down.The first step of decision-making process is shown in Fig. 10. A car brand ROI extracted from the input image is first subjected to the keypoint extraction and then compared to each SIFT pattern in the reference database. Each comparison results in a particular measure – a number of matches obtained for a single pattern. With a distance ratio r_d set to a restrictive value of 0.7, most of the patterns produce zero matches. Only few of them generate a number of positive responses. At this point, all of them are collected in a pattern matching vector $\mathbf{M}$ and delivered to the classifier.

2.4 Classification

The search for a trade-off between false positive and false negative rates moved the distance ratio r_d into a relatively small, restrictive value. That, however,

results in a low number of matching keypoints and makes the classification challenging. Let us consider several rules leading to a final decision:

1. **The D1 rule (direct match)**. If the maximum number of matches in **M** is produced by a single pattern, it is accepted as the winner and its car make becomes the car make assigned to the input image. D1 is quite robust, yet there are too many cases with multiple patterns producing the maximum number of matches; thus, no decision is made.
2. **The D2 rule (mean brand match)**. The mean number of matches is computed within each group G_i of brand patterns and the largest value determines the decision. D2 requires as uniform distribution of distinctive keypoints among patterns as possible. Moreover, if a specific car make covers miscellaneous brand patterns, they should be grouped in separate clusters to avoid undesirable reduction of the group measure.
3. **The D3 rule (top-of-the-list match)**. Drawbacks of D1 and D2 rules might be reduced by the following approach. Let us monitor the best matching N_t patterns and collect the total number of matches within groups of patterns. Group with the largest number of matches is accepted as the winner. D3 shows its best performance, when $N_t = k_t \cdot N_{ppb}$, with $k_t \in [1, 2]$.

Each of the above rules has its pros and cons. In many cases (especially for D1), there is no individual match produced by a decision. The experiments have shown, that with a balanced reference database, D2 provides best results. Thus, D2 becomes final, if it is unequivocal. Otherwise, the remaining decisions are inspected as deep as necessary: if D3 yields the sole winner, then it is the final one; if not, D1 is checked. If there is no effective rule, the final decision is: "unrecognized".

3 Results

The system has been evaluated using a dataset of 1225 images. In each experiment it has been divided into the reference database and the testing set. Table 1 shows the total system efficiency as a function of the distance ratio r_d and the number of reference patterns per brand N_{ppb}. The optimum values for these parameters have been set to 0.7 and 5, respectively. As a result, 796 cases have been recognized correctly, 249 incorrectly, whilst 23 have been considered "unrecognized". Therefore, the total efficiency reached 74.53%, with 76.17% for all definite decisions. Tables 2 and 3 show detailed analysis of the system accuracy for all classification rules and specific car makes, respectively.

The system fails mainly due to: (a) visual image poorness leading into the unstable feature extraction; (b) similarities between some car brands at available image quality (e.g. Nissan-Opel; Ford patterns produce most false positive hits); (c) small size/poor textural content of the car brand; visual dominance of non-brand textures leading into unpredictable feature extraction (BMW, Volvo, Chevrolet); (d) insufficient level of the reference database representativeness. Since the reference database generation is based on the ROC analysis of all

Table 1. System efficiency as a function of parameters r_d and N_{ppb}; each cell has a format: recognition efficiency **total efficiency** hits/misses/unrecognized

	N_{ppb}								
r_d	3			4			5		
0.65	71.1%	**65.9%**	741/301/83	74.7%	**71.7%**	787/267/43	76.1%	**73.6%**	787/247/35
0.70	67.4%	**64.6%**	725/351/47	70.7%	**69.2%**	757/313/24	76.1%	**74.5%**	796/249/23
0.75	66.3%	**65.0%**	729/371/22	71.1%	**70.0%**	766/312/16	73.8%	**73.6%**	786/279/3
0.80	64.2%	**63.4%**	711/397/13	70.2%	**69.6%**	762/324/9	72.8%	**72.6%**	776/290/3

Table 2. Efficiency of the classification rules ($r_d = 0.7$, $N_{ppb} = 5$)

Rule	Recognition eff.	Total eff.	Hits/misses/unrecognized
D1	68.05%	**50.84%**	543/255/270
D2	80.37%	**73.22%**	782/191/95
D3	76.00%	**69.66%**	744/235/89
Final	76.17%	**74.53%**	796/249/23

Table 3. System efficiency for specific car makes ($r_d = 0.7$, $N_{ppb} = 5$)

Make	Efficiency			Make	Efficiency		
Suzuki	100.0%	**100.0%**	11/0/0	Ford	67.2%	**65.0%**	39/19/2
Mitsubishi	100.0%	**100.0%**	1/0/0	Hyundai	64.3%	**64.3%**	9/5/0
Seat	91.7%	**91.7%**	13/1/0	Citroen	71.1%	**64.0%**	32/13/5
Volkswagen	90.9%	**90.3%**	159/16/1	Toyota	66.7%	**64.0%**	32/16/2
Honda	87.5%	**87.5%**	14/2/0	Kia	75.0%	**60.0%**	3/1/1
Fiat	87.7%	**83.3%**	50/7/3	Iveco	38.5%	**33.3%**	5/8/2
Opel	82.4%	**81.2%**	108/23/2	Volvo	27.3%	**27.3%**	3/8/0
Renault	79.6%	**78.3%**	11/0/0	Nissan	20.0%	**20.0%**	2/8/0
Mercedes	78.2%	**78.2%**	68/19/0	BMW	18.8%	**17.6%**	3/13/1
Peugeot	75.5%	**75.5%**	37/12/0	Chevrolet	0.0%	**0.0%**	0/1/0
Audi	75.4%	**75.4%**	43/14/0	Chrysler	0.0%	**0.0%**	0/1/0
Skoda	68.0%	**67.3%**	70/33/1	Dacia	0.0%	**0.0%**	0/3/1
Mazda	66.7%	**66.7%**	6/3/0				

available samples of a given car make, the recognition is more reliable in case of strongly represented makes.

The system time consumpion is presented in Table 4, where detailed information on mean times for subsequent stages of an algorithm are shown. Evaluation has been performed on workstation with CPU @ 3.40GHz, 16GB RAM, 64-bitWindows 7 OS and Matlab 7.14. (R2012a). Due to the image size and its reduction during image preprocessing, features are extracted in milliseconds. Since all operations except pattern matching take less than half a second of total time, the real-time abilities of a system depend on pattern matching. Mean time for a single pattern-to-pattern matching is shown in 4^{th} and mean time for a single pattern-to-database matching – in 5^{th} column of Table 4. The latter depends directly on the number of patterns in the reference database; both – on the mean number of keypoints per pattern.

Table 4. System time consumption analysis. Subscripts of t refer to acronyms of subsequent stages from Fig. 1; pattern matching is evaluated using 2 measures: pattern-to-pattern ($t_{PaMa,1}$) and pattern-to-reference database (t_{PaMa})

N_{ppb}	t_{ImPr}	t_{FeEx}	$t_{PaMa,1}$	t_{PaMa}	t_{Cl}	t_{total}
3	0.361 s	0.059 s	0.006 s	0.520 s	0.001 s	0.941±0.030 s
4	0.362 s	0.056 s	0.006 s	0.690 s	0.001 s	1.108±0.034 s
5	0.363 s	0.056 s	0.006 s	0.837 s	0.001 s	1.256±0.039 s

4 Conclusion

A robust system for automatic car make recognition has been presented. Using the scale invariant pattern recognition and matching tool, it enables classification of various car makes from low contrast images. Simplicity and flexibility of the system architecture makes it easy to adapt for various types of images, specifically of a better quality. Each block of a system – image preprocessing steps, feature extraction, pattern matching, and classification – works independently and might be improved separately according to potential requirements. The multicriteria classification framework provides adaptable inference, based on various pattern matching conclusions. Its possible adaptability to changing conditions and image specification might rely on learning techniques, e.g. in the decision weighting selection.

Currently the system is able to recognize almost 30 different car makes with 75% accuracy. The recognizable car collection corresponds to the cars driving on Polish roads. Since the system uses a well defined, yet open knowledge database, clustered into car brand patterns, additional car makes may be recognized without any changes to the decision-making process. Potential replacements of patterns into different ones, yielding more distinctive features, is also easy to accomplish. The study on distinctiveness and repeatability of a reference database and system recognition abilities remains an open task for future research.

References

1. Du, S., Ibrahim, M., Shehata, M., Badawy, W.: Automatic License Plate Recognition (ALPR): A State-of-the-Art Review. IEEE Trans. Circuits and Systems for Video Technology 23(2), 311–325 (2013)
2. Gu, H., Lee, S.: Car Model Recognition by Utilizing Symmetric Property to Overcome Severe Pose Variation. Machine Vision and Applications 24 (2013)
3. Baran, R., Glowacz, A., Matiolanski, A.: The Efficient Real- and Non-Real-Time Make and Model Recognition of Cars. Multimedia Tools and Applications, 1–20 (2013)
4. Vapnik, V.N.: The Nature of Statistical Learning Theory. Springer (1995)
5. Kazemi, F.M., Samadi, S., Poorreza, H.R., Akbarzadeh-T, M.R.: Vehicle Recognition Using Curvelet Transform and SVM. In: Proc. of the 4th Int. Conf. on Information Technology, pp. 516–521 (2007)

6. Bernardo, J.M., Smith, A.F.M.: Bayesian Theory. Wiley Series in Probability and Statistics (1994)
7. Pearce, G., Pears, N.: Automatic Make and Model Recognition from Frontal Images of Cars. In: 8th IEEE International Conference on Advanced Video and Signal-Based Surveillance (AVSS), pp. 373–378 (2011)
8. Lee, H.J.: Neural Network Approach to Identify Model of Vehicles. In: Wang, J., Yi, Z., Żurada, J.M., Lu, B.-L., Yin, H. (eds.) ISNN 2006. LNCS, vol. 3973, pp. 66–72. Springer, Heidelberg (2006)
9. Munroe, D., Madden, M.G.: Multi-Class and Single-Class Classification Approaches to Vehicle Model Recognition from Images. In: Proc. Irish Conf. on Artificial Intelligence and Cognitive Science, pp. 93–102 (2005)
10. Petrovic, V.S., Cootes, T.F.: Analysis of Features for Rigid Structure Vehicle Type Recognition. In: British Machine Vision Conference (BMVC 2004), pp. 587–596 (2004)
11. Negri, P., Clady, X., Milgram, M., Poulenard, R.: An Oriented-Contour Point Based Voting Algorithm for Vehicle Type Classification. In: Proc. of the 18th Int. Conf. on Pattern Recognition, ICPR 2006, pp. 574–577 (2006)
12. Bay, H., Ess, A., Tuytelaars, T., Van Gool, L.: Speeded-Up Robust Features (SURF). Comput. Vis. Image Underst. 110(3), 346–359 (2008)
13. Iqbal, U., Zamir, S.W., Shahid, M.H., Parwaiz, K., Yasin, M., Sarfraz, M.S.: Image Based Vehicle Type Identification. In: Proc. of the Int. Conf. on Information and Emerging Technologies, pp. 1–5 (2010)
14. AbdelMaseeh, M., Badreldin, I., Abdelkader, M.F., El Saban, M.: Car Make and Model Recognition Combining Global and Local Cues. In: 21st International Conference on Pattern Recognition (ICPR), pp. 910–913 (2012)
15. Badura, S., Foltan, S.: Advanced Scale-Space, Invariant, Low Detailed Feature Recognition from Images – Car Brand Recognition. In: Proceedings of the 2010 International Multiconference on Computer Science and Information Technology (IMCSIT), pp. 19–23 (2010)
16. Bernsen, J.: Dynamic Thresholding of Gray-Level Images. In: Int. Conf. Pattern Recognition, vol. 2, pp. 1251–1255 (1986)
17. Shih, F.Y.: Image Processing and Mathematical Morphology: Fundamentals and Applications. CRC Press Inc. (2009)
18. Otsu, N.: A Threshold Selection Method from Gray-Level Histograms. IEEE Trans. Syst., Man, Cybern. 9(1), 62–66 (1979)
19. Lowe, D.G.: Object Recognition from Local Scale-Invariant Features. In: 7th Int. Conf. Computer Vision, pp. 1150–1157 (1999)
20. Lowe, D.G.: Distinctive Image Features from Scale-Invariant Keypoints. Int. Journal of Computer Vision 60(2), 91–110 (2004)
21. Lindeberg, T.: Scale-Space Theory: A Basic Tool for Analysing Structures at Different Scales. Journal of Applied Statistics 21(2), 224–270 (1994)
22. Lindeberg, T.: Scale-Space Theory in Computer Vision. Kluwer/Springer (1994)

Retina Analysis in Optical Coherence Tomography Images

Wojciech Wieclawek and Ewa Pietka

Silesian University of Technology, Faculty of Biomedical Engineering,
Zabrze, Poland
Wojciech.Wieclawek@polsl.pl
http://ib.polsl.pl

Abstract. A new method of the OCT (Optical Coherence Tomography) image analysis is presented. It concerns eyeball examination in ophthalmology. Adaptive noise suppression algorithm, based on anisotropic diffusion, followed by multistep image analysis approach yield a segmentation and measurement of various layers within the retina structure. The proposed segmentation approach utilizes different image processing techniques including watershed transform, Fuzzy C-Means and H-Minima Transform. Both, anatomical and pathological cases have been subjected to the analysis. The results have been evaluated by an expert.

Keywords: segmentation, OCT, retina, eyeball, retina layers, macular edema, cysts.

1 Introduction

Optical Coherence Tomography is a relatively novel, non-invasive optical technique applied in medicine, providing imaging of the internal structure of semitransparent objects. This technique plays an important role, mainly in ophthalmology and dermatology. In ophthalmology it is often employed for the diagnosis of pathologies, ocular diseases detection and therapy aiding.

The first laboratory model of the optical tomograph was created in 1993, while three years later the first commercial apparatus was manufactured. Fast and efficient progress in the construction of these devices (following the development of optoelectronics) has been observed for the last ten years. Faster and more selective lasers have been applied and new image reconstruction techniques have been used.

The OCT technology acquires high-resolution images of the eyeball structures. One of the significant drawbacks of the OCT techniques is a high image granularity. Therefore, image quality improvement phase is required before a suitable image analysis or image segmentation procedure is applied.

The image analysis phase in ophthalmology exams starts with the detection of the retina layers. The anatomy of retina consists of 12 layers oriented almost parallel to each other (Fig. 1). However, only 8 of them including full-thickness

E. Pietka, J. Kawa, and W. Wieclawek (eds.), *Information Technologies in Biomedicine, Volume 3*, Advances in Intelligent Systems and Computing 283,
DOI: 10.1007/978-3-319-06593-9_22,

macular hole, central serous chorioretinopathy, macular edema, epiretinal membrane, vitreomacular traction and retinitis pigmentosa and chloroquine retinopathy are important in the medical diagnosis [1]. The most difficult task in the OCT image analysis is to outline the layers and measure distances between them. The first stage requires a correct detection of the Internal Limiting Membrane (ILM). The task is not trivial in healthy patients and becomes much more difficult in pathological cases. Macular edema that causes cysts (fluid-filled areas) in the macula serves as an example [2].

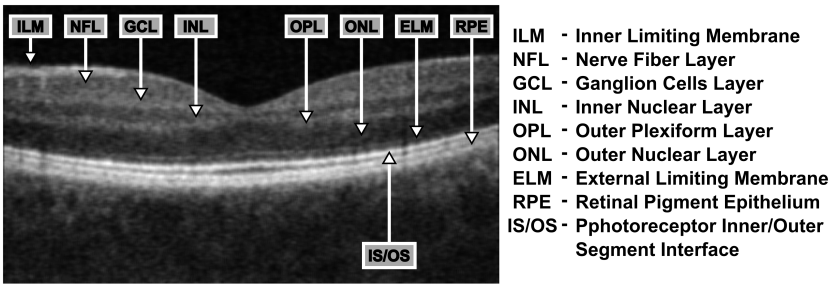

Fig. 1. The selected retina layers in OCT scan

Medical studies show that visual prognosis are based on cyst localization and cystoid fluid volume calculation. This problem induced motivation to develop a computer aided methodology dedicated to automatic cysts detection.

Already developed image analysis application are performed automatically [3–5] and semi-automatically [6]. Some authors [3, 6, 7] decompose the retina into cellular layers. Depending on the needs various number of layers is segmented using the 2D edge workflow [3], adaptive filtering technique with peak detection method [6] or active contour approach [4, 5]. A separate analysis of the anterior and posterior eye segment has also been reported [7]. Roychowdhury et al. [8] have followed the retina layers segmentation by the detection of the cystoid. Additionally, some studies [8] undertake the analysis of pathological cases like vitreomacular traction, drusen, macular holes (cysts) etc.

The paper is organized as follows. Section 2 presents the methodology divided into four parts: (1) image quality improvement, (2) segmentation of ILM layer and retina thickness measurement, (3) detection of NFL and RPE layers and (4) automatic cysts detection. Numerical results are discussed in Section 3. Section 4 concludes the paper.

2 Methodology

The methodology has been divided into several stages (Fig. 2). The image acquisition is followed by the quality improvement applied to every image in order to reduce the noise and granularity. Then, on the user request, the segmentation of the most important retina layers and cysts detection is performed.

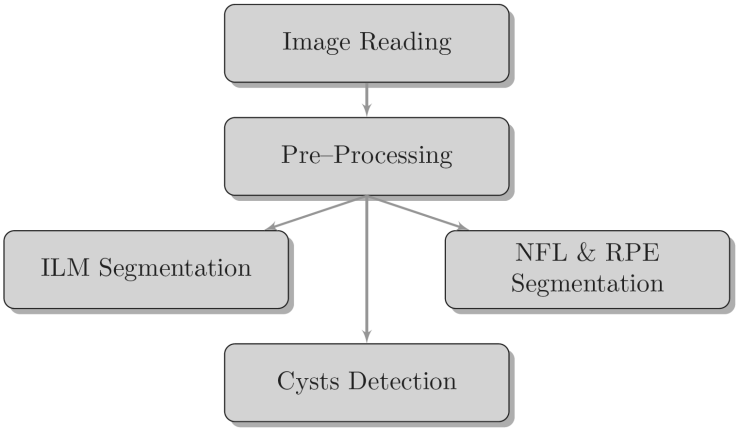

Fig. 2. Workflow

2.1 Pre-processing

Among filtering methods a technique preserving edges is required. The retina layers have to remain unblurred. Adaptive filtering is one of the methods that fulfils this demand. One of the possibilities is to use the diffusion process based on the heat equation. In the interior of a segment the nonlinear isotropic diffusion equation behaves almost like the linear diffusion filter but on the edges the diffusion is inhibited. Therefore, a noise occurring on the edges cannot be successfully eliminated by this process. To overcome this problem, the desired method should prefer diffusion along the edges to diffusion perpendicular to them. Anisotropic models take into account not only the modulus of the edge detector, but also its direction. Hence, such model behaves really anisotropically, suitably for this task. This method yields much better results, as the filtering kernel parameters are calculated separately for each image pixel. In this way impulse or Gaussian noise and small artefacts in the image can be removed without blurring off the relevant edges.

A mathematical model for diffusion is based on heat equation often presented as:

$$I^t(x, y, t) = div\left[c \cdot \nabla I\left(x, y, t\right)\right] \tag{1}$$

where div is a divergence operator, ∇ denotes a gradient operator and c is the diffusion coefficient. When c is constant (generally equal to 1) an analogous result as in convolving image $I(x, y)$ with a Gaussian of the standard deviation $\sigma = \sqrt{2 \cdot t}$ is obtained [9]. This case is known as a linear diffusion.

Using the linear heat equation as a paradigm Perona and Malik [10] have introduced a modification where diffusion coefficient c is a positive, monotonously decreasing function, which modulates the strength of the diffusion process [11]. Two functions for the diffusion coefficient are employed:

$$c_{PM_1}(x,y,t) = \frac{1}{1+\left(\frac{|\nabla I(x,y,t)|}{k_{PM}}\right)^2}, \tag{2}$$

$$c_{PM_2}(x,y,t) = e^{\left(\frac{|\nabla I(x,y,t)|}{k_{PM}}\right)^2}. \tag{3}$$

In this way nonlinear diffusion reducing the smoothing effect near edges is obtained.

The filtering model presented above is a isotropic case. However, in some applications the orientation has to be distinguished. Weickert in [12, 13] suggested an efficient anisotropic diffusion model. Anisotropic models do not only take into account the gradient magnitude $|\nabla I(x,y,t)|$, but also its direction. For this purpose the diffusion coefficient should be decomposed into a matrix:

$$c(x,y,t) = \begin{bmatrix} c_{11} & c_{12} \\ c_{21} & c_{22} \end{bmatrix}. \tag{4}$$

Additionally, eigenvectors v_1 and v_2 of the diffusion coefficient $c(x,y,t)$ satisfy the conditions:

$$v_1 || \nabla I_\sigma(x,y,t) \;\; v_2 \perp \nabla I_\sigma(x,y,t), \tag{5}$$

where $I_\sigma(x,y,t)$ is a Gaussian-smoothed version of $I(x,y,t)$ with kernel K_σ.

Most implementations of diffusion filters are based on finite difference methods. The partial derivatives are approximated by central difference quotients. Since the majority of retinal layers are aligned horizontally, this direction should be amplified during the calculation of partial differences by means of the differential calculus. Hence, not only the nearest neighbours are taken into consideration, but also remote neighbours, situated on the same horizontal line.

Benefits of application diffusion filter are clearly visible in figure (Fig. 3) shows images before and after adaptive filtering stage. Also visible in the figure image profiles (Fig. 3(c)–(d)) are a good indicator of pre-processing procedure. Main retina layers are easy to see while noise suppressing and edge locations preserving.

After the anisotropic diffusion stage, median spatial filtering is suggested as the final pre-processing operation before the segmentation stage. It is useful to suppress impulse noise.

2.2 Internal Limiting Membrane Segmentation

The preprocessed image features a sharpen retina region and suppressed background. At this stage a gradient-based watershed approach has been employed.

The watersheds idea is derived from the topography. It consists of areas splitting by finding watershed lines called also dams. These lines indicate the regions boundaries which are catchment basins for a drop of water falling on the area. Therefore, lines pass along the highest points of the land.

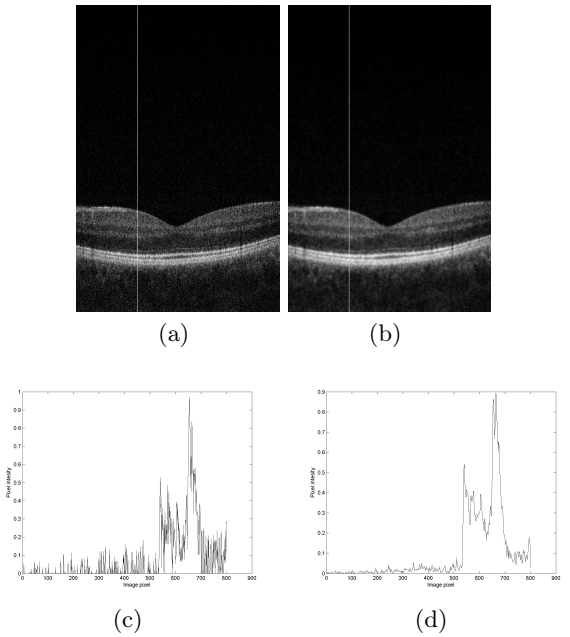

Fig. 3. Pre-processing based on anisotropic diffusion: (a) original image, (b) image after diffusion, image profiles of: (c) original image, (d) diffused image

In image processing the intensity value of each pixel stands for the height at this point. In order to assign the highest values to the edges the gradient preprocessed image is subjected to the watershed procedure, (Fig. 4).

Unfortunately, as is commonly known that the standard watershed algorithm generates a huge number of regions. To reduce the effect a modified version – the Marker-Controlled Watershed Segmentation – has been utilized.

This approach requires an additional image: marker image. Generally, it is a binary image indicating the regions of possible edge occurrence that can not be

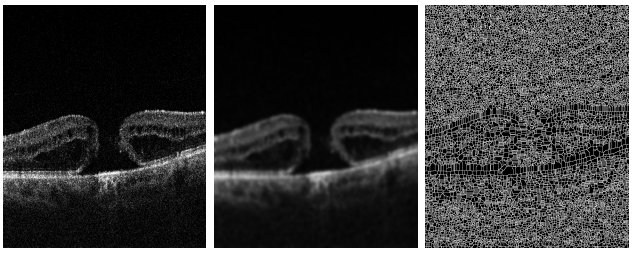

Fig. 4. Standard watershed algorithm: (a) original image, (b) pre-processed image, (c) final image

divided. To obtain a marker image, thresholding and mathematical morphology tools have been employed. The desirable shape of this binary image should indicate only the coarse of retina. Then, the watershed procedure does not generate any regions or edges inside the retina, yielding only the essential retina borders [14].

Additionally, the image gradient has to be modified. Since the gradient is very sensitive to local noise, the preprocessed image has been enhanced. This process sharpens clear edges while suppresses weak edges.

A way to obtain the final result of the ILM detection is shown in figure, (Fig. 5). Comparing images Fig. 4(c) and Fig. 5(c) one can see that the number of watershed regions is significantly reduced and any regions outside the marker have not been found. Such proceedings in most medical cases ensures a proper detection of Inner Limiting Membrane.

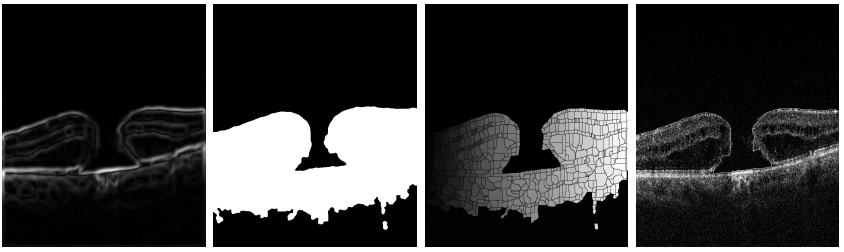

(a) (b) (c) (d)

Fig. 5. Detection of Inner Limiting Membrane: (a) modified gradient image, (b) marker image, (c) Marker-Controlled Watershed Segmentation, (d) final image

2.3 IS/OS and RPE Segmentation

Some of the clearly visible and diagnostically relevant layers are Photoreceptor Inner/Outer Segment Interface and Retinal Pigment Epithelium Layer. Anatomically both are rather parallel to ILM and are running across the whole retina visible in the OCT image. When the appearance and position of these layers are disturbed it reflects pathologies. Thus, the analysis has to start with the segmentation of IS/OS and RPE.

The proposed segmentation algorithm is based on the Fuzzy C-Means clustering (FCM) technique. Three classes that define low, medium and high intensity regions have been extracted, (Fig. 6(c)). The defuzzification is based on the maximum aggregate operator. As a result, a highlighted background, significant part of the retina, IS/OS and RPE layers have been separated. The latter region is the smallest surface area. Therefore, primarily the smallest class is chosen, (Fig. 6(d)). The shadows caused by blood vessels or a pathology are often the reason of discontinuity of the layer. Correction procedure that merges broken parts employs mathematical morphology operations. Moreover, the regions belonging to the same class, located outside segmented layers, are ignored, (Fig. 6(e)).

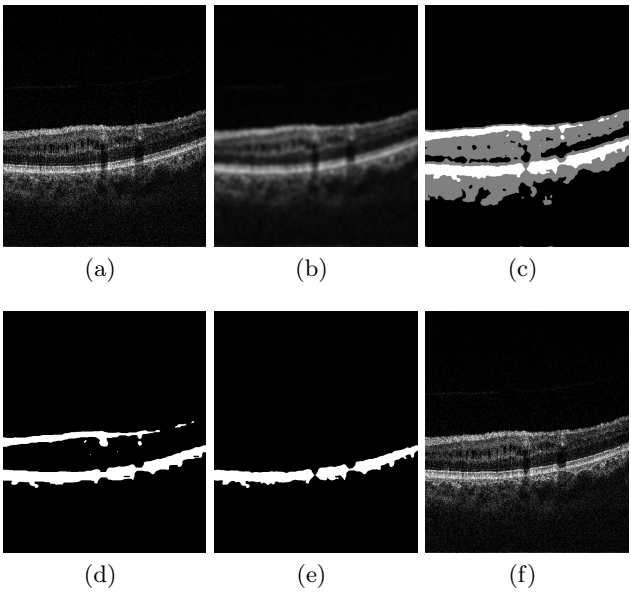

Fig. 6. Segmentation of IS/OS and RPE layer: (a) original image, (b) pre-processed image, (c) clustered image ($c = 3$), binary image (d) before, (e) after correction procedure, (f) final image

2.4 Cysts Detection

The final stage of the proposed methodology is an automatic cyst detection. This algorithm is processed in several stages. Image obtained after the anisotropic diffusion (Fig. 7(b)) is first subjected to grayscale morphology operations. Since the cysts resemble black blobs on relatively light background, H-Minima Transform has been used (Fig. 7(c)). Threshold H has been adjusted experimentally during the preliminary research performed on several OCT series. Thresholding function has yielded a binary image. Generally, except cysts other dark structures are segmented (Fig. 7(d)). To discard redundant regions, correction operations are employed. These manipulations rely on clearing border elements and deleting all structures which are located under the RPE layer. That is the brighter and thicker layer inside the retina that is possible to be detected (see Section 2.3). The final results are shown in Fig. 7(f).

3 Results

In this preliminary study the results have been evaluated by an expert. The proposed algorithm has been tested on a data set including anatomical cases as well as low quality images and pathologies. Among them are shadows from vasculature, vitreomacular traction, macular holes and cysts etc. The methodology has been compared with semi-manual segmentation that utilized Live-Wire

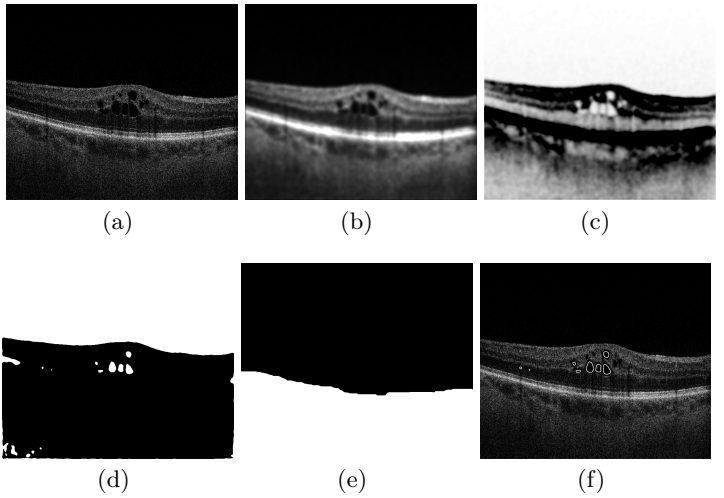

Fig. 7. The algorithm of cyst detection: (a) original image, (b) filtered image, (c) H-Minima Transform, (d) binary image, (e) segmentation of RPE, (f) final result

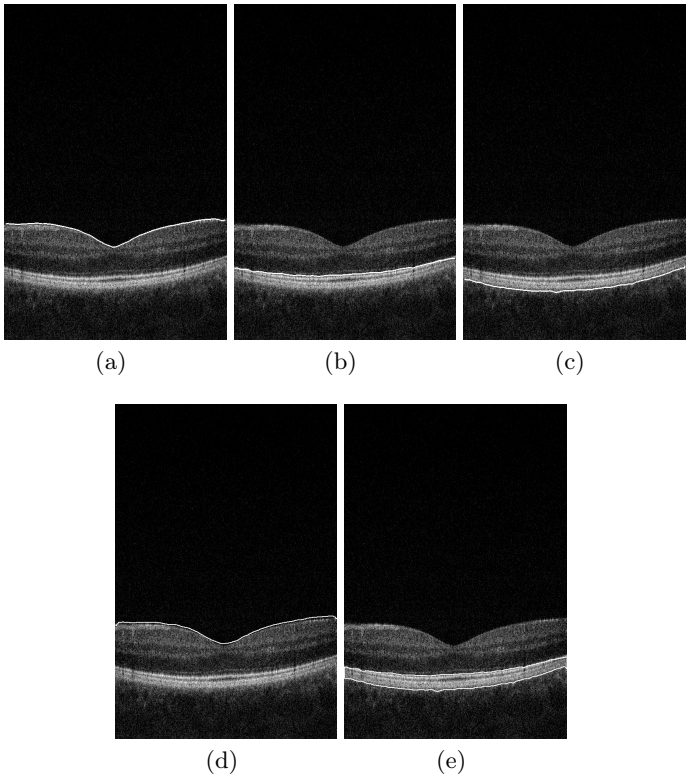

Fig. 8. Segmentation of ILM, IS/OS and RPE retina layer in anatomical case based on: (a)–(c) Intelligent Scissors, (d)–(e) proposed algorithm

(otherwise Intelligent Scissors) with FCM Clustering Algorithm [9]. Due to the possibility of manual correction of segmented edges, LW-FCM algorithm generate results accepted by an expert. Therefore, this method may be considered as a reference. Because each edge segmentation requires at least a pair of points each of the layers ILM, IS/OS and RPE is individually detected. Whereas in the proposed algorithm the segmentation of IS/OS and RPE layer proceeds simultaneously.

The simplest normal case is shown in Fig. 8. Both results obtained by the semi-automatic (based on Intelligent Scissors) and fully-automatic, proposed in this paper, algorithm have accepted by the expert.

The segmentation of images with vasculature shadows (Fig. 9) is also acceptable. However, it can be noticed that the proposed algorithm is more sensitive to shadows. Under certain conditions they may cause gaps within the layer.

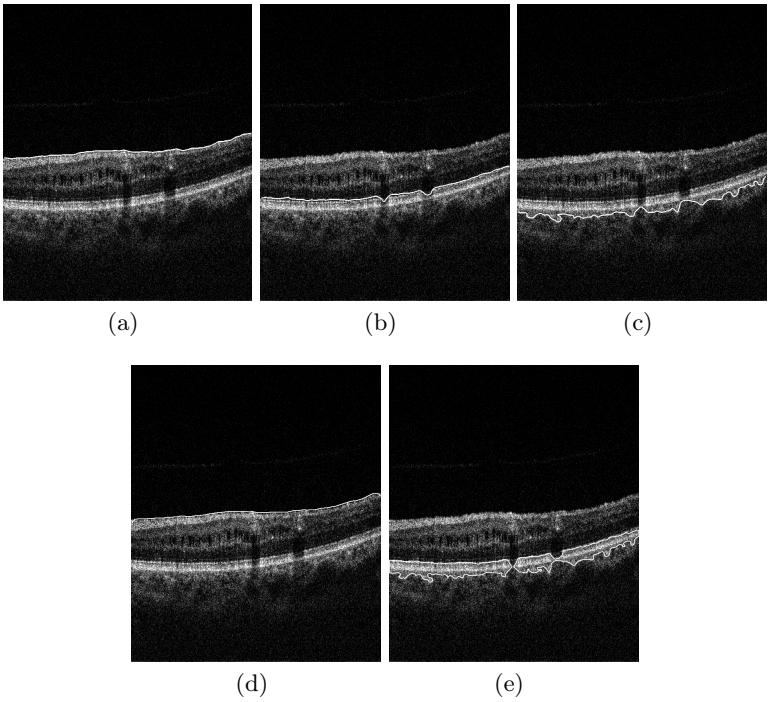

Fig. 9. Segmentation of ILM, IS/OS and RPE retina layer accept vasculature shadows based on: (a)–(c) Intelligent Scissors, (d)–(e) proposed algorithm

The OCT exam showing a macular hole has been segmented and results are given in Fig. 10. Automatic segmentation of ILM (Fig. 10(d)–(e)) is successful despite the ILM layer has a strongly complicated shape having sharp corners and rapid turns.

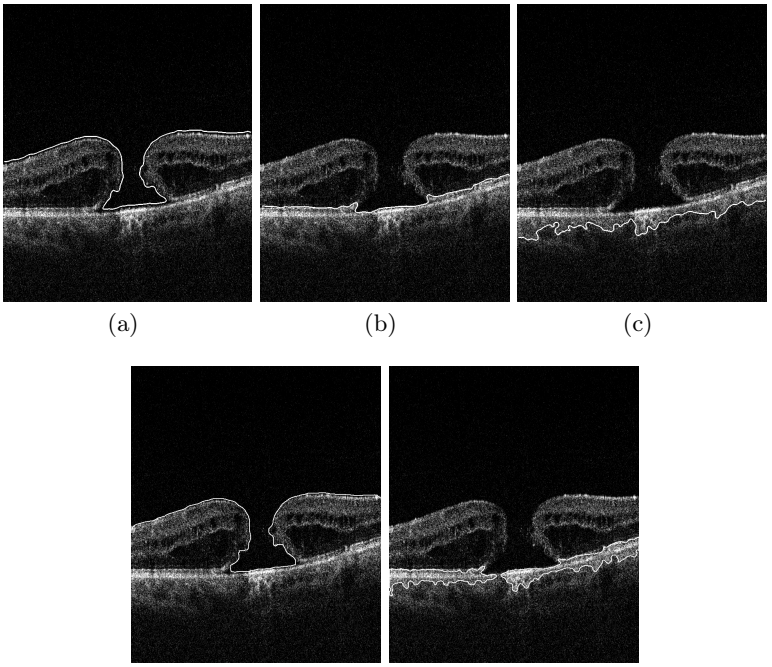

Fig. 10. Segmentation of ILM, IS/OS and RPE retina layer accept macular hole based on: (a)– (c) Intelligent-Scissors, (d)–(e) proposed algorithm

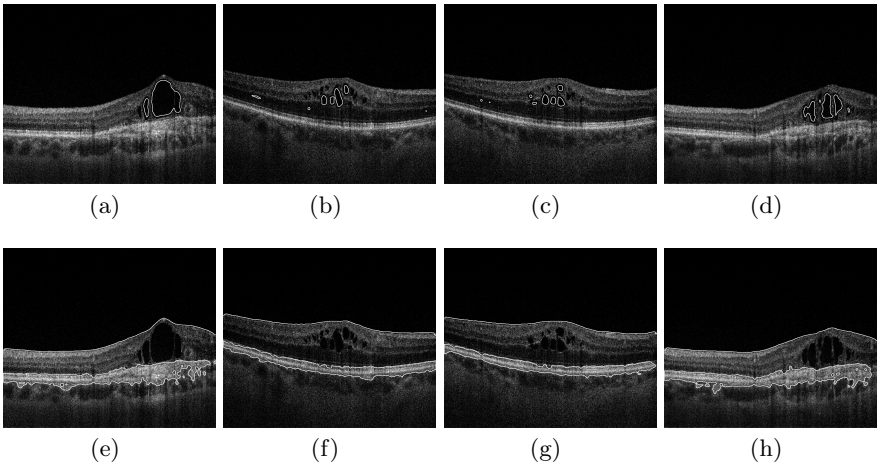

Fig. 11. Automatic cyst segmentation: (a)–(d) detection of all cyst, (e)–(h) ILM, IS/OS, RPE segmentation

The macula hole also caused some changes in IS/OS and RPE layers. Both layers are subjected to the analysis. This results in the lack of continuity. Nevertheless, the layers are delineated correctly.

The final test included automatic cysts detection from OCT series with different types, sizes and localization of cysts. As shown in figure (Fig. 11) despite aforementioned image properties correct cysts segmentation has been obtained.

Additionally, three basic layers ILM, IS/OS and RPE have been subjected to the segmentation procedure, (Fig. 11(e)–(h)). The results are acceptable to the expert. The figures (Fig. 11(e), (h)) show minor problems with segmentation near the image border. In this area the layers behave similarly to vasculature shadows.

A quantitative analysis on a large data base is being performed and will be published shortly.

4 Conclusion

Decomposition of the retina into its anatomical layers and detection of the cysts are medically important and frequently encountered in the literature as an unsolved problem. The fully automatic algorithm for the segmentation of layers and cysts presented in this paper follows this trend. The methodology is quite complex and is carried out in multiple stages, including pre-processing and segmentation of various retina layers.

Performance of the algorithm seems to be effective for OCT image series. The preliminary results are visually accepted by an expert. The algorithm returns the correct segmentation in many different medical cases including pathologies and low quality images. Comparison of the results with those obtained by a semi-automatic method (Intelligent Scissors), confirms its effectiveness and accuracy. The main advantage of the proposed algorithm is its automatic performance.

The proposed algorithm is the first step of the overall analysis of OCT scans of internal eyeball structure.

Acknowledgement. The authors would like to thank OPTOPOL Technology S.A. Zawiercie, Poland for valuable cooperation and providing the images.

References

1. Ko, T.H., Fujimoto, J.G., Schuman, J.S., Paunescu, L.A., Kowalevicz, A.M., Hartl, I., Drexler, W., Wollstein, G., Ishikawa, H., Duker, J.S.: Comparison of Ultrahigh- and Standard-Resolution Optical Coherence Tomography for Imaging Macular Pathology. Ophthalmology 112(11), 1922.e1–1922.e15 (2005)
2. Bernardes, R., Cunha-Vaz, J.: Optical Coherence Tomography: A Clinical and Technical Update. Biological and Medical Physics, Biomedical Engineering. Springer (2012)
3. Bagci, A.M., Shahidi, M., Ansari, R., Blair, M., Blair, N.P., Zelkha, R.: Thickness Profiles of Retinal Layers by Optical Coherence Tomography Image Segmentation. Amer. J. Ophthalmology 146(5), 679–687 (2008)

4. Cabrera, F.D., Villate, N., Puliafito, C.A., Rosenfeld, P.J.: Comparing Total Macular Volume Changes Measured by Optical Coherence Tomography with Retinal Lesion Volume Estimated by Active Contours. Invest. Ophthalmol. Vis. Sci. 45(5), 3072 (2004)
5. Yazdanpanah, A., Hamarneh, G., Smith, B., Sarunic, M.: Intra-Retinal Layer Segmentation in Optical Coherence Tomography Using an Active Contour Approach. In: Yang, G.-Z., Hawkes, D., Rueckert, D., Noble, A., Taylor, C. (eds.) MICCAI 2009, Part II. LNCS, vol. 5762, pp. 649–656. Springer, Heidelberg (2009)
6. Cabrera, F.D., Salinas, H.M., Puliafito, C.A.: Automated Detection of Retinal Layer Structures on Optical Coherence Tomography Images. Optics Express 13(25), 10200–10216 (2005)
7. Koprowski, R., Wróbel, Z.: Image Processing in Optical Coherence Tomography Using Matlab, Work funded by the Ministry of Science in 2009–2011, work number N518 427036, Sosnowiec (2011)
8. Roychowdhury, S., Koozekanani, D.D., Radwan, S., Parhi, K.K.: Automated Localization of Cysts in Diabetic Macular Edema Using Optical Coherence Tomography Images. Conf. Proc. IEEE Eng. Med. Biol. Soc. 2013, 14260–14290 (2013)
9. Wieclawek, W., Pietka, E.: Fuzzy clustering in Intelligent Scissors. Computerized Medical Imaging and Graphics 36(5), 396–409 (2012)
10. Perona, P., Malik, J.: Scale-Space and Edge Detection Using Anisotropic Diffusion. IEEE Trans. Pattern Anal. Mach. Intell. 12, 629–639 (1990)
11. Bao, Y., Krim, H.: Bridging Scale-Space to Multiscale Frame Analyses. In: Proceedings of the Acoustics, Speech, and Signal Processing, IEEE International Conference, ICASSP 2001, vol. 3, pp. 1953–1956 (2001)
12. Weickert, J.: A Review of Nonlinear Diffusion Filtering. In: ter Haar Romeny, B.M., Florack, L.M.J., Viergever, M.A. (eds.) Scale-Space 1997. LNCS, vol. 1252, pp. 1–28. Springer, Heidelberg (1997)
13. Weickert, J.: Anisotropic Diffusion In Image Processing. B.G. Teubner, Stuttgard (1998)
14. Wieclawek, W.: Detection of Retina Internal Limiting Membrane in Images. International Journal of Computer Assisted Radiology and Surgery, International Journal of CARS 7, S512 (2012)

Part II

Bioinformatics

Numerical Simulation of the Vascular Solid Tumour Growth Model and Therapy – Parallel Implementation

Krzysztof Psiuk-Maksymowicz, Damian Borys, Sebastian Student, and Andrzej Świerniak

Institute of Automatic Control, Silesian University of Technology, ul. Akademicka 16, Gliwice, Poland
{krzysztof.psiuk-maksymowicz,damian.borys,sebastian.student, andrzej.swierniak}@polsl.pl

Abstract. The main interest of the authors was to develop vascular solid tumour growth model, implement efficient numerical methods for simulations towards finding a solution of the model and trying to optimise influence of different types of therapies. A system of partial differential equations was introduced in order to simulate growth of tumour and normal cells as well as the dynamics of the diffusing nutrient and anti-angiogenic or chemotherapeutic factors within the tissue. Numerical simulations of our model were executed toward finding a suboptimal therapy protocol using stable FDTD (finite difference time-domain) method implementation. Combined therapy protocols has been selected by means of meta-heuristic algorithms. In this work we have selected genetics algorithms, ant colony algorithms and simulated annealing method. For those algorithms convergence to suboptimal solution was examined and compared, as well as average tumour size, average iteration count and average execution time.

Keywords: tumour growth model, parallel implementation, therapy optimisation, heuristic methods.

1 Introduction

Solid tumour progression is inseparably connected with vascular network surrounding its volume [1]. In order to grow, tumour needs oxygen and nutrition factors that will be delivered by the vascular network. It is crucial to consider the vascular network as well as its dynamics in a realistic models. In literature we can find many approaches of solid tumour modelling, among them one can distinguish models based on cellular automata [2], structured models [3], single cell-based models [4], and models based on physical mass and momentum equations [5]. In the process of carcinogenesis, it is possible to identify different phases of the (premalignant and malignant) tumour growth. There are many models which focus on the one particular phase, for example on the hiperplastic growth phase [6], tumour growth *in situ* [7], invasion [8], angiogenesis [9] or process of metastasis [10].

E. Pietka, J. Kawa, and W. Wieclawek (eds.), *Information Technologies in Biomedicine, Volume 3*, Advances in Intelligent Systems and Computing 283,
DOI: 10.1007/978-3-319-06593-9_23,

The microvascular network plays crucial role in development of the solid tumours. It constitutes a source of the nutrient for the tumour and enables its permanent growth. However, due to fast metabolism of the tumour cells, hypoxic regions may occur causing creation of necrotic lesions. The phenomenon of hypoxia is important because it may lead to the process of angiogenesis and simultaneously is a reason of lower efficiency of different therapies. The model taking into consideration above mentioned processes was developed and it's numerical solution has been performed. Independently of the type of mathematical model, calculation of its solution is always time and resources demanding (computations time or computer memory) [11]. Presented model of vascular tumour growth is described by set of partial differential equations. We have implemented FDTD (finite-difference time-domain) numerical method which was already shown to produce numerical stable solutions. In order to make calculations in larger space which include complex three-dimensional structure of capillaries a single processor computers are not sufficient. Hence there is need to use more computing power to obtain the results in a reasonable time. We are comparing the implementation of the numerical method for multi-computer system (cluster) with the message passing programming paradigm (MPI) [12] with massively parallel computing implementation using graphic computing accelerators (Nvidia CUDA) [13].

2 Materials and Methods

2.1 Model Simulations Material

Numerical simulations has been done on the basis of syntetic micro environment created to reflects real environment in the tissue. Except of the normal cells fraction, tumour cells fraction and ECM (see the model in Sec. 3), vascular network has been allocated, that underlies the distribution pathways for nutritients, oxygen and therapeutic agents. Parameters of the model has been based on a literature.

2.2 Numerical and Parallel Computation Methods

In order to find solution of the mathematical model appropriate numerical methods have been used. Among the explicit numerical methods one-step Lax-Wendroff method [14] for transport equations was chosen, and standard forward time centered space for the diffusion equations. Computations have been done in Mathworks Matlab for testing purposes (finding optimal and stable numerical method, non-parallel implementation), with use of C language for parallel version using MPI (Message Passing Interface) libraries, and CUDA based implementation.

2.3 Optimisation Methods

Suboptimal therapy protocols have been investigated by means of selected metaheuristic algorithms: simulated annealing (SA) [16], genetic algorithm (GA) [18]

and ant colony (AC) [17]. To compare computation time and the accuracy of the solution for each studied method selected performance indexes have been examined: tumour size, iteration count to reach the end of the algorithm and execution time. We define also the performance index as the measure of efficacy of the therapy treatment in a finite horizon T_{max} as

$$J = \int a(T_{max})d\Omega + w_1 \int_0^{Tmax} d_{ch}(t)dt + w_2 \int_0^{Tmax} d_a(t)dt, \qquad (1)$$

where Ω denotes the spatial domain; w_1 and w_2 denotes coefficients for the total amount of the delivered chemotherapeutic and antiangiogenic drug, respectively. The optimisation problem is to minimize the performance index under the additional constraints. They concern the maximum amounts of the delivered drugs within the computational time step:

$$0 \leq d_{ch} \leq D_{ch,max}, \qquad 0 \leq d_a \leq D_{a,max}. \qquad (2)$$

All the calculations were carried out using the computer cluster Ziemowit (`http://www.ziemowit.hpc.polsl.pl`) funded by the Silesian BIO-FARMA project No. POIG.02.01.00-00-166/08 in the Computational Biology and Bioinformatics Laboratory of the Biotechnology Centre in the Silesian University of Technology. Every node used for MPI calculations has 2 six-cores Intel Xeon CPUs and 36 GB RAM. Computer for CUDA computing was equipped with Nvidia Tesla C2075 graphic accelerator and Intel Xeon processor.

3 Mathematical Model

A set of partial differential equations was introduced in order to simulate growth of tumour and normal cells as well as the dynamics of the nutrient, hypoxic factors, anti-angiogenic and chemotherapeutic particles diffusing within the tissue. Different approaches are used for modelling the solid tumour growth. We use continuous description of the model, but unlike in [15] we do not distinguish proliferative, quiescent and apoptotic cells. Cell behaviour is determined by the oxygen concentration within the tissue. The equations for the cell dynamics originate from the multiphase theory [19, 20]. The main constituents of the multiphase part of the model are normal cells, tumour cells and extracellular matrix (ECM). Henceforth variable n denotes volume fraction of normal cells, a denotes volume fraction of tumour cells, and m denotes volume fraction of the ECM. Other continuous variables considered as volumeless includes: variable c stands for oxygen concentration, variable d_a stands for the concentration of anti-angiogenic treatment agent, variable d_{ch} stands for the concentration of chemical treatment agent, and variable p stands for hypoxic factor, *i.e.* vascular endothelial growth factor (VEGF). Additionally in the model exists discrete variable e denoting occurrence of blood capillaries in the space (binomial type of the variable). For the sake of simplicity, volume fraction of ECM is assumed to be homogeneous and constant. The model, in which the dynamics of the ECM

is investigated, can be find in work by Psiuk-Maksymowicz [20] (see the content for more models). The overall volume fraction occupied by the cells spread on the ECM must satisfy the inequality $\psi = n + a + m \leq 1$ to be consistent with the overall physical meaning. In order to close the model, the porous media assumption is applied [21]. In order to provide true physiological picture – spatial heterogeneity of concentration of the nutrient, hypoxic factors and xenobiotics is ensured. Mathematical model consists of six PDE equations:

$$\begin{cases} \frac{\partial n}{\partial t} = \nabla \cdot (n\, K\, \Sigma' \nabla \psi) + nF(c - c_P)[\alpha_n(1-\psi) - k_n d_{ch}] - \gamma_n nF(c_A - c), \\ \frac{\partial a}{\partial t} = \nabla \cdot (a\, K\, \Sigma' \nabla \psi) + aF(c - c_P)[\alpha_a(1-\psi) - k_a d_{ch}] - \gamma_a aF(c_A - c), \\ \frac{\partial c}{\partial t} = D_c \nabla^2 c - (k_{n_P} n + k_{a_P} a)F(c - c_P) - (k_{n_Q} n + k_{a_Q} a)F(c_P - c)F(c - c_A) + S_1(e), \\ \frac{\partial p}{\partial t} = D_p \nabla^2 p + \alpha_p F(c_A - c)(n + a) - \rho_p\, p\, e - \lambda_p p, \\ \frac{\partial d_a}{\partial t} = D_{da} \nabla^2 d_a + S_2(e) - k_{da} d_a e - \lambda_{da} d_a, \\ \frac{\partial d_{ch}}{\partial t} = D_{dch} \nabla^2 d_{ch} + S_3(e) - k_{dch}(n + a)F(c - c_P) - \lambda_{dch} d_{ch}. \end{cases} \tag{3}$$

where K is a coefficient related to the permeability of the medium, Σ is a stress function. Growth of the cells is of logistic type, where α_n and α_a stands for growth rate for normal and tumour cells, respectively. Normal and tumour cells undergo apoptosis with γ_n and γ_a rates, respectively. Growth and degradation of the cells is dependent on the oxygen availability, therefore in both terms sigmoid function $F(\cdot)$ is present. In growth terms it depends on the proliferation oxygen concentration c_P, and in degradation terms it is dependent on the apoptotic oxygen concentration c_A. Parameters k_n and k_a specify effectiveness of the chemotherapy on normal and tumour cells, respectively. Further four reaction-diffusion equations determine dynamics of volume-less model constituents; D_c, D_p, D_{da}, D_{dch} denote oxygen, VEGF, anti-angiogenic agent and chemotherapeutic agent diffusion coefficients, respectively. Source terms are denoted by $S_i(\cdot)$, $i \in \{1, 2, 3\}$ functions dependent on the position of the blood vessels. VEGF particles are produced with a rate α_p, and decay spontaneously or due to meeting with an endothelial cell. Similarly the drug particles decay spontaneously or due to meeting with selected cells (endothelial cells for the anti-angiogenic drug and proliferating cells for the chemotherapeutical drug).

In described model the velocity of the cells depend on the stress exerted within the tissue. Different types of stress-volume ratio relations can be taken into consideration. The simplest function characterising response to the stress (*c.f.* [21]) is such, that below the value ψ_0 it vanishes, increases for $\psi > \psi_0$, and tends to infinity as $\psi \to 1$. Such a function can have a form:

$$\Sigma(\psi) = E(1 - \psi_0) \left(\frac{\psi - \psi_0}{1 - \psi} \right)_+, \tag{4}$$

where $(f)_+$ denotes the positive part of f and E is the value of the derivative in$\psi = \psi_0$, a sort of Young's modulus for moderate compressions.

4 Results

Example of model result with the drugs acting on healthy and tumour cells can be seen in pictures collected in Figure 1. The colors correspond to density of the cells after anti-angiogenic therapy (top row) and after chemotherapy (bottom row). The cells in the top row develop preferentially around the vessels, whereas in bottom row cells are situated in distant regions due to action of chemotherapeutic drug.

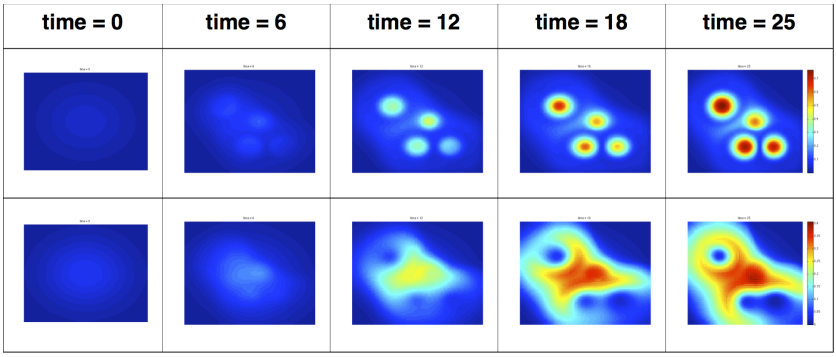

Fig. 1. Spatial changes of the cellular density due to anti-angiogenic therapy (top row) and chemotherapy

4.1 Parallel Implementation Methods Comparison

Main results of our work presents comparison of the speedup of parallel implementation with the basic Matlab computations (Fig. 2).

We have compared the speedups of MPI implementations with different domain calculation sizes (100x100 and 400x400). The speedup is increasing up to about 12 cores then is slightly lower. This is caused by the architecture – single computing machine has 12 physical cores and when increasing this number we are causing that processes needs to communicate through the computer network which is always slower than shared memory architecture (even for Infiniband QDR connection). When spatial computational domain was increased 16 times the speedup increased up to 8 and the absolute computation times ratio increased maximum to about 10 times. Comparing MPI (with 11 cores) and CUDA (Fig. 4) we can see that the speedup is higher for smaller domains but when increased the performance is significantly lower.

4.2 Therapy Protocol Optimisation

In this section we compare the usage of meta-heuristic methods (simulated annealing (SA), genetic algorithm (GA), ant colony (AC)) toward finding a suboptimal therapy protocols. One of the examples of the final suboptimal protocol

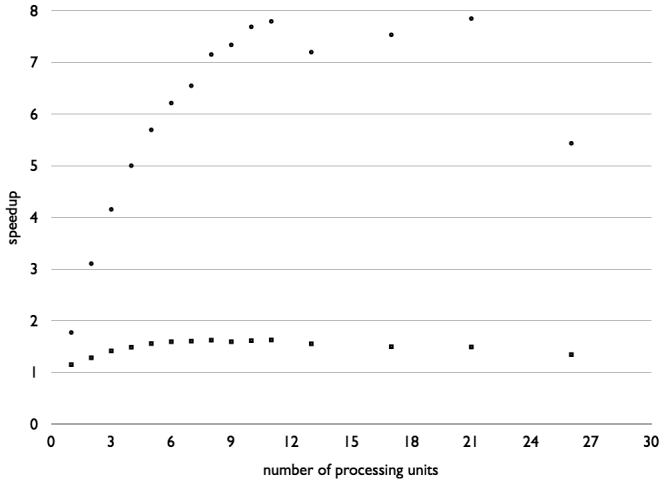

Fig. 2. Speedup of the calculations time in dependence with the number of processing units. Two series are compared - with smaller spatial domain (100x100, boxes) and with large domain (400x400, circles).

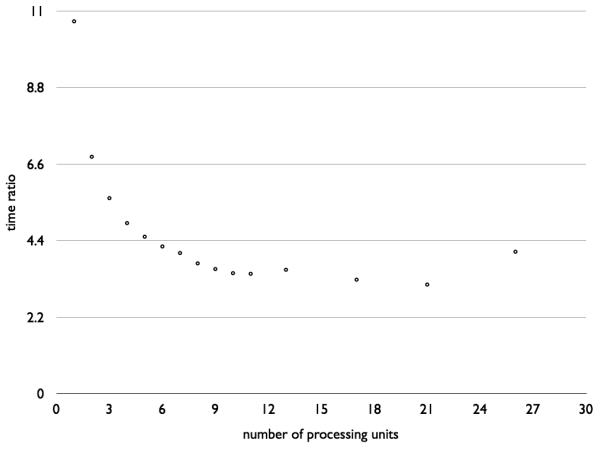

Fig. 3. Time ratio after 16 times increase of the spatial domain (T400/T100) depending the number of processing units

for chemo and anti-angiogenic therapy is presented in Figure 5. This plot shows a sequence of two combined therapies (alternation was not observed).

The optimisation algorithms were compared in terms of the number of iterations, the execution time, and the overall tumour size (see Fig. 6).

In Figure 7 all three methods has been compared for how fast they reach a suboptimal performance index leading to the optimal therapy schedule. In this

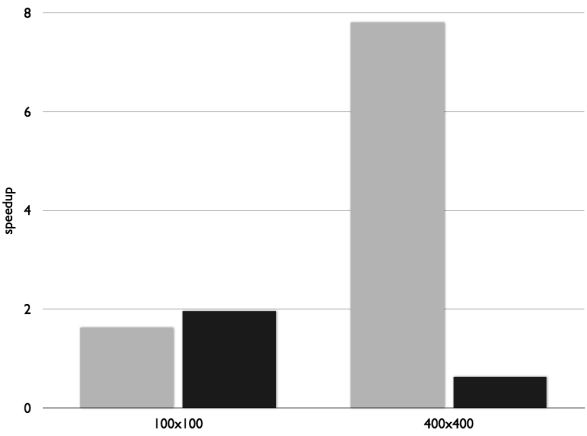

Fig. 4. Speedup of MPI with 11 cores (light grey colour) and CUDA (black) implementation for different spatial domain sizes (100x100 and 400x400)

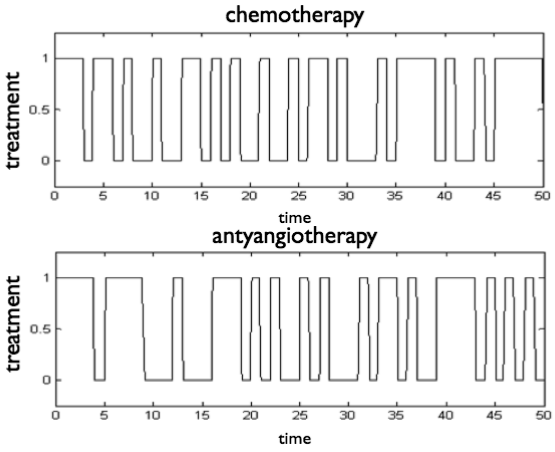

Fig. 5. Example of suboptimal solution for chemotherapy (upper) and antiangiogenic therapy

plots we represents the best protocol and dotted line represents average solution. As one can notice the GA method reach the best (minimal) performance index.

5 Discussion

For optimisation of the therapy in a finite time horizon we include implementation of meta-heuristic methods as simulated annealing, genetic algorithms and

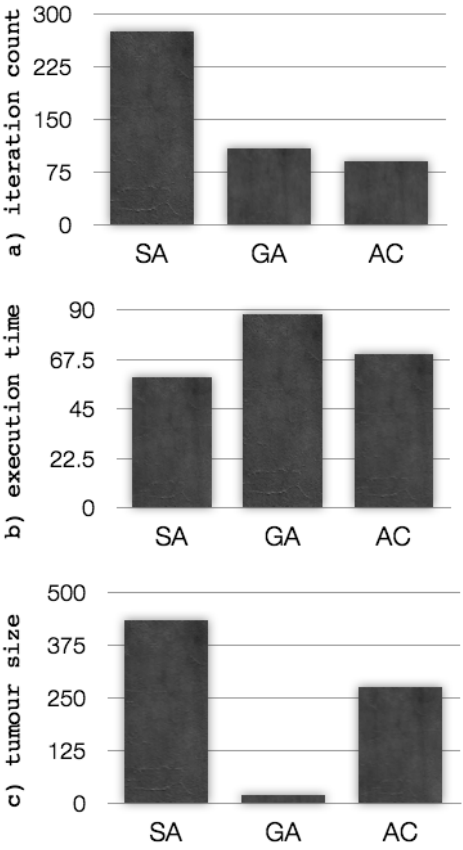

Fig. 6. Comparison of iteration counts (a), execution time (b) and the tumour size (c) for selected optimisation algorithms (SA, GA, AC)

ant colony optimisation to find the optimal solution. Presented results show that in spite of the fact that GA algorithm was slightly slower than the remaining algorithms, it demonstrated the best results in respect to the final tumour size. GA method has reached minimal performance index with the lowest tumour size (see Fig. 6). However regarding the protocol solution we couldn't find any general pattern for the treatment that would be a clear and simple indication for clinical use.

These results are inherently connected with multiple model simulation so even apparently small speedup of execution time multiplicated during optimisation step will contribute significantly to the overall execution time. Parallelization of presented numerical simulations serves us not only to study different methods of parallelization performance but it's a crucial step toward trying to find optimal therapeutic protocols of simultaneously implemented chemo- and anti-angiogenic therapies.

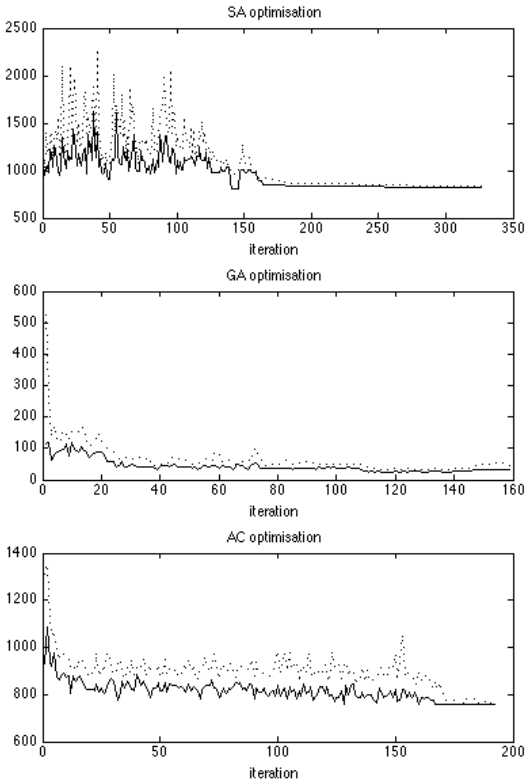

Fig. 7. Convergence to suboptimal solution, SA (upper), GA (middle) and AC (lower); dotted line presents mean solution while solid line is the best

Presented parallelization study results have show that when the computing problem is relatively small using MPI technique and the usage of big cluster architecture is not the best choice as long as the speedup is figurative, however using CUDA architecture we can obtain very interesting results. With the growth of the size of the problem CUDA meets it's limitations related to memory bandwidth limits and MPI implementation seems to be reasonable choice. We could also observe that if the problem can be solved using single multi-core machine it will give us slightly better performance than using more machines. While switching the computations of the model to the third spatial dimension only the MPI technique should be considered.

Acknowledgement. This work was supported by the National Science Centre (NCN) in Poland under Grant No. N- N519-647840.

References

1. Araujo, R.P., McElwain, D.L.S.: A history of the study of solid tumour growth: the contribution of mathematical modelling. Bull. Math. Biol. 66, 1039–1091 (2004)
2. Dormann, S., Deutsch, A.: Modeling of self-organized avascular tumor growth with a hybrid cellular automaton. Silico Biology 2, 393–406 (2002)
3. Billy, F., Clairambault, J., Delaunay, F., Feillet, C., Robert, N.: Age-structured cell population model to study the influence of growth factors on cell cycle dynamics. Math. Biosci. Eng. 10, 1–17 (2013)
4. Rejniak, K.A.: A single-cell approach in modeling the dynamics of tumor microregions. Math. Biosci. Eng. 2, 643–655 (2005)
5. Lowengrub, J.S., Frieboes, H.B., Jin, F., Chuang, Y.-L., Li, X., Macklin, P., Wise, S.M., Cristini, V.: Nonlinear modelling of cancer: bridging the gap between cells and tumours. Nonlinearity 23, R1–R9 (2010)
6. Mamontov, E., Koptioug, A., Psiuk-Maksymowicz, K.: The minimal, phase-transition model for the cell-number maintenance by the hyperplasia-extended homeorhesis. Acta Biotheor. 54, 61–101 (2006)
7. Bankhead III, A., Magnuson, N.S., Heckendorn, R.B.: Cellular automaton simulation examining progenitor hierarchy structure effects on mammary ductal carcinoma in situ. J. Theor. Biol. 246, 491–498 (2007)
8. Kam, Y., Rejniak, K.A., Anderson, A.R.: Cellular modeling of cancer invasion: integration of in silico and in vitro approaches. J. Cell Physiol. 227, 431–438 (2012)
9. Chaplain, M.A., Anderson, A.R.: Mathematical modelling, simulation and prediction of tumour-induced angiogenesis. Invasion Metastasis 16, 222–234 (1996)
10. Sherratt, J.A.: Predictive mathematical modeling in metastasis. Methods Mol. Med. 57, 309–315 (2001)
11. Evans, G., Blackledge, J., Yardley, P.: Numerical Methods for Partial Differential Equations. Springer, London (1999)
12. The Message Passing Interface (MPI) standard, `http://www.mcs.anl.gov/research/projects/mpi/`
13. Nvidia CUDA Toolkit, `https://developer.nvidia.com/cuda-toolkit`
14. Larsson, S., Thomee, V.: Finite Difference Methods for Hyperbolic Equations. Springer, Heidelberg (2003)
15. Macklin, P., Lowengrub, J.: Nonlinear simulation of the effect of microenvironment on tumor growth. J. Theor. Biol. 245, 677–704 (2007)
16. Kirkpatrick, S., Gelatt Jr, C.D., Vecchi, M.P.: Optimization by simulated annealing. Science 220, 671–680 (1983)
17. Bonabeau, E., Dorigo, M., Theraulaz, G.: Swarm Intelligence: From Natural to Artificial Systems. Oxford Univ. Press, New York (1999)
18. Cooper, L., Steinberg, D.: Introduction to Methods of Optimization. W. B. Saunders, Co., Philadelphia (1970)
19. Byrne, H., Preziosi, L.: Modelling solid tumour growth using the theory of mixtures. Math. Med. Biol. 20, 341–366 (2003)
20. Psiuk-Maksymowicz, K.: Multiphase modelling of desmoplastic tumour growth. J. Theor. Biol. 329, 52–63 (2013)
21. Ambrosi, D., Preziosi, L.: On the closure of mass balance models for tumor growth. Math. Models Meth. Appl. Sci. 12, 737–754 (2002)

Searching for Malignancy in Automated Urological Cytology

Boguslaw D. Pietka and Annamonika Dulewicz

Laboratory of Fundamentals of Computer-Aided Image Diagnostics
lnstitute of Biocybernetics and Biomedical Engineering, Polish Academy of Sciences
Ks.Trojdena 4, 02-109 Warsaw, Poland
darek@ibib.waw.pl
http://www.ibib.waw.pl

Abstract. There is a great advantage of early detection of bladder cancer on the basis of non-invasive voided urine cytological investigations. However, in spite of diagnostic potential of the method for discovering malignancy associated changes in cells before they start to form a tumor, the procedure seems to be underestimated by physicians as there is a common view its sensitivity, especially for early stages of the cancer, is relatively low. In this paper we are trying to support pathologists in making such diagnosis more accurate and reliable.

Keywords: cancer, digital cytology, content-based image retrieval.

1 Automated Cytological Investigations

Subjects related to automation and computer-aided support for cytological examination of biomedical smears are widely present in scientific projects and literature. In many cases this is the only method for early detection of a disease, especially cell cancerous transformations [3, 4]. Additionally, cytological screening is capable of detecting cancerous cells before they start to form a tumor or even allows identifying subtle precancerous changes of cell morphology known as dysplasia [2]. Although new technologies, related to biomarkers, emerging from molecular and cellular biology, turns out promising in identifying early stages of tumor progression, microscopic examination of smears is going to remain the standard procedure for grading tumors [1]. Actually, for a wide application of early detection of dangerous pathological changes, it is necessary to implement efficient mass screening projects. It is of particular importance when the collection of diagnostic material may be performed by means of a non-invasive procedure (e.g. blood, saliva, urine) as the cytological screening in such cases may become a part of a standard, preventive, medical investigation. On the other hand, the number of qualified cytopathologists will never be sufficient to manage mass screening tasks manually. Therefore, computers and reliable image processing software should be explored to support the work.

Computer-aided diagnostic concepts functionally fall into two categories, which are not mutually exclusive:

E. Pietka, J. Kawa, and W. Wieclawek (eds.), *Information Technologies in Biomedicine, Volume 3*, Advances in Intelligent Systems and Computing 283,
DOI: 10.1007/978-3-319-06593-9_24,

1. INDEPENDENT. Samples are scanned automatically and each of them is assigned a score basing on the potential for abnormalities as ascertained by the computer program. Those slides which are assigned a score higher than a predetermined threshold are subsequently re-screened by humans. Those which are assigned a score below the threshold are signed out as NRI (No Review Indicated) without human examination.

2. INTERACTIVE. The slide scanning process is also conducted automatically. However, after potentially abnormal cells or cell clusters are detected they are presented on a computer screen. Cytotechnologists and/or pathologists review these slide "abstracts" and make decision whether manual screening is required or not. If the decision is not to review a slide it is signed out as negative with no further follow-up.

The result of using either type of device, independent or interactive, or the two in combination, is always the same: selection of a group of slides which are subjected to one or more human screenings and a group of slides which are signed out as NRI and which are never manually screened by a human for the presence of cancerous symptoms. Both ideas, independent and interactive, are studied and implemented in our laboratory. This paper, however, is devoted to the latter one – an interactive approach. In the next sections you are going to find several arguments exposing the nature and advantages of interactive solution.

2 Urinary Bladder Cancer

In most leading countries efficacy of cancer diagnosis and therapy is considered an indicator of civilization progress. On the other hand, experts from the Polish Union of Oncology alarm that growth of morbidity from tumors in Poland outstrips increase of population. As bladder cancer is not widely discussed, people may believe it is a rare disease. Yet, this form of cancer occurs more often than one might think. In fact, it is the fourth most common cancer among men and the ninth most common among women in Poland (as well as in the United States and European countries). Bladder cancer is also the sixth most common reason of deaths among men. Fortunately, the majority of bladder tumors do not grow rapidly. Average period of disease development is evaluated from 10 to 30 or even 40 years [2]. Therefore, growths can be treated without major surgery. Thus, most patients with bladder tumors are not at risk of developing a cancer that will spread and become life-threatening if one but crucial condition is met – it must be recognized in early stage of development. When found and treated in the early stages, even cancerous bladder tumors are not likely to spread (Fig. 1).

3 Diagnostics – Current State and Perspectives

In lack of efficient mass screening programs it is usually a patient who discovers first symptoms of pathology. And so, hematuria (blood in urine) is the most

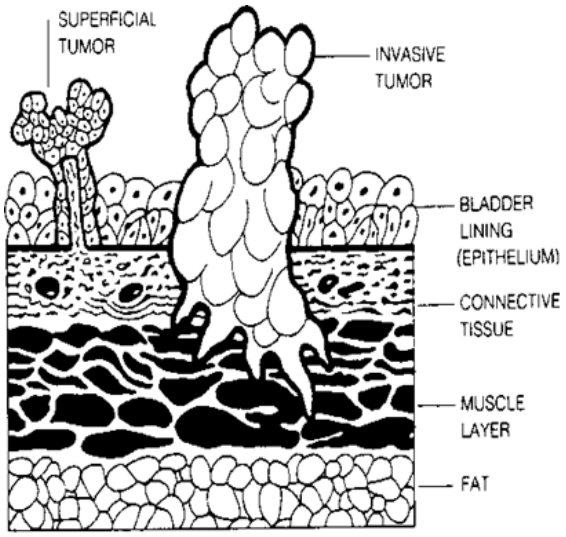

Fig. 1. A section of the bladder wall showing superficial and invasive bladder cancers; the superficial cancer is present only in the lining, not entering the other layers of the bladder wall

important and frequent phenomenon. It is observed in 60% of all bladder tumors. Others may be: dysuria (difficulties and pain while urinating), the need to urinate more frequently or urgently than usual (decrease of bladder capacity). Any of mentioned signs does not necessarily mean that a bladder tumour is present. People with kidney stones or urinary tract infections and men with enlarged prostate glands may experience these symptoms as well. It is therefore important to find the cause in each particular case. First-step tests in case of suspicion of bladder cancer may be performed by an urologist without requiring a patient to stay overnight in a hospital or to have anaesthesia. They are: intravenous pyelogram (IVP), urography or cystography that take advantage of a special liquid called a "contrast solution". When injected into a vein it passes quickly into the urine. X-rays of the urinary system, when the contrast solution is present, allow the urologist to see images of the kidneys, ureters, and bladder. In cystoscopy, a pencil-thin, telescope-like instrument with a light source and magnifying lenses (cystoscope) is inserted gently into the urethra and passed into the bladder to examine its lining. The cystoscope also permits the urologist to remove a tissue sample for biopsy. Urinary cytology is an important test in detecting bladder cancer. For this test, urine is examined under a microscope to search for cancer cells. To complete the review of all today available diagnostic methods it is necessary to mention techniques used afterward to estimate location and size of the growth or to detect metastases. They are: ultrasonography (USG), computer tomography (CT), magnetic resonance imaging (MRI/NMR), X-ray imaging of lungs, liver and kidney and radioactive tests of bones. These

methods are used as second-step approach to identify disease progress. Although still not widely used in clinical practice, molecular and genetic biomarkers seem to become the most forceful cancer diagnostic tool in the future. Generally, a biomarker is any substance or phenomenon that is measured biologically and associated with a stage or increased risk of disease. Practically, biomarkers are produced by tumors or they are generated by the human immunological system in reaction to cancer. Their occurrence and intensity may be measured in blood, urine or tissue. Molecular and genetic alterations offer the opportunity to specifically detect early tumour-related changes in cells and their DNA. This way, it is possible to detect very first origin of cancer and follow the progress of applied therapy. Determination of biomarkers level may help in selection of optimal therapy, adjusted to individual patient, and evaluation of the need for more aggressive treatment in case of high risk of disease progression. Finally, genetic alterations research achievements reveal another area where they could contribute. It is early and exact risk assessment. Among many biomarkers suitable for bladder cancer detection, recently special attention is drawn to the following gens and antigens: p53, p21, Ki67, bcl-2, MDR-1. Some of advanced molecular and genetic tests enter clinical practice. To name a few: BTA (bladder tumour antigen test), NMP22 (nuclear matrix protein test), AuraTek FDP (fibrin and fibrinogen degradation products), Vysis UroVysion FISH (Fluorescence In Situ Hybridization). Many efforts are undertaken in laboratories to make such tests cheaper and easier in order to be performed by a patient at home [2].

4 Early Risk Detection – The Essence of Thing

Although a primary tumour can usually be successfully controlled with local therapy, most cancer deaths are caused by metastatic disease. Therefore, the goal of screening and early detection is to identify tumors at early stages of development. Unfortunately, clinically available screening and early detection modalities detect many tumors at a relatively late stage in their development because they are applied to patients with some clinical symptoms rather than patients from mass screening. As already mentioned, new technologies emerging from molecular and cellular biology, have been shown to identify genetic alterations and antigenic changes during early stages of tumour progression. Some of these could show promise as markers of pre-malignant lesions but it is hard to imagine their wide utilization in near future because of their complexity and price.

As stated earlier, cystoscopy is probably the most frequently applied method of diagnosing bladder tumors. Physicians use cystoscope to see the inside of the bladder and urethra. Many cystoscopes have extra tubes to guide other instruments to collect samples of tissue. Cystoscopy is very effective in detecting visible tumors. On the other hand, the method is invasive and may evoke infections. Alternative, or better to say, complementary method of initial neoplasia detection is urine cytology. This kind of investigation is able to identify cancer cells in the urine on microscopic level. The method shows high specificity (low rate

of false-positive diagnosis) but sensitivity is still not satisfactory (relatively high rate of false-negative results), particularly in case of superficial and low grade tumors. It is also highly subjective test, depending on the knowledge, experience and condition of pathologist performing visual inspection. Nevertheless, among all non-invasive methods, urinary cytology promises the best chances of early diagnosis since pathological alterations may be detected before visible symptoms appear. Assuming a model situation, when cancer test would be a part of routine urine analysis, we can expect great improvement of cancer development prevention. There are two main obstacles in implementing the model. One of them is of just economical nature and the second is lack of cytologists to perform this enormous work. On the other hand, as we can define the problems, quite reasonable are efforts to support mass screening programs introducing advanced computer hardware and software technology.

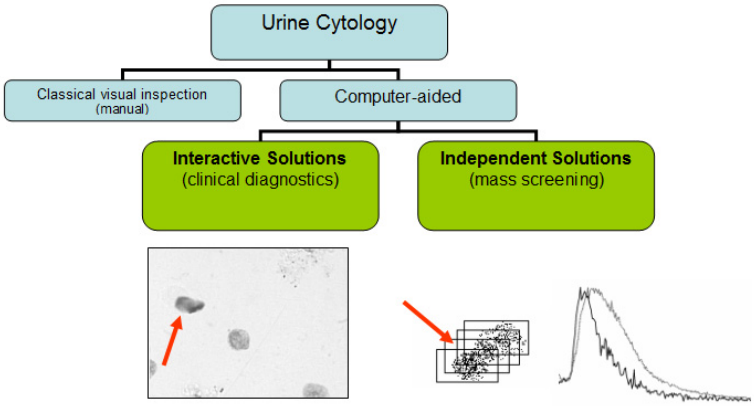

Fig. 2. Different types of information in interactive system (presentation of suspicious objects) and independent one (evaluation of entire slide on the basis of statistical features of the whole cell population)

As a consequence of distinguishing two, mentioned earlier, diagnostic directions there are two different ideas of realizing computer-aided support in cytology (Fig. 2). Independent systems are devoted for mass screening projects while interactive ones are dedicated for clinical tests. A simplified illustration of how the idea is realized in interactive system is shown in Fig. 3.

5 Detecting Malignancy in an Interactive System

The aim of support in interactive system is not to suggest a diagnosis but, after automatic analysis of microscopic smear, presentation of objects and smear regions that potentially contain malignancy associated changes (MAC). To get

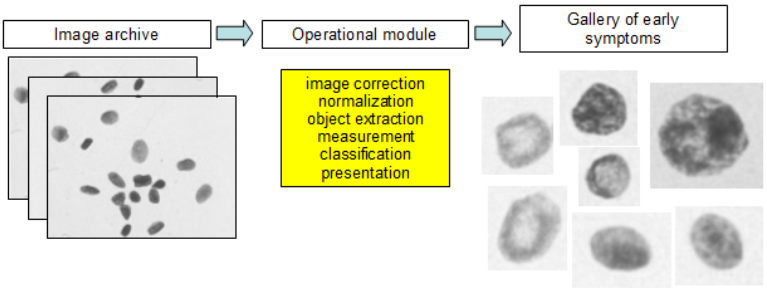

Fig. 3. Acquisition, digital processing and presentation of suspicious objects

correct view of procedures and algorithms presented here it is necessary to be aware of the position of the machine in the entire diagnostic chain. It is a common view among pathologists that the system should play a role of a quality control unit. It has to check pre-selection performed by cytotechnician. It means, there is great need to make a kind of re-screening of all samples classified as negative (no signs of pathology)[8]. This is because here is the main reason of relatively low sensitivity of cytological investigations for early cancer stages (Fig. 4). The

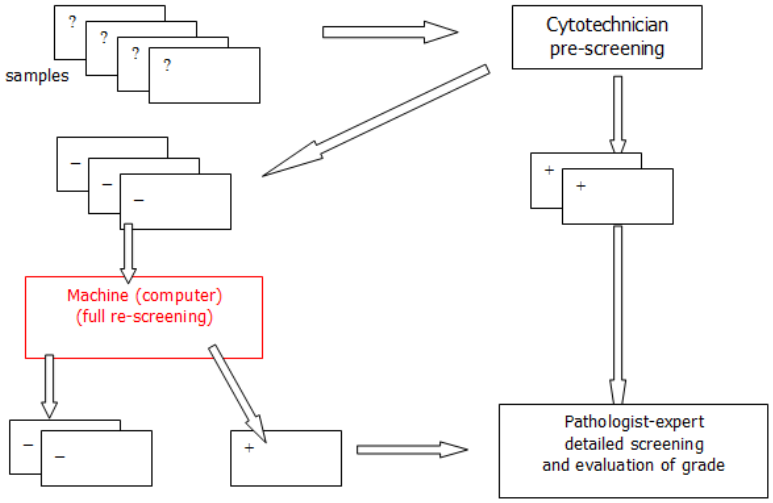

Fig. 4. Location of the machine support in the cytodiagnostic chain

place interactive system is located determines the way it operates. Pathologist expectations and postulates are following:

1ST POSTULATE: The most important is reduction of false-negative errors made by human inspector during visual (manual) pre-screening.

2ND POSTULATE: It is not useful to analyse and present in pathological symptoms gallery obvious cases. Therefore, do not show me objects of no diagnostic value (like artefacts – Fig. 5). Also, do not present in gallery pathological symptoms that are clearly visible and can not be missed in practice by a cytotechnician (e.g. nuclear clusters – Fig. 6) or highly irregular shaped nuclei (Fig. 7).

3RD POSTULATE: What I actually expect from a computer support is to help me in the task which is most difficult for me. This is not to overlook but detect almost every early cancerous (or even precancerous) changes which are known to occur in the chromatin structure of quite regular shaped nuclei (circular or oval – Fig. 8).

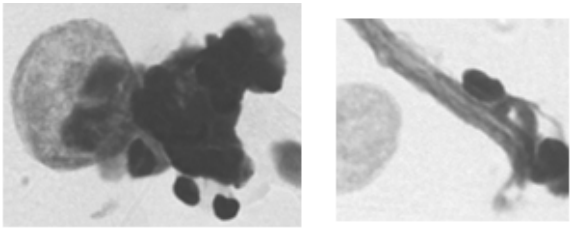

Fig. 5. Artifacts found frequently in urine samples

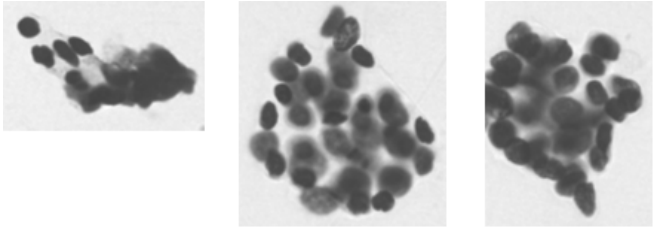

Fig. 6. Easy-to-detect cases – large nuclear clusters

A good illustration of the point of interactive support may be found in Fig. 9. It is quite natural tendency, during visual inspection, that the supervisor attention is drawn to some strong pictorial phenomena found in subsequent scenes. They may be clumps of normal nuclei or even artefacts. Meanwhile, what is really important for early detection of risk, small changes of the chromatin structure in a nucleus located on the periphery of the image frame, are usually omitted.

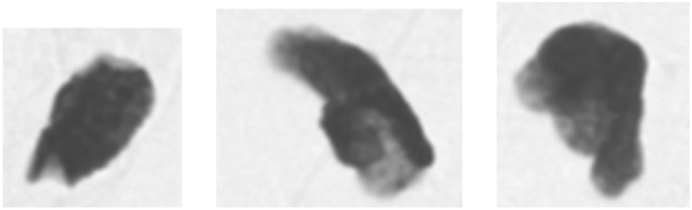

Fig. 7. Objects of clearly visible suspicious morphology

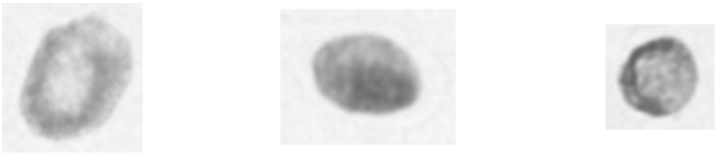

Fig. 8. Suspicious but easy-to-overlook changes of chromatin structure

Finally, sensitivity of detecting such early symptoms decreases radically. And here is the place for a machine (computer), making quality control of a human work by re-screening negative cases. Moreover, computer pays special attention to objects that are known to be hard cases for a human inspector. It works 24 hour a day, without breaks, without tiredness, all the time applying the same, objective evaluation criteria.

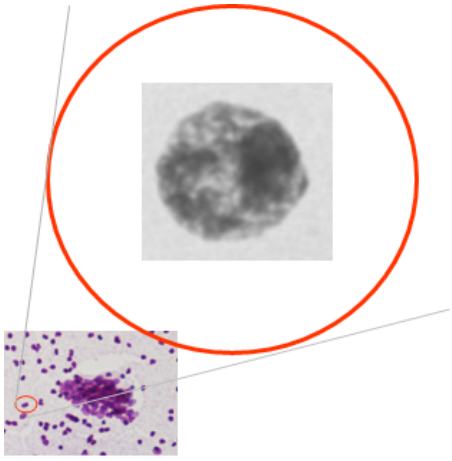

Fig. 9. The point of low sensitivity of early cancerous changes detection

6 Detecting Abnormalities with the Help of Pathomorphological Image Database

Starting the work we apply simple, bimodal classification scheme. A training set of objects was divided into two groups: NORM vs PATHOLOGY (Fig. 10). The GLCM (Grey Level Coocurence Matrix) texture descriptors were used to create feature vectors of each object.

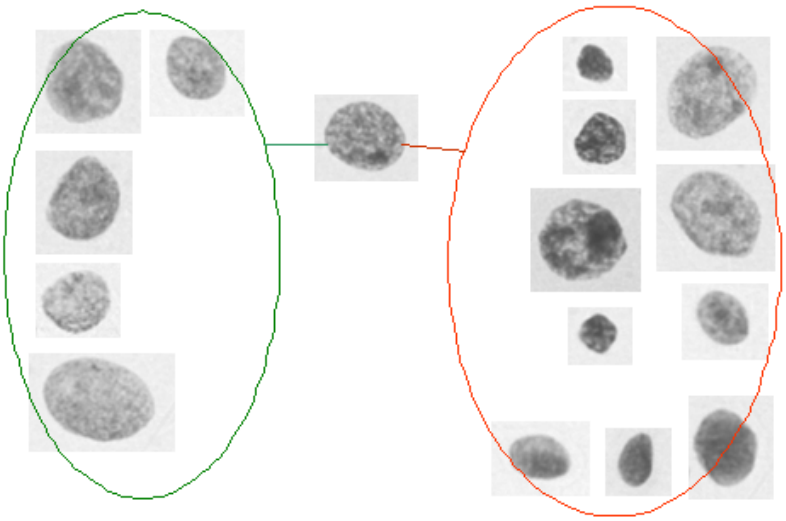

Fig. 10. Initial division of training set: NORM (left) vs PATHOLOGY (right)

However, as the number of images in the training set was increasing, a significant decrease of classification specificity was observed. And the reason of this was quite natural since intra-classes difference was increasing and inter-class distance was decreasing at the same time. Then, decrease of classification specificity was the reason of low specificity of resulting gallery of pathological symptoms. The frequency of finding normal nuclei in the gallery could not be accepted (specificity 50-60%). Further investigations allowed obtaining increase of specificity by changing the classification tools. Instead of discriminant analysis the k-NN algorithm was applied (specificity increased to 70%). However, in contrast to analytical form of discriminant analysis, this requires an object under study to be compared with every element (image) of reference (Fig. 11).

And here we come to the fundamental switch in the classification scheme. We put aside rigid, analytical discrimination procedures and try developing algorithms to measure image similarity, thus approaching CBIR (Content Based Image Retrieval) and QBE (Query by Example) concepts.

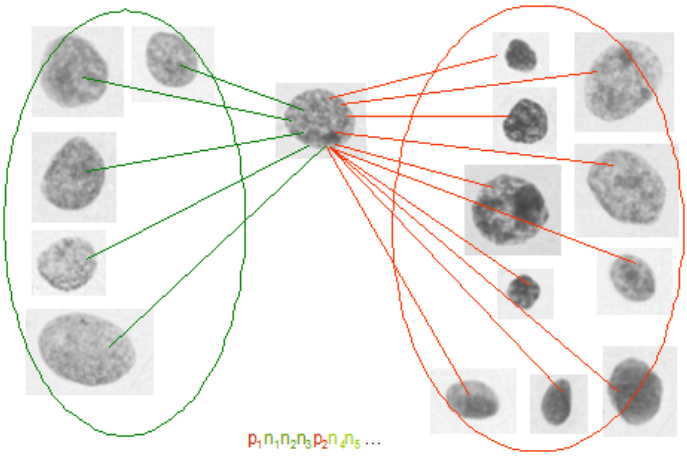

Fig. 11. Object classification by means of k-NN procedure

As the classification procedure becomes more complicated there is a need to rethink the role of image database. It can not be just a simple collection of data used to calculate an analytical classification rule. On the contrary, it starts to be actively used in the discrimination process. Finally, it is necessary to add to former postulates a new one:

4TH POSTULATE: Object identification and classification during automatic screening of a smear should not be realized on the basis of rigid, persistent discrimination rules. It should be performed by the help of pathomorphological image database. The database is created and may be modified dynamically by experts (pathologists). The search and exploration procedures should be based on CBIR/QBE techniques.

As for now, despite the database management is more powerful, the database itself still remains divided into NORM and PATHOLOGY classes. However, there are several important reasons that make such an organization not to be the best solution for the task at hand. Most significant in this context is the opinion of pathologists. They claim the database bimodal organization may be only accepted in mass screening systems (as there is a hidden assumption we deal with a control group and any aberrance is suspicious). On the contrary, in clinical applications, this is not the case and things become more complicated. It often happens; cytological investigations in pathological laboratories are carried out to monitor a patient therapy progress. Many of therapeutic techniques (radiotherapy, immunotherapy, BCG injection etc.) have significant influence on the image of urine sample. Even an experienced pathologist is not able to give

reliable diagnosis without information from many external sources. The same image of urine specimen may be classified suspicious in one case and may be the effect of different treatments in another one. Thus, having so many different and important sources of diagnostic information that should be taken into account, a computer, which knowledge is limited to cytological images only, should not decide what is normal and what is not. The system is only to supply additional data to that already in hand, to allow for better diagnosis. However, it is always a physician (pathologist) who takes full responsibility for a final result. Taking

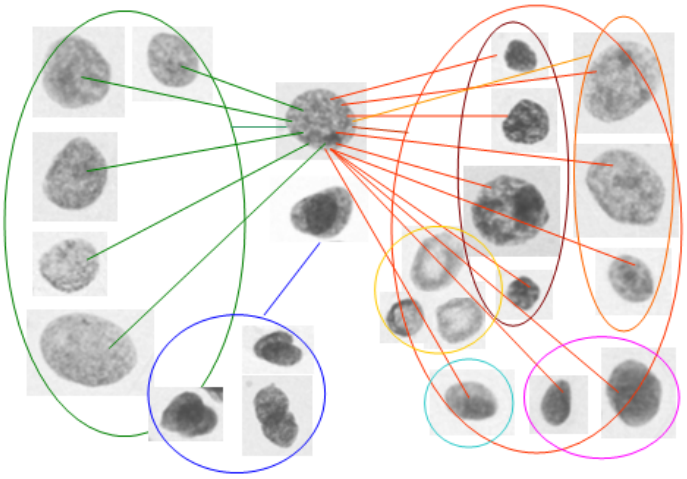

Fig. 12. The final organization of pathological image database according to experts

all above into consideration it seems necessary to formulate last but very important postulate regarding organization and usage of pathomorphological image database:

5TH POSTULATE: The reference database, created and modified by experts and used as a basis for classifying cytological objects must not define NORM or PATHOLOGY a-priori. Let it be divided into different classes containing different, distinctive types of objects (nuclei). Let it be pathologist who decides, before running the test, what phenomena and types of morphological alterations are interested and should be included in the gallery of diagnostically significant symptoms (Fig. 12).

7 Experiments and Implementation

Among conventional texture analysis methods, the best one for our purposes appeared to be GLCM and it was implemented initially in our study. However,

still, the search was continuing to find a technique that would be better suited for particular structures at hand. GLCM, similarly as Fourier spectral methods, are obviously right choices for regular, periodic textures. Moreover, as an input data they require rectangular pieces of a texture and our nuclear objects are not characterized by those features. We know, it is necessary to have a structure descriptor to preserve information about topology of more and less dense regions but there is no any periodicity in our case. Then, we analyzed the method known as SGF (Statistical Geometric Features) [5]. Shortly speaking, it relays on input image decomposition by thresholding into a stack of binary images (Fig. 13). From every elementary image several geometric parameters of connected regions (both dark and bright) are computed. This way we get statistical distribution as a function of threshold t. Appropriate statistics derived from those distributions become descriptors of the texture under study. As we get the structure features

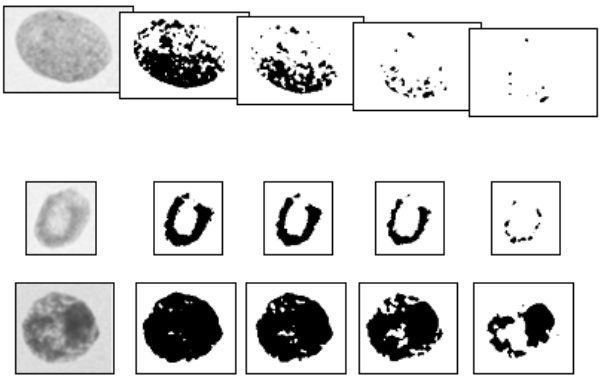

Fig. 13. The idea of texture analysis by means of SGF

space it is necessary to select a metric to compute similarity between different spatial chromatin distributions. Our experiments were carried out with the following distance measures:

1) Manhattan (L1)
2) Euclidian (L2)
3) Mahalanobis
4) Weighted-Mean-Variance (WMW)
5) Chebychev (Linf.)
6) Canberra
7) Bray-Curtis
8) Squared Chord
9) Squared Chi-Squared

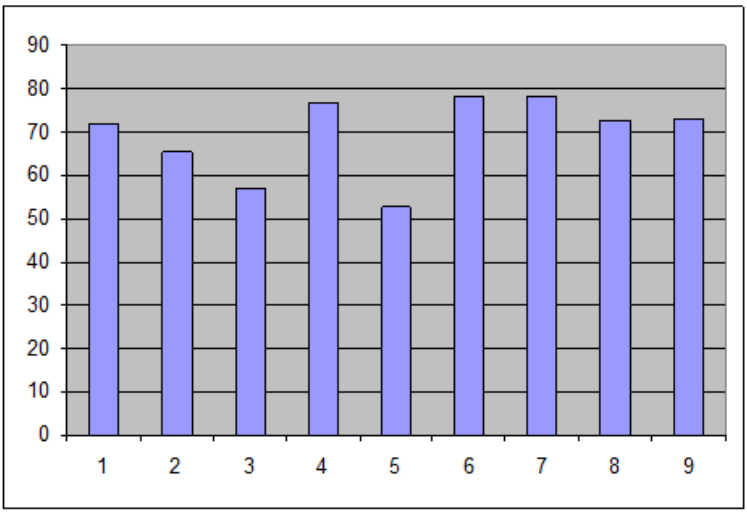

Fig. 14. Specificity of the gallery for different distance measures

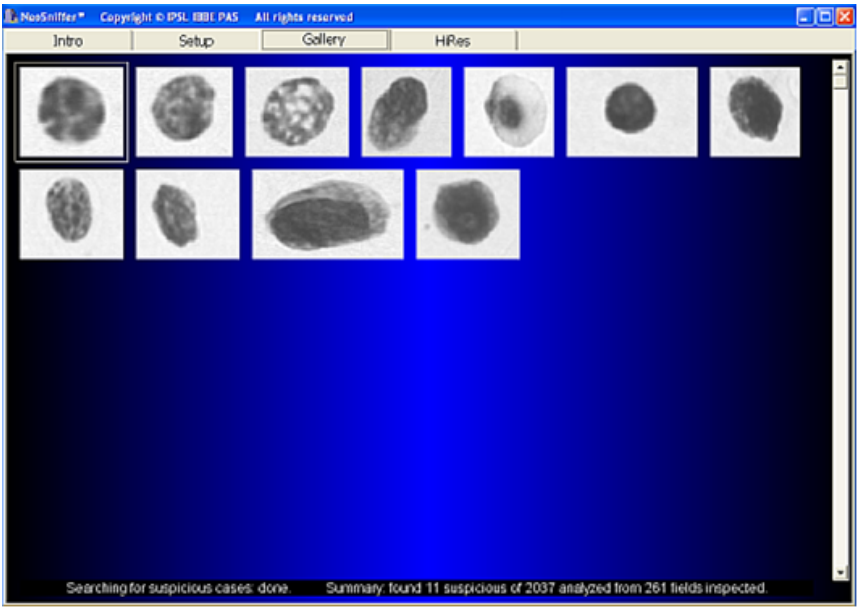

Fig. 15. Symptoms of malignancy associated changes in NeoSniffer output gallery

Averaged test results performed for five randomly selected specimens are shown in Fig. 14. Thanks to the experiments it was possible to select the optimal solution as the Bray-Curtis metric which is relatively easy to compute and gives us the best results. In our current model, pathomorphological database of chro-

matin patterns contains 70 images of nuclei divided into seven classes, 10-items each: 1) normal nuclei, 2) normal nuclei with highly visible nucleoli, 3) overlapping nuclei having overall shape and size similar to a single nucleus image, 4), 5), 6), 7) four different, but characteristic and distinct, types of chromatin distribution. The algorithms and procedures described above were implemented in a model of interactive system for computer-aided diagnosing of bladder cancer. The look of a final screen containing gallery of possible cancer symptoms is shown in Fig. 15. For a typical urine smear, containing 10-20 thousand cytological objects, some 30-40% of them are going to be analyzed in the system as only they are single, isolated, circular/oval cell nuclei. Created galleries contain from dozens to several hundred objects. Of course, you can find artefacts (from diagnostic point of view) in output gallery. However, the total number of them is kept on reasonable level (10-20%). Moreover, there is no risk they influence diagnosis thanks to the principle of interaction between the system and pathologist.

References

1. Dulewicz, A., Pietka, B.D., et al.: Computer Identification of Neoplastic Urothelial Nuclei from the Bladder. Analiytical and Quantitative Cytology And Histology 23(5) (October 2001)
2. Pirtskalaishvili, G., Konety, B., Getzenberg, R.: Update on urine-based markers for bladder cancer. How sensitive and specific are the new non-invasive tests? ostgraduate Medicine 106(6) (November 1999)
3. Intersociety Working Group for Cytology Technologies: Proposed Guidelines for Primary Screening Instruments for Gynaecologic Cytology. Acta Cytologica 41(3) (May-June 1997)
4. Intersociety Working Group for Cytology Technologies: A Proposed Methodology for Evaluating Secondary Screening (Rescreening) Instruments for Gynaecologic Cytology. Acta Cytologica 41(3) (May-June 1997)
5. Harlow, D.G., Wei, R.P., Wang, M.Z.: Statistical analysis of constituent particles in 7075-T6 aluminium alloy. A Metallurgical and Materials Transactions 37(11) (November 2006)

microRNA 3'-end Modification Detection Algorithm and Its Usage Example for Tissue Classification

Marta Danch[1], Damian Borys[1], Tomasz Stokowy[1], Knut Krohn[2], and Krzysztof Fujarewicz[1]

[1] Institute of Automatic Control, Silesian University of Technology, ul. Akademicka 16, 44-100 Gliwice, Poland
marta.danch@polsl.pl
[2] Interdisciplinary Center for Clinical Research, University of Leipzig, Germany

Abstract. Recent studies indicates that cellular cancerogenesis is connected with microRNA (miRNA) expression levels. In particular, different miRNAs can serve as classification features for distinguishing different cancer types. This paper provides classification attempt using miRNA isoforms with 3'-end modification as classification features. microRNA samples was obtained using next generation sequencing method. Data was preprocessed using authors algorithm developed in R. Support Vector Mashines and Partial Least Square methods were used to classify two types of miRNA samples: Follicular Adenoma and Follicular Thyroid Cancer. It was observed that only several miRNA modified isoforms were identified as the most differentiating for analyzed samples. Obtained results indicate that miRNA 3'-end modifications can be used as cancer tissue classification features.

Keywords: microRNA, 3'-end modification, detection algorithm, classification, partial least square.

1 Introduction

Folicular Thyroid Cancer (FTC) constitute about 10% of all cancer diagnosis and is the second most common cancer type among people [22]. Unfortunately, distinguishing between FTC and its benign form Follicular Adenoma (FA) is extremely difficult. Based on histopathological studies only, classification efficiency varies from 11% to 69%. Large discrepancy is due to discrepancies in the data provided by various research centers [22].

Based on genetic data, several models for tissue classification between FTC and FA were developed. For models classifying this type of tissue, in the literature one can find different performance indicators. These indicators are calculated only on the basis of a few selected miRNAs, and not all of the sequences present in the cells. Indicators in question can reach the level of about 80% for the accuracy [26] or 100% sensitivity and 86% specificity [11], depending on the

E. Pietka, J. Kawa, and W. Wieclawek (eds.), *Information Technologies in Biomedicine, Volume 3*, Advances in Intelligent Systems and Computing 283,
DOI: 10.1007/978-3-319-06593-9_25,

data and feature selection methods. The best classification models differentiating between FTC and FA, for now, can reach the performance indicators up to 100% sensitivity and 94% specificity. However, these indicators were calculated basing on selected genes, not miRNAs [27]. These are highly satisfying results, but only from a statistical point of view. In fact, a certain number of patients still remains misdiagnosed.

microRNA (miRNA) are short (15 - 27 base pairs), non-coding nucleotide sequences responsible for a number of mechanisms of controlling post–transcriptional processes in the cell. The study confirmed that miRNAs are involved in almost every cellular process. In mammals, they are responsible for about 50% of genes activity, for which they are specific inhibitors [12]. In case of humans more than 2 thousand miRNA sequences have been identified and described [19]. They are not only species specific, but tissue specific. miRNA expression levels determines type of tissue origin and cell cycle stage. Based on miRNA presence and its expression levels one can identify acquired materials.

Recent three-year studies [12] has shown that miRNAs are not only involved in post-transcriptional gene processing, but they have its own post-transcriptional processing path. Specific modifications were detected at the 3 'end of mature miRNAs, which consist of up to 3 additional bases [20], with the most frequent modification is adenine (A) [28, 20, 15]. Additional bases do not come from unmatures miRNA (hairpin) sequences. Exemplary modified sequences shown in Tab. 1.

In tested samples specific diversity of modification was detected, which rules out random base addition [14]. Modification processes are not yet fully understood, but it is known that these processes are biologically regulated [1, 28].

At the moment, there are few reports on the biological function of 3'-end miRNAs modification. It is supposed, that modifications are stabilizing part of miRNAs structure, so it is not immediately degraded [12]. Since many researches confirm species and tissue diversity of 3'-end modifications, it is not possible to create a global modification pattern [1, 14, 15, 20, 28]. Thanks to this, there is a possibility that the expression levels of modified miRNAs or characteristic modifications could constitute set of features allowing tissue classification.

2 Algorithm Overview

Next Generation Sequencing (NGS) provides genomic data of accuracy that could not be achieved before. Thus NGS data requires advanced processing algorithms to handle its precision in the most convenient manner. Here we present algorithm designed to cope with miRNA NGS data, especially to detect miRNAs 3'end modifications and expression levels of miRNA isoforms. Algorithm allow to indicate origin of each detected sequence and provides miRNA isoform abundance to be used in the further analysis. Algorithm use R environment [7], bowtie2 [13] and cutadapt [17] tools. Link for script download: `http://cellab.polsl.pl/index.php/software`.

Table 1. Exemplary isoforms table with occurrence number and their percentage share for miRNA sample (here: hsa-miR-486-5p); modification bases detected in data are labelled with bold font

	Isoform	Amount	%
miRNA reference	TCCTGTACTGAGCTGCCCCGAG		
detected in data miRNA sequences	TCCTGTACTGAGCTGCCCCGAG	1042	51.20
	TCCTGTACTGAGCTGCCCCG	15	0.74
	TCCTGTACTGAGCTGCCCCGA	217	10.66
	TCCTGTACTGAGCTGCCCC	2	0.10
hairpin reference	ATCCTGTACTGAGCTGCCCCGAGGCCCT		
detected in data hairpin sequences	TCCTGTACTGAGCTGCCCCGAGG	6	0.29
	ATCCTGTACTGAGCTGCCCCGA	1	0.05
	ATCCTGTACTGAGCTGCCCCGAG	1	0.05
	TCCTGTACTGAGCTGCCCCGAG**A**	591	29.04
	TCCTGTACTGAGCTGCCCCGAG**T**	124	6.09
	TCCTGTACTGAGCTGCCCCGAG**AT**	9	0.44
	TCCTGTACTGAGCTGCCCCGAG**GT**	2	0.10
	TCCTGTACTGAGCTGCCCCGAG**GAG**	1	0.05
	TCCTGTACTGAGCTGCCCCGAG**TA**	5	0.25
	TCCTGTACTGAGCTGCCCCGAG**GA**	1	0.05
	TCCTGTACTGAGCTGCCCCGAG**AA**	10	0.49
	TCCTGTACTGAGCTGCCCCGAG**C**	1	0.05
	TCCTGTACTGAGCTGCCCCGAG**TT**	1	0.05
	TCCTGTACTGAGCTGCCCCGAG**AGA**	1	0.05
	TCCTGTACTGAGCTGCCCCGAG**TAA**	1	0.05
	TCCTGTACTGAGCTGCCCCGAG**AG**	1	0.05

2.1 Reference Preparation

Algorithm requires three different references to operate properly:

- mature miRNA - miRNA
- hairpin miRNA - hairpin
- recent version of human genome - hg19.

MiRNA and hairpin references were created from the mirBase database entries. Hg19 is available in public and was downloaded from UCSC Genome Bioinformatics database.

2.2 Isoforms Recognition

The algorithm performs following steps to recognize isoforms (see Fig. 1):

1. Removal of Illumina adapters using Cutadapt program - selection of sequences with length between 15 and 30 bp;
2. Data alignment using Bowtie2 to hairpin reference with `--local mode`, `--trim3 3 -N 1 and --norc` parameters - choosing isoforms which might derive from hairpin miRNA sequences;

3. Data alignment using Bowtie2 to miRNA reference from miRBase database with `-end-to-end mode, --score-max C,0 -L 8 -a and --norc` parameters - choosing none but miRNA isoforms;
4. Data alignment using Bowtie2 to hairpin reference from miRBase database with `-end-to-end mode, --score-max C,0 -L 8 -a and --norc` parameters - choosing none but hairpin isoforms;
5. Data alignment using Bowtie2 to hg19 reference with `-end-to-end mode`, `--score-max C,0 -L 8 -a and --norc` parameters-choosing other genome isoforms whiteout mismatches;
6. Data alignment using Bowtie2 to hairpin reference with `--local mode`, `--trim3 3 -N 1 and --norc` parameters - preparing data to next step by determining sequence references;
7. Data comparison using R script - choosing isoforms without mismatches in miRNA sequence with additional bases at 3'-end;
8. Data alignment using Bowtie2 to hg19 reference with `-end-to-end mode`, `-N 1 -L 8 -a and --norc` parameters - choosing genome isoforms;
9. Data alignment using Bowtie2 to hairpin reference with `--local mode`, `--trim3 3 -N 1 and --norc` parameters - definition of probable references for sequences with higher mismatches value;

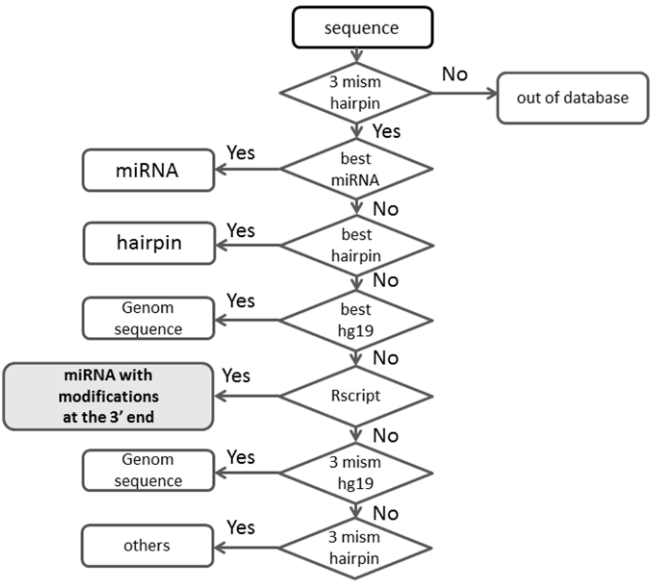

Fig. 1. Algorithm block diagram representing steps 2 - 9

2.3 Output Data Tables

MirMod as a final results produces four miRNA isoform tables:

- "ALL_izof.txt" - containing count table for all isoforms in all samples
- "ALL_PROC_izof.txt" - containing percentage table for all isoforms in all samples
- "ALL_filtr_izof.txt" - containing count table for isoforms with higher number of occurrences than "threshold" at least in one sample
- "ALL_filtr_PROC_izof.txt"- containing percentage table for isoforms with higher number of occurrences than "threshold" at least in one sample

To obtain percentage values in both "PROC" files we normalized count table values dividing each by total number of sequences received from step 2 (see section Isoforms recognition) for each sample. Normalized value allows to compare relative isoform expression level between samples.

MirMod script assigns to each isoform in each sample a miRNA reference name and one of four different attributes - type of isoform:

- miRNA - means that isoform is an exact miRNA sequence
- hairpin - means that isoform is an exact hairpin sequence
- hairpin+mod - means that isoform is an exact miRNA sequence with additional modification at 3'-end
- hairpin+N1 - means that isoform is an miRNA or hairpin sequence with mismatches

MirMod script produces other files with detected miRNA sequences, divided into different origin classes in each file which may be used for further analyses.

2.4 Exemplary Output Data Table

Tab. 2 shows exemplary output data table for two Illumina sequenced samples. Each column contains respectively:

- 1st column: miRNA reference sequence name from miRBase database;
- 2nd column: Type of detected sequence origin (see step 3 of isoform recognition);
- 3th column: Detected sequence;
- 4thand 5th: expression levels of detected sequence in the samples (count or percentage values, depends on file type, see step 3 of isoform recognition)

3 Materials and Methods

The algorithm was tested on miRNAs samples, isolated from thyroid cancer tissues FA (Folicular Adenoma) and FTC (Folicular Thyroid Cancer). The study used 20 miRNA samples from the FTC and FA tissues obtained by deep sequencing method (often referred as next generation sequencing - NGS) by Illumina

Table 2. Exemplary output table for two samples with expression percentage values

miRNA Reference	Type	Isoform	Sample 1[%]	Sample 2[%]
hsa-let-7a-3p	miRNA	CTATACAATCTACTGTCTTTC	0.008786	0.023931
hsa-let-7b-5p	miRNA	TGAGGTAGTAGGTTGTGTGGTT	4.62E-05	0.000155
hsa-let-7b-5p	miRNA	TGAGGTAGTAGGTTGT	0.000348	0.001005
hsa-let-7b-5p	hairpin	TGAGGTAGTAGGTTGTGTGGTTT	3.30E-05	9.35E-05
hsa-let-7b-5p	hairpin+mod	TGAGGTAGTAGGTTGTGTGGTTA	1.52E-05	3.90E-05
hsa-let-7b-5p	hairpin+mod	TGAGGTAGTAGGTTGTGTGGTTG	6.29E-06	1.17E-05
hsa-let-7b-5p	hairpin+N1	TGAGGTAGTAGGTTGTATGGTAA	6.29E-06	1.17E-05
hsa-let-7b-3p	hairpin+N1	CTATACCACCTACTGCCTTCCT	1.15E-05	2.73E-05

platform [9]. This technology, from year to year more and more popular, using fluorescent additives to nucleic acids, allows detection of all available cell genetic material in a relatively short period of time. In cases when sequences under test repeat themselves, like RNA sequences, basing on data from NGS one can specify the levels of expression of these sequences, and thus the approximate concentrations of proteins present in the tested cells.

Expression levels of individual miRNA isoforms detected in each sample were used as features set for classification models. Classification models were created using supervised methods of analysis: Support Vector Machine (SVM) [5, 6, 25, 23, 10], and the Partial Least Squares (PLS) method [21, 8, 24]. For model validation boostrap632 method (combination of classic bootstrap and resubstitution method) [3, 4] was used and set of 10 differentiating features was selected from the data using Wilcoxon test. In order to determine the quality of the classification three most common indicators were used: sensitivity, specificity, and accuracy. The whole analysis was performed using libraries and R language scripts.

4 Results

As shown in the Fig. 2 classification based on PLS obtained higher values of quality indicators than SVM method. For both methods relations between indices are very similar. Sensitivity value is significantly larger than specificity value, which is caused directly by specifics of classification methods in question - uncertain sample is put in class number 1. Accuracy index is arithmetic mean from sensitivity and specificity values. Minor difference between sensitivity and specificity values allows to conclude that classification process is of high quality.

In analyzed data 424 miRNA isoforms with 3'-end modification were identified. For purpose of creating models about 50% of them were used.

To create classification models, set of five most often used isoforms were selected. Tab. 3 presents isoforms used for classification and percentage utilization in models for different validation methods.

In case of bootstrap validation method presented features are those with the largest percentage of use, but the values are much lower than in case of

resubstitution method. Because the resubstitution method uses more features than bootstrap method to build classification model, such model is more complete, and therefore more reliable.

Polinucleotide modified isoforms were the most differentiating features in created classification models, despite singlenucleotide modified isoforms have the highest expression levels in used samples.

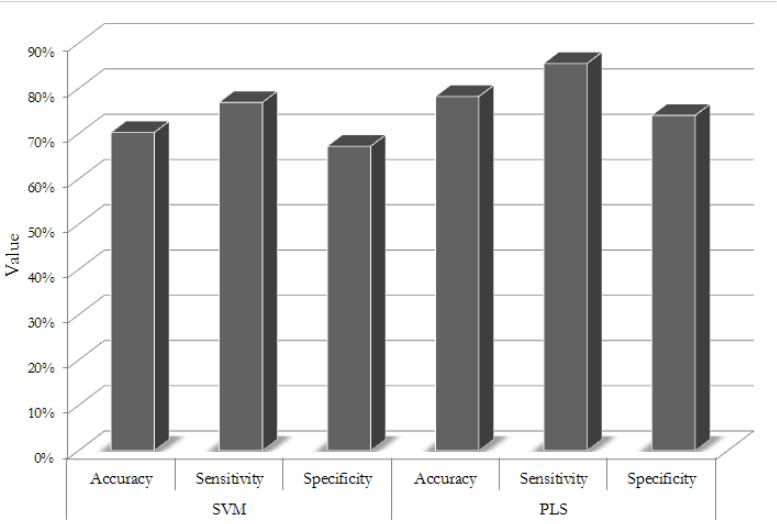

Fig. 2. Obtained performance indicators for classification methods used in the paper

Table 3. Most commonly used isoforms in classification models; abbreviations stands for validation methods: boot – bootstrap method, res – resubstitution method; modification bases detected in data are labeled with bold font

miRNA Reference	**Isoform**	**Percentage usage [%]**	
		boot	res
hsa-mir-30e-5p	TGTAAACATCCTTGACTGGAAG**CTT**	64	100
hsa-mir-21-5p	TAGCTTATCAGACTGATGTTGA**CC**	59	100
hsa-mir-486-5p	TCCTGTACTGAGCTGCCCCGAG**AG**	51	100
hsa-mir-222-3p	AGCTACATCTGGCTACTGGGTCTC**A**	43	100
hsa-mir-28-3p	CACTAGATTGTGAGCTCCTGGA**AA**	37	100

5 Discussion

Based on the results obtained in the work one can conclude that modifications of 3'-end miRNA work well as a feature classifying the different types of tissues.

Modified miRNA isoform expression levels differentiates two classes of samples at a satisfactory level. This confirms thesis cited in the introduction [1, 14, 15, 20, 28] that modifications are tissue-specific.

Modified isoforms detected in data suggest that these modification sequences are not random. According to what was previously described [15, 20, 28], the most common modification is Adenine. Not all modified isoform expression levels have statistically significant differences, what confirms omitting a large part of them during creating classification models. It is highly possible that those sequences are characteristic for thyroid tissue or general malignancy indicators. Comparing obtained results with different set of data from the above mentioned thyroid tissue, could assist in confirm or overthrow this hypothesis.

In literature several differentiating sequences are described. Among the most frequently mentioned, there are hsa-mir-21, hsa-mir-192, hsa-mir-197, hsa-mir-222, hsa-mir-328, hsa-mir-346 [11, 16, 22, 26]. Two of above mentioned miRNA isoforms (hsa-mir-21, hsa-mir-222) were identified in this paper, as the most differentiating for analyzed samples (see Table 3).

In this paper one of the simplest and most intuitive feature selection test(non-parametric Wilcoxon test) was used. There is a possibility to define better classification model using another more precised method. Another alternative method of feature selection could base on biological approach. Knowledge of thyroid cancer specific miRNA could be good way to select differentiating FA and FTC isoforms.

6 Conclusions

It is not surprising, that classification models based only on modified isoforms cannot reach 100% accuracy with thyroid cancer tissues classification. Nonetheless, 70-80% efficiency of classification allows to locate the 3'-end miRNA modification between other markers, such as individual genes and miRNAs. One classification model created basing on all these features i.e. genes, miRNAs, modified miRNAs, could improve already existing schemes and provide reliable classifications.

Classification problem mentioned in this paper was solved basing on twenty tissue samples. Supposing that satisfactory obtained results are not accidental, additional amount of data could clarify created models, and thus improve classification quality.

Significant growth of interest in the 3'end miRNA modification shows up in growing amount of publications, providing information that could complement this paper with new facts and probably extend data set required for further classification problem.

7 Further Work

Based on already created algorithm, it is possible to determine mutations places and types occurring in miRNA sequences and estimate their expression levels

in analyzed data. Such analysis would make possible selecting specific sequences interesting for further study. In further work extending created software to pre-miRNA analysis is planned.

MiRNA sequences are responsible for a number of mechanisms of controlling processes in the cell [12]. These sequences mutation could influence its binding potential with other cellular particles (RNAs, proteins), thus on cell lifecycle. Basing on sequence analysis described above, further experiments can be designed, which should explain mutation influence on miRNA-particles binding productivity and other phenomenon in cellular processes.

Acknowledgments. This work was supported by the Polish National Science Center under grant DEC-2012/05/B/ST6/03472 and by Silesian University of Technology.

References

1. Burroughs, A.M., et al.: A comprehensive survey of 3' animal mirna modification events and a possible role for 3' adenylation in modulating mirna targeting effectiveness. Genome Research 2, 1398–1410 (2010)
2. Dudoit, S., Fridlyand, J.: Classification in microarray experiments. Bioconductor Manual (September 2002)
3. Efron, B.: Estimating the error rate of a prediction rule: improvement on cross-validation. J. Amer. Stat. Assoc. 78(382), 316–331 (1983)
4. Fujarewicz, K.: A multi-gene approach to differentiate papillary thyroid carcinoma from benign lesions: gene selection using support vector machines with bootstrapping. Endocrine-related Cancer 14(3), 809–826 (2007)
5. Fujarewicz, K.: A note on classification of gene expression data using support vector machines. Journal of Biological Systems 11(01), 43–56 (2003)
6. Fujarewicz, K.: Improved classification of gene expression data using support vector machines. J. Med. Inf. Technol. 6 (2001)
7. Gentleman, R.C., et al.: Bioconductor: open software development for computational biology and bioinformatics. Genome Biol., R80 (2004)
8. Hoskuldsson, A.: PLS regression methods. J. Chemom. 2(3), 211–228 (1988)
9. Illumina company website, `http://www.illumina.com`
10. Jarzab, B.: Gene expression profile of papillary thyroid cancer: sources of variability and diagnostic implications. Cancer Research 65(4), 1587–1597 (2005)
11. Keutgen, X.M., et al.: A panel of four micrornas accurately differentiates malignant from benign indeterminante thyroid lesions of fine needle aspiration. Clinical Cancer Research (2012) (published online February 20, 2012)
12. Krol, J., et al.: The widespread regulation of microrna biogenesis, function and decay. Nature Reviews 11 (2010)
13. Langmead, B., Salzberg, S.L.: Fast gapped-read alignment with Bowtie 2. Nat. Methods 9, 357–359 (2012)
14. Lee, L.W., et al.: Complexity of the microrna repertoire revealed by nextgeneration sequencing. RNA 16, 2170–2180 (2010)
15. Li, S.C., et al.: Microrna 3'-end nucleotide modification patterns and arm selection preference in liver tissues. In: 23rd International Conference on Genome Informatics GIW 2012 (2012)

16. Marini, F., et al.: Microrna role in thyroid cancer development. Journal of Thyroid Research, 2011 ID: 407123 (2011)
17. Martin, M.: Cutadapt removes adapter sequences from high-throughput sequencing reads. EMBnet. Journal 17, 10–12 (2011)
18. Mevik, B.H., Wehrens, R.: The pls package: Principal component and partial least squares regression. Journal of Statistical Software 18 (2007)
19. Mirbase database website, `http://www.mirbase.org`
20. Newman, M.A., et al.: Deep sequencing of microrna precursors reveals extensive 3'-end modification. RNA 17 (2011)
21. Nguyen, D.V., Rocke, D.M.: Tumor classification by partial least squares using microarray gene expression data. Bioinformatics 18(1), 39–50 (2002)
22. Rossing, M., et al.: Classification of follicular cell-derived thyroid cancer by global rna profiling. Journal of Molecular Endocrinology (2013)
23. Simek, K., et al.: Using SVD and SVM methods for selection, classification, clustering and modeling of DNA microarray data. Engineering Applications of Artificial Intelligence 17(4), 417–427 (2004)
24. Student, S., Fujarewicz, K.: Stable feature selection and classification algorithms for multiclass microarray data. Biology Direct 7(1), 33 (2012)
25. Vapnik, V.: The Nature of Statistical Learning Theory. Springer, New York (1995)
26. Weber, F., et al.: A limited set of human microrna is deregulated in follicular thyroid carcinoma. The Journal of Clinical Endocrinology and Metabolism 91(9), 3584–3591 (2006)
27. Weber, F., et al.: Genetic classification of benign and malignant thyroid follicular neoplasia based on a three-gene combination. The Journal of Clinical Endocrinology and Metabolism 90(5), 2512–2521 (2005)
28. Wyman, S.K., et al.: Post-transcriptional generation of mirna variants by multiple nucleotidyl transferases contributes to mirna transcriptome compexity. Genome Research 21, 1450–1461 (2011)

A Machine Learning Approach to Identify Prostate Cancer Areas in Complex Histological Images

Sadri Salman[1], Zhaoxuan Ma[2], Sambit Mohanty[3], Sanica Bhele[3], Yung-Tien Chu[1], Beatrice Knudsen[2,3], and Arkadiusz Gertych[1,3,4]

[1] University of Southern California, Department of Biomedical Engineering, Los Angeles, CA 90048, USA
[2] Cedars-Sinai Medical Center, Department of Biomedical Sciences,
[3] Cedars-Sinai Medical Center, Department of Pathology and Laboratory Medicine,
[4] Cedars-Sinai Medical Center, Department of Surgery, Los Angeles CA 90048, USA
arkadiusz.gertych@cshs.org

Abstract. Separating benign glands, and cancer areas from stroma is one of the vital steps towards automated grading of prostate cancer in digital images of H&E preparations. In this work we present a novel tool that utilizes a supervised classification of histograms of staining components in hematoxylin and eosin images to delineate areas of benign and cancer glands. Using high resolution images of whole slide prostatectomies we compared several image classification schemes which included intensity histograms, histograms of oriented gradients, and their concatenations to the manual annotations of tissues by a pathologist, and showed that joint intensity histograms of hematoxylin and eosin components performed with the highest accuracy.

1 Introduction

Prostate cancer (PCa) is the most commonly diagnosed cancer in men in developed countries despite steadily declining trends of new incidences and deaths per annum[1]. Microscopic evaluation of needle biopsies and prostatectomies is the gold standard for PCa diagnosis, as well as one of the most important criteria in the pathological assessment of prostate cancer and in predicting clinical outcomes. PCa develops from glands, that are visually evaluated according to the Gleason grading system which is based on the tumor growth patterns. Microscopically, normal glands are large and well separated by stroma. As the PCa develops the glands shrink, cluster and become tightly packed with little or no intervening stroma. A large variety of geometric configurations of glands pose significant challenge to a manual grading system [1, 2] which is laborious, requires extensive experience and is associated with poor inter-observer reproducibility particularly in determining tumors with Gleason 3 (G3) and Gleason 4 (G4) patterns.

[1] American Association for Cancer Research Cancer Progress Report 2013: cancerprogressreport.org/2013/Documents/2013_AACR_CPR_FINAL.pdf.

E. Pietka, J. Kawa, and W. Wieclawek (eds.), *Information Technologies in Biomedicine, Volume 3*, Advances in Intelligent Systems and Computing 283,
DOI: 10.1007/978-3-319-06593-9_26,

Existing approaches to computer-assisted evaluation of histopathological preparations of the prostate employ gland histomorphometry or context-based gland quantification to distinguish benign, and low- and high-grade cancer zones [3–9]. However, in order to perform any quantifications the glands are usually first separated from stroma. This task is difficult and prone to detection errors due to a large spectrum of gland architectures in benign and cancer areas. Most if not all of the computer-assisted gland segmentation techniques utilize the presence of the glandular lumen as a prominent feature that governs more sophisticated image processing routines. Yet, they usually leave off when the lumen is obscured or occluded by artifacts such as corpora amylacea (large circular shapes of thickened secretions with strong eosinophilic staining), when glands form clusters such as in cribriform G4 and also in G3 areas, or in cases when the lumen is very small or not present at all such as in non-cribriform G4 carcinoma or in the highest grade tumors.

Towards the development of a pattern recognition-based grading of prostate cancer we evaluate intensity histograms of hematoxylin and eosin images to reliably separate stroma from benign and cancer areas. Segmentation results were quantitatively compared with manual annotations generated by a pathologist.

2 Materials

Radical prostatectomy specimens from 20 patients with a diagnosis of G3 or G4 prostate cancer according to the contemporary grading criteria [1, 2] were retrieved from archives in the Pathology Department at our institution. Slides were digitized by a high resolution whole slide scanner (Leica SCN400F) dedicated to pathology research. The scanning objective was set to x20. The focusing was automatically adjusted by the scanner. The output was a color RGB image with the pixel size of $0.5\mu m$ x $0.5\mu m$ and 8bit intensity depth for each color channel. We implemented freely available libraries from `OpenSlide.org` [10] to import Leica (.scn) images and select histopathologically important fields of view that were converted to TIFFs for methods development. Furthermore, the fields of view were split into smaller images (1200x1200 pixels) manageable for analysis. Of the total 200 images obtained in this way, three sets including 25 images each containing stroma (ST) and: a) benign (BN) glands, b) G3 glands, and c) G4 areas were randomly selected by collaborating genitourinary pathologists who manually delineated all these areas directly on images. The sets were named as ST-BN, ST-G3 and ST-G4 respectively. In the 75 images obtained in this way the fraction of image area occupied by BN, G3 or G4 areas versus ST varied from low percentage of ST in G4 to moderate in G3 and high in BN images.

3 Methods

Hematoxylin and eosin are dyes that differentially stain the DNA, RNA and proteins in tissues. Hematoxylin binds and stains DNA in purple-blue, and eosin

binds to proteins in cytoplasm and stains them in pink (Fig. 1(a)). Our methodology was developed based on three main observations: a) the density of epithelial nuclei in BN glands and cancer areas is higher than the density of nuclei in ST, b) the intensity of eosin is different in ST versus the BN glands and areas of cancer, and c) hematoxylin and eosine image texture in glands is different from that seen in stroma. Hence, we propose to utilize the differential information embedded in the intensity characteristics of eosin and hematoxylin to quickly classify areas of the prostate tissue and arrive at a mask showing where the BN, G3 and G4 areas are located.

3.1 Histograms of Hematoxylin and Eosin Components

All 75 images selected for methodology development were subjected to colour deconvolution [11] to obtain hematoxylin and eosin images (Figure 1). Next, for a single pixel in the input H&E image one intensity histogram of hematoxylin component Hist(H) and one intensity histogram of eosin component Hist(E) were derived from a 64x64 pixel window centred at that pixel. For the same window, histograms of oriented gradients (HOG) [12] namely: HOG(H) and HOG(E) were respectively calculated in hematoxylin and eosin images. HOG(.) histograms were calculated using a freely available code[2]. Each Hist(.) was sorted into 18, and each HOG(.) into 9 equally spaced bins. Interestingly, Hist(.) and HOG(.) are independent features and describe different image characteristics. Histograms Hist(H), Hist(E), HOG(H), and HOG(E) for an entire image were collected using a sliding window method.

3.2 Training Set and Classification

Training features were derived from 20 stromal and 20 glandular training windows found in 5 representative images selected from each of the 25 belonging to ST-BN, ST-G3, and ST-G4 image sets. The remaining 60 images were left for methods testing. To capture a large variety of intensity and texture characteristics of glands some of the training windows were placed at the boundary of luminal areas in glands, some at the boundary of gland and background, and some entirely covered the glands or cancer areas with no lumen. Stromal windows included: areas between the glands, blood vessels with blood cells, blood vessel lumen, clusters of immune cells and a nerve. No windows were selected at the interface of stroma and glands. The histogram collection procedure was carried out until three separate training sets for ST-BN, ST-G3, and ST-G4 were completed. In total 120 different training windows were selected. Histograms in respective sets were labelled according to the tissue type (Fig. 2). Images left for testing were classified by means of several *knn* classifiers. Prior to classification both the training features and features derived from testing images were normalized using means and standard deviations from the training

[2] Chris McCormick, Hog Descriptor in MATLAB: `chrisjmccormick.wordpress.com/2013/05/09/hog-descriptor-in-matlab/`, visited 01.2014.

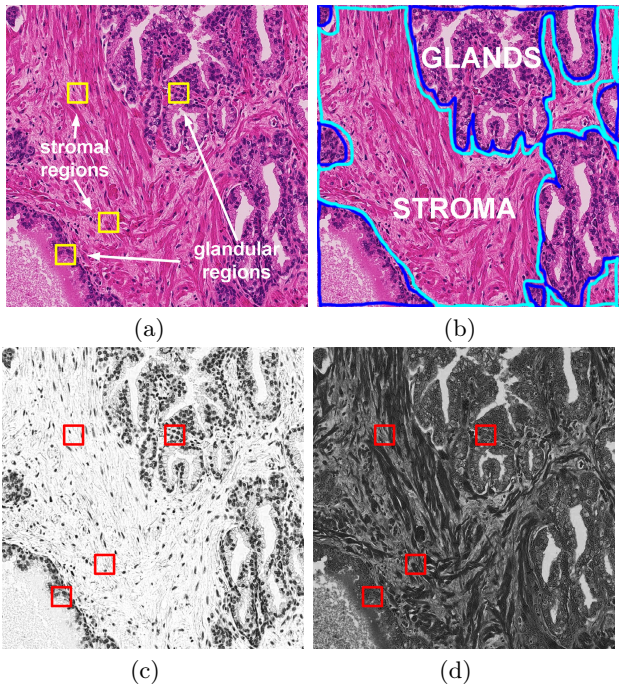

Fig. 1. Example H&E image with BN glands and stroma: (a) original H&E image, (b) pathologist outlines, (c) hematoxylin and (d) eosin images deconvoluted from (a). 64x64 pixel windows superimposed on (a), (c) and (d) indicate example location for histogram extraction shown in Figure 2. Note the differential staining in glands and stroma.

sets. To determine whether the texture or intensity-based features yield better classification, the experiment was separately performed in three steps: a) individual histograms: HOG(H), HOG(E), Hist(E), Hist(H), b) combined intensity histograms - Hist(HE) and combined gradient histograms - HOG(HE), and c) combined selected intensity and gradient histograms including: HOG(H)Hist(H), HOG(H)Hist(HE), and HOG(HE)Hist(HE). In a) the length of the feature vector was 9 for a gradient and 18 for an intensity histogram, in b) the length of the feature vector was 36 for Hist(HE) and 18 for HOG(HE), and in c) it was 27 for HOG(H)Hist(H), 45 for HOG(H)Hist(HE) and 54 for HOG(HE)Hist(HE) due concatenations of the respective histograms. The *knn* classification scheme was tested for neighbourhood $n = 1 : 7$ with odd increments.

3.3 Validation

Validation was carried out using measures of agreement that are frequently used when a computed result (C) is compared to a manual ground truth (G) by pathologist. Area overlap (Ov), Jaccard similarity coefficient (Ji), and Rand

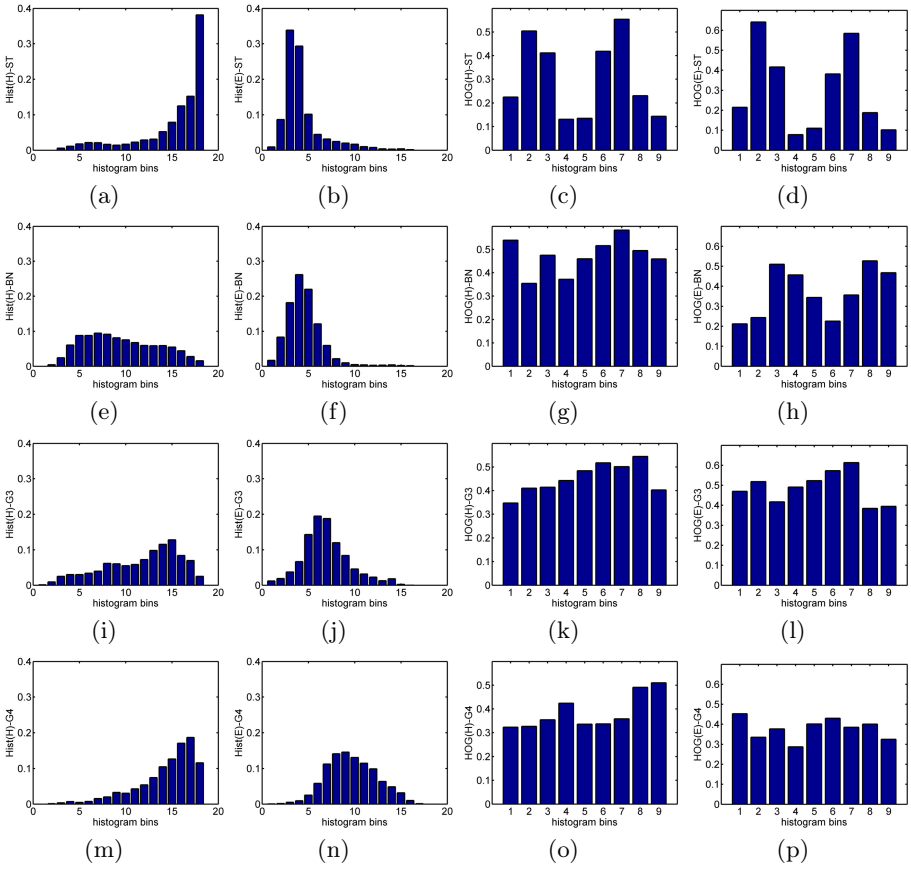

Fig. 2. Example histograms from small windows in hematoxylin and eosin images: (a)-(d) ST, (e)-(h) BN, (i)-(l) G3, and (m)-(p) G4 tissue components; consecutive columns (from left to right) represent: Hist(H), Hist(E), HOG(H), and HOG(E) histograms

index (Ri) [13] defined as follows: $Ov = |G \cap C|/|G|$, $Ji = |G \cap C|/|G \cup C|$, and $Ri = (a+b)/G_2^{n_{samples}}$, where: a is the number of pairs of elements that are in the same set in G and in the same set in C, b is the the number of pairs of elements that are in different sets in G and in different sets in C, and $G_2^{n_{samples}}$ is the total number of possible unordered pairs in the dataset. The Rand index is particularly useful in evaluating classification and clustering methods. (Ov), (Ji), and (Ri) reach 1 for a perfect agreement and 0 for a complete disagreement between (G) and (C). Background areas including lumens were removed from (G) and (C) before the validation.

4 Results

Utilizing clinical image data and the newly developed analytical framework we selected four different intensity and texture features (histograms) and tested their

ability to discriminate between prostate glands and stroma. Features described in Sections 3.1 and 3.2 in three separate training sets were used to train *knn* classifiers that were subsequently applied to ST-BN, ST-G3, and ST-G4 testing images.

Since no single measure fully quantifies segmentation performance, we compared our results using three different methods (Table 1). While *Ov* only reports true positive gland detection rate, *Ji* is the number of true positive detections divided by the sum of true positive, false positive (miss-detections) and false

Table 1. Prostate tissue classification performance ($knn, n = 3$) for different feature vectors obtained from individual and concatenated intensity histograms Hist(.) and histograms of oriented gradient HOG(.); best performances in respective categories are bolded

Feature vector	Measure	Tissue complex			Mean performance (all tissue images)
		ST-BN	ST-G3	ST-G4	
Hist(H)	*Ov*	0.824	0.747	0.806	0.795
	Ji	**0.671**	0.501	0.722	0.624
	Ri	0.765	0.610	0.734	0.715
Hist(E)	*Ov*	0.788	0.877	0.757	0.798
	Ji	0.445	0.541	0.606	0.542
	Ri	0.661	0.610	0.652	0.643
Hist(HE)	*Ov*	**0.894**	**0.923**	0.825	**0.871**
	Ji	0.645	**0.611**	**0.736**	**0.678**
	Ri	**0.803**	**0.648**	**0.743**	**0.732**
HOG(H)	*Ov*	0.791	0.836	0.724	0.724
	Ji	0.473	0.523	0.633	0.609
	Ri	0.697	0.602	0.684	0.664
HOG(E)	*Ov*	0.869	0.863	0.588	0.737
	Ji	0.439	0.552	0.513	0.505
	Ri	0.669	0.619	0.646	0.644
HOG(HE)	*Ov*	0.810	0.774	0.832	0.810
	Ji	0.468	0.528	0.706	0.595
	Ri	0.691	0.618	0.714	0.681
HOG(H)Hist(H)	*Ov*	0.783	0.615	0.831	0.758
	Ji	0.529	0.459	0.725	0.600
	Ri	0.735	0.612	0. 729	0.698
HOG(H)Hist(HE)	*Ov*	0.843	0.911	0.732	0.811
	Ji	0.546	0.559	0.648	0.597
	Ri	0.738	0.614	0.694	0.683
HOG(HE)Hist(HE)	*Ov*	0.820	0.824	**0.841**	0.831
	Ji	0.514	0.553	0.717	0.619
	Ri	0.719	0.626	0.722	0.694

negative (lack of) detections occurring in stroma. Since both Ji and Ov do not consider true negative findings, it is advantageous to juxtapose them with Ri which quantifies accuracy using virtually all positive and negative findings. The best overall classification performance was yielded by the $knn(n = 3)$ classifier. Figures: 3-5 and 6 illustrate tissue classifications in example images from various tissue complexes. All remaining knn classification schemes resulted in worse performances.

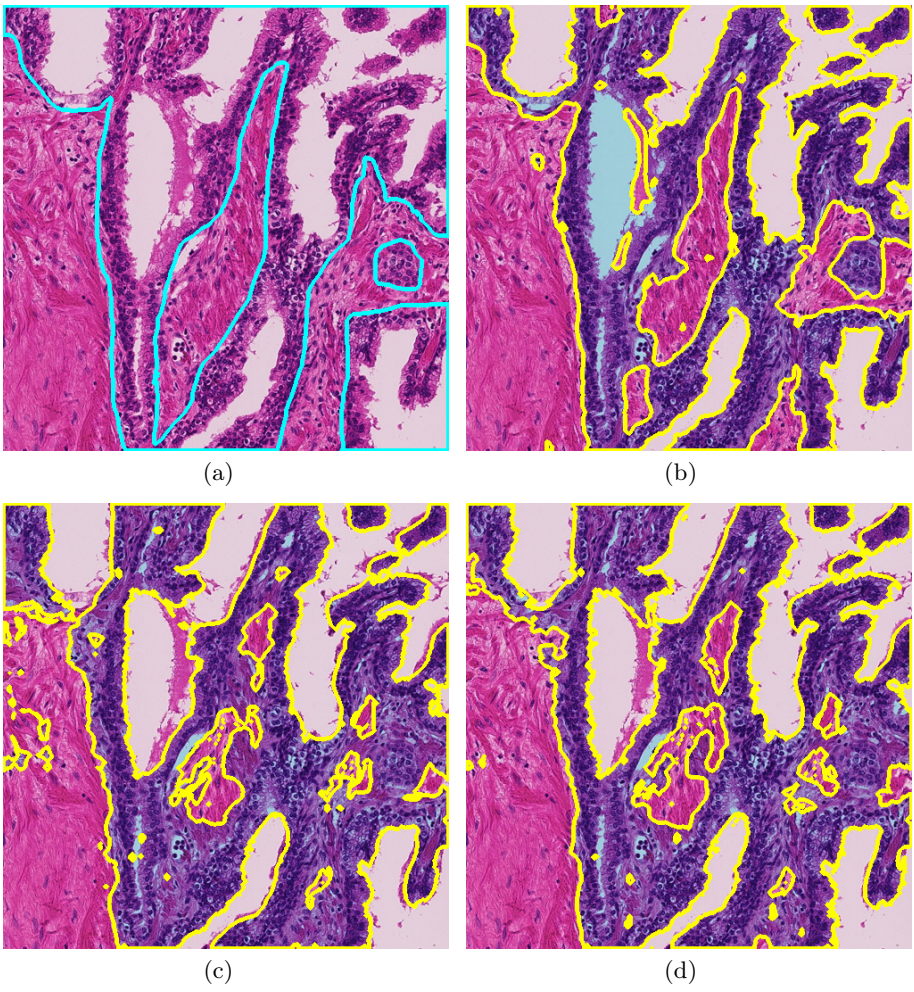

Fig. 3. Example knn-based classification results in BN areas: (a) ground truth, (b) using Hist(HE) (c) using HOG(H), and (d) using HOG(H)Hist(HE)

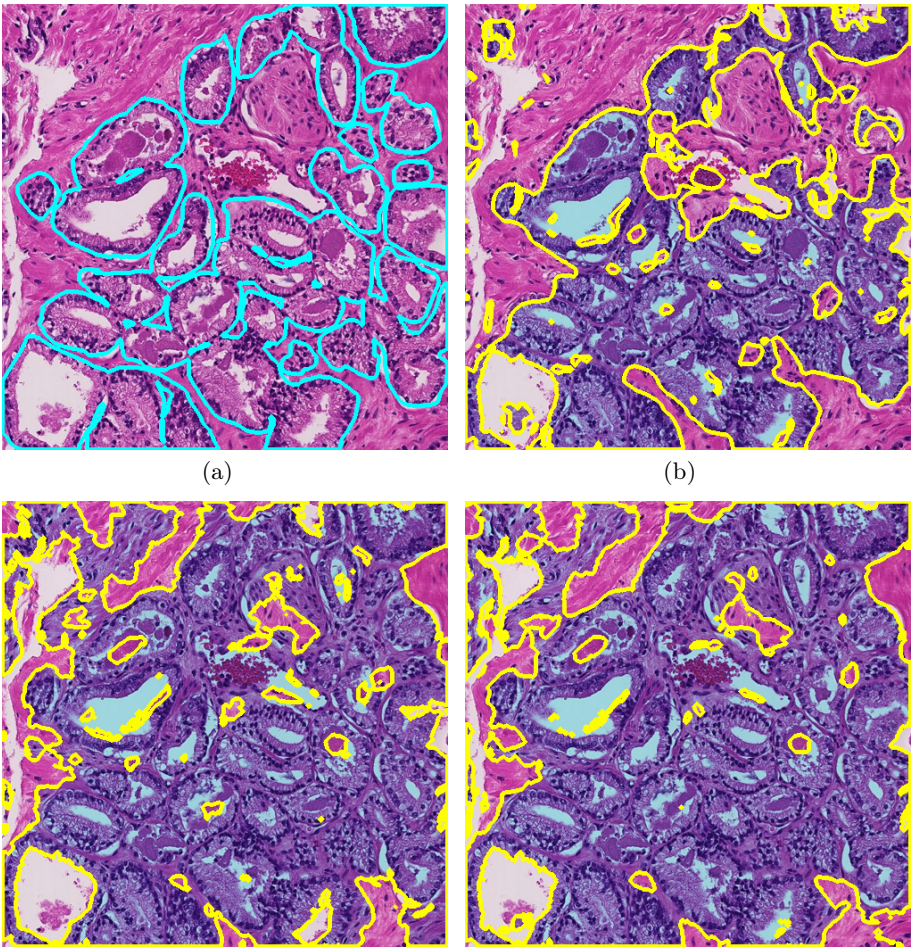

Fig. 4. Example *knn*-classification results in clustered G3 areas: (a) ground truth, (b) using Hist(HE) (c) using HOG(H), and (d) using HOG(H)Hist(HE)

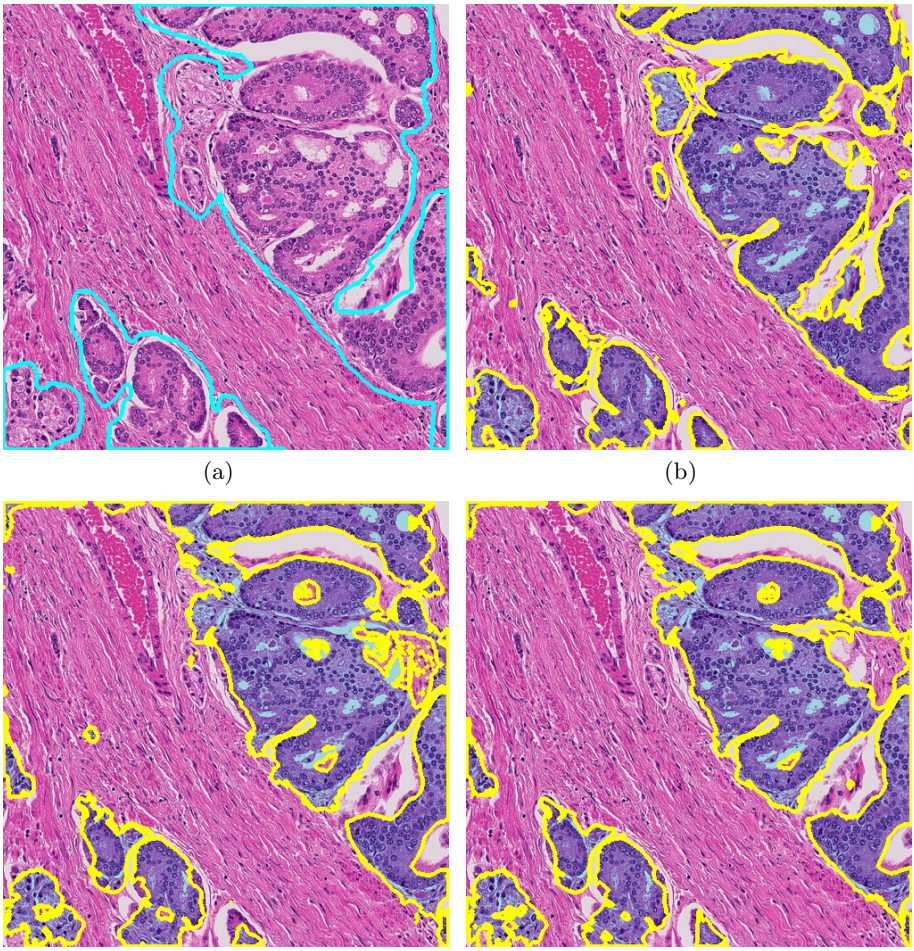

Fig. 5. Example *knn*-based classification results in dense cribriform G4 areas: (a) ground truth, (b) using Hist(HE) (c) using HOG(H), and (d) using HOG(H)Hist(HE)

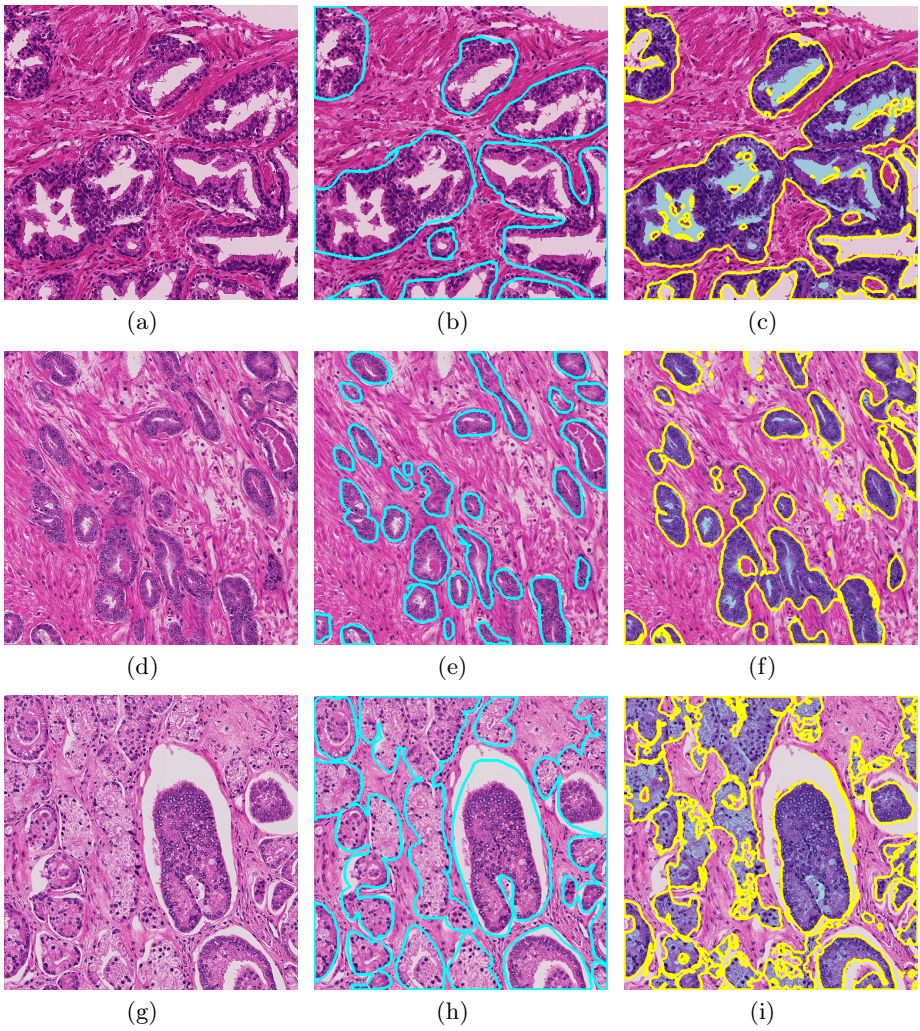

Fig. 6. Example classification results in complex areas: (a), (d), (g) original images, (b), (e), (h) pathologist outlines, and (c), (f), (i) image classified by means of Hist(HE) features and $knn(n = 3)$ classifier; individual BN, non-cluster G3 with artifacts and diverse cribriform G4 areas are shown in first, second and third row respectively

5 Discussion

The main goal of this study was to devise a method that could automatically pre-process prostate tissue images for a more comprehensive computer-assisted analysis. The pre-processing is meant to yield a mask covering areas of interest, so that the digital grading techniques can focus on the glands rather than on the entire fields of view which may include large patches of stroma that provide no

vital information in prostate cancer grading. Towards developing a methodology that distinguishes stroma, and cancer with different Gleason grades we tested the capacity of several machine learning approaches. Areas of interest were best separated from stroma by the algorithm that utilized the $knn(n = 3)$ classifier and Hist(HE) features. Our success was demonstrated by the high average measures of Ov, Ji, and Ri that reached respectively 0.871, 0.678 and 0.732 across all images, indicating a high concordance with the manual rater. Ov rates in ST-BN and ST-G3 areas were above average and higher than in ST-G4 areas. However, Ji indices in ST-BN and ST-G3 were lower than the average. Although our new method was tested on a limited set of images, it achieved a Ji index higher than 0.66 which was reported in [8]. In addition, our method performed well in different type of glands, a point that was not evaluated in [8].

We attribute the high rates of gland segmentation to the Hist(HE) features which were able to better discern the specific prostate cancer image characteristics than all HOG(.), Hist(E) and Hist(H) features alone. As illustrated by histograms in Figure 2, stroma has a lower amount of highly concentrated hematoxylin and a higher amount of highly concentrated eosin per unit area compared to glands. These characteristics allowed to use the high density of nuclei in all types of glands as a unique feature distinguishing stromal components including blood vessels, fibroblasts, and immune cells from glands. The classification of glands and stroma was straightforward in our method. In contrast, [8] required k-means clustering algorithm in the RGB color space, searching of lumen edges, recognizing of nuclei to generate lunimal and glandular outlines. Peng's method [7] used principal components on color of RGB images, k-means clustering to identify lumen, cytoplasm, nuclei and stroma and post-processing procedures with region-growing seed selection to determine the glandular mask.

Another factor contributing to the success of our analytical method was the selection of training windows in a way that they partially contained areas with no tissue (gland lumen, blood vessel lumen, or background). Such selection had a positive impact on the classification performance. As a result, most of the glands in G3 and BN areas with visible lumen even if occupied by corpora amylacea were correctly segmented out. Using our new technique; whole, single, clustred or cribriform glands as well as partial glands can be reliably detected. Individual results may however depend on the training set which may need to be optimized for best performances. Results suggest that our technique can significantly improve gland segmentation including those that have an obscured or compressed lumen and constitutes a valid alternative to several published methods [3, 6, 8, 7] which frequently ignore, or fail to segment such glands.

6 Conclusions

We have developed an analytical framework to separate glands and cancer areas from stroma in high resolution images of radical prostatectomies. The approach can serve as a first step preceding the quantification and stratification of anatomic tissue structures by providing a mask of components of interest for further analysis.

Acknowledgement. This work was supported by grants from the Department of Surgery at Cedars-Sinai Medical Center.

References

1. Fine, S.W., Amin, M.B., Berney, D.M., et al.: A contemporary update on pathology reporting for prostate cancer: biopsy and radical prostatectomy specimens. Eur. Urol. 62(1), 20–39 (2012)
2. Brimo, F., Montironi, R., Egevad, L., et al.: Contemporary Grading for Prostate Cancer: Implications for Patient Care. Eur. Urol. 63(5), 892–901 (2013)
3. Dole, S., Feldman, M.D., Shih, N., Tomaszewski, J., Madabhushi, A.: Cascaded discrimination of normal, abnormal, and confounder classes in histopathology: Gleason grading of prostate cancer. BMC Bioinformatics, 13–282 (2012)
4. Gorelick, L., Veksler, O., Gaed, M., et al.: Prostate Histopathology: Learning Tissue Component Histograms for Cancer Detection and Classification. IEEE Transactions on Medical Imaging 32(10), 1804–1818 (2013)
5. Loeffler, M., Greulich, L., Scheibe, P., Kahl, P., Shaikhibrahim, Z., Braumann, U.D., Kuska, J.P., Wernert, N.: Classifying prostate cancer malignancy by quantitative histomorphometry. J. Urol. 187(5), 1867–1875 (2012)
6. Doyle, S., Hwang, M., Shah, K., Madabhushi, A., Feldman, M., Tomaszewski, J.: Automated grading of prostate cancer using architectural and textural image features. In: 4th IEEE International Symposium on Biomedical Imaging: From Nano to Macro, pp. 1284–1287 (2007)
7. Peng, Y., Jiang, Y., Eisengart, L., Healy, M.A., Straus, F.H., Yang, X.J.: Computer-aided identification of prostatic adenocarcinoma: Segmentation of glandular structures. J. Pathol. Inform. 2, 33 (2011)
8. Nguyen, K., Sarkar, A., Jain, A.K.: Structure & Context in Prostatic Gland Segmentation and Classification. In: Ayache, N., Delingette, H., Golland, P., Mori, K. (eds.) MICCAI 2012, Part I. LNCS, vol. 7510, pp. 115–123. Springer, Heidelberg (2012)
9. Tabesh, A., Teverovskiy, M., Pang, H.Y., Kumar, V.P., Verbel, D., Kotsianti, A., Saidi, O.: Multifeature prostate cancer diagnosis and Gleason grading of histological images. IEEE Trans. Med. Imaging 26(10), 1366–1378 (2007)
10. Goode, A., Gilbert, B., Harkes, J., Jukic, D., Satyanarayanan, M.: OpenSlide: A vendor-neutral software foundation for digital pathology. J. Pathol. Inform. 4, 27 (2013)
11. Ruifrok, A.C., Johnston, D.A.: Quantification of histochemical staining by color deconvolution. Analytical & Quantitative Cytology and Histology 23(4), 291–299 (2001)
12. Dalal, N., Triggs, B.: Histograms of Oriented Gradients for Human Detection. In: Int. Conference on Computer Vision & Pattern Recognition, vol. 2, pp. 886–893 (2005)
13. Rand, W.M.: Objective criteria for the evaluation of clustering methods. Journal of the American Statistical Association 66(336), 846–850 (1971)

Spectral Classification of Dual Nuclear p16/Ki67 Positivity in Pap Smears

Sukhveer Sandhu Singh[1] and Arkadiusz Gertych[1,2,3]

[1] University of Southern California, Department of Biomedical Engineering, Los Angeles, CA 90048, USA
[2] Cedars-Sinai Medical Center, Department of Pathology and Laboratory Medicine
[3] Cedars-Sinai Medical Center, Department of Surgery, Los Angeles CA 90048, USA
arkadiusz.gertych@cshs.org

Abstract. An automated detection and quantification of high-risk human papillomavirus immunostains in Pap smears can potentially improve the drawbacks of human observes, reduce the number of equivocal or misinterpreted cytologic specimens and increase the throughput of slide screening. Towards increasing the accuracy and efficacy of Pap smear screening, we tested a spectral imaging approach to quantify the dual p16/Ki67 immunoreactivity of epithelial cell nuclei in Pap smears. We demonstrated that the classification of spectral signatures extracted from nuclear pixels is helpful in detecting nuclei of cells that are positive for p16 and Ki67 and distinguishing them from other nuclei that are positive only for one or negative for both markers. Sensitivity of the proposed method was 84.4% whereas the specificity was 99.9%. Although our results are preliminary, they suggest that the implementation of spectral imaging and spectral classifications can potentially offer better nuclei screening performances than methods utilizing conventional RGB imaging.

1 Introduction

Cervical cytology, generally known as the Pap test, is the most effective way to detect precursor lesions, stratify women at risk for cervical cancer, and ultimately prevent its development [1, 2]. In liquid-based technology cervical cells are first collected with a cytobrush, then separated from blood, mucus, and debris and finally transferred onto a slide. After staining, slides are examined by a trained cytotechnologist or cytopathologist using a transmitted light microscope to determine the presence of abnormal cells. Evaluating the morphology of each cell is time consuming, labor intensive, subjective, and costly. Intra- and inter-observer variability in the diagnosis of precursor lesions as well as occasional false positive and false negative diagnoses of cancer negatively affect the efficacy of manual screening. Nearly all cervical intraepithelial neoplasias (CIN) and carcinomas are caused by high-risk human papillomaviruses (hrHPV). Whereas the majority of low-grade HPV lesions spontaneously regress without treatment, persistent

E. Pietka, J. Kawa, and W. Wieclawek (eds.), *Information Technologies in Biomedicine, Volume 3*, Advances in Intelligent Systems and Computing 283,
DOI: 10.1007/978-3-319-06593-9_27,

infection is associated with progression to high-grade precursor lesions and cervical cancer that warrants treatment. The development of immunochistochemical biomarkers that are overexpressed in most hrHPV associated cervical carcinomas and dysplasias has the potential to significantly enhance the capabilities of manual screening [4, 3, 5, 6]. CINtec®PLUS (MTM laboratories,Westborough, MA), a dual immunostain that simultaneously detects p16 and Ki67 over-expression, has been shown to be useful in detecting high-grade CIN and in resolving cytomorphological ambiguities for cervical cancer risk stratification. P16 is a cyclin-dependent kinase inhibitor that is over-expressed in high-grade CIN and invasive cervical squamous carcinoma, and has also been shown to be useful in the triage of atypical squamous cells of undetermined significance and low-grade CIN [3]. Ki67 is a nuclear protein that is also over-expressed in high-grade CIN [5]. Nuclei of cells that overexpress Ki67 have a red color. P16 positive cells have a brown appearance of the whole cell and nuclei. Cells that stain negative for p16 and Ki67 exhibit blue counterstaining in the nucleus and a bluish staining in the cytoplasm. According to manufacturer's guidelines the presence of at least one cell that simultaneously overexpresses both biomarkers constitutes a positive Pap test result. However, it is difficult for the human eye to: (a) distinguish dual-stained cells from cells that stain for one of these biomarkers, and (b) interpret co-localized brown and red tones.

An automated detection and scoring of immunostains in Pap smears can potentially improve the drawbacks of human observes, reduce the number of equivocal or misinterpreted cytologic specimens and increase the throughput of screening [6, 9]. However, the development of tools to detect and classify the dual p16 and Ki67 positive (p16+/Ki67+) overexpressions in Pap smears is a new field. So far, the analyses were performed in color (RGB) images and revealed that colocalization of red and brown colors in the nuclei of cervical epithelial cells can be detected and quantified. Yet, a reliable detection of the dual overexpression remains challenging due to presence of areas of low and high staining intensity of p16 and Ki67 even within one cell.

Multispectral imaging can capture band-separated signals of visible light transmitted through an object of interest. Separately captured wavelengths represent responses of the object to the light passing through it, and allow forming if spectral signatures which uniquely identify object's colorimetric properties. Towards increasing the accuracy and efficacy of Pap smear screening, in this work, we tested a spectral imaging approach to quantify the dual p16/ki67 immunoreactivity of cell nuclei in Pap smears. Such studies have not been so far undertaken. We implemented a set of spectral signatures to classify nuclear pixels, and then the entire nucleus with the aim to improve sensitivity and specificity of the detection of dual positive p16/Ki67 (p16+/Ki67+) cells. Detection performances of the spectral classification were compared with the performances of RGB classifications previously reported.

2 Materials

2.1 Specimens and Image Acquisition

The experimental data were obtained from 10 liquid-based (SurePathTM) cervical Pap smears (8 diagnosed with abnormal cells and 2 diagnosed as negative for malignant and dysplastic cells). The process of specimen staining for p16 and Ki67 dual overexpression was described in [4, 3]. Slide preparation was followed by a manual screening performed by experienced cytopathologists who manually annotated the abnormal cells with the assistance of a conventional compound microscope.

5 to 20 non-overlapping areas were selected in each slide. Imaging was performed on a whole slide imager platform Vectra 2 (Perkin-Elmer, CA) dedicated for tissue biomarker discovery and validation. The equipment comprised a spectral image acquisition device, coupled with a scientific-grade CCD camera, and image acquisition software (Nuance). High power 20x objective, 4ms exposure time and 1x1 pixel binning were set to acquire a single image array with 1040x1392 pixels (pixel size = 0.5μm x 0.5μm) covering each area. Spectral range was 420nm to 720 nm with 10nm increments. Each area was represented by a spectral cube containing 31 images, each representing optical density for one wavelength from the above range. In total 99 spectral cubes were collected. Acquired cubes were flat-field corrected using an area with no cells. Each spectral image (a component of the spectral cube representing an optical density for a wavelength in the spectral range) was exported as a TIFF file. Separately, RGB images with areas containing dual p16/Ki67 positive cells were acquired to validate results from our spectral analyses and to perform nuclei segmentation.

2.2 Spectral Signatures

Our main goal was to identify all p16+/Ki67+ cells among other cells that are positive solely for one marker either for p16 (p16-/Ki67+), or for Ki67 (p16+/Ki67-), or negative for both markers (p16-/Ki67-). Localization of all p16+/Ki67+ cells was known as they were already identified directly on the slide by pathologists. Example nuclei are shown in Figure 1. 28 nuclei were singled out. Each nucleus was marked as either p16+/Ki67+, p16-/Ki67+, p16+/Ki67-, or p16-/Ki67-, and subjected to manual extraction of signatures from spectral images. Each signature was represented by an ordered set of averaged optical densities from all nuclear pixels. Signatures were normalized by dividing each averaged optical density by the maximal optical density in the signature. The normalization of spectral signatures is a process frequently preceding a quantitative analysis of tissue samples. It diminishes the difference between amplitudes of strongly and weakly stained specimens and preserves the shape of signatures. Signatures of optically dense nuclei had low amplitudes and were scaled up, whereas signatures of nuclei with low optical density were scaled-down. During this process the maximal amplitude of all signatures was set to 1. Normalized

signatures of 28 nuclei (Fig. 2) were labeled according to the p16/Ki67 colorimetric pattern, and saved as a library of signatures for classification of nuclear pixels in the subsequent steps of image analysis.

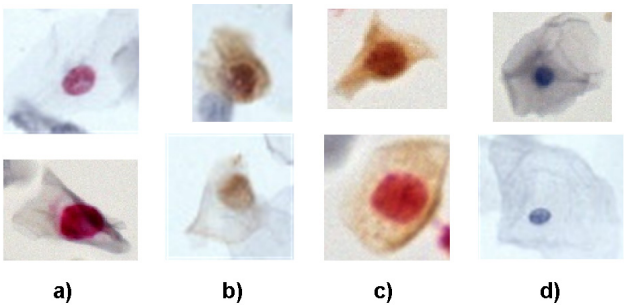

Fig. 1. Example cells with different p16/Ki67 immunoreactivity: a) p16-/Ki67+, p16+/Ki67-, p16+/Ki67+, and p16-/Ki67- cells

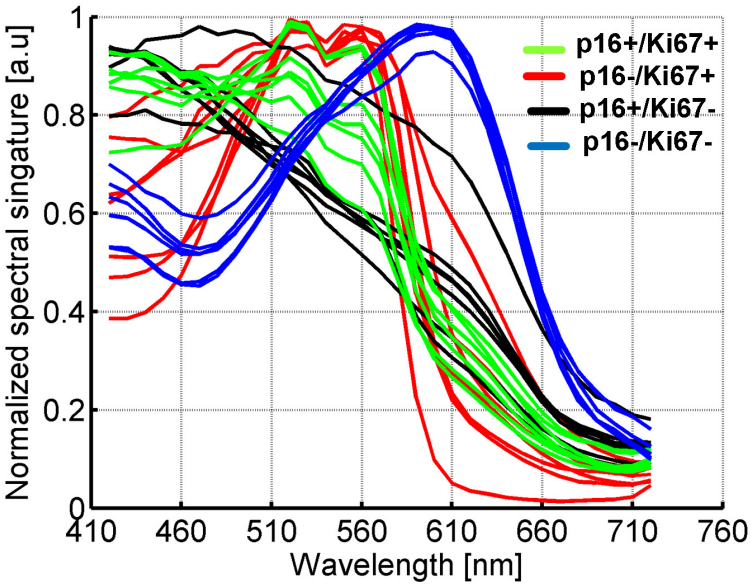

Fig. 2. Spectral signatures of nuclei with different p16/ki67 immunoreactivity

3 Methods

3.1 Workflow

We designed a workflow for the analysis of spectral images of Pap smears (Fig. 3). It consists of three main steps: a) segmentation of nuclei, b) extraction and

classification of nuclear pixels, and c) classification of whole nuclei to one of the four classes: p16+/Ki67-, p16-/Ki67+, p16+/Ki67+, or p16-/Ki67- based on the pixel-based classification. The output is a colored image representing classification results in individual nuclei.

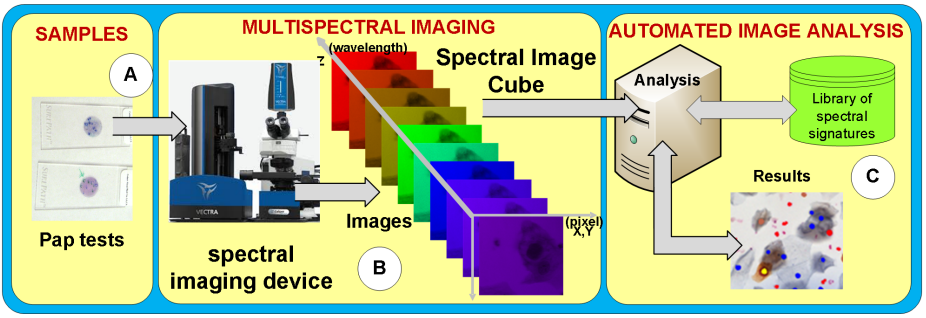

Fig. 3. General workflow of Pap smear analysis

3.2 Segmentation of Nuclei

In the first step the RGB color image captured during image acquisition was loaded up, and nuclei were segmented by means of our previously developed method [9]. This method utilized a radial symmetry transform followed by an adaptive thresholding of the symmetry image to delineate nuclear areas in single cells and cell clumps. The output of the nuclei segmentation is a binary nuclear mask in which each binary object represents a segmented nucleus (Fig. 4).

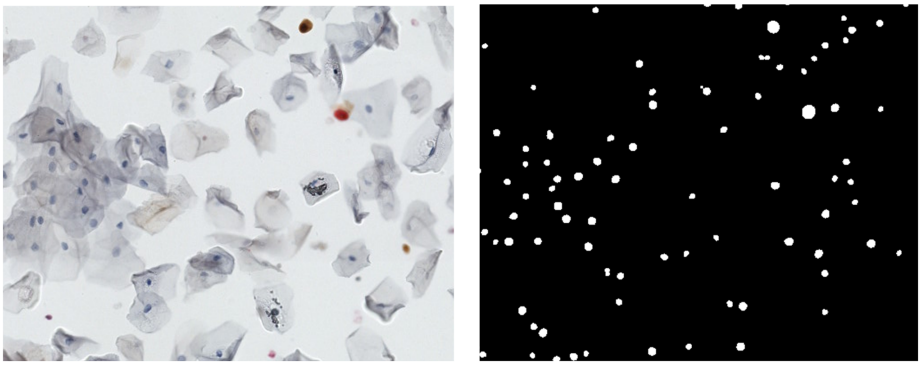

Fig. 4. Nuclei segmentation in Pap smears: a) original image, b) binary mask of nuclei

3.3 Pixel and Whole Nucleus Classifications

In the second step the objects (nuclei) in the binary mask were labeled, and a spectral cube corresponding to the binary mask was retrieved. Spectral signatures were extracted from the spectral cube for each labeled nucleus. The number of spectral signatures was equal to the number of pixels in the labeled nucleus. Next, spectral signatures of all pixels were normalized to perform pixel-based classifications.

In the third step a *knn* classifier with a neighbourhood size n=5 and signatures collected in the spectral library were used to classify individual pixels. The classifier compared each pixel's signature with all signatures in the library. During the classification spectral signatures from the library were ordered based on similarity to the pixel's spectral signature, and the most frequent p16/Ki67 color pattern of the 5 top ranked signatures was assigned to that pixel. The classification was carried on until all pixels of all nuclei were processed. In many nuclei all pixels were uniformly classified to the same class. However, there were nuclei which ended up with a blend of differently classified pixels. For example, in some p16+/Ki67+ cells the intensity of red coloring in the nucleus was strong in one area and weak in another. Several other p16+/Ki67+ cells possessed a much stronger brown coloring (p16) than a red coloring (Ki67) in the nuclear area. In some p16+/Ki67- cells the nucleus was partially brown and partially blue.

The final classification of the nucleus was determined by a series of steps based off of logic pathways prioritizing the voting for dual p16/Ki67 positive areas. If there was a single, uniform classification (c=1) for the entire nucleus, then that given classification was automatically assigned. If the number of unique classifications were two (c=2) then the majority pixel classification ended up defining the nucleus. However in the case of a 50% tie, a set of hierarchy was setup. Essentially, all classifications related to red, brown or both colors were regarded higher than a negative classification. For example if it is 50% red and 50% negative then red is the nuclear classification. Additionally if it was 50% brown and 50% red then by definition the nucleus was expressing red-and-brown colors so it was given a dual nuclear classification. See the Figure 5 for a graphical representation. In the case of three unique classifications (c=3) within the nucleus a unique set of circumstances was followed. The first check was if there were more than 33% of dual pixels in the nucleus. If there was a majority of dual pixels then the nucleus was classified as dual. However, if there was a majority of another classification, that particular classification was given precedence. In the case where the percentage of dual pixels was less than 33% the hierarchy given when c=2 was used. Everything was given precedence over blue color, however in this case if there were red and brown pixels within the nucleus, for example 12 red pixels and 15 brown pixels, then the 12 red pixels and 12 of the brown pixels were automatically changed to dual type pixels. In the end there were 24 new dual pixels, 0 red, and 3 brown pixels. Afterwards the majority of the pixel count (voting) was taken as the nuclear classification. In the case of four unique classifications (n=4) within a particular nucleus, the first step was to eliminate

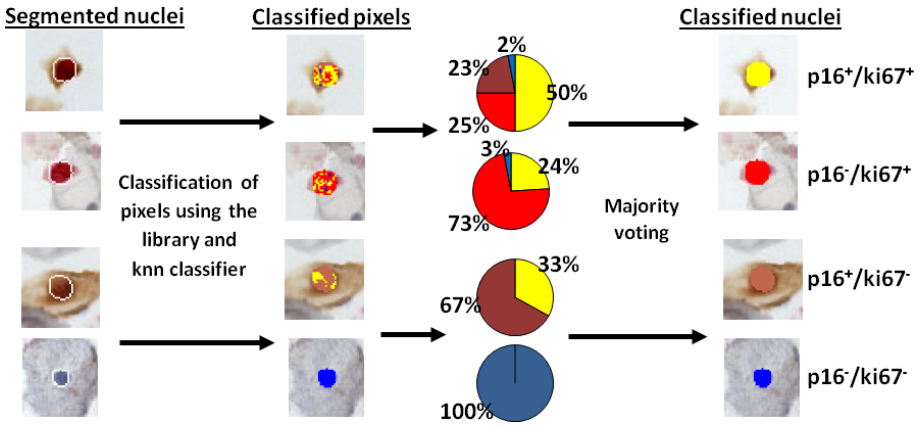

Fig. 5. Example pixel-based classifications and classified nuclei of cells with different p16/Ki67 immunoreactivity

at least one of the unique classifications. Red, brown or both were eliminated by combining them to create dual, much like we did at the end of the c=3 classification case. From there we implemented the rest of the c=3 classification logic. In the above approach we attempted to favour the dual classification over the other color combination instances. The rationale for this approach was to provide a unified classification result in case the staining pattern within a nucleus was not uniform. After all nuclei are analyzed the program returns the pixel-based and the whole nucleus-based classifications.

4 Results

We have developed a pilot workflow for a spectral quantification of nuclei in Pap smears stained with two p16 and Ki67 biomarkers which employ red and brown dyes to indicate biomarker's overexpression. Spectral signatures of automatically segmented nuclei were classified through a cascade of pixel-based and whole nucleus-based classifications. The primary goal of this study was to correctly identify nuclei with the presence of dual p16+/ Ki67+ coloring in the nucleus. In order to verify our results we utilized manually annotated p16+/Ki67+ cells from our previous study [9].

A correct whole-nucleus classification was counted as a true positive (TP) detection. A true negative (TN) detection occurred in case of nucleus classification to either: p16-/Ki67-, p16+/Ki67-, or p16-/Ki67+ which was correct. A false negative (FN) detection indicated an assignment of a truly p16+/Ki67+ nucleus to either: p16-/Ki67-, or p16+/Ki67-, or p16-/Ki67+ category. A false positive (FP) detection occurred when a nucleus positive for one of the markers or negative for both markers was detected with the dual p16+/Ki67+ overexpression. Implementation of our methods ultimately led to the following statistics:

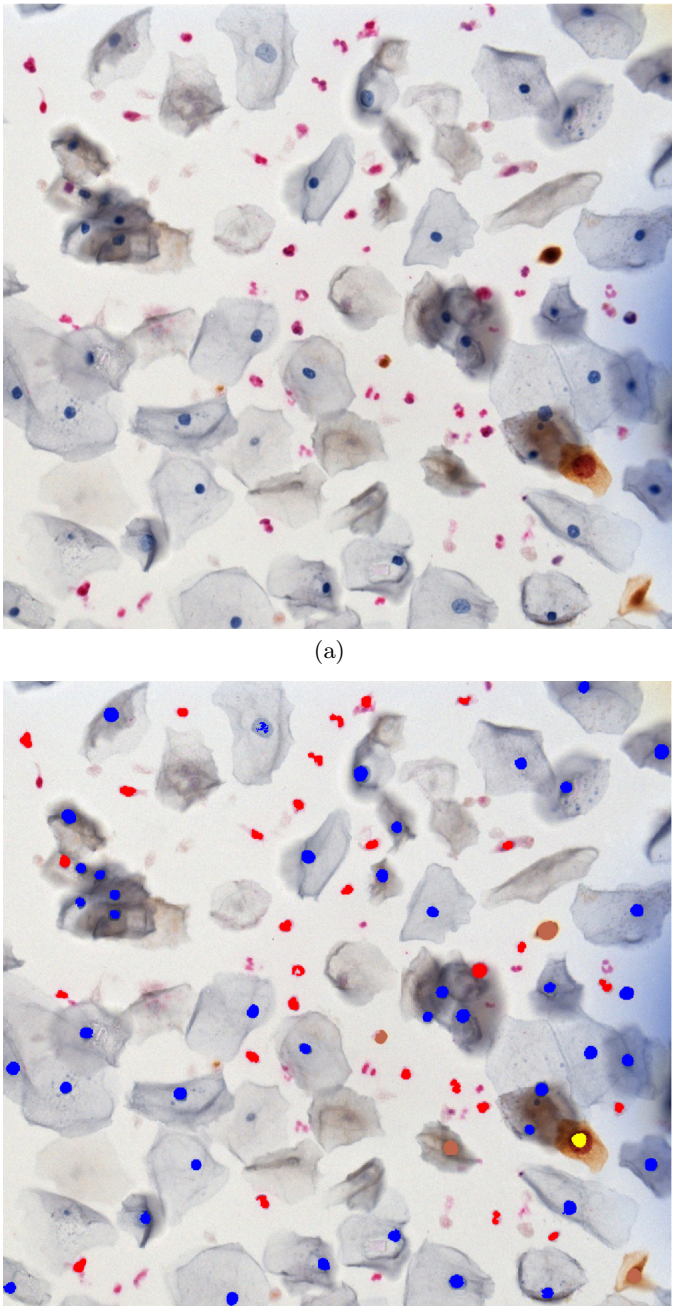

(a)

(b)

Fig. 6. Final nuclei classification: a) original image, b) classified nuclei. Yellow color indicates p16+/Ki67+ nuclei, red p16-/Ki67+, brown p16+/Ki67-, and blue p16-/Ki67- nuclear detections

TP=67, FN=12, TN=33113, and FP=4. The sensitivity ($TP/(TP+FN)$) of the p16+/Ki67+ nuclei detection was 84.81%, and the specificity ($TN/(TN+FP)$) was 99.9%. Example classification results for an area containing multiple cells is shown in Figure 6. In our previously reported method [9] sensitivities measured against two pathologists were 82.6% and 77.1% respectively, whereas the specificity was 99.6%.

5 Discussion

Spectral analysis of cytopatholgical specimens has been shown to be potentially useful as an adjunct tool to manual screening [8, 7]. However, with the advent of immunochistochemical biomarkers that are overexpressed in most hrHPV associated cervical carcinomas and dysplasias that also have the potential to significantly enhance the capabilities of manual screening, the development of tools adopted for computerized screening of immunohistochemically stained cytological specimens will follow. Computerized analysis of dual positive p16 and Ki67 nuclei in Pap smear images based on the brown and red color of dyes is a challenging task. The first challenge is detecting the nuclei, and the second is quantifying the various intensities that arise from the local concentration of two dyes in the nuclear region. Although the two dyes possessed very different spectral signatures (Fig.2), some signatures resulting from a colocalization of the dyes were either more similar to the brown (p16+/Ki67-) or the red (p16-/Ki67+) signatures due to a higher concentration of one marker versus the other. However, we demonstrated that the combined pixel-based classification of spectral signatures followed by the voting-based analysis of classified groups of pixels implemented in this study was capable to distinguish the four types of nuclear coloring patterns. Sensitivity of the proposed method was better by as much as 7.7% (4.9% on average) than the method we proposed in [9] which was based on the RGB imaging.

6 Conclusions

In this paper a method for spectral quantification of Pap smears stained by two immunohistochemical biomarkers is presented. We were able to build it upon the previously implemented and tested nuclei detection and quantification technique. Our major challenge was to deal with the presence of two markers in the nucleus area. We so far addressed it by the classification of spectral signatures derived from the nucleus, to deliver a proof of concept. Although our results are preliminary, they suggest that the implementation of spectral imaging and spectral classifications can potentially offer better nuclei screening performances than methods utilizing conventional RGB imaging.

Acknowledgement. This work was supported by grants from the Department of Surgery at Cedars-Sinai Medical Center.

References

1. Sirovich, B.E., Welch, H.G.: The frequency of Pap smear screening in the United States. Journal of General Internal Medicine 19(3), 243–250 (2004)
2. Nanda, K., McCrory, D.C., Myers, E.R., Bastian, L.A., Hasselblad, V., Hickey, J.D., Matchar, D.B.: Accuracy of the Papanicolaou test in screening for and follow-up of cervical cytologic abnormalities: a systematic review. Annals of Internal Medicine 132(10), 810–819 (2000)
3. Loghavi, S., Walts, A.E., Bose, S.: CINtec (R) PLUS dual immunostain: a triage tool for cervical pap smears with atypical squamous cells of undetermined significance and low grade squamous intraepithelial lesion. Diagnostic Cytopathology 41(7), 582–587 (2013)
4. Walts, A.E., Lechago, J., Bose, S.: P16 and Ki67 immunostaining is a useful adjunct in the assessment of biopsies for HPV-associated anal intraepithelial neoplasia. The American Journal of Surgical Pathology 30(7), 795–801 (2006)
5. Nam, E.J., Kim, J.W., Hong, J.W., Jang, H.S., Lee, S.Y., Jang, S.Y., Lee, D.W., Kim, S.W., Kim, J.H., Kim, Y.T., et al.: Expression of the p16 and Ki-67 in relation to the grade of cervical intraepithelial neoplasia and high-risk human papillomavirus infection. Journal of Gynecologic Oncology 19(3), 162–168 (2008)
6. Wentzensen, N., Bergeron, C., Cas, F., Eschenbach, D., Vinokurova, S., von Knebel Doeberitz, M.: Evaluation of a nuclear score for p16INK4a-stained cervical squamous cells in liquid-based cytology samples. Cancer 105(6), 461–467 (2005)
7. Gertych, A., Galliano, G., Bose, S., Farkas, D.L.: Automatic recognition of abnormal cells in cytological tests using multispectral imaging. In: Proc. SPIE Medical Imaging 2010: Computer-Aided Diagnosis, vol. 7624, p. 762435 (2010)
8. Siddiqi, A.M., Li, H., Faruque, F., Williams, W., Lai, K., Hughson, M., Bigler, S., Beach, J., Johnson, W.: Use of hyperspectral imaging to distinguish normal, precancerous, and cancerous cells. Cancer 114, 13–21 (2008)
9. Gertych, A., Joseph, A.O., Walts, A.E., Bose, S.: Automated Detection of Dual p16/Ki67 Nuclear Immunoreactivity in Liquid-Based Pap Tests for Improved Cervical Cancer Risk Stratification. Ann. Biomed. Eng. 40(5), 1192–1204 (2012)

Simulation Analysis of the ATR Module as a Detector of UV-Induced DNA Damage

Monika Kurpas, Katarzyna Jonak, and Krzysztof Puszyński

Faculty of Automatic Control, Electronics and Computer Science, Silesian University of Technology, Akademicka 16, 44-102 Gliwice, Poland
monika.kurpas@polsl.pl

Abstract. Maintaining the integrity of the DNA in the cell is essential for the proper functioning of the organism. For this purpose detection, amplification and transduction of the signal about DNA damage to the effector module is necessary. This results with cell cycle arrest, DNA repair or apoptosis. In some of the eukaryotic cells, like human, two modules play roles as DNA damage detectors: ATM (ataxia telangiectasia mutated), which responds to the formation of double DNA strand breaks and ATR (ataxia telangiectasia mutated and Rad3-related), which is responsible for detecting single-strand damage. Simulation analysis of a constructed mathematical model of ATR pathway is a subject of this study. Our results show that ATR is an effective system for damage detection and amplification of the signal. The activation of this module is fast: detection takes place within a few seconds after the occurrence of the damage. The created novel mathematical model explains the mechanism of single-strand breaks detection, enables testing of the impact of modifications of proteins belonging to the ATR-p53 signaling pathway. Additionally the model explains that the basic activation of p53 protein signaling pathway observed in cells, may be caused by persistent cellular stress levels.

Keywords: ATR, DNA, damage, detection, model, SSB.

1 Biological Background

Thousands of DNA lesions are formed daily in each cell in the human organism. They can be induced either endogenously and exogenously - by physical and chemical agents from outside of the body. Endogenous factor causing DNA damage can be replication errors, tautomeric shift and replication slippage. Chemical agents causing DNA lesions are base analogs, deaminating factors, alcylating factors, intercalating agents, platinum derivatives, polycyclic aromatic hydrocarbons and reactive oxygen species. Physical damaging agents are ionizing irradiation (IR), ultraviolet radiation (UV), changing temperature and pH [1, 2].

There are several types of DNA damage, from small chemical modifications and single-stranded DNA breaks (SSBs) through the photoproducts and adducts caused by UV irradiation, to the potentially most dangerous double-strand breaks (DSBs).

E. Pietka, J. Kawa, and W. Wieclawek (eds.), *Information Technologies in Biomedicine, Volume 3*, Advances in Intelligent Systems and Computing 283,
DOI: 10.1007/978-3-319-06593-9_28,

The existence of such a large number of abnormalities in many cells may cause death of the single cell, but also of the whole organism, after a very short time. During evolution number of mechanisms that protect cell from damages evolved to prevent cell death and lesions transformation to future generations. There are several pathways of DNA repair depending on nature of damage, their review can be found in [3]. For all of these complex mechanisms of repair, it is necessary to detect DNA damage just after it arises and spread the information about it to the proper regulatory units. This process takes place in a manner specific to the type of lesion. ATR module is activated by presence of single-stranded DNA areas, which are caused by resection of various types of lesions or by stalled replication forks. DSBs are detected indirectly by ATM which is linked to the ATR pathway. Various stages of DNA damage detection by ATR and ATM and its further amplification are presented in Fig. 1.

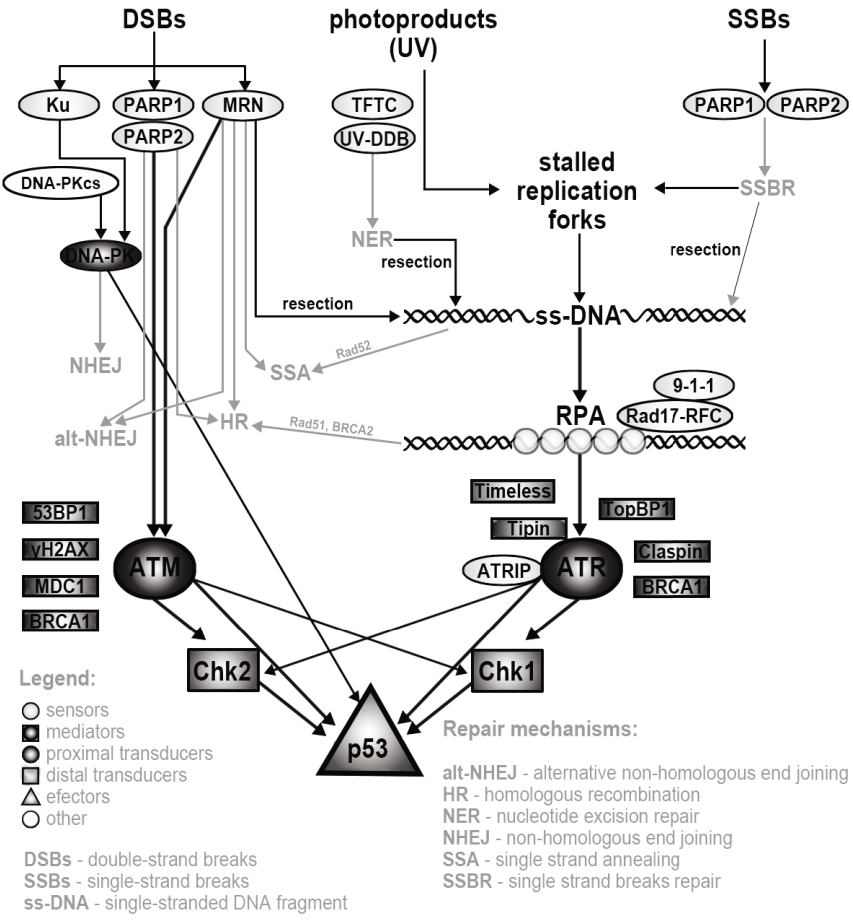

Fig. 1. DNA damage detection and signal amplification

The first step in damage detection by ATR module is joining RPA (replication protein A) complexes to single-stranded DNA (ssDNA) region. This causes independent movement of Rad17-RFC2-5, Rad9-Rad1-Hus1 (9-1-1 complex) and ATR-ATRIP complexes to the damaged site. ATRIP (ATR interacting protein) acting in ATR-ATRIP complex, is capable of attaching themselves to RPA-ssDNA, what induces autophosphorylation of ATR. Moreover, to the ss-DNA fragment binds as well Rad17-RFC2-5 complex, what allows the attachement of the 9-1-1 complex to the site of damage. Rad9 subunit of the 9-1-1 complex phosphorylated by ATR recruits TopBP1 (DNA topoisomerase 2-binding protein 1), which presence is necessary for full activation of ATR. ATR combined with TopBP1 phosphorylates many proteins from this pathway, including Rad17, and mounted by it claspin, which is necessary to recruit cell cycle checkpoint kinase 1 (Chk1). The signal strength of the checkpoint cascade is dependent on the length of RPA- ssDNA regions and possibility of ATR molecules to locate closely to each other. Other ATR phosphorylation targets are RPA subunits (RPA70 and RPA32), ATRIP, TopBP1, Chk2, p53 and histone H2AX [4, 5]. ATR module function is essential for cell viability and disruptions of ATR signaling cause genomic instability.

DSBs are detected by repair complexes like Mre11-Rad50-Nbs1 complex (MRN). MRN binds to DNA damage site and recruits ATM kinase, that after its autophosphorylation interacts with several proteins in the pathway (Chk1, Chk2, p53, Mdm) and leads to p53 stabilization. Damage detected by ATM, after resection may be recognized by ATR module [3].

A major effector for both pathways is tumor suppresor p53, known as "the guardian of the genome" which is a transcription factor that regulates, e.g. cell cycle, repair and apoptosis.

2 Methodology

2.1 Mathematical Modeling

In the process of modeling the cellular signaling pathways, we use the basic laws known from biochemistry: the law of mass action and Michaelis-Menten kinetics. The kinetic parameters for our model are obtained from the results of biological experiments known from literature. To estimate relative changes in the levels of the proteins from the ATR-p53 pathway, we use program [6]. Unknown parameters are estimated by fitting the model to the known data.

The proposed model is based on Haseltine-Rawlings postulate [7] which binds deterministic and stochastic approach. Here we use ODE (ordinary differential equations, Runge-Kutta fourth order method) to simulate fast reactions (e.g. protein-protein interactions) and direct Gillespie method [8] to simulate slow reactions (enabling genes and DNA lesions number).

2.2 Model of ATR-p53 Pathway

The presented model is an extension of the model of p53 signaling pathway developed by K. Puszyński [9]. To our knowledge, ATR-p53 model is innovative

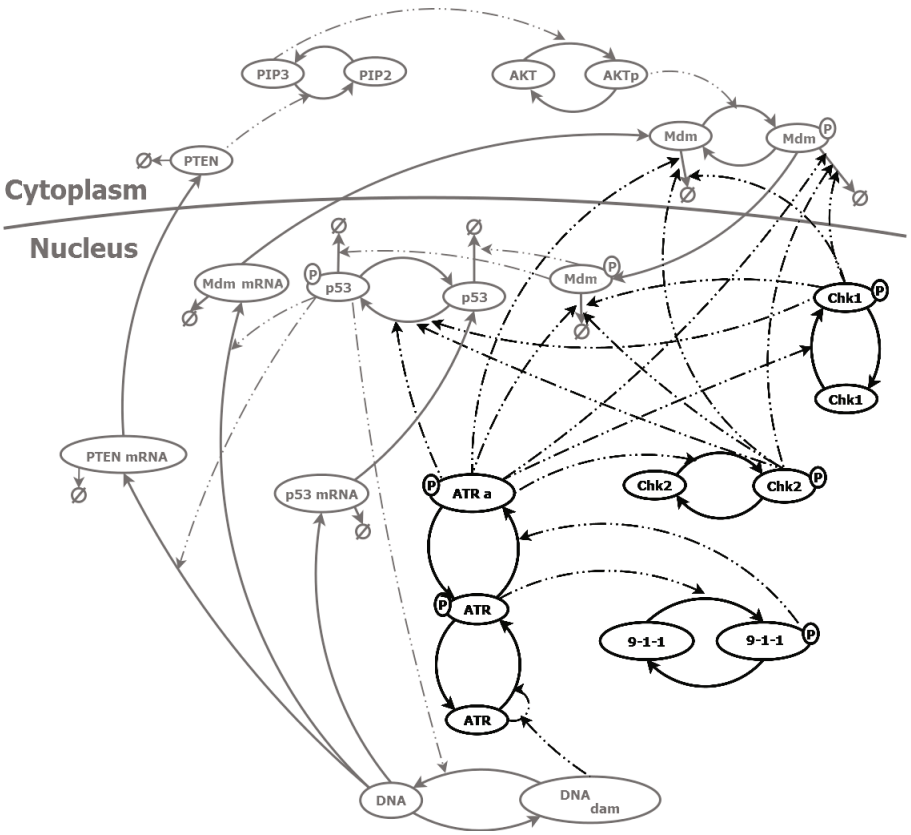

Fig. 2. DNA damage detection model vizualization; solid lines represent change of protein form; dashed lines describe the interactions that occur in the path; components of ATR module are marked

because it introduces expanded path of the UV-induced DNA damage response, which we do not observe in the models found in the literature. Only in the model proposed in [10] the authors show simplified interaction between ATR, p53, Mdm and Wip1. Our model is extended to other interactions which we find essential in the process of DNA damage detection in real life and during the simulaion analysis. The big advantage of our model is that it takes into account the impact of positive loop including PTEN (phosphatase and tensin homolog), which is responsible for many cancers. In addition, the authors of [10] do not take into account stochastic elements in their simulations. Stochastic in our models allows to observe the damage response of the cell population. Authors of [10] do not perform the analysis of the impact of various modifications in their model, e.g. impact of mutations in proteins belonging to the pathway.

Lack of similar models was one of the reasons of our interest in modeling this pathway. Another reason was the fact that this module is highly connected to

the p53 pathway, on which we were working previously [9], as well as to ATM module, on which we are working now.

Described model is a simplification of a real signaling pathway existing in the cell. The model is activated by UV irradiation which results in the occurrence of DNA SSBs. The output of the model is the level of p53 protein which determines cell fate: DNA damage repair or cell apoptosis. Spontaneous DNA damage formation implemented in presented model results in basic ATR-p53 pathway activation. The core of the model are states of ATR: inactive protein, its phosphorylated state, and fully activated form. In this model, there are two feedback loops: positive, with the participation of PTEN, and negative, containing p53 suppressor called Mdm (Fig. 2). In turn, phosphorylated p53 is a transcription factor for Mdm. Mdm activated in cytoplasm by Akt protein is transported to the nucleus where performs ubiquitination of p53, leading to its rapid degradation in proteasomes. The positive feedback loop blocks the effects of Mdm loop. P53 induces the production of PTEN which then inactivates PIP3 hydrolyzing it to PIP2 unable to activate Akt. Consequently, p53 blocks its own inhibitor Mdm, because without active form of the Akt, Mdm does not penetrate to the nucleus, and thus can not accelerate degradation of p53. Details about p53 signaling pathway are available in [9].

The model distinguishes the nucleus and cytoplasm. It was assumed that each gene has two copies. None of them can be active, one of them or both can be active. For some proteins production and degradation was not modeled directly, assuming that they are equal and protein only change the form (active to inactive and vice versa). In presented model, a simplified DNA repair was implementing depending on the number of p53 tetramers, repair rate and the amount of repair complexes, which is limited. Apoptosis condition is recognized as a permanently elevated level of the p53 protein (over 6 hours). Then the cell dies and all of its elements are degraded, thus further protein levels and the number of lesions are not taken into account.

3 Results

We examined cell response to different doses of UV radiation during the simulation analysis. We set the threshold of detection and apoptosis, as well as showed spontaneous activation of the ATR/p53 pathway. Deterministic and stochastic (for 100 cells) experiments were performed. At time t=24 hours after setting up the experiment, simulated cells were irradiated by a specific dose of UVC, and then observed over the next 48 hours. The model was verified based on the results of biological experiments from the literature.

According to [11] DNA damages caused by radiation dose of 10 J/m^2 UVC are repaired within 15 hours. This dose will cause 150 500 SSBs [12]. Under the assumption that number of SSBs depends on dose in linear manner, we examined that 1 J/m^2 causes 15 050 SSBs. Our model is based on the above assumption.

In [13] it was presented that 12 hours after irradiation with 20 J/m^2 UVC, the level of total p53 increases threefold. This information allows the estimation of the increase in number of p53 molecules in response to the damage.

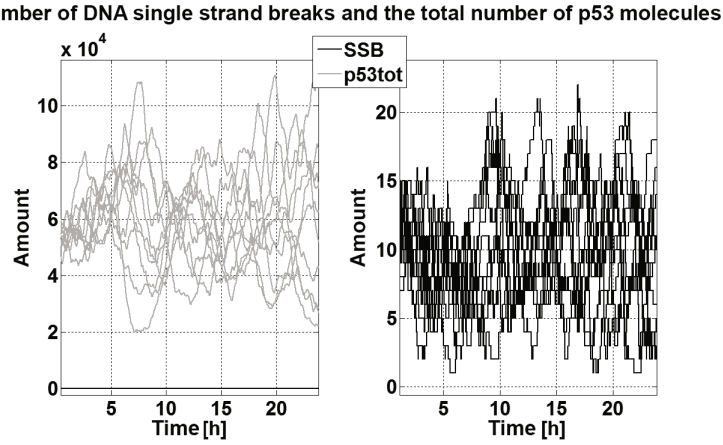

Fig. 3. Spontaneous DNA damage formation and p53 activation; result of 10 stochastic simulations

It was observed that two hours after irradiation with dose of 15 J/m^2 the total level of ATR within the cell increases about seven times [5]. As a result of dose of 50 J/m^2 Chk1 level increases eightfold after 1.5 hours [14], and the level of Chk2 increases sixteen-fold after 2 hours after irradiation [15].

3.1 Basic Activation

According to [16], in every cell of the human organism, daily about 55 000 SSBs are formed. They are responsible for base activation of the ATR-p53 pathway. We used this number in the model as an activation parameter of the model (Fig. 3).

3.2 Damage Detection Threshold

We examined the response of the model (Fig. 4A) to radiation dose causing one SSB (0.0665 mJ/m^2). We can observed that the lesion generated after 24 hour of experiment is detected by ATR module.

3.3 Apoptotic Death Threshold

Based on the observation of simulation results, the dose of 18 J/m^2, in which more than half of the cell becomes apoptotic, was taken as the threshold for apoptosis (Fig. 4B). For comparison, the dose 17 J/m^2 causes death of 44/100 cells. We assumed that apoptosis occurs when the level of p53 is increased by more than 6 hours (in simulation exceeding the threshold $2.1 \cdot 10^5$). Further experiments were run for the radiation dose of 18 J/m^2.

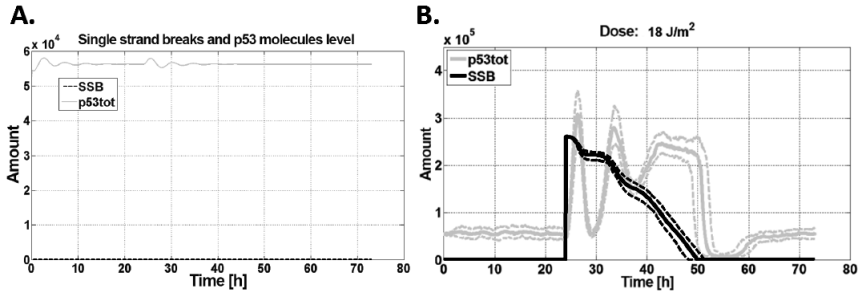

Fig. 4. A. Response to one lesion occurrence; B. Apoptotic death threshold; result for 100 stochastic simulations; solid line – median; dashed line – upper and lower quartile of result

3.4 Disabling Selected Effects

Disabling Phosphorylation of p53. Inhibition of the p53 phosphorylation caused by Chk1 and Chk2 kinases results in the reduction of apoptotic fraction size (Fig. 5A: 17/100 cells for the Chk1 and 14/100 cells to Chk2, for which plot appears almost identical), and a significant prolongation of DNA repair time. This effect of blocking is difficult to achieve biologically, because Chk1 and Chk2 phosphorylate mainly the same serine residue (Ser-20) of the p53 protein and it is difficult to separate their effects.

In the case of the inhibition of the ATR-dependent p53 activation (Fig. 5B), the apoptotic fraction decline was smaller (size of fraction was 46/100 cells). The blocking is, however, possible to obtain biologically by mutation of Ser-15 phosphorylated mainly by ATR [17].

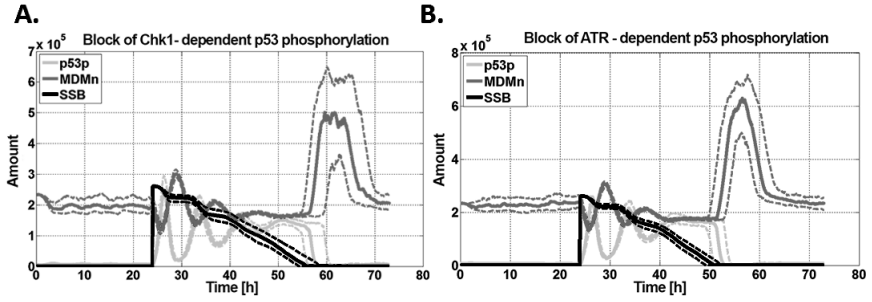

Fig. 5. Disabling mediated by Chk1(A.) and ATR (B.) p53 phosphorylation; results for 100 stochastic simulations; solid line – median; dashed line – upper and lower quartile of results

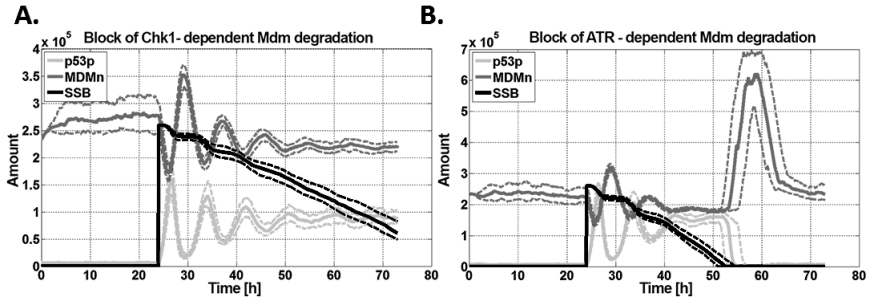

Fig. 6. Disabling mediated by Chk1(A.) and ATR (B.) Mdm degradation; results for 100 stochastic simulations; solid line – median; dashed line – upper and lower quartile of results

Disabling Degradation of Mdm. A stronger effect was obtained excluding Chk1 (Fig. 6A) and Chk2 dependent degradation of Mdm. None of the cells entered the state of apoptosis. It is possible to achieve biologically through modification of a relevant amino-chain residues of Mdmx. In our study we don't treat separately Mdm2 and Mdmx, what is complicated to model, but we focus on their common interaction. Chk1 phosphorylates Mdmx in Ser-342 whereas the Chk2 phosphorylates Mdmx in Ser-367. Mdmx phosphorylation leads to its Mdm2-mediated ubiquitination and degradation. Mdmx devoid of Mdm2 is unable to effectively bind p53 and can not lead to its degradation [18]. As in the previous case, less system response change was observed for the ATR (Fig. 6B). Apoptotic fraction size was 20/100. Biologically this condition may be obtained by modification of appropriate serine (Ser-407) of Mdm2 protein. Phosphorylation of Mdm2 in this residue reduces its affinity for HAUSP (deubiquitylating enzyme) that is a stabilizing factor of Mdm2 and Mdmx level in the absence of stress factor. Increased degradation of Mdm2 and MdmX results in lack of inhibition of p53 [18, 19].

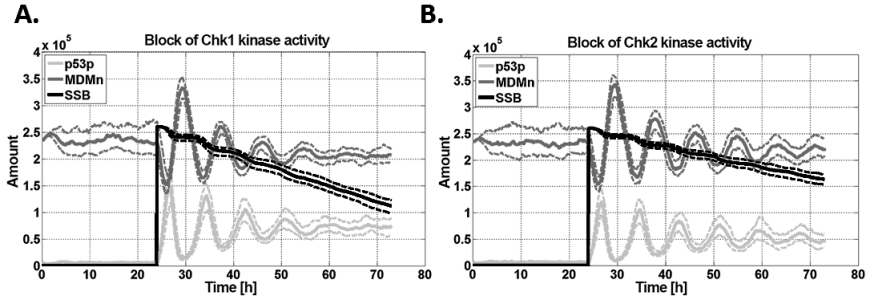

Fig. 7. Disabling total kinase activity of Chk1(A.) and Chk2 (B.); results for 100 stochastic simulations; solid line – median; dashed line – upper and lower quartile of results

Disabling Total Kinase Activity of Chk1 and Chk2. When total Chk1 (Fig. 7A) or Chk2 (Fig. 7B)protein kinase activity is blocked, none of the cells reach the state of apoptosis. This effect could be obtained in the case of a mutation in a gene fragment encoding protein kinase domains of Chk1 and Chk2 or mutation in the amino acid residues which are the target of the ATR-mediated phosphorylation. Also absence of mediators (e.g., claspin in the case of Chk1) may cause such an effect.

4 Conclusions

Simulation analysis show the correct functioning of the model stress response which effect is known from the literature. ATR module is able to detect a single-strand break caused by UVC appearing in the cell and enhance the signal so as to cause an increase in p53 protein level. Changes of protein levels observed in the simulation correspond to these found in the literature. We plan to perform the laboratory experiments in order to obtain the kinetic parameters for the model and confirm the results obtained during the simulation.

The threshold of apoptosis in the healthy cell is 18 J/m^2. However, if the pathway is defective, apoptotic threshold shifts. Despite extensive damage, the cells may not die, but transfer incorrect genetic material to daughter cells (because DNA damage repair takes a lot longer). This state could potentially be a cause of cancer and other genetic diseases.

The presented model can be used to study the behavior of cells with specific mutations without the need for costly and time-consuming experiments in the laboratory.

We plan to combine the model presented in this study with the model of the ATM-p53 pathway and to create links between these pathways to make a more accurate and universal model of DNA damage detection.

Acknowledgement. The project was financed by the National Science Centre, grant number DEC-2012/05/D/ST7/02072.

References

1. Brown, T.A.: Genomy. Państwowe Wydawnictwo Naukowe PWN, Warszawa (2001)
2. Friedberg, E.C., Walker, G.C., Siede, W.: DNA Repair and Mutagenesis. ASM Press, Washington DC (1995)
3. Ciccia, A., Elledge, S.J.: The DNA Damage Response: Making It Safe to Play with Knives. Molecular Cell 40, 179–204 (2010)
4. Zou, L., Elledge, S.J.: Sensing DNA Damage Through ATRIP Recognition of RPA-ssDNA Complexes. Science 300, 1542–1548 (2003)
5. Liu, S., Shiotani, B., Lahiri, M., Marechal, A., Tse, A., Leung, C.C.Y., Glover, J.N.M., Yang, X.H., Zou, L.: ATR Autophosphorylation as a Molecular Switch for Checkpoint Activation. Molecular Cell 43, 192–202 (2011)

6. Jonak, K., Jędrasiak, K., Polański, A., Puszyński, K.: Application of Image Processing in Proteomics: Automatic Analysis of 2-D Gel Electrophoresis Images from Western Blot Assay. In: Bolc, L., Tadeusiewicz, R., Chmielewski, L.J., Wojciechowski, K. (eds.) ICCVG 2012. LNCS, vol. 7594, pp. 433–440. Springer, Heidelberg (2012)
7. Haseltine, E.L., Rawlings, J.B.: Approximate simulation of coupled fast and slow reactions for stochastic chemical kinetics. Journal of Chemical Physic. 117(15), 6959–6969 (2002)
8. Gillespie, D.T.: Exact stochastic simulation of coupled chemical reactions. The Journal of Physical Chemistry 81(25), 2340–2361 (1977)
9. Puszyński, K., Hat, B., Lipniacki, T.: Oscillations and bistability in the stochastic model of p53 regulation. Journal of Theoretical Biology 254, 452–465 (2008)
10. Batchelor, E., Loewer, A., Mock, C., Lahav, G.: Stimulus-dependent dynamics of p53 in single cells. Molecular Systems Biology 7(488), 53 (2011)
11. Fornace, A.J.J., Kohn, K.W., Kann, H.E.J.: DNA single-strand breaks during repair of UV damage in human fibroblasts and abnormalities of repair in xeroderma pigmentosum. Biochemistry 73(1), 39–43 (1976)
12. Fornace, A.J.J.: Detection of DNA Single-Strand Breaks Produced during the Repair of Damage by DNA-Protein Cross-Linking Agents. Cancer Research 42, 145–149 (1982)
13. Maki, C.G., Howley, P.M.: Ubiquitination of p53 and p21 is differentially affected by ionizing and UV radiation. Molecular and Cellular Biology 17(1), 355–363 (1977)
14. Liu, Q., Guntuku, S., Cui, X.S.: Chk1 is an essential kinase that is regulated by Atr and required for the G 2/M DNA damage checkpoint. Genes and Development 14, 1448–1459 (2000)
15. Matsuoka, S., Rotman, G., Ogawa, A., Shiloh, Y., Tamai, K., Elledge, S.J.: Ataxia telangiectasia-mutated phosphorylates Chk2 in vivo and in vitro. In: Proceedings of the National Academy of Sciences, vol. 97(19), pp. 10389–10394 (2000)
16. Kohn, K.W.: Genomic Instability and DNA Repair. In: Alison, M.R. (ed.) The Cancer Handbook, 2nd edn. (2002)
17. Tibbetts, R.S., Brumbaugh, K.M., Williams, J.M., Sarkaria, J.N., Cliby, W.A., Shieh, S.Y., Taya, Y., Prives, C., Abraham, R.T.: A role for ATR in the DNA damage-induced phosphorylation of p53. Genes and Development 13, 152–157 (1999)
18. Wade, M., Wang, Y.V., Wahl, G.M.: The p53 orchestra: Mdm2 and Mdmx set the tone. Trends in Cell Biology 20(5), 299–309 (2010)
19. Shinozaki, T., Nota, A., Taya, Y., Okamoto, K.: Functional role of Mdm2 phosphorylation by ATR in attenuation of p53 nuclear export. Oncogene 22, 8870–8880 (2003)

Protein Hotspot Prediction Using S-Transform

Jan Kasparek[1], Denisa Maderankova[1], and Ewaryst Tkacz[1,2]

[1] Brno University of Technology, Faculty of Electrical Engineering, Department of Biomedical Engineering, Technicka 3058/12, 616 00 Brno, Czech Republic
xkaspa26@stud.feec.vutbr.cz
[2] Institute of Theoretical and Applied Informatics Polish Academy of Sciences, Bałtyka Street 5, 44-100 Gliwice, Poland

Abstract. Since experimental techniques of protein hotspot prediction are still financially extremely demanding and time consuming there is a strain to produce sufficiently reliable computational techniques for this particular task. We propose an algorithm based on Resonant Recognition Model relying heavily on signal processing techniques. Processed numerical signal is obtain solely form protein sequence using physical quantity EIIP. We therefore use no information of protein structure. The key element here is a time-frequency analysis tool – S-transform. This allows us to determine exact residues responsible for majority of performance on protein's characteristic frequency. We achieve basic sensitivity of 85 % and PPV 49 %, while demanding very little computing resources, because simplicity is one of the biggest advantages of our approach.

Keywords: Protein hotspots prediction, signal processing, electron-ion interaction potential, resonant recognition model, protein sequence, S-transform, time-frequency analysis.

1 Introduction

For more than a decade there have been efforts to compose a map of protein-protein interactions [1–3]. Although these maps are steadily growing and gaining more and more complexity, all they actually reveal is that particular interaction takes place at some point of cell's lifetime. There is no doubt this information is useful and even crucial for further study, however it still is just a mere observation of processes of which we have no deeper insight.

To acquire this insight we need to look closer at particular proteins and search for information on how these proteins actually interact with their partners to see what the exact mechanisms of each interaction are. Studies indicate that two interacting proteins align certain areas of their surface called binding sites [4]. These are rather large areas composed of tens of residues [5]. However not each residue contributes to the bond equally, in fact only a few residues are responsible for a vast majority of binding free energy [6]. In the past these residues were called active sites [7] and Rajamani once denoted them as anchor residues [8]. Today one can rarely find a paper referring to them in any other way than hotspots.

E. Pietka, J. Kawa, and W. Wieclawek (eds.), *Information Technologies in Biomedicine, Volume 3*, Advances in Intelligent Systems and Computing 283,
DOI: 10.1007/978-3-319-06593-9_29,

1.1 Alanine Scanning Mutagenesis

The first attempts to identify these hotspots were conducted in laboratories via means of daunting wet work. The procedure is known as Alanine Scanning Mutagenesis (ASM) [9]. It relies on mutating protein residues to alanine one at a time and then measuring change in binding free energy ($\Delta\Delta G$) produced during interaction with its counterpart. In the case of the mutated residue producing significantly less energy than the original wild-type protein, this residue is then regarded as a hotspot. So far there is no commonly accepted threshold value differentiating hotspot residues from non-hotspot residues. Most often researchers use $\Delta\Delta G = 1$ kcal/mol as a threshold value, however this is not always the truth [10]. Anyway, basically all experimental data available on hotspots were produced via means of this particular procedure and often their authors provided exact values of observed $\Delta\Delta G$ allowing readers to make their own conclusion [11].

As easy as it may sound ASM is in fact no simple task. Each mutated residue requires creation of whole new strain of bacteria – often Escherichia Coli – to produce mutated protein in sufficient amount for the change in free energy to be measurable. In fact this is so demanding that even proteins studied by ASM are not subjected to it in their full length. Only a few interesting residues are chosen to be mutated to alanine. In average their number usually lies around ten percent of protein's total length. Results of such experiments can be found in Alanine Scanning Energetics database. The financial and time requirements of ASM are one of the main reasons for high demand for different means of hotspot determination [11].

1.2 Existing Computational Methods of Hotspot Prediction

As an answer to these demands several computational techniques of protein hotspot prediction have emerged. Since even for the most demanding algorithms computational time is always significantly cheaper than lab work, this remains to be a trend.

At first there was focus on molecular docking techniques using information of protein structure. This brought up methods like MAPPIS [12], Hotpoint [13], Hotsprint [14], pyDockNIP [15] and several others. These approaches generally yield fairly good efficiency, but they also suffer one significant drawback. Their core idea requires the availability of protein structural data. Often it is not just any structural data that are acceptable and only high resolution structural data are to be used. Since only around 1 % of all known proteins' structure has been solved [16], this can be considerably restricting.

Lately we can see new approaches utilizing purely protein sequence, which gives them an edge over those described above. Although one group of these algorithms uses machine learning techniques including neural networks [16] and support vector machines [17], even these techniques did not come up with any generally applicable hotspot predictor. Another group of methods concentrates on signal processing techniques like digital filtering [18] and time-frequency analysis [19]. Furthermore these methods tend to have significantly lower computational requirements.

2 Proposed Algorithm

The algorithm we here propose utilizes signal processing techniques, namely S-transform, which is a time-frequency analysis tool. We therefore need only protein sequence and any data on protein structure are entirely unnecessary.

2.1 From Sequence to Numerical Signal

To employ any signal processing techniques, the first step inevitably has to be the conversion of the protein sequence to numerical signal. To do this we use a physical quantity called electron-ion interaction potential (EIIP). See Table 1 for its distribution among individual residues. EIIP describes average energy of residues' valence electrons and is often stated in Rydbergs (1 Ry = $2.18{\cdot}10^{-18}$ J). Since energy can only be positive, sequence of such values introduces an offset to the signal. Such an offset needs to be eliminated before further processing takes place. This is done by subtracting average value of each sequence from itself.

Table 1. Distribution of EIIP among 20 residues encoded in human genome

Residue	EIIP [Ry]	Residue	EIIP [Ry]
Alanine	0.0373	Leucine	0.0000
Arginine	0.0959	Lysine	0.0371
Asparagine	0.0036	Methionine	0.0823
Aspartic acid	0.1263	Phenylalanine	0.0946
Cysteine	0.0829	Proline	0.0198
Glutamic acid	0.0058	Serine	0.0829
Glutamine	0.0761	Threonine	0.0941
Glycine	0.0050	Tryptophan	0.0548
Histidine	0.0242	Tyrosine	0.0516
Isoleucine	0.0000	Valine	0.0057

2.2 Resonant Recognition Model and Characteristic Frequency

The basic idea of our algorithm – together with most of other signal-processing-based algorithms – is provided by Resonant Recognition Model [20]. This model claims that proteins sharing common function also share common frequency component in their Fourier spectra [21]. This common frequency component is then referred to as characteristic frequency [18]. For sake of simplicity we call these proteins of common function as related proteins.

So far the only way to obtain value of characteristic frequency is multiplying spectrum of particular protein with spectra of its related proteins until only one significant peak is visible in the product spectrum, which is often called consensual spectrum. This calculation can be described by following equation [18]:

$$S(e^{j\omega}) = |X_1(e^{j\omega}) \cdot X_2(e^{j\omega}) \cdot \cdots \cdot X_1(e^{j\omega})| \tag{1}$$

where $X_i(e^{j\omega})$ is Fourier spectrum of i-th related protein and $S(e^{j\omega})$ is consensual spectrum. To ensure equal length of all protein sequences we pad the shorter ones with zeroes.

There is no way to tell how many of these related proteins' sequences will be needed to obtain single significant peak in consensual spectrum and therefore the characteristic frequency. It can be as few as two, but often this number exceeds ten. From proteins in our dataset the highest number of related proteins used is twelve. When we have sufficient number of related proteins' sequences available, the consensus spectra may look like one shown in Fig. 1.

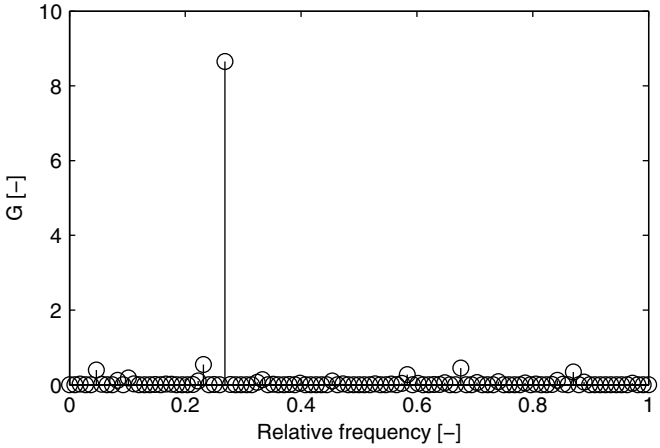

Fig. 1. Consensus spectrum of human growth hormone (3hhr chain A) after 8 multiplications with spectra of related proteins; characteristic frequency for this particular protein is 0.26852

To obtain related proteins' sequences we use proteins performing the same function, but found in different organisms. In our example of human growth hormone, some of its related proteins are rabbit growth hormone, chicken growth hormone, bull growth hormone and so on.

The way consensual spectrum is calculated highlights that we are in fact operating with evolutionary information. In protein interactions, hotspots are so important that the cell rarely survives mutation at their locus without impaired function. This is the reason why hotspots are highly conservative, which is an attribute we exploit during consensual spectrum computation [5].

The ability to determine protein's characteristic frequency is a crucial premise for successful use of our algorithm. If we cannot guarantee sufficient number of related sequences and therefore characteristic frequency determination, then any results we may obtain will be highly questionable and with high probability even useless.

2.3 S-Transform

Once we acquire the characteristic frequency, the next task is to determine which residues are responsible for majority of performance on this frequency. We do this by employing the S-transform (ST), which is a powerful time-frequency analysis tool. ST is similar to Short Time Fourier Transform (STFT), but introduces some very useful advantages. ST provides frequency dependent resolution similar to wavelet transform, while retaining easy to interpret output. Unlike STFT, ST is always invertible and thus allows for time-frequency filtering simply by modifying the ST spectrum.

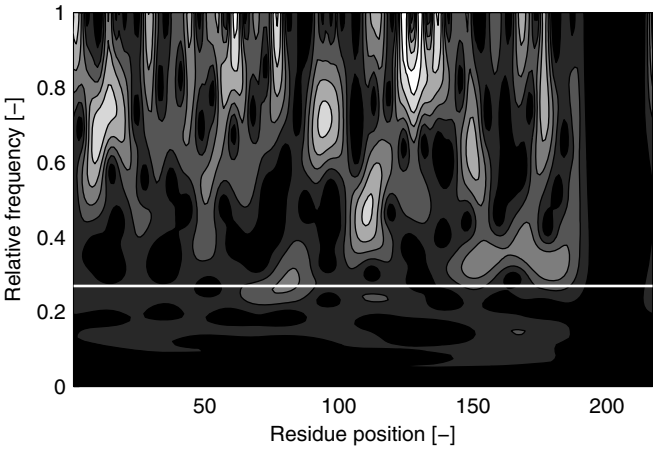

Fig. 2. ST spectrum of human growth hormone; white line marks characteristic frequency; area with zero performance on the right hand side is a result of zero padding

Mathematically, ST is defined as follows [22]

$$S(\tau, f) = \int_{-\infty}^{\infty} x(t)\omega(\tau - t, f)e^{-j2\pi ft}dt \tag{2}$$

where $x(t)$ is time varying signal as the transformation's input, $S(\tau, f)$ is sample of the output corresponding to time shift τ and frequency f. Window ω is then defined as

$$\omega(t, \sigma) = \frac{1}{\sigma(f)\sqrt{2\pi}} e^{\frac{t^2}{2\sigma^2(f)}} \tag{3}$$

where σ is window width defined as

$$\sigma(f) = \frac{1}{|f|} \tag{4}$$

2.4 Thresholding

The ultimate signal we use for hotspot prediction itself is a slice of the ST spectrum at characteristic frequency marked by a white line on Fig. 2. Waveform of this signal is shown in Fig. 3 together with reference data of known hotspot and non-hotspot residues. This signal is then subjected to thresholding and above threshold residues are deemed hotspots. Default threshold value is set to match mean value of ST spectrum slice, it can however be moved up or down to achieve desired results.

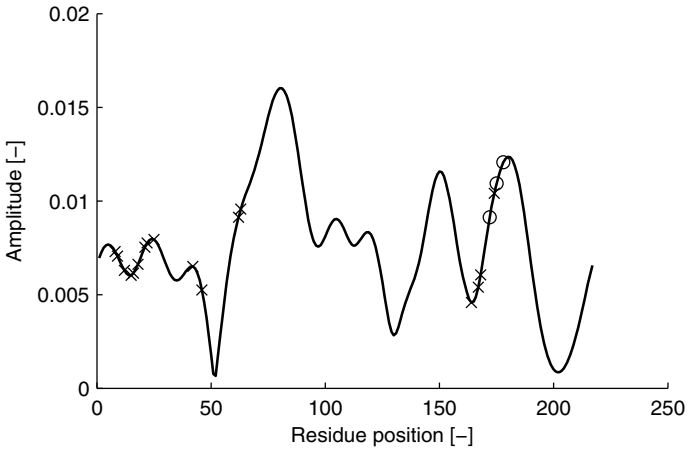

Fig. 3. Slice of ST spectra at characteristic frequency; crosses denote a priori known non-hotspot residues, while circles denote a priori known hotspot residues

2.5 Recapitulation

To summarize the course of algorithm: First, we convert amino acid sequence of examined protein and all its related proteins to numerical signal using EIIP values for individual residues. Secondly, we pad all these numerical sequences with zeroes to obtain sequences of equal length. Thirdly, we compute consensual spectrum to obtain value of characteristic frequency. Failure to accomplish this step will force us to abort as a result of insufficient number of related proteins' sequences or their poor choice. Fourthly, we use S-transform to obtain course of characteristic frequency over individual residues. Finally we apply thresholding on characteristic frequency waveform obtained in step four. Succession of all mentioned steps is clearly shown in Fig. 4.

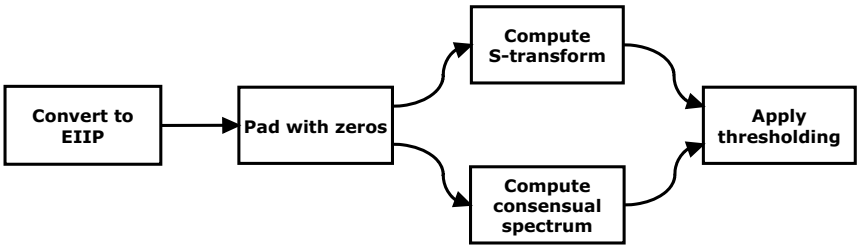

Fig. 4. Block scheme of the proposed algorithm

3 Results

3.1 Dataset

As a basis for our testing set of protein sequences we took a dataset put together by Nguyen with an aim to introduce representative sample of known protein families and thus form a reasonable training set for a machine learning technique published in [23]. It was pieced together from previous works of Tuncbag [24], Cho [25] and Kortemme [26]. The dataset includes no proteins achieving more than 35 % of mutual sequence identity. It only takes in account information obtained via means of ASM which is still the single most authoritative method of hotspot localization. Residues in the dataset marked as hotspots achieved $\Delta\Delta G \geq 2$ kcal/mol, while those marked as non-hotspots $\Delta\Delta G < 0.4$ kcal/mol [23].

Table 2. Protein sequences in our dataset

PDB ID	Chain ID	Name
1a22	A	Somatotropin
1a4y	A	RNAse inhibitor
1a4y	B	Angiogenin
1brs	D	Barstar
1bxi	A	Colicin E9 immunity protein
1cbw	D	Pancreatic trypsin inhibitor
1dan	T	Soluble tissue factor
1fcc	C	Streptococcal protein (C2 fragment)
1jrh	I	Interferon-gamma receptor alpha chain
1jtg	B	Beta-lactamase inhibitory protein
3hhr	A	Human growth hormone
3hhr	B	Human growth hormone receptor

Unfortunately we could only find sufficient number of related proteins for about half of the proteins in Nguyen's original set. This means we ended up with 12 proteins with suitable properties for our algorithm. Proteins composing this reduced dataset can be found in Table 2.

3.2 Achieved Efficiency

Table 3 clearly shows achieved efficiency of our algorithm in comparison with some other published methods. We can see that our algorithm provides the best value of sensitivity, on the other hand we are falling behind in terms of positive predictive value (PPV).

Table 3. Achieved efficiency of proposed algorithm compared to some of competitive approaches

Method	Sensitivity [%]	PPV [%]
ISIS	15	89
ROBETTA	69	71
MAPPIS	66	63
Hotpoint	59	70
pyDockNIP	43	75
Nguyen	58.9	74.8
ST filtering	83.33	62.5
Proposed	85.32	49.7

We have mentioned before that the actual threshold value can be moved. In doing so we should always bear in mind that the individual waveform of each protein's characteristic frequency can vary significantly. Therefore we have based the value of threshold offset on standard deviation of characteristic frequency waveform. The values displayed in Table 3 have been achieved with zero threshold offset from its default value matching mean value of slice of ST spectrum on characteristic frequency. By moving it up by 0.9 times of the standard deviation we can significantly boost achieved PPV value up to 57.57 % at the cost of sensitivity dropping to 57.86 %. Efficiency values of competing algorithms were all achieved on different datasets with an exception of Nguyen's algorithm.

4 Conclusion

We have introduced a protein hotspot prediction method based on theory of Resonant Recognition Model using S-transform as a time-frequency analysis tool. Although the proposed method achieves lower PPV than other mentioned approaches, its main advantage is in its simplicity and low computational requirements which is especially truth in comparison with molecular-docking-based methods. Another benefit of our approach is no need for structural data, on the other hand it was shown that even our need for sequences of related proteins can still prove to be restrictive. Even so, it is a considerably lower limitation.

Acknowledgement. Authors are very grateful to Nguyen et al. [23] for releasing their dataset for free use, this is exactly the kind of work hotspot-seeking community needs. This paper has been supported by the Program Project UMO-2012/07/B/ST6/01238 and authors would like to express their appreciation for that.

References

1. Ito, T., Tashiro, K., Muta, S., Ozawa, R., Chiba, T., Nishizawa, M., Yamamoto, K., Kuhara, S., Sakaki, Y.: Toward a protein-protein interaction map of the budding yeast: A comprehensive system to examine two-hybrid interactions in all possible combinations between the yeast proteins. Proc. Natl. Acad. Sci. USA 97, 1143–1147 (2000)
2. Schächter, V., Wojcik, J.: Protein-protein interaction map inference using domain profile pairs. Bioinformatics 17, S296–S305 (2001)
3. Davy, A., Bello, P., Thierry-Mieg, N., Vaglio, P., Hitti, J., Doucette-Stamm, L., Thierry-Mieg, D., Reboul, J., Boulton, S., Walhout, A.J., Coux, O., Vidal, M.: A protein-protein interaction map of the Caenorhabditis elegans 26S proteasome. EMBO Rep. 2, 821–828 (2001)
4. Hobohm, U., Sander, C.: Enlarged representative set of protein structures. Protein Sci. 3, 522–524 (1994)
5. Ma, B., Elkayam, T., Wolfson, H., Nussinov, R.: Protein-protein interactions: structurally conserved residues distinguish between binding sites and exposed protein surfaces. Proc. Natl. Acad. Sci. USA 100, 5772–5777 (2003)
6. Clackson, T., Wells, J.A.: A Hot Spot of Binding Energy in Hormone-Receptor Interface. Science 267, 383–386 (1995)
7. Cosic, I., Hearn, M.T.W.: Protein Active Sites are Defined as Resonant Spots in Protein 3D Structure. Engineering in Medicine and Biology Society, 206–207 (1992)
8. Rajamani, D., Thiel, S., Vajda, S., Camacho, C.J.: Anchor residues in protein-protein interactions. Proc. Natl. Acad. Sci. USA 101, 11287–11292 (2004)
9. Bogan, A.A., Thorn, K.S.: Anatomy of hot spots in protein interfaces. J. Mol. Biol. 280, 1–9 (1998)
10. Fernández-Recio, J.: Prediction of protein binding sites and hot spots. Wiley Interdiscip. Rev. Comput. Mol. Sci. 1, 680–698 (2011)
11. Thorn, K.S., Bogan, A.A.: ASEdb: a database of alanine mutations and their effects on the free energy of binding in protein interactions. Bioinformatics 17, 284–285 (2001)
12. Shulman-Peleg, A., Shatsky, M., Nussinov, R., Wolfson, H.J.: MAPPIS: Multiple 3D alignment of protein-protein interfaces. In: Berthold, M., Glen, R.C., Diederichs, K., Kohlbacher, O., Fischer, I. (eds.) CompLife 2005. LNCS (LNBI), vol. 3695, pp. 91–103. Springer, Heidelberg (2005)
13. Tuncbag, N., Keskin, O., Gursoy, A.: HotPoint: hot spot prediction server for protein interfaces. Nucleic Acids Res. 38, W402–W406 (2010)
14. Guney, E., Tuncbag, N., Keskin, O., Gursoy, A.: HotSprint: database of computational hot spots in protein interfaces. Nucleic Acids Res. 36, D662–D666 (2008)
15. Grosdidier, S., Fernández-Recio, J.: Identification of hot-spot residues in protein-protein interactions by computational docking. BMC Bioinformatics 9, 447 (2008)
16. Ofran, Y., Rost, B.: Protein-protein interaction hotspots carved into sequences. PLoS Comput. Biol. 3, e119 (2007)

17. Lise, S., Buchan, D., Pontil, M., Jones, D.T.: Predictions of hot spot residues at protein-protein interfaces using support vector machines. PLoS One 6, e16774 (2011)
18. Ramachandran, P., Antoniou, A.: Identification of Hot-Spot Locations in Proteins Using Digital Filters. J. Sel. Top. Signal Process. 2, 378–389 (2008)
19. Ramachandran, P., Antoniou, A., Vaidyanathan, P.P.: Identification and location of hot spots in proteins using the short-time discrete fourier transform. Conf. Rec. Thirty-Eighth Asilomar Conf. Signals, Syst. Comput. 2, 1656–1660 (2004)
20. Veljković, V., Ćosić, I., Dimitrijević, B., Lalović, D.: Is It Possible to Analyze DNA and Protein Sequences by the Methods of Digital Signal Processing? Trans. Biomed. Eng. BME-32, 337–341 (1985)
21. Cosic, I.: Macromolecular bioactivity: is it resonant interaction between macromolecules? – Theory and applications. IEEE Trans. Biomed. Eng. 41, 1101–1114 (1994)
22. Stockwell, R.G., Mansinha, L., Lowe, R.P.: Localization of the Complex Spectrum: The S Transform. Trans. Signal Process. 44, 998–1001 (1996)
23. Nguyen, Q., Fablet, R., Pastor, D.: Protein Interaction Hotspot Identification Using Sequence-Based Frequency-Derived Features. Trans. Biomed. Eng. 60, 2993–3002 (2013)
24. Tuncbag, N., Gursoy, A., Keskin, O.: Identification of computational hot spots in protein interfaces: combining solvent accessibility and inter-residue potentials improves the accuracy. Bioinformatics 25, 1513–1520 (2009)
25. Cho, K., Kim, D., Lee, D.: A feature-based approach to modeling protein-protein interaction hot spots. Nucleic Acids Res. 37, 2672–2687 (2009)
26. Kortemme, T., Baker, D.: A simple physical model for binding energy hot spots in protein-protein complexes. Proc. Natl. Acad. Sci. USA 99, 14116–14121 (2002)
27. Sahu, S.S., Panda, G.: Efficient Localization of Hot Spots in Proteins Using a Novel S-Transform Based Filtering Approach. Trans. Comput. Biol. Bioinforma. 8, 1235–1246 (2011)

Extended Spatial Evolutionary Games and Induced Bystander Effect

Michał Krześlak and Andrzej Świerniak

Silesian University of Technology,
Faculty of Automatic Control, Electronics and Computer Science,
Department of Automatic Control,
Gliwice, Poland
krzeslak.michal@gmail.com, andrzej.swierniak@polsl.pl

Abstract. The main goal of the study is modelling of radiation induced bystander effect using evolutionary game theory. A payoff table for three different phenotypes (game-theoretic strategies) contains: costs/profits of bystander effect, choice of apoptotic pathway, producing growth factors and resistance against bystander effect. Games are played on a lattice and for that purpose two kinds of spatial evolutionary games are presented and compared. Moreover different polymorphic equilibrium points dependent on model parameters and cells reproductions are discussed.

Keywords: evolutionary games, biomathematical modelling, carcinogenesis, cellular automata, polymorphism.

1 Introduction

The game theory has been frequently used as efficient methodology for processes simulation and analysis where decision-making is a key factor. The new viewpoints in such areas as genetics, ecology or etiology of diseases have been unlocked by evolutionary game theory (EGT) initiated by John Maynard Smith and George Price [1]. Their ideas link the mathematical tools of game theory with Darwinian fitting and species evolution. As a result the new approach provides new understanding of the game and players as well. Individuals, without any rationality, compete or cooperate with each other to obtain better position in the population. Payoffs measure a change in the degree of fitness resulting from interactions of the individuals. A good example for the introduction of mathematical approaches is fundamental evolutionary model: Hawk and Dove [2]. To delineate the results of such a game, the concept of Evolutionary Stable Strategy (ESS) was introduced in [2]. A phenotype, which is ESS, is resistant to the emergency and impact of the other or even new phenotypes (as a result of environmental migration or mutation) and also cannot be repressed by them. On the other hand, the opposite situation is possible, so that whenever ESS arises within a population then it can coexist stably with other phenotypes or even dominate the population. In addition ESS is always in Nash equilibrium, but reverse implication is generally not true [3]. Application of evolutionary game

E. Pietka, J. Kawa, and W. Wieclawek (eds.), *Information Technologies in Biomedicine, Volume 3*, Advances in Intelligent Systems and Computing 283,
DOI: 10.1007/978-3-319-06593-9_30,

theory to mathematical modelling of processes during carcinogenesis is based on the following assertions:

- in an organism, cells compete for space and nutrients, while cells with different phenotypes are players in the game.
- cooperation and even evolutionary altruism can occur.
- mutation (appearing in tumour cells) occurs in cell division due to various reasons.
- an advantage of tumour cells over healthy ones is a signature of cancer.
- environmental factors can affect different cells to varying degrees.

To our knowledge the first tumour's phenomena modelled by evolutionary game theory are avoidance of apoptosis and production of growth factors presented by Tomlinson and Bodmer [4]. Within the first model the authors proposed three kinds of phenotypes: two of them produce a factor to prevent apoptosis either in paracrine or autocrine fashion and the third one is neutral gaining benefits from paracrine factors. The second model is an extract of the first one - there is no phenotype producing factors in autocrine fashion. This paper has triggered a series of other studies, where evolutionary game theory has been applied to present different tumour phenomena (see [5, 6] for survey). On the other hand, game theory models show only single phenomena occurring in a very complicated process of cancer evolution (results represent quantitative, but not qualitative description). To track the evolution of different phenotypes in the population it is feasible to simulate equations for replicator dynamics [7]. They show how frequencies of different strategies change in time, thereby effecting the composition of studied population. Results from replicator dynamics and models used for the simulation are commonly called mean-field models. Another way to track the phenotypes' evolution is created by methodology of spatial evolutionary games which enables study of players' allocation. A crucial difference between non-spatial and spatial models is lack of perfect mixing. Due to this feature the various local structures of cells could have an impact on the course of the game and the results. Comparison of the results between the mean-field and the spatial model was done by Bach et al [8]. We followed this line adding new kinds of cells reproduction and applying spatial games to various, carcinogenesis models (see [6]) including [9, 10] where we have presented results and discussion for a model of radiation induced bystander, which is also the main topic of this paper. Using spatial algorithm from [8] and our previous results of bystander model [10] we propose an extension by presenting a new way of payoff updating.

2 Spatial Evolutionary Games

The spatial games which we consider follow one global algorithm, which is used every single interaction among players placed on the lattice forming torus:

- payoff updating – determination of local fitness for players in their neighbourhoods.

- cell mortality – choosing 10% of the players from the lattice.
- reproduction by competition – defining a new player on the empty place.

The main difference between both kinds of spatial games are definitions of the player and payoff updating:

- a standard approach – each player follows only one strategy. Local adaptation is calculated as a sum of payoffs (taken from payoff matrix describing the game) of interaction between players in the neighbourhood.
- a population game – each player is treated as entire population containing different strategies (presented as frequency of occurrences). The payoff due to interaction between two players is calculated as a sum of the interactions between each strategies multiplied by their frequency of occurrences. Then, as in the standard game, the local adaptation is the sum of such payoffs.

Taken as an example Hawk and Dove game with two players (two populations consist of 20% H, 80% D and 40% H, 60%D) the payoff due to interaction between these two players shall be (p – means the payoff value due to interaction between individuals):

$$20\% \cdot 40\% \cdot p(H,H) + 20\% \cdot 60\% \cdot p(H,D) + 80\% \cdot 40\% \cdot p(D,H) + 80\% \cdot 60\% \cdot p(D,D) \tag{1}$$

The same calculation as in (1) should be done for rest of the neighbours and then the sum should be taken to determine final value of local adaptation for the player. In this paper we are using semi–synchronous updating. This technique allows for biologically realistic situation for the first game. In case of the second game more reasonable could be synchronous update (all populations interact between each other every single iteration), however simulations show that this way of updating assumes a global controller of the system. Moreover for the comparison purposes it is better to choose the same way of cell mortality for both games. Semi–synchronous updating could be treated as a kind of temporal isolation between populations. Last way of choosing players (asynchronous one – only one player is chosen during iteration) presented in [8] implies vanishing of small cell clusters impossible. Yet another discrepancy between spatial games is that in the standard game a chosen player is removed from the lattice, in the population game he/she stays alive and takes active part in the game. The authors [8] have suggested two kinds of reproduction, which in their general understanding could be applied for both spatial games presented by us:

- deterministic reproduction – in competition of empty place the winner is the strongest player with highest local adaptation.
- probabilistic reproduction – each player's local adaptation is divided by the sum of the local scores among its neighbourhood.

Additionally we introduce [10] two other ways of reproduction: quantitative (assumes cooperation between players with the same strategies) and switching (depending on the size of diversity between scores, quantitative or deterministic reproduction is chosen). In addition at least three another reproductions could be determined for the population game:

- weighted mean of the strongest players – the weighted mean (players' payoffs are the weights) is taken for the players with highest scores (additional parameter defines number of players).
- weighted mean of the best interval – players are sorted according to their payoffs, then the range of the local payoff is divided onto intervals (additional parameter defines number of intervals). At the end the weighted mean is taken for the players in the strongest interval.
- spreading reproduction – here we introduce small alteration, because the chosen player instead of being changed affects rather the neighbours. The weighted mean is taken for the main player and those neighbours (each separately) whose payoffs are smaller than the main player's payoff multiplied by the correcting factor (additional parameter defined in percentage).

Moreover similarly as in the standard approach we can introduce the switching reproduction, that could be performed between deterministic reproduction and for instance the weighted mean of the strongest players. For this paper we mainly concentrate on deterministic and probabilistic reproduction, following the line of reasoning that it is better for comparison purposes and taking into account a crucial fact that both spatial games provide vast amount of possible configurations. Every competition results giving tie are settled randomly in the case of the standard game. For the population games the average between frequency of occurrences of strategies from each population in tie is taken. The difference between described spatial games occurs also within their graphical representation. In the standard approach we can assume that one colour corresponds to one strategy (say the phenotype H is red and D is blue), for the population one we need to mix the colours. So in case when a player obtains 40% H and 60% D the resulting colour should be a shade of violet. This entails more results in the meaning of different spatial structures, however the analysis is more complex. For the spatial simulations two initial lattices (30 x 30 cells) were generated randomly, which provides substitute of perfect mixing.

3 Radiation Induced Bystander Effect

Recent studies have shown that cells exposed to ionizing radiation can trigger reactions affecting non-targeted neighbouring cells. Phenomenon known as radiation based bystander effect has been widely reviewed in literature [11]. Irradiated cells release signals which lead to damage in nearby, non–irradiated cells and reduction in survival of adjacent cells. Moreover the signalling is mutual, so the irradiated cells can also receive signals from non-irradiated neighbours. The induced bystander effect in non-irradiated cells can be exposed in couple ways: reduction of survival, delay of cell's death, oxidative damage in DNA and the genomic instability, micronuclei induction, lipid peroxidation and apoptosis. Besides that those systems are documented, the mechanisms responsible for bystander phenomena are still complex and seem to be dependent on many circumstances. Intercellular signalling, so important for bystander effect, is correlated

with reactive oxygen species, nitric oxide, cytokines such as interleukin 8 or TGF-β. Also significant role is played by gap junction communication and presence of soluble mediators. The bystander effect can be induced also by chemotherapy, ultraviolet radiation and photo-chemotherapy. The UV radiation may lead to skin cancer, basal and squamous-cell carcinoma and to the emergence of malignant melanoma. Oxidative stress, which can also be a result of UVB radiation, is an important mediator of bystander effect induced by ionizing radiation [12]. The radiation induced bystander may have positive and negative effects, since the factors issued by irradiated cells may lead to mutation and second neoplasia. If healthy cells are damaged then the effect is harmful and could increase the adverse effect of radiotherapy in the form of actinic complications. Those positive and negative effect may also be visible in case of radiotherapy. If cancer cells directly absorbing ionizing radiation energy damages, by their signaling, the cells in the neighbourhood or initiates differentiation of these cells then this is the positive and desired effect. However if the healthy cells are damaged (epithelial and endothelial cells, fibroblasts, leucocytes), then it may be seen as unfavourable and undesired result of radiotherapy in the guise of different, radiation side effects, complication and secondary neoplasm. Radiation induced bystander effect occurs especially in the case of very low doses of alpha radiation (mGy and cGy), but also after irradiation of cells by radiation with low linear energy transfer coefficient (radiation X and gamma) even in the higher, conventionally used doses. There are a number of different reports showing that 1% of radiated cells with the increase in dose results in death of 30% of the cells, and then above a certain dose threshold effect disappeared. On the other hand, other sources indicate that this effect is visible at both low and high doses. As we have mentioned before, genetic instability is also observable within this phenomenon, the delayed effect of the changes and the death of cells in distant generations previously irradiated as well. Furthermore, radiation-induced cell clones emit cytotoxic agents. Another phenomenon that accompanies the impact of low radiation doses is adaptive radioresistance, which could increase the resistance for the next even thousand times higher doses. Unfortunately the mechanisms of this phenomenon are not sufficiently understood. The irradiation leads to disruption of the balance between the state of signaling molecules acting prooxidant and antioxidant. One such molecules might be the nitric oxide (NO). Delayed reproductive death (DRD) is expressed in the lower performance of cloning, which probably is not caused by the process of apoptosis or necrosis, although an increase in the percentage of apoptosis is also one of the markers of radiation induced bystander. DRD is mainly observed in the cells with undisturbed repairing mechanism of double strand DNA damage, however does not occur in cells with not proper mechanisms [14]. Apart from described phenomena some others could be listed too:

- irradiated cells harm surrounding cells.
- it is possible to increase a count of non–irradiated neighbours.

– a growth of cells that have received a high dose of radiation through signalling from cells irradiated by low-dose may appear.
– paracrine fashion of intercellular interaction.

From the modelling point of view some of the conditions and phenomena detected within bystander effect could be covered by Tomlinson's model of growth factors [4] and production of cytotoxic substances [13]. The former is a very basic model showing the bystander effect in a way of paracrine signalling between cells, incurring losses due to factors productions and some passive group of individuals that receive benefits from other actions. The latter shows the phenomenon of cytotoxic substances production, which perfectly illustrates production of free radicals and immunity induction (also observed in bystander effect studies). In a similar way of basic and overall modelling fashion we present game theoretic model strictly assigned to radiation induced bystander effect. Adding to this different ways of solving game theoretical models, it allows for observations of complicated and various responses and results of intercellular signalling and communication.

4 Model

We consider three different strategies/phenotypes of cells:

– escape to apoptosis – frequency of appearance: X (blue colour)
– production of growth and mutation factors – frequency of appearance: Y (green colour)
– neutrality – frequency of appearance: Z (red colour)

Table 1. Payoff matrix

	X	Y	Z
X	$1-k$	$1-i+j-p$	$1-p$
Y	$1-k+j$	$1-i+j$	$1+j$
Z	$1-k$	$1-i+j$	1

Parameters of the model:

k – cost of apoptosis/profit from bystander effect
j – profit of cell contact with growth factors
i – cost of producing the growth factors
p – cost/advantage from resistance to bystander effect

Results from the replicator dynamics equations (and the same, from the mean-field, non-spatial analysis) show that population can reach different states [9]. The resulting trimorphic, dimorphic or monomorphic populations may be independent from initial frequencies (in case when the equilibrium point is an

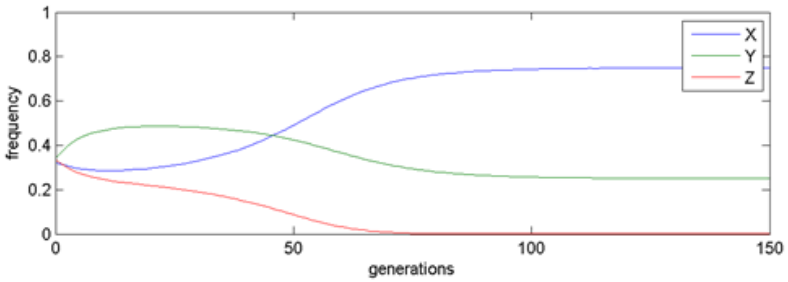

Fig. 1. Replicator dynamics results for parameters i=0.4, j=0.8, k=0.1, p=0.4

attractor), or dependent on them (equilibrium point is a repiler). Within this paper main aim focuses on comparison between different spatial games, however some references to replicator dynamics results should be also considered.

First set of parameters leads to dimorphic population with X and Y cells (Z cells have been repressed) for non-spatial game (Fig. 1). This is a case when the equilibrium point (X=0.25, Y=0.5, Z=0.25) is a repiler, which means that final result depends on initial frequencies. In case of spatial simulation, starting frequencies are equal for all three phenotypes and for all kind of games. Taking the same initial frequencies and changing them (for instance X, Y to 0.3 and Z to 0.4) result in dimorphic population consisting of Z and Y cells (Fig. 2). Such change does not have any simple impact on results of spatial games. First of all, the change is not so significant for spatial consideration. Such alteration could affect the results while changing predefined clusters of the phenotypes within the initial lattice (but not in the case of lattices generated randomly).

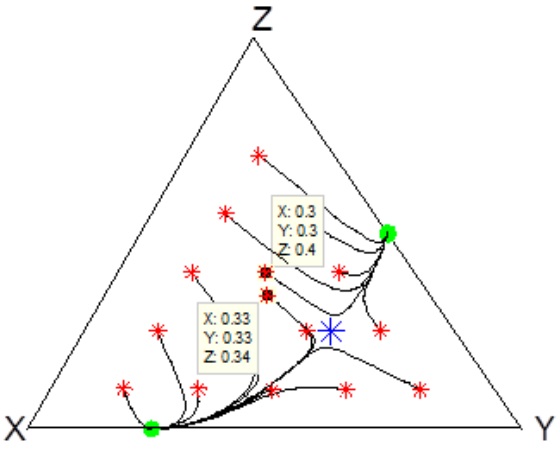

Fig. 2. Different initial frequencies. Parameters i=0.4, j=0.8, k=0.1, p=0.4

Returning to the spatial results, in both games the outcomes are different than in the mean-field game for the same initial frequencies (Fig. 3 and Fig. 4). So the most dominant are Z and Y cells, however probabilistic reproduction in population games allows to set up some clusters of pure X phenotype and in case

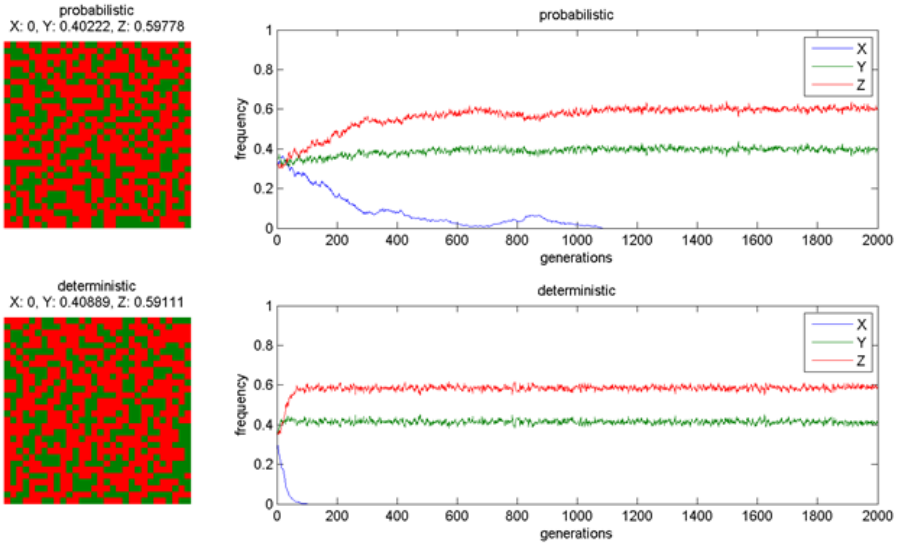

Fig. 3. Standard spatial game for parameters i=0.4, j=0.8, k=0.1, p=0.4

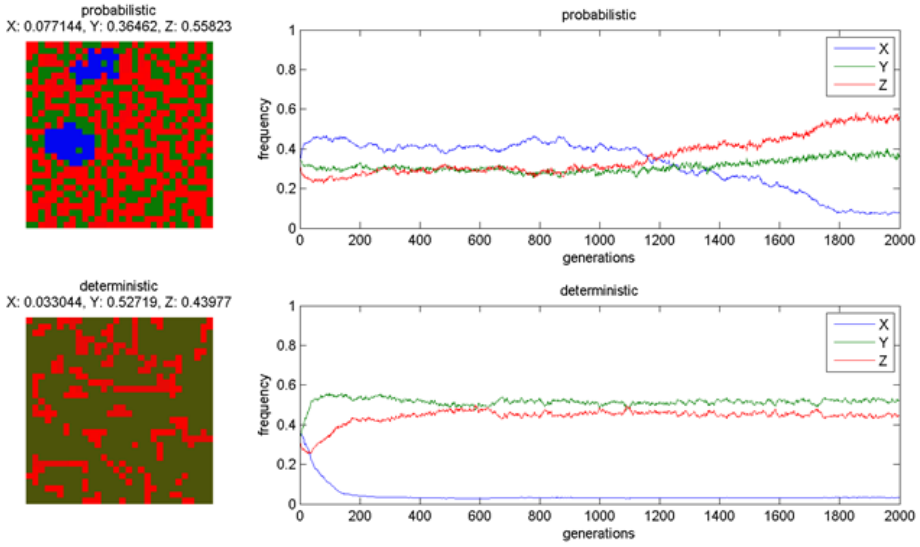

Fig. 4. Phenotype spatial game for parameters i=0.4, j=0.8, k=0.1, p=0.4

of deterministic one the small amount of X also stays alive within population. The results from the standard game show similar pair of dominating phenotypes.

Mean-weighted reproductions give almost the same result as deterministic reproduction in population game, but with more frequent phenotype Y (which disagrees with standard results, where Z-cells are the dominating ones). Yet another feature of the mean-weighted reproduction is that in most cases the entire lattice is covered by one kind of population.

The trimorphic population in non-spatial game is feasible for the second set of parameters. Both probabilistic reproductions give similar result, however the leadership within the population is swamp (Fig. 5 and Fig. 6). Again it is worth to mention that in the probabilistic reproduction within the population game scheme apart from mixed populations there are some structures with mainly one phenotype. Quite interesting phenomenon is observed among the results of deterministic reproductions. It seems the very beginning is similar (at least from the frequency of occurrences point of view), but then Z-cells are repressed from the population in case of standard game. First thought could be that this difference is a result of semi-synchronous player choosing, which in fact introduces some randomization into the algorithm. However vast amount of simulations have shown that the results are the same even for different initial lattices. It indicates that despite of mentioned randomness and even various configurations for some set of pay-off parameters the behaviour and results are the same every each simulation. In the same way as for previous set of parameters the mean-weighted reproductions give the same result as deterministic one (again the players' structure is much more variable).

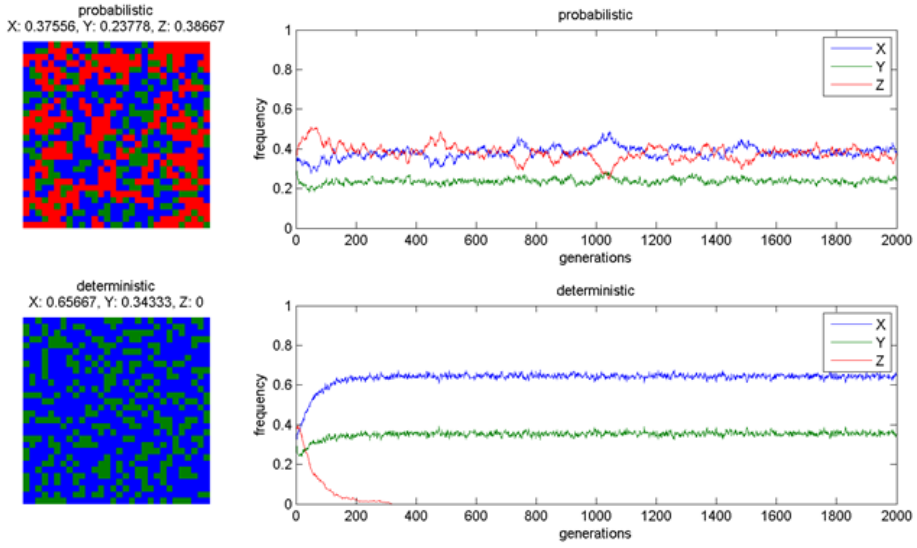

Fig. 5. Classic spatial game for parameters i=0.5, j=0.7, k=-0.1, p=-0.3

Last set of parameters results in stable dimorphic population with X and Z in almost all cases. In the mean-field model the frequencies of occurrences for X and Z are equal, in spatial games Z-cells are the dominating ones, but the advantage over X is not so great. Within probabilistic reproduction in population game the difference between these two phenotypes is even smaller and survival of the Y-cells is possible in small quantities (the frequency of phenotype Y is even greater for mean-weighted reproductions).

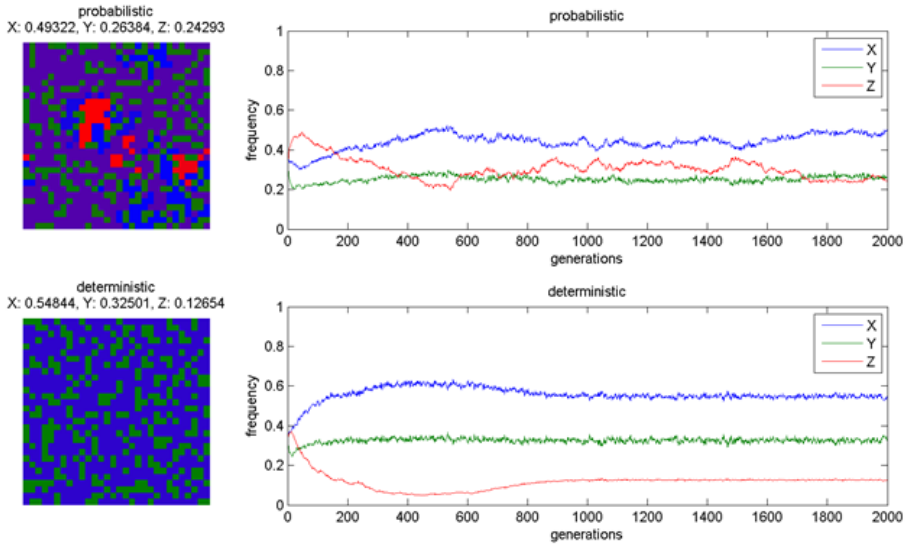

Fig. 6. Phenotype spatial game for parameters i=0.5, j=0.7, k=-0.1, p=-0.3

5 Remarks

We have proposed an extension of the evolutionary spatial games introduced by Bach et all [8] and enhanced in [10]. The main difference is that each simple player shall be treated either as entire population (monomorphic or polymorphic) or as more complex individual containing phenotypes with diverse proportions. The new way of solving spatial games has inherited two kinds of reproduction from its ancestors, but also announced some new methods. So called mean-weighted reproductions use the new interpretation of the players and provide possibility to simulate mixing between populations, due to their interactions. On the other hand, within such approach it is unlikely to emergence some stable clusters of different populations, in contrast to deterministic or probabilistic reproductions in the standard and the population spatial games as well. Within this paper we have neglected some chosen sets of parameters like initial lattice, the size of the neighbourhood or the way of choosing players. Also quantitative and switching reproductions are not taken into account (the results could be found in [6, 10]). In fact switching one could provide other new possibilities of reproductions by

mixing different basic kinds. Despite numerous parameters and possible configurations of spatial games other possibilities for different results are provided by various values within payoff table. We showed three sets of model parameters which lead to quite similar results, in terms of phenotypes quantities, for standard and population approach (still a bit different than in mean-field games). The reason of similarities could be the evolutionary game factor, which in fact should have the biggest and the most basic impact on the results. So independently of different players interpretation and kinds of reproductions if the phenotypes have got strong evolutionary adjustment then the results shall be alike. Such analysis of quantitative results is appropriate for making a comparison between different spatial games and their mean-field counterparts. One could find interesting results in dynamics of players' structure changes on the lattice. Spatial games show that cooperation and forming common cells clusters are possible. Moreover, it is feasible, that monomorphic players are able to survive in population games among the players with mixed phenotypes. New possibilities of spatial evolutionary games have been presented by using the game theoretic model of radiation induced bystander effect. The effect mechanisms could be better understood by spatial factor, the more that some results may be matched with biological phenomena. Unfortunately till now those results are still qualitative, so biological interpretation is possible if such phenomena could appear, but not exactly on which conditions in quantitative sense. Further studies could reveal a way to obtain a proper experiments that will allow to estimate the fitness matrix parameters according to the real results. Then the possible more biologically accurate simulation results could have also quantitative impact on cancer evolution studies. Nevertheless the spatial evolutionary games seem to be the next stage (introducing players allocation) in carcinogenesis phenomena modelling, especially if we remember that various scenarios could be studied according to different configurations. Other possible extensions could be done not by modification of spatial algorithms and new parameterization, but by improvement of the payoff matrix for instance with time dependent variables or more complex functions dependent on external parameters and even lattices. For bystander effect studies it could be dose concentration mentioned at the very beginning of this article. It could be modelled using yet another spatial layer of the game and linked to the main lattice having at the same time impact on the game itself. Additionally spatial games could be developed from the computing point of view by adding new phenotypes, increasing size of the lattice or player's neighbourhood.

References

1. Maynard Smith, J., Price, G.R.: The logic of animal conflict. Nature 246(5427), 15–18 (1973)
2. Maynard Smith, J.: Evolution and the theory of games. Cambridge University Press (1982)
3. Myerson, R.B.: Game theory: analysis of conflict. Harvard University Press (1991)

4. Tomlinson, I.P.M., Bodmer, W.F.: Modelling the consequences of interactions between tumour cells. British J. Cancer 75, 157–160 (1997)
5. Basanta, D., Deutsch, A.: A game theoretical perspective on the somatic evolution of cancer. In: Bellomo, N., Chaplain, M., Angelis, E. (eds.) Selected Topics in Cancer Modeling: Genesis, Evolution, Immune Competition, and Therapy, pp. 1–16 (2008)
6. Świerniak, A., Krześlak, M.: Application of evolutionary games to modeling carcinogenesis. Mathematical Biosciences and Engineering 10(3), 873–911 (2013)
7. Hofbauer, J., Shuster, P., Sigmund, K.: Replicator dynamics. J. Theor. Biol. 100, 533–538 (1979)
8. Bach, L.A., Sumpter, D.J.T., Alsner, J., Loeschcke, V.: Spatial evolutionary games of interactions among generic cancer cells. Journal of Theoretical Medicine 5, 47–58 (2003)
9. Świerniak, A., Krześlak, M.: Game theoretic approach to mathematical modeling of radiation induced bystander effect. In: Proc of the 16 Nat. Conf. on Applications of Mathematics in Biology and Medicine, pp. 99–104 (2010)
10. Krześlak, M., Świerniak, A.: Spatial evolutionary games and radiation induced bystander effect. Archives of Control Sciences 21, 135–150 (2011)
11. Wideł, M., Przybyszewski, W., Rzeszowska-Wolny, J.: Radiation-induced bystander effect: The important part of ionizing radiation response. Potential Clinical Implications. Postępy Hig. Med. Dośw. 63, 377–388 (2009) (in Polish)
12. Wideł, M.: Bystander effect induced by UV radiation; why should we be interested? Postępy Hig. Med. Dośw (Online) 66, 828–837 (2012)
13. Tomlinson, I.P.M.: Game-theory models of interactions between tumour cells. Eur. J. Cancer 33, 1495–1500 (1997)
14. Herok, R., Konopacka, M., Polańska, J., Świerniak, A., Rogoliński, J., Jaksik, R., Hancock, R., Rzeszowska–Wolny, J.: Bystander effects induced by medium from irradiated cells: similar transcriptome responses in irradiated and bystander K562 cells. Int. J. Radiat. Oncol. Biol. Phys., 244–252 (2010)

Prediction of the Behavior of Mammalian Cells after Exposure to Ionizing Radiation Based on the New Mathematical Model of ATM-Mdm2-p53 Regulatory Pathway

Katarzyna Jonak, Monika Kurpas, and Krzysztof Puszyński

Silesian University of Technology, Faculty of Automatic Control, Electronics and Computer Science, Akademicka 16, 44-102 Gliwice, Poland
{katarzyna.jonak,monika.kurpas,krzysztof.puszynski}@polsl.pl

Abstract. Eukaryotic cells are exposed continuously to the genotoxic stresses caused by various sources, such as ionizing radiation (IR) that generates DNA double-strand breaks (DSBs). In order to maintain genomic integrity, the DNA damage response is activated. DSBs are detected by ATM protein kinase that stabilizes and activates p53 tumor suppressor, which target genes are involved in cell cycle arrest, DNA repair and apoptosis. We propose a preliminary mathematical model that explains p53 regulation based on ATM-dependent detector system. We linked the existing p53-Mdm2 pathway model with checkpoint kinase 2 that inhibits p53 degradation, and MRN complex that activates ATM upon DSBs induction. Moreover, recent works shown that the critical component of ATM-dependent signaling pathway is played by phosphatase Wip1 that regulates dephosphorylation events. Additionally, in the presented model we included Wip1 transcriptionally dependent on p53. The preliminary results of simulation analysis show that ATM pathway is an effective system for DSBs detection with strong amplification signal for Wip1 and p53 and quick response. Furthermore, we observed strong dependence of the cellular response to the DNA damage on Wip1, what leads to the conclusion that it plays a role as a gatekeeper in the ATM-Mdm2-p53 regulatory loop.

Keywords: ATM, p53, Wip1, double strand breaks, simulation analysis.

1 Introduction

DNA double strand breaks (DSBs) are known to be one of the most cytotoxic lesions, caused by exposure to ionizing radiation (IR), clastogenic drugs [1], but also formed endogenously during DNA replication or as an effect of reactive oxygen species (ROS) [2]. In order to maintain genomic integrity, the DNA damage response (DDR) is activated. DNA DSBs triggers series of events that determine cell fate. Incorrect mechanisms of DDR may lead to pathological changes transmitted to daughter cells, uncontrolled proliferation and tumor growth. During

E. Pietka, J. Kawa, and W. Wieclawek (eds.), *Information Technologies in Biomedicine, Volume 3*, Advances in Intelligent Systems and Computing 283,
DOI: 10.1007/978-3-319-06593-9_31,

evolution a number of mechanisms that protect the cell from damages and from passing them in the form of mutations to future generations was developed.

The tumor suppressor p53 (cellular tumor antigen p53) is a main component of DDR pathway, which increased production and activation may lead to various cellular responses to the damage: from cell cycle arrest and DNA repair processes to cell death, like apoptosis. All of these complex mechanisms have one thing in common. In order to maintain the proper cellular response, the precise, fast and error-free damage detection is necessary with the proper signal transduction inside the cell.

1.1 Double Strand Breaks Detection

The fundamental pathway responsible for the activation of the DDR upon DSBs induction is ATM-dependent pathway. ATM (ataxia telangiectasia mutated) is a protein kinase that exists in cell in form of inactive dimmer, which after DSBs is phosphorylated and degraded into active monomers. The activation is dependent on the detection of DNA breakages through multi-protein complex of Mre11, Rad50 and Nbs1 (MRN complex) [3]. DNA damages induce ATM autophosphorylation in the position of Ser1981, what leads to the signal amplification [3, 4]. Activated ATM phosphorylates the component of MRN complex, Nbs1, and H2AX histone [5], which binds to MDC1 (mediator of checkpoint signaling protein 1) and amplificates the DDR signal through the recruitment of the MRN complexes and ATM monomers [5]. Phosphorylated MDC1 recruits RNF8 ligase what leads to the degradation of active H2AX and recruitment of the 53BP1 (p53 binding protein 1), as well as tumor suppressor BRCA1 (breast cancer type 1 susceptibility protein) [6]. These proteins are phosphorylated by ATM and are responsible for activation of such processes as repair pathways.

ATM is involved in cell cycle arrest by phosphorylation of checkpoint kinases 1 (Chk1) and 2 (Chk2). The signal of DSB is amplified by autophosphorylation of Chk2 [6]. Chk1 is involved in the DDR pathway through ATR kinase (ataxia telangiectasia and Rad3 related protein) that is a detector module of single stranded DNA (ssDNA) also called DNA single strand breaks (SSBs). The main function of Chk2 is to stop cell cycle through the inactivation of Cdc25 phosphatase or activation of p53 [6, 7]. Moreover, Chk2 regulates the activity of BRCA1 in the transcriptional level and by phosphorylation [8].

1.2 P53–Dependent Cellular Response

One of the key proteins involved in the DDR pathway is p53 transcription factor, which regulates hundreds of genes that encode proteins responsible for DNA repair, apoptosis or ATP synthesis [9]. P53 regulates also transcription of main p53 inhibitor − Mdm2 (E3 ubiquitin-protein ligase, double minute 2 homolog). Phosphorylated p53 by ATM and Chk2 kinases activates the transcription of Mdm2 that in turn ubiquitinates and degrades p53 [10, 11]. At the same time p53 induces expression of PTEN (phosphatase and tensin homolog), which regulates phosphorylation of Mdm2 by the control of Akt kinase activation [12]. This

positive feedback loop allows to maintain the high level of p53 protein in stress condition, what may lead to programmed cell death.

1.3 The Role of Wip1

An essential component in regulation of the DDR pathway is phosphatase Wip1 encoded by *PPM1D* gene. It functions as a deactivation agent for the key proteins involved in the pathway. Its main role is to regulate the level of activated proteins, mostly after succeed process of repair. The transcription of Wip1 gene is induced in a p53-dependent manner, thus the level of Wip1 is much higher in cancer cells, for example in breast cancer cell lines [13]. The most important part of cell response to DSBs regulation by Wip1 is associated with inactivation of ATM detector module [11, 13], cell cycle checkpoints and p53 [13]. Moreover, Wip1 dephosphorylates multi-phosphorylated inactive form of Mdm2 in the ATM phosphorylation site [13].

2 Theoretical Models of ATM–Dependent Damage Response

There are few mathematical models concerning ATM-dependent damage response pathway including the effects of the damage on p53 regulatory loop [14–18]. However, to our knowledge, most of the models are simplified. They do not include macromolecules directly involved in the activation or inactivation of ATM and p53, such as MRN complex and PTEN feedback loop, as well as different compartments of such proteins as Mdm2. We found it essential during cellular damage response and for simulation analysis of ATM-Mdm2-p53 pathway.

In recent works [15, 16], the authors use ordinary differential equations (ODE) in order to describe the dynamics occurring in the single cell after the treatment with IR. Both of the models, as well as the one described in [17], are reduced and are built using molar concentration equations to describe the dynamics of the cellular processes. Moreover, the model described in [16] focuses mainly on G2 phase of cell cycle instead of trying to cover the whole system of cell cycle with no dependence of the cycle phase.

In [15], the authors present the model divided into two compartments: nucleus and cytoplasm. However, their work does not include the DDR components responsible for detection of DSBs, such as H2AX histone or MRN complex, which are important in the first phase of DSBs detection. Their various levels may lead to different cellular response to the damage, such as activation of different repair pathways. The original models based on ATM [18] treats this kinase as a direct measure of DNA damage, without considering the oscillations of this module.

In our opinion, the molecules omitted in the above mathematical models provide important delays to the system dynamics.

3 ATM–Mdm2–p53 Model Formulation

Mathematical model of ATM-Mdm2-p53 regulatory pathway (Fig. 1) is based on the mathematical model of p53 signaling pathway described by K. Puszyński [19]. Most of the assumptions, equations and parameters are obtained from two previous work [19] and [20].

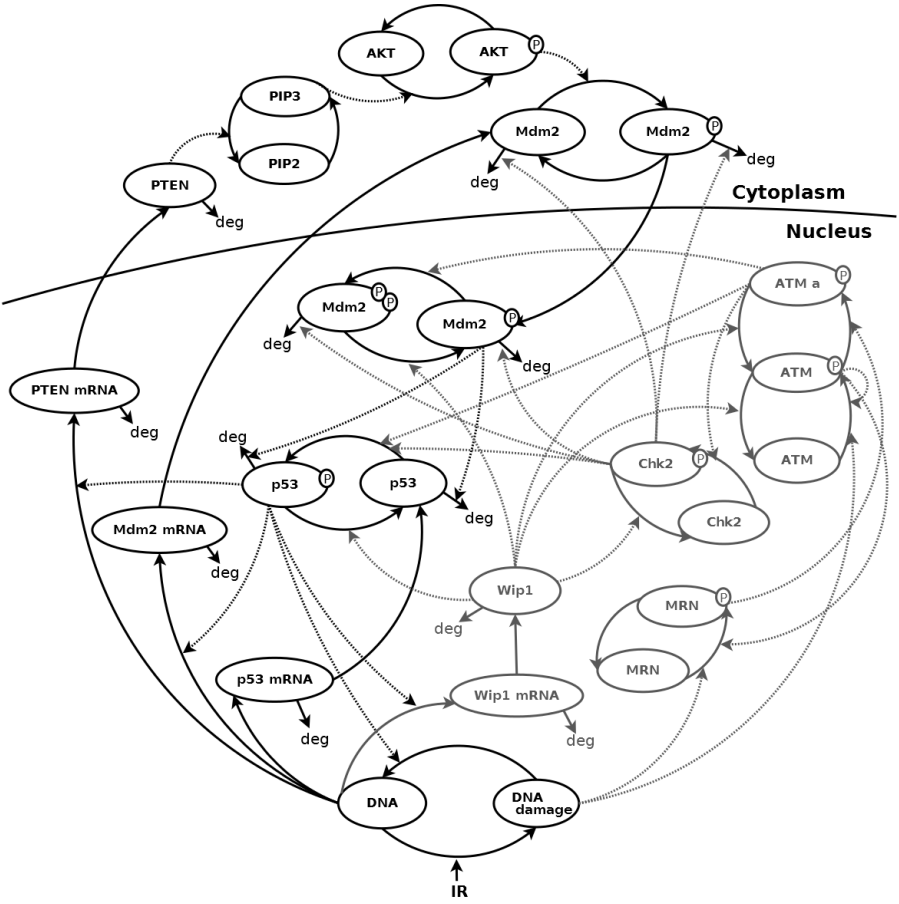

Fig. 1. Schematic of the ATM-Mdm2-p53 model including interactions with Wip1 phosphatase; dotted lines with arrow-heads are positive regulation between components, solid lines are transitions between states of the components, *deg* is degradation of the protein or transcript, and P is phosphorylated form of the protein; a in ATM case means fully active form of this kinase; the components of p53 model are colored in black and the components of ATM are grey

3.1 Methods

Mathematical model is built using set of equations that allow to simulate the behavior of cells treated with different doses of IR. The model is presented as a set of stochastic and deterministic equations according to the Haseltine-Rawlings postulate. Stochastic description and following Gillespie direct method based simulation are used for slow reactions, like states of genes change, while deterministic description based on ODE and following Runge-Kutta fourth order simulation method are used for description of quick reactions, like activation or degradation of the proteins.

3.2 Basic Assumptions of the Model

The interactions between components included in the model can be described shortly. Transcription processes of PTEN, Mdm2 and Wip1 are regulated by p53 transcription factor. The positive feedback loop is between p53 and PTEN. The negative feedback is between Mdm2 and p53, as well as p53 and Wip1. Wip1 dephosphorylates multi-phosphorylated Mdm2, what leads to the activation of Mdm2 and increased degradation of p53. The important role in the model is also played by Chk2, which activates p53 and increases degradation rate of Mdm2. Moreover, PTEN hydrolyzes PIP3 to its inactive form PIP2. Akt is activated by PIP3, thus by its inactivation PTEN acts as Akt inhibitor.

The proteins involved on the pathway are presented mainly in two main states: active (phosphorylated) and inactive (without phosphorylation). ATM is a protein which can be described in another additional state, as fully active (phosphorylation with high level of attachment to the DNA damaged site). Moreover, most of the proteins considered in the model contain their transcriptional forms (messanger RNA, mRNA): PTEN, Mdm2, p53 and Wip1. Here, the degradation rate of the proteins and mRNAs is taken into account. For these components without the production state (PIP, Akt, TM, Chk2, MRN complex) the degradation process is omitted. It is assumed that the production rate for that type of components is equal to degradation rate.

In the model, two Mdm family members, Mdm2 and MdmX, are described as Mdm2 what simplifies model description.

The model includes the compartments of Mdm2: cellular and nuclear.

The model has an assumption that each gene has two copies (allele) and among them one can be in an active state, both, or none (gene not transcribed). The transcription and translation rates of p53, PTEN and Mdm2 are set according to the information from [20], while the transcription rate of Wip1 is set to 0.05/s.

Activation of the model takes place by the application of IR in different doses. The activation process of the whole system is based on the activation of p53-NF-κB mathematical model described in [20] without considering the effect of TNFα (tumor necrosis factor alpha).

The output of the model is p53 level that determinates cell fate: apoptosis or survival. In this model cell death is recognized as a permanently increase p53 level, then the cell is considered as an apoptotic and its elements are degraded.

This cell is no longer able to proliferate and to transmit the damages and mutations to next generations. When the level of p53 is lower and oscillations occur it is assumed that the cell survives with ability to proliferate.

3.3 Model Equations

The equations and parameters for PTEN protein and mRNA form, PIP and Akt, as well as p53 and Mdm2 mRNA forms were obtained from [19]. We used the number of substrates instead of molar concentrations assuming that the ratio of the cytoplasm to nucleus is equal to 5 [19]. The values of the parameters that were not obtained from [19] and [20] were estimated to receive the typical behavior of the mammalian cell after the treatment with IR known from the literature.

Variables in the ATM-Mdm2-p53 model

- AKT_p – active form of cytoplasmic Akt
- ATM_p – phosphorylated form of nuclear ATM monomers
- ATM_a – fully active form of nuclear ATM monomers
- $CHK2_p$ – phosphorylated active form of nuclear Chk2
- MDM_t – Mdm2 transcript
- MDM – inactive form of cytoplasmic Mdm2
- MDM_p – phosphorylated active form of cytoplasmic Mdm2
- MDM_{np} – phosphorylated active form of nuclear Mdm2
- MDM_n – multi-phosphorylated inactive form of nuclear Mdm2
- MRN_p – active form of nuclear MRN complex with phosphorylated Nbs1 by ATM
- $P53_t$ – p53 transcript
- P53 – inactive form of nuclear p53 dimers
- $P53_p$ – phosphorylated active form of nuclear p53
- $PTEN_t$ – PTEN transcript
- PTEN – cytoplasmic PTEN
- PIP3 – active form of cytoplasmic PIP
- $WIP1_t$ – Wip1 transcript
- WIP1 – nuclear Wip1
- DSB – number of DSBs in one cell
- AF – number of apoptotic factors in one cell
- GPTEN – state of PTEN gene
- GMDM2 – state of Mdm2 gene
- GP53 – state of P53 gene
- GWIP1 – state of Wip1 gene

Equations

- **MDM2:**
  Cytoplasmic inactive Mdm2, MDM: The first term describes Mdm2 synthesis and inactivation of Mdm2 phosphorylated form, while the second term describes Mdm2 activation forced by Akt and degradation (spontaneous and forced by Chk2 kinase)

$$\frac{d}{dt}MDM(t) = t_0 MDM_t(t) + c_2 MDM_p(t) - a_4 AKT_p(t) MDM(t) \\ -(d_0 + d_1 \frac{CHK2_p(t)}{CHK2_p(t) + mm_4}) MDM(t). \quad (1)$$

Cytoplasmic active Mdm2, MDM_p: The first term describes Mdm2 activation and the second inactivation of Mdm2, import from cytoplasm to nucleus and degradation of this active form

$$\frac{d}{dt}MDM_p(t) = a_4 AKT_p(t)MDM(t) - c_2 MDM_p(t) - i_0 MDM_p(t) \\ -(d_0 + d_1 \frac{CHK2_p(t)}{CHK2_p(t) + mm_4})MDM_p(t). \quad (2)$$

Nuclear active Mdm2, MDM_{np}: The first term describes Mdm2 import from the cytoplasm to nucleus and dephosphorylation forced by Wip1, while the second term describes the degradation and phosphorylation of mono-phosphorylated Mdm2 forced by ATM

$$\frac{d}{dt}MDM_{np}(t) = i_0 MDM_p(t) + c_3 WIP1(t)MDM_{np} \\ -a_1 \frac{ATM_a(t)}{ATM_a(t) + m_3}MDM_n(t) - (d_0 + d_1 \frac{CHK2_p(t)}{CHK2_p(t) + mm_4})MDM_{np}(t). \quad (3)$$

Nuclear inactive Mdm2, MDM_n: The first term describes the multi-phosphorylated Mdm2 inactivation by following phosphorylation and the second term describes activation and degradation of mono-phosphorylated form

$$\frac{d}{dt}MDM_n(t) = a_1 \frac{ATM_a(t)}{ATM_a(t) + m_3}MDM_n - c_3 WIP1(t)MDM_{np} \\ -(d_0 + d_1 \frac{CHK2_p(t)}{CHK2_p(t) + mm_4})MDM_n(t). \quad (4)$$

– **P53:**
Nuclear inactive p53, $P53$: The first term describes p53 synthesis and its inactivation, while the second term describes p53 activation forced by Chk2 or ATM, and degradation (spontaneous and forced by Mdm2)

$$\frac{d}{dt}P53(t) = t_2 P53_t(t) + (c_4 + c_5 \frac{WIP1(t)}{WIP1(t) + m_2})P53_p(t) \\ -ma_4(ATM_a(t) + CHK2_p(t))P53(t) - (d_3 + d_4 MDM_{np}^2(t))P53(t). \quad (5)$$

Nuclear active p53, $P53_p$: The first term describes p53 activation and the second inactivation and degradation of the protein

$$\frac{d}{dt}P53_p(t) = ma_4(ATM_a(t) + CHK2_p(t))P53(t) \\ -(c_4 + c_5 \frac{WIP1(t)}{WIP1(t) + m_2})P53_p(t) - (d_3 + d_4 MDM_{np}^2(t))P53_p(t). \quad (6)$$

– **ATM:**
Nuclear phosphorylated form of ATM, ATM_p: The first term describes ATM phosphorylation by DSBs induction and inactivation of fully active form forced by Wip1, while the second term describes activation of ATM in fully active state by MRN complex and inactivation of phosphorylated form of ATM in not fully active state

$$\frac{d}{dt}ATM_p(t) = (ma_0\frac{DSB(t)}{DSB(t)+mm_0})(ATM_{tot}(t) - ATM_p(t) - ATM_a(t))^2 + (mc_0 + mc_2\frac{WIP1(t)}{WIP1(t)+mm_2})ATM_a(t) - ma_1MRN_p(t)ATM_p(t) - (mc_0\frac{WIP1(t)}{WIP1(t)+mm_2})ATM_p(t). \quad (7)$$

Nuclear fully active form of ATM, ATM_a: The first term describes activation of fully active state of ATM by MRN complex and the second inactivation

$$\frac{d}{dt}ATM_a(t) = ma_1MRN_p(t)ATM_p(t) - (mc_0 + mc_2\frac{WIP1(t)}{WIP1(t)+mm_2})ATM_a(t). \quad (8)$$

– **WIP1:**
Nuclear Wip1, *WIP1*: The first term describes Wip1 synthesis and the second its degradation

$$\frac{d}{dt}WIP1(t) = mt_0WIP1_t(t) - md_1WIP1(t). \quad (9)$$

Wip1 transcript, $WIP1_t$: The first term describes Wip1 transcription (state of gene) and the second Wip1 mRNA degradation

$$\frac{d}{dt}WIP1_t(t) = ms_0GWIP1(t) - md_0WIP1_t(t). \quad (10)$$

– **CHK2:**
Nuclear active form of Chk2, $CHK2_p$: The first term describes Chk2 activation by ATM and the second described spontaneous inactivation

$$\frac{d}{dt}CHK2_p(t) = (ma_3\frac{ATM_a(t)}{ATM_a(t)+mm_3})(CHK2_{tot}(t) - CHK2_p(t)) - mc_3CHK2_p(t). \quad (11)$$

– **MRN complex:**
Nuclear active form of MRN complex, MRN_p: The first term describes activation of MRN complex by phosphorylated form of ATM and the second describes spontaneous inactivation of MRN complex

$$\frac{d}{dt}MDM_p(t) = (ma_2\frac{ATM_p(t)}{ATM_p(t)+mm_1})(MRN_{tot}(t) - MRN_p(t)) \\ -mc_2MRN_p(t). \quad (12)$$

Table 1. Parameters of the model equations described in 3.3 *Model equations*

Parameter	Value	Parameter	Value	Parameter	Value
a_1	$1x10^{-3}$/s	mc_1	$1x10^{-3}$/s	mm_0	60
a_4	$7.5x10^{-9}$/s	mc_2	$1x10^{-2}$/s	mm_1	5000
ma_0	$1x10^{-8}$/s	mc_3	$1x10^{-3}$/s	mm_2	26
ma_1	$3x10^{-6}$/s	d_0	$4.37x10^{-5}$/s	mm_3	4000
ma_2	$1x10^{-4}$/s	d_1	$2.4x10^{-4}$/s	mm_4	17623
ma_3	$5x10^{-4}$/s	d_3	$1x10^{-4}$/s	ms_0	0.05/s
ma_4	$3.8x10^{-6}$/s	d_4	$1x10^{-13}$/s	t_0	0.5/s
c_2	$1x10^{-4}$/s	md_0	$6.5x10^{-5}$/s	t_2	0.5/s
c_3	$2.5x10^{-9}$/s	md_1	$3.9x10^{-5}$/s	mt_0	0.6/s
c_4	$2.5x10^{-9}$/s	i_0	$5x10^{-4}$/s	ATM_{tot}	100000
c_5	$2.5x10^{-9}$/s	m_2	25	$CHK2_{tot}$	100000
mc_0	$1x10^{-2}$/s	m_3	4000	MRN_{tot}	100000
$DSB_{Induction}$	40/Gy	$DSB_{RepairSaturation}$	50		

4 Results of Simulation Analysis

Deterministic simulation for the single cell was performed. The applied doses after 24 hours of simulation were 2 Gy and 5 Gy. Cells were observed for next 48 hours. The preliminary results presented here are number of phosphorylated p53 molecules in nucleus ($P53_p$), number of active Mdm2 in nucleus (MDM_{np}), number of active PIP ($PIP3$) and active Akt (Akt_p) in cytoplasm, and number of Wip1 in nucleus ($Wip1$).

4.1 High Production of Wip1

The simulation was performed for cells irradiated with 2 Gy and 5 Gy. The production of Wip1 was high. The level of active p53, which depends on number of Wip1 molecules, reaches about $3x10^5$ molecules for irradiation with 2 Gy (Fig. 2A), and about $4x10^5$ molecules for irradiation with 5 Gy (Figure 2B). These are expected results, due to the fact that p53 is stimulated by DSBs through ATM and Chk2 systems.

The oscillations of Mdm2 and p53 appear after 24 hours when the appropriate dose of IR is added. These oscillations are the result of the action of the repair

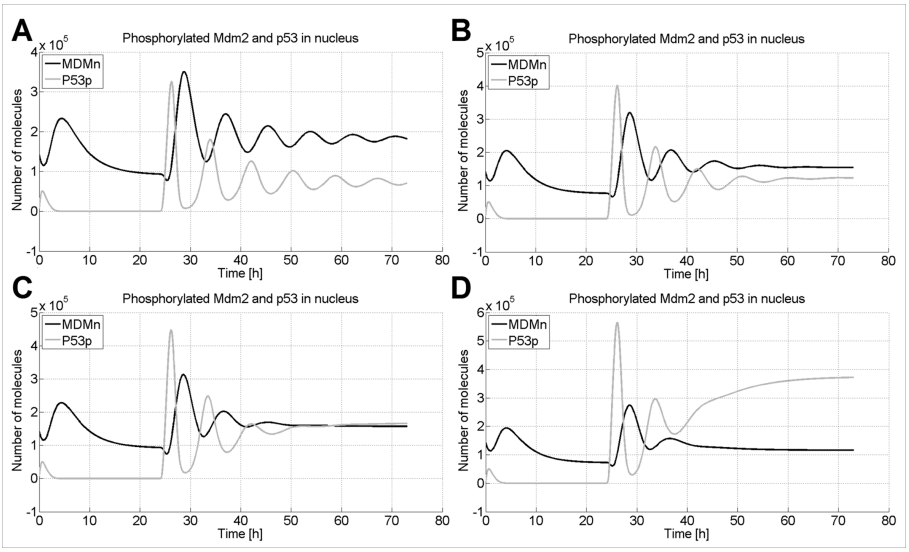

Fig. 2. The level of active Mdm2 in nucleus (black) and active p53 in nucleus (grey); **A:** High level of Wip1 and IR dose of 2 Gy; **B:** High level of Wip1 and IR dose of 5 Gy; **C:** Blocked production of Wip1 and IR dose of 2 Gy; **D:** Blocked production of Wip1 and IR dose of 5 Gy

processes and interactions with other molecules included in ATM-Mdm2-p53 model. If there are more oscillations of active p53 in a lower level, the cell has more chance to survive. For higher IR dose the oscillations are extinguishing faster, however with the presence of highly active Wip1 the level of p53 does not reach the apoptotic phase.

By comparing the levels of Wip1 in the cell after irradiation with 2 Gy and 5 Gy (Figure 4A and 4B, respectively), the increase of Wip1 level is observed. For lower dose there are no oscillations when Wip1 reaches the highest level (about $12x10^6$ molecules). If the IR dose is higher, the level of Wip1 is similar, however, this high state is reached faster.

4.2 Blocked Production of Wip1

For the blocked production of Wip1 the oscillations of p53 and Mdm2 are extinguishing faster. The cell is driven to the apoptotic pathway when irradiated with higher dose (here 5 Gy, Figure 2D). P53 just after irradiation reaches $4x10^5$ molecules, which is more than in case of irradiation with high production of Wip1. For lower dose (Figure 2C), p53 reaches the level of Mdm2 50 hours after set up the experiment. The maximum level of p53 reaches about $5x10^5$ molecules, which is more than in case of active Wip1.

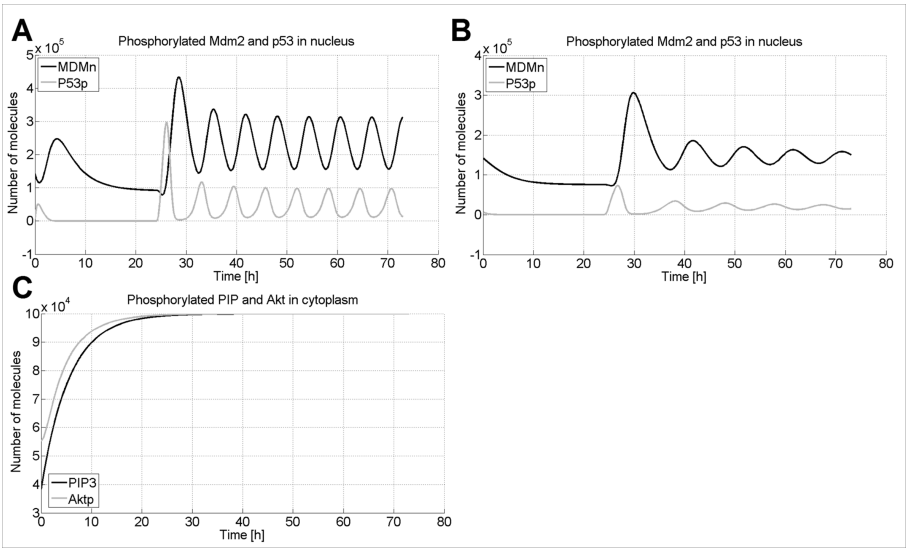

Fig. 3. The level of Mdm2, p53, PIP and Akt for the cell with high production of Wip1; **A:** Active Mdm2 (black) and p53 (grey) in nucleus with blocked production (mRNA) of PTEN; **B:** Active Mdm2 (black) and p53 (grey) in nucleus with blocked activation of Chk2 protein; **C:** Active PIP (black) and Akt (grey) in cytoplasm with blocked production (mRNA) of PTEN

4.3 Blocked Production of PTEN

With high production of Wip1 and blocked production of PTEN the simulation was performed. The cell was irradiated after 24 hours of experiment with dose of 5 Gy. It was observed that both Mdm2 and p53 cannot stabilize when PTEN is not included in the model (Figure 3A). The maximum level of p53 reaches no more than $3x10^5$ molecules that is much lower than comparing to the level of p53 with active PTEN. These results indicate how essential for the prediction of cell behavior is this positive feedback loop. Moreover, with blocked production of PTEN the level of active PIP and Akt are stabilizing (Figure 3C).

The level of Wip1 is lower when the production of PTEN is blocked. In Figure 4C, the oscillations are observed when Wip1 reaches the maximum level. The oscillations are stabilizing. That is an effect of the lower activation of Mdm2, what results in higher activation of p53 and then higher production of Wip1.

4.4 Blocked Activation of Chk2

The simulation analysis was performed for the cells with high production of Wip1 and blocked Chk2 activation (Figure 3B). With blocked Chk2 the response to the damage is weaker, what results in higher level of Mdm2 (Chk2 increases degradation rate of Mdm2). The oscillations have very low amplitude. The results indicate that Chk2 in an active form is essential in the DDR pathway.

For blocked activation of Chk2 the level of Wip1 reaches maximum level of $2.3x10^6$ molecules (Figure 4D). This level is much lower than with blocked production of PTEN. Chk2 interacts directly with p53, therefore, the signal about inactivation of Chk2 is sending faster to Wip1 than the signal about inactivation of PTEN. Thus, Wip1 cannot reach the higher level and the amplitude of the oscillations is decreasing.

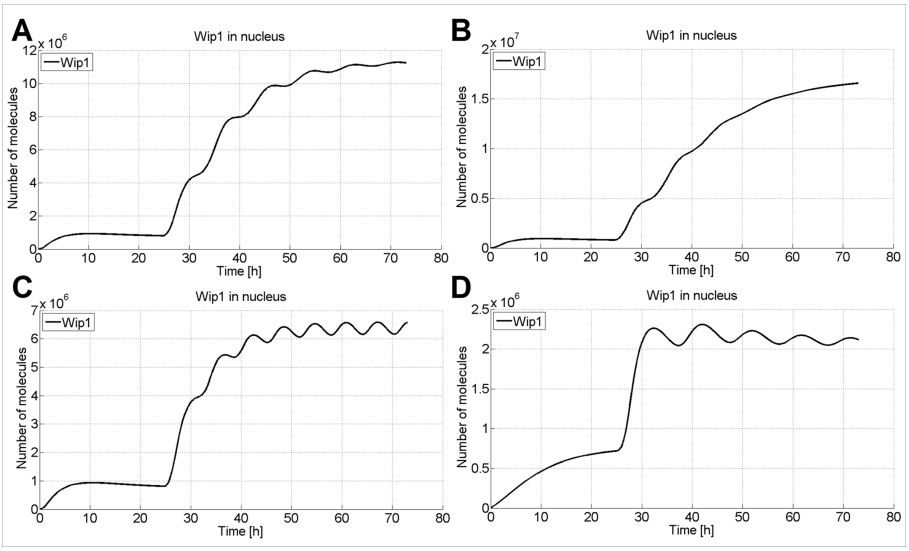

Fig. 4. The level Wip1 for the cell with high production of Wip1; **A:** IR dose of 2 Gy; **B:** IR dose of 5 Gy; **C:** IR dose of 5 Gy and blocked production of PTEN; **D:** IR dose of 5 Gy and blocked activation of Chk2

5 Conclusion and Future Work

Simulation analysis of the preliminary ATM-Mdm2-p53 model show the typical behavior of the mammalian cells after exposure to IR, known from the literature, what leads to the conclusion that the further work on this pathway is promising.

With the higher dosage of IR more DSBs occur in DNA strands, what leads to the higher activation of ATM pathway and p53. High level of p53 results in activation of repair pathways, cell cycle arrest, activation of some of the genes, such as *PPM1D*, or apoptosis. The absence of the components of ATM and p53 pathways, as well as Wip1, are very noticeable. With the highly active Wip1 it is possible for cell to survive. However, using this model we cannot predict if the cell will survive with repaired DNA damages or if the mutations caused by damages will be passed to the future generations. Thus, for some of the experiments the apoptotic way is more preferred.

The future work will be based mainly on the expanding the ATM module to the interactions between ATM and Chk2 genes. Moreover, the experiments

will be performed in order to investigate the parameters of the model, such as degradation rates or transcription rates. The ATM-Mdm2-p53 model will be connected to existing NF-κB pathway model described in [20], and ATR detection module. All the data obtained will be analyzed in terms of, e.g. apoptotic fraction of cells, and verified with biological experiments. The simulations will be performed also in a stochastic way for at least 1000 cells. The future ATM-p53-NF-κB model will be used in studies of cells behavior without the need for costly and time-consuming biological experiments.

Acknowledgement. This project is funded by the Polish National Center for Science granted by decision number DEC-2012/05/D/ST7/02072.

References

1. Lindahl, T., Barnes, D.E.: Repair of endogenous DNA damage. Cold Spring Harb. Symp. Quant. Biol. 65, 127–133 (2012)
2. Lopez-Contreras, A.J., Fernandez-Capetillo, O.: Protein Phosphorylation in Human Health, 1st edn. InTech (2012)
3. Bakkenist, C.H., Kastan, M.B.: DNA damage activates ATM through intermolecular autophosphorylation and dimer dissociation. Nature 421, 499–506 (2003)
4. Lee, J.H., Paull, T.T.: ATM activation by DNA double-strand breaks through the Mre11-Rad50-Nbs1 complex. Science 308(5721), 551–554 (2005)
5. Derheimer, F.A., Kastan, M.B.: Multiple roles of ATM in monitoring and maintaining DNA integrity. FEBS Letters 584, 3675–3681 (2010)
6. Ahn, J., Urist, M., Prives, C.: The Chk2 protein kinase. DNA Repair 3, 1039–1047 (2004)
7. Matsui, T., Katsuno, Y., Inoue, T., Fujita, F., Joh, T., Niida, H., Murakami, H., Itoh, M., Nakanishi, M.: Negative regulation of Chk2 expression by p53 is dependent on the CCAAT-binding transcription factor NF-Y. J. Biol. Chem. 279(24), 25093–25100 (2004)
8. Perona, R., Moncho-Amor, V., Machado-Pinilla, R., Belda-Iniesta, C., Sanchez-Perez, I.: Role of Chk2 in cancer development. Clinical and Translational Oncology 10, 538–542 (2008)
9. Maclaine, N.J., Hupp, T.: The regulation of p53 protein function by phosphorylation. In: Ayed, A., Hupp, T. (eds.) p53 Molecular Biology Intelligence Unit. Landes Bioscience and Springer Science+Business Media LCC (2010)
10. Moll, U.M., Petrenko, O.: The MDM2-p53 interaction. Mol. Cancer Res. 1(14), 1001–1008 (2003)
11. Lu, X., Ma, O., Nguyen, T.A., Jones, S.N., Oren, M., Donehower, L.A.: The Wip1 Phosphatase acts as a gatekeeper in the p53-Mdm2 autoregulatory loop. Cancer Cell 12(4), 342–354 (2007)
12. Cantley, L.C., Neel, B.G.: New insights into tumor suppression: PTEN suppresses tumor formation by restraining the phosphoinositide 3-kinase/ AKT pathway. Proc. Natl. Acad. Sci. USA 96, 4240–4245 (1999)
13. Lowe, J., Cha, H., Lee, M.O., Mazur, S.J., Appella, E., Fornace, A.J.: Regulation of the Wip1 phosphatase and its effects on the stress response. Frontiers in Bioscience 17, 1480–1498 (2012)

14. Batchelor, E., Loewer, A., Mock, C., Lahav, G.: Stimulus-dependent dynamics of p53 in single cells. Mol. Syst. Biol. 7, 488 (2011)
15. Elias, J., Dimitrio, L., Clairambault, J., Natalini, R.: The p53 protein and its molecular network: Modelling a missing link between DNA damage and cell fate. Biochim Biophys Acta. 1844(1 Pt. B), 232–247 (2014)
16. Zhang, W., Cheng, Y.M., Liew, K.M.: A mathematical analysis of DNA damage induced G2 phase transition. Applied Mathematics and Computation 225, 765–774 (2013)
17. Kim, D.H., Rho, K., Kim, S.: A theoretical model for p53 dynamics: identifying optimal therapeutic strategy for its activation and stabilization. Cell Cycle 8(22), 3707–3716 (2009)
18. Dimitrio, L., Clairambault, J., Natalini, R.: A spatial physiological model for p53 intracellular dynamics. Journal of Theoretical Biology 316, 9–24 (2013)
19. Puszynski, K., Hat, B., Lipniacki, T.: Oscillations and bistability in the stochastic model of p53 regulation. Journal of Theoretical Biology 254, 452–465 (2008)
20. Puszynski, K., Bertolusso, R., Lipniacki, T.: Crosstalk between p53 and nuclear factor-kB systems: pro- and anti-apoptotic functions of NF-kB. IET Syst. Biol. 3(5), 356–367 (2009)

Euler's and Taylor's Expansion Method Applied on Non-linear Pharmacokinetics Model

Daniela Gombárska and Mariana Beňová

University of Žilina, Faculty of Electrical Engineering,
Žilina, Slovakia
{daniela.gombarska,mariana.benova}@fel.uniza.sk

Abstract. There are many applications in pharmacokinetic described and modelled by linear or non-linear differential equation systems. These non-linarities can be considered in pharmacokinetic model parameters and the pharmacokinetics of drug action. The Euler's- and Taylor's expansion methods are applied for numerical solution pharmacokinetic equations. A fictitious exciting functions method makes possible numerical solution of this DE system with non-stationary matrices. The solutions of warfarin target-mediated drug disposition are presented as well.

Keywords: non-linear pharmacokinetic models, non-linear equations, Euler's and Taylor's expansion method.

1 Introduction

Models of many biological systems are often described by system of ordinary differential equations — ODEs. By the nature of these systems the equations are usually non-linear. Unfortunately, only a few non-linear systems can be solved explicitly. Therefore, the solving should be taken on a numerical scheme to approximate the solution as accurately as possible.

A fictitious exciting functions method makes possible numerical solution of differ-ential equation system with non-stationary matrices. The paper deals with Euler's- and Taylor's expansion methods applied for numerical solution of pharmacokinetic — pharmacodynamic of warfarin using Matlab.

A system of differential equations — DEs

$$\begin{array}{l} \frac{\mathrm{d}x_1}{\mathrm{d}t} - a_{11}x_1 - a_{12}x_2 = -b_{11}u_1 \\ \frac{\mathrm{d}x_2}{\mathrm{d}t} - a_{21}x_1 - a_{22}x_2 = -b_{22}u_2 \end{array} \tag{1}$$

can be written in matrix state-space form as follows

$$\frac{\mathrm{d}}{\mathrm{d}t}\begin{pmatrix} x_1 \\ x_2 \end{pmatrix} = \begin{pmatrix} a_{11}\ a_{12} \\ a_{21}\ a_{22} \end{pmatrix}\begin{pmatrix} x_1 \\ x_2 \end{pmatrix} + \begin{pmatrix} b_{11}\ b_{12} \\ b_{21}\ b_{22} \end{pmatrix}\begin{pmatrix} u_1 \\ u_2 \end{pmatrix} \rightarrow \frac{\mathrm{d}x}{\mathrm{d}t} = \mathbf{A}\bar{x} + \mathbf{B}\bar{u} \tag{2}$$

E. Pietka, J. Kawa, and W. Wieclawek (eds.), *Information Technologies in Biomedicine, Volume 3*, Advances in Intelligent Systems and Computing 283,
DOI: 10.1007/978-3-319-06593-9_32,

where $\mathbf{A}$, $\mathbf{B}$ are the system and transition matrices; $\bar{x}$, $\bar{u}$ are state-variables and exciting vectors. If a_{11} and a_{12} elements of $\mathbf{A}$ matrix are non-stationary and b_{12}, b_{21}, b_{22} and $u_2 = 0$ the formula (2) takes form

$$\frac{\mathrm{d}}{\mathrm{d}t}\begin{pmatrix} x_1 \\ x_2 \end{pmatrix} = \begin{pmatrix} 0 & 0 \\ a_{21} & a_{22} \end{pmatrix}\begin{pmatrix} x_1 \\ x_2 \end{pmatrix} + \begin{pmatrix} b_{11} & 1 & 1 \\ 0 & 0 & 0 \end{pmatrix}\begin{pmatrix} u_1 \\ a_{11}x_1 \\ a_{12}x_2 \end{pmatrix} \rightarrow \frac{\mathrm{d}\overline{x}}{\mathrm{d}t} = \mathbf{A_f}\overline{x} + \mathbf{B_f}\overline{u}_f \quad (3)$$

where $\mathbf{A_f}$, $\mathbf{B_f}$ are the modified (fictitious) system and transition matrices; $\overline{u}_f$ is fictitious exciting vector, and $a_{11}x_1$, $a_{12}x_2$ are fictitious exciting functions.

Using Euler explicit method can the previous system be written

$$\overline{x}_{n+1} = (\mathbf{E} + h\mathbf{A_f})\overline{x}_n + h\mathbf{B_f}\overline{u}_{fn},$$

where h is integration step and $\mathbf{E}$ is unity matrix. This method is sensitive on integration step h.

The Euler implicit method yields

$$\overline{x}_{n+1} = (\mathbf{E} - h\mathbf{A_f})^{-1}\left[\overline{x}_n + h\mathbf{B_f}\overline{u}_{fn}\right],$$

where $\mathbf{F} = (\mathbf{E} - h\mathbf{A_f})^{-1}$ is fundamental matrix of the system. This method is for negative real part of eigenvalues absolutely stable (A-stabile) for any positive step h.

And by applying Taylor's expansion methods for numerical solution are

$$\mathbf{F} = \exp(h\mathbf{A}) = \sum_{n=0}^{\infty} \frac{h^n \mathbf{A}^n}{n!},$$

and similarly

$$\mathbf{G} = h\sum_{n=0}^{\infty} \frac{h^n \mathbf{A}^n}{(n+1)!}.$$

Choosing appropriated number of series member gives

$$\overline{x}_{n+1} = \mathbf{F}\overline{x}_n + \mathbf{G}\overline{u}_{fn}.$$

All discrete equations carried-out by Euler explicit-, implicit- and Taylor expansion methods are easily solvable by numerical computing because their modified (fictitious) matrices are stationary ones [3, 11].

2 Pharmacokinetics of Warfarin

Coagulation as an important part of hemostasis, provides a complex process in which blood forms clots, prevents bleeding and begins repair of the damaged part on a blood vessel walls. Wide group of diseases and clinical conditions can result in disor-ders of coagulation which lead to an increased risk of bleeding (hemorrhage) or ob-structive clotting (thrombosis). Those leading into thrombosis

require a treatment with anticoagulants. The occurrence of thrombophilic states can be caused by many factors as chronic lung disease, endoprosthesis, prolonged immobility or paralysis, prior venous thromboembolism, cancer, surgery (lower extremities, pelvis or gynecological surgery), varicose veins, congestive heart failure, estrogen use, obesity and plenty others. Warfarin belongs to most widely used coumadin anticoagulants applied in case of thromboembolism risk factors, especially in treatment of atrial fibrillation, hearth valve prosthesis, deep vein thrombosis or pulmonary embolism. However, usage of warfarin can be potentially harmful due to very narrow therapeutic range and very individual range of sensitivity to dose. Inappropriate dosage for more sensitive patients can cause hemorrhagic complication and lead to serious life threating bleeding. In case of lower than therapeutic concentration is the patient endangered by occurrence of thrombophilic state. Also age, gender, co-administration with medication and dietary interaction from food containing vitamin K causes difficulties in proper dose assessment. Vitamin K takes an opposite action to warfarin in process of forming coagulation factors [12].

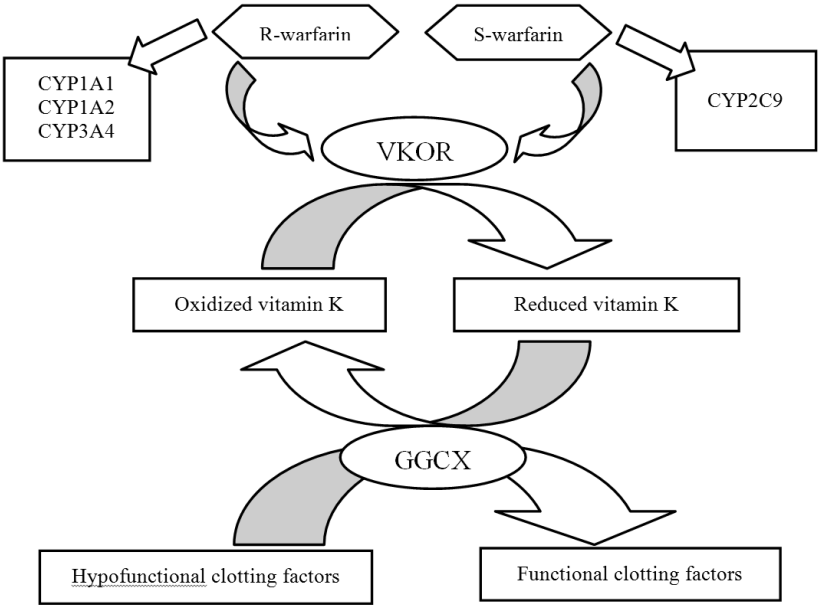

Fig. 1. Warfarin in vitamin K cycle — effect on forming of clothing factors; [12] warfarin is usually administered as racemic mixture of two enantiomers R and S warfarin; R-warfarin is metabolized by cytochromes CYP1A1, 2 and CYP3A4, S warfarin is metabolized by CYP2C9; vitamin K epoxide reductase (VKOR) is inhibited by warfarin, it is the target of warfarin; by inhibition of VKOR enzymatic activity warfarin prevents the forming of functional clotting factors by means of γ-glutamyl carboxylase (GGCX)

The anticoagulation effect of warfarin is based on its suppression of synthesis of the vitamin K-dependent coagulation factors II, VII, IX and X. It acts trough the interference with vitamin K cycle in the liver, which leads to secretion of inactive clotting factors and reduction of the coagulation factors synthesis in 30 to 50 with decreasing of its biological activity. Because of the life time of clothing factors a full effect can be observed within few days (2 to 7), during which are the coagulation factors gradually eliminated from the circulation [12].

Since lot of commonly used medications and foods interacts with warfarin, in order to keep the anticoagulation effect of warfarin as stable as possible in the therapeutic range, the activity of warfarin has to be monitored by blood testing. Warfarin is usually administered by oral and is completely absorbed. After, almost all (99%) absorbed warfarin is bounded to plasma proteins (mainly albumin) and remaining 1% of free warfarin is biologically active in liver where it inhibits vitamin K epoxide reductase (VKOR). VKOR is a key enzyme system for regeneration of reduced vitamin K. The shortage of reduced vitamin K in cycle leads to inhibition in forming of functional clotting factors by means of γ-glutamyl carboxylase (GGCX).

3 Pharmacokinetic Model

The study of drug disposition in the body focuses on the changes in drug plasma concentration. The plasma concentration of any drug after its administration changes over time, depending on the rates of three processes: absorption, distribution, and elimination.

- Absorption of a drug refers to rate of transport into blood plasma from other tissues; usually strongly depends on the way of administration and physical characteristic of the drug.
- Distribution of a drug represents the process of a drug transport from the bloodstream into the target organs and tissues.
- Elimination of a drug from the blood proceeds in two ways: as biotransformation of a drug to its metabolites in tissues (primarily metabolism in the liver); and as the excretion of the drug or its metabolites (in the kidneys).

Physiologically based pharmacokinetic models describe drug disposition, characterize the time behavior of drug concentrations in plasma (blood) and also in important organs and tissues, usually on a compartment basis. Such model can provide information about the role of various physiologic perturbations on these concentrations [11].

Target-mediated drug disposition (TMDD) represents an assumption that a significant proportion of the drug (relative to dose) is bound with high affinity to a receptor, enzyme, or transporter [8] and the pharmacokinetic model of drug disposition in TMDD is shown on Fig. 2.

Central compartment represents free drug by concentration C_p in distribution volume V_c. The input rate ($I_n(t)$) to the free drug compartment C_p can

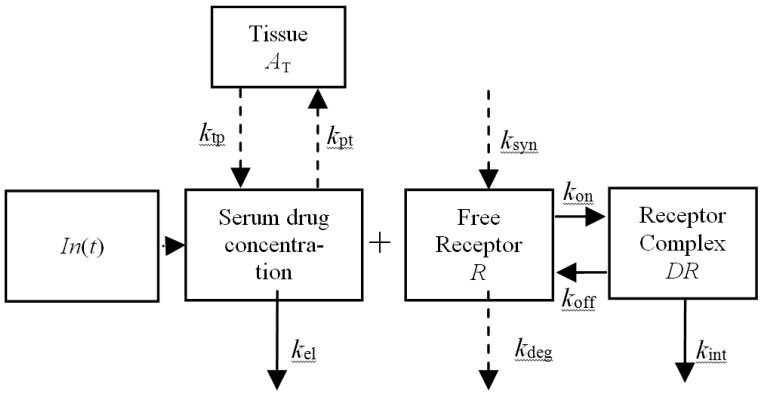

Fig. 2. Pharmacokinetic model of TMDD according to [1]; Free drug is represented by its concentration (C_p); drug binds to free receptors (R) with the rate (k_{on}) and forms a drug-receptor complex (DR); free drug could be distributed also to a nonspecific tissue-binding site (A_T); the dose is represented by input rate $I_n\,(t)$ to the free drug compartment; free drug C_p, free receptor R, and drug receptor complex DR are in $\mu\mathrm{gl}^{-1}$ concentrations, A_T in moles

be realized by IV bolus, zero-order infusion, first-order absorption with rate of absorption (k_a), etc. The drug within first compartment binds with rate k_{on} to free receptors and forms a drugreceptor complex DR with total binding capacity R_{max}. Amount of free receptors available for binding represents R. Created DR leaves the compartment in two ways; it can dissociate (rate constant k_{off} or internalize (rate constant k_{int}). Unbound drug can be eliminated directly from plasma with rate constant k_{el} or pass to non-specific tissue binding (A_T, k_{pt}, k_{tp}). Such model can be described by following system of differential equations

$$\frac{\mathrm{d}A_d}{\mathrm{d}t} = -k_a A_d \tag{4}$$

$$\frac{\mathrm{d}C_p}{\mathrm{d}t} = \frac{k_a}{V_c}A_d + \frac{I_n(t)}{V_c} - (k_e l + k_p t)C_p - k_{on}RC_p + k_{off}DR + k_t p\frac{A_T}{V_c} \tag{5}$$

$$\frac{\mathrm{d}A_T}{\mathrm{d}t} = k_{pt}C_p V_c - k_{tp}A_T \tag{6}$$

$$\frac{\mathrm{d}DR}{\mathrm{d}t} = k_{on}R\ C_p - (k_{off} + k_{int})DR \tag{7}$$

$$\frac{\mathrm{d}R}{\mathrm{d}t} = k_{syn} - k_{deg}R - k_{on}R\ C_p - k_{off}DR \tag{8}$$

where k_{syn} is production constant and kdeg degradation rate of free receptor. Tissue compartment and internalization k_{int} are in this type of model optional

and nonspecific tissue binding was not included in model. Because the system is assumed to be stationary, the production rate is defined as

$$k_{syn} = k_{deg} R(0)$$

where $R(0)$ is initial condition of free receptors, the receptor density in absence of drug.

Parameters used in model for racemic warfarin adopted from literature [8, 9] are listed in Table 1.

Value $t_{1/2}$ represents biological half-life of warfarin which varies in different sources. We use value 35 hours.

Applying the above mentioned methods and by modification of the pharmacokinetic model equations (4) to (8) to the form of formula (3) we obtain system

$$\frac{\mathrm{d}}{\mathrm{d}t}\begin{pmatrix} A_d \\ C_p \\ DR \\ R \end{pmatrix} = \begin{pmatrix} -k_a & 0 & 0 & 0 \\ \frac{k_a}{V_c} & -k_{el} & k_{off} & 0 \\ 0 & 0 & -(k_{off}+kint) & 0 \\ 0 & 0 & -k_{off} & -kdeg \end{pmatrix} \begin{pmatrix} A_d \\ C_p \\ DR \\ R \end{pmatrix} + \tag{9}$$

$$+ \begin{pmatrix} 0 & 0 & 0 \\ 1 & -k_{on} & 0 \\ 0 & k_{on} & 0 \\ 0 & -k_{on} & 1 \end{pmatrix} \begin{pmatrix} \frac{I_n(t)}{V_c} \\ R\ C_p \\ k_{syn} \end{pmatrix}$$

Initial conditions used in model are for oral administered dose

- $A_d(0) = Dose$
- $C_p(0) = 0$
- $DR(0) = 0$
- $DR(0) = R_{max}$

Table 1. Parameters used in model for racemic warfarin adopted from literature [8, 9]

Parameter	Value	Unit
k_a	1.19	$\mathrm{hr}^{-}1$
k_{on}	0.126	$\mu\mathrm{M}^{-1}\mathrm{hr}^{-1}$
k_{off}	0.0405	$\mu\mathrm{M}^{-1}\mathrm{hr}^{-1}$
k_{deg}	1	$\mu\mathrm{M}^{-1}\mathrm{hr}^{-1}$
k_{int}	0.1	hr^{-1}
R_{max}	0.167	$\mu\mathrm{moleskg}^{-1}$
k_{el}	$ln(2)/t_{1/2} = ln(2)/35$	hr^{-1}

4 Results

Warfarin belongs to drugs with TMDD which produces complex nonlinear pharmacokinetic profiles. We present a simulation approach based on the application of Euler's explicit, implicit and Taylor's expansion method for calculation of drug, free receptor and drug-receptor complex concentration in time.

Model and simulation is performed in Matlab environment. Results of simulation for single dose in 24 hours and all Euler and Taylor methods are shown on Fig. 3, 4 and 5. Dose amount in μg used in simulations is D1=500, D2=1000, D3=1500.

All the used expansion methods are showing good agreement in results of the model.

Fig. 3, 4 and 5 show (a) concentrations of free drug C_p in central compartment, (b) concentration of free receptors R and (c) concentration of drug-receptor complex DR in time 24 hours after single dose oral administration.

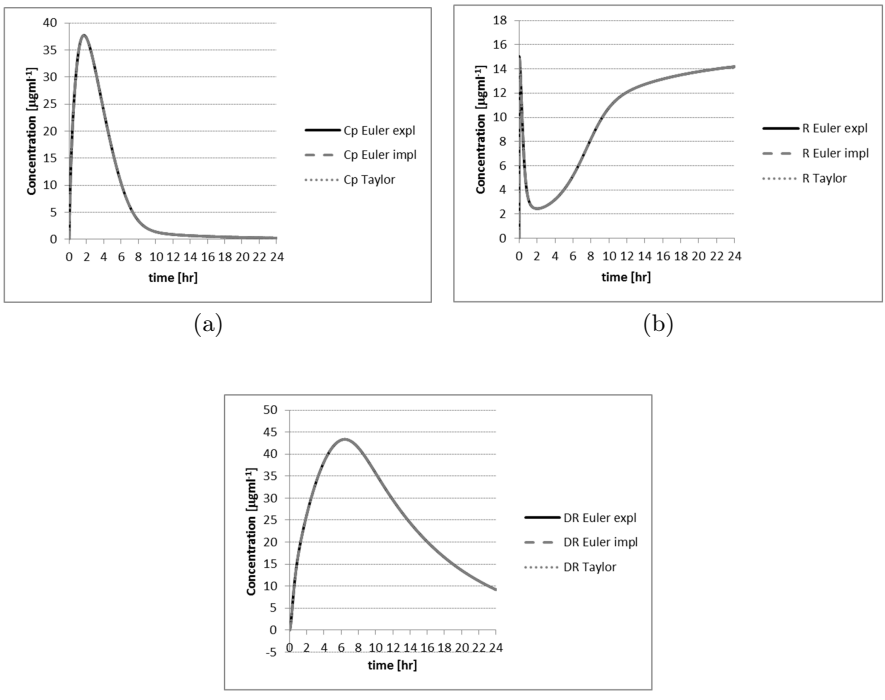

(a) (b)

(c)

Fig. 3. Concentration of (a) free drug C_p, (b) free receptor R, (c) bounded drug-receptor complex DR for dose D1

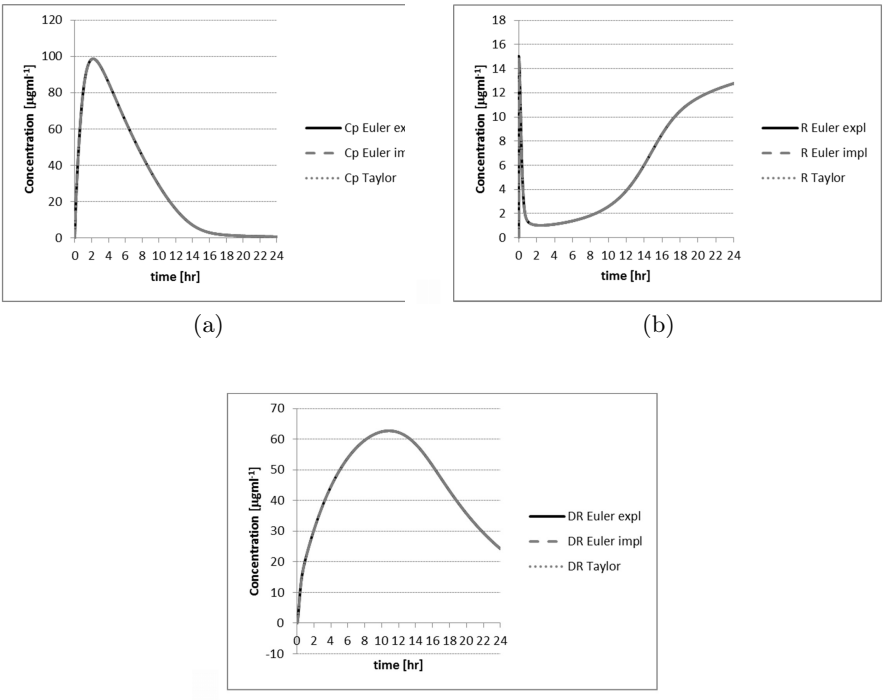

Fig. 4. Concentration of (a) free drug C_p, (b) free receptor R, (c) bounded drug-receptor complex DR for dose D2

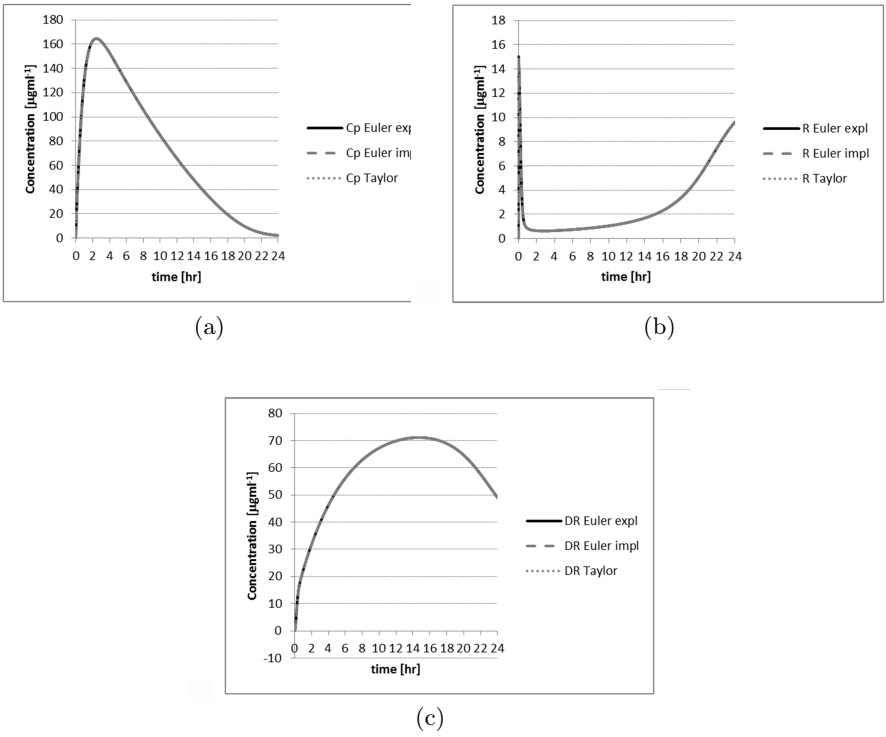

Fig. 5. Concentration of (a) free drug C_p, (b) free receptor R, (c) bounded drug-receptor complex DR for dose D3

5 Conclusion

Pharmacokinetics model was performed for simulation of single dose warfarin oral administration using Taylor's expansion method. The calculated plasma drug concentration free receptor and receptor-drug complex were shown. Simulations were per-formed for three values of dose. It is necessary to note that results of simulations have strictly theoretical character and were not compared with any clinic data. The solutions of modelling of warfarin concentrations were presented with using Euler's explicit, implicit and Taylor's expansion method for next numerical solution.

References

1. Wagner, J.G.: Modern View of Pharmacokinetics. Journal of Pharmacokinetics and Biopharmaceutics 1(5), 363–401 (1973)
2. Marsh, R., Fuite, J., Tuszynski, J.A.: Fractal Space and Time - Sources of Nonlinearity in Drug Elimination. In: Proceedings of ECC 2003, p. 478 (2003)

3. Benova, M., Dobrucky, B., Marcokova, M.: On Specific Utilization of Infinite Series for Periodical Non-Harmonic Functions in Electrical Engineering. Journal of Applied Mathematics 3(3), 1–14 (2010)
4. Principles of pharmacology, Pharmacokinetics (2002), http://www.us.elsevierhealth.com/-media/us/samplechapters/9781416066279/Chapter%2002.pdf
5. Levy, R.H.: Time-dependent pharmacokinetics. Pharmac. Ther. 17, 383–397 (1982)
6. Mager, D.E., Jusko, W.: General pharmacokinetic model for drugs exhibiting target-mediated drug disposition. J.J. Pharmacokinet Pharmacodyn 28, 507–532 (2001)
7. Levy, G., Mager, D.E., et al.: Comparative pharmacokinetics of coumarin anticoagulants L: Physiologic modeling of S-warfarin in rats and pharmacologic target-mediated warfarin disposition in man. J. Pharm. Sci. 92(5), 985–9894 (2003)
8. Gibaldi, M., Perrier, D.: Pharmacokinetics, 2nd edn. Marcel Dekker, New York
9. Levy, G.: Pharmacologic target-mediated drug disposition. Clin. Pharmacol. Ther. 56, 248–252 (1994)
10. Gong, I.Y., et al.: Clinical and Genetic Determinants of Warfarin Pharmacokinetic and Pharmacodynamic during Treatment Initiation. Plos One 6, e27808 (2011)
11. Benova, M., Dobrucky, B., Gombarska, D.: Using Euler's and Taylor's expansion method for solution of non-linear differential equation system in pharmacokinetics. Electrical Review 89(2a), 259–261 (2013)
12. Gombarska, D., Benova, M.: Computer model of anticoagulation treatment. Electrical Review 89(2a), 262–263 (2013)

Prokaryotic DNA Signal Downsampling for Fast Whole Genome Comparison

Karel Sedlar[1], Helena Skutkova[1], Martin Vitek[1,2], and Ivo Provaznik[1,2]

[1] Department of Biomedical Engineering, Brno University of Technology, Technicka 12, CZ 616 00 Brno, Czech Republic
sedlar@feec.vutbr.cz
[2] International Clinical Research Center - Center of Biomedical Engineering, St. Anne's University Hospital Brno, Pekarska 53, CZ 656 91 Brno, Czech Republic

Abstract. Classification of prokaryotes is mainly based on molecular data, since next-generation sequencing platforms provide fast and effective way to capture prokaryotes' characteristics. However, two different bacterial strains of the same genus can differ in the specific parts of their genomes due to copious amounts of repetitive and transposable parts. Thus, finding an ideal segment of genome for comparison is difficult. Conventional character-based methods rely on multiple sequence alignment, rendering them extremely computationally demanding. Only small parts of genomes can be compared in reasonable time. In this paper, we present a novel algorithm based on the conversion of the whole genome sequences to cumulative phase signals. Dyadic wavelet transform (DWT) is used for lossy compression of phase signals by eliminating redundant frequency bands. Signal classification is then performed as cluster analysis using Euclidean metrics where sequence alignment is replaced by dynamic time warping (DTW).

Keywords: prokaryotes, genomic signal, cumulated phase, compression, classification, dwt, dtw.

1 Introduction

The classification of organisms is one of the fundamental questions in biology. It is based mainly on molecular characters since DNA is the carrier of heredity [1]. However, new sequencing techniques allow cheap assembly of the entire genomes, particularly prokaryotic genomes formed by single circular chromosomes, since the classical methods of comparison are still unable to process whole chromosomes. This is caused by multiple sequence alignment that is computationally too demanding, even impossible for sequences of length of several Mbp. Only small parts of chromosomes, e.g. single genes, can be processed. Unfortunately, various genes are evolving at different rates, which may not reflect the evolutionary development rate of the whole organism. On the other hand, the conversion from character sequence to numeric signal brings the possibility of using digital

E. Pietka, J. Kawa, and W. Wieclawek (eds.), *Information Technologies in Biomedicine, Volume 3*, Advances in Intelligent Systems and Computing 283,
DOI: 10.1007/978-3-319-06593-9_33,

signal processing techniques for lossy compression. Despite lossy compression, we are able to preserve reasonable amounts of information and significantly reduce the computational demands, so that whole genomes can be compared in a very short time. Several digital signal processing techniques can be used for compression. Here, we present an approach using dyadic wavelet transform (DWT) [2] for its speed and effectiveness.

Other disadvantage of sequence alignment is the necessity of using scoring matrices. Comparison of several sequences based on various scoring matrices leads to a number of different results. This is caused by presumptions concerning the specific speed of evolution of an organism, which is unknown. Multiple sequence alignment can be replaced by dynamic time warping (DTW). It is an algorithm of dynamic programming used for signal alignment. Unlike the multiple sequence alignment, DTW is not dependent on substitution matrix and works with individual nucleotides changes. The previous utilization of DTW in DNA signals alignment can be found in [3].

2 Materials and Methods

A set of several bacterial whole genome sequences was used for comparing our approach with the classical character processing method performed on 16S rRNA, which are the most commonly used short barcode sequences for prokaryotes' identification [4]. Later study shows that using only short sequences can brings many imprecisions [5]. Sequences were obtained from GenBank database at NCBI (`http://www.ncbi.nlm.nih.gov/genbank/`). The characterization of sequences used for analysis is summarized in Table 1.

2.1 Sequence Conversion

A number of techniques for for converting DNA sequences to genomic signals have been published [6], though not all of them can be used for whole genome classification. The preservation of all biological properties is the essential condition during conversion. Thus, we chose cumulated phase signal representation [7]. In this representation each of the nucleotides A, C, G, T occurring in the DNA is reflected in the complex plane in manner such that appropriate complex numbers maintain information on the nucleotides' chemical similarities, see Figure 1(a). Every character along a sequence is replaced by its complex number during transformation: A [1,j]; C [-1,-j]; G [-1,j];T [1,-j].

By the definition, the complex number phase have values $(-\pi, +\pi\rangle$. Using trigonometric functions, we can easily calculate the phase of our four numbers:

$$\{\varphi_A, \varphi_C, \varphi_G, \varphi_T\} = \left\{\frac{\pi}{4}, -\frac{3\pi}{4}, \frac{3\pi}{4}, -\frac{\pi}{4}\right\}. \quad (1)$$

Table 1. The specifications of sequences from seven organisms

Organism	Chr accession	Chr length (bp)	16S length (bp)
Escherichia coli str. K-12	NC_000913.2	4639675	1403
Lactobacillus casei	NC_008526.1	2895264	1568
Lactobacillus crispatus	NC_014106.1	2043161	1552
Lactobacillus gasseri	NC_008530.1	1894360	1579
Salmonella bongori	NC_015761.1	4460105	1542
Salmonella enterica CT18	NC_003198.1	4809037	1542
Salmonella enterica LT12	NC_003197.1	4857432	1542
Thermococcus ga. EJ3	NC_012804.1	2045438	1539
Thermococcus sp. 4557	NC_015865.1	2011320	1496
Pyroccocus fu. COM1	CP_003685.1	1909827	1519
Bibersteinia trehalosi	NC_020515.1	2407846	1528
Proteus mirabilis HI4320	NC_010554.1	4063606	1542
Bordetella per. Tohama I	NC_002929.2	4086189	1992
Acidovorax ebreus TPSY	NC_011992.1	3796573	1971
Thauera sp. MZ1T	NC_011662.2	4496212	1985

The actual signal is gained using cumulating phase numbers (1) of appropriate nucleotides along the sequence or it can be computed directly from character sequence by:

$$\theta_{cum} = \frac{\pi}{4} \left[3 \left(n_G - n_C\right) + \left(n_A - n_T\right)\right], \tag{2}$$

where n_X is number of nucleotide X in the sequence, from the first to the current location.

The representation of the DNA sequence by cumulated phase keeps the positional information, which enables the mutual comparison of two sequences. Also it maintains the chemical and structural information about the original sequence [7, 8]. The main reason for choosing cumulated phase signals is their large scale feature [9]. The shape of prokaryotic whole genome cumulated phase signal is typical for each organism. Moreover, signals of related organisms are more alike than the signals of evolutionary farther ones. Although in a negligible number of cases, two different strains of genomes of the same genus can be more dissimilar due to horizontal transfer of genetic information, which is common in prokaryotes [10]. The downsampled cumulated phase signals of seven organisms are shown in Figure 1(b).

The shape of a signal is mainly formed by the ratio of purines and pyrimidines, especially by those with strong bonds. Almost linear purines-rich subsequences alternating linear pyrimidines-rich subsequences along the DNA are evident. Signals usually end with the phase close to zero because of the second Chargaff's rule [11]. Due to these features, signals are suitable for massive downsampling.

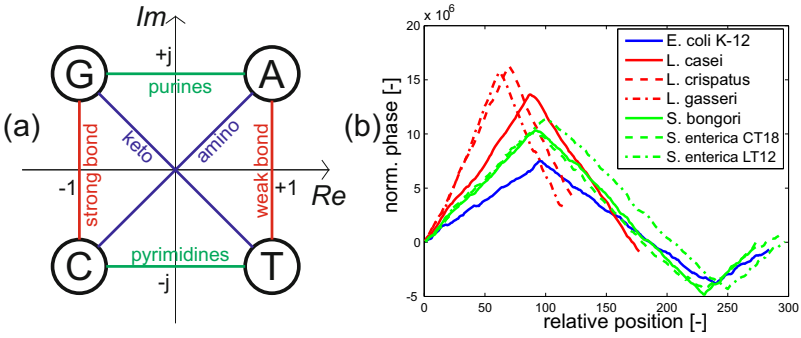

Fig. 1. (a) Complex representation of nucleotides, (b) Downsampled cumulated phase of DNA sequences of seven different organisms

2.2 Analysis of Signals

Genomic signals are discrete signals with progression along the DNA sequence; thus, they can be processed using any discrete transformation [12]:

$$\langle f(n), \psi(n) \rangle = \sum_{-\infty}^{+\infty} f(n)\psi(n), \tag{3}$$

where $f(n)$ represents sequence of signal samples and $\psi(n)$ belongs to the basis functions that determine the type of transformation.

Unlike other biological signals e.g. ECG, where sampling rate f_s is given by resolution of the sensing device, the sampling frequency of genomic signal is equal to the length of the DNA sequence. This makes it many times higher than f_s of other biological signals and massive downsampling is needed. Spectral analysis provided by discrete Fourier transform (DFT) can show possibilities of downsampling. To be able to perform DFT, the signal has to be periodic. The cumulated phase is defined at interval $\langle 1, N \rangle$, where N is number of nucleotides in the sequence, which could be taken as one period of signal on $(-\infty, +\infty)$. Consequently, the frequency axis can be divided into N equal units $\Omega = 2\pi/NT$ and DFT can assign to signal $f(n)$ new coefficients of discrete spectrum series $F(k)$ in the frequency domain, having the same length:

$$DFT\{f(n)\} = F(k) = \sum_{n=1}^{N} f(n)\ e^{-jk\Omega nT}. \tag{4}$$

The spectrum of *Escherichia Coli* in the Figure 2 had to be zoomed in due to the fact that the peripheral spectral lines are more than 10^{10} high making other lines unable to be observed. In the zoomed spectrum, only up to 10^5 other lines can be observed. These higher frequency components show changes to adjacent nucleotides and form only a noisy background of the genome. This information

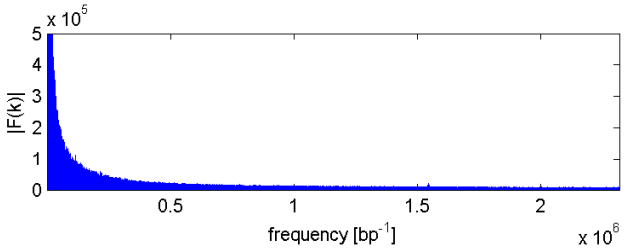

Fig. 2. Limited Fourier spectrum for *E. Coli*

is redundant, for comparison useless because these components are very similar to all genomes. On the contrary, low frequencies carry information about large scale features of signal, e.g. upward parts of signals formed by purines-rich subsequences or downward parts made of pyrimidines-rich subsequences. These components are species-specific. Thus, we are able to reduce a significant part of the spectrum by removing higher frequency components without compromising large scale information. Removing part of the spectrum allows us to downsample the signal, avoiding aliasing. Theoretically, simple lowpass filter could preprocess the signal for downsampling. Very long impulse response of the filter would be needed since the signal sampling frequency is equal to its length.

2.3 Signal Downsampling

We avoided the necessity of very long filter impulse response by using another transformation for discrete signals - discrete time wavelet transform ($DTWT$). For our purpose, the special case of wavelet transform - dyadic $DTWT$, was employed. This technique is characterized by utilizing parameters that are power of two. Using the relation between correlation and convolution, we can define dyadic wavelet transform for genomic signal as discrete convolution:

$$y_m(n) = \sum_{i=-\infty}^{+\infty} x(i)h_m(2^m n - i) = \sum_{i=-\infty}^{+\infty} h_m(i)x(2^m n - i), \tag{5}$$

as a signal decomposition by bank of discrete octave filters with impulse responses $h_m(n)$. Then the sampling frequency of signal $y_m(n)$ on output of m^{th} filter is 2^m times lower than the sampling rate f_s of the input signal $x(n)$.

There are two parameters that we had to set, the shape of the wavelet and the extent of the degree of decomposition. To reduce the organism comparison analysis time, we tested several simple wavelets. The best results were obtained using the basic Haar wavelet [13]. The shape of this wavelet is rectangular, thus computation of the transform is extremely fast. We found more complex wavelets as unsuitable because they can change the shape of the signal inappropriately

and the computation is more demanding. The Haar wavelet stands for two simple filters with impulse responses:

$$h_h(n) = \{-0.7071; 0.7071\} \tag{6}$$

$$h_d(n) = \{0.7071; 0.7071\}. \tag{7}$$

To determine the maximum possible downsampling factor, we used percentage root-mean-square difference (PRD) between the original signal and the downsampled signal by dyadic wavelet decomposition, that was resampled to the initial sampling rate:

$$PRD = \sqrt{\frac{\sum_{i=1}^{n}(x_0(i) - x_r(i))^2}{\sum_{i=1}^{n}(x_0(i) - \bar{x_0})^2}} \cdot 100\%, \tag{8}$$

where x_0 stands for original signal and x_r for resampled signal, both of length n.

PRD dependency of tested signals on the degree of decomposition with error bars along the curve is shown in Figure 3. Up to level 14 of the decomposition, the dependency shows a linear trend with reasonable values of percentage root-mean-square difference and its standard deviations. From level 15 of the decomposition, the dependency changes to a quadratic trend with high values of PRD and its standard deviations. As optimum, we selected decomposition degree of 14. Further analysis with higher level of decomposition leads to unsatisfactory results due to the loss of too much information. On the contrary, lower level of decomposition takes more computational time without any benefits.

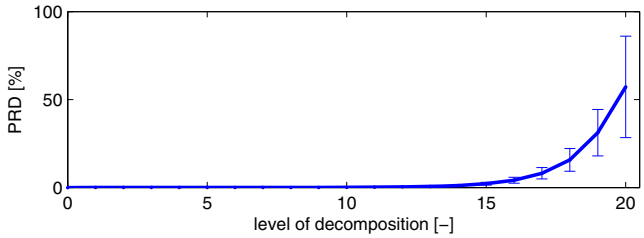

Fig. 3. Percentage root-mean-square difference as a function of degree of decomposition for 7 tested organisms

Of course the same degree of decomposition has to be used for all analyzed signals in order to maintain the ratio of lengths among the signals. Figure 1(b) shows the batch of our downsampled signals that were used for PRD analysis. The length of signals is only about 300 samples, unlike the original length of sequences in milions of bases.

2.4 Signal Alignment

Signals have to be aligned prior to conducting genome comparison. Since the lengths of various genomes can vary, multialignment of more signals would bring

about the incorporation of high number of gaps. Therefore, we decided to use pairwise alignment of every signal pair instead. This leads to maximum preservation of the genetic information for each comparison. We utilized dynamic time warping algorithm (DTW) [3, 14], which is similar to Needleman-Wunsch [15] or Smith-Waterman [16] algorithms for character sequence alignment. DTW is based on minimizing the distance between the pair of signals to be aligned.

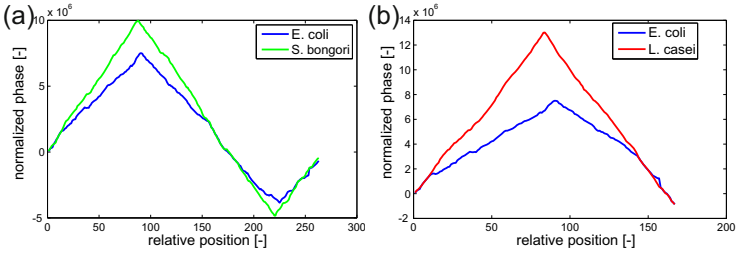

Fig. 4. (a) Alignment of *E. coli* and *S. bongori* signals of similar length, (b) Alignment of *E. coli* and *L. casei* signals of different lengths

When both signals are approximately of the same length, DTW is similar to global alignment as shown in Figure 4(a), where complete information from both signals were used. When the signals of different lengths are aligned, DTW is similar to local alignment where corresponding purines-rich and pyrimidines-rich subsequences are aligned and other parts of the longer signal are eliminated as shown in Figure 4(b). In both cases, maximum signal information is maintained.

2.5 Organism Comparison

The aligned pair of signals has the same length n. Their distance can be computed using the Euclidean metric:

$$d = \sqrt{\sum_{i=1}^{n} [x(i) - y(i)]^2}, \tag{9}$$

where $x(n)$ and $y(n)$ are aligned signals.

From the distances of each pair of signals we were able to construct the distance matrix and process it by cluster analysis. We used the unweighted pair group method with arithmetic mean ($UPGMA$) for achieving the best distinction of clusters [17]. The entire method was compared to the standard analysis based on multialignment of 16S rRNA sequences processed by the same clustering method. To prove that the parameters of the proposed method are correct and applicable in general, we added the rest of organisms from Table 1 to cluster analysis.

Table 2. Taxonomical classes of tested organisms

Class	Assigned number
Betaproteobacteria	1
Thermococci	2
Bacilli	3
Gammaproteobacteria	4

Selected organisms belong to four different taxonomical classes. Each class is assigned a number according to Table 2. These numbers are used for describing the organisms in cluster analysis shown in Figure 5.

Figure 5(a) representing the results of the proposed method. Four clusters correspond to real taxonomical classes. The results show that two different strains of

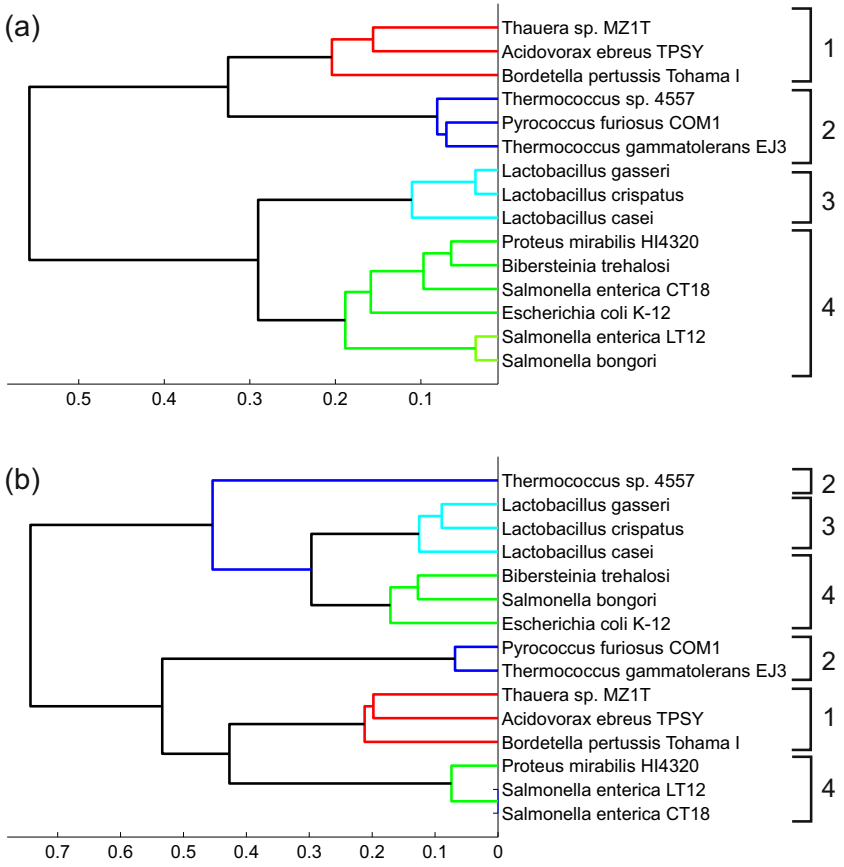

Fig. 5. (a) Cluster analysis based on whole genome signals, (b) Cluster analysis of 16S rRNA sequences

Salmonella enterica have quite diverse genomes, but they are still assigned to the *Gammaproteobacteria* cluster. The method is not dependent on the length of a genome but rather on information it contains. It assigns *Bibersteinia trehalosi* to the cluster of related organism despite its genome having half the length beside other *Gammaproteobacteria*. This is probably caused by two possible behavior of DTW, which can be similar to global or local alignment according to the specific situation. The result of the classical character processing method is shown in Figure 5(b). This approach cannot distinguish between the various strains of bacteria because 16S rRNA sequences are very commonly the same for different strains of the same genus. It splits *Gammaproteobacteria* into two very distant clusters. Also *Thermococci* cluster is split in an inappropriate way.

Whole genome comparison is significantly more robust. Redundant information that can be the source of bias was filtered out during signal downsampling. Only two signals are compared at a time, which leads to maximum utilization of the relevant information. Short 16S rRNA sequences should contain similar information across all genomes; however, multiple sequence alignment brings much imprecision to the analysis because of its high complexity.

3 Conclusion

In this paper, we present a novel method for classifying whole genome DNA sequences. Due to the use of sequences conversion to cumulated phase signals and massive downsampling, the method has low computational requirements in comparison to traditional methods. Thus, extremely long sequences with lengths of millions pair of bases, like whole genomes, can be processed. The method was tested on complete genome sequences records of prokaryotic organisms obtained from the GenBank database at NCBI.

Current bioinformatics does not provide an adequate technique for preprocessing whole genome signals; the proposed approach can be used as a new standard for this purpose. Although the genomic signal processing is a relatively new scientific field, it provides a high number of conversion techniques for obtaining genomic signal from character sequence. The cumulated phase signal representation was chosen for its specific properties suitable for downsampling. The low frequency band, formed by purines/pyrimidines ratio, carries the main information about the genome. The results of whole genome signals spectral analysis were used for designing appropriate downsampling technique, which allows downsampling of extremely large signals like whole prokaryotic genomes by more than ten thousand times. The dyadic wavelet transform was chosen for its ability to easily downsample signals with very high sampling rate. The level 14 of decomposition by DWT was set according to the percentage root-mean-square difference analysis of the selected signals; the percentage losses of original signals information do not exceed 1 percent.

Sequence multiple alignment, one of the most problematic issues in traditional DNA classification methods, was replaced by modification of dynamic time warping for genomic signals. The principal utilization of DTW does not

provide faster or less computationally demanding result, the calculation speed up is given only by the previous signal decimation step. However, the alignment of genomes in signal form using DTW offers another advantage; it is not necessary to choose specific parameters for sequence alignment like scoring matrix or gap penalization based on DNA biological properties. The genomic signal carries biological and chemical properties in a specific shape of signal, further biological adaptation of the alignment process is not necessary.

The results of the proposed method were compared to the traditional character processing technique based on multiple alignment of short parts of sequences represented by common phylogenetic marker 16S rRNA genes. Our approach reproduced the real taxonomical division with higher success than the traditional method and due to the independence on the genome length, it is now possible to conduct an extensive comparative analysis that would, otherwise, not be realizable by conventional techniques.

Acknowledgement. Supported by European Regional Development Fund - Project FNUSA-ICRC (No. CZ.1.05/1.1.00/02.0123) and by the grant project GACR P102/11/1068 NanoBioTECell.

References

1. Mayr, E., Bock, W.J.: Classifications and other ordering systems. Zool. Syst. Evol. Research 40, 169–194 (2002)
2. Cohen, A., Daubechies, I., Vial, P.: Wavelets on the Interval and Fast Wavelet Transforms. Applied and Computational Harmonic Analysis 1(1), 54–81 (1992)
3. Skutkova, H., Vitek, M., Babula, P., Kizek, R., Provaznik, I.: Classification of genomic signals using dynamic time warping. BMC Bioinformatics 14, S1 (2013)
4. Bittner, L., Halary, S., Payri, C., Cruaud, C., de Reviers, B., Lopez, P., Bapteste, E.: Some considerations for analyzing biodiversity using integrative metagenomics and gene networks. Biology Direct 5 (2010)
5. Chapple, D.G., Ritchie, P.A.: A Retrospective Approach to Testing the DNA Barcoding Method. PloS One 8(11) (2013)
6. Anastassiou, D.: Genomic Signal Processing. IEEE Signal Processing Magazine 18(4), 8–20 (2001)
7. Cristea, P.D.: Conversion of nucleotides sequences into genomic signals. Journal of Cellular and Molecular Medicine 6(2), 279–303 (2002)
8. Yau, S.S.T., Wang, J.S., Niknejad, A., Lu, C., Jin, N., Ho, Y.K.: DNA sequence representation without degeneracy. Nucleic Acids Research 31(12), 3078–3080 (2003)
9. Cristea, P.D.: Large scale features in DNA genomic signals. Signal Processing 83, 871–888 (2003)
10. Hao, W., Golding, G.B.: Patterns of Bacterial Gene Movement. Mol. Biol. Evol. 21(7), 1294–1307 (2004)
11. Sorimachi, K.: A Proposed Solution to the Historic Puzzle of Chargaff's Second Parity Rule. The Open Genomics Journal 2(1), 12–14 (2009)
12. Jan, J.: Digital signal filtering, analysis and restoration. Institution of Electrical Engineers (2000)
13. Daubechies, I.: Ten lectures on wavelets. CBMS-NSF conference series in applied mathematics. SIAM Ed (1992)

14. Berndt, D., Clifford, J.: Using dynamic time warping to find patterns in time series, New York, vol. 398, pp. 359–370 (1994)
15. Needleman, S.B., Wunsch, C.D.: A general method applicable to the search for similarities in the amino acid sequence of two proteins. Journal of Molecular Biology 48(3), 443–453 (1970)
16. Smith, T.F., Waterman, M.S.: Identification of common molecular subsequences. Journal of Molecular Biology 147(1), 195–197 (1981)
17. Sokal, R., Michener, C.: A statistical method for evaluating systematic relationships. University of Kansas Science Bulletin 38, 1409–1438 (1958)

Using Analysis Algorithms and Image Processing for Quantitative Description of Colon Cancer Cells

Anna Wójcicka[1,2], Przemysław Jędrusik[2], Mateusz Stolarz[2], Robert Kubina[3], and Zygmunt Wróbel[2]

[1] Department of Technology and Engineering of Material, Pedagogical University, Institute of Technology, ul. Podchorążych 2, 30-084 Cracow, Poland
aniawojcicka@gmail.com
[2] Department of Computer Biomedical Systems, University of Silesia, Institute of Computer Science, ul. Będzińska 39, 41-200 Sosnowiec, Poland
pjedrusik@tlen.pl, mateusz_stolarz@yahoo.com, zygmunt.wrobel@us.edu.pl
[3] Department of Pathology, Medical University of Silesia, School of Pharmacy with the Division of Laboratory Medicine in Sosnowiec, ul. Ostrogórska 30, 41-200 Sosnowiec, Poland
rkubina@sum.edu.pl

Abstract. Nowadays, many diagnostic methods based on providing information about the patient in the form of photographs, projections, cross-sections. Almost impossible to conduct an effective and efficient treatment without the use of modern tools to support the process of medical analysis. The main goal of this work is to develop a tool for medical diagnosis of colorectal cancer in order to determine the level of cell growth. As part of the work developed and tested the processing and analysis algorithms microscopic images of the colon cancer cells, leading to a quantitative description of the local parameters of the object, include the quantity, the growth and cell growth over time. The proposed algorithm has been written in the Matlab.

Keywords: Image processing, algorithms, colon cancer.

1 Introduction

In the era of ubiquitous computerization the diagnostic systems used in medicine are gaining lot of popularity. Almost impossible is to conduct an effective and efficient treatment without the use of modern tools to support the process of medical analysis. Virtually all diagnostic methods are based on providing information about the patient in the form of images, projection and cross-section received from research like X-ray, medical ultrasonography, magnetic resonance imaging, nuclear medicine, scintigraphy, computed tomography, positron emission tomography, endoscopy, elastography, tactile imaging, echocardiography. Through the introduction of computer image analysis for routine and scientific research in the diagnosis may improve the quality of the investigation results.

E. Pietka, J. Kawa, and W. Wieclawek (eds.), *Information Technologies in Biomedicine, Volume 3*, Advances in Intelligent Systems and Computing 283,
DOI: 10.1007/978-3-319-06593-9_34,

By increasing the accuracy of the measurements is possible to determine the image parameters which are not possible to determine by human in routine medical investigation [9]. Algorithms for quantitative analysis excludes mistakes that can make by human due to inattention or fatigue.

Colon cancer arises from uncontrolled cell growth of the colon wall [5, 10]. The large intestine is the final section of the digestive tract, occupying a large part of it. It is positioned between the small intestine and the rectum. The vast majority of colorectal cancer (90%) is colorectal adenocarcinoma [5]. Symptoms and treatment of various cancers various parts of the large intestine may differ materially. The main parts of the large intestine are: cecum, ascending colon, transverse colon, descending colon and rectum. Cancer can occur in any of these parts (mostly occurs in the rectum) [5]. For the first signs of cancer can include changes to the rhythm of defecation, usually in the form of constipation, between which there may be diarrhea. Bleeding from the rectum, observed as the presence of visible blood in the stool, it should be a warning about the disorder that can be serious [2, 4, 13]. Depending on the location of cancer, the blood can be "live red" or in the form of a thrombus (grounds). In less advanced stages of proper treatment of colorectal cancer is partial or total colectomy, often with a large margin of surrounding tissue. Complete excision of the tumor is possible and gives cure, but the patient must be monitored due to the further possibility of recurrent colorectal cancer [4, 11].

Cancer of the colon is a social problem not only in Europe but also in the world [10]. In Europe and the US it is the second biggest cause of deaths due to malignant neoplasms, the world's third. Worldwide is about 1 230 000 people who suffer from cancer, of whom die each year 609 000 of them [11]. More than 450 000 citizens in Europe are newly diagnosed every year with the disease [11]. Annually on colorectal cancer dies 230 000 in Europe, and 52 045 people in the US [7]. Colorectal cancer is more common in men. Rarely occurs before the age of 40, mostly above 50 years of age with a peak incidence falls on the 7th decades of life. Approximately 175 million European citizens aged 50 - 69 years of age suffering from colon cancer [6]. Worse, the incidence is increasing over the years, it is estimated that 2,020 years this growth reaches 9,7% in the world. Permanent increase in the incidence of colorectal cancer is associated with a change in eating habits to a more "lazy", smoking, obesity, as well as population growth and the aging of society makes that the colorectal cancer is becoming a disease of civilization. Despite extensive research into the cause of formation the cancer, not all aspects are explained. It is known that the etiology is multifactorial and despite a number of well-known causative agents, still all the factors affecting its development are not known.The analysis of microscopic images of cancer cells allows to count and classify objects visible and to determine their morphological parameters and thus maybe closer to the answer concerning the formation and development of the disease like neoplasms [8, 11].

As part of the work developed and tested analysis and processing algorithms microscopic images in order to show level of growth of tumor cells of the colon in time. For this purpose, determine the quantitative parameters cells, like the number of cells and pace of their growth in time. Then compared these parameters,

in respect which better reflects the level of cell growth in time. The results of this study may help to accelerate research on the pathogenesis of colon cancer, and improve the process of medical diagnosis.

2 Materials and Experiment

In the study used microscopic images of the colon cancer cell line colorectal carcinoma cells HCT0020116 ATCC® CCL-247^{TM}. The cell line of colon cancer HCT 116 derived from colony ATCC was cultured in accordance with the manufacturer's instructions using the modified McCoy's medium (PAA Culture Company) supplemented with 10% bovine serum (FBS, PAA Culture Company). Cells were cultured in flasks with 25 cm^2 surface area (PAA) in a particular environment with the addition of penicillin at 100 $\mu l/ml$, streptomycin 100 $\mu l/ml$ and amphotericin B 0.25 $\mu l/ml$. A series of microscopic images was performed in the Department of Pathology, Medical University of Silesia, Katowice, using compact fluorescent microscope JULI Digital BioTechnology. Images of the same area of sample were recorded every 10 minutes. The image in digital form is saved as a bitmap with a resolution of 640x512 pixels — 96 dpi. A series of 140 images were analyzed using a proprietary algorithm written in Matlab.

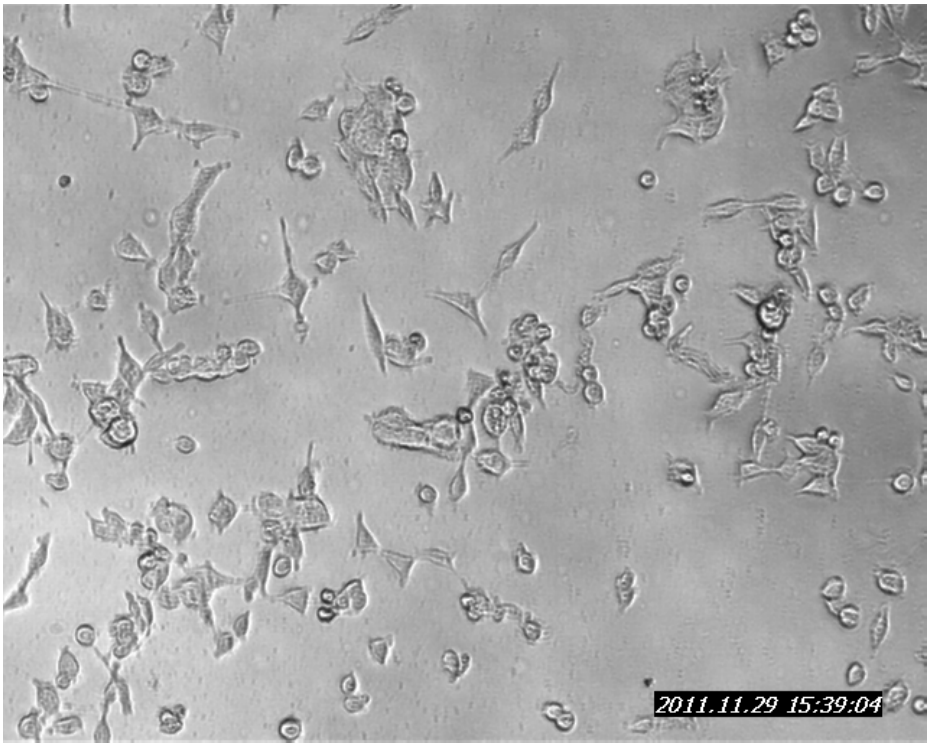

Fig. 1. The source image of the colon cancer cells

3 Result

An example of the resulting image source, subjected to the analysis shown in Figure 1. The focus and lighting of an image on the stage of the acquisition have a significant impact on the usefulness of the image for further analysis and the application of image pre-processing. The enlarged portion of the digitized image acquired for testing does not have many observable artifacts outside blur the edges of objects. Blur it was probably created as a result of wrong focus.

To increase the efficiency of algorithms of segmentation and identification of objects in the microscopic images was applied pre-processing of the image [1, 3, 12]. Its purpose is to eliminate the image of irrelevant or interfering elements from the point of view of the intended aims of analysis. Therefore, the images were cut to the size of 640x474 pixels in order to remove the information regarding the date and time the photo was taken. The removal of these data has no significant effect on the test result. The prepared a series of microscopic images of the colon cancer cells were subjected by operations which was shown in the schematic of actions the algorithm — Figure 2.

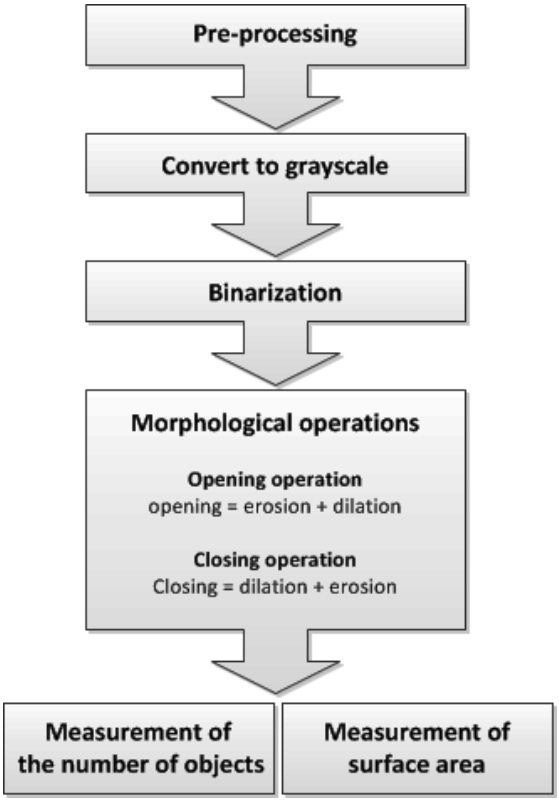

Fig. 2. The scheme of the algorithm

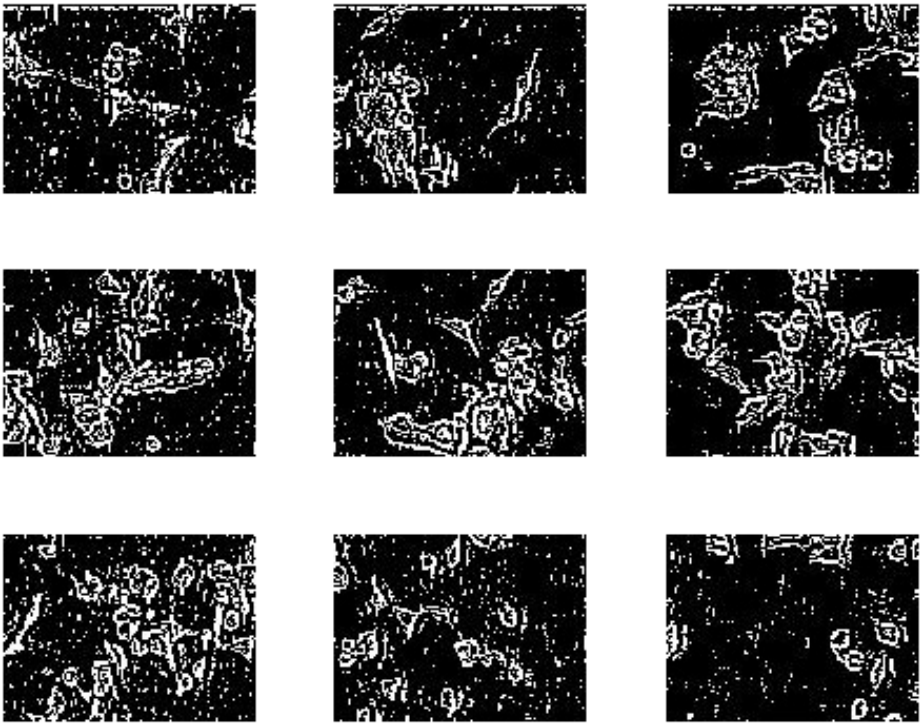

Fig. 3. The image after the adaptive binarization

Each of the series of images was divided into 3x3 regions and subjected to grayscale conversion. In order to obtain information on the level of cell growth in time was determined the quantitative parameters of image, first surface of area elements. The surface area is relatively simple to define the parameter and may be determined with high accuracy. However, for the outcome is highly influenced by the manner of conducting binarization, preceding the measurement. Even a small change in the threshold of binarization can have a significant impact on the resulting surface area, due to the significant reduction in the amount of information contained in the image [12]. He test images were subjected adaptive binarization with the local window size (11), additional global threshold (C = 0.03) with the mean. The adaptative binarization is dynamic search local binarization threshold, for better effect resulting image due to poor global threshold. Image after binarization is shown in Figure 3.

Then, in order to remove the image elements which is not significant to the result were applied morphological operations. Two basic morphological transformations which are erosion and dilatation have a common drawback — as a result of their activities the surface of object will change dramatically. The erosion reduces the object surface area, while dilatation increases it. The way to get rid of this imperfection is the use of these two transformations in tandem to

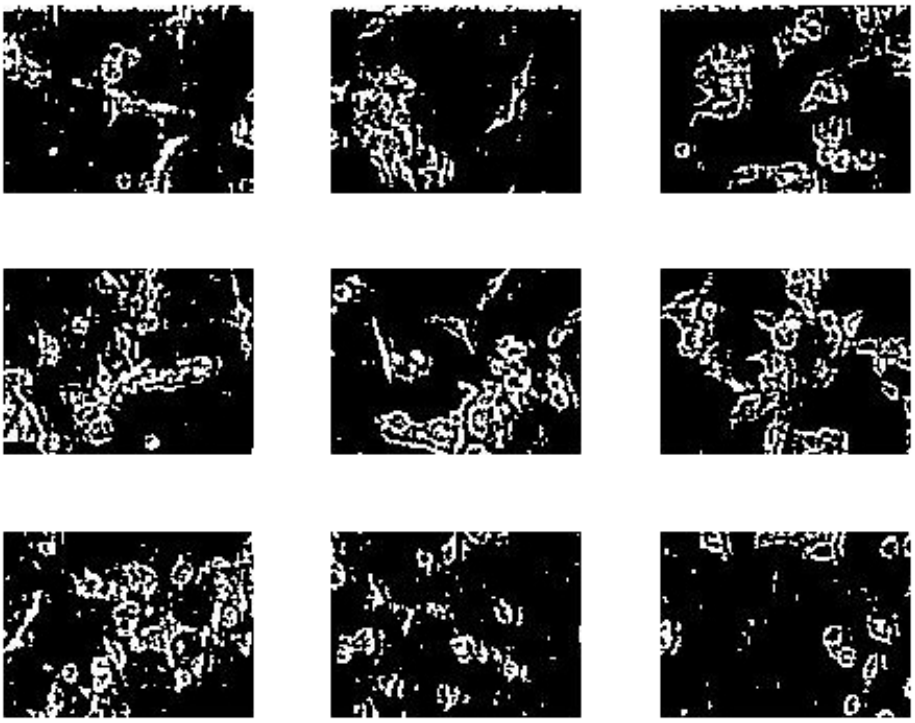

Fig. 4. The image after the application of the morphological operations of opening and closing

eliminate the above mentioned drawbacks. Using open operation as a consisting of the erosion and dilation, and closing - dilation and erosion, does not change the shape of the object's dimensions. Opening operation removes small objects and details which are not changing the size of the main part of the elements and also can detach objects with constrictions. Closing operation fills small voids, indentations in the object without changing the shape and dimensions of the object in contrast to the open operation can combine objects which are close to each other [12]. First for the tested images were performed opening operation, then closure operation. As a result of the applied morphological operations obtained an image of an important reducing unnecessary elements, but keeping the original shape and size of objects. Figure 4 shows the objects after morphological operations.

As a result of the applied morphological operations was obtained images from which to obtain information regarding surface area occupied by the tumor cells. The measurement of the surface area is done by counting the pixels belonging to an interesting object — cancer cells. After administration of the actual distance corresponding to the distance, in pixels, the measurement result can be obtained in such units which was required. The result of measurement of surface area is shown in Figure 5. The table shows sample data for the 20 analyzed images.

No. of images	Surface area
1	4,31
2	4,32
3	4,62
4	4,59
5	4,69
6	4,68
7	4,83
8	4,84
9	4,89
10	4,82
11	4,93
12	5,45
13	5,48
14	5,44
15	5,38
16	5,43
17	5,32
18	5,23
19	5,38
20	5,57

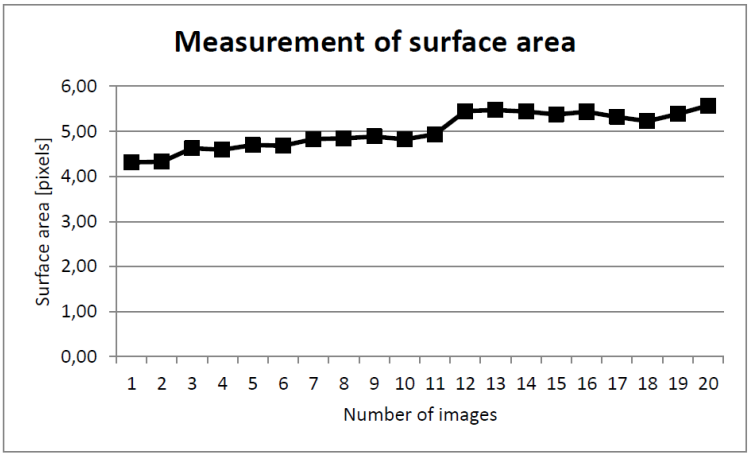

Fig. 5. The result of measurement of surface area

The second quantitative parameter, which will assess the level of cell growth in time is the analysis of the number of cells. Quantitative analysis of tumor cells was performed on the images of the original size. For test images were applied segmentation with template matching with some level of sensitivity. Segmentation by matching the template is a method that examines the degree of similarity between the stencil mask — circle for object shape which are searching in the images. Because the shape of segmented object is known and takes the form of an ellipse and their assemblies, the method used is appropriate to the studied images. The result of segmentation is shown in Figure 6.

Figure 7 shows a quantitative analysis of colon cancer cells. The table shows sample data for the 20 analyzed images. This situations reflect the quantitative results presented in the figure where the number of objects in consecutive images may be equal or less than in preview images.

Number of found objects for individual images depends on the arrangement of the cells and their shape. It often happens that the objects overlap, or their shape is strongly deviate from the assumed looking stencil. This situations reflect the quantitative results presented in the Figure 6, where the number of objects in consecutive images may be equal or less than the previous images. However, analyzing all possible images, show that a global score shows a significant increase in the number of examined cells.

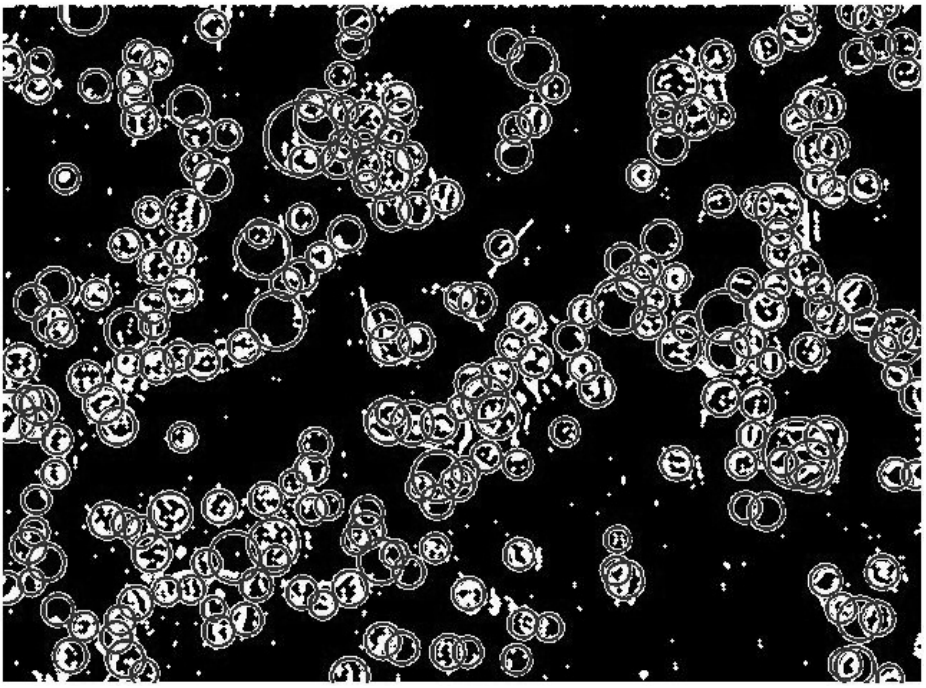

Fig. 6. The result of segmentation

No. of images	Number of objects/cells
1	255
2	256
3	287
4	275
5	289
6	293
7	298
8	282
9	310
10	301
11	297
12	322
13	315
14	317
15	337
16	336
17	319
18	312
19	331
20	324

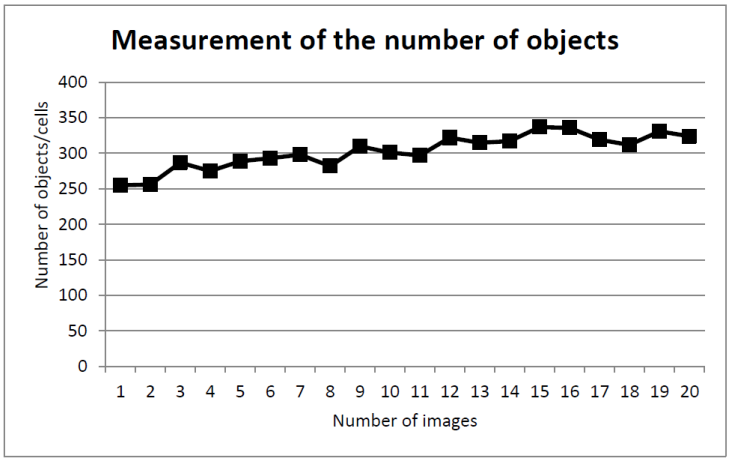

Fig. 7. A quantitative analysis of colon cancer cells

4 Conclusions

The study shows that both the quantitative parameters to assess the level of cell growth show a significant (expected) increase in the surface area occupied by the tumor cells and increase their numbers. The fact is that number of search objects is dependent on the arrangement of cells, their overlapping, confluent with the background and their shape which is sometimes difficult to identify. So the analysis of the area occupied by the cell searches is a better way to solve the problem to determine the level of cell growth in time. The analysis shows that the proposed algorithm can be a useful tool in the study of microscopic images of cancer cells of the colon. In an automatic manner can be monitored growth of the cell in time by studying the quantitative parameters of the image. It should be noted that in clinical research performed by human there is a reasonable suspicion that a person can make mistakes in counting and recognizing cancer cells. Moreover, in the case of such images, where the field of view is about 300 object the visual fatigue may cause errors.

Pre-processing of images, and the application of appropriate morphological operations significantly simplifies the process of analysis. Tests have shown that the case of the segmentation algorithm is significantly important fit parameters and the choice of an appropriate method for the detection of objects. The next step in the analysis examined images will be attempt to assess the ability of cell migration.

Through the use of such modern tools is possible to perform efficient and effective treatment. The role of programs to analyze medical image is constantly growing, allowing for more perfect diagnosis, treatment, rehabilitation and getting better explore the mysteries of the human body, the principles of its operation and treatment. Informatics tools like proposed algorithm may plays an important role in the pathogenesis of many diseases, including cancer.

Acknowledgments. Anna Wójcicka and Mateusz Stolarz are a beneficiary of Silesian Cooperation: Innovations For Efficient Development (SWIDER). Project realized within Human Capital Operational Programme, Priority VIII: Regional human resources for economy, 8.2 Transfer of knowledge, Sub-measure 8.2.1 Support to cooperation of scientific environment and enterprises. Project partially funded from European Union Project based on European Social Funds; University of Silesia, Katowice, Poland.

References

1. Ray, A.K.: Image Processing - Principles and Applications. Wiley InterScience (2006)
2. Macaskill, B.A., Chan, P., Katelaris, S.F., Irwig, P.H., Most, L.: bowel cancer symptoms do not indicate colorectal cancer and polyps: a systematic review. BMC Gastroenterology 11(65) (2011), doi:10.1186/1471-230X-11-65
3. Tannenbaum, E., Mathematical, A.: methods in medical image processing. Bulletin of the American Mathematical Society 43, 365–396 (2006)

4. Astin, M., Griffin, T., Neal, R.D., Rose, P., Hamilton, W.: The diagnostic value of symptoms for colorectal cancer in primary care: a systematic review. The British Journal of General Practice: The Journal of the Royal College of General Practitioners 61(586), 231–243 (2011), doi:10.3399/bjgp11X572427
5. Bochenek, A., Reicher, M.: Anatomia Człowieka. 2, Wydawnictwo Lekarskie PZWL, pp. 239–267 (2004)
6. Cunningham, D., Atkin, W., Lenz, H.J., Lynch, H.T., Minsky, B., Nordlinger, B., Starling, N.: Colorectal cancer. Lancet 375(9719), 1030–1047 (2010), doi:10.1016/S0140-6736(10)60353-4
7. Diggsa, D.L., Myersa, J.N., Banksa, L.D., Niaza, M.S., Hoodb, D.B., Roberts, L.J., Ramesha, A.: Influence of dietary fat type on benzo(a)pyrene [B(a)P] biotransformation in a B(a) P-induced mouse model of colon cancer. The Journal of Nutritional Biochemistry 24(12), 2051–2063 (2013)
8. Eadie, L.H., Reid, C.B., Fitzgerald, A.J., Wallace, V.P.: Optimizing multidimensional terahertz imaging analysis for colon cancer diagnosis. Expert Systems with Applications 40(6), 2043–2050 (2013)
9. Koprowski, R., Korzyńska, A., Zieleźnik, W., Wróbel, Z., Małyszek, J., Stępień, B., Wójcik, W.: Influence of the measurement method of features in ultrasound images of the thyroid in the diagnosis of Hashimoto's disease. BioMedical Engineering OnLine 11, 91 (2012)
10. The Cancer Genome Atlas Network.: Comprehensive molecular characterization of human colon and rectal cancer. Nature 487(7407), 330–337 (2012), doi:10.1038/nature11252
11. International Agency for Research on Cancer, World Health Organization. IARC launches the definitive cancer statistics resource GLOBOCAN 2008 201 (2010), `http://globocan.iarc.fr/`
12. Wróbel, Z., Koprowski, R.: Praktyka przetwarzania obrazów z zadaniami w programie Matlab. Published: Exit, Warsaw (2012)
13. Yamada, T., Alpers, D.H., Kalloo, A.N., Kaplowitz, N., Owyang, C., Powell, D.: Principles of clinical gastroenterology, p. 381. Wiley-Blackwell, Chichester (2008) ISBN 978-1-4051-6910-3

Relationship of Bacteria Using Comparison of Whole Genome Sequences in Frequency Domain

Vladimira Kubicova[1] and Ivo Provaznik[1,2]

[1] Department of Biomedical Engineering, Brno University of Technology, Brno, Czech Republic
kubicova@feec.vutbr.cz
[2] International Clinical Research Center - Center of Biomedical Engineering, St. Anne's University Hospital Brno, Brno, Czech Republic

Abstract. Developing sequencing techniques provide understanding the molecular phylogeny at the whole genome level. The phylogeny derived from 16S rRNA gene is the universally accepted DNA sequence-based method today; so far there is no widely accepted approach to infer phylogenetic relationships from complete genome data. If the entire genome is used, the data reflect organismal evolution, not the evolution on a single gene level. We propose a new method for determination of relationship of bacteria based on whole genome data. The method compares whole genomic DNA sequences in frequency domain. The proposed method was tested on phyla level on 168 bacteria from four phyla and on order level – 121 bacteria from phylum *Proteobacteria*, class *Gammaproteobacteria* were classified. The classification on both levels was successful in more than 82%.

Keywords: relationship of bacteria, whole genome comparison, DNA spectrogram.

1 Introduction

Identification of bacteria plays a key role in medicine to identify the pathogens isolated from a patient or in food industry for identification of a microbial contaminant responsible for food spoilage. Microbial taxonomy is essential for accurate identification of microorganisms, because it organizes huge amounts of organisms into meaningful groups. Classification is a prerequisite for identification [1]. Morphological and metabolic features may be used to infer relationships, but developing sequencing techniques provide understanding the molecular phylogeny at the whole genome level.

Approaches to the classification based on the study of genotypic data, involve the study of GC content, study of small genetic variations (insertions and deletions) [2] or study the conserved genes. Species phylogenies have traditionally been constructed by measuring evolutionary divergence in particular proteins. The most commonly used sequence is small subunit ribosomal RNA (16S rRNA gene). The phylogeny derived from 16S rRNA gene is the universally accepted

E. Pietka, J. Kawa, and W. Wieclawek (eds.), *Information Technologies in Biomedicine, Volume 3*, Advances in Intelligent Systems and Computing 283,
DOI: 10.1007/978-3-319-06593-9_35,

DNA sequence-based method today [3, 4]. The 16S rRNA genes are found in all organisms, they are highly conserved among different species and they have evolved relatively slowly, so it permits to construct phylogenies between distant organisms. However, bacteria may have multiple copies of this gene and this can make interpretation difficulties when base pair changes exist among copies. High levels of sequence variation have been observed, even between strains of the same species. Further, the 16S rRNA gene sequence does not contain enough discriminating power to delineate species within certain groups and some bacterial taxa have identical 16S rRNA genes [5].

Several attempts were introduced to infer bacterial phylogeny from complete genomes. If the entire genome is used, the data reflect organismal evolution, not the evolution of single genes. It does not make sense to align two complete genomes since every species has its own gene content and gene order, not to mention the different sizes of the genomes. Methods which infer whole genome phylogeny are usually based on study the gene content. The method, based on the proportion of homolog genes shared between two genomes, is presented in [6]. Method based on the presence and absence of gene families was presented in [7]. Distance between two species can be measured as the number of homologous genes divided by the total number of genes, or its variants [8]. Then, the genomes can be compared using gene order. Distance between two species is defined as the minimum number to get the same order of genes. The breakpoint distance counts the minimal number of breakage events that are necessary to transform one genome into another. The inversion distance is the edit distance under the single allowed event of inversion [9]. Another approach takes into account score forming by both the gene content measure and gene order measure [10]. The main disadvantage of mentioned method, which are based on study the gene content, is the requirement of gene identification and an fact, that searching for homologous genes is time consuming.

Another method, which infers phylogeny from whole genome sequences, takes into account the distribution of sequence strings, where frequency of amino acid K-strings in their complete genomes or proteomes is found [11].

Time consuming multiple alignment of symbolic or numeric sequences in whole-genome analysis can be treated using specific signal processing techniques. Dynamic time warping was previously used and validated in dendrogram construction using cluster analysis [12].

Today, the Bergey's manual of Systematic Bacteriology [13] is considered the highest authority and the taxa which have been correctly described are reviewed in. The classification comprises both the genotypic and phenotypic features, called polyphasic taxonomy. The extensive application of polyphasic taxonomy has led to marked improvements in the classification of prokaryotes.

So far there are no widely accepted ways to infer phylogenetic relationships from complete genome data. There is an urgent need to develop new phylogenetic methods utilizing the increasing amount of molecular data, in particular, the complete genomes of organisms.

We propose a new method for determination of relationship of bacteria based on whole genome data. Our method compares the whole genomic DNA sequences in frequency domain. DNA spectral analysis was proposed in [14]. In spectrograms of biological sequences, we observe some patterns, which are created by nucleotide repetitions, often related to the sequence function or structure. For example 3 bp pattern occurs in coding regions; such periodicity is related to distributions of codons [15]. Biological sequences are often built from tandem repetitive regions (mostly in noncoding regions), which are clearly visible in spectrogram. Spectrograms can reveal periodicities related to helical structure, the periodicity related to folding around nucleosomes is considered the periodicity around 10 bp [16, 17]. In our method, distance between two organisms is derived from the similarity of spectrograms. We compared our results to the taxonomy in Bergey's manual of Systematic Bacteriology.

2 Methods

2.1 Spectrogram Construction

Spectrograms of DNA sequences give a combined view of the local periodicity throughout the nucleotide sequence. If we transform the DNA sequence into a sequence of numbers, we can compute DNA sequence spectrum. By computing the spectrum in short windows, sliding in a sequence, we can construct spectrogram by depicting single spectrum from one window as a one column of spectrogram image. Depicting many spectra from sliding windows we obtain spectrogram. Spectrogram can be depicted as RGB image or as non-RGB (classical) spectrogram.

In [18], there is suggested to compute spectrum from one sliding window in 4 steps: convert DNA sequence to numerical sequences, Discrete Fourier transform (DFT) of numerical sequence, mapping of DFT values to RGB colors and normalizing the pixel values.

For conversion of DNA to numerical sequence, the binary representation is widely used [14, 19]. The symbolic DNA sequence is first converted to four binary indicator sequences, $u_A(n)$, $u_T(n)$, $u_C(n)$ and $u_G(n)$, which indicate the presence or absence of four nucleotides, A, T, C and G, respectively, at the n-th position. For example, sequence GTACCATAG is represented by binary vectors:

$$\begin{aligned} u_A(n) &= 001001010 \\ u_T(n) &= 010000100 \\ u_C(n) &= 000110000 \\ u_G(n) &= 100000001 \end{aligned}$$

Numerical sequences were transformed to frequency domain using DFT:

$$U(k) = \sum_{n=0}^{N-1} u(n) e^{-j \frac{2\pi n k}{N}} \tag{1}$$

where N is the length of signal $u(n)$, $n = 0, 1, \ldots, N$ and k is frequency. To obtain RGB spectrogram, the four spectra were reduced to three:

$$\begin{aligned} x_R &= U_T[n] + \tfrac{1}{3}U_G[n] \\ x_G &= U_C[n] + \tfrac{1}{3}U_G[n] \\ x_B &= U_A[n] + \tfrac{1}{3}U_G[n] \end{aligned} \tag{2}$$

The thymine occurrence is registered in red layer of RGB spectrogram, the cytosine occurrence in green layer of RGB spectrogram, the adenine occurrence in blue layer of RGB spectrogram and finally, the guanine occurrence in all three layers of RGB spectrogram. Then every layer was normalized from 0 to 1. For computing the spectrograms, the length of sliding window was set to 5000 bp. In Fig. 1, spectrograms for *Melissococcus plutonius*, *Staphylococcus epidermidis* and *Mycobacterium bovis* are shown.

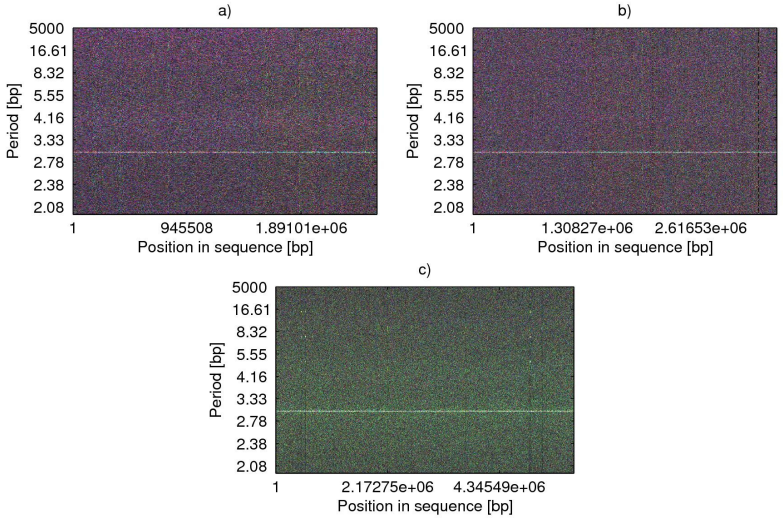

Fig. 1. RGB spectrograms of a) *Melissococcus plutonius* (phylum *Firmicutes* class *Bacilli*, order *Lactobacillales*), b) *Staphylococcus epidermidis* (phylum *Firmicutes*, class *Bacilli*, order *Bacillales*) and c) *Mycobacterium bovis* (phylum *Actinobacteria*, class *Actinobacteria*, subclass *Actinobacteridae*, order *Actinomycetales*); length of sliding window was set to 5000 bp. (Note: See color version of figure which is available in electronic version of paper)

2.2 Spectrogram Comparison

Relation between bacteria can be seen from color of RGB spectrograms; for closely related bacteria, RGB spectrograms show similar color properties (Fig. 1 a, b) unlike for distant bacteria RGB spectrograms are visually different (Fig. 1 a, c). For evaluation of similarity of two spectrograms we used the spatial distribution

of colors, which was designed to achieve image and video segment retrieval based on similarity. The algorithm for color layout descriptor was published in [20].

For every studied genome, DNA spectrogram was computed and every pair of spectrograms was compared to get a distance matrix. The spectrogram image is first split to n uniform rows and n uniform columns and every of $n*n$ regions is described separately. The average RGB color from region is counted and new image of n rows and n columns is obtained. This RGB image is transformed to YC_bC_r color space, which is defined as:

$$\begin{aligned} Y &= 0.299R + 0.587G + 0.114B \\ C_b &= -0.169R - 0.331G + 0.5B \\ C_r &= 0.5R - 0.419G - 0.081B \end{aligned} \tag{3}$$

Each of three matrixes (Y, C_b, C_r) is transformed by Discrete cosine transform (DCT) using formula:

$$B_{pq} = \alpha_p \alpha_q \sum_{m=0}^{M-1} \sum_{n=0}^{N-1} Y_{mn} cos \frac{\pi(2m+1)p}{2M} cos \frac{\pi(2n+1)q}{2N} \tag{4}$$

where M and N are row and column size of Y, respectively. If $p=0$ then $\alpha_p = \frac{1}{\sqrt{M}}$, else $\alpha_p = \sqrt{\frac{2}{N}}$. We obtain three sets of DCT coefficients. The set of DCT coefficients is called color layout descriptor. For every pair of spectrograms, Euclidian distance is counted from the DCT coefficients. By counting distances for each pair of spectrograms, we obtain the distance matrix. To evaluate the relationship between bacteria, we constructed a distance tree using Neighbor joining algorithm.

To determine relationship between bacteria, several parameters can be modified: number of rows and columns n, the color space of image and the number of DCT coefficients. Impact of these parameters on determination of relationship is discussed in next paragraph.

3 Results

3.1 Comparison on Phylum Level

We compared bacteria from four different phyla using proposed method. Chosen bacteria come from NCBI (National Center for Biotechnology Information) list of reference bacteria, downloaded from NCBI database [21]. Four phyla with more than 10 organisms were chosen – *Firmicutes* (52 organisms), *Actinobacteria* (23 organisms), *Tenericutes* (12 organisms) and *Proteobacteria* (81 organisms). Length of the whole genome sequences was between 138927 bp and 10467782 bp. Total sequence length was 547083155 bp. The NCBI taxonomy database is not a primary source for taxonomic or phylogenetic information because it attempts to incorporate phylogenetic and taxonomic knowledge from a variety of sources. We took the taxonomy of bacteria from Bergey's manual of Systematic Bacteriology [13].

We analyzed the classification of bacteria for every pair of studied phyla. In Fig. 2, a distance tree for *Firmicutes* and *Actinobacteria* is shown. Name of each leaf is created from name of the phylum, NCBI access number and name of the organism. In Fig. 2, two groups of organisms are shown. Organisms from phyla *Actinobacteria* are classed together by upper branch, while organisms from phyla *Firmicutes* by lower branch. Four *Actinobacteria* occur in group of *Firmicutes* incorrectly. The success of sorting to two groups were counted as probability that organism was included in the correct branch. For the distance tree in Fig. 2, probability that organism from phyla *Firmicutes* is placed in the correct branch is $\frac{52}{52+0} = 1$. On the other hand, the probability, that organism from phyla *Actinobacteria* is placed in the right branch is $\frac{19}{19+4} = 0.83$. Probabilities for all pairs of studied phyla are listed in Table 1.

Table 1. Probability of correct separation, if pair of phyla is analyzed

		YC_bC_r **model, all DCT coeffs, image 10x10**		**RGB model, all DCT coeffs, image 10x10**		YC_bC_r **model, 12 DCT coeffs, image 10x10**		YC_bC_r **model, all DCT coeffs, image 20x20**	
Phylum 1	**Phylum 2**	**P1**	**P2**	**P1**	**P2**	**P1**	**P2**	**P1**	**P2**
Firmicutes	*Actinobacteria*	1	0.83	1	0.65	1	0.65	1	0.83
Tenericutes	*Actinobacteria*	1	0.83	0.83	1	1	0.83	1	0.83
Tenericutes	*Firmicutes*	0.83	0.88	**0.50**	1	**0.50**	1	**0.50**	1
Proteobacteria	*Firmicutes*	**0.57**	1	**0.57**	1	**0.57**	1	**0.57**	1
Proteobacteria	*Actinobacteria*	**0.43**	0.65	**0.58**	0.65	**0.43**	0.65	**0.43**	0.65
Proteobacteria	*Tenericutes*	1	0.83	1	0.83	1	0.83	1	0.83

We compared results for RGB model and YC_bC_r color model. Probabilities of correct classification of bacteria are listed in third and fourth column of Table 1. Probability of correct separation of *Tenericutes* from *Firmicutes* decrease and overall, three probabilities of correct classification are lower than 0.6 (highlighted in table). In case of YC_bC_r color model, only two probabilities are lower than 0.6. Therefore the YC_bC_r color model is considered being more appropriate.

We investigated number of DCT coefficients, which are necessary to determine the relationship between bacteria. According to [20], the best choice for considering tradeoff is total 12 coefficients (6 coefficients of Y, 3 for C_b and 3 for C_r). We found that the best choice for determination of relationship is to consider all of the DCT coefficients, not only low frequency coefficients as mentioned. In the fifth and sixth row of Table 1, there are shown the results considering 12

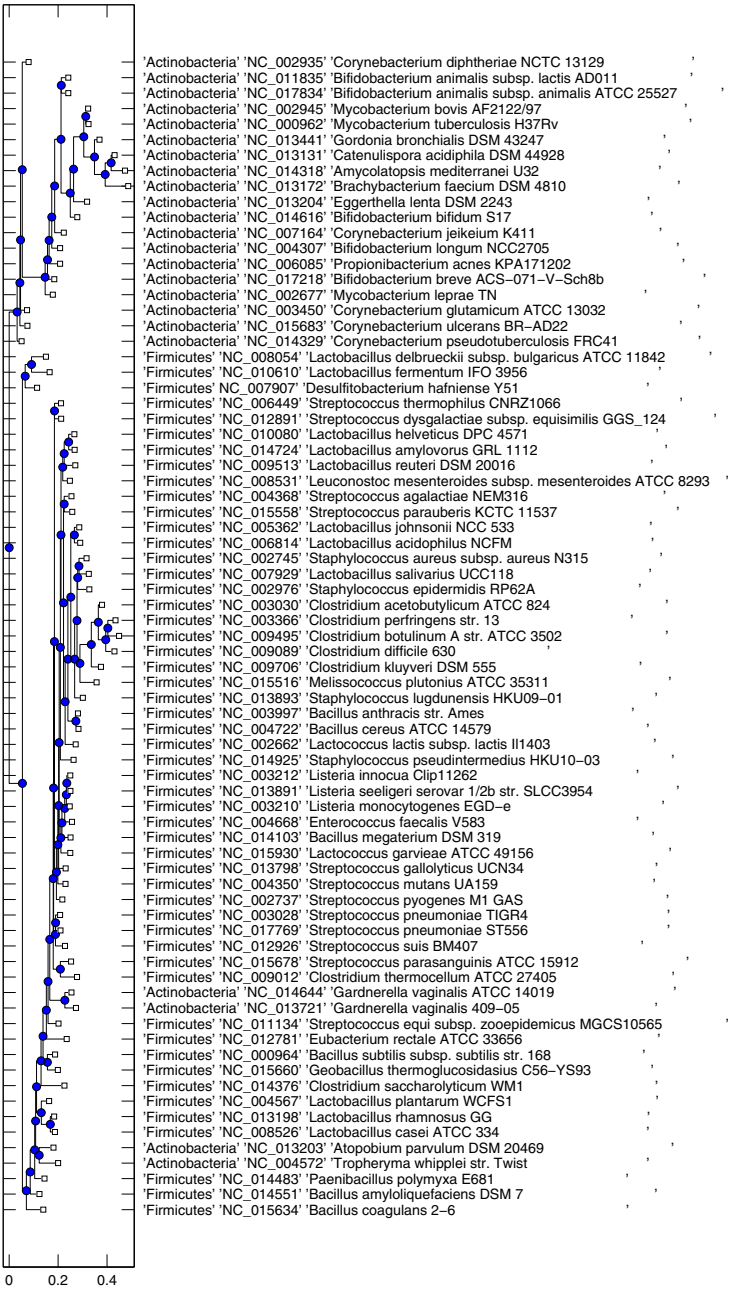

Fig. 2. Distance tree for *Firmicutes* and *Actinobacteria*

DCT coefficients. Results considering all DCT coefficients show better results for classification of *Tenericutes*. On the contrary, there are 3 probabilities lower than 0.6.

We examined the number of regions $n*n$ in which the image is divided. We compared results for splitting the image into 10 uniform rows and columns and 20 uniform rows and columns. In last two columns of Table 1, there is shown the probability of correct separation in case of splitting the image into 20x20 regions. Probability of correct separation of *Tenericutes* from *Firmicutes* is lower than in the method consider splitting the image into 10x10 regions.

Based on these findings, the best results give us the method considering the YC_bC_r color model, splitting the image into 10x10 regions and using all DCT coefficients for analysis. Results using these parameters are summarized in Table 2. Cells show the probability that bacteria from phylum in corresponding column will be separated from bacteria from phylum in corresponding row. Results presented in ROC space are shown in Fig. 3 a). Problem arises with separation of *Proteobacteria*, which is phenotypically most diverse division among prokaryotes. The average probability for classification of bacteria from all four phyla is 0.82.

Table 2. Probability that bacteria from phylum in corresponding column will be separated from bacteria from phylum in corresponding row

	Firmicutes	*Actinobacteria*	*Tenericutes*	*Proteobacteria*
Firmicutes	-	0.83	0.83	0.57
Actinobacteria	1	-	1	0.43
Tenericutes	0.88	0.83	-	1
Proteobacteria	1	0.65	0.83	-

3.2 Comparison on Order Level

Proteobacteria is the largest and phenotypically most diverse division among prokaryotes. This phylum encompasses bacteria with a wide variety of phenotype and physiological attributes and habitats [22]. *Proteobacteria* has been classified based on the homology of 16S ribosomal RNA or by hybridization of ribosomal DNA with 16S and 23S ribosomal RNA. It has been subdivided in five major classes: α-, β-, γ-, δ- and ϵ- [23].

We tried to classified orders of phylum *Proteobacteria*, class *Gammaproteobacteria*. 8 orders were chosen, *Alteromonadales* (23 organisms), *Enterobacteriales* (38 organisms), *Chromatiales* (9 organisms), *Oceanospirillales* (7 organisms), *Pasteurellales* (15 organisms), *Pseudomonadales* (15 organisms), *Xanthomonadales* (9 organisms) and *Thiotrichales* (5 organisms) using method presented above. Genomes were chosen from NCBI list of representative bacteria genomes. Length of the whole genome sequences was between 113685 bp and 7215267 bp.

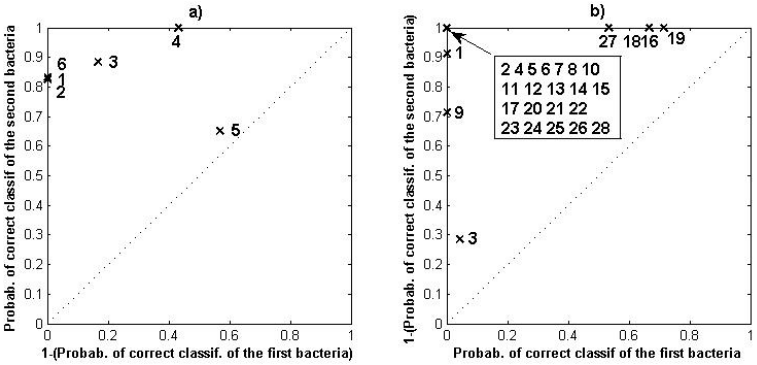

Fig. 3. Results of classification presented in ROC space a) Results on phylum level are shown, pairs of phyla are numbered as follows: 1 - *Firmicutes* and *Actinobacteria*, 2 - *Tenericutes* and *Actinobacteria*, 3 - *Tenericutes* and *Firmicutes*, 4 - *Proteobacteria* and *Firmicutes*, 5 - *Proteobacteria* and *Actinobacteria*, 6 - *Proteobacteria* and *Tenericutes*. b) Results on order level are shown, pairs of orders are numbered as follows: 1 - *Ent.* and *Alt.*, 2 - *Alt.* and *Chrom.*, 3 - *Alt.* and *Ocean.*, 4 - *Alt.* and *Pas.*, 5 - *Alt.* and *Pseud.*, 6 - *Alt.* and *Thiotr.*, 7 - *Alt.* and *Xant.*, 8 - *Ent.* and *Chrom.*, 9 - *Ent.* and *Ocean.*, 10 - *Ent.* and *Pas.*, 11 - *Ent.* and *Pseud.*, 12 - *Ent.* and *Thiotr.*, 13 - *Ent.* and *Xant.*, 14 - *Ocean.* and *Chrom.*, 15 - *Chrom.* and *Pas.*, 16 - *Chrom.* and *Pseud.*, 17 - *Chrom.* and *Thiotr.*, 18 - *Chrom.* and *Xant.*, 19 - *Ocean.* and *Pas.*, 20 - *Ocean.* and *Pseud.*, 21 - *Ocean.* and *Thiotr.*, 22 - *Ocean.* and *Xant.*, 23 - *Pseud.* and *Pas.*, 24 - *Pas.* and *Thiotr.*, 25 - *Pas.* and *Xant.*, 26 - *Pseud.* and *Thiotr.*, 27 - *Pseud.* and *Xant.*, 28 - *Thiotr.* and *Xant.* (*Alt.* = *Alteromonadales*, *Ent.* = *Enterobacteriales*, *Chrom.* = *Chromatiales*, *Ocean.* = *Oceanospirillales*, *Pas.* = *Pasteurellales*, *Pseud.* = *Pseudomonadales*, *Thiotr.* = *Thiotrichales*, *Xant.* = *Xanthomonadales*)

Total sequence length was 486687188 bp. For evaluation the success of classification similar bacteria into one group, we used the method described above. Table 3 shows results, where probabilities lower than 0.5 are highlighted. Results presented in ROC space are shown in Fig. 3 b). In [24], comparative genomic analyses based on concatenated sequences for 13 and 36 universally distributed proteins and the maximum like hood phylogenetic tree was used and the order *Oceanospirillales* and *Alteromonadales* were not separated clearly. Our method cannot separate *Oceanospirillales* from *Alteromonadales*, neither. Results indicated very similar DNA content for those orders. Results of our method are not satisfactory for separation of *Oceanospirillales* from *Pasteurellales*, *Chromatiales* from orders *Pseudomonadales* and *Xanthomonadales*, *Pseudomonadales* from order *Xanthomonadales*. The closed relationship is shown for *Chromatiales* and *Xanthomonadales* in [24]. But, probability of correct separation for other group of organisms (52) is 1 or close to 1. The average probability is 0.93.

Table 3. Probability that bacteria from order in corresponding column will be separated from bacteria from order in corresponding row (*Alt.* = *Alteromonadales*, *Ent.* = *Enterobacteriales*, *Chrom.* = *Chromatiales*, *Ocean.* = *Oceanospirillales*, *Pas.* = *Pasteurellales*, *Pseud.* = *Pseudomonadales*, *Thiotr.* = *Thiotrichales*, *Xant.* = *Xanthomonadales*)

	Alt.	*Ent.*	*Chrom.*	*Ocean.*	*Pas.*	*Pseud.*	*Thiotr.*	*Xant.*
Alteromonadales	-	1	1	**0.29**	1	1	1	1
Enterobacteriales	0.91	-	1	0.71	1	1	1	1
Chromatiales	1	1	-	1	1	1	1	1
Oceanospirillales	0.96	1	1	-	1	1	1	1
Pasteurellales	1	1	1	**0.29**	-	1	1	1
Pseudomonadales	1	1	**0.33**	1	1	-	1	1
Thiotrichales	1	1	1	1	1	1	-	1
Xanthomonadales	1	1	**0.33**	1	1	**0.47**	1	-

4 Conclusion

We developed a new method for determination of relationship between bacteria based on whole genome information. The method based on spectrogram is created from whole genomes, which were retrieved from NCBI.

We analyzed the success of classification on level of phyla and order. In the first case, we classified 168 organisms from 4 phyla. We evaluated the success of separation of bacteria into groups by counting the probability, that bacteria will be separated into the correct group, if pair of phyla is analyzed. Problem arises with separation of *Proteobacteria*. Some organisms from phyla *Proteobacteria* were placed into one branch with bacteria from *Firmicutes* and *Actinobacteria*. No organism from *Firmicutes* was placed into branch with *Proteobacteria*. The average probability of successful classification on phyla level was 0.82.

A total of 121 *Gammaproteobacteria* from 8 orders were analyzed to assess the success of the classification in orders level. Most of the bacteria from order *Oceanospirillales* were placed incorecctly into one branch with *Alteromonadales* and *Pasteurellales*. Similarly, most of the organisms from order *Chromatiales* are assigned to *Pseudomonadales* and *Xanthomonadales*. The average probability of successful classification on order level was 0.93.

The proposed method is suitable for classification of organisms on phyla and order level. Method does not need to choose subsequences for analysis to the contrary in gene content comparison based methods or other methods, which used searching the similar parts of genetic information (e.g. K-strings method).

Acknowledgement. This work has been supported by grant project GACR P102/11/1068 and European Regional Development Fund - Project FNUSA-ICRC (No. CZ.1.05/1.1.00/02.0123).

References

1. Priest, S.T., Williams, S.T.: Computer-assisted identification. In: Handbook of New Bacterial Systematics, pp. 362–381. Academic Press, London (1993)
2. Gupta, R.S., Griffiths, E.: Critical Issuea in Bacterial Phylogeny. Theoretical Population Biology, 423–434 (2002)
3. Choi, B.K., Wyss, C., Gobel, U.B.: Phylogenetic analysis of pathogen-related oral spirochetes. Journal of Clinical Microbiology, 1922–1925 (1996)
4. Claridge, J.E.: Impact of 16S rRNA Gene Sequence Analysis for Identification of Bacteria on Clinical Microbiology and Infectious Diseases. Clinical Microbiology Reviews, 840–862 (2004)
5. Cathy, P.A.: Detection and Identification of Microorganisms by Gene Amplification and Sequencing. Medical Microbiology, 1108–1114 (2007)
6. House, C.H., Fitz-Gibbon, S.T.: Using Homolog Groups to Create a Whole-Genomic Tree of Free-Living Organisms: An Update. Journal of Molecular Evolution, 539–547 (2002)
7. Fitz-Gibbon, S.T., House, C.H.: Whole genome-based phylogenetic analysis of free-living microorganisms. Nucleic Acids Research, 4218–4222 (1999)
8. Snel, B., Bork, P., Huynen, M.: Genome phylogeny based on gene content. Nature Genetics, 108–110 (1999)
9. Moret, B.M., Warnow, T.: Advances in Phylogeny Reconstruction from Gene Order and Content Data. Methods in Enzymology, 673–700 (2004)
10. Khiripet, N.: Bacterial Whole Genome Phylogeny Using Proteome Comparison and Optimal Reversal Distance. In: Computational Systems Bioinformatics Conference Workshops (2005)
11. Qi, J., Wang, B., Hao, B.I.: Whole Proteome Prokaryote Phylogeny Without Sequence Alignment: A K-String Composition Approach. Journal of Molecular Evolution, 1–11 (2004)
12. Skutkova, H., Vitek, M., Babula, P., Kizek, R., Provaznik, I.: Classification of genomic signals using dynamic time warping. BMC Bioinformatics 14(suppl. 10), S1 (2013)
13. Garrity, G.M., Bell, J.A., Lilburn, T.G.: Taxonomic Outline of the Prokaryotes – Bergeys Manual of Systematic Bacteriology. Springer, New York (2004)
14. Anastassiou, D.: Frequency-domain Analysis of Biomolecular Sequences. Bioinformatics 16, 1073–1081 (2000)
15. Tiwari, S., Ramachandran, S., Bhattacharya, A., Bhattacharya, S., Ramaswamy, R.: Prediction of Probable Genes by Fourier Analysis of Genomic Sequences. CABIOS 113, 263–270 (1997)
16. Rhodes, D., Klug, A.: Helical periodicity of DNA determined by enzyme digestion. Nature 286, 573–578 (1980)
17. Klug, A., Lutter, L.C., Rhodes, D.: Helical periodicity of DNA on and off the nucleosome as probed by nucleases. Cold Spring Harbor Symposium on Quantitative Biology 47, 285–292 (1983)
18. Dimitrova, N., Cheung, Y.H., Zhang, M.: Analysis and Visualization of DNA Spectrograms: Open Possibilities for the Genome Research. In: Proceedings of the 14th Annual ACM International Conference on Multimedia, New York (2006)
19. Zhou, H., Du, L., Yan, H.: Detection of Tandem Repeats in DNA Sequences Based on Parametric Spectral Estimation. IEEE Transaction on Information Technology in Biomedicine (2009)

20. Kasutani, E., Yamada, A.: The MPEG-7 color layout descriptor: a com-pact image feature description for high-speed image/video segment retrieval. Image Processing (2001)
21. National Center for Biotechnology Information. National Center for Biotechnology Information, U.S. National Library of Medicine, http://www.ncbi.nlm.nih.gov/
22. Gupta, R.S.: The phylogeny of proteobacteria: relationships to other eubacterial phyla and eukaryotes. FEMS Microbiology Reviews, 367–402 (2000)
23. Woese, C., Stackebrandt, E.W.: The phylogeny of purple bacteria: the alpha subdivision. Systematic and Applied Microbiology, 315–326 (1984)
24. Gao, B., Mohan, R., Gupta, R.: Phylogenomics and protein signatures elucidating the evolutionary relationships among the Gammaproteobacteria. International Journal of Systematic and Evolutionary Microbiology, 234–247 (2009)

Three-Step Framework of Feature Selection for Data of DNA Microarray Experiments

Pawel Trajdos, Adam Kamizelich, and Marek Kurzynski

Wroclaw University of Technology, Department of Systems and Computer Networks
Wyb. Wyspianskiego 27, 50-370 Wroclaw, Poland
pawel.trajdos@pwr.wroc.pl

Abstract. Dimensionality reduction of attribute set is a common preprocessing step used in machine learning. This step is especially important for high-dimensional data with low-dimensional representation such as gene expression data. Feature reduction is essential in the case of microarray data because most of the microarray data attributes are believed to be unrelated to observed classes. This paper proposes a three-step feature selection framework based on feature clustering, multi-criteria assessment (Borda count) and Markov blanket. The proposed framework is a filter method so it can be used with any classification algorithm. Its classification performance and selection stability were assessed. The experimental studies were performed on 10 microarray data sets. The experimental evaluation showed that the Markov blanket filter produces results comparable to state-of-art methods in terms of classification performance. However it tends to produce unstable solutions.

Keywords: Feature selection, Feature clustering, Feature filtering, Microarray, Borda count, Markov blanket, Stability.

1 Introduction

In many data mining problems there are data sets with extreme asymmetry between the high-dimensional data and its low-dimensional representation. Typical examples of such data are DNA microarrays, or gene chips, which are an important new technology for genomic research [16]. Analysis of microarray data is a fundamental process in the characterization of gene functions and detection of correlated gene expression, which can be useful in the medical decision strategy, e.g. recognition of tumor types, prediction of the clinical outcome, disease detection, to name only a few [24, 7]. Usually, the microarray data contain the expression of thousands of genes (features) and – due to considerable time and logistic costs – microarray studies are limited to a small number of experiments (patients). It means, that in microarray data the number of features is much larger than the number of samples, which denotes the problem commonly known in machine learning as *the curse of dimensionality* [21].

Although the microarray data contains a large number of genes (features), only few of them are associated with a medical decision problem under

E. Pietka, J. Kawa, and W. Wieclawek (eds.), *Information Technologies in Biomedicine, Volume 3*, Advances in Intelligent Systems and Computing 283,
DOI: 10.1007/978-3-319-06593-9_36,

consideration [13]. This observation leads to the conclusion that in the analysis of microarray data feature selection procedures play a crucial role.

Feature selection denotes a process of removing irrelevant features from the original set of genes so as to retain the most informative genes useful for a further decision problem. There are many effective methods of feature selection which have been used in the microarray experiments. A detailed review of the feature selection techniques used for gene expression data can be found in [8].

In this paper we proposed a novel method of feature selection based on the three-step scheme described in [21], in which first the data set is clustered, then features in clusters are evaluated and the top-rated features from each cluster are gathered, and finally the collected features are subjected to the procedure of optimal feature selection.

The paper is organized as follows. Section 2 provides an insight into algorithms of feature selection and methods for evaluation of their results. Section 3 describes in detail the procedures applied in the three-step framework of feature selection. In Section 4 the experiments conducted are shown and the results with discussion are presented. Section 5 concludes the paper.

2 Feature Selection

2.1 Preliminaries

The data of microarray experiments are summarized in the matrix:

$$\mathbf{X} = \begin{pmatrix} x_{1,1} & x_{1,2} & \dots & x_{1,N} \\ x_{2,1} & x_{2,2} & \dots & x_{2,N} \\ \dots & \dots & \dots & \dots \\ x_{M,1} & x_{M,2} & \dots & x_{M,N} \end{pmatrix}$$

where $x_{i,j} \in \Re$ is an expression level of j-th gene in i-th experiment, M is the number of objects (experiments) and N is the number of features (genes).

Let

$$E_i = [x_{i,1}, x_{i,2}, \dots, x_{i,N}] \in \Re^N \tag{1}$$

denotes data coming from the i-th experiment ($i = 1, 2, \dots, M$), and

$$G_j = [x_{1,j}, x_{2,j}, \dots, x_{M,j}]^T \tag{2}$$

denotes a vector of observations of j-th gene expression in different experiments ($j = 1, 2, \dots, N$). Additionally, we suppose that microarray data set has a form of training set, i.e. each feature vector E_i is associated with class number (label) $L_i \in \mathcal{L}$, where $\mathcal{L}$ denotes class number set. Class label may have a different practical meaning resulting from a given medical problem – for example, it may be a type of tumor or a disease name.

In feature selection procedure we select (for given number n) the subset of n features from the entire set of N features so as to minimize (maximize) adopted

criterion $Q(\cdot)$ or alternatively – for given value of criterion $Q(\cdot)$ we select the subset of n features so as to minimize the number n.

Feature selection procedures can essentially be divide into filters, wrappers, embedded methods and hybrid methods.

Filter methods are based on criteria functions calculated from the training set, so they are independent of the learning methods used in the next stage of the analysis. The undeniable advantage of the filter approach is its low computational complexity. Filter methods were used to reduce microarray data sets in [25]. Filter methods can also be employed as one of the processing steps in feature selection framework [21, 28].

In wrapper methods there is feedback between the applied machine learning algorithm and the method of attribute reduction. The subset evaluation criterion is based on the quality of the results obtained by the chosen method of learning. Wrapper methods generally outperform filters [23]. However, they require more calculations. Wrapper methods are often criticized as being similar to brute force methods [8]. They were also proved to be overfitting-prone [23]. An Example use of the wrapper methods can be found in [21].

Embedded methods select a subset of features during the process of classifier learning. This approach considerably reduces calculation effort in comparison to wrapper methods. However, the quality of the results is comparable [23]. It should be noted that embedded methods are built for a specific machine learning algorithm. One of the best known examples of these methods is the SVM-RFE [9].

Hybrid methods combine the above mentioned approaches in order to overcome their drawbacks and enhance their strengths. An example of a hybrid method was shown in [21].

2.2 Evaluation of Feature Selection Process

In order to compare feature selection methods some evaluation criteria must be developed. In many cases the feature selection process is preceded by the classification step, so classification quality can be used as an evaluation criterion. The classification error criterion allows us to asses the loss of information caused by the selection process. The classification quality is evaluated experimentally using the training and test set. In the case of small data sets classification quality is assessed using the K-fold Cross-validation. Classifier performance can be assessed using a few criteria. Error rate (3) is one of the frequently used criteria.

$$E_r = \frac{a}{a+b} \tag{3}$$

Where a and b are the numbers of incorrectly and correctly classified objects, respectively.

On the other hand, it is crucial to asses stability of selected subset of attributes. Stability means the sensitivity of the selection algorithm used to small, random changes in the training set. Stability is assessed by examining the variability of the resulting set for different data sets, generated from the same

probability distribution [10]. The outcome of stability assessment is the data distribution results from comparison of all pairs of the reduced sets. These sets are compared using a given criterion [10]. Stability can be evaluated using several measures such as Tanimoto measure:

$$T(A,B) = \frac{|A \cap B|}{|A \cup B|}. \tag{4}$$

A and B are reduced subsets and $|\cdot|$ is set cardinality.

The above mentioned evaluation criteria and leave-one-out scheme were used during experimental study.

3 Methods

Our approach is based on the three-step method described in [21]. The original concept is described below. In the first step feature clustering using the K-means algorithm is performed. In the next step attributes in clusters are evaluated using the SNR(Signal to Noise Ratio) criterion. Then, for each cluster a representative feature is selected. The representative is the best-assessed attribute of the cluster. At the final stage, a subset of features is selected using the wrapper algorithm based on swarm optimization. The aim of using the clustering algorithm is to diverse the selected feature subset. Each cluster contains attributes similar in terms of a given criterion. The attribute set at the next stage contains representatives of each cluster. This prevents the set from being dominated by similar, highly rated attributes. The second step is performed in order to filter out irrelevant attributes before applying the third step. The filtration is conducted using a ranking search. Each attribute is evaluated individually and then the best attributes are selected (a detailed comparison of common evaluation criteria can be found in [15]). Ranking search is based on an implicit assumption that the used criterion is additive. However, this assumption is not fulfilled in most cases. The structure of the selection method does not consider the case when several poorly rated attributes may together have a greater discriminatory power than a highly rated attribute [8]. Moreover, it tends to include many redundant features in the output set.

The third step, whose computational complexity is the highest of all the steps, selects the final set of attributes.

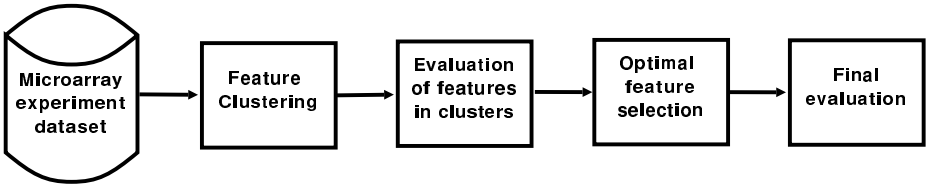

Fig. 1. Block diagram of the three-step feature selection framework

After analyzing the described method we proposed the following modifications.

– Replacing the clustering algorithm with the hierarchical clustering algorithm.
– Changing the SNR criterion into the multi-criterion based on Borda Count[25].
– Replacing the wrapper method with the Markov blanket [27] based filter.

The abandonment of K-means was motivated by the following flaws. Clusters obtained by K-means depend strongly on initial solution. Therefore it is necessary to perform many times the clustring and then select the best solution. The algorithm works well with clusters of the shape similar to a multidimensional sphere. Therefore, instead of the K-means algorithm we decided to use the hierarchical classification algorithm. We used Ward's criterion for cluster merging

$$D_w = \arg\min_{i,j \in 1,2,\cdots,M} \left[\sum_{l \in C_i \cup C_j} \left\| E_l - V_{C_i \cup C_j} \right\|^2 - \sum_{k=i}^{k=j} \sum_{l \in C_k} \left\| E_l - V_{C_k} \right\|^2 \right]. \tag{5}$$

Where C_k represents a cluster, E_l is data point in the cluster and V_k is a centroid of the cluster. The hierarchical clustering algorithm is a deterministic algorithm. This makes determining optimal number of clusters less computationally expensive than in the case of the K-means method. The cluster dendrogram is computed once, and then the dendrogram is cut at a given level. In order to choose an appropriate number of clusters a suitable criterion must be chosen. In this paper the average silhouette index [14] was used.

In the proposed approach the second step was changed. The representative of the cluster is not an attribute but a set of attributes. The number of the representatives depends on cluster cardinality and it is proportional to ηN, where $\eta \in (0, 1]$.

Authors of [25] showed that the above mentioned disadvantages of the filter approach can be overcome by using several different criteria, and then combining the results. Therefore, we proposed to use the method called Borda Count [25]. The Borda Count combines several rank-filter approaches in overall ranking. The attributes are evaluated using given criteria. So m rankings are created. In each of these rankings the best attribute gets N points, the second one $N - 1$ points and so on. The final score is the sum of points scored in all rankings.

A Bayesian network is a model of the relationships between random variables. It is represented by a Directed Acyclic Graph, in which vertices represent events, while the arcs represent connections between these events [27]. Let F be the set of attributes, and $L \notin F$ be the set of labels, the Markov blanket of a random variable L is the smallest subset that generates L statistically independent of the other random variables. Less formally, it is a set of parents, descendants and other descendants of the parent node in a Bayesian network [4]. It was proven that the Markov Blanket is an optimal subset of features for the classification [26]. However, the computational complexity of Markov blanket induction is prohibitive in the case of microarray data (detailed review of Markov blanket

induction algorithms can be found in [5]). Therefore in our approach, Markov blanket was preceded by two low-computational-complexity filters. Their main task is to reject the irrelevant attributes.

The scheme of our approach is showed in Fig. 1.

4 Experiments

4.1 Experiment Setup

In order to study the performance of the developed framework, i.e. its stability and discriminatory power of the determined feature vector, some computer experiments were made. The experiments were conducted in the R [18] environment. The discriminatory power was assessed using evaluating classification quality. It was decided to use K-NN (the number of neighbours was set to 5) and SVM classifiers. The classification quality was assessed using the error rate criterion (3). Due to a small number of objects in data sets it was decided to apply the leave-one-out cross-validation scheme.

Stability was assessed using Tanimoto index (4). Bootstrap method was used to create $B_r = 100$ $M-$element sets. Then we computed the Tanimoto indices for all pairs of selected subsets. The mean values of the obtained Tanimoto measure distribution were compared to assess the methods.

The statistical significance of obtained results was assessed using the Friedman test [3] and the post-hoc Nemenyi test [3]. The significance level was set to $\alpha = 0.05$. The critical difference for the Nemenyi test given α test is $CD_c = 3.320$ for classification and $CD_s = 2.849$ for a stability test.

4.2 Databases

The benchmark databases used in the experiments were taken from the Broad Institute Repository (BIR) [29], Princeton University Collection (PUC) [30] and some sets from *datamicroarray* package (DMP) [19]. A brief description of the databases is given in Table 1. For each data set feature vectors were subjected to appropriate pre-processing procedures and normalized. Details can be found in the literature cited in Table 1.

4.3 Methods Used for Comparison

In classification experiment the following methods of feature reduction were used:

1. The ReliefF.
2. The Information Gain filter.
3. Minim Description length (MDL) filter.
4. Borda count filter without previous clustering.
5. The two-step framework.
6. Random selection

7. The three-step framework.
8. Selection of full attribute set(without selection).

The same methods were used in the experiment with stability criterion except the selection of full attribute set.

The first method is based on the ReliefF algorithm. The ReliefF is a version of the Relief algorithm adapted to multi-class problems. Relief based algorithms were described in [20]. Next ranking method used in framework was a criterion based on the Normalized Information Gain

$$\mathrm{NIG}(G_i) = \frac{I(L, G_i)}{H(L)}, \tag{6}$$

where $I(L, G_i)$ is mutual information and $H(L)$ is entropy of L. The last criterion was based on Minimum Description Length (MDL). It was proposed in [12].

4.4 Results and Discussion

Results for classification are presented in Table 2 and Table 3. The results show that the three-step framework outperforms other methods in the case of the K-NN classifier. However, there is no significant difference, in terms of classification error, between the three-step framework and the other attribute selection methods.

Based on the obtained results (Table 4) it can be concluded that the stability obtained by the three-step framework is the lowest in comparison with the other examined methods. Moreover, there is no statistically significant difference between the stability results obtained by the three-level framework and the result obtained by the random selection. However, for the other methods such differences exist. On the other hand, distances between other methods, except Information Gain filter, and the three-step framework are smaller than CD_s. Obtained stability profiles are shown in Fig. 2, Fig. 3 confirmed this observations. In the given profiles (Fig. 3) it can be seen that the three-step framework usually achieves a similar level of stability, regardless of the number of features provided

Table 1. The databases used in the experiments

Data set	Source	#Features (Genes)	#Objects	#Classes
Leukemia [6]	BIR	3051	38	2
Carcinoma [16]	PUC	3553	36	2
Colon [1]	PUC	2000	62	2
Adenoma [16]	PUC	3556	8	2
Khan [11]	BIR	2308	63	4
Prostate [22]	BIR	2135	102	2
Gravier [7]	DMP	2905	168	2
Sorlie [24]	DMP	456	84	5
Brain [17]	BIR	5597	42	5
Christensen [2]	DMP	1413	217	3

Table 2. Classification error for K-NN classifier and $\eta = 0.02$ (methods are numbered as in subsection 4.3)

	1	2	3	4	5	6	7	8
Adenoma	0.00	0.00	0.00	0.00	0.00	0.50	0.00	0.50
Brain	0.36	0.38	0.36	0.38	0.24	0.79	0.48	0.26
Carcinoma	0.08	0.06	0.06	0.03	0.03	0.47	0.03	0.03
Christensen	0.05	0.00	0.04	0.01	0.02	0.66	0.02	0.00
Colon	0.29	0.29	0.29	0.29	0.31	0.48	0.16	0.18
Gravier	0.32	0.34	0.31	0.32	0.31	0.38	0.29	0.36
Khan	0.29	0.32	0.25	0.33	0.29	0.67	0.21	0.06
Leukemia	0.18	0.21	0.18	0.21	0.24	0.58	0.21	0.03
Prostate	0.14	0.25	0.15	0.25	0.18	0.49	0.18	0.13
Sorlie	0.51	0.48	0.51	0.38	0.36	0.72	0.55	0.18
Avg. Rank	4.50	4.75	3.95	4.45	3.90	7.95	3.80	2.70

Table 3. Classification error for SVM classifier and $\eta = 0.02$ (methods are numbered as in subsection 4.3)

	1	2	3	4	5	6	7	8
Adenoma	0.00	0.00	0.00	0.00	0.00	0.88	0.00	0.12
Brain	0.24	0.24	0.24	0.24	0.19	0.76	0.48	0.12
Carcinoma	0.06	0.06	0.08	0.03	0.06	0.53	0.06	0.03
Christensen	0.06	0.00	0.22	0.01	0.01	0.71	0.02	0.00
Colon	0.16	0.16	0.16	0.16	0.16	0.48	0.19	0.16
Gravier	0.28	0.28	0.24	0.29	0.30	0.35	0.29	0.26
Khan	0.16	0.06	0.16	0.11	0.10	0.60	0.19	0.00
Leukemia	0.05	0.03	0.05	0.03	0.05	0.37	0.21	0.00
Prostate	0.14	0.25	0.18	0.10	0.12	0.46	0.13	0.09
Sorlie	0.42	0.38	0.48	0.42	0.41	0.69	0.47	0.11
Avg. Rank	4.55	3.45	5.00	3.55	3.75	8.00	5.65	2.05

Table 4. Mean values of 1-Tanimoto (lower is better) and average ranks over data sets for $\eta = 0.02$ (methods are numbered as in subsection 4.3)

	1	2	3	4	5	6	7
Adenoma	0.10	0.00	0.71	0.57	0.60	0.99	0.75
Brain	0.00	0.00	0.97	0.83	0.83	0.99	0.91
Carcinoma	0.92	0.62	0.89	0.92	0.92	0.99	0.95
Christensen	0.94	0.41	0.88	0.83	0.84	0.99	0.92
Colon	0.00	0.00	0.98	0.84	0.84	0.99	0.94
Gravier	0.95	0.86	0.94	0.94	0.94	0.99	0.97
Khan	0.79	0.02	0.79	0.83	0.83	0.99	0.94
Leukemia	0.07	0.00	0.96	0.81	0.81	0.99	0.92
Prostate	0.61	0.03	0.52	0.79	0.80	0.99	0.92
Sorlie	0.95	0.82	0.91	0.94	0.93	0.99	0.94
Avg. Rank	3.50	1.10	3.70	3.30	3.90	7.00	5.50

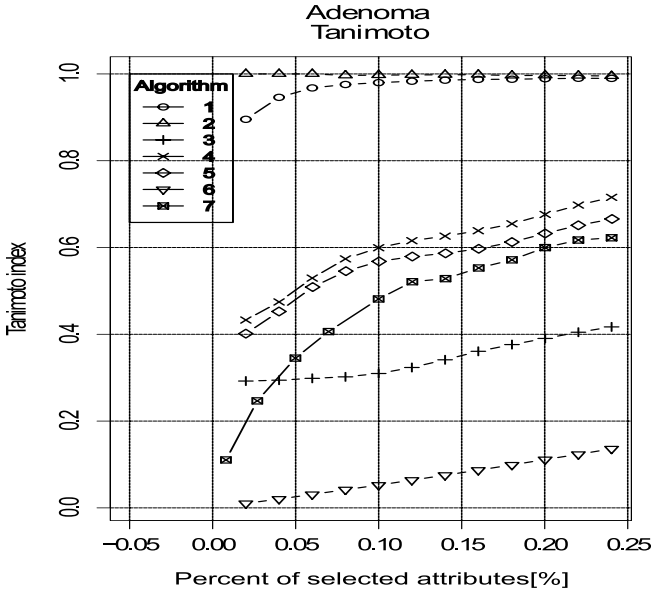

Fig. 2. Stability profile for Adenoma set

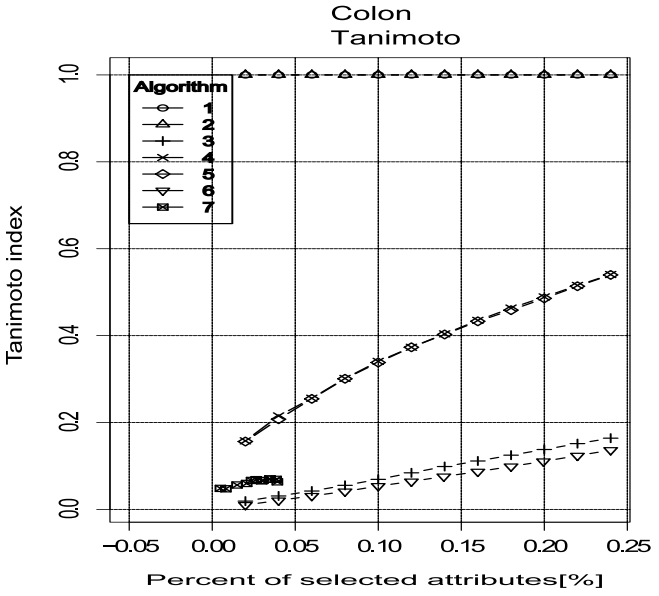

Fig. 3. Stability profile for Colon set

by the first two stages. The only data set for which three-step framework behaves differently is Adenoma (Fig. 2). It can be concluded that the induction of Markov blanket is sensitive to changes in the input set. Poor stability can also be caused by presence of many redundant features in the data sets.

5 Conclusion

In this paper we proposed the tree-steps feature selection framework based on ranking filters, Borda Count, attribute clustering and Markov blanket. The proposed framework was compared to its components. The classification error and set stability were assessed using 10 real microarray data sets.

The conducted experiments made it possible to draw the following conclusions:

- The results obtained by the two-step framework are not worse than the worst result obtained using the base criteria (in terms of overall ranking). This applies to both the quality of the classification and the stability of the solution.
- The two-step framework achieves results similar to the Borda Count method applied to the full feature set (without attribute clustering)
- The number of relevant attributes returned by the three-step framework is usually lower than the number of attributes returned by the two-step framework.

The obtained results provide the basis for further research. First, the following issues should be considered:

- Use of a different clustering algorithm, another method of determining the optimal number of clusters, and a change in distance measure between attributes should be considered.
- Use of another multi-criteria feature selection method should be considered.
- Due to its instability, the third framework's step should be modified.
- Due to large discrepancy of the classification results, the three-step framework should be assessed using other classifiers such as the naive Bayes classifier or an artificial neural network classifier.

Acknowledgments. This work was financed from the National Science Center as a research project No S30011/K0402.

This research was supported in part by PL-Grid Infrastructure.

References

1. Alon, U., Barkai, N., Notterman, D.A., Gish, K., Ybarra, S., Mack, D., Levine, A.J.: Broad patterns of gene expression revealed by clustering analysis of tumor and normal colon tissues probed by oligonucleotide arrays. Proc. Natl. Acad. Sci. USA 96(12), 6745–6750 (1999)

2. Christensen, B.C., Houseman, E.A., Marsit, C.J., Zheng, S., Wrensch, M.R., Wiemels, J.L., Nelson, H.H., Karagas, M.R., Padbury, J.F., Bueno, R., Sugarbaker, D.J., Yeh, R.F., Wiencke, J.K., Kelsey, K.T.: Aging and Environmental Exposures Alter Tissue-Specific DNA Methylation Dependent upon CpG Island Context. PLoS Genet. 5(8), e1000602+ (2009)
3. Demšar, J.: Statistical comparisons of classifiers over multiple data sets. The Journal of Machine Learning Research 7, 1–30 (2006)
4. Dernoncourt, D., Hanczar, B., Zucker, J.D.: An empirical analysis of markov blanket filters for feature selection on microarray data. Machine Learning in Systems Biology, 19–23 (2011)
5. Fu, S., Desmarais, M.C.: Markov blanket based feature selection: a review of past decade. Proceedings of the World Congress on Engineering 1, 321–328 (2010)
6. Golub, T.R., Slonim, D.K., Tamayo, P., Huard, C., Gaasenbeek, M., Mesirov, J.P., Coller, H., Loh, M.L., Downing, J.R., Caligiuri, M.A., Bloomfield, C.D., Lander, E.S.: Molecular classification of cancer: class discovery and class prediction by gene expression monitoring. Science 286(5439), 531–537 (1999)
7. Gravier, E., Pierron, G., Vincent-Salomon, A., Gruel, N., Raynal, V., Savignoni, A., De Rycke, Y., Pierga, J.Y., Lucchesi, C., Reyal, F., Fourquet, A., Roman-Roman, S., Radvanyi, F., Sastre-Garau, X., Asselain, B., Delattre, O.: A prognostic dna signature for t1t2 node-negative breast cancer patients. Genes Chromosomes Cancer 49(12), 1125–1134 (2010)
8. Guyon, I., Elisseeff, A.: An introduction to variable and feature selection. J. Mach. Learn. Res. 3, 1157–1182 (2003)
9. Guyon, I., Weston, J., Barnhill, S., Vapnik, V.: Gene selection for cancer classification using support vector machines. Mach. Learn. 46(1-3), 389–422 (2002)
10. Kalousis, A., Prados, J., Hilario, M.: Stability of feature selection algorithms: A study on high-dimensional spaces. Knowl. Inf. Syst. 12(1), 95–116 (2007)
11. Khan, J., Wei, J.S., Ringner, M., Saal, L.H., Ladanyi, M., Westermann, F., Berthold, F., Schwab, M., Antonescu, C.R., Peterson, C., Meltzer, P.S.: Classification and diagnostic prediction of cancers using gene expression profiling and artificial neural networks. Nat. Med. 7(6), 673–679 (2001)
12. Kononenko, I.: On biases in estimating multi-valued attributes. In: Proceedings of the 14th International Joint Conference on Artificial Intelligence, IJCAI 1995, vol. 2, pp. 1034–1040. Morgan Kaufmann Publishers Inc., San Francisco (1995)
13. Liu, H., Wu, X., Zhang, S.: Feature selection using hierarchical feature clustering. In: Proceedings of the 20th ACM International Conference on Information and Knowledge Management, CIKM 2011, pp. 979–984. ACM (2011)
14. Liu, Y., Li, Z., Xiong, H., Gao, X., Wu, J.: Understanding of internal clustering validation measures. In: Proceedings of the 2010 IEEE International Conference on Data Mining, ICDM 2010, pp. 911–916. IEEE Computer Society, Washington, DC (2010)
15. Napolitano, A., Dittman, D., Wald, R., Khoshgoftaar, T.: Similarity analysis of feature ranking techniques on imbalanced dna microarray datasets. In: Proceedings of the 2012 IEEE International Conference on Bioinformatics and Biomedicine (BIBM 2012), pp. 1–5. IEEE Computer Society, Washington, DC (2012)
16. Notterman, D., Alon, U., Sierk, A., Levine, A.: Transcriptional gene expression profiles of colorectal adenoma, adenocarcinoma, and normal tissue examined by oligonucleotide arrays. Cancer Research 61, 3124–3130 (2001)

17. Pomeroy, S.L., Tamayo, P., Gaasenbeek, M., Sturla, L.M., Angelo, M., McLaughlin, M.E., Kim, J.Y.H., Goumnerova, L.C., Black, P.M., Lau, C., Allen, J.C., Zagzag, D., Olson, J.M., Curran, T., Wetmore, C., Biegel, J.A., Poggio, T., Mukherjee, S., Rifkin, R., Califano, A., Stolovitzky, G., Louis, D.N., Mesirov, J.P., Lander, E.S., Golub, T.R.: Prediction of central nervous system embryonal tumour outcome based on gene expression. Nature 415(6870), 436–442 (2002)
18. Core Team, R.: R: A Language and Environment for Statistical Computing. R Foundation for Statistical Computing, Vienna (2012) ISBN 3-900051-07-0
19. Ramey, J.A.: Datamicroarray, R package version 0.2.2 (2013)
20. Robnik-Šikonja, M., Kononenko, I.: Theoretical and empirical analysis of relieff and rrelieff. Mach. Learn. 53(1-2), 23–69 (2003)
21. Sahu, B., Mishra, D.: A novel feature selection algorithm using particle swarm optimization for cancer microarray data. Procedia Engineering 38, 27–31 (2012); International Conference on Modelling Optimization and Computing
22. Singh, D., Febbo, P.G., Ross, K., Jackson, D.G., Manola, J., Ladd, C., Tamayo, P., Renshaw, A.A., D'Amico, A.V., Richie, J.P.: Gene expression correlates of clinical prostate cancer behavior. Cancer Cell 1(2), 203–209 (2002)
23. Somol, P., Novovicova, J., Pudil, P.: Efficient Feature Subset Selection and Subset Size Optimization. InTech (2010)
24. Sørlie, T., Perou, C.M., Tibshirani, R., Aas, T., Geisler, S., Johnsen, H., Hastie, T., Eisen, M.B., van de Rijn, M., Jeffrey, S.S., Thorsen, T., Quist, H., Matese, J.C., Brown, P.O., Botstein, D., Lønning, P.E., Børresen-Dale, A.L.: Gene expression patterns of breast carcinomas distinguish tumor subclasses with clinical implications. Proc. Natl. Acad. Sci. USA 98(19), 10869–10874 (2001)
25. Yang, F., Mao, K.Z.: Robust feature selection for microarray data based on multicriterion fusion. IEEE/ACM Trans. Comput. Biol. Bioinformatics 8(4), 1080–1092 (2011)
26. Yaramakala, S., Margaritis, D.: Speculative markov blanket discovery for optimal feature selection. In: Proceedings of the Fifth IEEE International Conference on Data Mining, ICDM 2005, pp. 809–812. IEEE Computer Society, Washington, DC (2005)
27. Zeng, Y., Luo, J., Lin, S.: Classification using markov blanket for feature selection. In: IEEE International Conference on Granular Computing, GRC 2009, pp. 743–747 (2009)
28. Zhu, Z., Ong, Y.S., Dash, M.: Markov blanket-embedded genetic algorithm for gene selection. Pattern Recogn. 40(11), 3236–3248 (2007)
29. Broad institute repository, `http://www.broadinstitute.org/`
30. Princeton university collection, `http://genomics-pubs.princeton.edu/oncology/`

Author Index